Testing and refining the chronology and correlation of Mediterranean pollen records of late Last Glacial age using tephrochronology

Mark John Hardiman

Thesis submitted for the degree of Doctor of Philosophy at the University of London

September 2012

Institution of study:
Department of Geography
Royal Holloway, University of London

Declaration

This thesis presents the results of original research undertaken by the author and none of the results, illustrations or text are based on the published or unpublished work of others, except where specified and acknowledged.

The following published paper includes orginal results reported in this PhD Thesis:

1. Lowe, J., Barton, N., Blockley, S., Ramsey, C.B., Cullen, V.L., Davies, S.W.G., Gamble, C., Grant, K., **Hardiman, M.**, Housley, R., Lane, C.S., Lee, S., Lewis, M., MacLeod, A., Menzies, M., Muller, W., Pollard, M., Price, C., Roberts, A.P., Rohling, E.J., Satow, C., Smith, V.C., Stringer, C.B., Tomlinson, E., White, D., Albert, P., Arienzo, I., Barker, G., Carandente, A., Civetta, L., Farrand, W., Ferrier, C., Gaudelli, J-L., Karkanas, P., Koumouzelis, M., Muller, U.C., Orsi, G., Pross, J., Rosi, M., Shalamanov-Korobar, L., Sirakov, N., Tzedakis, P.C. & Boric, D. (2012) Volcanic ash layers illustrate the resilience of Neanderthals and early modern humans to natural hazards. Proceedings of the National Academy of Sciences of the United States of America. 109 (34), 13532-13537.

Signature: **Date:** 18/09/2012

Abstract

Six terrestrial basin sites from across the Mediterranean region were investigated for cryptotephra content in order to construct site-specific tephrostratigraphies, with a focus on the latter part of the Last Glacial period. Two of the sequences were located in Spain (Padul, Villarquemado), one in Italy (Fimon), two in Greece (Tenaghi Philippon, Kopais) and one on the Greek Island of Lesvos. High resolution pollen stratigraphies and other proxy records were available for each sequence, characteristics of which have been used (in previous research) to form chronological frameworks and correlations between the records. This project aimed to use tephra isochrones to (1) test and refine the age models that underpin each of the records, and (2) correlate between the palaeo-records. The geographical spread of the sites studied here also allows the current tephrostratigraphic framework for southern Europe to be extended into areas for which tephra layers dating to the Last Glacial period had not previously been reported.

The two Spanish sites contained no or insignificant amounts of tephra. The other four sites each contained a number of tephra layers. Over 30 discrete tephra layers were identified, most of which were classified as cryptotephra. Geochemical characterisation of major, minor and trace elements were obtained using EPMA-WDS, LA-ICP-MS and SIMS micro-analytical methods. Correlations of tephra layers were based on graphical comparison of the geochemical data-sets to a developing data-base of the representative glass chemical compositions of European proximal and distal tephra deposits. The age estimates of key tephra isochrones were compared with other chronological information using Bayesian-based methods to develop revised age-depth models for each palaeo-record, the results being compared with the original age-depth models generated for each record.

The key outcomes of this study are: (1) some important tephro-correlations enable the degree of synchronicity of proxy response to rapid climatic shifts to be assessed across broad geographical regions; (2) the new tephrochronological results reveal significant chronological off-sets between records previously aligned using curve or *'wiggle'* matching and by other independent chronological methods; and (3) previously unknown tephra layers originating from Santorini have been detected and their placement within the existing tephrostratigraphic framework of the Eastern Mediterranean proposed.

Acknowledgments

I would like to express my deep gratitude and thanks to the following people whose willingness to provide samples, data and assistance made this thesis possible:

Ulrich Müller and **Jörg Pross** (Institute of Geosciences, Goethe University Frankfurt) – For allowing me to sample the Tenaghi Philippon core and general help and advice.

Chronis Tzedakis and **Vasiliki Margari** (Department of Geography, University College London) – For allowing me to sample the Lesvos and Kopais sequences and general help and advice in interpreting results.

Roberta Pini and **Cesare Ravazzi** (C.N.R. - Istituto per la Dinamica dei Processi Ambientali, Laboratorio di Palinologia e Paleoecologia, Milano) – For facilitating access to the Fimon core sequence and the lovely tour of Milano.

José E. Ortiz, Trino Torres and **Arantxa Díaz-Bautista** (Laboratory of Biomolecular Stratigraphy, E.T.S.I. Minas de Madrid, Madrid) – For providing access to the Padul core sequences and the lovely hospitality while I was in Madrid.

Ana Moreno and **Blas Valero-Garcés** (Pyrenean Institute of Ecology, Zaragoza) – For providing access to the Villarquemado core and their fantastic tours of Zaragoza.

Sabine Wulf (GeoForschungsZentrum, Potsdam) – For providing data from the Lago Grande di Monticchio sequence.

Lusia Ottolini (CNR-Istituto di Geoscienze e Georisorse, Pavia) – For carrying out SIMS analysis.

I would also like to thank all the RESET members (and associates) who have provided great discussion and assistance during this work, and in particular (though not exhaustively): **Paul Albert**, **Vicky Cullen**, **Clive Gamble**, **Katharine Grant**, **Rupert Housley**, **Christine Lane**, **Sharen Lee**, **Christina Manning**, **Chris Satow**, **Victoria Smith**, **Emma Tomlinson** and **Dustin White**.

Also to all other staff and PhD students in Geography who have been wonderful in giving their support and discussion during the last four years: **Anna Bourne**, **Ian Candy**, **Robyn Christie**, **Lauren Davies**, **Katy Flowers**, **Claire Gallant**, **Paul Lincoln**, **Alison Macleod**, **Ian Matthews**, **Adrian Palmer**, **Jenni Sheriff**, **Elaine Turton** and **Gareth Tye**.

Thanks also my Family, Friends and especially my lovely girlfriend **Becky Dowding** who encouraged me always during the seemingly never-ending journey that is a PhD (the h stands for hassle, the D for devotion required).

Finally I would like to thank my supervisors **John Lowe**, **Simon Blockley** and **Martin Menzies** whose continued guidance, support and intellectually enriching debate kept me going during times when I was not always sure I was going to make it. I will be forever grateful.

List of Figures

Chapter 5: Results

Chapter 6: Correlation of Tephra Layers

Chapter 7: Testing and Refining Existing Age–Depth Models

Chapter 8: Disscussion

List of Tables

Chapter 7: Testing and Refining Existing Age–Depth Models

Chapter 8: Disscussion

Foreword

RESET Project

This thesis is tied to the NERC funded RESET Project[1] the overarching aim of which is to improve the chronological framework of European archaeological, marine and terrestrial sediment sequences via the use of widespread volcanic ash layers. Using these distal volcanic ash layers as time-parallel signatures allows a detailed tephrostratigraphic framework or 'lattice' to be developed. The RESET Project covers the period from the last interglacial to the start of the Holocene with the central remit to test quantitatively whether major shifts in hominin development were linked to Abrupt Environmental Transitions (AETs). There are many interconnected strands to the RESET Project which integrates studies of archaeological transitions, environmental shifts (within both the terrestrial and marine realms), geochemical fingerprinting of proximal volcanic deposits and improved existing age modelling techniques, and finally the overall information synthesis of the data.

While the work presented within this thesis forms an important component of the RESET project, it has distinct stand-alone aims and objectives which focus upon the latter part of the Last Glacial, the Late Last Glacial (LLG; defined here as 50–20 ka BP) within terrestrial palaeo-records of Southern Europe. This timeframe represents a period of considerable climatic variability over decadal to millennial timescales. Although these climate signals are best expressed at higher latitudes, they are increasingly being recognised at the global scale. Synchronising these records is however hampered by chronological uncertainties that are frequently overcome by alignment or 'wiggle matching' between records, but this assumes synchronous timing of events and that an individual climate signal has been imprinted over large spatial areas. This thesis aims to test these connections using isochronic volcanic ash layers to link terrestrial palaeo-records during the LLG. This information is important to other RESET strands where, for example, the same tephra layers are discovered in other realms (e.g. in archaeological or marine deposits) or important new geochemical datasets can be used to help the understanding of the proximal volcanic record.

[1] RESET (RESponse of humans to abrupt Environmental Transitions).
Website: http://c14.arch.ox.ac.uk/reset/embed.php?File=index.html

1.0 INTRODUCTION

1.1 General context

The Quaternary is the most recent geological period and spans 2.58 Ma ago to present (Gibbard *et al*., 2010) and is dominated by a cooling trend globally with successive (increasingly severe) warmer and colder episodes controlled principally by orbital forcing (Milankovitch, 1941; Hays *et al*., 1976), the latter known as glacial–interglacial cycles. Understanding the physical, chemical, biological, atmospheric and human-induced processes that initiated and controlled environmental changes at all spatial and temporal scales during this timeframe is of key importance to Quaternary scientists (Lowe *et al*., 2007).

Since the early 1990s the importance of much shorter duration sub-orbital climatic events has become apparent during, although not confined to, the Late Last Glacial[2] (e.g. Siddall *et al*., 2010). This short duration climatic variability was first described from the Greenland ice-core records and were termed Dansgaard–Oeschger (D–O) events (Johnsen *et al.,* 1997; NGRIP Members, 2004). Coupled to this were the almost coeval discovery of Heinrich (H) events, described from North Atlantic marine records (Heinrich, 1988; Broecker *et al*., 1992). Since these discoveries, similar climate signals have started to be described from a large selection of geographically scattered marine and terrestrial palaeoenvironmental records (Allen *et al*., 1999; Sánchez Goni *et al*., 2000). These data suggest a climate mechanism that affected large parts of the Northern Hemisphere, not just higher latitudes. Understanding these types of climatic variability is also important for providing important insights into the future of the Earth system (Schrag and Alley, 2004; Snyder, 2010).

This introduction briefly outlines 1) the definition and expression of these events from the records where they were first recognised, 2) their suggested expression in the southern European Quaternary record and finally 3) current chronological methods used to date and link the records.

[2] The Late Last Glacial (LLG); defined here as 50–20 ka BP.

1.2 Rapid climatic variability during the late Last Glacial (50-20 ka BP)

1.2.1 Millennial to centennial scale climate variability; D-O cycles and Heinrich events in the North Atlantic

Expression and timing

D-O cycles occur over centennial to millennial time frames (Alley *et al*., 1993; Dansgaard *et al*., 1993; NGRIP Members, 2004; Rasmussen *et al*., 2006). There are 12 D–O cycles recognised in the Greenland ice cores in the 50-20 ka BP time interval (labelled GI-13 to GI-2; see Fig. 1.1). D–O cycles display a strong, non-trivial climate signal, typically encompassing around 50% of glacial-interglacial amplitude as seen in Greenland inferred palaeo-temperatures (Wolff *et al*., 2010).

A D–O cycle is formed of a Greenland Interstadial (GI) and Greenland Stadial (GS) event and begins with a rapid transition from a GS to GI with an enrichment of ~6 $\delta^{18}O$ permil that is interpreted as a 10-15^{0}C warming; this shift can occur within a couple of decades (Schwander *et al*., 1997; Huber *et al*., 2006; Johnsen & Vinther, 2007; inferred temperatures ranging from -31 -37°C; see Table 1.1). After this sudden warming there is a gradual depletion in oxygen isotope values (~3-5 $\delta^{18}O$ permil) indicating decreasing temperatures, a phase that can last from between 200 to 2500 years and which is followed by a very rapid decadal depletion in $\delta^{18}O$ into full Greenland stadial conditions (temperatures ranging from -46 to -54°C; Schwander *et al*., 1997; Huber *et al*., 2006).

During the LLG there is subtle variability in the structure of D–O cycles, with, for example, GI events 8 and 12 having much longer durations (c.1640 and 2580 years respectively) compared to the two shortest which operated on centennial scales GI-3 and GI-9 (c.240 and 260 years). The same is true of the GS component of D–O cycles with longer durations present in GS-3 and GS-5 (c.4200 and 3100 years) compared with, for example, GS-4 and GS-10 (c.820 and 640 years; see Table 1.1 for an overview). It is also the case that some D–O cycles had higher amplitude isotopic enrichments at the initiation of GI events suggesting some D–O cycles were warmer than others (e.g. GI-12 compared to GI-9). Finally the duration and amplitude of GI events appears to have a relationship with the gradient at which isotopic depletion

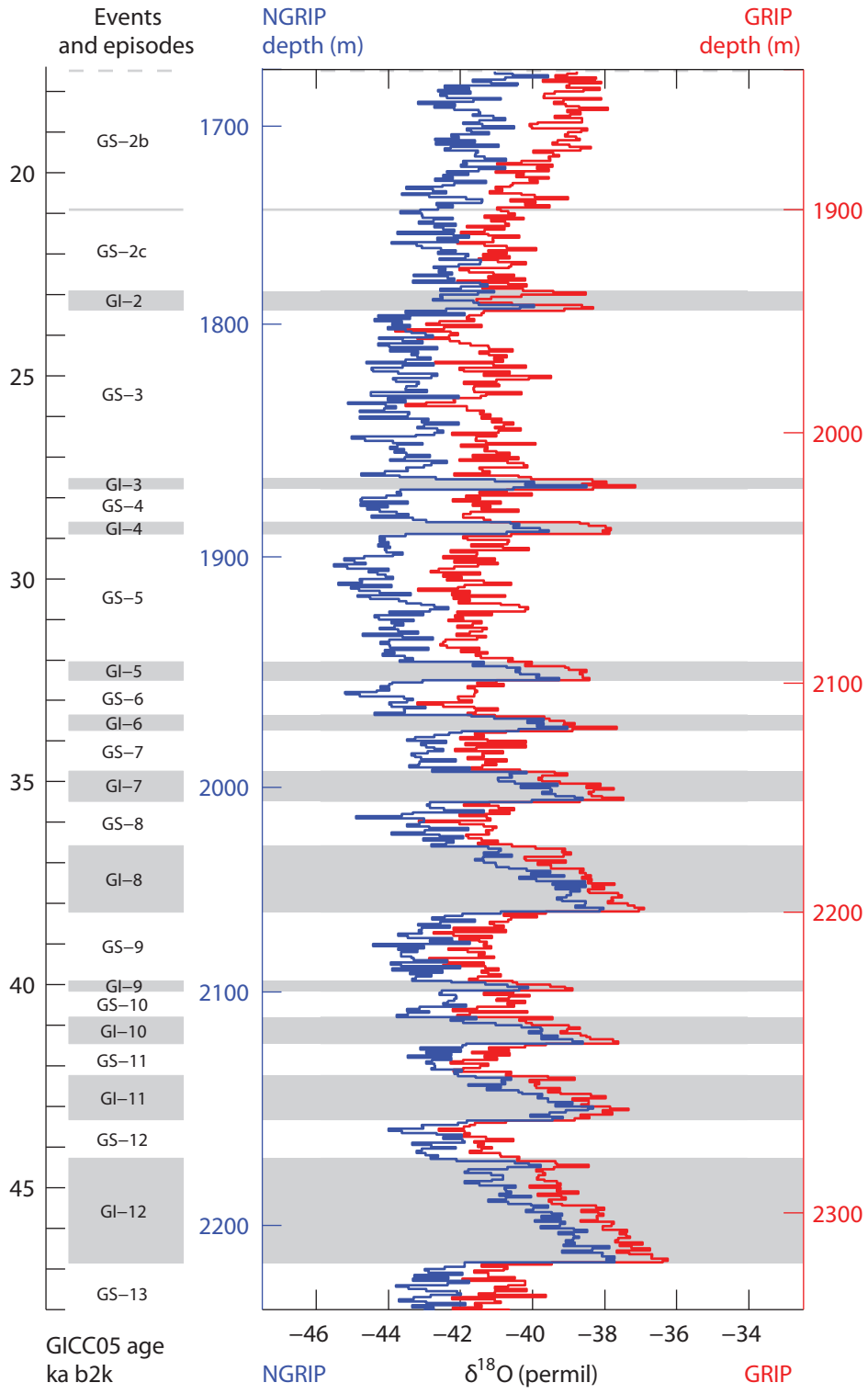

Figure 1.1 – The GRIP and NGRIP $\delta^{18}O$ stratigraphy on the GICC05 timescale (b2k; years before AD 2000) for the Late Last Glacial showing the Greenland Interstadial and Stadial events (2-13) described within the main text. Diagram adapted from Blockley *et al.,* (2012).

occurs, with shorter, lower–amplitude GI events depleting at a much faster rate and *vice versa* (see Fig. 1.2).

Although D–O cycles are primarily defined from the $\delta^{18}O$ signal in the Greenland record, as described above, many other proxies (studied from the same ice–core sequences) co-vary with GI and GS events showing the same rapidity of change (i.e. often decadal).

Table 1.1 – Summary of the timing, duration and inferred temperature jumps of GI Events during the LLG. The transitions are defined following Lowe *et al*. (2008), Rasmussen *et al.* (2006) and Svensson *et al.* (2008). GICC05 ages have been adjusted from b2k to years BP (1950).

Start of GI / GS Event	GICC05 age (years BP)	Max counting error (~2 σ) (years)	Duration of GI /GS Event (years)	Reference/s	Magnitude of Temperature change (°C)	Reference/s
GS-2b	20850	482	–	1,2	–	–
GS-2c	22850	573	2000	1,2	–	–
GI-2	23290	596	440	1,2,3	–	–
GS-3	27490	822	4200	1,2	–	–
GI-3	27730	832	240	1,2,3	–	–
GS-4	28550	887	820	1,2	–	–
GI-4	28850	898	300	1,2,3	12 ± 5	6
GS-5	31950	1103	3100	2,5	–	–
GI-5	32450	1132	500	2,3	7 ± 5	6
GS-6	33310	1191	860	2,5	–	–
GI-6	33690	1212	380	2,3	7 ± 5	6
GS-7	34690	1286	380	2,5	–	–
GI-7	35430	1321	740	2,3	9 ± 3	6
GS-8	36530	1397	1100	2,5	–	–
GI-8	38170	1449	1640	2,3	11 (+3;–6)	7
GS-9	39850	1569	1680	2,5	–	–
GI-9	40110	1580	260	2,3	9 (+3;–6)	7
GS-10	40750	1615	640	2,5	–	–
GI-10	41410	1633	660	2,3	11.5 (+3;–6)	7
GS-11	42190	1682	780	2,5	–	–
GI-11	43290	1736	1100	2,4	+15 (+3;–6)	7
GS-12	44230	1780	940	2,5	–	–
GI-12	46810	1912	2580	2,4	12 ± 2.5	8
GS-13	–	–	–	–	–	–
GI-13	49230	–	–	4	8 (+3;–6)	7

References: 1: Lowe *et al.* (2008); 2: Rasmussen *et al.* (2008); 3: Andersen *et al.* (2006); 4: Svensson *et al.* (2008); 5: Blockley *et al.* (2012); 6: Sanchez-Goni *et al.* (2008); 7: Huber *et al.* (2006); 8: Landais *et al.* (2004)

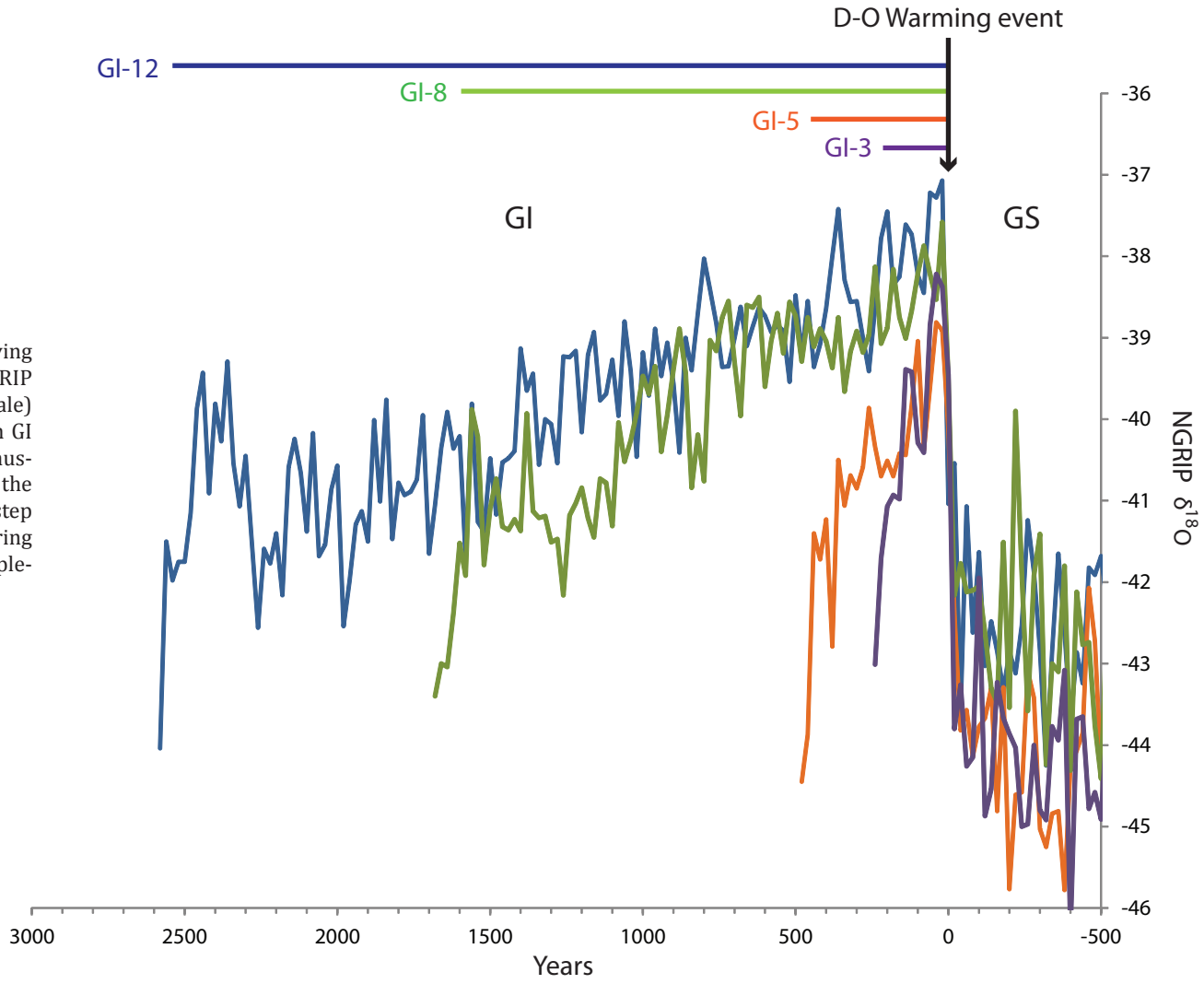

Figure 1.2 – Diagram showing the varying anatomy of D–O events 3,5,8 and 12 in the NGRIP $\delta^{18}O$ stratigraphy (on the GICC05 timescale) which have been aligned to the start of each GI event (as defined by Lowe et al., 2008; Rasmussen *et al.,* 2008; Andersen *et al.,* 2006) until the onset of the succeeding GS event. Each data step represents 20 ice-core years. Note the differing amplitude, durations and rate of isotopic depletion of each GI Event shown here.

In particular these include: 1) measured ice layer thicknesses which are twice as thick during GIs compared to GSs, probably due to warmer air delivering more moisture during GIs (Wolff *et al*., 2010); 2) terrestrial dust which rapidly decreases at the onset of GIs staying subdued until increasing again in GS intervals (Fuhrer *et al*., 1999; Ruth *et al*., 2007); 3) Sea salt concentrations decrease rapidly at the initiation of GIs building again during GS intervals, which is thought to occur due to an interplay between atmospheric circulation and sea ice extent (Wolff *et al*., 2010); and 4) methane concentrations, which show very significant variability, often in excess of 50% of that seen in the amplitude of glacial-interglacial transitions (Wolff *et al.,* 2010), are low in GS intervals and high during GIs (Brook *et al*., 2000; Flückiger *et al*., 2004). This constellation of evidence responds in symphony to the $\delta^{18}O$ shifts which define D–O cycles and represents different elements of the climatic and environmental system (for example methane concentrations) which supports the idea that geographically areas far distant from Greenland were influenced by these events (Wolff *et al*., 2010).

Between 50-20 ka BP four Heinrich (H) Events (HE2-HE5) are identified in the North Atlantic (Bond *et al*., 1992; Broecker *et al*., 1992; see Fig. 1.3) they are most distinct in the so-called Ice Rafted Debris (IRD) Belt (40°N–55°N; Standford *et al*., 2011). During the LLG H Events occurred quasi-periodically at a frequency of between 5000-14000 yrs (Hemming, 2004; Standford *et al*., 2011). Heinrich Events should be differentiated from Heinrich layers found in ocean cores which are characterised by high magnetic susceptibility peaks, coarse lithic-grain (IRD) peaks, high detrital carbonate concentrations and anomalies in $\delta^{18}O$ (Heinrich, 1988; Grousset *et al*., 1993; Snoeckx *et al*., 1999; Hemming, 2004). Heinrich layers are thought to be formed via "armadas of icebergs" (Broecker *et al*., 1992) or by vast increases in sea ice extent (Hemming, 2004). It should be noted however that smaller IRD layers, so-called 'inter-Heinrich' layers, have also been observed in the LLG timeframe (Grousset *et al*., 2000; Scourse *et al*., 2000).

H layers appear to be deposited very rapidly, with sharp sedimentary contacts and buried fossil burrows observed between H layers and underlying marine sediments (Bond *et al*., 1992; Broecker *et al*., 1992; McCave, 1995) at sub-millennial timescales (495±255 years (1σ) Hemming, 2004). Unlike HEs, which are defined here as spanning the time frame from the large resultant input of meltwater and effects on sea surface temperature, deep water and atmospheric circulation and which can last much longer

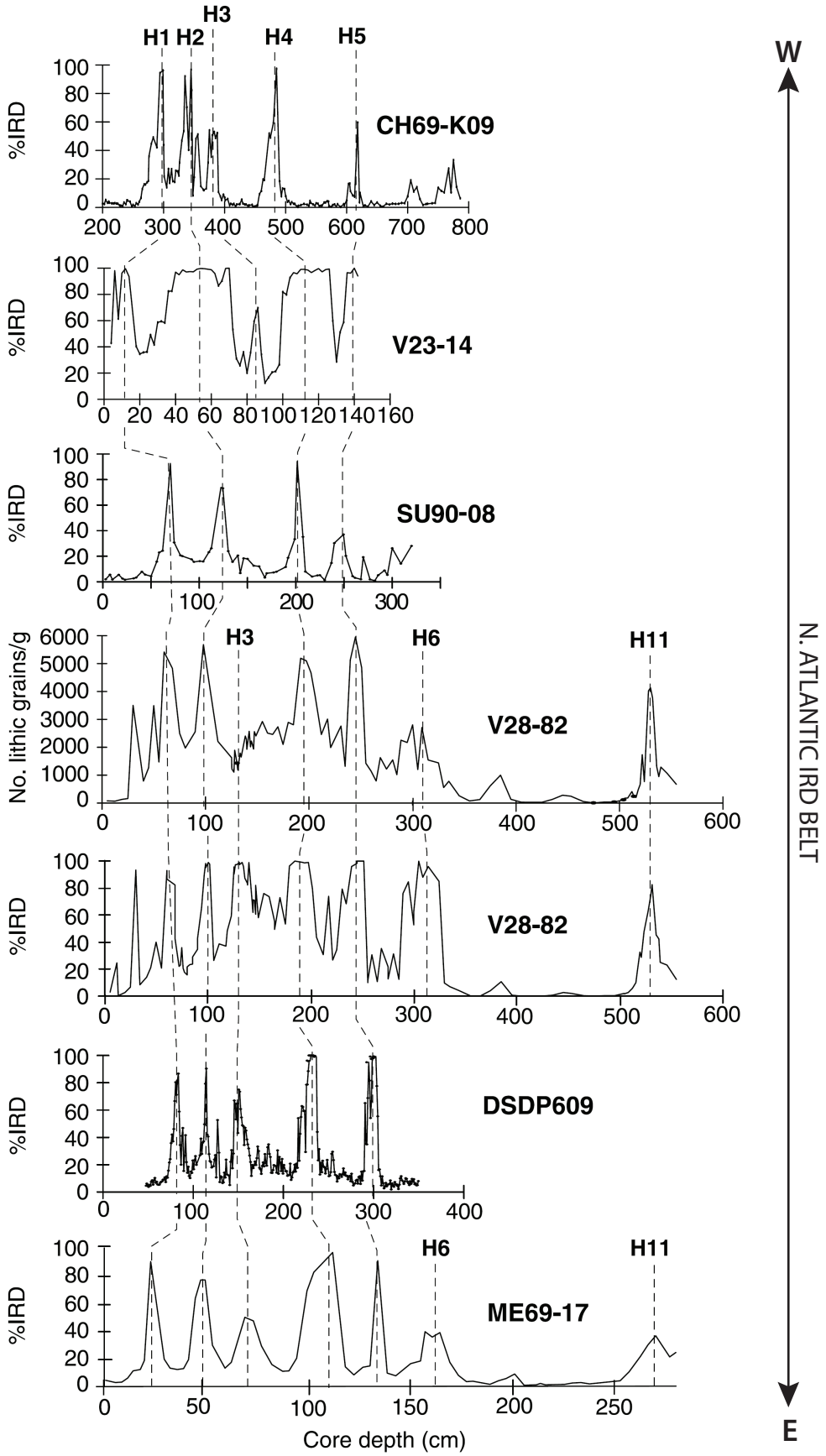

Figure 1.3 – Ice-rafted detritus (IRD) data for marine sequences across the North Atlantic (W to E) with correlated Heinrich layers. Data from sources for each core are: CH69-K09 (Labeyrie *et al.,* 1999); V23-14 (Hemming and Hajdas, 2003); SU90 08 (Grousset *et al.,* 1993); V28-82 (Gwiazda *et al.,* 1996; McManus *et al.,* 1998; Hemming *et al.,* 1998); DSDP609 (Broecker *et al.,* 1992; Bond *et al.,* 1992); and ME69-17 (Heinrich, 1988). Diagram adapted from Hemming (2004).

(e.g. Cortijo *et al*., 2005), both often preceding and outlasting the deposition of Heinrich layers.

Hemming (2004) has noted that H layers 2, 4 and 5 show very similar characteristics including: 1) the geographical area covered by IRD deposition of these layers in the North Atlantic (~2 x 10^6 km^2); 2) "razor-sharp" bases which suggest very rapid onsets 3) very high IRD flux, and finally, 4) very rich detrital carbonate concentrations. By contrast, H layer 3 appears to have a much smaller, or indeed absent, IRD flux imprint in the north Atlantic (see Fig. 1.3), covers a smaller geographical area (0.7 x 10^6 km^2) and appears to lack the detrital carbonate component. Gwiazda *et al*. (1996) even concluded that H layer 3 may not really be an ice rafting event at all in much of the IRD belt but instead represent a low foraminifera interval, artificially increasing IRD percentages. One suggested reason for this difference between these H layers is contrasting provenance with H layers 2, 4 and 5 sourcing primarily from the Hudson Strait in the Eastern North Atlantic and H layer 3 sourcing mostly from smaller European ice–rafted sources (Grousset *et al.,* 1993; Gwiazda *et al.,* 1996).

Elliot *et al.* (2002) provided average ages and durations for HEs calculated from seven ocean sediment cores (Bond and Lotti, 1995; Cortijo *et al*., 1997; Vidal *et al*., 1997; Labeyrie *et al*., 1999) placing HE2 at 21250±850, HE3 at 26750±650 and HE4 at 34400±500 ^{14}C yr BP this largely encompasses the age ranges from other sites H layers (see Table 1.2 for comparisons). The age of HE5 is not well defined but probably occurs around 50-47 ka BP (Sánchez Goni *et al*., 2008). Unfortunately no comprehensive attempt has been made to place either HEs or H layers on a calendar time scale based upon independent age information, although a notable exception is Thouveny *et al.* (2000) who do provide calibrated age ranges for HEs from an Iberia margin core. Uncertainties relating to marine reservoir offsets during the Last Glacial period and the absence of a widely accepted radiocarbon calibration curve before 26 ka BP until relatively recently (Reimer *et al.,* 2009) probably explain this absence. Instead HEs have mostly been placed on comparable timescales via alignment techniques (see below and section 1.2.2).

Table 1.2 – Summary of the core locations, timing and duration of H layers 2, 3 and 4 during the LLG. Dates in bold italics are average ages based on several cores (see main text). Source references are given at the bottom.

Heinrich Layer	Core	Top (cm)	Base (cm)	Thickness (cm)	Date of Top (^{14}C years)	Date of Base (^{14}C years)	Duration of event (^{14}C years)	Reference/s
H2	HU75–55	181	250	69	19410	21050	1640	1
	HU90–29	–	–	–	20040±130	21450±120	–	2
	NA87–22	482	505	23	21200	22800	1600	3
	SU90–08	118	128	10	20700	–	–	3,4
	SU90–09	82	92	10	20160	–	–	5
	GGC31	97	112	15	20443	–	–	6
	V23–81	327	329	2	20570	20990	420	7,8
	DSDP609	112	117	5	21110	21875	765	7,8
	OMEX-2K	–	–	–	20560±140	22130±160	1570	9
	MD95–2040	–	–	–	20410±220	20650±140	240	10
	MD95–2042	–	–	–	21026±297	21181±661	87	11
	Multiple				***20400±0.1***	***22100±0.8***	***1700***	12
H3	TP88–9P	–	–	–	~25000	~27000	~2000	13
	DSDP609	–	–	–	25970	29570	3600	8
	V23–16	–	–	–	28240	31250	3010	7
	MD95–2040	–	–	–	–	25430±250	–	10
	MD95–2042	–	–	–	26597±509	26844±1469	–	11
	Multiple				***26100±0.6***	***27400±1.6***	***1300***	12
H4	SU90–08	192	210	18	33450	35730	2280	3,4
	MD95–2040	–	–	–	–	32420±490	–	10
	MD95–2042	–	–	–	34019±948	34368±1182	–	11
	Multiple				***33900±0.7***	***34900±1.1***	***1000***	12

References: 1: Andrews *et al.* (1994); 2: Rashid *et al.* (2002); 3: Vidal *et al.* (1997); 4: Cortijo *et al.* (1997); 5: Grousset *et al.* (2001); 6: Bond and Lotti (1995); 7: Bond *et al.* (1992); 8: Bond *et al.* (1993); 9: Scourse *et al.* (2000); 10: de Abreu *et al.* (2003); 11: Thouveny *et al.* (2000); 12; Elliot *et al.* (2002); 13: Van Kreveld *et al.* (1996).

Mechanisms and links

The precise mechanisms which control or trigger these D–O cycles has yet to be fully understood, though the most widely accepted theory is that changes in meridional overturning circulation in the North Atlantic region changed the amount of effective heat being delivered to the North Atlantic region (e.g. EPICA Community Members,

2006), with some authors pointing to a near or complete shutdown of deep water formation during stadial events in the north Atlantic (Maslin *et al*., 2001; Elliot *et al*., 2002). Many authors have also pointed out that any large scale change to the meridional overturning circulation would have led to distinct shifts in atmospheric circulation gradients, affecting wind and precipitation patterns across the North Atlantic region (Chapman and Shackleton, 1998; Rasmussen & Thomsen, 2004; Grimm *et al*., 2006).

Various mechanisms have been proposed to explain the formation/trigger of Heinrich layers including both internal and external forcings of the ice sheets. Internal modes include MacAyeal's (1993) "binge-purge" model, that envisages ice sheets building up slowly (binge) before increasing internal base friction which causes catastrophic destabilization. Alternatively, Johnsen and Lauritzen (1995) proposed that repetitive jökulhlaups could produce large fresh-water pulses when ice dams failed. A more wide scale ice shelf build up and collapse model has also been suggested by Hulbe (1997). A triggering mechanism of ice load-induced earthquakes has also been proposed (Hunt and Malin, 1998). External mechanisms include minor variations in solar energy flux (Heinrich, 1988) or harmonics of orbital variations which could also correspond to the timing of Heinrich events (Broecker, 1994; Hagleberg *et al*., 1994). More recently sea level changes (probably induced by D–O cycles) have been suggested as a triggering mechanism, the forcing agent being the undercutting of the Laurentide ice sheet (van Kreveld, 2000).

Maslin *et al*. (2001) have stated that HEs should not be considered in isolation to the general climatic instability that characterized the LLG and indeed soon after the initial discovery of H layers Bond *et al.* (1993) and Broecker (1994) both noted the timing of these features appeared to relate to the climate fluctuations expressed in the Greenland ice cores. This relationship between Heinrich Layers and Greenland D–O cycles has been primarily implied via proxy alignment of $\delta^{18}O$ variations of planktonic forams in marine records to $\delta^{18}O$ fluctuations in the Greenland ice cores (Bond *et al.,* 1993). The main conclusions of this (and later work) is that HEs occur during GS events, with HE2, HE3, HE4 and HE5 being coincident with GS-3, GS-5, GS-9 and GS-13 respectively, all just preceding the initiation of a corresponding GI. Sanchez Goñi & Harrison (2010) have noted that the overall length of these events may differ, with for example HE2 and HE3 being shorter in duration than the GS-3 and GS-5 events, although the duration of HE4 may be a similar length to GS-9.

Although some independent chronology supports these interpretations in the North Atlantic via the identification of tephra horizons present in both marine and ice-core records (Austin *et al.,* 2004; Davies *et al.,* 2008), it is apparent that not all D–O cycles are associated with Heinrich events, and where they do exist, H events are not represented as more extreme temperatures in the Greenland ice cores, although they do appear to be related to longer duration GS intervals (Wolff *et al.,* 2010). Also some H layers occur just before large increases in SSTs, whereas others do not (e.g. H1 and H3) suggesting that the relationship between HEs and D–O cycles is a complex one.

1.2.2 The Mediterranean terrestrial palaeo-environmental record during the Last Glacial period

Over the last few decades various new palaeo-data records have helped increase our understanding of the rapid climatic and ecological changes that have occurred in the Mediterranean region during the LLG (e.g. Allen *et al*., 1999; Sánchez Goni *et al*., 2000; 2008; Tzedakis *et al*., 2002; 2004; Voelker *et al*., 2002). In particular the apparent detection of Dansgaard–Oeschger (D-O) cycles and Heinrich events (HEs) during this time in southern Europe from both ocean cores (Cacho *et al*., 1999; Fletcher & Sánchez Goni, 2008) and terrestrial sequences (e.g. Allen *et al*., 1999; Bartov *et al*., 2003; Gutiérrez *et al*., 2006; Wohlfarth *et al.,* 2008; Pini *et al*., 2010; Müller *et al*., 2010) has been put forward using evidence obtained from a wide array of proxy indicators. Figure 1.4 (taken from Fletcher *et al*., 2010) highlights these suggested climate linkages in both Mediterranean terrestrial and marine records (note however many of the palaeo-records in 1.4 are based upon tuned chronologies; see below). These data suggest that the D–O cycles, first detected from $\delta^{18}O$ variations within the Greenland ice cores during the last glacial cycle (Bond *et al*., 1993; Dansgaard *et al*., 1993), are to some extent also expressed in southern European records.

Teleconnections to the climate shifts and events described above have largely been achieved via alignment or 'wiggle-matching' of palaeo–records to the Greenland ice core records or to key marine records (e.g. Bond *et al*., 1993; Tzedakis *et al*., 2004; Pini *et al*., 2010). On this basis, some authors have concluded that fluctuations in the southern European proxy record are largely synchronous with the Greenland D–O cycles (Sánchez-Goni *et al*., 2002; Roucoux *et al*., 2005). This has mostly been attributed to the D–O events being a result of large shifts in meridional overturning

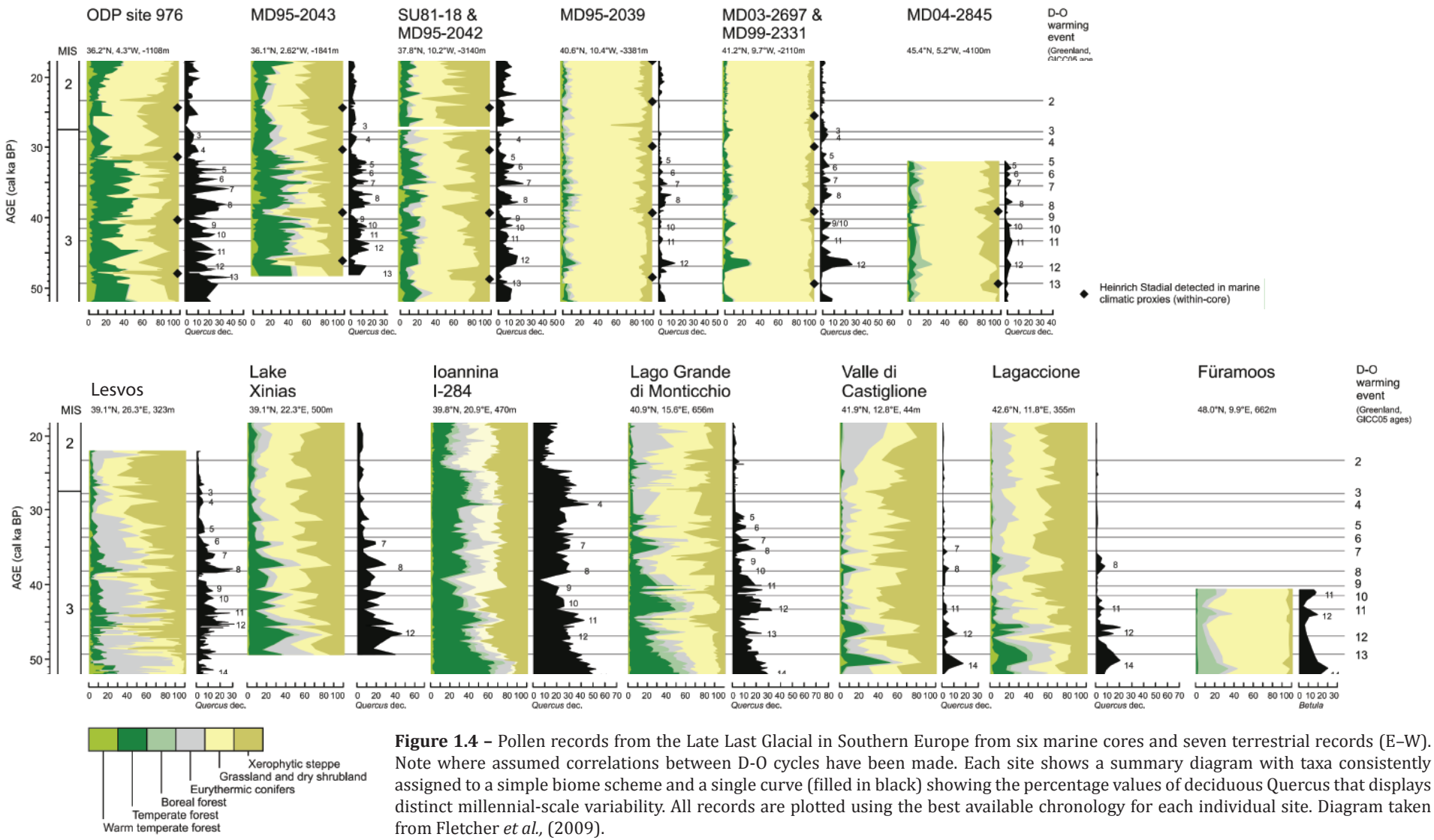

Figure 1.4 – Pollen records from the Late Last Glacial in Southern Europe from six marine cores and seven terrestrial records (E–W). Note where assumed correlations between D-O cycles have been made. Each site shows a summary diagram with taxa consistently assigned to a simple biome scheme and a single curve (filled in black) showing the percentage values of deciduous Quercus that displays distinct millennial-scale variability. All records are plotted using the best available chronology for each individual site. Diagram taken from Fletcher *et al.,* (2009).

circulation in the North Atlantic (e.g. EPICA community members, 2006) and thus evidence of a rapid atmospheric shift being expressed across Europe.

The advantage of aligning records is that it by-passes current chronological limitations that hamper the dating of the LLG in southern Europe (see Section 1.3). Von Grafenstein *et al.* (1998) justify this process of synchronising isotope records, by arguing that it is unlikely that very similar patterns could appear by accident or with a time–lag without being changed in shape. Tzedakis *et al.* (2001) made a similar case when interpreting land-ocean correlation based on pollen stratigraphy, stating that pollen curves have unique shapes and expressions that allow direct correlation between sites. Tzedakis *et al.* (2004) argued that although such alignment of records precludes the ability to assess leads or lags between palaeo-records, currently the error ranges on most age estimates available for the Last Glacial period from non-varved terrestrial sequences are greater than the duration of the climate shifts under examination thus making this a 'moot' point. Alternatively, Wunsch (2006) and Blaauw (2012) have questioned these viewpoints suggesting that visual similarity between records does not necessarily imply any causal relationship, especially in the case of the high frequency D–O events. In their view, the result of any alignment is always an assumption and by itself, leads to untested inferences. Skinner (2008) takes this further (p.792) stating, "All palaeoenvironmental inference hinges on chronostratigraphy. Without a way to accurately link and order our observations spatially and temporally, they remain at best of ambiguous, and at worst of dubious, significance".

Within the Mediterranean terrestrial record during the LLG the vast majority of alignment based chronological schemes are based upon palynostratigraphic correlations as primarily pollen is commonly preserved in terrestrial sequences and has been widely studied since the inception of Quaternary science as a discipline (von Post, 1916; 1918) and continues to be. Usually pollen signals, which record an environmental response, are cross correlated to differing proxy types such as oxygen isotopes, which record a climate signal. This is because these proxies are those available from marine and ice-core records which have the most prized chronological schemes and coupled high resolution palaeoenvironmental data available. From here dates from external records are either directly imported to form a site specific chronology (e.g. Pini *et al.* 2010) or extra-regional correlations are implicitly

suggested as, for example, of particular pollen signals to specific HEs (e.g. Ortiz *et al.,* 2010).

A number of studies from the Holocene period, where high precision radiocarbon chronologies are possible, have highlighted where previously assumed synchronous pollen signals (or events) are, in fact, diachronous in nature (e.g. Juvigné *et al.,* 1996; van den Bogaard *et al.,* 2002). Other studies have highlighted the lag times between proxy responses, for example Lauterbach *et al.* (2011) describe a vegetation lag of up to 500-750 yrs between the first occurrence of trees and an oxygen isotope shift related to early Holocene warming from a varved record located in the north-eastern Alps. A number of factors have been recognised that may lead to either asynchronous pollen signals or erroneous pollen correlations over both large extra-regional and much smaller inter-site geographical scales. These include the size and nature of the depositional basin which influences pollen deposition which may distort pollen signals (Prentice, 1985; Newham & Lowe, 1999), vegetation migration lag times and complexities in defining regions which should display uniform patterns of changes in vegetation communities (Bennett, 1988), as an example of this final point geographical regions which may have acted as areas of refugium due to specific physiography could be easily miscorrelated.

In LLG aged sequences palynostratigraphic tuning, as described above, assumes a greater importance as a chronological tool than dating techniques. For example, radiocarbon give less precise ages and are increasingly subject to other uncertainties (see section 1.3.1). To demonstrate the scale of this problem Figure 1.5 shows both the Lago Grande di Monticchio (LGdM) biome data (derived via a DCA analysis from pollen spectra) alongside the NGRIP oxygen isotope record both plotted on their individual independent timescales with associated errors (Allen *et al.,* 1999; Andersen *et al.,* 2006; Svensson *et al.,* 2006). When constrasted, although the records appear to show more variability during MIS 3 it is difficult to match any specific Greenland interstadial or stadial event with the LGdM pollen fluctuations, and in places the records seem to diverge completely (e.g. 50-45 ka BP). This could reflect the coarser proxy resolution of the Lago Grande di Monticchio pollen record, though comparison is further confounded significantly by the large error margins in the age models including the recently available counting errors inherent in the NGRIP age model (see Andersen *et al*., 2006). Also plotted on Figure 1.5 is the MD95-2042 marine record from the

Alboran Sea (Cacho *et al*., 1999) the chronology of this record is based upon tuning to the GISP2

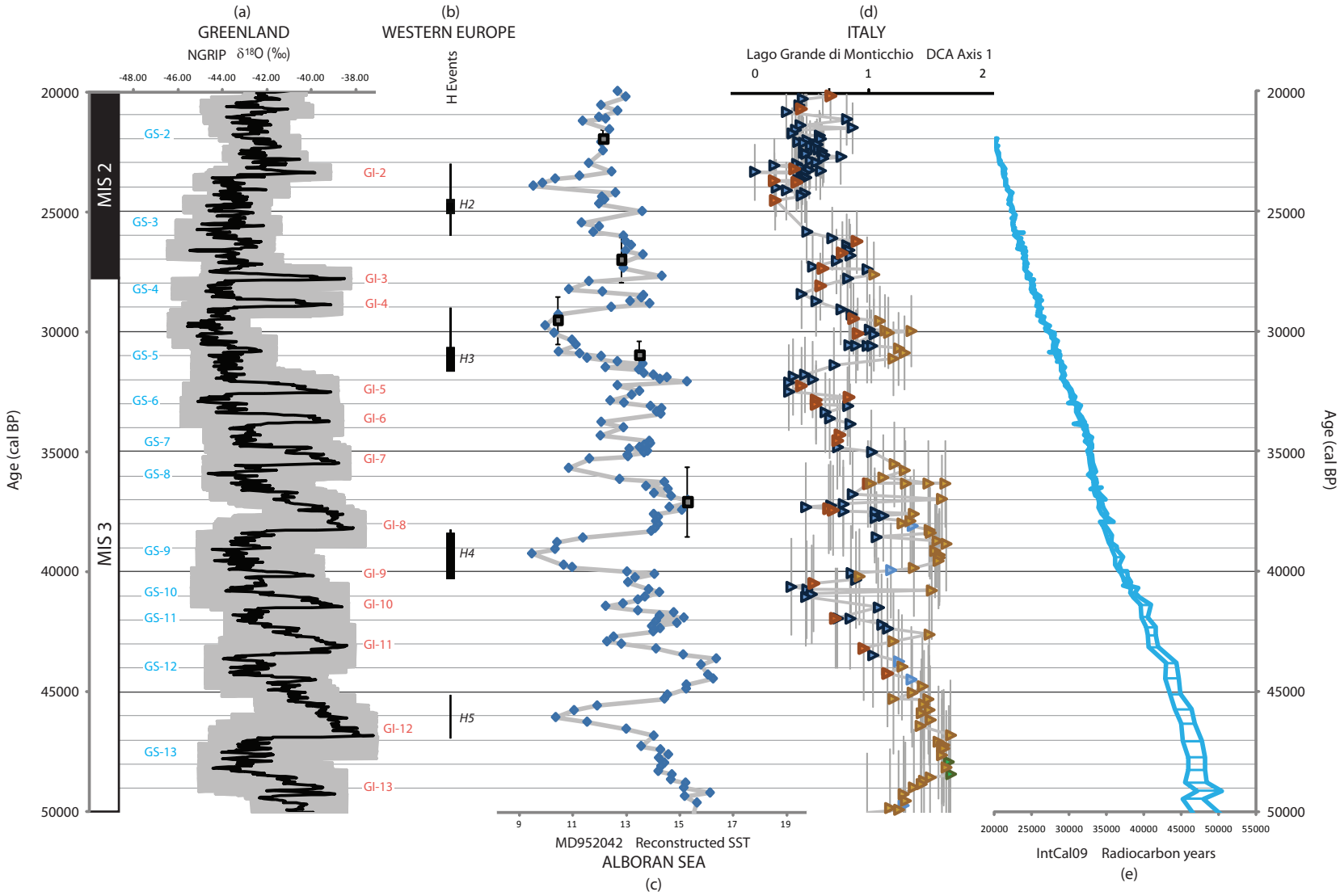
(a)
GREENLAND
NGRIP δ18O (‰)
-48.00
-46.00
-44.00
-42.00
-40.00
-38.00
(b)
WESTERN EUROPE
H Events
H2
H3
H4
H5
(d)
ITALY
Lago Grande di Monticchio DCA Axis 1
0
1
2
Age (cal BP)
20000
25000
30000
35000
40000
45000
50000
MIS 2
MIS 3
GS-2
GS-3
GS-4
GS-5
GS-6
GS-7
GS-8
GS-9
GS-10
GS-11
GS-12
GS-13
GI-2
GI-3
GI-4
GI-5
GI-6
GI-7
GI-8
GI-9
GI-10
GI-11
GI-12
GI-13
9
11
13
15
17
19
MD952042 Reconstructed SST
ALBORAN SEA
(c)
20000
25000
30000
35000
40000
45000
50000
55000
IntCal09 Radiocarbon years
(e)

Figure 1.5 (Previous Page) – Synthesis of palaeoclimate records during the LLG (MIS stages shown in left hand bar). (**A**) NGRIP Sixty year running average $\delta^{18}O$ record from Andersen *et al.* (2006) and Svensson *et al.* (2006). Grey shading represents estimated counting error and 20 year $\delta^{18}O$ range. Record adjusted to ka BP. (**B**) Calibrated age ranges for Heinrich (H) events 2, 3, 4 and 5. From data from western Europe (Bard *et al*., 2000; Sánchez Goñi *et al*., 2002; de Abreu *et al*., 2003) (thin lines) and calculated ages (Thouveny *et al*., 2000) (black boxes). (**C**) Reconstructed SST from Alboran sea core MD952043 calculated from C37 alkenone data (Cacho *et al*., 1999). Note the age model is based upon artificial correlation to the GISP2 oxygen isotope record, the calibrated radiocarbon dates obtained from the core are also shown. (**D**) DCA axis based on pollen data from Lago Grande di Monticchio, Italy. Two forest and three steppe biomes are represented: cool mixed forest (Light blue triangles), temperate deciduous forest (green triangles), wooded steppe (yellow triangles), warm steppe (orange triangles) and cold steppe (dark blue triangles). From Allen *et al.* (1999). (**E**) The Intcal09 calibration curve (Reimer *et al.,* 2009).

oxygen isotope record, and available radiocarbon dates for the record have been calibrated and plotted demonstrating the independent age errors for marine records.

Testing the synchronicity ('leads' and 'lags') and specific regional expression (if existent) of D–O cycles and Heinrich events registered in southern European terrestrial palaeo-records is therefore an important goal for studies of the Last Glacial period. This point is particularly illustrated by both the recent findings of Roberts *et al.* (2012) who describe evidence for an east–west climate see–saw during the Late Quaternary in the Mediterranean region (any similar climate mode during the LLG may be 'hidden' or masked via chronological uncertainties) and the synthesis attempted by Tzedakis *et al.* (2004) of three LLG pollen profiles from Greece, which appear to reflect differing ecological thresholds and response characteristics between sites, caused by localised environmental conditions. Furthermore a number of studies have suggested asynchronous or time-transgressive changes in climatic shifts over some areas (Coope & Lemdahl, 1995; Lowe, 2001), or show steep temperature gradients (Coope *et al*., 1998). In a study of several marine cores located off the Iberian coastline Sánchez Goñi *et al.* (2008) have also demonstrated differing ecological amplitude response during the last glacial. Rapid vegetation shifts are clearly reflected in southern European pollen records (see Fig. 1.4) but how or whether these shifts are related to D–O cycles or even how these events correspond on a more regional scale is difficult to establish without more robust temporal controls and more secure inter-site correlations.

Vegetation response to climate may be directly compared where pollen may be analysed within a marine sequence (e.g. Shackleton *et al.,* 2002; Sánchez Goni *et al.,* 2002), thus by-passing the alignment uncertainties outlined above. Although these records are undeniably valuable they also suffer from a set of limitations such as having complex or undefined pollen source areas which can make reliable interpretation difficult. Combourieu *et al.* (2009) and Beaudouin *et al.* (2007) for example have suggested that marine pollen records are heavily biased towards pollen produced from higher mountain areas and river outflows respectively. Another issue is that pollen source areas may change significantly over time in marine records (Magri & Parra, 2002). It is then still desirable for terrestrial pollen records to be analysed and placed on timescales comparable with other palaeorecords, despite the difficulties encountered achieving this goal.

Coupled to this point, more is now known about the occurrence and timing of anatomically modern humans (*Homo sapiens sapiens*[3]) and Neanderthals (*Homo neanderthalensis*) in southern Europe between 50-20 ka (e.g. Conard & Bolus, 2003; d'Errico *et al*., 1998) who lived on the terrestrial landscape. One of the most important human transitions during this time frame is the disappearance of the Neanderthals who appear to go extinct between ~40 to 30 ka BP (Balter, 2006; Davies, 2007). There has been much lively debate on the extinction of the Neanderthals (see Finlayson *et al*., 2004; d'Errico & Sánchez Goñi, 2004) and whether climatic changes, the Campanian Ignimbrite (CI) volcanic eruption, or the arrival of modern humans, or elements of all of these factors caused this disappearance. Better understanding of rapid ecological changes over large spatial transects could be made possible by more detailed site chronologies within southern Europe during this time frame, and may clarify how these changes affected human dispersal and development throughout Europe. As an example of this recently Lowe *et al.* (2012) used tephrostratigraphy, specifically the CI tephra, to synchronise high-resolution terrestrial and marine palaeo-records to archaeological sites in the Mediterranean region. Lowe *et al.* (2012) conclude that the CI and climatic deterioration failed to have lasting effects on the Neanderthals inferring that modern humans probably proved the greater threat to Neanderthal populations.

[3] *Homo sapiens sapiens* will be referred to as 'AMH' here; this term will also be used to envelope what are sometimes termed 'Cro-Magnons' in some of the literature. Also within the text the term human encompasses both moderns and Neanderthals.

1.2.3 The Greenland ice core record as a regional event stratigraphy?

The INTIMATE[4] Group has underlined the importance of the Greenland ice–core record by recommending it as a regional stratotype event stratigraphy for the North Atlantic and for wider geographical areas, as this archive is considered to provide the best-resolved and most complete record of climatic variability during the last glacial cycle in this region. Initially this stratotype sequence was proposed for the Last Termination (only 15-11 ka BP; Björck *et al*., 1998; Walker *et al*., 1999; Lowe *et al*., 2001) but later extended by Lowe *et al.* (2008) to include the past 30 ka BP (including the Holocene) and further extended into the Last Glacial to 48 ka BP by Blockley *et al*. (2012). The eventual aim of the INTIMATE Group is to extend this event stratigraphy to 60 ka BP. A key goal has been to define 'events' in the Greenland record (Fig. 1.1) and in particular their precise timings and dating errors (Table 1.1), not to replace existing local/regional terminology for climatic events, but to be used as a benchmark (or 'yardstick') for comparison with means to test independently–dated records, in order to test the synchronicity of events.

There have been some misunderstandings surrounding this approach, in particular the idea that this event stratigraphy is meant to replace local or regional schemes, which would essentially promote alignment of records instead, whereas the very opposite is being proposed (see Lowe *et al*., 2001). Edwards *et al.* (2000) questioned whether the Greenland record could be compromised as an Event stratigraphy if it does not record more regional climatic oscillations. In fact the Event stratigraphy 'yardstick' approach aims to highlight differences (if they exist) between records. For example Austin *et al.* (2012) found evidence for a warm interval from several marine cores dated to c.25 ka BP, which is apparently absent from the Greenland ice–core record. Comparison using independent timescales can allow these differences to emerge however direct chronostratigraphic comparisons between sites are only possible if 1) different dating techniques are comparable and 2) robust age uncertainty errors may be defined. The most commonly used dating techniques for the LLG will now be discussed and these issues explored.

[4] INTegration of Ice-core, MArine and TErrestrial records– a core programme of the INQUA Palaeoclimate Commission.

1.3 Age vs Depth: building independent chronologies for Last Glacial terrestrial palaeo-records

1.3.1 Radiocarbon dating

Radiocarbon dating is the most commonly deployed independent method for dating the last 50 ka BP (currently the effective limit of the technique) and has been applied to a large range of LLG terrestrial palaeo-records (e.g. Allen *et al*., 1999; Tzedakis *et al*., 2004; Blaauw *et al*., 2008; Margari *et al*., 2009; Müller *et al*., 2011). Radiocarbon ages are calculated from the ratio of the radioactive carbon isotope ^{14}C to one of the stable isotopes (^{12}C or ^{13}C) in the sample compared to a standard (Reimer & Reimer, 2007). The precision and accuracy of radiocarbon dates are checked by four groups of uncertainty: (a) analytical uncertainty, (b) geological and stratigraphical integrity of the dated material, (c) reservoir effects (e.g. hard water effects) and (d) calibration procedures (Lowe *et al.,* 2007; 2008). Each of these factors will now be discussed in relation to constraining the ages of palaeoenvironmental changes during the LLG.

The analytical precision of a radiocarbon date is produced from uncertainties relating to modern standards used, background samples and fractionation processes and are straightforward to quantify via error propagation formulae (Scott, 2007; Cook & van der Plicht, 2007). Within the LLG radiocarbon analytical errors can range from 100 – 3000 radiocarbon yrs, tending to increase with older ages. This error is important as it effectively determines the potential error range achievable at the calibration stage (see below). Towards the effective limit of radiocarbon time large analytical uncertainties can, for example, mean that only minimum ages can be determined (e.g. Margari *et al*., 2009).

Understanding the integrity of any dated carbon material is crucial to understanding how the final calibrated age relates to the 'true' age. There are many reasons why there may be offset or outlier ages including reworking of older material within a sequence, contamination introduced when sampling and isotopic fractionation (Griffiths, 2001), as well as growth of modern bacteria in stored material. A demonstration of this problem is that even if 0.5 per cent modern carbon is added to a sample dating to 40,000 ka BP, the resultant calculated age would become 35,600 ka BP (Higham, 2011). A particular issue towards the limit of radiocarbon time is the so-called asymptotic radiocarbon effect (Blockley *et al*., 2008; Higham, 2011) where ages do not become infinite in age but instead return ages close to the limit of radiocarbon

(40–50,000 radiocarbon yrs) sometimes at sites where other dating techniques indicate Last Interglacial ages (e.g. Chappell *et al*., 1996).

Hard water errors primarily manifest in lake settings where radiocarbon determination produce ages which are too old. There are various causes which lead to this effect but the most common two causes are the dissolution of ^{14}C depleted carbon from geologically old carbon or groundwater input containing ^{14}C depleted carbon (from leaching old soils or volcanic activity; Blaauw *et al*., 2011). This is particularly prevalent in (although not constrained to) the Mediterranean region, where active volcanic systems and large carbonate basins are common.

Radiocarbon time is not linear as atmospheric ^{14}C is not constant over time (van der Plicht, 2007) which also means that radiocarbon age is incomparable to other timescales unless calibrated to the calendar age scale (usually 1950 A.D.). Radiocarbon ages can be corrected using calibration curves created by ^{14}C dating of archives that offer alternative age controls such as tree rings for example, which allows the divergence between radiocarbon and 'real' time to be calculated and modelled.

IntCal09 (Reimer *et al*., 2009) is the current internationally accepted calibration curve and it extends to the limit of radiocarbon time (c.50,000 yrs). It is built from tree rings from the present to 12,550 cal BP but before this is based on U/Th dated marine coral datasets (e.g. Fairbanks *et al.,* 2005) and radiocarbon measurements from Cariaco Basin and Iberian Margin marine sediment records (Hughen *et al*., 2006; Bard *et al*., 2004a, 2004b; Shackleton *et al*., 2004) which have been tuned or aligned to the Chinese Hulu Cave speleothem $\delta^{18}O$ record (Wang *et al.,* 2001). There are thus increasing uncertainties and assumptions in the IntCal09 calibration curve before 12,550, including marine reservoir offsets which are assumed to be constant over time. Although this is currently the only feasible approach for correcting marine reservoir offsets, it is demonstrably unlikely to be true particularly during H Events (e.g. Thornalley *et al.,* 2011). The alignment of marine records to Hulu Cave is also problematic as it involves many assumptions inherent to the practice of wiggle–matching (see Wunsch, 2006; Blaauw, 2012) while also assuming the Hulu Cave U–Th chronology to be reliable. The relationships between these records and their intra–comparisons must therefore be considered a work still in progress (Reimer *et al*., 2009).

Despite these problems the IntCal09 calibration curve does provide an internationally approved curve on which to calibrate back to ~50 ka BP, allowing chronological comparison between radiocarbon and other dating techniques throughout the LLG. In the future it is possible that more reliable calibration curves based on independent timescales may become available for parts of the LLG, which would help to circumvent some of the aforementioned problems (Turney *et al*., 2010; Nakagawa *et al*., 2012).

1.3.2 Tephrochronology

Tephrochronology has also been used for dating LLG records, thus far primarily where visible layers have been found within sediment records. Crystals formed within volcanic eruptions can be both directly dated via Argon-Argon ($^{40}Ar/^{39}Ar$) or Potassium-Argon ($^{40}K/^{39}Ar$) (see Twyman, 2007) and indirectly dated via other chronological techniques (e.g. radiocarbon dating) which can then be imported into sites where the tephra layer is located.

The direct dating of tephra layers via both $^{40}Ar/^{39}Ar$ and $^{40}K/^{39}Ar$ is possible during the entirety of the LLG however with the errors of $^{40}Ar/^{39}Ar$ usually being centennial, whereas $^{40}K/^{39}Ar$ often has much larger millennial scale uncertainty. This is due to $^{40}Ar/^{39}Ar$ having a much greater degree of analytical precision than $^{40}K/^{39}Ar$ dating (Walker *et al.,* 2005). Where multiple lines of chronological evidence are available direct dating of tephra layers by these means show good agreement for both $^{40}K/^{39}Ar$ and $^{40}Ar/^{39}Ar$ techinques. For example the St Angelo Tuff has been dated by $^{40}K/^{39}Ar$ to 17,800±3200 and by varve chronology to 15,820±790 (Poli *et al.,* 1987; Wulf *et al.,* 2008). In another example the Tufi Biancastri tephra has been dated to 17,900±500 via $^{40}Ar/^{39}Ar$ and to 18,500±920 via varve chronology (Pappalardo *et al*., 1999; Wulf *et al*., 2008). Direct dating of volcanic products by $^{40}Ar/^{39}Ar$ or $^{40}K/^{39}Ar$ can, however, be problematic and result in age determinations which are too old; this effect is due to xenocrystic contamination. This is where older crystals are incorporated into younger eruptive product and is a problem with $^{40}Ar/^{39}Ar$ dates acquired using the more traditional laser incremental heating method rather than more recently available techniques which allow single crystal measurements (Di Renzo *et al*., 2010).

Thermoluminescence (TL) dating has also been carried out on the crystal component (e.g. quartz and plagioclase) of tephra although the errors achievable using this type of dating are often multi- millennial (Guerin, 1983).

Even where a tephra layer age may not be known they can be used as isochronous marker horizons that allow synchronization of palaeo-records for that time horizon (Lowe, 2011). Tephra layers are also found in a wide array of depositional environments including cave, marine, peat and lacustrine contexts (e.g. Lowe *et al.,* 2012). Tephrochronology is discussed in more detail in Chapter 2.

1.3.3 Other dating methods

Other chronological techniques applied to the LLG will now be briefly discussed. Optically simulated luminescence (OSL) and Infrared stimulated luminescence (IRSL) dating have both been applied to long palaeo-records that span this time–frame (e.g. Vandergoes *et al*., 2005; Wohlfarth *et al.,* 2008). The application of luminescence is limited to sequences where quartz and/or potassium feldspar are present and that have been exposed to adequate sunlight dose before deposition (Lian, 2007). This technique has generated results that show agreement with independent dating methods (e.g. Murray and Olley, 2002) although more recent dating of LLG records age models based on using OSL and IRSL chronologies appear to diverge significantly from age models based on both radiocarbon (Blaauw *et al*., 2008) and biostratigraphy (e.g. Lowick *et al*., 2010). Luminescence ages tend to have large millennial–scale error ranges (often reported at 1 s.d.) but provide an important alternative technique to radiocarbon as it can be applied to events that date beyond the limit of radiocarbon (e.g. 50 ka BP) and in many sites where no datable carbon is available.

Another dating technique which potentially allows a very high temporal resolution is varve chronology, though this is prone to increasing absolute errors with age, as varve counting errors are incremental, typically with a ±3% counting error (Ojala *et al.,* 2012). This factor alone generates errors of 600 yrs at 20 ka and 1500 yrs at 50 ka. Despite this problem, reliable varve chronologies can permit events to be differentially dated with a high annual/decadal precision. Even if the 'absolute' age error is large, this offers great potential in terms of dating the duration and speed of palaeoenvironmental transitions or their precise temporal relationship to, for example preserved tephra layers (see Blockley *et al*., 2012). Unfortunately very few annually-laminated records cover the full span of the LLG, with the aforementioned Lago Grande di Monticchio lacustrine record representing a rare example.

U-series dating has also been applied to LLG deposits particularly to speleothems (e.g. Bar-Matthews *et al*., 1999) where the carbonate material sometimes enables determination of U/Th ratios with 2 sigma age errors of centennial precision. U-series has also been carried out on carbonate lake sediments spanning the LLG, where good agreement has been demonstrated with coeval radiocarbon chronologies (Haase-Schramm *et al*., 2004). Obtaining reliable U-series ages from lake carbonates can be difficult, however, due to large amounts of detrital inclusions which can affect the U/Th ratio (Kaufman, 1993). U/Th has also been applied to peat records of LLG age (e.g. Ortiz *et al*., 2004), although very few such studies have parallel age estimates based on other chronological techniques obtained from the same sequence, to allow the accuracy of the U-series dates to be tested.

1.3.4 Age–depth modelling approaches

The above section briefly outlined some of the difficulties in generating precise and accurate ages for LLG events. It is impossible to date every level within a natural sequence and thus once a set of ages are available some form of modelling is required to interpolate ages for undated levels. Indeed the construction of robust age–depth profiles is an important goal for the Quaternary geochronology community, though it is often a non-trivial task (Telford *et al.,* 2004).

Many approaches are currently applied that allow age–depth relationships to be defined for southern European records that span the LLG (see Fig. 1.6 for a visual summary). Frequently used models include simple line plots, both through mean calibrated radiocarbon ages (e.g. Vogel *et al.,* 2010; Müller *et al.,* 2011; Fig. 1.6C) or their 2 s.d. error ranges (e.g. Bourne *et al.,* 2010; Fig. 1.6E). Linear and polynomial regression curves have also been applied (e.g. Ortiz *et al.,* 2004; Lowe *et al.,* 2004; Fig. 1.6B,D) and are often validated by intercept R^2 values. Although these techniques are relatively straight forward and transparent, there are considerable limitations (Telford *et al.,* 2004). For example, polynomial curves often produce age reversals even where there are no significant 'outlier' ages, only subtle differences between the mean ages. Clearly this violates the law of superposition and is often adjusted for by reducing the order of regression model used or by subjective removal of problem ages. Another problem with the above methods is that they cannot robustly estimate the errors of interpolated ages, often underestimating them (see Fig. 1.6).

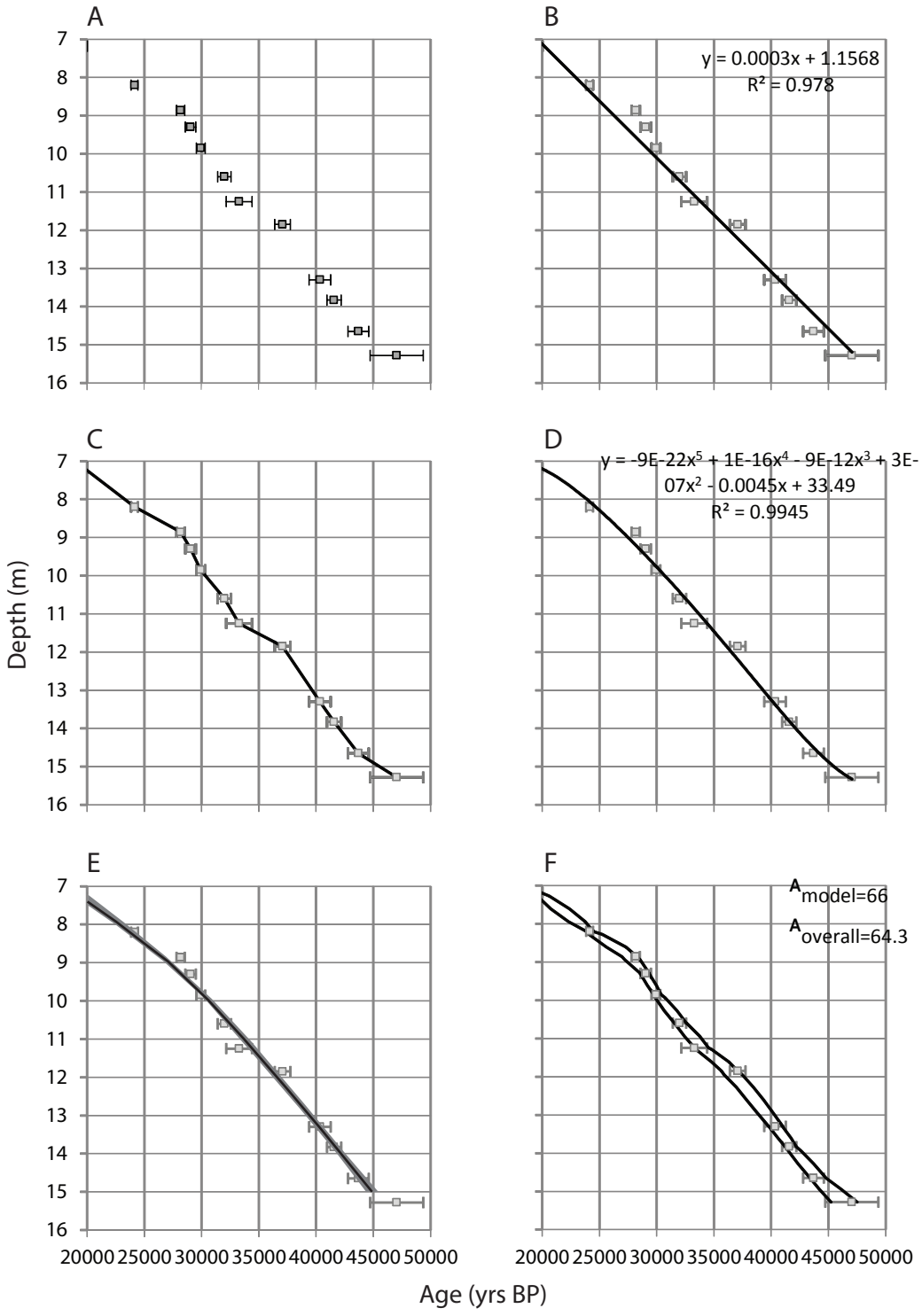

Figure 1.6 – Comparison of different age-depth modelling approaches of the Late Last Glacial of Tenaghi Philippon (Muller *et al.,* 2010). (**A**) The set of calibrated radiocarbon with mean age shown. (**B**) Linear trend line age–depth model. (**C**) Simple line plot through the mean calibrated ages. (**D**) A fifth order polynomial calculated through the mean calibrated ages. (**E**) Smoothing spline model with grey 95% confidence intervals (smoothing parameter 0.6, produced using clam (Blauuw, 2010)). (**F**) Ages modelled using Oxcal (version 4.1) P_Sequence depositional model (at 95.4% confidence limits).

These limitations have led to the development of more sophisticated techniques including; in particular, radiocarbon wiggle–matching and Bayesian statistical modelling (e.g. Blockley *et al.,* 2004; Blaauw *et al.,* 2004; Yeloff *et al.,* 2006), applied to records dating to within the Last Glacial interval (e.g. Wohlfarth *et al*., 2008; Blaauw *et al*., 2008; see Fig. 1.6F). Blockley *et al.* (2007a) compared the precision and accuracy of these two different approaches and found that although most can provide robust determinations of age at different depths, Bayesian statistical modelling performed best in complex stratigraphies (e.g. where sedimentation rate may be variable). Also this type of modelling can incorporate age estimates based on a variety of methods, whereas wiggle–match dating is limited to radiocarbon information alone.

In essence Bayesian modelling works via a uniform *prior* model (i.e. ***Sequence*** models; see Bronk Ramsey, 2000) which is based upon two key assumptions to build this *prior* (1) that a probability density function for a calibrated date range can be derived from a calibration curve and (2) that the law of superposition restricts the probability densities for a series of dates obtained from the same sequence (Blockley *et al.,* 2007a). One of the most widely used modelling software programs currently available is OxCal (Bronk Ramsey, 1995; 2001; 2008) which in its latest form (version 4.1) allows Poisson depositional models (***P_Sequences***) to be undertaken with which unlike *Sequence* models, allows utilisation of depth information without enforcing a uniform linear sedimentation rate (Blockley *et al.,* 2007a). There are, of course, good reasons to assume rates of deposition can change considerably within a sediment sequence (due to changes in lithology, hiatuses etc.) and this information can be placed within Bayesian models as ***Boundary*** functions. Also functions have become available recently to detect outliers in a more objective way within *P_Sequence* models (Bronk Ramsey, 2009).

Although there is no consensus 'correct' age–depth modelling approach, and indeed different methods can be appropriate depending on the type and nature of the age–depth information (Blockley *et al*., 2008) approaches, like *P_Sequences* allow robust calculation of undated depths (see Fig. 1.6F). It is only when using these more complex methods that robust error ranges can be quantified, which is fundamental in allowing comparison between separate palaeo-records on objective and independent time scales.

1.3.5 Summary of limitations and potential for improvement

All age modelling is however highly dependent on the amount and quality of the independent dating information available, which as discussed above is often problematic for large parts of LLG. It is for this reason that many authors chose to artificially synchronize or align LLG proxy records to well dated sequences (such as NGRIP or Hulu Cave) as it allows these chronological limitations to be essentially by-passed. It is however important for these assumptions to be tested and also for more independent chronologies to be available to test questions of environmental synchronicity and regional expression.

One suggested approach to improve the geochronology of the LLG, suggested by both the INTIMATE and RESET groups (Lowe *et al*., 2008) is the wider detection of non-visible distal ash layers, also known as cryptotephra layers (Lowe *et al*., 2001). As previously touched upon tephra layers can be used as powerful geochronological tools as they offer both the ability to import precise independent ages into sequences (e.g. tephrochronology) and also can be used as isochronous marker beds (e.g. tephrostratigraphy). Thus they provide great potential for the precise correlation of southern European LLG sedimentary records with many widespread highly explosive tephra dispersals originating from the Italian and Hellenic volcanic centres between c.50-20 ka. The Lago Grande di Monticchio sequence forms one of the most comprehensive tephrostratigraphic sequences currently available in the central Mediterranean (which is also coupled with a detailed palaeoenvironmental record, see above) with over thirty visible tephra layers between c.50-20 ka BP. Extending this tephrostratigraphic framework to other palaeo-records using non-visible tephra extraction techniques is of key importance.

1.4 Aims and Objectives

The overarching aim of this investigation is to test current chronological models for Mediterranean terrestrial palaeorecords during the LLG using tephrochronology, and to then use tephra layers as isochronic markers to improve correlation between these sequences.

The key objectives are:

1. To follow INTIMATE protocols and produce age-models that are chronologically independent for comparison with other independently dated palaeo-records (e.g. NGRIP).

2. Undertake tephra investigations of long records that cover the LLG, including systematic search for cryptotephra.

3. Extending the current tephrostratigraphic framework during the LLG over larger geographical ranges.

4. Use identified tephra layers to test and improve existing age models.

5. Test whether abrupt proxy (e.g. pollen) shifts (linked to rapid ecological changes) can be chronologically constrained and correlated across sites using tephrochronology and tephrostratigraphy.

1.5 Thesis structure

This introduction briefly considered: (a) the expression, timing and probable relationships of climatic variability during the LLG from the key North Atlantic palaeorecords, (b) the degree to which these climatic signals are expressed in southern European records and (c) the techinques used to derive age models for these records. The main body of this thesis is divided into eight chapters (plus appendices), with the following progression:

Chapter 2 – Tephra Studies

This chapter outlines the principles of tephrochronology, describes the major eruptions which produced far travelled tephra during the LLG, and provides a data synthesis.

Chapter 3 – Methods

This chapter outlines the key methods and approaches applied within this thesis, in particular focusing on 1) the detection and quantification of cryptotephra abundance, 2) assessing the precision and accuracy of geochemical data, and 3) the age modelling procedures utilised.

Chapter 4 – Site Descriptions

The sites sampled for this study are described in this chapter in terms of their: location, lithostratigraphy, existing palaeoenvironmental data (and importance), current chronological controls, and any tephrostratigraphic data previously reported for each site.

Chapter 5 – Results

A full detailed description of the tephra results obtained for each sequence examined in this project is provided in this chapter, including records of variations in volcanic shard abundance, morphology and the geochemical properties and classification of the tephra layers.

Chapter 6 – Correlation of Tephra layers

The tephra layers described in chapter 5 are compared primarily to the RESET database for geochemical data obtained from proximal volcanic deposits and also to other important data-sets obtained from distal volcanic ash archives (e.g. Lago Grande di Monticchio). Correlations of tephra layers are based first upon geochemical affinity and second stratigraphic superposition and relationships, before thirdly existing chronological data.

Chapter 7 – Testing and Refining Age-Depth Models

This chapter uses the tephra layers defined and correlated in chapter 5 and 6 as chronostratigraphic tools to test existing age models for each of the studied records. All available independent age data (e.g. radiocarbon dates) are then employed to construct new Bayesian age models for each record. The palaeoenvironmental implications of these new age models for each individual sequence are then discussed.

Chapter 8 – Discussion

This chapter examines the significance of the interpretations presented in chapters 6 and 7 with respect to the southern European tephra lattice for the LLG and the validity of the tephra isochron approach as adopted within this investigation. Finally the sequences investigated here are firstly compared to one another to test for regional synchrony and then to other independently–dated palaeo-records to test for synchrony at a larger scale and assess the palaeo–climate/environmental implications.

Chapter 9 – Conclusions

This chapter briefly outlines the key findings that emerged from this PhD project and how well the aims and objectives proposed have been met. It also suggests ways in which the research could have been improved with the emergence of new research findings and techniques that were not available during the course of this investigation. Finally ways in which this research can be taken forward in future work are proposed.

Appendices

Three appendices (I, II and III) are provided which give full datasets for (I) the tephra shard counts obtained for each sequence described in chapters 4 and 5 (II) the full geochemical data-sets for all tephra layers studied in this investigation, including the raw standard data (these data will also be made available on the RESET online database) and (III) site specific age modelling statistics. Please note appendices are provided electronically (on CD) located on the back cover of this thesis.

2.0 TEPHRA STUDIES

2.1 Principles of Tephrochronological Research

This chapter will explore the key definitions, principles and history of tephrochronological research before focussing on the tephrochronological research that has already been carried out in the Mediterranean region during the LLG.

The word tephra is derived from the Greek word τεφρα which means 'ash' and was first introduced into the academic literature by Sigurdur Thorarinsson in his 1944 doctoral thesis (written in Swedish) where he used it to describe all solid fragmented material ejected from a volcano during an eruption. The term tephra applies to all size fractions including ash (<2.0 mm), lapilli (2.0–64.0 mm) and blocks and bombs (>64 mm). There are two principle strands to tephra studies, tephrostratigraphy and tephrochronology. Tephrostratigraphy is where sites may be directly correlated via the presence of time-equivalent ashes and tephrochronology is where an age for a tephra, derived either directly or indirectly (see section 1.3.2 for details), may be imported into a sequence where the tephra layer is detected. It is often the case that the term tephrochronology is used to encompass both of these terms (Lowe, 2011). Tephra deposits are very useful stratigraphic tools for two main reasons:

Firstly, volcanic eruptions take place over very short periods of geological time (e.g. from hours to months) and, secondly, depending on the type and size of eruption a tephra may be transported over vast distances. This is particularly true of very explosive eruptions (e.g. Plinian or Ultra Plinian) which usually form sustained high energy explosions which can produce volcanic plumes capable of penetrating the high stratosphere (Sparks *et al.,* 1997) forming 'umbrella' clouds. In the case of the largest explosive eruptions these giant ash clouds are controlled by a balance between gravity and Coriolis forces forming large bodies that can be insensitive to predominating wind patterns (Baines & Sparks, 2005) allowing dispersal over continental size areas. More commonly eruptive events tend to spread in patterns closely following stratospheric winds direction, commonly in very elongated elliptical patterns. This can be seen from both the mapping of fallout from volcanic plumes using isopach contours (for past geological eruptions) and also via satellite observations of modern volcanic plumes during actual transport (Davies *et al.,* 2010a). Finally this allows tephra from both these eruption styles to travel over hundreds, even thousands of square kilometres from source. Pyle (1989) observed that as distance from source increases an

exponential thinning of tephra layers deposit can be observed. This means that tephra layers, depending on the distance from source, can range from millimetres to metres in thickness forming discrete visible layers which can 'blanket' sea and landscapes thus being preserved in many sediment archive types (Alloway *et al.,* 2007). Further from source tephra layers preserved in sedimentary records may be invisible to the naked eye, these tephra are termed 'cryptotephra' layers, deriving crypto from the Greek work 'kryptein' which means to hide conveying the concealed nature of these deposits.

Detection of tephra layers and volcanic eruptions

The detection of these non-visible distal ash horizons has been achieved using a large array of techniques and methods which can be divided into those where cryptotephra are indirectly detected before extraction (e.g. via magnetic susceptibility or sulphate peaks; Calanchi *et al.,* 1998; Dunbar & Kurbatov, 2011) or increasingly via direct sediment processing and extraction (Turney *et al*., 1998; Blockley *et al*., 2005). A more detailed discussion of these various techniques can be found in section 3.3. The detection of cryptotephra layers is allowing smaller to medium as well as large eruptions to be traced at increasing geographical distance from source (e.g. Blockley *et al*., 2008; Bourne *et al*., 2010).

Volcanic eruptions may also be identified where no tephra is preserved but via chemical signatures which record the presence of volcanically derived aerosols such as H_2SO_4. These aerosols may be transported between hemispheres which mean these types of records record global as well as more regional volcanic activity; currently this type of research is limited to ice-core records (e.g. Zielinski *et al.,* 1996) where these signals may be detected.

Dating tephra layers

As discussed in section 1.3.2, tephra layers may be dated both directly via analysis of mineral ($^{40}Ar/^{39}Ar$, $^{40}K/^{39}Ar$ and TL) and glass components (Fission track) formed during the volcanic eruption and also indirectly from age data gained from sediment material associated with tephra fallout, this includes radiocarbon dating of organic material, OSL dating and also incremental dating (i.e. varve chronologies).

Tephrostratigraphic relationships may also be used to determine ages of tephra layers. Modelling of one, or several, lines of different age information may also be performed in order to form more precise age estimates, often using Bayesian methods (Blockley *et al.,* 2007b).

Characterising tephra layers

Not all tephra deposits can be directly dated using the techniques outlined above as the minerals needed for direct dating (i.e. zircon) may not be formed during the eruptive event or, a more common problem, are not present in distal tephra deposits (the glass fraction travels further than the mineral component which has a much higher specific gravity; Juvigné and Porter, 1985). The best direct dating then can often only be carried out in proximal or medial proximal areas (e.g. De Vivo *et al.,* 2001; Ton-That *et al.,* 2001).

There is therefore a need to produce robust (both precise and accurate) characterisation of tephra layers which allows correlation between deposits (i.e. tephrostratigraphy) which allows precise direct (or indirect dates) to be transferred between sequences. Even where no age estimates are available for tephra layers, being able to link them is still a very powerful stratigraphic tool. A wide array of techniques have been developed (via a variety of methods) with this goal of tephra 'fingerprinting' in mind. These include detailed optical analysis of mineral assemblages (e.g. angle of distinction, birefringence) and also analytical analysis using X-Ray Fluorescence (XRF; Lowe, 2011). Grain-specific morphological and textural information like vesicularity or shard shape (Polacci *et al.,* 2003) and also by study of grain-specific optical properties such as refractive indexes (Enache & Cumming, 2006).

Although all these methods may be very successful in particular circumstances, they are much less so over larger geographical distances and particularly when considering cryptotephra layers. This is due to the mineral component often being absent in distal tephra layers (as previously mentioned), shard morphology characteristics often being ineffective at discriminating between fine-grained distal tephra deposits (Lane, 2008). Likewise refractive indices measurement often does not have the precision required to allow robust distinction between similar distal tephra layers (Lowe, 2011).

Increasingly and by far the most commonly adopted technique used to characterise tephra glass is via the shard specific measurement of major, minor and trace elements via a range of techniques including: Electron Probe Micro-Analysis (EPMA) for major and minor elements and Laser Ablation Inductively Coupled Plasma Mass Spectrometry (LA-ICP-MS) and Secondary Ion Mass Spectrometry (SIMS) for trace element acquisition (Lowe, 2011). These techniques allow robust precise quantified measurement of over 20 elements and can be increasingly applied on very small tephra shards often encountered in cryptotephra research (Pearce *et al.,* 2011b; Haywood, 2012). Despite these important advances there may still be instances where tephra layers from the same volcanic system have very similar (if not identical) geochemical signatures which cannot be distinguished, where this is the case tephra layers may have to be correlated on stratigraphic principles and other chronological controls (Lowe, 2011).

2.2 A Tephrochronological framework for the Mediterranean Region during the LLG

2.2.1 Volcanic provinces

Multiple volcanic centres have generated volcanic eruptions potentially capable of delivering ash to the southern European region during the LLG period and these include the Italian and Hellenic Arc volcanic systems which are currently observed to produce the most far-travelled tephra distributions in the Mediterranean during this timeframe (Keller *et al.,* 1978; Narcisi & Vezzoli, 1999). Alongside these, the Icelandic, Azores, Massif Central, Eifel District and Anotolian volcanic centres have also been volcanically active, although the geographical extent of tephra resultant from these eruption episodes remains less clear over the Mediterranean region, nevertheless these will also be briefly considered here. The location and key volcanoes from these centres are shown in Figure 2.1 and are described below before a chronological and geochemical synthesis of current available data is carried out in section 2.2.2.

Italian Region

The Italian Region was probably one of the most productive volcanic ash producing regions in the Mediterranean region during the LLG with many significant eruptions

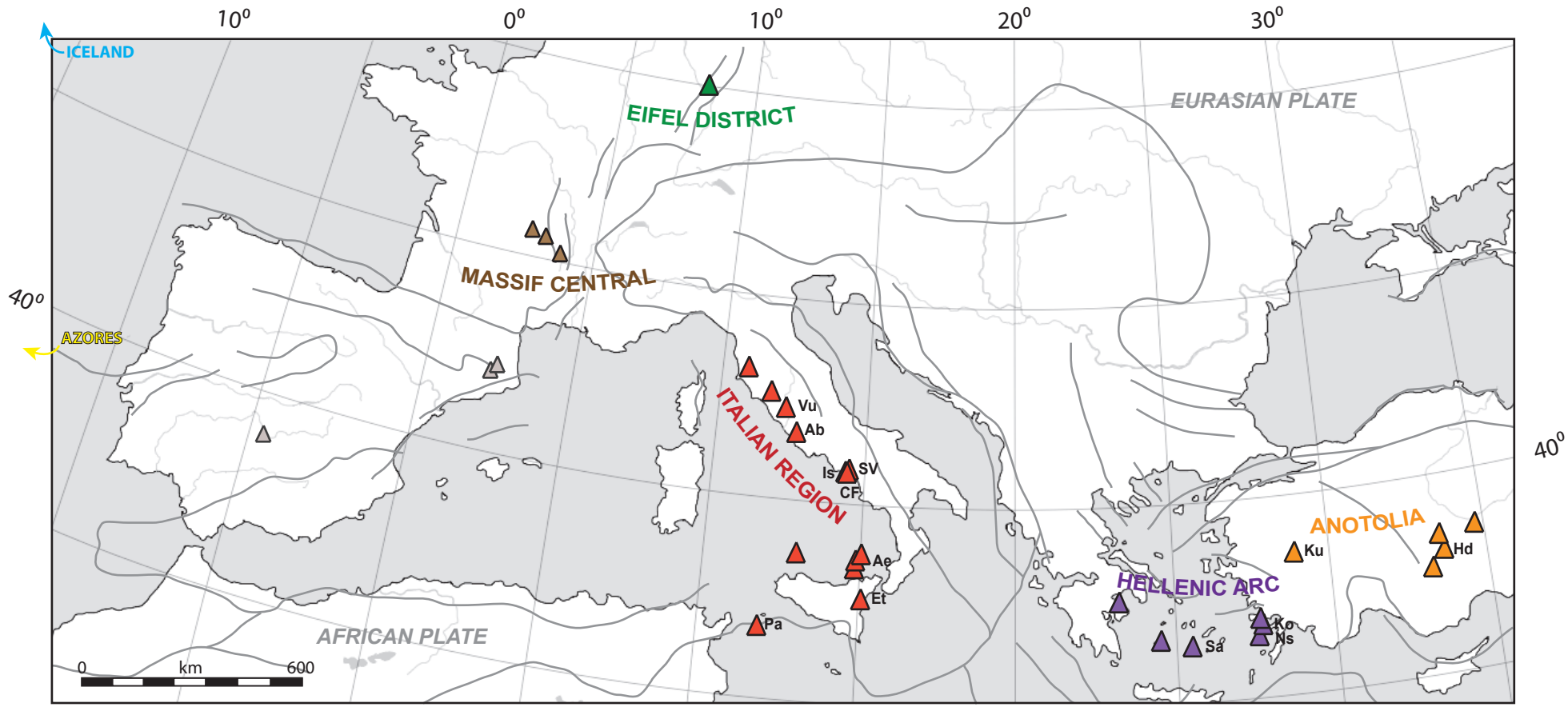

Figure 2.1 – Locations of volcanic regions known to be active during the Quaternary, minor and major fault lines also shown. For the Italian Region the following volcanoes are labelled: Vu: Vulsini Hills Ab: Alban Hills Is: Ischia SV: Somma-Vesvius CF: Campi Flegrei (Phlegrean Fields) Ae: Aeolian Islands Et: Etna Pa: Pantelleria. For the Hellenic Arc: Sa: Santorini Ko: Kos, Ns: Nisyros and Anotolia: Ku: Kula Hd: Hasan Dagi.

which are described here. Two key regions which were very active were the Campi Flegrei and Somma-Vesuvius. Ischia, Etna and Pantelleria were also active. This volcanic activity will now be briefly outlined.

The Campi Flegrei (CF) region is a major caldera forming complex that has produced several eruptions during the LLG. The earliest of these is the Santa Lucia eruption, dated via $^{40}Ar/^{39}Ar$ to around 51 ± 3 ka BP (Di Vito *et al.,* 2008). Between this eruption and the next largest (the Campanian Ignimbrite, discussed below) several eruptive events are recognised in the volcanostratigraphy by Pappalardo *et al.* (1999) and Di Vito *et al.* (2008). Many of these eruptions are likely to have had large eastward dispersals (Tomlinson *et al.,* 2012a). The largest eruption of the CF during the LLG by far was the caldera forming Campanian Ignimbrite, thought to be one of the largest eruptions that occurred during the Last Glacial within the Mediterranean (Pyle *et al.,* 2006). The Campanian Ignimbrite has been dated numerous times via $^{40}Ar/^{39}Ar$ dating to between 34–41 ka (Deino *et al.,* 1994; Watts *et al.,* 1996; Ton-That *et al.,* 2001; Lanphere, 2003; Rolandi *et al.,* 2003) although the most commonly used age is that obtained by De Vivo *et al.* (2001) who produced a very precise age of 39,280 ± 110 ($^{40}Ar/^{39}Ar$). After the CI eruption the next largest eruption was the Tufi Biancastri which is $^{40}Ar/^{39}Ar$ dated to around 18 ka BP (Pappalardo *et al.,* 1999) and which also had a large eastward dispersal (Wulf *et al.,* 2004).

Somma-Vesuvius produced at least three large eruptions during the LLG including the Verdoline (or Greenish) eruption at around 16 ka BP (Andronico *et al.,* (1995) the caldera forming Pomici di Base eruption which occurred between 20–22 ka BP (Andronico *et al.,* 1995) and the Codola eruption dating to around 25 ka BP (Guest *et al.,* 2003).

Pantelleria is known to have produced one very large eruption during the LLG, the Green Tuff which is dated to around 50 ka BP (Cornette *et al.,* 1983; Civetta *et al.,* 1988; Madhood & Hildreth, 1986). This tephra is known to have travelled very far, including into the Eastern Mediterranean (Margari *et al.,* 2007). Ischia was also active during the LLG producing several smaller eruptions between 43 to 44 ka BP recognised proximally as the Citara-Serrata-Fontana Formation (Poli *et al.,* 1987).

Hellenic Arc

The Hellenic Arc produced several widespread ash layers during the LLG including the Cape Riva (Y–2) eruption of Santorini, which proximal expression was described in detail by Druitt (1985) with the Cape Riva formed of 4 large units. Pichler & Friederich (1976) and Eriksen *et al.* (1990) both attained radiocarbon determinations from these units suggesting an eruption age of around 22 ka BP. This eruption had a very wide dispersal across the Eastern Mediterranean region both to the north and southeast (Vinci, 1987; Asku *et al.,* 2008; Wulf *et al.,* 2002; Roeser *et al.* 2012). Marine sequences within the Aegean Sea document another eruption older than the Cape Riva termed the Y–4 which is also thought to have also originated from Santorini volcano around 30 thousand years ago (Vinci, 1985) although its geographical extent appears much more limited (Asku *et al.,* 2008). The Yali (or Yali-C) tephra is also found within marine cores in this region sourcing from Yali (see Fig. 2.1). The only dates for this tephra are based upon oxygen isotope stratigraphy (Federman & Carey, 1980) suggesting an age of around ~31 ka and on astronomically tuned ages of sapropels (Smith *et al.,* 1996) suggesting an age of ~35 ka.

The Yali caps the proximal volcanostratigraphy of the volcanic Island of Nisyros and overlies two precursory eruptions; the Upper and Lower Nisyros both of which have been recognised as distally discrete tephra horizons (e.g. Vinci, 1985; Margari *et al.,* 2007). Asku *et al.* (2008) describe the age of these Nisyros layers as in flux, as various discordant ages have been determined ranging from 30 to >50 ka years.

Anotolian

The Anotolian volcanic province is located within the Eastern Mediterranean region and can be separated into two volcanic areas, the Western and Central Anatolian Volcanic Province's (the WAVP and CAVP). Much remains unknown about the Anotolian eruptive history during the LLG although Kuzucuoglu *et al.* (1998) do describe several tephra layers from sedimentary sequences that are situated in close proximity (~50 km) to the CAVP. These layers were dated indirectly between c.20 to 70 ka BP and source from various volcanoes within the CAVP. More precise $^{40}K/^{39}Ar$ ages are available for two specific eruptions from the Hasan Dag stratovolcano at 33±2 and 29±1 ka BP (Kuzucuoglu *et al.,* 1998). Multiple eruptions are also described during the period ~24–70 ka BP originating from the Gölcük volcano in the WAVP (Platevoet *et al.,* 2008).

Massif Central

The Massif Central is an intra-plate volcanic province situated in mainland northern Europe (Nowell *et al.,* 2006; see Fig. 2.1) and there is evidence of frequent volcanic activity which, although much of it probably relatively minor, most likely produced at least some tephra forming eruptions during the LLG, particularly before around 25 thousand years ago (see synthesis below) . The majority of this volcanic activity has been dated via thermoluminescence (TL) dating, which is subject to fairly large chronological uncertainties (e.g. Guérin, 1983). Two tephra layers are described proximally, the Le Fau Tephra which is dated to around 35–47 ka BP (Sanzelle *et al.,* 2000) and the La Vestide du Pal Tephra thought to have erupted between 42–52 ka BP (Guerin & Gillot, 2007) it is currently unclear if either of these tephra layers travelled a significant distance from source.

Eifel District

Like the Massif Central the Eifel District is also an intra-plate volcanic province situated in mainland northern Europe (Nowell *et al.,* 2006). The Eifel District is the source of a very large eruption which occurred just before the onset of the Younger Dryas (c.13 ka BP), the Laacher See Tephra which had a wide N–S distribution across central Europe reaching up into southern Sweden and into Italy (van den Bogaard & Schmincke, 1985; Turney *et al.,* 2006). Much less is known about the eruptive history of this region during the LLG and activity appears to have been very episodic. Two eruptions from this source have been recognised and dated to the LLG, these are the Eltviller Tuff (Semmel, 1969; Juvigné & Semmel, 1981) which has been recognised in a sequence distal from source by Antoine *et al.* (2001). The age of this tephra layer is thought to be around 18-22 ka BP on the basis of IRSL and TL datings (Zöller *et al.,* 1988; Antoine *et al.,* 2001; Bibus *et al.,* 2007). The Les Echets Tephra in contrast was first recognised more recently by Veres *et al.,* (2008) from a palaeo-record in France. This tephra is thought to date to around 42–45 ka BP and has a stratigraphical relationship with a small interstadial event potentially relating to GI-11. Veres *et al.* (2008) have suggested a volcanic source for this tephra located in the West Eifel region, perhaps relating to the formation of the Meerfelder Maar (Mertes, 1983). The

presence of this tephra layer in France could be evidence of a very large geographical distribution over Europe.

Finally electron spin resonance (ESR) and Alpha-recoil track (ART) dating from Woda *et al.* (2001) and Gögen & Wagner (2000) suggest the Germündener Maar was active some time between c.26–40 ka BP. It is however, unclear if any widespread tephra layers were generated from this activity.

Azores

The Azores is situated on the Mid-Atlantic Ridge and is formed of multiple volcanic Islands, there is evidence of large caldera forming eruptions originating from the largest Island forming the archipelago, São Miguel. These occur during the LLG with at least four large eruptions between c.40–18 ka BP many of these source from the highly active Furnas Volcano (Moore, 1991; Guest *et al.,* 1999). The distal geographic extent of tephra distribution from these eruptions remains very uncertain although they did travel into the medial-distal marine record (Huang *et al.,* 1979). And it is worth noting that there is very tentative evidence of Azores ash reaching as far east as Ireland during the Holocene (I. Matthews, *pers .comm.*).

Iceland

Iceland is also situated on the Mid-Atlantic Ridge and is currently formed of 30 active volcanic systems (Larsen *et al.,* 1999; Thordarson & Larsen, 2007). During the LLG at least 7 distal tephra layers have been recognised, largely these have been observed primarily from the Greenland Ice core record (Davies *et al.,* 2008; 2010) where very precise ages from the GRIP and NGRIP chronologies (Rasmussen *et al.,* 2006; Svensson *et al.,* 2008) can be obtained for these layers (Davies *et al.,* 2008; 2010). LLG tephra layers are also recognised from within the North Atlantic marine record (e.g. Wåstegard *et al.,* 2006). Two widely dispersed layers are the Faroe Marine Ash Zones (FMAZ) II and III which originate from the Hekla-Vatnafjöll and Grimsvötn volcanic systems and are both dated within the NGRIP ice core to 26,690 ± 390 and 38,122 ± 673 ka BP respectively (Davies *et al.,* 2008; 2010). These layers form important tie points in the INTIMATE Event stratigraphy with the FMAZ II (also known as the Fugloyarbanki Tephra) sitting at the start of GS-3 and the FMAZ III situated at the near

onset of GI-8 (Blockley *et al.,* 2012). Other tephra layers during the LLG occur at c. 27.2, 27.5, 29.1 and 30.6 ka BP and all originated from the Eastern Volcanic Zone (Davies *et al.,* 2010).

Despite their distance from the Mediterranean Region, Icelandic eruptions are worthy of consideration as both modern volcanic product (e.g. from the 2010 Eyjafallajökull eruption) and Late Quaternary Icelandic tephra (e.g. the Vedde Ash) have both been observed to have very large dispersals reaching areas as far south as northern Italy (Lane *et al.,* 2012) and in the case of the Eyjafallajökull eruption even Iberia (Revuelta *et al.,* 2012)

2.2.2 Synthesis of geochemical and age data for volcanic eruptions

In this section a synthesis of the current available dating information as well as geochemical data are synthesised. Firstly all geochemical data currently within the RESET database (this includes previously published information alongside currently unpublished RESET data) was accessed and divided into the volcanic provinces described above. This information was not defined to the LLG period alone as volcanic systems may produce similar trends over long time periods (Lowe, 2011) which are useful to observe when assessing general patterns (a more tailored LLG geochemical dataset is outlined in chapter 6). The synthesis here is shown in Figure 2.2 and general geochemical compositions will be briefly described along with an assessment of how geochemically distinctive different volcanic provinces are when compared and contrasted with a SiO_2 vs Al_2O_3 biplot to show major elements and Th vs Zr biplot for trace elements. These particular plots have been chosen because SiO_2 and Al_2O_3 often represent the two highest concentration (wt %) elements in tephra glass and are thus usually measured with the most precision, also SiO_2 is important for assessing degrees of evolution. For trace elements comparison is shown between two High Field Strength Elements (HFSEs; i.e. Zr, Nb, Th and U) as these should form uniform compositional trends that relate to magma chamber conditions (Pearce & Peate, 1995).

From Figure 2.2 it can be observed that very little data exists for the Massif Central province which appears to show a compositional range from a basaltic to trachydacite and even rhyolitic compositions. This suggests tephra from this region can be more evolved (i.e. silica rich) than has previously been suggested (Davies *et al.,* 2002; Pyne-

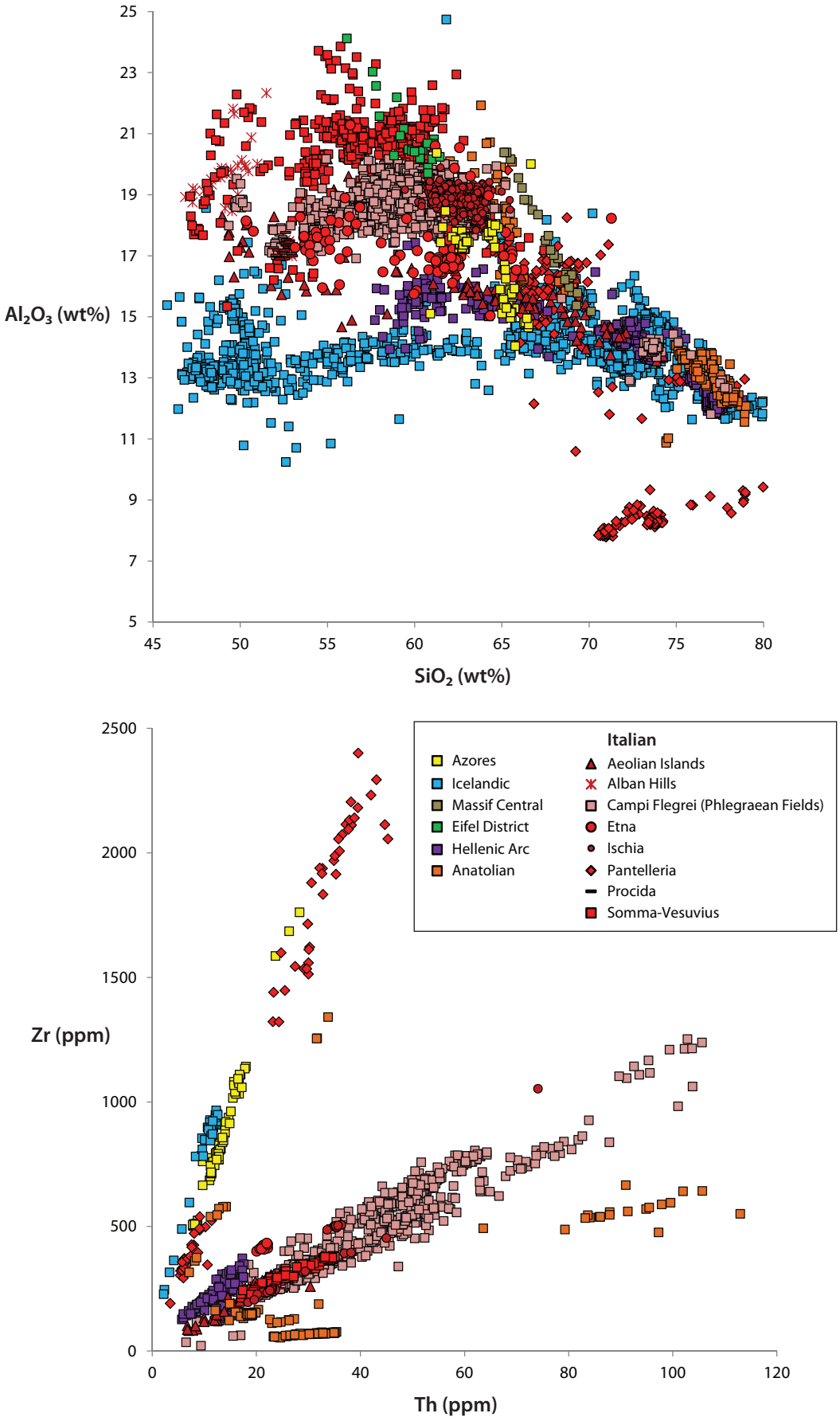

Figure 2.2 – Major and Trace element biplots of tephra layers as defined by volcanic region. Data accessed from the RESET Database (30/05/12).

O'Donnell, 2007). Unfortunately no trace element data are currently available for this region, which may allow finer distinction. Like the Massif Central only small geochemical datasets are available for the Eifel District and Azores provinces. The Eifel District geochemical data does however suggest a very distinctive geochemical fingerprint (even though only major elements are available). The Azores and Iceland both also have similar (but importantly distinguishable) geochemical trends which is perhaps unsurprising considering they both sit upon the Mid-Atlantic ridge. Anatolian region tephra layers produce both trachytic and rhyolitic compositions and this is reflected in a wide array of geochemical evolution trends which can be seen on trace elements; this is perhaps unsurprising considering the Anatolian volcanic provinces (i.e. East and Central) lie over a diverse range of geological settings. The Hellenic Arc tephra layers, in comparison, have compositions ranging from andesitic up to highly evolved rhyolites and have a more clustered trace element range than Anatolian tephra. Italian region tephra layers probably form the most detailed geochemical dataset (when trace elements are included) of any of the volcanic provinces being considered within the present study and within Fig. 2.2 geochemistry from this region has been divided into smaller individual volcanic areas which make up this highly active region. The most geochemically distinctive Italian volcanic areas are Pantelleria, Aeolian Islands, Prochida, Etna and the Alban Hills. Volcanic eruptions from Pantelleria in particular form very distinctive melts, called pantellerites, which are very geochemically distinctive on both major and trace elements. Geochemical distinction between Campi Flegrei, Ischia and Somma-Vesuvius tephra is, in comparison, more difficult to distinguish and requires more careful biplot comparison.

A data synthesis of tephra ages was also carried out for LLG for each of the volcanic provinces described above. This was done as very few tephrochronological review papers cover or focus upon the LLG timeframe in detail. For example Davies *et al.* (2002) focused upon the Last Termination (18.5-8 ^{14}C ka BP) and Narcisi & Vezzoli (1999) discuss only the very large eruptions which are known to have had a widespread distribution across the Eastern Mediterranean during the last ~500 ka BP. Also, since the publication of these papers a plethora of new tephrochronological information has become available (e.g. Wulf *et al.,* 2004; Margari *et al*., 2007). Coupled to this newly available radiocarbon calibration curves (e.g. IntCal09 and Marine09) which allow calibration of radiocarbon dates back to ~50 ka cal BP can be utilised to provide comparable calendar ages for where tephra layers are dated via this method (Reimer *et al.,* 2009).

Over 150 direct (e.g. $^{40}Ar/^{39}Ar$, $^{40}K/^{39}Ar$ ages) and indirect (e.g. radiocarbon, varve ages) dates have been collected from the literature for tephra layers spanning LLG from the regions outlined above (except for Anotolia which has very little chronological data currently available). All uncalibrated radiocarbon ages gathered have been calibrated using either IntCal09 or Marine09. Marine dates were readjusted where reservoir effects had been applied. All dates have been adjusted to a comparable cal BP (1950) min and max age range. Ages relating to eruptions or tephra layers mentioned in section 2.2.1 have been labelled. This synthesis is presented in Figure 2.3. All the synthesis references are presented in the Figure 2.3 caption. This forms the basis of the tephrochronological stratigraphy to be tested and/or expanded within this study.

2.2.3 Overview of current Mediterranean terrestrial tephrostratigraphy

As this project is concerned with extending the tephrostratigraphic framework across terrestrial palaeo-records the final part of this chapter will consider the key existing tephrostratigraphic records of this region.

Figure 2.3 (Next Page) – Dated tephra layers or large tephra forming eruptions from key volcanic regions with known or the potential for distal tephra dispersal over parts of southern Europe within the LLG (50-20 ka BP). Dates are plotted to their mean value to the y-axis with the errors also shown on the x-axis. Coupled to this other reported dates for some correlated tephra have been calculated relative to the mean 'key' date in order to show the variation in the date estimates for some tephra layers with minus figures representing younger ages and vice versa (Note that this does not represent an absolute comparison). Stratigraphic order of some of the tephra layers shown here may not be correct, since the precise order of superposition may not have been fully determined. For Italian Region tephra the Lago Grande di Monticchio record has been used to form the stratigraphical order based upon the varve chronology ages for the tephra layers (Allen *et al.,* 1999). All dates have been adjusted to a 1950 BP timescale and calibrated using IntCal09 and the Marine09 curves, a -400 yrs correction has been applied on marine radiocarbon dates. The literature sources for the tephra ages from different volcanic centres are: **Azores** (Moore, 1990; Guest *et al.,* 1999); **Iceland** (Rasmussen *et al.,* 1996; 1998; Wåstegard *et al.,* 2006; Davies *et al.,* 2008; 2010); **Massif Central** (Gillot *et al.,* 1979; Guérin & Valladas, 1980; Guérin *et al.,* 1981; Condomines *et al.,* 1982; Guérin, 1983; Raynal *et al.,* 1985; Etlicher *et al.,* 1987; de Goër de Herve *et al.,* 1993; Paste *et al.,* 1994; Sanzelle *et al.,* 2000; Guérin & Gillot, 2007); **Eifel District** (Zöller *et al.,* 1988; Gögen & Wagner, 2000; Antoine *et al.,* 2001; Woda *et al.,* 2001; Bibus *et al.,* 2007; Veres *et al.,* 2008); **Italian Region** (Aleisio *et al.,* 1976; Cornette *et al.,* 1983; Civetta *et al.,* 1988; Lirer *et al.,* 1991; Deino *et al.,* 1994; Andronico *et al.,* 1995; Oris *et al.,* 1996; Watts *et al.,* 1996; Pappalalardo *et al.,* 1999; De Vito *et al.,* 2001; 2008; Ton-That *et al.,* 2001; Siani *et al.,* 2001; 2004; Buccheri *et al.,* 2002a,b; Rolandi *et al.,* 2003; Lanphere, 2003; Sulpizio *et al.,* 2003; Munno & Petrosino, 2004; Wulf *et al.,* 2004; 2008; Anastasakis & Pe-piper, 2006); **Hellenic Arc** (Pichler & Freidrich, 1976; Federman & Carey, 1980; Keller *et al.,* 1989; Eriksen *et al.,* 1990; Limberg & Varekamp, 1991; Smith *et al.,* 1996; Margari *et al.,* 2007; Aksu *et al.,* 2008). Also shown is the volcanic sulphate concentrations from the GISP2 core (Zielinski *et al.,* 1996).

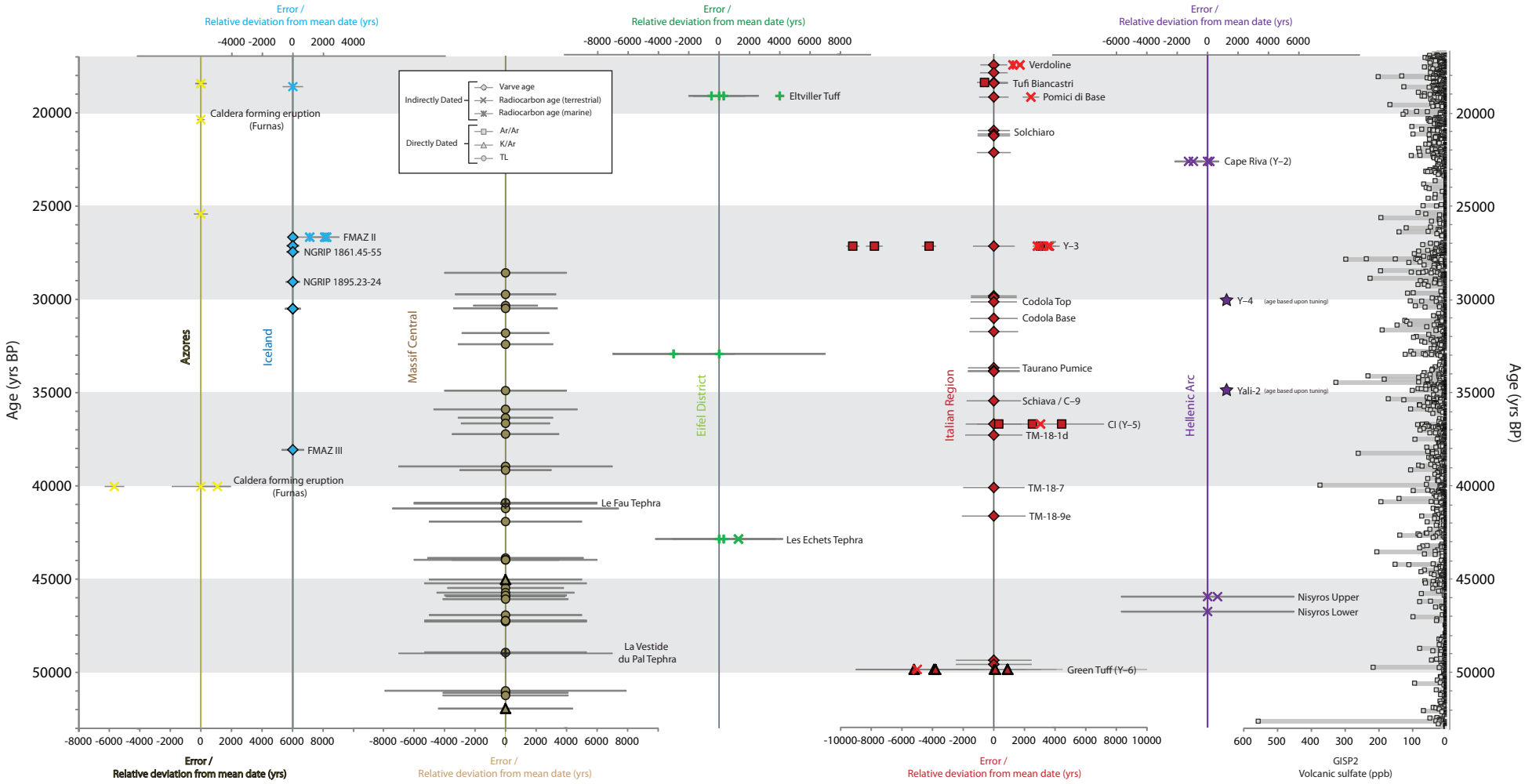
Error /
Relative deviation from mean date (yrs)
Age (yrs BP)
Azores
Iceland
Massif Central
Eifel District
Italian Region
Hellenic Arc
Indirectly Dated
Varve age
Radiocarbon age (terrestrial)
Radiocarbon age (marine)
Directly Dated
Ar/Ar
K/Ar
TL
Caldera forming eruption (Furnas)
FMAZ II
NGRIP 1861.45-55
NGRIP 1895.23-24
FMAZ III
Caldera forming eruption (Furnas)
Le Fau Tephra
La Vestide du Pal Tephra
Eltviller Tuff
Les Echets Tephra
Verdoline
Tufi Biancastri
Pomici di Base
Solchiaro
Y–3
Codola Top
Codola Base
Taurano Pumice
Schiava / C–9
CI (Y–5)
TM-18-1d
TM-18-7
TM-18-9e
Green Tuff (Y–6)
Cape Riva (Y–2)
Y–4 (age based upon tuning)
Yali-2 (age based upon tuning)
Nisyros Upper
Nisyros Lower
GISP2
Volcanic sulfate (ppb)

Lago Grande di Monticchio, Italy

Lago Grande di Monticchio (LGdM) is a maar lake in Southern Italy located 120 km east of Naples and is recognised as one of the most comprehensive records of tephra layers in the Mediterranean region (Bourne *et al.,* 2010). LGdM is one of two maar lakes that formed during a phreatomagmatic eruption of Monte Vulture, dating to around 132 ± 12 ka (Wulf *et al.,* 2004). The sedimentary sequence has the advantage of having a varve-based chronology available (Brauer *et al.,* 2000). During the LLG 25 discrete ash layers are currently recognised (see Table 2.1), most of which have been geochemically analysed (Wulf *et al.,* 2004; 2006; 2008). The location of the sequence 120 km east of the Phlegraean Fields makes it an ideal medial-distal archive for recording eruptive events as it is on the dispersal axis of most eruptions from this volcanic region.

The LGdM record of volcanism during the LLG originates primarily from Campi Flegrei, but eruptions are also thought to be present from the Alban Hills, Ischia, Etna, Somma-Vesuvius and Procida (Wulf *et al.,* 2004; 2006; 2008; *pers. comm.*) which are highlighted in Table 2.1. These tephra layers are labelled TM (Tephra Monticchio) and numbered on the basis of stratigraphy (e.g. TM-18 underlies TM-8). No tephra layers from volcanic provinces other than the Italian Region have been detected in the LGdM record.

Table 2.1 – LGdM tephra for the LLG with varve ages, and suggested sources and correlations also listed. References presented.

Tephra Coding	***Varve Age***	***Source***	***Volcanic Eruption***	***Reference***
TM-12	17,560 ± 880	SV	Verdoline	Wulf *et al.* (2004, 2008)
TM-12-1	17,980 ± 900	ET	Ante-Biancavilla ?	Wulf *et al.* (2008)
TM-12-2a	18,500 ± 920	CF	Tufi Biancastri ?	Wulf *et al.* (2008)
TM-12-2b	18,540 ± 930	CF	Tufi Biancastri ?	Wulf *et al.* (2008)
TM-13	19,280 ± 960	SV	Pomici di Base	Wulf *et al.* (2004, 2008)
TM-14a	21,070 ± 1050	PR	Solchiaro CD1-b	Wulf *et al.* (2004, 2006)
TM-14b	21,260 ± 1060	PR	Solchiaro, white facies	Wulf *et al.* (2004, 2006, *in review*)
TM-14-1	21,350 ± 1070	IS	Faro di Punta Imperatore?	Wulf (*pers. comm.*)
TM-14-2	22,250 ± 1110	AB?	—	Wulf (*pers. comm.*)
TM-15	27,260 ± 1360	CF	Y-3	Wulf *et al*. (2004, 2006, *in review*)
TM-17a	29,920 ± 1500	CF	-	Wulf *et al*. (2004) Wulf (*pers. comm.*)
TM-17b	30,000 ± 1500	CF	-	Wulf *et al*. (2004) Wulf (*pers. comm.*)
TM-16a	30,240 ± 1510	SV	Coldola Top	Wulf *et al*. (2006)
TM-16b	31,120 ± 1560	SV	Codola Base	Wulf *et al*. (2006, in review)

TM-17bc	31,830 ± 1590	AB	Albano Unit 7	Wulf *et al*. (2004, in review)
TM-17c	33,770 ± 1690	CF	Taurano Pumice	Wulf *et al*. (2004) Wulf (*pers. comm.*)
TM-17d	33,920 ± 1700	CF	Taurano Pumice	Wulf *et al*. (2004) Wulf (*pers. comm.*)
TM-17e	33,360 ± 1700	CF	Taurano Pumice	Wulf *et al*. (2004) Wulf (*pers. comm.*)
TM-17-2	35,530 ± 1780	SV	Schiava, C-9	Wulf *et al*. (2006) Wutke (*submitted*)
TM-18	36,770 ± 1840	CF	Campanian Ignimbrite	Wulf *et al*. (2004, 2006, *in review*)
TM-18-1d	37,360 ± 1870	CF	SMP1-a	Wulf *et al*. (2006) Wutke (*submitted*)
TM-18-4	38,600 ± 1930	CF	—	Wulf (*pers. comm.*)
TM-18-7	40,170 ± 2010	PR ?	—	Wulf (*pers. comm.*)
TM-18-9e	41,690 ± 2090	IS	Citara	Wulf *et al.* (2006)
TM-18-12b	49,410 ± 2470	CF	Santa Lucia, C-15	Wulf *et al*. (2006)

Sources: AB: Alban Hills, CF: Ischia, ET: Etna, CF: Campi Flegrei, SV: Somma-Vesuvius, PR: Procida.

San Gregorio Magno Basin, Italy

The San Gregorio Magno basin is located in the Southern Apennines and records evidence of four eruptions during the LLG. These are all present as visible sandy layers between 20 to 60 cm in thickness and are presented in Table 2.2 (Munno & Petrosino, 2007). Geochemical analysis of these horizons allowed correlation of these tephra layers to the LGdM sequences and associated volcanic eruptions (shown in Table 2.2).

Table 2.2 –Depth, source and correlation to LGdM layer and volcanic eruptions for LLG tephra layers in the San Gregorio Magno Basin (Munno & Petrosino, 2007).

Tephra Coding	***Depth (cm)***	***Source***	***Correlation to LGdM layer***	***Volcanic Eruption***
S20	5.80–6.00	SV	TM-12	Verdoline
S19	6.65–6.80	CF	TM-15	Y–3
S18	6.80–7.00	SV	TM-16	Codola
S17	7.90–8.50	CF	TM-18	Campanian Ignimbrite

Sources: CF: Campi Flegrei, SV: Somma-Vesuvius.

Lake Ohrid, Albania and Macedonia

Many tephrostratigraphic studies have been carried out on Lake Ohrid during the LLG, including cryptotephra analyses (Caron *et al.,* 2010; Vogel *et al.,* 2010) and it forms a key terrestrial record for picking up Italian tephra layers with an eastward dispersal that cross the Adriatic. In total six tephra layers have been identified from the Ohrid sequence during the LLG (see Table 2.3) which have been geochemically analysed and

correlated to three LGdM layers relating to the Verdoline, Coldola and CI eruptions as well as a tephra not found within LGdM, the Green Tuff of Pantelleria.

Table 2.3 –Volcanic source, correlation to LGdM tephra layer and volcanic eruption for LLG tephra layers in Lake Ohrid cores Co1202 and JO 2004 (Caron *et al.,* 2010; Vogel *et al.,* 2010).

Tephra Coding (Co1202)	***Tephra Coding (JO 2004)***	***Source***	***Correlation to LGdM layer***	***Volcanic Eruption***
OT0702-4	JO-187	CF	TM-15	Verdoline (Greenish)
OT0702-5	–	SV	TM-16	Codola
OT0702-6	JO-244	CF	TM-18	Campanian Ignimbrite
OT0702-7	–	PA	–	Green Tuff

Sources: CF: Campi Flegrei, SV: Somma-Vesuvius, PA: Pantelleria

Tenaghi Philippon, Greece

Tenaghi Philippon has been studied for its tephrostratigraphy in two studies (St Seymour *et al.,* 2004; Müller *et al.,* 2011) both of which describe two visible tephra layers within the LLG timeframe the Cape Riva tephra and the CI, both of which form discrete visible layers (between 2 to >25 cm in thickness respectively; see Table 2.4). Tenaghi Philippon therefore records ashfall from more than one volcanic centre, the Italian Region and the Hellenic Arc. Thus far only visible layers have been researched in the Tenaghi Philippon basin, which would seem likely to contain additional cryptotephra layers.

Table 2.4 –Depth, source and correlation to LGdM layer and volcanic eruption for LLG tephra layers in the Tenaghi Philippon basin (St Seymour *et al.,* 2004; Müller *et al.,* 2010).

Tephra Coding (Ph cores)	***Tephra Coding (TP 2005)***	***Source***	***Correlation to LGdM layer***	***Volcanic Eruption***
Ph-2	TP 7.61	SA	–	Cape Riva
Ph-3	TP 12.87	CF	TM-18	Campanian Ignimbrite

Sources: CF: Campi Flegrei, SA: Santorini

Lesvos, Greece

Like Tenaghi Philippon only visible tephra layers have been analysed in the Lesvos sequence (Margari *et al.,* 2007), located further to the east than Tenaghi Philippon. Six tephra layers are described from the Lesvos sequence which covers the entirety of the LLG (See Table 8.4). Four of these layers originate from volcanic centres located in the Hellenic Arc such as Santorini (e.g. the Cape Riva) and Nisyros (Upper and Lower Nisyros) and two tephra layers originating from the Italian Region, the Green Tuff and CI.

Table 8.5 –Depth, source and correlation to LGdM layer and volcanic eruption for LLG tephra layers in Lesvos (Margari *et al.,* 2007).

Tephra Coding	***Depth (cm)***	***Source***	***Correlation to LGdM layer***	***Volcanic Eruption***
ML-1	1.80–1.82	SA	–	Cape Riva
ML-2	5.50–5.63	CF	TM-18	Campanian Ignimbrite
ML-3	10.33–10.50	NI	–	Upper Nisyros
ML-4	11.89–12.00	NI	–	Lower Nisyros
ML-5	24.21–24.25	PA	–	Green Tuff
ML-6	28.41–28.42	–	–	–

Sources: SA: Santorini, CF: Campi Flegrei, NI: Nisyros, PA: Pantelleria.

2.2.4 Summary

The tephrostratigraphy from the sites described above are summarised in Figure 2.4, with tephrocorrelations between sites shown, site specific tephra labelling as well as related volcanic eruption. Sometimes where no proximal equivalent may be found for a distally preserved tephra layer these are known by their distal name (e.g. Y–3) in order to avoid confusion within Figure 2.4 these distal names are shown in brackets (sometimes alongside the associated proximal eruptions where names are used interchangeably within the literature).

It is clear that the dispersal of volcanic ash to the west of Italy remains poorly understood as it does also to the north. Clearly tephra layers which currently have very large geographic distributions will form key targets within this investigation. These include the Cape Riva, Y-3, CI and the Green Tuff. The methods applied within this study will be outlined in the next chapter before the study sites chosen to meet the aims of this study are described and discussed in Chapter 4.

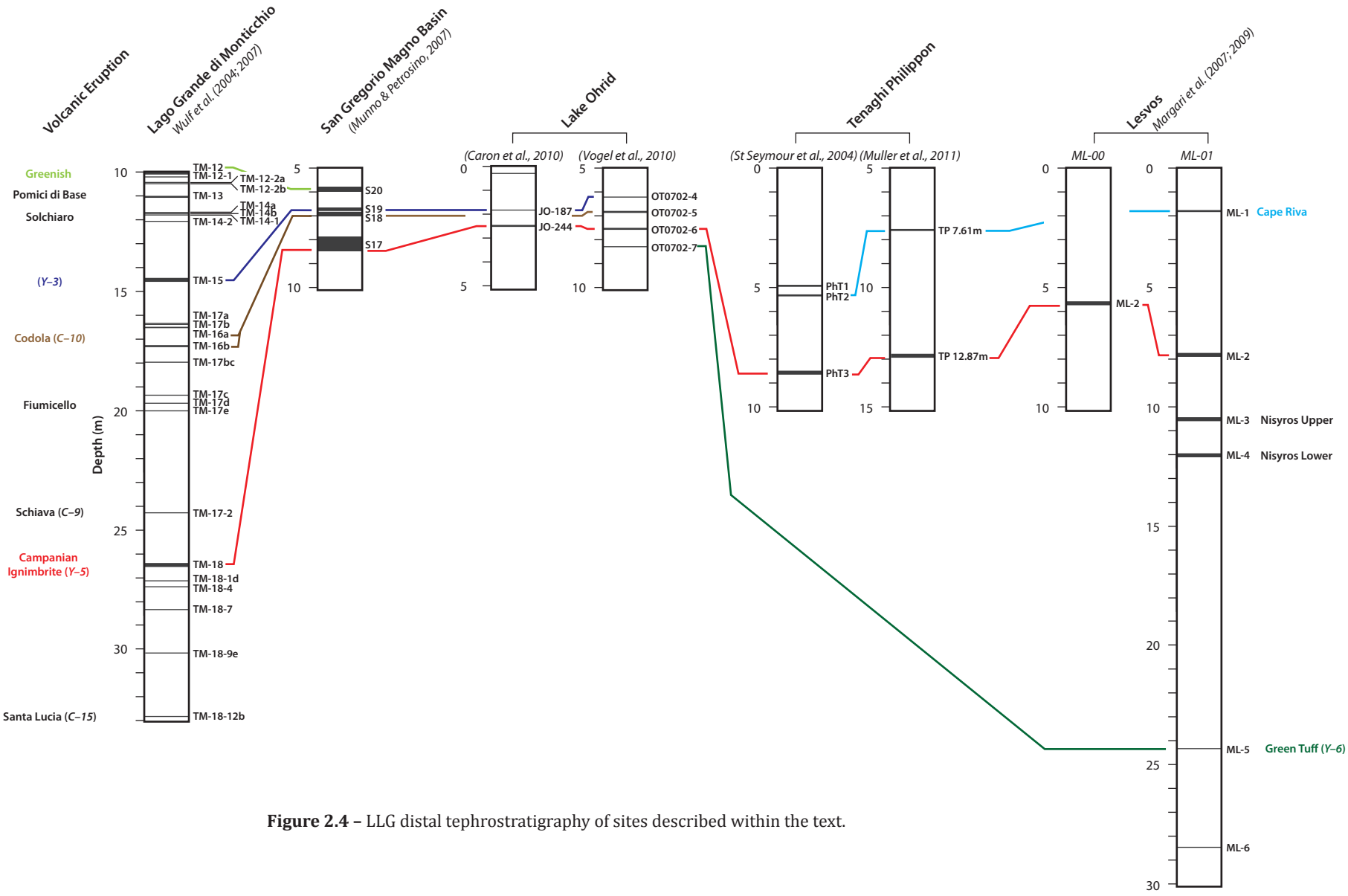

Figure 2.4 – LLG distal tephrostratigraphy of sites described within the text.

3.0 METHODS

3.1 Field Methods

3.1.1 Assessment of core quality

As all cores worked on within this study were previously recovered and stored sometimes for decades, and often already heavily worked upon or sub-sampled, an assessment of sediment quality was carried out on all cores prior to further sub-sampling (see Table 3.1). This was to ensure that newly taken samples could be related to the original worker's depths/code system to guarantee a good correspondence between previous palaeo-proxy work and the new tephrostratigraphic investigations being carried out within this project. Sites where significant core shrinkage (5-10%) had taken place were still deemed suitable only if the original proxy sample holes (with depths) were still visible and could be used to calibrate for shrinkage and hence pinpoint exact correspondence between the new analyses and pre-existing proxy records.

Table 3.1 – Description of the qualitative assessment criteria and scoring system undertaken:

Criteria	**Score system**		
Storage conditions	Freezer	Cold store	No cooling
Core moisture	Dried out	Some moisture	Still moist
Sediment softness	Hard	Firm	Soft
Core shrinkage	Very severe (>5%)	Minimal (<1%)	None (0%)

Overall core sample quality:	**Unsuitable for sub-sampling/work.**	**Acceptable**	**Good**

3.1.2 Sediment description

Fine sediment detail is usually best observed when core material is first extracted and still moist. Because of this and the often very dry condition of the older cores worked upon in this study, the initial investigator's sediment descriptions were primarily used

throughout this investigation. Basic notes on core condition and cracks, etc. were taken at the time of sub-sampling.

3.1.3 Sediment sub-sampling methods

Most sub-sampling took place in various laboratories across Europe and because the cores could not be removed to RHUL, sub-sampling both of the 'scan' samples (5 or 10 cm lengths) and 1 cm high resolution sub-samples was conducted simultaneously in order that, in the cases where tephra was found, high-resolution work could be carried out immediately and with accuracy. This approach avoids the potential problem of mis-sampling during subsequent further work, something that is particularly problematic if different persons are involved. In the case of moist/soft sediments, L-channels were taken where possible which enabled further sub-sampling back in the RHUL laboratory.

All sub-sampling was undertaken on sediment surfaces that were meticulously cleaned with a scalpel. All sampling equipment was washed thoroughly with deionised water in-between each sub-sample. Slightly differing sub-sampling techniques were employed for different sites depending upon the sediment type and condition (see Table 3.1 above).

3.2 Laboratory Methods

3.2.1 Sediment storage

On return to the RHUL laboratories samples were further sub-sampled (if required), logged into the laboratory records system and stored in the RHUL Geography Department cold store at c.5°C until required (except for the samples obtained from the sites which had already been kept at room temperature for many years).

3.2.2 Contamination protocols

In distal tephrochronology, any small amount of tephra contamination can lead to unnecessary further lab work and more importantly erroneous results. Thus great care was taken to try and limit any potential contamination when working:

- All sediment preparation was performed under a laminar flow cabinet and all work surfaces were cleaned before use to minimise the contamination risk.
- Detailed log books are present in all labs and records of all work undertaken is mandoratory, this enables extra care to be exercised when working in a laboratory where tephra-rich core materials had previously been handled. This also may allow a suspected contamination 'event' to be traced to source.
- The use of an 'extra-clean' tephra laboratory which is reserved only for sites with low tephra content is either suspected or detected during the scan phase.
- Multiple filtering of sodium polytungstate (SPT) through very fine sieve sizes (see section 3.3.1 below).
- Regular robust cleaning of all the laboratories.

3.3 Tephra Extraction and Identification

3.3.1 Extraction of tephra shards

Numerous techniques have been employed to detect cryptotephra within sedimentary records. These techniques utilise both direct (e.g. extraction of volcanic glass) and indirect (e.g. magnetic signals) approaches and the relative advantages and limitations of each method are outlined in Table 3.2.

Increasingly however the most widely used method is that advocated by Turney *et al.* (1997), Turney (1998) and Blockley *et al.* (2005) and involves a stepped density separation using the inert heavy liquid sodium polytungstate ($Na_6(H_2W_{12}O_{40})H_2O$; Plewinski & Kamp, 1984). Firstly a 'cleaning' float (specific gravity of 1.98 g/cm^{-3}) is performed to remove organics and diatoms, and then an 'extraction' float (specific gravity of 2.55 g/cm^{-3}) is carried out to separate the tephra shards from the heavier minerogenic material. The main reasons this method was chosen are as follows:

Table 3.2 – Summary of the range of techniques employed to detect and/or extract cryptotephra layers.

Technique	Principle/s	Advantages	Limitations	Reference/s
Slide mounts	Creating slide 'smears' which are then scanned for tephra shards	No lab set up is required.	Very time consuming to analyse; all material has to be scanned as there is no refinement stage.	Griffiths (2001)
Magnetic susceptibility peaks	Tephra layers often include mineral suites which have a distinctive magnetic susceptibility signal compared to sediment background.	Not as time consuming compared to other techniques. Non-destructive.	Does not detect all cryptotephra layers. False positives also common.	Calanchi *et al.* (1998); Abbott (2005); U Muller (*pers. comm.*)
Magnetic Separation	Method for extracting glass shards that are high in iron content (e.g. basaltic glass).	Enables extraction of high iron content shards from minerogenic sediments.	Only extracts high iron content glass; time consuming.	Froggatt and Gosson, 1982; Mackie *et al*, (2002); Davies *et al*. (2005)
Removal of organic component via combustion	Removal of any organic component via combustion (at 550-650°C). This allows remaining material to be mounted and scanned for cryptotephra.	Relatively quick method as it can avoid the need for further refinement stages. Preserves all tephra glass densities (e.g. basaltic and rhyolitic)	Only effective on highly organic material (c.95-99%). The high temperatures required for combustion has been shown to alter tephra glass chemistry.	Dugmore *et al.* (1992); Dugmore *et al.* (1995)
Removal of organic/biogenic silica component via chemical treatment	Using chemicals such as nitric acid or NaOH to remove organic or biogenic materials.	Can remove biogenic silicates which often impede tephra identification. Effective on higher organic material.	Use of reactive chemicals has been shown to alter glass geochemistry.	Dugmore (1989); Dugmore *et al.* (1995); Rose *et al*. (1996) Pilcher & Hall (1992); Chambers *et al*. (2004)
Heavy liquid density separation	Allows enumeration of glass shards via a stepped density separation using heavy liquids.	Enables extraction of tephra glass with much less exposure to reactive chemicals or temperatures. Also effective on all sediment types (e.g. higher organic and very minerogenic).	Time consuming. Glass with higher densities (e.g. with large mineral inclusions and high in iron) may not be extracted.	Pilcher & Hall (1992); Turney *et al*. (1997); Turney (1998); Blockley *et al.* (2005)

Table 3.2 (Cont)

Light reflectance and luminescence properties	Uses the unique light properties of volcanic glass against background signal.	Relatively fast technique and non-destructive.	Untested on very small cryptotephra shard concentrations. Only suitable on peat?	Caseldine *et al*. (1999)
Sulphate peaks	Volcanic eruptions produce sulphates which can be recorded in ice cores and used to locate coeval tephra.	Non-destructive, allows fast pinpointing of possible tephra shards.	Only used within ice core contexts; Sulfate peaks do not always occur alongside tephra shards.	Dunbar & Kurbatov (2011) Davies *et al.* (QRA Meeting Poster, 2009)
Identification within thin section	Identifying cryptotephra within thin section.	Allows a detailed micromorphological analysis (at micron scales) of cryptotephra within a sediment package. Useful for detecting tephra reworking and 'input' event.	Can miss very small cryptotephra layers. Very time consuming.	Wulf *et al*. (2004); A. MacLeod and I. Matthews (*pers. comm.*)

- It extracts a high percentage yield of the tephra shards present (see Blockley *et al.,* 2005) increasing the chances that tephra shards present within the sediment will be detected
- It does not involve the use of more reactive chemicals which can alter tephra shard geochemistry (Dugmore, 1989)
- It is applicable to a wide array of unconsolidated sediments types
- It can be used with highly organic material (e.g. peats) if an ashing stage is carried out first to remove organic materials.

As with any method there are disadvantages, the key one being that of which is this method will potentially not extract glass shards with a higher specific gravity than the optimal SPT densities used, such as basaltic glass, which have high iron content or glass shards rich in mineral inclusions. Despite this draw-back the specific gravity values cited above have been carefully tested by Blockley *et al.* (2005) to show optimal extraction of the majority of tephra shards encountered in several European volcanic sources (e.g. Icelandic, Italian and Eifel).

The final procedure followed is an adaptation of that outlined in Blockley *et al.* (2005) and is shown as a step diagram in Fig. 3.1. Once extracted samples were mounted onto slides for analysis (see section 3.3.3). Samples were sieved at >125μm and then at either 25μm or 15μm. 25μm is commonly used for cryptotephra studies as a smallest sieve size (Blockley *et al.,* 2005) although some researchers do utilise smaller sieve fractions to maximise shard numbers (e.g. 15μm and smaller; e.g. Kuehn & Froese, 2010). Using these smaller particle size ranges does however start to increase overall analysis time, also smaller shards are harder to geochemically analyse due to minimum spot sizes (see section 3.4). Because of this the smaller 15μm sieve was only used on sites very distal from volcanic sources and there typical dispersal axis's (e.g. sites in Spain).

3.3.2 Extraction of tephra shards for geochemical analysis

The stepped density separation extraction technique described above was also used when extracting shards for geochemical analysis, but avoiding the ashing step (step 4, see Fig. 3.1) as exposure of glass shards to high temperatures is known to alter the chemistry (Dugmore *et al.,* 1995). It was also used on visible tephra layers as it helps to separate the purer vitreous tephra from any associated volcanic minerogenic

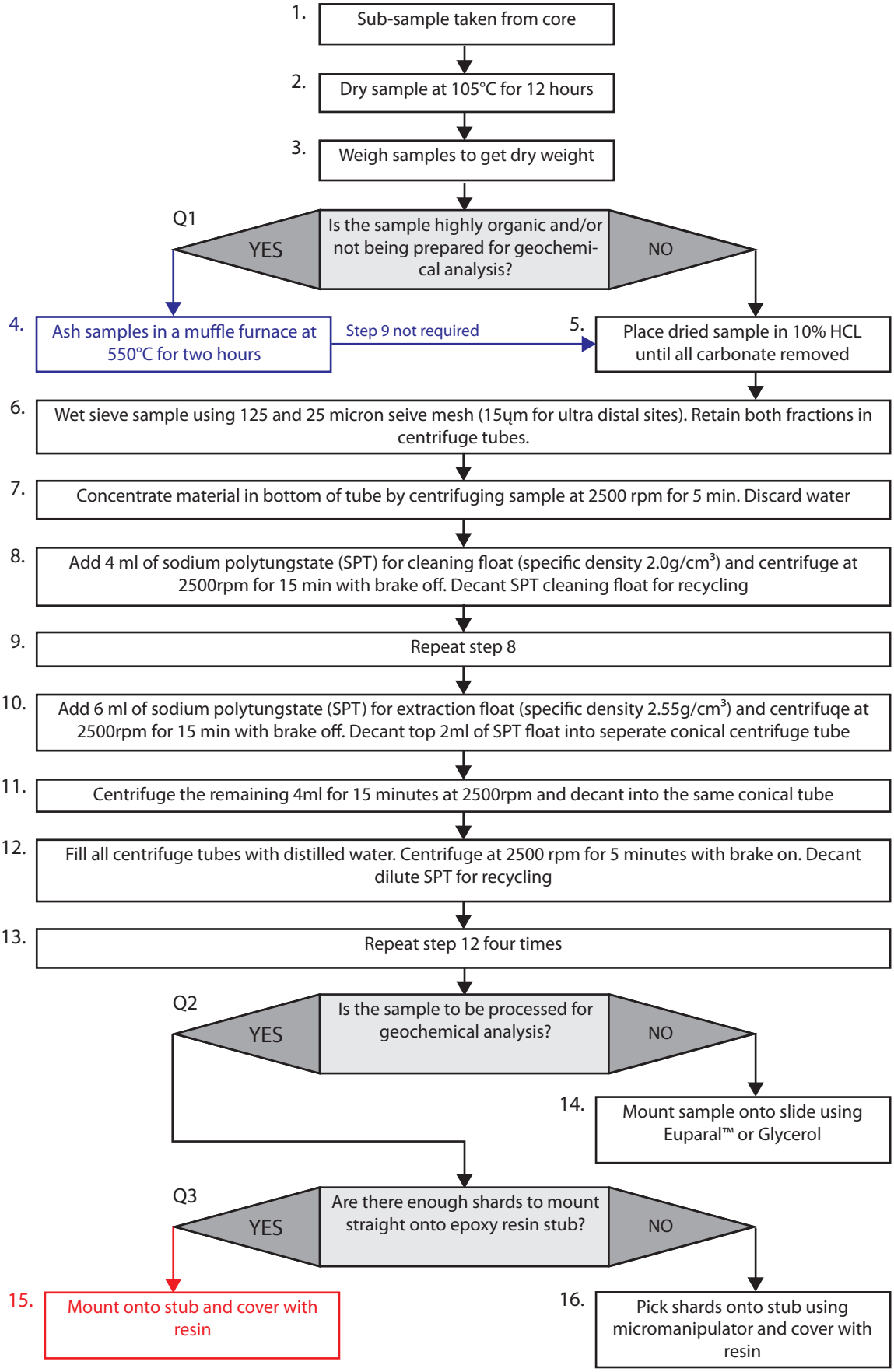

Figure 3.1 – Flow diagram of stepped flotation method adopted in this study (adapted from Blockley *et al.*, 2005).

material. Figure 3.1 and section 3.4.1 provide more details on procedures for preparing tephra shards for geochemical analysis.

3.3.3 Tephra analysis by optical microscopy

Tephra slides were analysed using an Olympus CX-41 binocular transmitted light microscope with cross polarising filters (also known as Nicols) and x10, x40 and x100 magnification objectives. The x10 magnification lens was found to be optimal for scanning for tephra shards whereas the x40 and x100 objectives were useful for checking both less certain tephra shards and morphological features in greater detail. The whole extracted sample residue was scanned, on multiple slides where necessary. Extensive use of the Royal Holloway tephra reference collection was undertaken in order to learn the main visual characteristics and optical properties of a wide variety of tephra layers from several volcanic sources. Key distinguishing features of shard morphologies are shown and described in Fig. 3.2.

Tephra shard optical analysis is subjective, this is demonstrated in Table 3.3 where three slides were recounted for total tephra amounts at intervals of 3 months, note how counting error increases as tephra concentrations increase. Positive identification of tephra shards can be challenging due to the presence of tephra 'mimics' such as biogenic silica and other minerals which are often not cleansed out during the stepped density separation due to them having a similar density to glass shards (Sedov *et al.,* 2003). Also physical and chemical weathering of tephra shards can hamper identification (see Fig. 3.2).

Table 3.3 – Results of recounting three tephra slides with different tephra concentrations over 3 month intervals.

	Nov 2010	**March 2011**	**August 2011**	**Standard deviation**
Slide x	15	15	15	0
Slide y	389	371	380	9
Slide z	1328	1263	1314	34.21

One effective way of distinguishing between tephra shards and similar non-tephra minerals is by using cross-polarised light which will cause anything with a crystalline structure (anisotropic) to show birefringence colours and 'glow'. This is useful as glass

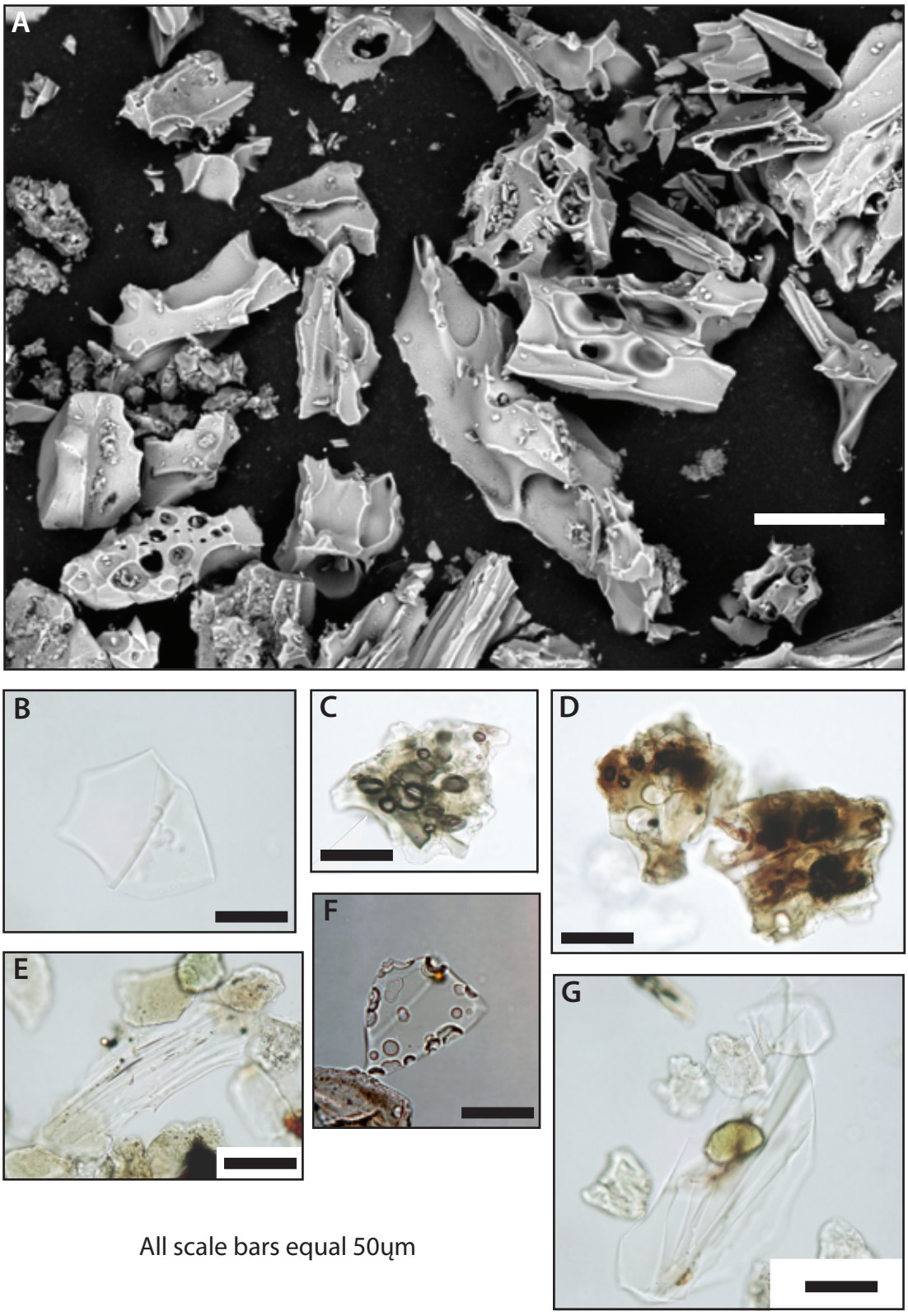

Figure 3.2 – SEM images and microphotographs under transmitted light of tephra shards. (**A**) SEM image of multiple tephra shards from the Campanian Ignimbrite tephra. The shards present are mostly 50-125µm in length and are blocky with both planar and curviplanar intersecting surfaces, note also the finer grained volcanic material sticking to the surfaces of the coarser ash grains. There are examples of both well and poorly developed spherical and ovoid vesicles some of which are showing coalescence and many containing fillings (probably made up of smaller shard fragments and crystallites). A few lithic fragments are also present. (**B**) A platy shard with curviplanar fracture surfaces. (**C**) A blocky shard with a high vesicularity and containing many mineral inclusions. (**D**) Two brownish shards with both enclosed and broken spherical and ovoid vesicles. (**E**) An elongate highly fluted shard. (**F**) Post deposition alteration features on a platy shard due probably to geochemical processes. (**G**) A fluted shard.

is isotropic and will 'extinguish' (appear black) under cross-polarised light (see Fig. 3.3). It is worth noting that even under cross-polarised light the outside edge of tephra shards can still sometimes be seen to glow slightly, which may be due to weathering or hydration of the glass. Distinguishing biogenic silicates (e.g. phytoliths and diatoms) from tephra via optical analysis can be far more challenging, firstly, because they are isotropic like glass shards, and secondly they often share similar morphological features to tephra shards (especially when weathered or degraded). In these cases using the refractive index (RI; see Nesse, 2000) of the tephra and non-tephra particles can be a useful way of distinguishing between them (Matthews, 2003; 2009; Enache and Cumming, 2006). Biogenic silicates have much higher SiO_2 contents (95-98% wt) when compared to tephra which is c.42-77% wt SiO_2, the remainder of the composition being formed of metallic elements (K, Na, Fe etc.). Due to these geochemical differences biogenic silicate has a maximum RI of 1.47 and tephra a minimum RI of 1.485 (Matthews, 2009). Using a mounting media that spans these RI values thus allows optical distinction (via subtle colour differences) between glass and non-glass material, which is aided by use of the Becke line method (see Enache and Cumming, 2006).

A number of different mounting media have been used in cryptotephra studies including Naphrax® (RI = 1.7), Canada balsam (RI = 1.55), Euparal™ (RI = 1.483) and Glycerol (RI = 1.475). In this study, use of Euparal™ and Glycerol was preferred, firstly because they have RI indices between 1.47 and 1.485, optimal for optical distinction between biogenic silicate and tephra (see above). Secondly, they allow tephra glass with lower RIs to be seen much more readily (e.g. many Italian tephra shards) than can be achieved using mounting media such as Canada balsam, which is better for distinguishing volcanic glass with higher SiO_2 values (see Fig. 3.4).

3.3.4 Quantification of Cryptotephra

There are many techniques available for the quantification of non-visible tephra concentrations including absence/presence data (e.g. Dunbar & Kurbatov, 2011), vertical thickness (Wulf *et al.,* 2004), relative abundance scales (e.g. Austin *et al.,* 2012), measurement of tephra shards per volumetric space (e.g. tephra shards/cm^3; Pyne-O'Donnell *et al.,* 2007; 2008) and also tephra shards estimated against sample weight, wet or dried (e.g. tephra shards/g; Brendryen *et al.,* 2010).

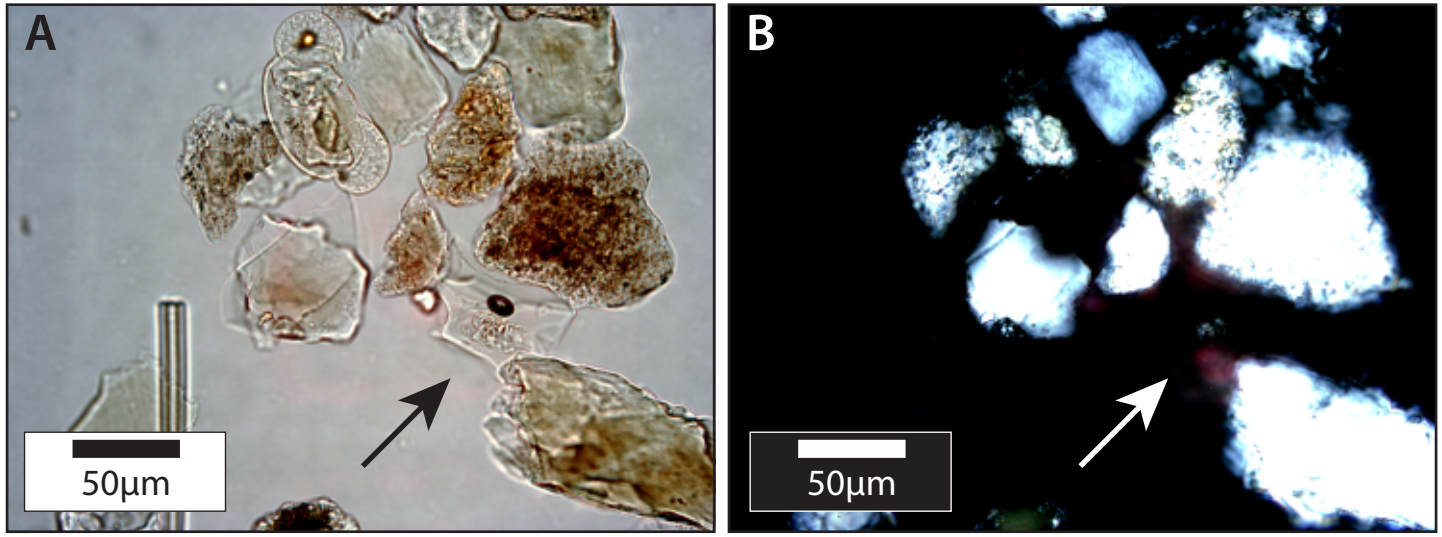

Figure 3.3 – The same microphotograph of a tephra shard under (**A**) normal transmitted light and (**B**) Cross-polarised light. Note how the minerals above the tephra shard show strong birefringence and 'glow'. In comparison the tephra shard highlighted, and also an elongate phytolith and pollen grain (*Pinus*), extinguish as they are all isotropic.

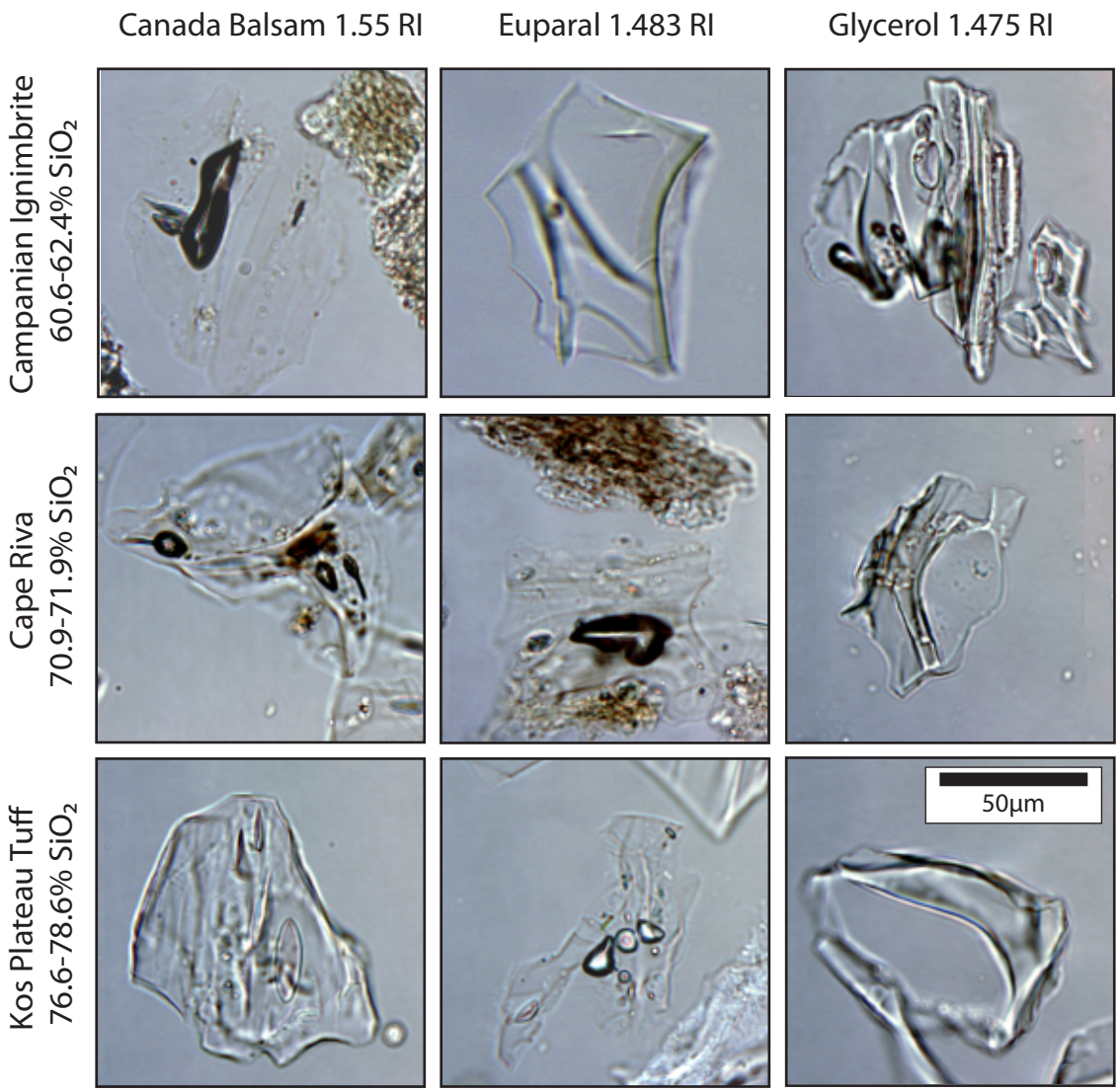

Figure 3.4 – Microphotographs of tephra shards from three different volcanic eruptions (the CI, Cape Riva and Kos Plateau Tuff) which have differing SiO_2 concentrations (presented as normalised values here) mounted in three different media. Note how the less SiO_2 rich CI tephra shard is less clear in Canada Balsam with very faint edges and only the vesicle making the shard apparent. The rhyolitic Cape Riva and Kos Plateau Tuff glass shards are far clearer in Canada Balsam due to higher SiO_2 contents. This situation is reversed when the samples are mounted in Euparal™ with the CI glass shard edges becoming far clearer (note also the green colour produced). The Cape Riva is also visible though slightly fainter, the KPT becomes very faint although the edges are still discernible. The tephra all look distinguishable within glycerol, however as this mounting media is not permanent Euparal™ was preferred during the course of the research. The Cape Riva sample was from Tenaghi Philippon, Greece (7.59m), the CI from Lesvos, Greece (ML-2) and the KPT from LC-21, a marine core situated in the Aegean (12.465m; sample supplied by C. Satow).

In this study the total tephra shards were measured against dry weight, because water content can be highly variable between samples. This procedure is relatively straightforward: it allows detailed quantification of shard numbers, vertical thickness (or spread) to be calculated and also time-efficient sub-sampling. Volumetric sampling, by comparison, is much more time-consuming. However it is important to note that most of the sediment sequences analysed within this study are not isotaphonomic which influences tephra counts by weight because some minerogenic sediments can weigh more than others affecting the calculations. This was not considered a significant problem in this project as most of the cryptotephra distributions (see section 3.3.5) are recorded within the same sediment type. Care must be exercised, however, when directly comparing tephra concentrations between and within sites, as many factors affect the taphonomy of cryptotephra layers (Pyne-O'Donnell, 2011). Tephra concentrations were counted only up to totals of 10,000 shards per gram using an automated counter ('clicker'), as very few cryptotephra layers within this study contained higher shard concentrations.

3.3.5 Cryptotephra stratigraphic positions and volcanic eruptive events

In tephrochronology the concept of an ash layer representing a synchronous coeval blanket over large areas within various sedimentary archives is fundamental (see section 2.1 for more discussion). Central to this understanding is defining the volcanic event (e.g. period of eruption) in any sediment archive where tephra is present. This can be complex even where visible ash layers are concerned. Although contact between the tephra layer and the underlying sediment is often interpreted as the air-fall event, processes such as secondary reworking (Boygle, 1999) and density-induced emplacement (Anderson *et al.,* 1984) can create layers which can be too young or too old with respect to the volcanic event they represent.

With cryptotephra the situation is equally complex; typically the peak in shard concentration is used to represent the volcanic event (Davies *et al.,* 2007). Many distinctive types of tephra horizons have now been described for terrestrial depositional environments and these are shown and classified into schematic types in Figure 3.5. Various interpretations of how these different tephra horizon types relate to their respective volcanic events are also outlined in Figs. 3.5A-G. These types are used throughout the text to describe various tephra shard distributions uncovered

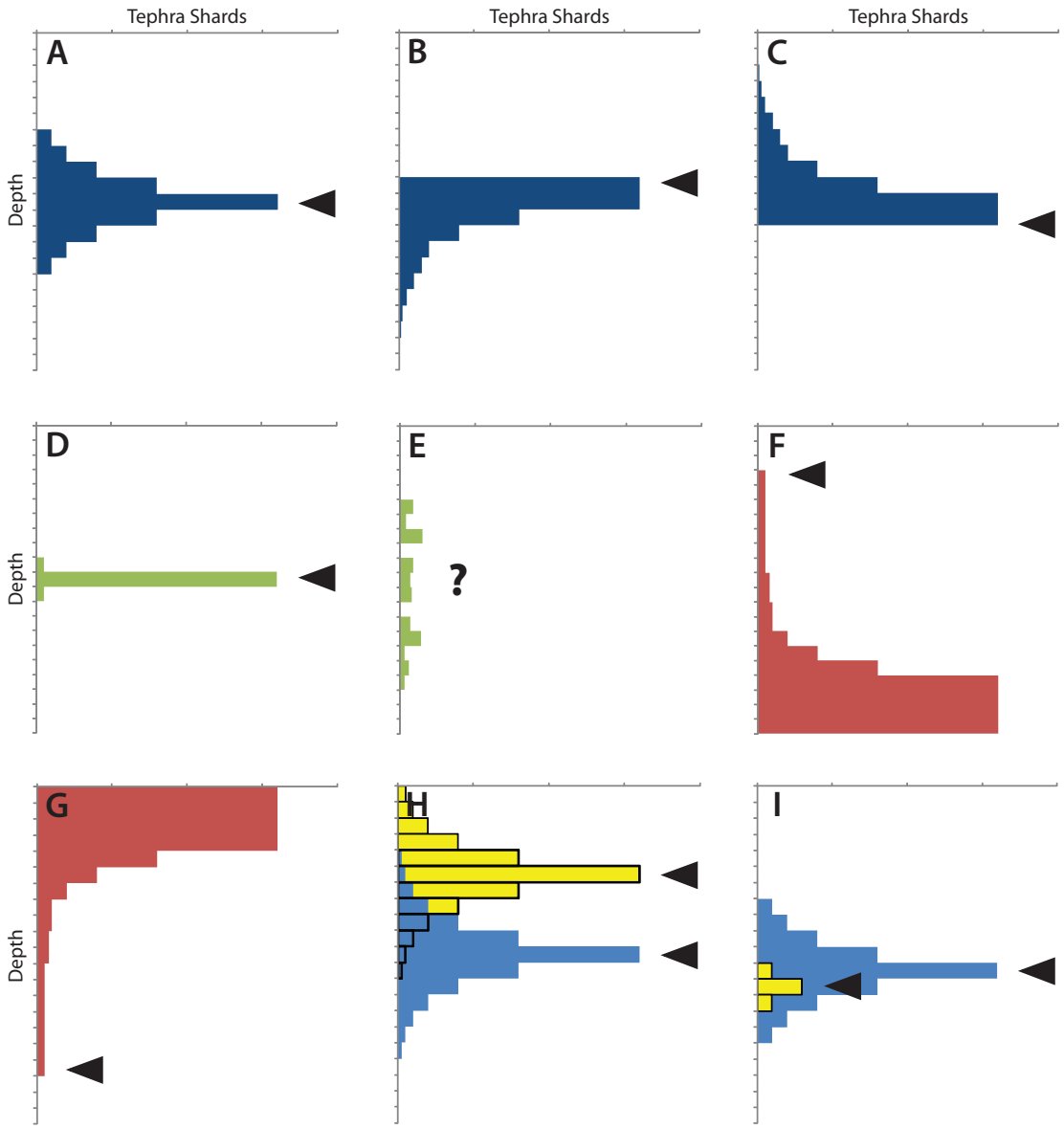

Figure 3.5 – Schematic diagrams showing common idealised tephra distributions both found within this study and described within the literature (see main text for details). Black triangles represent the first input event of tephra. (**A**) Shows a normal distribution (i.e. tephra reworking occurring both ways) with the peak representing the tephra input. (**B**) Also shows a layer where the peak in tephra represents the initial input however reworking has only occurred down profile. (**C**) shows that the base of tephra peak represents the input with stratigraphic reworking occurring only upwards through the profile. (**D**) A very well defined tephra peak with minimal vertical stratigraphic reworking. (**E**) A very dispersed tephra horizon with no apparent peak. (**F**) The input event is not represented by maximum shard numbers instead significant downward reworking has occurred, this has been demonstrated in soft sediments where large tephra input can result in density-induced emplacement (Anderson *et al.,* 1985). (**G**) A tephra where the input event does not record a peak but only the onset of tephra deposition, one reason this may occur is due to snow trapping the majority of tephra and releasing this only when they melt over time and completely at a later date (e.g. Davies *et al.,* 2007). (**H**) Showing the effect of two type A tephra events occurring close in time creating a double peak feature. (**I**) A smaller tephra input event masked by a larger tephra input event, here morphological or geochemical differences may be the only way to realise to events are present.

within this study. The distribution around the 'peak' in tephra shards should always be regarded as the stratigraphic error. A sedimentological (e.g. types F-G) and geochemical (e.g types H-I) based approach should always be taken when interpreting layers as the peak may not represent the volcanic event. The most common types of tephra horizons found within this research was type's A-E.

Distinctive tephra peaks (e.g. types A and D) are more useful marker horizons as they allow a smaller stratigraphic horizon to be assigned an age (if available) and more precisely linked to a palaeo-environmental signature, such as subdued tree expansion or higher tree pollen percentages reflected in a pollen diagram. However even when a tephra horizon is diffuse and lacks a distinct peak (e.g. type E), often an imported tephra age (with a large error) is larger than depth errors so it can have little effect on the final chronology.

Within this study the sampling resolution was carried out at 10 or 20 cm for 'scan' samples and 1 or 2 cm for high resolution sampling. These intervals are arbitrary but are used firstly because they are on a simple metric scale and secondly because often (especially for scan samples) the amount of material taken at these depths can be counted on minimal slides. Reduction at 1 to 2 cm is necessary to allow detailed tephra distributions and peaks to be defined; however it is clear that the sampling resolution can have a large effect upon the observed tephra distribution as shown in Figure 3.6.

3.4 Geochemical analysis of tephra shards

3.4.1 Preparing tephra shards for geochemical analysis

Samples with very high concentrations of tephra shards could be mounted directly onto resin stubs after floatation and covered with resin (see section 3.4.2 below). For samples where shard concentrations were very low (c.>3 non tephra shards: 1 tephra shard) a 5ųl gas chromatography syringe fitted with a 110ųm diameter needle micromanipulator was used to capture or 'pick' individual shards and transfer them onto the stub (Fig. 3.7). Collecting volcanic shards in this way is time consuming but greatly increases the amount of geochemical data that can be gained from volcanic glass.

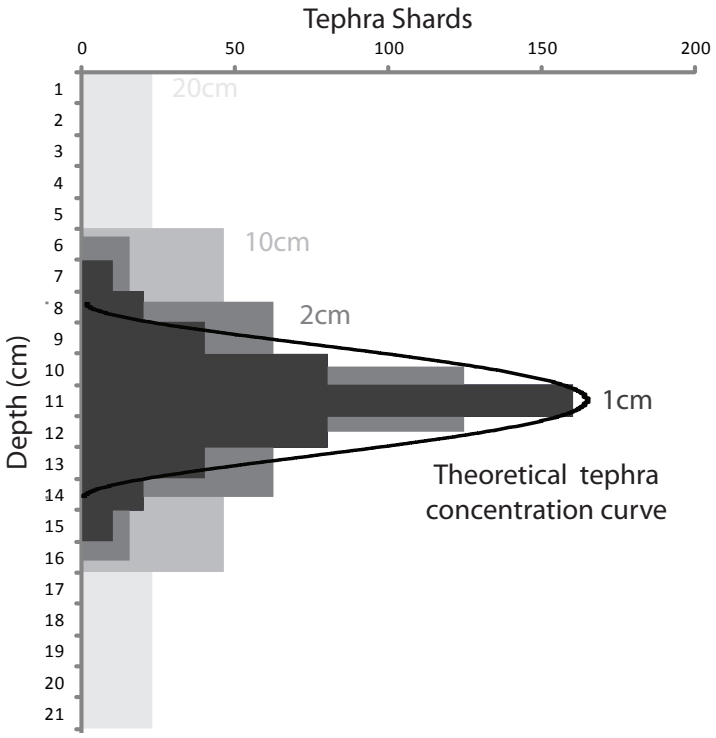

Figure 3.6 – Diagram highlighting how differences in sampling resolution affect the final tephra distribution when based around a hypothetical tephra concentration curve. Note how as the sampling resolution is increased the peak and stratigraphic spread of the tephra can be better resolved and hence more precisely defined.

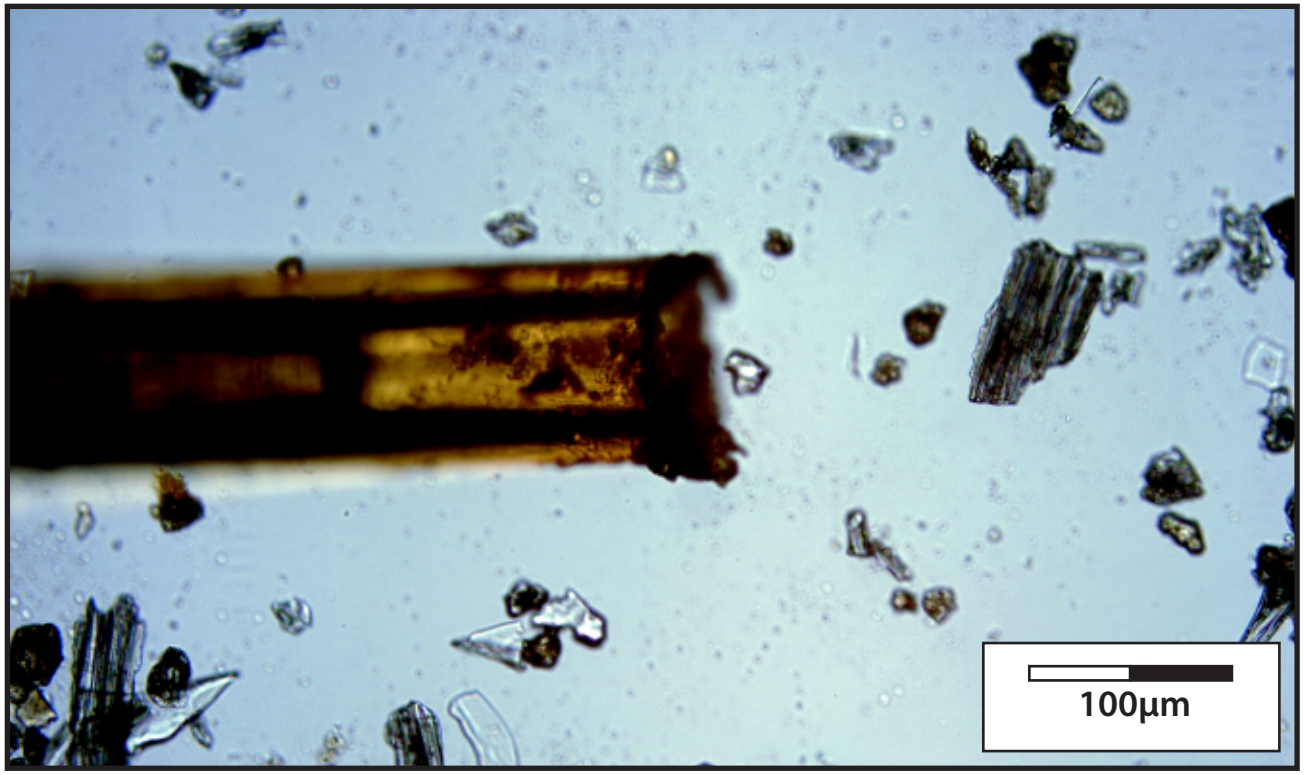

Figure 3.7 – A microphotograph showing the 110µm diameter fused silica needle used to 'pick' individual shards. All picking was carried out within a well slide in water using a Olympus CX-41 binocular transmitted light microscope at 10x magnification. Once a tephra shard was located the micromanipulator was used to position the needle for capture of the shard by the use of an attached 5µl gas chromatography syringe.

3.4.2 Resin stub preparation

Resin stubs were prepared broadly following the RHUL geochemical stub preparation procedure (A. Macleod and E. Turton, *pers comm*.) which is outlined below:

1. A phenolic ring is placed in a blue rubber mould and filled with specifix™ resin (2.5 parts resin: 1 part hardener) until filled.
2. This is then cured (hardened) in an oven at 50°C for 4 hours.
3. The 'stub' is then allowed to cool and further harden overnight.
4. The blue rubber mould can be removed and the stub is flattened to within 20-10μm using increasingly fine grades of silicon carbide grinding paper, starting with coarse grades between P120-P240 and then finer grades between P400-P1200-P2500-P4000. This is achieved by placing the stub within a hand polishing guide.
5. The sample can then be added to the stub surface (see section 3.4.1).
6. The stub is then covered with more specifix™ resin as in steps 1-3 above.
7. The sample is now ready for sectioning to expose tephra shard surfaces.

3.4.3 Exposing and polishing tephra shard surfaces

Once covered with resin the sample is placed in the Beuhler hand polishing guide and taken through decreasing coarse silicon carbide grinding papers ranging through P120-P240-P1200-P2500. P4000 paper is used between these steps to allow optical examination with an Olympus CX-41 binocular transmitted light microscope using both reflected and transmitted light, in order to constantly monitor how much resin remains above the covered tephra shards. Once the shard surfaces become exposed, the sample is removed from the hand grinder and preparation is completed on a Beuhler grinding/polishing machine using 9 and 3μm diamond suspension and finally 0.3μm aluminium oxide powder on MasterTex papers. These stages are designed to produce a good final polish and to ensure that exposed shard surfaces are as flat as possible, both of which are important to help generate geochemical data (see section 3.4.5).

3.4.4 Mapping stub shard surfaces

Once shard surfaces had been exposed, the stub surfaces were imaged so that the precise locations of individual shards analysed on the EPMA-WDS could be referenced and therefore subsequently targeted for LA-ICP-MS or SIMS trace element analyses (see sections 3.4.6 and 3.4.7). As the research progressed it became increasingly apparent that this process was very time-consuming, especially for stubs containing thousands of shards. Instead a Cartesian co-ordinate system was adopted, as this was found to be much less time-consuming and more precise. Three reference points were made in the stub using a scalpel; grid co-ordinates (*x*–*y*) were then taken during EPMA-WDS and were recorded automatically for all analyses. The data can then be translated onto another system (e.g. the LA-ICP-MS or SIMS) simply by calibrating the three reference points, using a co-ordinate conversion utility (see Kuehn and Froses, 2010) using Microsoft Excel.

3.4.5 Rationale of techniques chosen to gain geochemical data in this study

Within tephra studies Electron Probe Micro-Analysis (EPMA) forms the key technique for determining the major and minor element composition of individual glass shards (Lowe, 2011). The EPMA technique directs a focused beam of electrons onto a sample which generates X-rays which are of specific energies and wavelengths which relate to individual elements, the intensities of these allow measurement of specific element abundances (Hunt & Hill, 1993).

Within EPMA there are two widely used techniques; wavelength-dispersive spectrometry (WDS) and energy-dispersive spectrometry (EDS). EDS analysis is relatively quick compared to WDS as all X-ray energies produced are measured simultaneously according to their energy (Coulter *et al.,* 2010) whereas WDS uses a spectrometer crystal to diffract X-rays one element at a time over the course of an analysis. The main advantage of WDS, despite longer analysis times, is that higher beam currents can be used allowing greater spectral resolution which gives improved peak to background ratios and lower limits of detection (Spray & Rae, 1995). A disadvantage of the higher beam current used during WDS (coupled with longer analysis times) is that this can lead to mobilisation of Na as the sample heats up (Hunt and Hill, 2001; Reed, 2005) although there are ways to mitigate this effect (see section 3.4.6).

Overall WDS-EMPA allows greater accuracy and precision (Turney *et al.,* 2005; Coulter *et al.,* 2010) which is why it was used within this study (see section 3.4.7 for more details).

Trace element geochemical data is becoming an increasingly important proxy within the toolkit of the tephrochronologist; this is primarily because improvements in spatial resolution (e.g. spot size) and machine sensitivity (e.g. precision and accuracy) of Laser Ablation Inductively Coupled Plasma Mass Spectrometry (LA-ICP-MS) which has allowed the technique to be applied to increasingly small shard sizes (e.g. Pearce *et al.,* 2007; 2011a; 2011b; Tomlinson *et al.,* 2010). Alongside LA-ICP-MS Secondary Ion Mass Spectrometry (SIMS) which uses an ion probe- is also now being utilised to acquire trace element geochemical data. The SIMS system is less destructive to the sample glass than LA-ICP-MS due to the ion probe using 'sputtering' instead of ablation, allowing far less removal of material. This makes SIMS useful for analysis of smaller (and especially thinner) tephra glass shards (Lowe, 2011). The SIMS system does however take much longer for each analysis (x60); it is also far more expensive, thus here it is used more sparingly only for important samples where LA-ICP-MS could not be utilised due to inadequate tephra shard sizes. Trace elements are useful in addition to the more commonly available major elements as they allow more robust correlation/discrimination as well as providing important information on volcanic provenance and magmatic evolution trends (Lowe, 2011).

LA-ICP-MS and Secondary Ion Mass Spectrometry (SIMS) are two techniques (which along with EPMA) which allow shard specific geochemical data to be acquired. This is important because often geochemical fields of specific tephra are non-normal or even bi-modal thus making 'bulk' geochemical data generally of little use or even misleading (see Fig. 3.8). On top of this using shard specific techniques means that pure tephra glass can be better targeted, allowing for example mineral inclusions to be avoided and also for detection of subtle heterogeneous geochemical variations (Mokgalaka & Torresdey, 2006). This cannot be achieved with Inductively Coupled Plasma Mass Spectrometry (ICP-MS) alone as a potentially geochemically complex bulk glass sample is taken, then dissolved and homogenised into one sample value. Because of this both LA-ICP-MS and SIMS have been utilised during the course of this research (see sections 3.4.8 and 3.4.9 for more details of these techniques). Importantly SIMS and LA-ICP-MS have been shown to produce comparable data (E. Tomlinson,

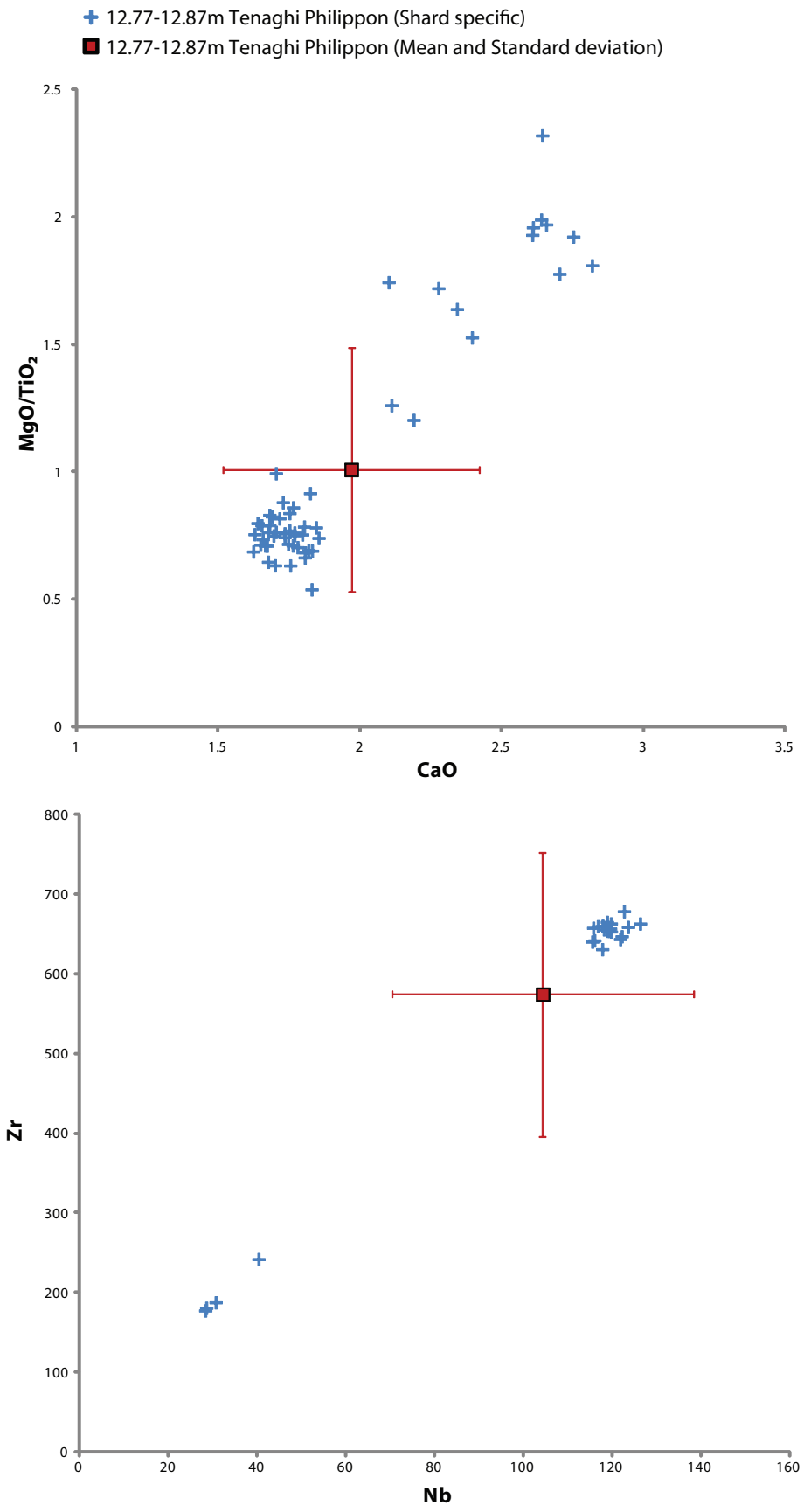

Figure 3.8 – Geochemically bimodal tephra analysed within this study demonstrating the potential pitfalls of utilising mean and standard deviation values.

unpublished data) and secondary standards can be used to provide independent measures of both accuracy and precision (see section 3.4.10).

3.4.6 Number of geochemical assays per sample

There is some debate on how many geochemical assays per sample are required for robust geochemical correlation of tephra layers with some authors suggesting as many as 50 shards per sample may be required (Lowe, 2011) and others using statistical methods to suggest that in some cases as few as 6 data points may be sufficient for robust correlation (C. Lane, *pers. comm.*). In large part this question probably changes on a case-by-case basis dependent on firstly geochemical 'uniqueness' and secondly on levels of geochemical homogeneity or otherwise of individual tephra layers.

Typically, during this research, attempt was made to assay at least 20 individual tephra shards per sample for major, minor and trace elements in order to fully assess geochemical homogeneity and allow large enough datasets for detailed comparison. This however was not always possible due to either very few shards being available for analysis (usually in more distal sites) or when thin and highly vesicular glass makes analysis difficult. During the research an average of 17.2 assays per sample was achieved for major and minor element analysis (2-47, min and max) and an average of 10.1 assays per sample for LA-ICP-MS (3-24, min and max). Successful sample analyses for SIMS was lower (3-6 assays per sample) as analysis time is much longer compared to LA-ICP-MS (x60) thus fewer shards could be analysed per sample stub.

3.4.7 Wavelength Dispersive Electron Probe Micro-Analysis (EPMA-WDS)

Major (SiO_2, TiO_2, Al_2O, FeO, MnO, MgO, CaO, Na_2O, K_2O) and minor element (P_2O_5, Cl) compositions were almost all analysed at the Research Laboratory for Archaeology and the History of Art, University of Oxford using a Jeol JXA8600 wavelength-dispersive electron microprobe, equipped with 4 spectrometers and SamX software. Prior to analysis samples were carbon coated to prevent surface charging. To minimize Na migration an accelerating voltage of 15 kV, 6 nA beam current and a defocused 10μm beam were used (as recommended by the International focus group on Tephrochronology And Volcanism (INTAV) group; Kuehn *et al.,* 2011). The instrument was calibrated using a suite mineral standards before an analysis run.

Different count times were used for different elements: 10 seconds for Na; 30 seconds for Si, Al, K, Ca, Fe, Mg Ti, Mn and 60 seconds for P and Cl. A range of MPI-DING glasses were used throughout the period of study as secondary standards (see Jochum *et al.,* 2006) including GOR128, GOR132, ATHO-G and StHs6/80. These standards incorporate Basalts, an Andesite and a Rhyolite and thus have a good range of geochemical diversity.

For two samples a smaller beam size than 10μm was required due the tephra layers only having very small tephra shards size distributions (typically with A-axis less than 25μm leading to <10μm exposed shard surfaces on the stub). These samples were analysed at the Tephra Analytical Unit (TAU) at the University of Edinburgh by a CAMECA SX-100 wavelength-dispersive electron microprobe which is equipped with five spectrometers. The Edinburgh probe system is set up to operate at smaller beam diameters and a 5μm operating beam was applied (see Hayward, 2012). Both major (SiO_2, TiO_2, Al_2O, FeO, MnO, MgO, CaO, Na_2O, K_2O) and minor (P_2O_5, Cl, F) elements were measured. The probe operating conditions were an accelerating voltage of 15 kV, a beam current of 2 nA for Si, Al, Fe, Mg, Ca, Na and K and a current of 80 nA for Ti, Mn, P, S, F and Cl. The secondary standards used were Lipari Obsidian and MPI-DING glass BCR-2G. The secondary standards are bracketed throughout the runs on both probe machines to check for drift and allow accuracy and precision to be determined (see section 3.4.10 for more details).

Inevitably not all the produced EPMA data produced represents volcanic glass, thus the data has to go through a 'cleansing' process to remove geochemical assays of quartz, biogenic silica and feldspars. Quartz and biogenic silica can be identified with ease as they have very high SiO_2 values (98-100%) not possible in volcanic glass. Likewise feldspars can be recognized via high alkali values (1-11%) but very low TiO_2, FeO and MgO percentages.

3.4.8 Laser Ablation Inductively Coupled Plasma Mass Spectrometry (LA-ICP-MS)

LA-ICP-MS was carried out in the Department of Earth Sciences, Royal Holloway University of London. Analyses of proximal tephra samples were performed using an Agilent 7500ce coupled to a Resonetics 193 nm ArF excimer laser-ablation system (RESOlution M-50 prototype) with a two-volume ablation cell (Müller *et al.,* 2009;

Tomlinson *et al.,* 2010). The laser sampling strategy used was single circular 'spot' analyses, with spot sizes used ranging from 54, 44, 34 and 25μm, larger spot sizes were always used if possible to increase precision (see section 3.4.10). The repetition rate was 5 Hz and the count time was 40 s (200 pulses) on the sample and 20 s on the gas blank (background) either side of the analysis. The elements measured were Sc, Ti, V, Ni, Rb, Sr, Y, Zr, Nb, Ba, La, Ce, Pr, Nd, Sm, Eu, Gd, Dy, Er, Yb, Lu, Ta, Pb, Th and U (always as ppm unless otherwise stated). See Tomlinson *et al.* (2010) for further details of operating parameters.

The secondary standards used were the same MPI-DING glasses used as for EPMA-WDS including GOR128, ATHO-G and StHs6/80 for constancy and also to allow full comparison. The secondary standards are bracketed throughout the runs to check for drift and allow accuracy and precision to be determined (see section 3.4.10 for more details). Alongside this MPI-DING glass NIST612 was used as the internal calibration standard, and was analysed at the start and end of each run and also bracketed each secondary standard analysed. Si values imported from EMPA-WDS analyses were used as the internal standard for unknowns and GeoRem values for standards (Jochum *et al.,* 2006). This allows any variation in ablation yield during analysis of unknown samples (run between standards) to be corrected for (See Pearce *et al.,* 2007). Machine conditions were recorded on the day of each run.

Data reduction was performed manually using a Microsoft Excel macro provided by E. Tomlinson (RHUL), this allowed removal of any phenocryst or vesicle components. The resin of the stub does not contribute to the background signal allowing small amounts of ablation without impacting the elements measured (although the signal will reduce, impacting upon the precision that can be achieved; Tomlinson *et al.,* 2010). All processing and acceptance of geochemical data adhered to RESET protocols, including acceptable accuracy (calculated as %Bias) and precision (calculated as %RSE and 2S.E.; see section 3.4.10 for more details) limits of secondary standards and minimum glass ablation time (or time slices) needed for a statistically acceptable analysis.

3.4.9 Secondary Ion Mass Spectrometry (SIMS)

SIMS was carried out by Lusia Ottolini at the Istituto di Geoscience e Georisorse (IGG), Unità di Pavia, Italy. EPMA samples were polished (to remove the carbon coats from

EPMA analysis) and Pt-coated. Samples were analysed using a Cameca IMS 4f ion microprobe using a 0.5-0.7 nA current intensity with a spot diameter of 5-8 μm. There was a waiting time of 450 s necessary to obtain steady-state sputtering conditions, and four acquisition cycles with the following counting times per cycle: Li (5s), Be (5s), Si (2s), K (2s), Sc (5s), Ti (4s), V (5s), Cr (5s), Rb (5s), Sr (5s), Y (5s), Zr (5s), Nb (5s), Cs (8s), Ba (8s), La (10s), Ce (10s), Nd (10s), Sm (15s), Dy (20s), Er and Yb (15s each), Th and U (20s each). For Eu and Gd a deconvolution procedure was used to remove BaO, CeO and NdO interferences from Eu and Gd isotopes, respectively.

Two international reference materials were used as secondary standards including NIST-SRM 610 and BCR-2G (see Jochum *et al.,* 2006), alongside these two well characterised internal standards (BB and WY1) were analysed during the sample runs (L. Ottolini, *pers. comm*.).

3.4.10 Calculating machine drift, precision and accuracy using standard glass analyses

Understanding the drift, accuracy and precision at which elemental concentrations can be measured is important for understanding the comparability and robustness of the geochemical data produced. Within this section the ATHO-G standard is used to explore how these three variables can be assessed and measured. Machine drift can occur for various reasons; both analytical and external (e.g. changes in atmospheric conditions). Figs. 3.9 and 3.10 show the major element analyses for the ATHO-G standard over the course of this study, in chronological order, compared against the international standard concentrations (MPI-DING) for ATHO-G as defined in Jochum *et al.* (2006). Overall it can be seen that there is very little drift apparent, and where machine drift may be present it remains within the acceptable standard range. From Figs. 3.9 and 3.10 an assessment of precision can also be made and certain elements (e.g. K_2O) have a very high precision whereas others (e.g. MnO) do not.

Accuracy can be measured quantitatively using %Bias (%Bias = $100*(x\text{-}x_a)/x_a$) where x is the standard concentrations defined within this study and x_a is the certified MPI-DING standard values. Figure 3.11 shows the %Bias values for the major, minor and trace elements of the ATHO-G standard analysed within this study, it can be seen that accuracies are typically below 5% for trace elements and for SiO_2, Al_2O_3. K_2O and CaO. The precision for the lower abundance elements are much lower (e.g. MgO and

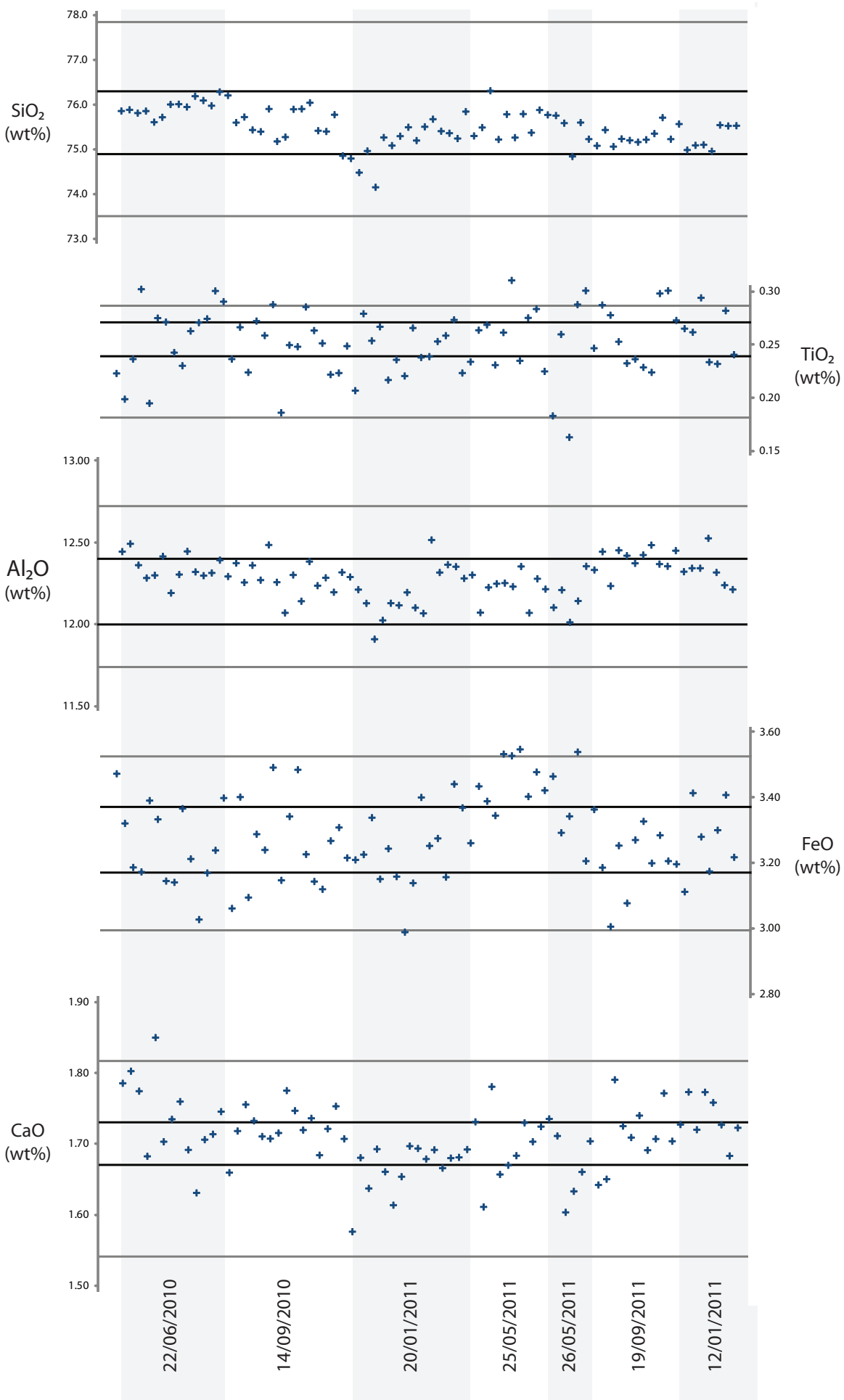
SiO2 (wt%)
78.0
77.0
76.0
75.0
74.0
73.0
TiO2 (wt%)
0.30
0.25
0.20
0.15
Al2O (wt%)
13.00
12.50
12.00
11.50
FeO (wt%)
3.60
3.40
3.20
3.00
2.80
CaO (wt%)
1.90
1.80
1.70
1.60
1.50
22/06/2010
14/09/2010
20/01/2011
25/05/2011
26/05/2011
19/09/2011
12/01/2011

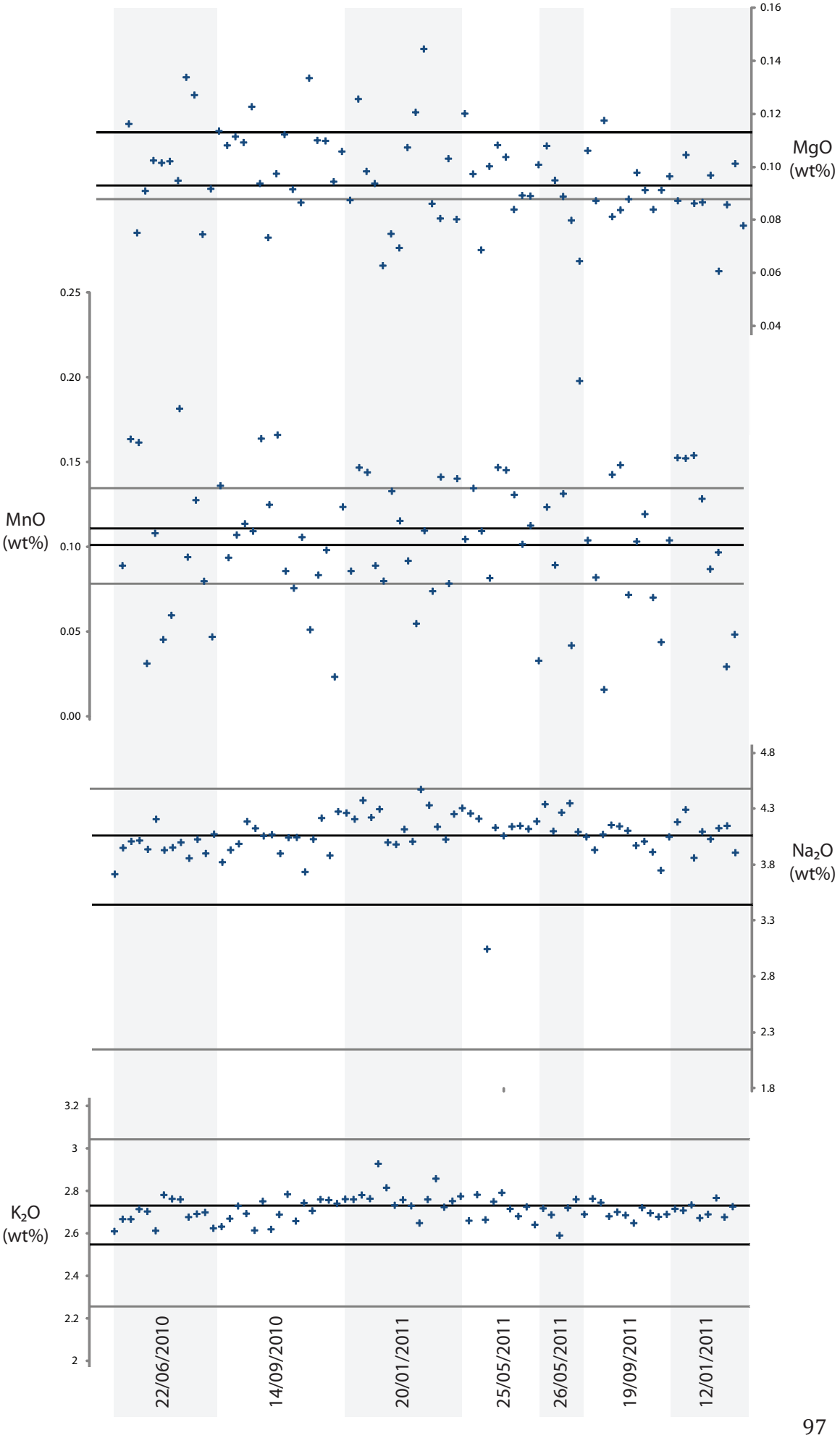
MgO (wt%)
0.16
0.14
0.12
0.10
0.08
0.06
0.04
MnO (wt%)
0.25
0.20
0.15
0.10
0.05
0.00
Na2O (wt%)
4.8
4.3
3.8
3.3
2.8
2.3
1.8
K2O (wt%)
3.2
3
2.8
2.6
2.4
2.2
2
22/06/2010
14/09/2010
20/01/2011
25/05/2011
26/05/2011
19/09/2011
12/01/2011

Figure 3.9 (Previous page x2) – SiO_2, TiO_2, Al_2O, FeO and CaO values (un-normalised) for the ATHO standard assayed during analytical runs over the course of this study (between June 2010 to January 2011). Black lines indicate the 95% confidence level from different analytical techniques whereas lighter grey lines indicate the standard deviation from EPMA analysis alone (comparison standard data from Jochum *et al.*, 2006).

Figure 3.10 (Previous page) – MgO, MnO, Na_2O and K_2O values (un-normalised) for the ATHO standard assayed during analytical runs over the course of this study (between June 2010 to January 2011). Black lines indicate the 95% confidence level from different analytical techniques whereas lighter grey lines indicate the standard deviation from EPMA analysis alone (comparison standard data from Jochum *et al.*, 2006).

MnO). In Figure 3.11 data points shown in red represent runs which were rejected due to poor agreement with the internationally accepted standard concentrations (these points are also shown in Figs. 3.12 and 3.13). Na_2O values appear to show a positive %Bias compared to the standard (Figs. 3.10 and 3.11). This could be due to relatively recent recommendations to analyse Na_2O first in order to reduce migration and mobilisation of this element in EPMA-WDS analysis (see section 3.4.7). A historical bias maybe prevalent within the compiled MPI-DING values, this would indicate that care should be taken when using Na_2O to compare to data taken from the literature that was not analysed via EPMA in this order. Precision can be measured via the percentage of Relative Standard Error (%RSE). This calculation is based upon the internal dataset, not comparison with external international standards. Most high abundance major elements display very high <5% precision (Si_2O – CaO), trace elements have a slightly larger precision ranges (4-15%).

A limitation with both %Bias and %RSD are that they assume that the standard glasses are homogenous, which is not always the case (Jochum *et al.,* 2006). This may overestimate differences between the standards measured here and those based on MPI-DING mean values (and those measured comparatively internally).

Precision has been calculated as a 2S.E. error for each trace element geochemical assay and are lower for larger spot sizes due to machine sensitivity improving with ablative yield (Tomlinson *et al.,* 2010; see Fig. 3.13). All standard data are presented in the appendices.

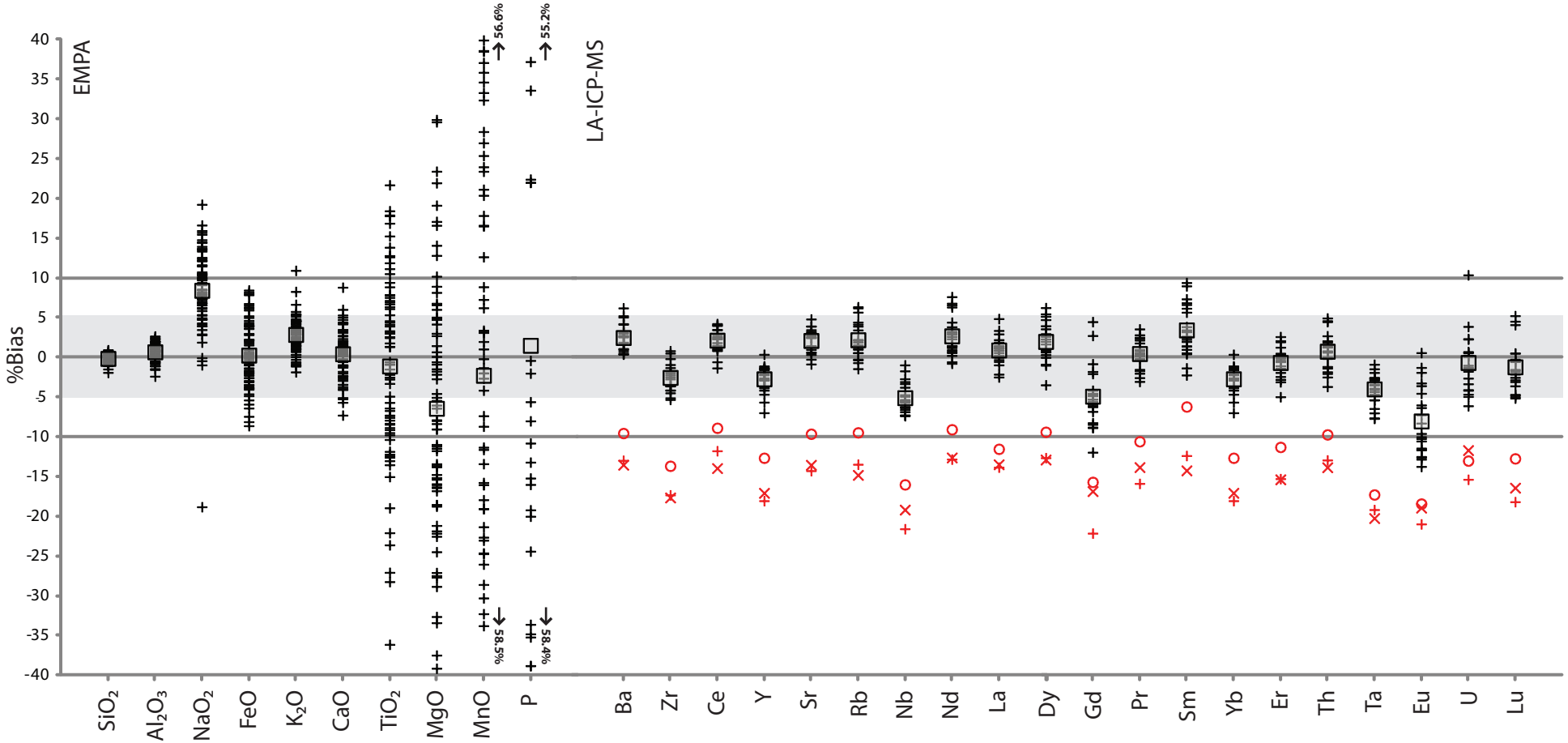

Figure 3.11 – %Bias of all major, minor and trace the elements analysed during the course of this study for the ATHO-G standard.

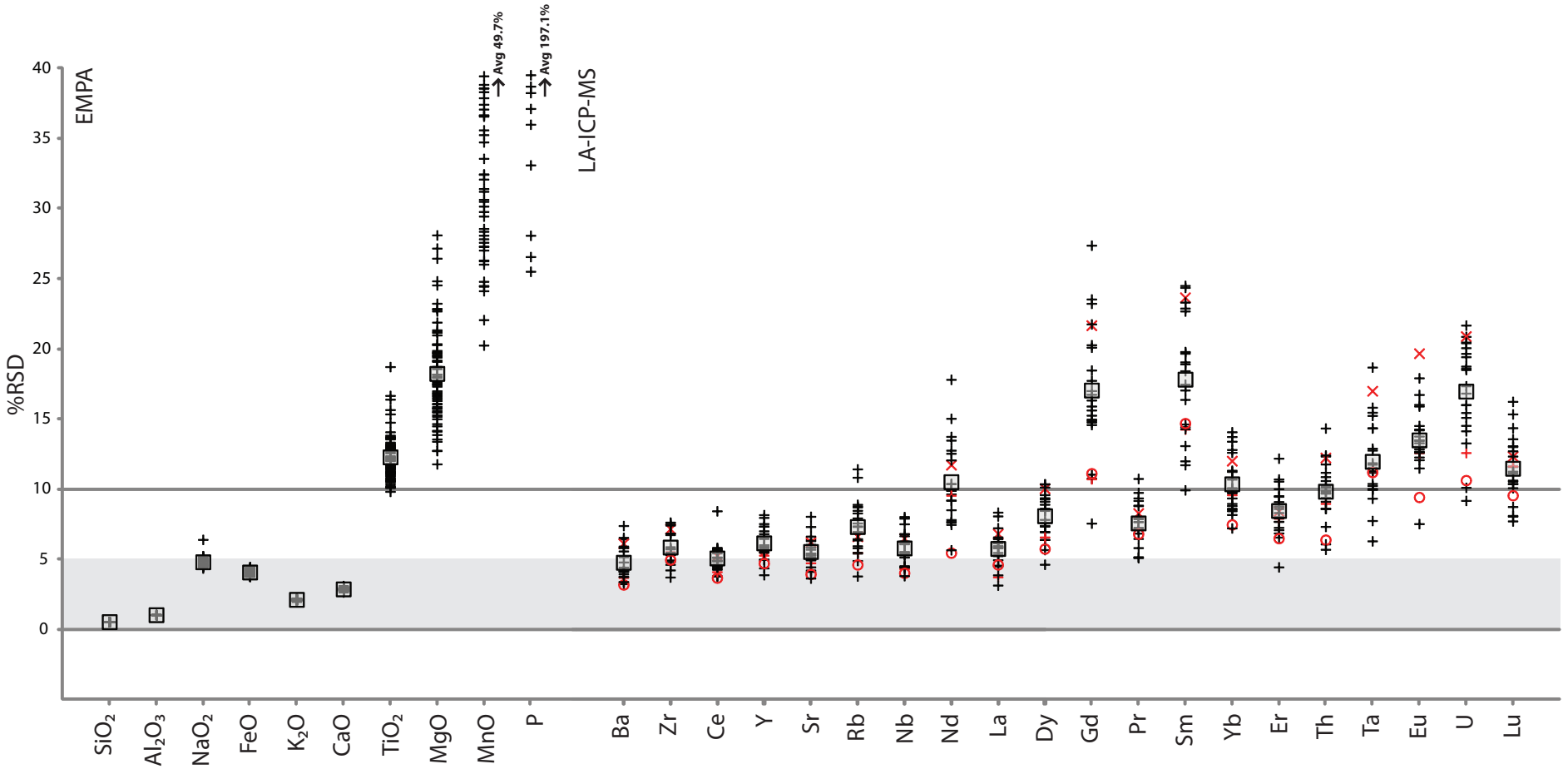

Figure 3.12 – %RSD values of all major, minor and trace elements analysed during the course of this study for the ATHO-G standard.

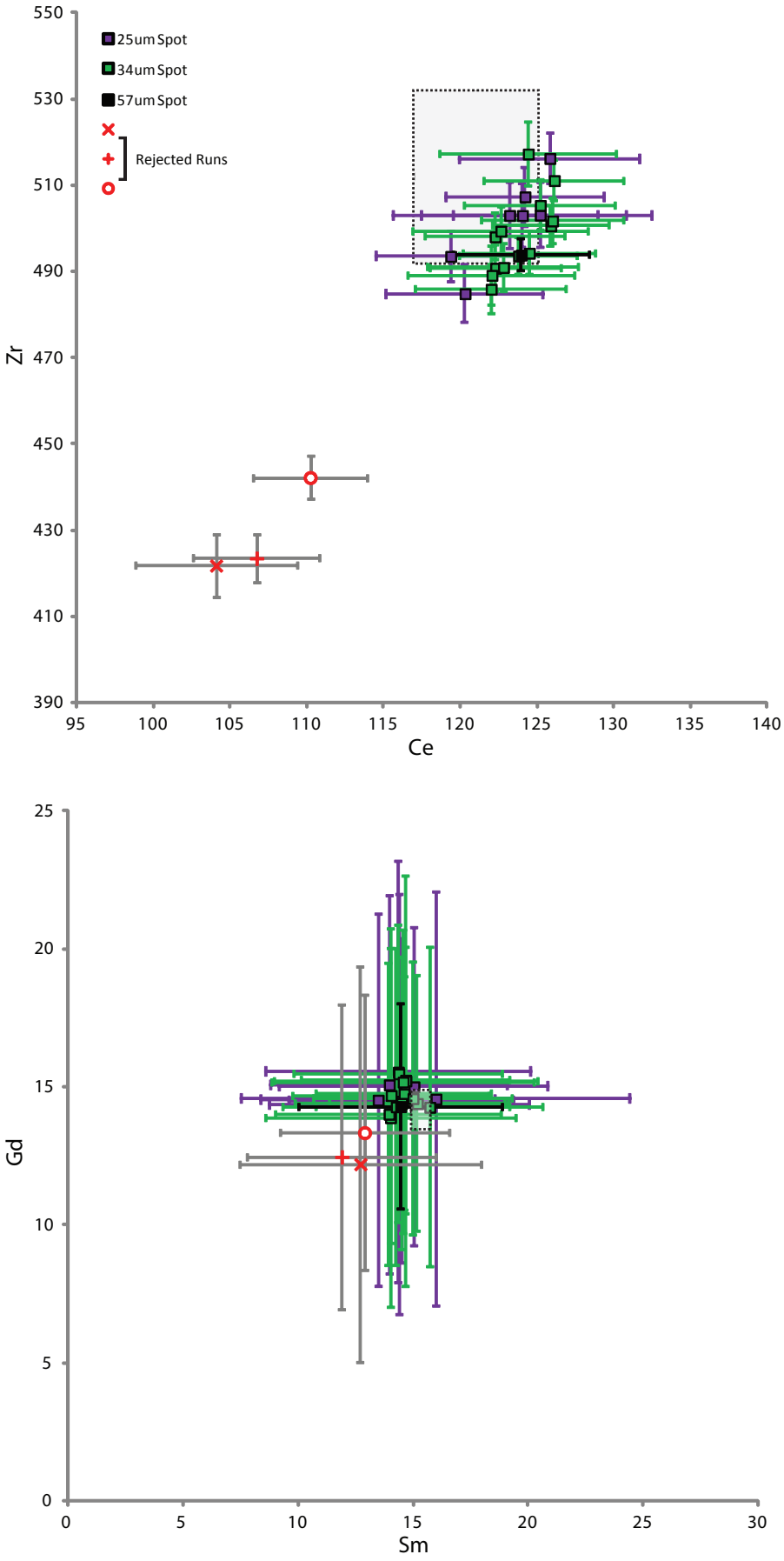

Figure 3.13 – Comparison of different LA-ICPMS spot sizes and rejected runs on the ATHO-G standard, shown with RSE error. Reference dataset is at 95% confidence level from different analytical techniques and shown as a grey box (from Jochum *et al.,* 2006).

3.5 Geochemical data exploration methods

3.5.1 Correlating tephra layers; bivariate and multivariate approaches

Correlating tephra layers primarily via differences or affinities in geochemical compositions is at the cornerstone of tephrochronology. Despite this there is neither one agreed method nor statistical measure for validating a correlation between, for example, a distal and proximal tephra unit. Most commonly correlating Quaternary tephras has been undertaken via qualitative graphical means such as bivariate x-y (element-element) biplots. Pearce *et al.* (2008) have described how this allows straight forward visual analysis of often complex datasets including allowing the:

- Range of composition and trends to become apparent.
- Detection of outliers.
- The observation of compositional overlaps or differences between samples.

It is possible to generate 45 separate x-y plots from 10 major elements and many multiples more when considering 25 trace elements, although there is software freely available which allows rapid plotting and exploration of large geochemical datasets. Within this study data exploration was carried out with GCDKit 3.0 Beta (available for free download online; Janoušek *et al.,* 2006). Even with bespoke software, exploring data in this way is time consuming but allows simple clear comparison between two elements, and also it does not provide a quantitative measurement of how robust the correlation is. An overlapping composition between two samples on all possible x-y biplots would however be strongly suggestive of a correlation, although other lines of evidence may preclude this (e.g. sedimentology, stratigraphy or chronology; Davies *et al.,* 2012).

Many statistical and multivariate techniques have been applied to tephra geochemical datasets in an attempt to provide more quantitative correlations including: statistical distance analysis, cluster analysis, *t*-test comparisons of means, similarity coefficients and Principal Component Analysis (PCA) and Discriminant Function Analysis (DFA) (Lowe, 2011). Some of these methods (e.g. cluster analysis, *t*-test) only test the similarity of the mean values which is problematic where many tephra display bimodal (see Fig. 3.12) or indeed unimodal distributions thus resulting in potentially erroneous correlations. PCA and DFA compare the overall distribution of the data as well as the mean and have been used alongside graphical biplots to help quantify correlations (e.g. Bourne *et al.,* 2010). Davies *et al.* (2012) suggest that these statistical

techniques may be able to readily disprove a correlation but to confirm a correlation requires more than just the statistical approach because of the risk of incorrect correlation. Multivariate statistics also cannot account for precision or accuracy issues already discussed, although some low precision elements can be removed from the analysis (e.g. MnO or P). These may, however, be useful for distinguishing between tephra within certain volcanic regions.

Because of these current uncertainties within this study, biplots are used to firstly explore the geochemical datasets and to distinguish and correlate tephra layers on the basis of known useful elements (these are dependent on volcanic region/source).

3.5.2 The unit sum problem

Major and Trace element data is always expressed and compared as percentage data with elements presented as part of a whole (wt % of 100% or parts per million, ppm). Therefore by defining an oxide concentration as a percentage, involves not only that concentration but also the sum of all the remaining oxides (Pollard *et al*., 2006). This means that the data are not truly independent of each other, for example if in a tephra layer SiO_2 represents 60% of the sample the next element must be 40% or less. This effect is known as the unit sum problem and can introduce false negative relationships between elements in biplots and is particularly problematic when using multivariate statistics (Aruga, 2004) which have not been applied in this study.

3.5.3 Un-normalised vs normalised data

The major and minor oxide values from EPMA-WDS analysis are always presented as percentages of sample weight and the sum of the oxide percentages for each element measurement should equal 100% (as discussed above). However this is rarely ever achieved for both geological and analytical reasons including:

1) The water content of volcanic glass which has been shown to be as high as 10% (WoldeGabriel *et al.,* 2005), this process of hydration can also occur post-deposition (Blockley *et al.,* 2005).
2) Deficient sample polish.

3) Poor beam spot targeting or small surface areas for the electron beam to interact with.
4) The mobilisation of certain elements (Pollard *et al.,* 2006).
5) The presence of unmeasured minor elements such as fluorine (Turney *et al.,* 2004).

Because of the natural possibility of high water content in glass many have proposed that all geochemical data should be normalised to 100% to produce 'real' weight percentage values that are more comparable (Froggatt, 1992) and that EPMA assays returning totals of as low as 90-92% are acceptable as this is a geological possibility. Others, in contrast, have argued that as analytical issues can affect the totals, normalisation should be avoided and samples returning analytical totals below 95% should also be rejected (Hunt and Hill, 1993). Shane (2000) and Kuehn *et al.* (2011) have however both reported tephra glasses where consistently low totals (92-94%) were apparent and reflective of true natural high water contents.

Within this study the majority of the tephra layers analysed via EMPA produced assays where analytical totals were mostly above 95% and displayed low variability (>3%). In the few cases where low totals (92-94%) were returned consistently from a single sample this was considered to be real evidence of high glass water content. All EMPA data within this study are presented as normalised values because of the reasons outlined above and as this reduces scatter within the data thus resulting in more consistent element abundances (Pearce *et al.,* 2008). Stokes and Lowe (1988) have shown that the use of normalised data vs un-normalised actually made little difference in correlating glass to its volcanic source. All EMPA data are presented as un-normalised with analytical totals in appendix II.

3.6 Age modelling techniques

3.6.1 Constructing age-depth models

Age modelling was applied in this study to allow robust age estimates to be calculated for tephra layers and to provide robust statistically valid age-depth models for each site investigated based, solely using independent age information (e.g. radiocarbon dates and Ar–Ar ages).

Age models were constructed utilising Bayesian deposition modelling (with Markov Chain Monte Carlo analysis or MCMC; Blockley *et al*., 2004) and was undertaken in OxCal ver 4.1 (Bronk Ramsey, 2001, 2009), using the internationally agreed IntCal09 calibration curve (Remier *et al.,* 2009). The advantage of Bayesian age modelling (employing MCMC) over calibrating radiocarbon dates on a one by one basis is that, due to the non-linear relationship between radiocarbon and calendar time-scales (Yeloff *et al*., 2006) non-normal probability distributions exist in most calibrated radiocarbon ages. Bayesian MCMC analysis can help in this issue by running thousands of 'random walks' through the non-normal probability distributions of the posterior data in order to find the most likely calibrated age for each date. By doing this outliers and dates which statistically do not fit the age-depth model are not only being removed but can be mathematically defined in terms of an ***Agreement Index (AI)*** value, both in terms of the model overall and for each individual date (Bronk Ramsey, 1999; 2008).

All site datasets were processed using the ***P_Sequence*** function within OxCal 4.1 (see Bronk Ramsey, 2008). This approach uses the relative position of dated horizons in order to produce more constrained age-depth models (see section 1.3.4 and Fig. 1.5) and employs a Poisson depositional model, which treats the deposition of sediment as a poisson process where individual particles of sediment build up over time, this approach allows variable sedimentation rates between dated layers and produces realistic age estimates for undated horizons. ***Boundary*** functions essentially 'reset' sedimentation rate modelling where changes in deposition rate may occur and were placed where described lithological changes exist or where a suspected hiatus was possible in the record; see Blockley *et al.* (2004). *Boundary* functions were also placed where large gaps were present between dated horizons. The applicability of this approach to depositional modelling was tested and verified in Blockley *et al.* (2007) in theoretical simulations and has also produced reliable age estimates for tephra layers of known age in studies on real sites (Blockley *et al.,* 2008)

The *P_Sequence* requires a user defined ***K value*** (a Poisson constraining parameter) which sets the number of accumulation events per unit depth (Bronk Ramsey, 2008). A high *K value* would thus constrain the data very rigidly but a low one allows higher model flexibility. To find an optimal/realistic *K value* all models were run initially using a low *K value* of 0.001 (as recommended by Bronk Ramsey, 2008 and Blockley *et al*., 2007) and at this stage dates with very low AIs were removed. To avoid any

circularity only a few dates (which had the lowest agreement index issues) were removed at a time and the model was re-run until the total model *Agreement Index* ($A_{overall}$ and A_{model}) was higher than 60% (Bronk Ramsey, 2008). After a satisfactory model was achieved with an overall agreement index above 60% no more dates were removed but the model was rerun in steps using larger parameter K values, this was done in order to try and constrain the age-depth model while still producing statistically valid model agreement indexes above 60% (Bronk Ramsey, 1999).

All age-model parameters and output data are presented in the appendix III for each age-depth model produced within this thesis to allow independent evaluation and replication. All modelled ages and age-depth relationships are plotted and described at 95.4% confidence limits.

3.6.2 Combining multiple age estimates

Sometimes multiple ages are available for both dated horizons or for a dated tephra layer. Within OxCal the ***R_Combine*** and ***Combine*** function can be used to combine several radiocarbon ages prior to calibration (e.g. *R_Combine*) or alternatively to combine multiple calendar ages based upon probability density functions (*Combine*). This allows assessment of whether differing ages are statistically similar and allows production of more precise ages.

4.0 SITE DESCRIPTIONS

4.1 Site Selection Criteria

In order to resolve the aims and objectives outlined in section 1.4, each site selected for inclusion within this research project needed to meet the following criteria. Firstly sites were targeted which represented a spatial improvement with the potential to extend the current European tephrostratigraphic framework, either with the first discovery of tephra or via cryptotephra layers. Key sites disscussed in section 2.2.3 are shown in Fig 4.1 alongside sites sampled within this study.

Selected sites also required a detailed palaeoenvironmental proxy record (e.g. based on pollen, isotopes, etc.) to be available. This is important as it allows palaeoenvironmental inferences and inter-site comparisons to be made where co-registered tephra layers are present. Existing chronological data was also required (results based on a combination of independent methods were preferred) coupled with correlations based on biostratigraphic alignment. This information allows the relevant sediment sequence depths to be targeted with respect to the timeframe of interest to this study (i.e. 50-20 ka BP) for tephra content. They also provide age models that can be tested independently using Bayesian statistical procedures and tephrochronology.

For many sites several (often quite dissimilar) chronologies have been derived. Where this was the case, tephra sampling was designed to ensure that all depths that had been interpreted to potentially cover the Late Last Glacial (LLG; 50-20 ka BP) were sampled. Of course all chronological models are by definition subject to some degree of error. In order to take account of error ranges therefore, care was exercised to ensure that broad depth intervals were sampled over the extended time interval of c.70-10 ka BP, as defined by existing age models, to be more certain that the target interval was covered.

Where possible, contiguous sampling was undertaken over the defined depth intervals, rather than attempting to estimate the time/depth intervals in which large eruptions might be found. Focusing in such a selective way limits the robustness with which age models are tested and may also introduce bias that leads to false affirmation of the existing age-depth models. A selective strategy also assumes perfect knowledge of the local eruptive history (i.e. considering ‘known knowns’ only) and fails to take

into account potential 'unknowns', previously undetected eruptions that may be present within a sediment sequence. This is a vital point, because the detection of previously undiscovered tephra layers is a key step in the development of a fuller tephrostratigraphic framework for the Mediterranean region during the LLG.

In the remainder of this chapter, the degree to which the sites selected for study meet the above criteria is outlined.

4.2 Site descriptions and current chronological information

4.2.1 Padul, Andalusia, Spain

Site history

Padul is located in Andalusia in the southern part of Spain (see Fig. 4.1). The Padul site has a long history of Quaternary research tracing back to pollen diagrams published in the 1970's and subsequently (Florshutz *et al*., 1971; Pons and Reille, 1988; Fig 4.2). Florshutz *et al.* (1971) correlated the base of the original sequence to older than the Holstein Stage (MIS 11) based on pollen stratigraphy, which they interpreted as reflecting two warm intervals predating the last interglacial. These original pollen diagrams remain difficult to interpret in relation to more recent climatostratigraphic information (e.g. SPECMAP; Imbrie *et al*., 1984) due to often poor pollen preservation which may relate to desiccation phases (Florshutz *et al*., 1971; de Beaulieu *et al*., 2007).

Despite this drawback, Padul is one of the very few long terrestrial palaeoenvironmental records available from southern Iberia. Because of this a new longer core was obtained in 1997 (Nestares & Torres, 1998; see Table 4.1), from the deepest part of the basin. This core is 107 metres in length and has been dated via radiocarbon and U/Th dating on peat in addition to amino acid racemization dating on ostracod shells in the older part of the core; the base of this new core is thought to be around 1 Ma BP (Ortiz *et al*., 2004; see Fig. 4.3). A range of proxies have been analysed for the core including a new pollen diagram for the upper part of the core (Valle *et al*., 2003; see Fig. 4.4) and $\delta^{13}C$ isotopes and *n*-alkane content (Ortiz *et al*., 2004; 2010).

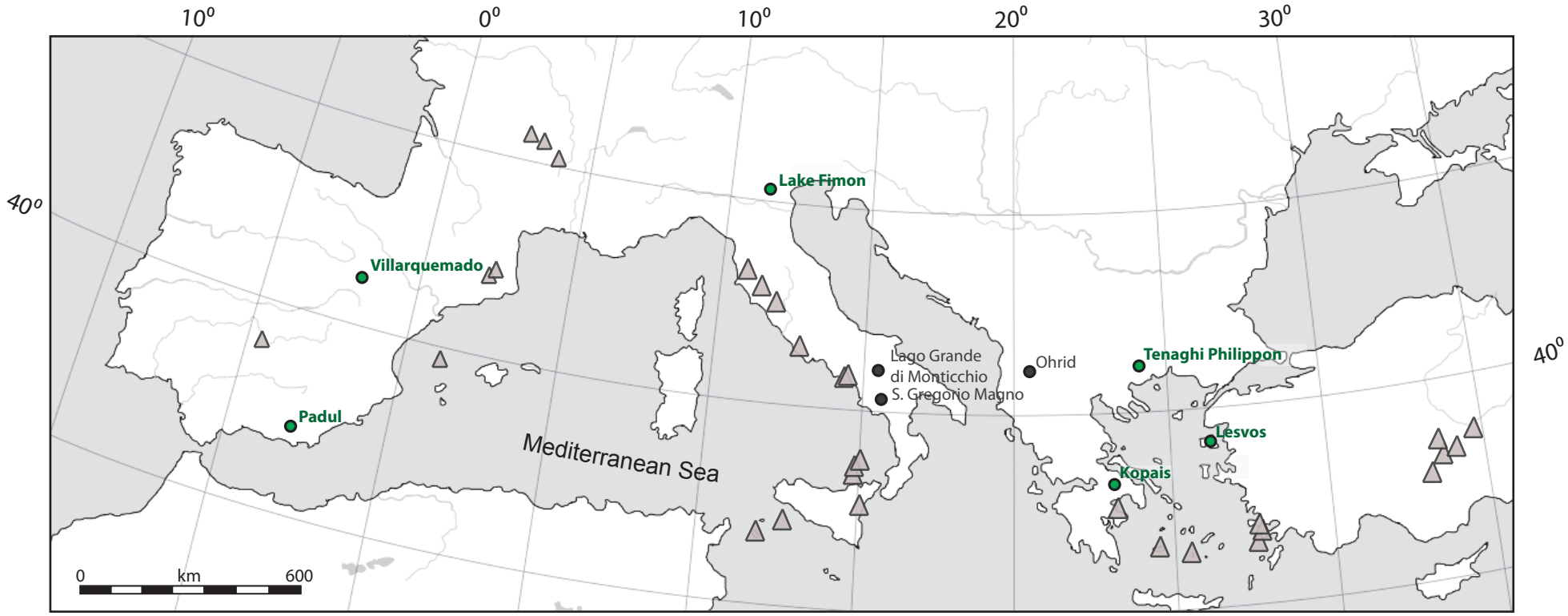

Figure 4.1 – Locations of sites sampled for this study (in green) and other aforementioned sites. Volcanoes known to be active during the Quaternary are also highlighted as triangles.

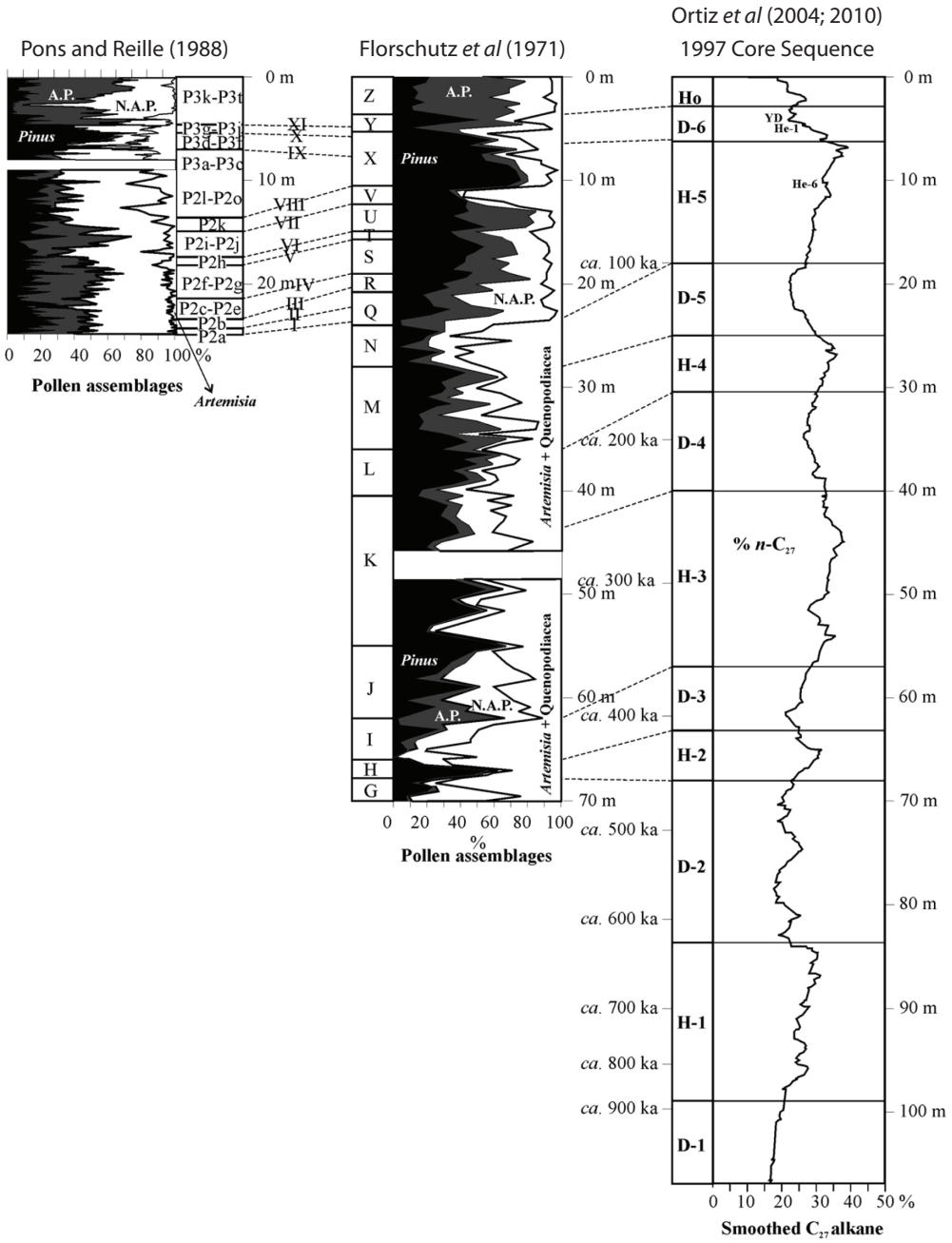

Figure 4.2 – The pollen stratigraphies for Padul produced by Florschuitz *et al.* (1971) and Pons and Reille (1988) (A.P. (arboreal pollen); N.A.P. (Non-arboreal pollen)) compared to the new 1997 core (smoothed profile of C_{27} alkane displayed). Tentative correlations have been made between the cores on the basis of the palaeoenvironmental episodes recognised. Diagram from Ortiz *et al.* (2010).

Padul 1997 Core Sequence

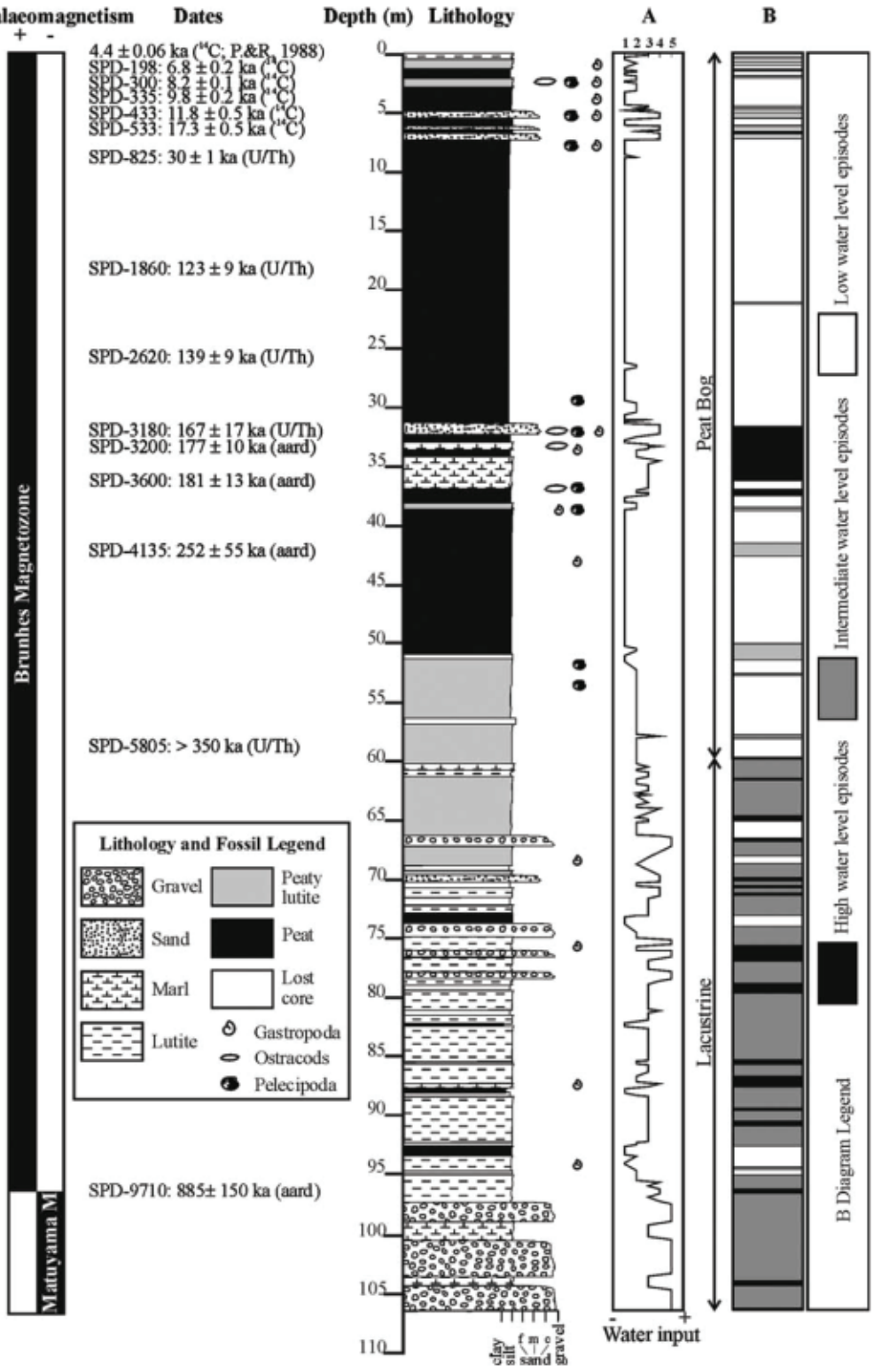

Figure 4.3 – Lithostratigraphy and chronology of the 1997 Padul peat bog core with water-input (**A**; based upon the sedimentology) and water level episodes (**B**) based upon the palaeoenvironmental proxies. Diagram from Ortiz *et al.* (2004).

Padul 1997 Core Sequence

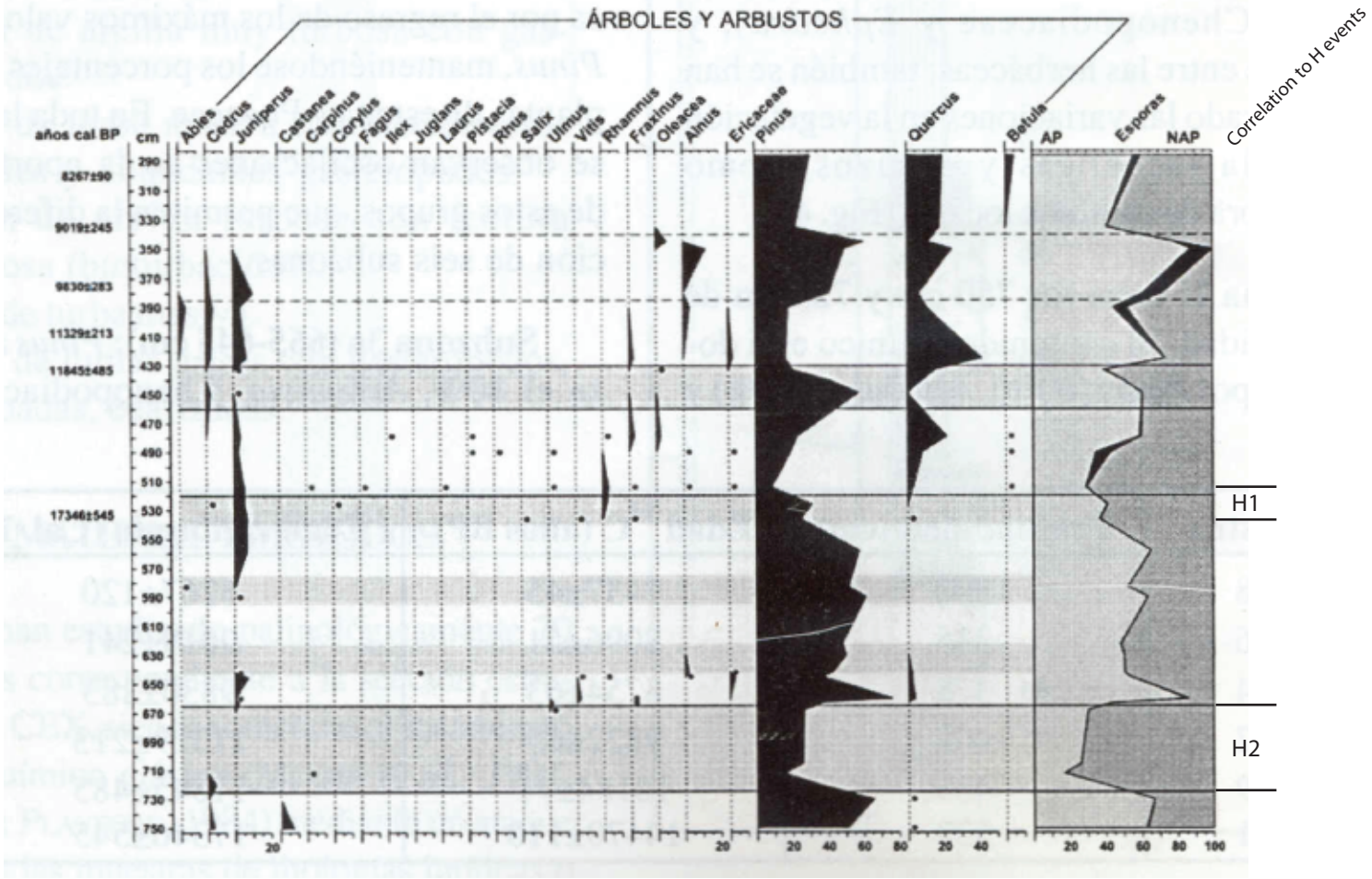

Figure 4.4 – Pollen profile from the new 1997 Padul core, adapted from Valle *et al* (2003). The pollen stratigraphy covers the very upper part of the sequence and correlations to Heinrich Events have been highlighted (Valle *et al.*, 2003).

Table 4.1 – Summary of Padul setting and available palaeo-data.

Site Name:	Padul
Country:	Spain
Grid Ref.	37°01'01"N 3°36'07"W
Modern Setting:	Peat bog
Core Code:	Padul Borehole
Sedimentology:	Peat, marls and leutite with rare sand horizons
Proxy data available:	Pollen, $\delta^{13}C$ isotopes, TOC, *n*-alkanes, C/N ratios

Palaeoenvironmental significance for the LLG

The original pollen diagrams of Florschütz *et al.* (1971) and Pons and Reille (1988) show evidence of tree expansions and contractions during the LLG, though poor age control (and often poor sample resolution) has limited what can be interpreted from these environmental shifts on a more regional scale. The palaeoenvironmental record obtained from the new 1997 core sequence has been studied using a multi-proxy approach at higher stratigraphic resolution, which improves understanding of the climatic changes at Padul during the LLG. Ortiz *et al.* (2004; 2010) have recorded shifts in *n*-alkane percentages (Fig. 4.5) at 10.2, 9, 7.7, 6.8 and 5.9m which they attribute to drier phases that are tentatively related to Heinrich Events 5 to 1 respectively. Following these dry climatic events, there is evidence that regional precipitation and temperatures increased, allowing the re-expansion of trees as reflected in the pollen record (Valle *et al*., 2003; Fig. 4.4).

Current chronology for the LLG

The current chronology of the part of the new Padul core considered to represent the LLG is based on 3 bulk ^{14}C ages and 1 U/Th age estimate (Ortiz *et al*., 2004). No outliers have been identified within the sequence and no age reversals are evident, although there is a large gap in dates between 8.25 and 18.6m, an interval in which many important environmental shifts have been inferred (see above). No detailed chronology has been proposed for the site although Ortiz *et al.* (2004) did interpolate age estimates for undated levels using a polynomial curve (R^2=0.996). The age information put forward by Ortiz *et al.* (2004) for the LLG is shown in Fig. 4.6. At the

Padul 1997 Core Sequence

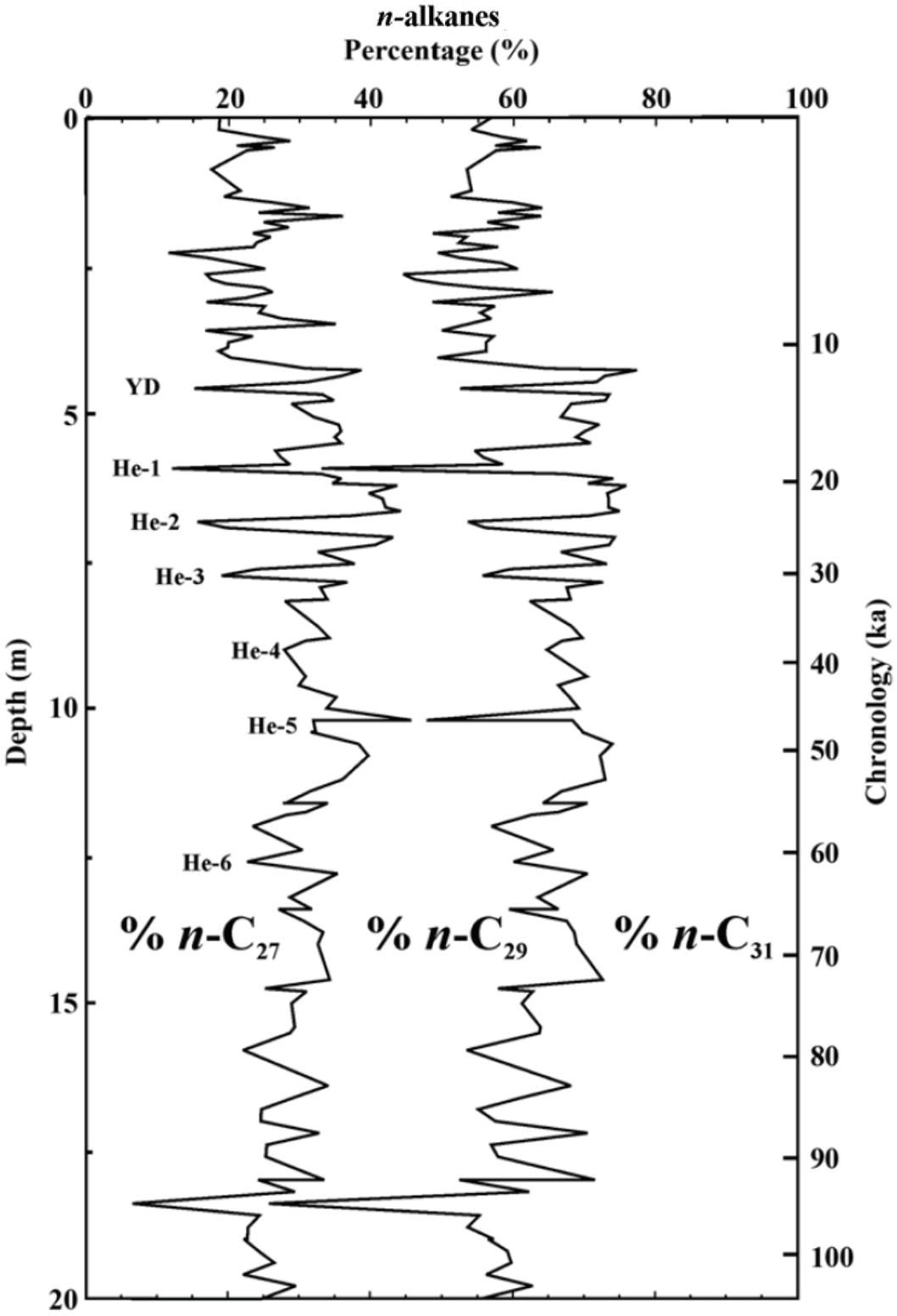

Figure 4.5 – n-Alkane profile (percentages of C_{27}, C_{29} and C_{31} isomers in relation to the total sum) for the upper 20m of the 1997 Padul sequence. The Ortiz *et al.* (2004) age model is also shown (See Fig. 4.6 for details). Palaeoenvironmental interpretations are presented (He: Heinrich Events; YD: Younger Dryas). Diagram from Ortiz *et al.* (2010).

time of commencement of this PhD project, no visible tephra layers had been observed from the Padul sequence and no previous cryptotephra studies had been undertaken.

Tephra sampling

The Padul core (1997) was sampled for tephra in July 2009. Depth interval 6-15m was sampled (the core quality was deemed acceptable for this study; see Table 3.1). The sedimentology of this interval is almost entirely peats with some ostracod–rich horizons; two sand horizons were also present at around 6m. According to the Padul chronology this time interval equates to c.20-80 ka BP (see Fig. 4.6). The core material above 6m meters was in a poor condition (broken up with many gaps from previous sampling) and thus was considered unsuitable for sub-sampling and inclusion within this study.

Site–specific aims

The specific aims for this site were to firstly test if cryptotephra are deposited in this part of Iberia, and, if so, to chemically fingerprint the potential volcanic sources, and secondly to attempt to use the tephra results to test and improve the Padul age model, particularly for the parts of the sequence for which chronological information is sparse (below 8m).

4.2.2 Villarquemado, Aragon, Spain

Site history

The Villarquemado sequence is located in the Teruel province in NE Spain (see Fig. 4.1). The site was discovered in the early 2000's on a coring exploration of this region of Spain where a 74m core was extracted (B. Valero-Garcés, *pers. comm.*). This area is undergoing tectonic subsidence which is thought to have allowed this long sequence to have formed. 18 AMS ^{14}C dates are now available as well as 5 OSL ages for the lower part of the core (Valero-Garcés *et al*., 2007), which is thought to span from 0-120 ka BP (Moreno *et al*., 2012), making Villarquemado potentially very important for understanding environmental and climatic shifts in this part of Spain during the last glacial-interglacial cycle.

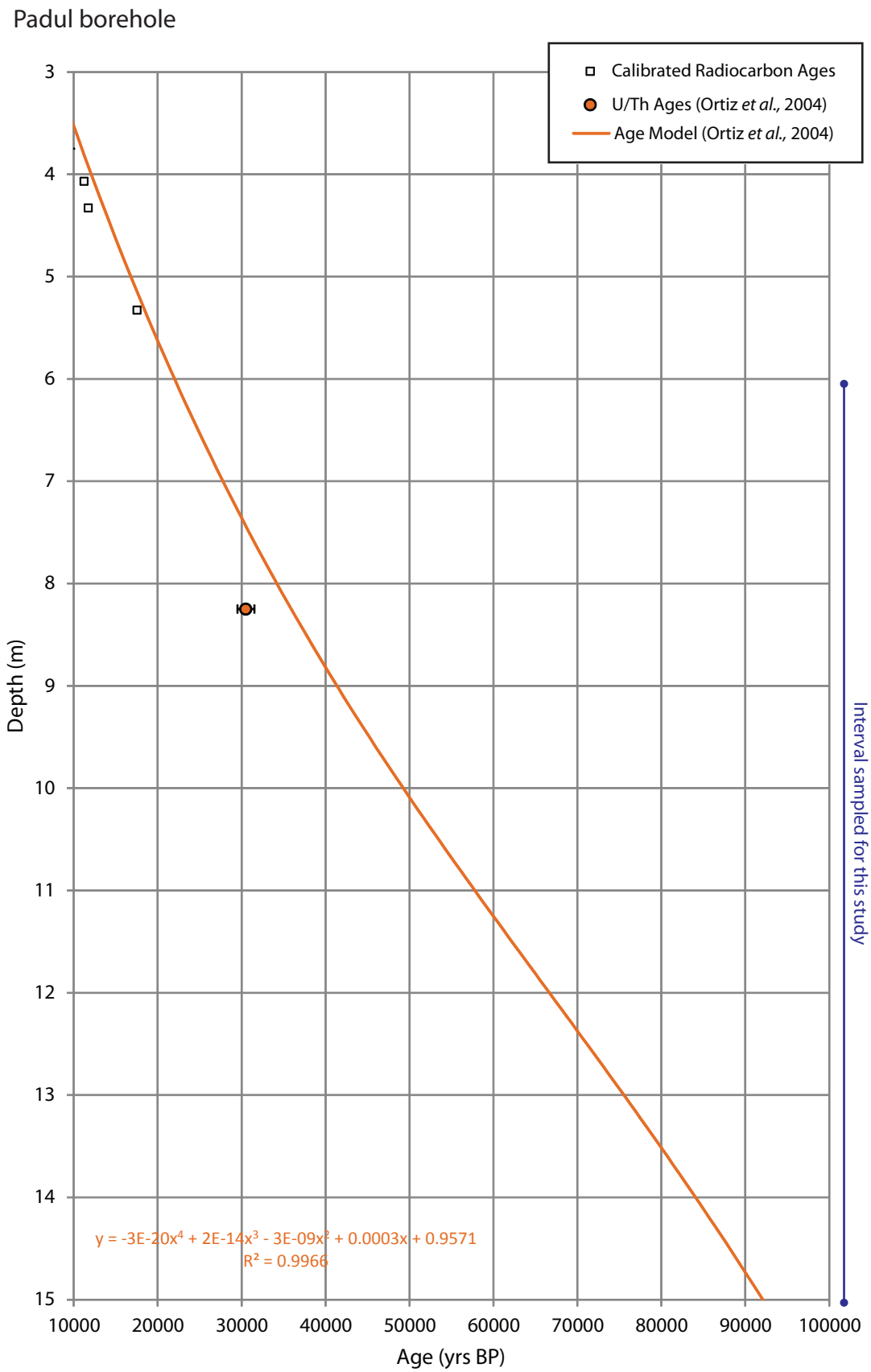

Figure 4.6 – The Ortiz *et al.* (2004) age profile and independant ages (2 sigma error) for Padul borehole (3-15m metres). The interval sampled for this study is highlighted.

Palaeoenvironmental significance for the LLG

The palaeoenvironmental signal from Villarquemado is complicated due to the active tectonism that would have been on-going within the basin coupled with poor pollen preservation for most of the LLG sequence (B.Valero-Garcés & A. Moreno, *pers. comm.*). On the basis of the lithostratigraphic facies units and XRF results (particularly Ca), Moreno *et al.* (2012) have identified the beginning of MIS 3 and inferred it to have been a very arid period, with evidence of alluvial fan deposition. However this changed and the local conditions briefly became increasingly moist around c.42-21 ka BP with evidence of shallow lake formation. This humid phase although punctuated with arid intervals continued through to MIS 2, with apparently relatively humid conditions prevailing during the LGM. The key lithostratigraphic, chronological and proxy information for the full Villarquemado sequence is shown in Fig. 4.7 and Table 4.2.

Table 4.2 – Summary of Villarquemado setting and available palaeo-data.

Site Name:	Villarquemado
Country:	Spain
Grid Ref.	40°30'N 1°18'W
Modern Setting:	Wetland
Core Code:	Villarquemado
Sedimentology:	Peats, sands and silts.
Proxy data available:	XRF, MS, TOC, TIC, Pollen

Current chronology for the LLG

The current chronology of the LLG in the Villarquemado core, based upon 18 bulk radiocarbon dates and one OSL age (see Fig. 4.8), reveals age reversals within the radiocarbon chronology with several outliers identified (B.Valero-Garcés & A. Moreno, *pers. comm.*). No detailed age model has yet been proposed for Villarquemado, and currently no visible tephra layers have been observed and no previous cryptotephra studies had been undertaken at the time this PhD project commenced.

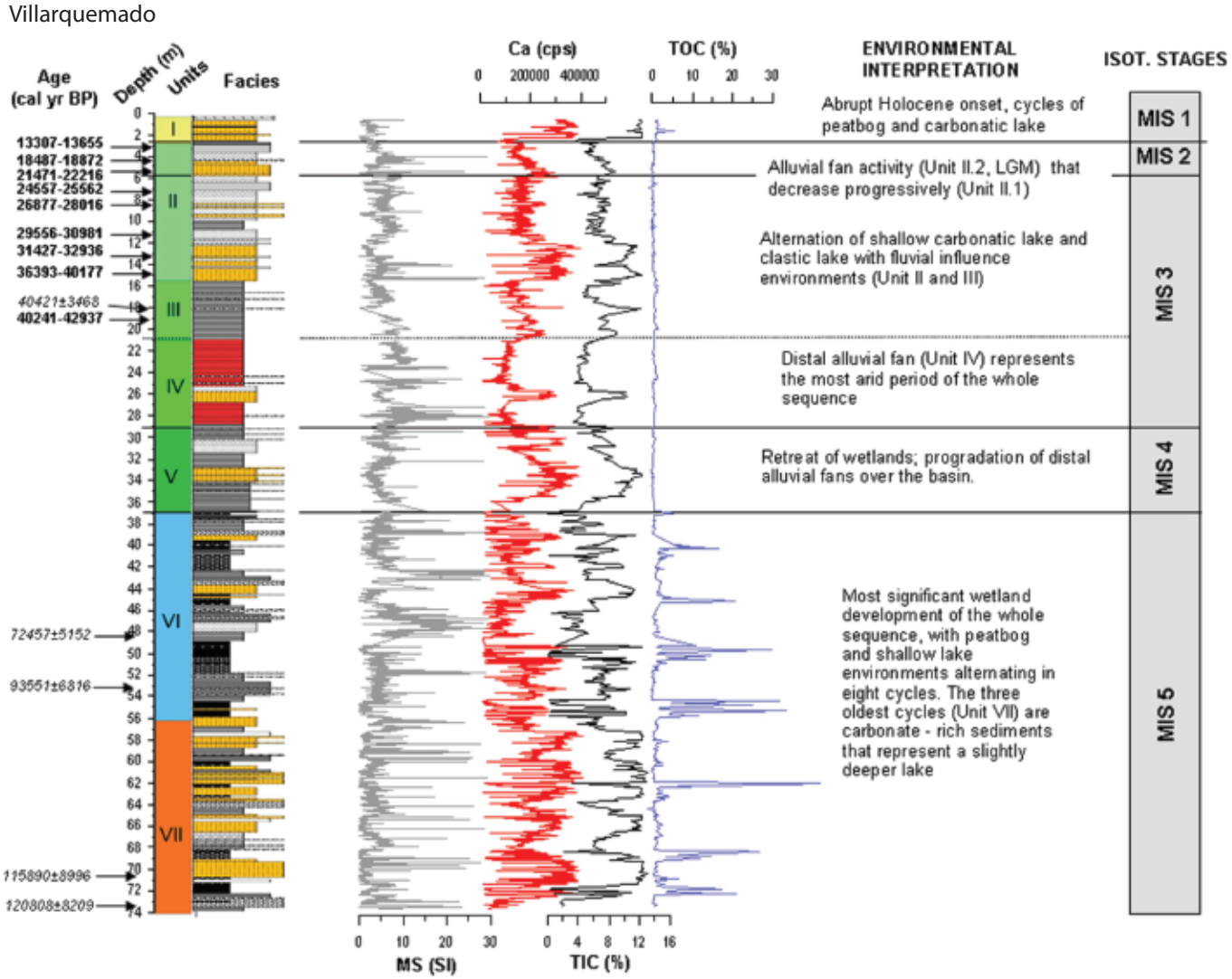

Figure 4.7 – Overview of the Villarquemado palaeo-record. From Left to Right: chronological information (calibrated radiocarbon dates in bold, OSL ages in Italics), Sedimentary units and facies, magnetic susceptibility (MS), Ca (via XRF), total organic carbon (TOC) and interpretations of the depositional environments and correlation to Marine Isotope Stages. Diagram taken from Moreno *et al.* (2012).

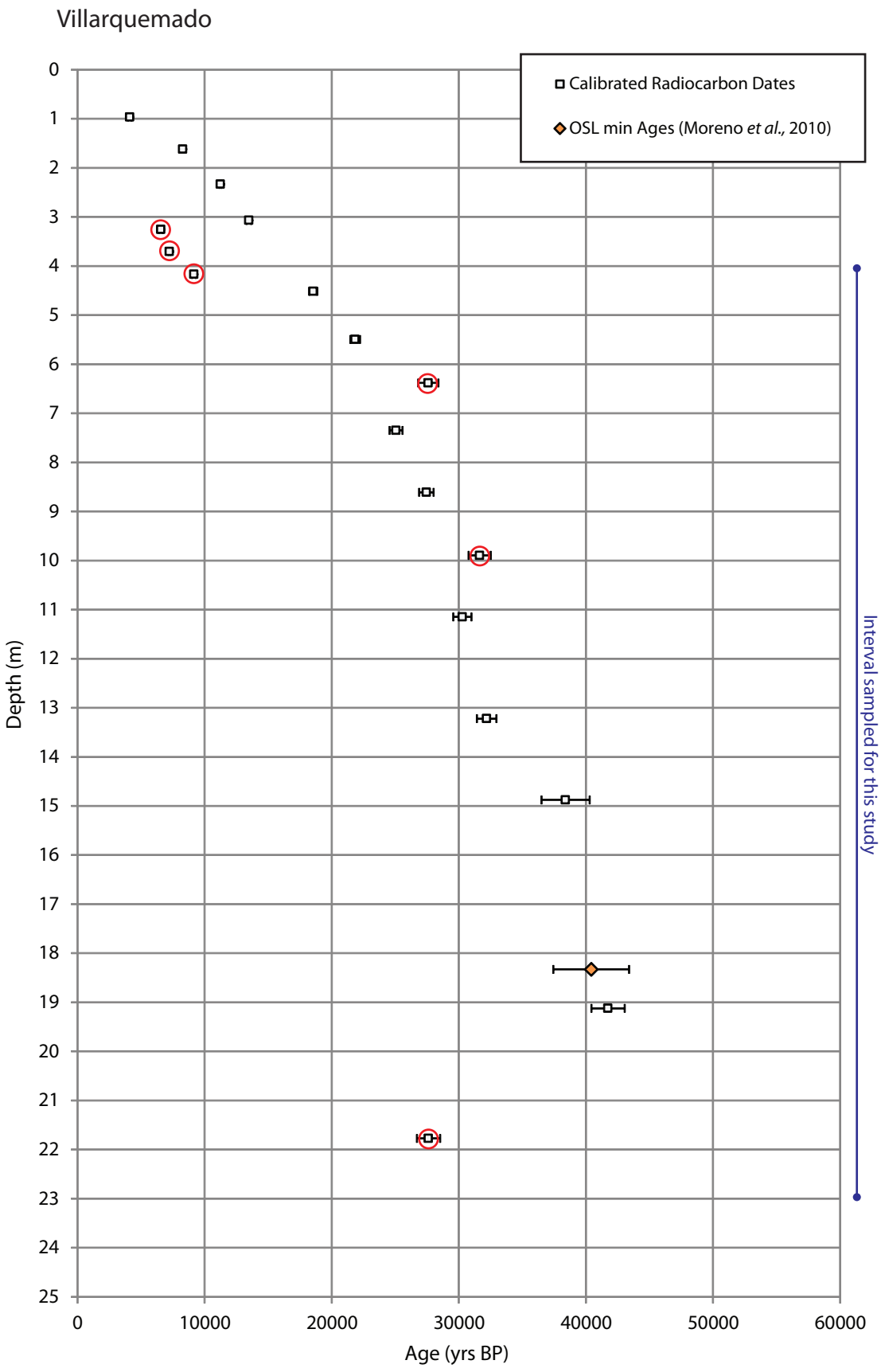

Figure 4.8 – Dating controls available for the Villarquemado sequence (with error ranges at 2 standard deviations). Radiocarbon dates with red circles indicate ages which have been identified as potential outliers (B. Valero-Garcés, *per comm*). The interval sampled for this study is highlighted.

Tephra sampling

The Villarquemado cores were sub-sampled in two separate sampling trips, one undertaken in late 2008 and the other in early 2009, on both occasions based at the Instituto Pirenaico de Ecología-CSIC, Zaragoza, Spain. The depth interval 4 to 23m was sampled contiguously and analysed for cryptotephra content. The core condition was mostly good. Lithological units sampled included clay and silt beds with some interspersed fine sandy units. According to the radiocarbon and OSL ages, this sampled interval roughly equates to the interval 15-50 ka BP (see Fig. 4.7 and 4.8).

Site-specific aims

As with Padul, the key aims were to ascertain if cryptotephra layers were deposited in this part of Iberia, and, if so, whether their potential volcanic sources could be determined using geochemical methods. A further aim was to use any tephra results to test and, if possible, enhance, the Villarquemado age model.

4.2.3 Fimon, Vicenza, Italy

Site history

The modern Lake Fimon (45°28'N 11°32'E) is situated on the northern side of the Berici Hills (NE Italy; see Fig. 4.1). The modern lake sits upon valley-fill deposits, much of which is formed of lacustrine sediments deposited in the previously much larger palaeolake Fimon. These more extensive former lake deposits were only discovered very recently after an extensive drilling campaign (See Pini *et al.,* 2010; Monegato *et al.,* 2011). The genesis of this palaeolake system is still largely unknown and research on this and its relationship to the local fluvial geomorphology is still on-going (C. Ravazzi, *pers. comm.*). The underlying bedrock is formed primarily of Oligocene marine limestones, Eocene marls and mafic volcanic dykes which cut through these beds (Macera *et al*., 2003).

There are three cores from the Fimon region that have been investigated (Monegato *et al*., 2011). Of these three cores, Fimon core Ponte sulla Debba (PD; see Table 4.3) has been studied in the most detail, with fourteen radiocarbon dates determined and a pollen record generated (Pini *et al*., 2010; see Fig. 4.9). Pini *et al.* (2010) suggest this

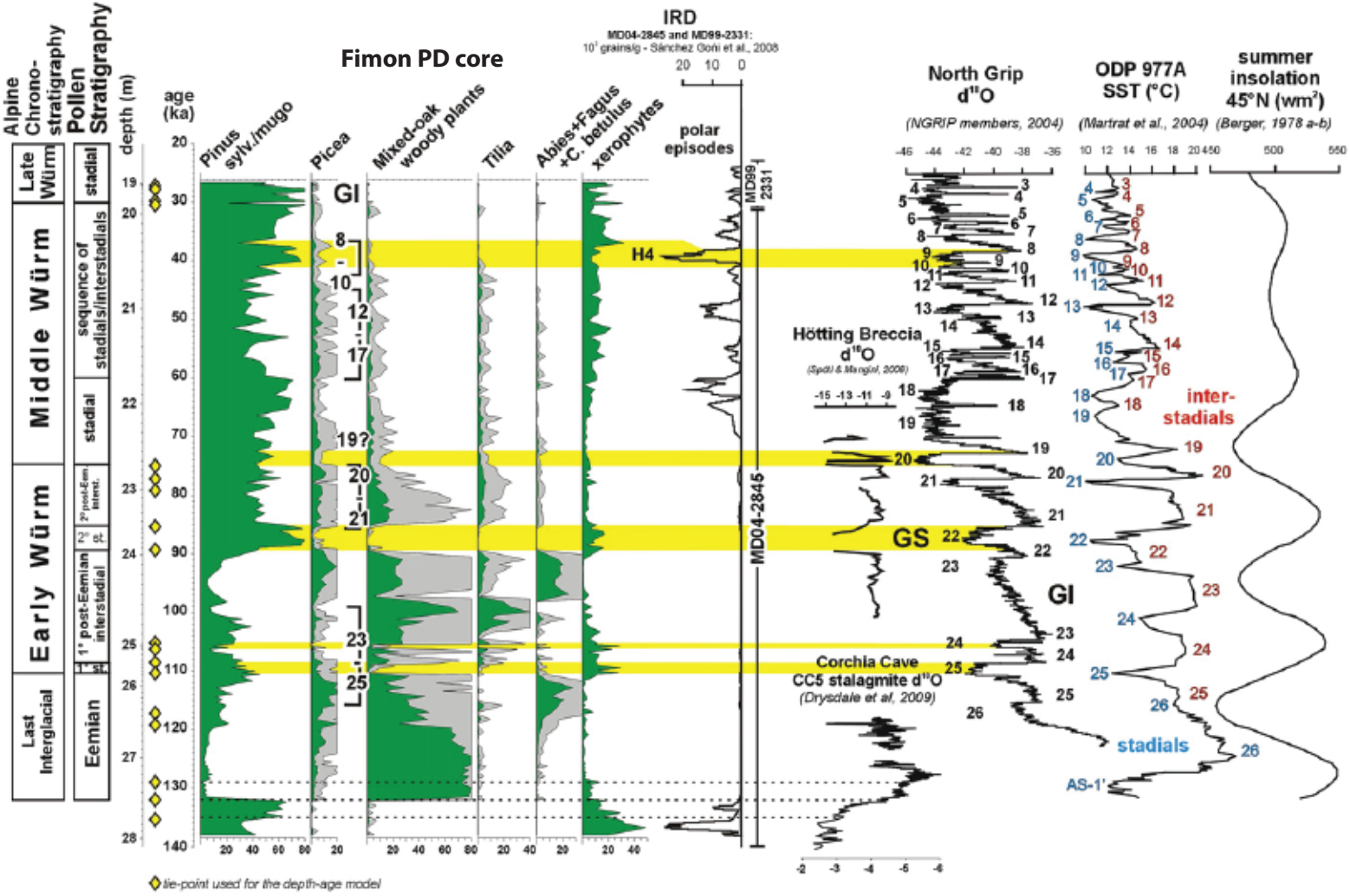

Figure 4.9 – Fimon PD pollen record and correlation to other palaeoenvironmental records and climatic events. From Pini *et al.* (2010).

record forms a continuous record extending from the late glacial to the Last Interglacial.

Table 4.3 – Summary of Fimon (PD) setting and available palaeo-data

Site Name:	Lake Fimon
Country:	Italy
Grid Ref.	45°28'49"N 11°32'34"E
Elevation:	23m
Modern Setting:	Former lake basin
Core Code:	Ponte sulla Debba core (PD)
Sedimentology:	Shaled gyttja peat, siltly gyttja, organic silts and inorganic and organic clays.
Proxy data available:	Pollen stratigraphy, Loss On Ignition, Magnetic Susceptibility, Radiocarbon dates, Petrographic information.

Palaeoenvironmental significance for the LLG

Based on the current accepted age model, Pini *et al.* (2010; see Fig. 4.9 and 4.10) recognise D-O like vegetation fluctuations during the middle part of the last glacial, though they do not attempt to correlate these to Greenland interstadial events due to the low pollen-stratigraphic resolution currently available for this part of the core. However, within this interval, Pini *et al.* (2010) do attribute a pollen peak in xerophytic taxa and the last occurrence of continous *Tilia* pollen at 20.45m to Heinrich Event 4. One of the key inferences made from the Fimon data is the evidence for persistent afforestation (of *Pinus* and other warm-temperate tree species) during the middle part of the last glaciation, which they considered to be suggestive of sustained high precipitation during this interval.

The Fimon PD core is the most detailed palaeoenvironmental record currently available from the southern Alpine foreland. Very few other palaeo-records extending this far back into the Late Pleistocene are currently available from this region. Fimon PD is thus of key importance to understanding environmental and climatic changes in this area during the Last Glacial cycle and before.

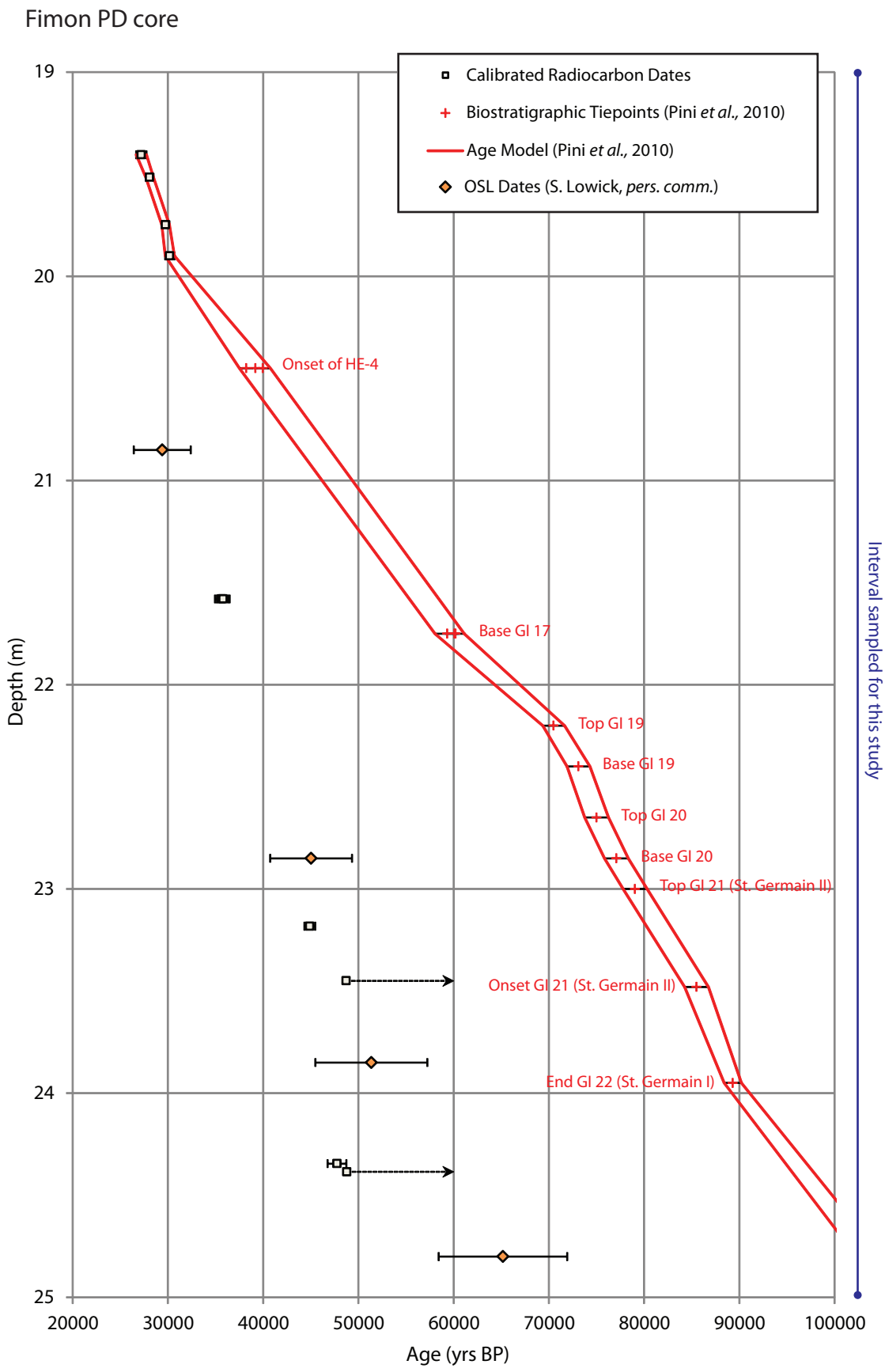

Figure 4.10 – Fimon PD age information from Pini *et al.* (2010), OSL ages were supplied by Sally Lowick, Bern University (*pers. comm.*). Biostratigraphic alignment point ages were imported from various palaeo-records including ice-cores, marine cores and speleothems, see Pini *et al.* (2010). The interval sampled for this study is highlighted. Error ranges are plotted at 2 standard deviations except for the OSL ages shown with 1 sigma errors.

Current chronology for the LLG

Pini *et al.* (2010) have developed a very detailed chronostratigraphic scheme for the Fimon PD core which is tied to the radiocarbon dates until c.30 ka BP and then is based upon 18 pollen-stratigraphic alignment points back to c.130 ka BP. Pini *et al.* (2010) import the ages (and errors) for these climatic events using other records, such as the NGRIP isotope sequence, and more regional speleothem records (Martrat *et al.,* 2004; Holzkämper *et al.,* 2005; Spötl & Mangini, 2006; Meyer *et al.,* 2008; Drysdale *et al.,* 2009) directly into the Fimon PD chronology (see Fig. 4.10). This age model is discordant with the radiocarbon information available for the lower part of the core, which Pini *et al.* (2010) reject on the basis of the pollen-biostratigraphy, which they consider indicates a "natural contamination not removed by the pre-treatment process" (p.3127) leading to anonymously young radiocarbon ages. Subsequently, a number of OSL ages became available for the Fimon PD sequence during the course of this research, and these appear to show broad agreement with the radiocarbon chronology beyond c.30 ka BP (S. Lowick, *pers. comm.*). This new age information is included in Figure 4.10.

At the time this PhD project commenced, no visible tephra layers had been observed from the Fimon sequence, but an initial cryptotephra study was on-going during the course of the research presented here. This was being carried out by B. Giaccio (Istituto di Geologia Ambientale e Geoingegneria, CNR) who focused on the narrow depth interval of 22.40-22.45m in an attempt to locate tephra of the Campanian Ignimbrite eruption, because this part of the core was interpreted as representing the beginning of the Heinrich 4 event by Pini *et al.* (2010) which dates to around c.40 ka BP, also the widely accepted age of the CI eruption (De Vivo *et al.* 2001).

Tephra sampling

The Fimon core was sub-sampled in July 2010 in Milano, Italy. The depth interval 19 to 25m was sampled contiguously and analysed for cryptotephra. Lithological units sampled included gyttja, peats, organic silts and clays. The core condition was very good, though some bioturbation features were evident (Pini *et al*., 2010). According to the radiocarbon and OSL ages, this sampled interval roughly equates to 25-60 ka BP (Pini *et al*., 2010; S. Lowick, *pers. comm.*), but the biostratigraphically based age-depth model favoured by Pini *et al.* (2010) suggests the age range to be c.25-100 ka BP.

Site-specific aims

Testing the robustness of the age model proposed by Pini *et al.* (2010) against the rejected chronological information (see Fig. 4.10) is an important aim for Fimon. Also Fimon is, as far as this author knows, one of the first pre-Lateglacial records in the north of Italy to be investigated for cryptotephra. Thus Fimon can be used to test if any eruptions during the LLG had a northwards dispersal. In particular the Campanian Ignimbrite is predicted to leave a visible ash horizon just 200 km to the south of Fimon (Pyle *et al*., 2006) and is potentially a key chronostratigraphic marker to seek within the Fimon sequence.

4.2.4 Kopais, Boeotia, Greece

Site history

Lake Kopais is situated in Boeotia, central Greece. The catchment covers an area of 2000 km^2 and is primarily fed by the River Kephissos and River Melas as well as other small inlets (Griffiths, 2001). The Kopais basin depression formed as a result of tectonic subsidence during the Pliocene and Pleistocene, and also was enhanced by solution of the limestone bedrock (Papadopoulou-Vrynioti, 1990). The underlying bedrock is predominately formed of Mesozoic limestones.

Lake Kopais has been significantly managed beginning as long ago as 3.5 ka BP by the Mycenaean civilization when the Kopais basin was occupied by a fen (Knauss, 1984; 1987). Evidence suggests the Mycenaean's undertook major engineering works (including cutting large drainage channels into the limestone bedrock) to increase drainage of the basin, probably to decrease the chance of flooding or to make the area more suitable for agricultural use (Kenny, 1935). The lake was drained more fully during the 1880s by the Lake Kopais Company (Tzedakis, 1999). The Quaternary palynology of the site was first investigated by Greig & Turner (1974) who showed clear vegetation change attributed to the late Holocene. Since then a number of researchers have produced pollen diagrams based on cores taken from Kopais: Turner & Greig (1975) provided the first evidence of pre-Holocene glacial climate from the site. Allen (1986; 1990) investigated the sedimentary and environmental history of the late Quaternary of Kopais and reported the results of the first radiocarbon determinations.

The geometry of the lake basin was subsequently constructed from data obtained from 45 cores taken by the Greek Institute of Geological and Mineral Exploration (IGME). One of the longer cores, K-93 (c.60m), taken from the centre of the Kopais basin was studied in detail by Tzedakis *et al.* (1999) primarily for its pollen stratigraphy and then by Griffiths (2001) and Griffiths *et al.* (2002) for isotope stratigraphy (see Figs. 4.11 and 4.12 and Table 4.4.), with MIS 3 and MIS 4 studied in particular detail. Because of the rich amount of proxy evidence available this core sequence was chosen for inclusion within this study and is discussed in more detail below. Coeval to these investigations, a separate research group have also carried out palynological investigations (Okuda *et al.,* 1999; 2008) on the longest core taken from Kopais by the IGME to the east of the basin (c.120m). This sequence is interpreted as extending back to at least Stage 11 and probably older. No tephra horizons were reported from this sequence.

Table 4.4 – Summary of Kopais (K-93) setting and available data

Site Name:	Kopais
Country:	Greece
Grid Ref.	38°26'16"N, 23°03'01"E
Elevation:	92.4m
Basin Size:	2000 km^2
Modern Setting:	Drained lake basin
Core Code:	K-93
Sedimentology:	Calcareous lake silts and clays with rare organic layers.
Proxy data available:	Pollen, LOI, Mag Sus, O and C isotopes, Radiocarbon dates (AMS), TOC, Colourimetry, CaCO3, Ostracod fauna.

Suggested age models for the LLG

The primarily calcareous inorganic lithology of core K-93 makes it particularly problematic to date; all available radiocarbon dates (AMS) for the core are based on picked charcoal pieces (see Table 4.5 and Fig. 4.13). Because of a lack of dates for the sequence below 20 m, the first age model proposed for the site by Tzedakis (1999) utilised variations in the pollen stratigraphy and also the lithostratigraphy, which suggest that no major hiatuses have interrupted sedimentation except perhaps at 42.59-42.65 m where an organic layer could be evidence that the lake completely

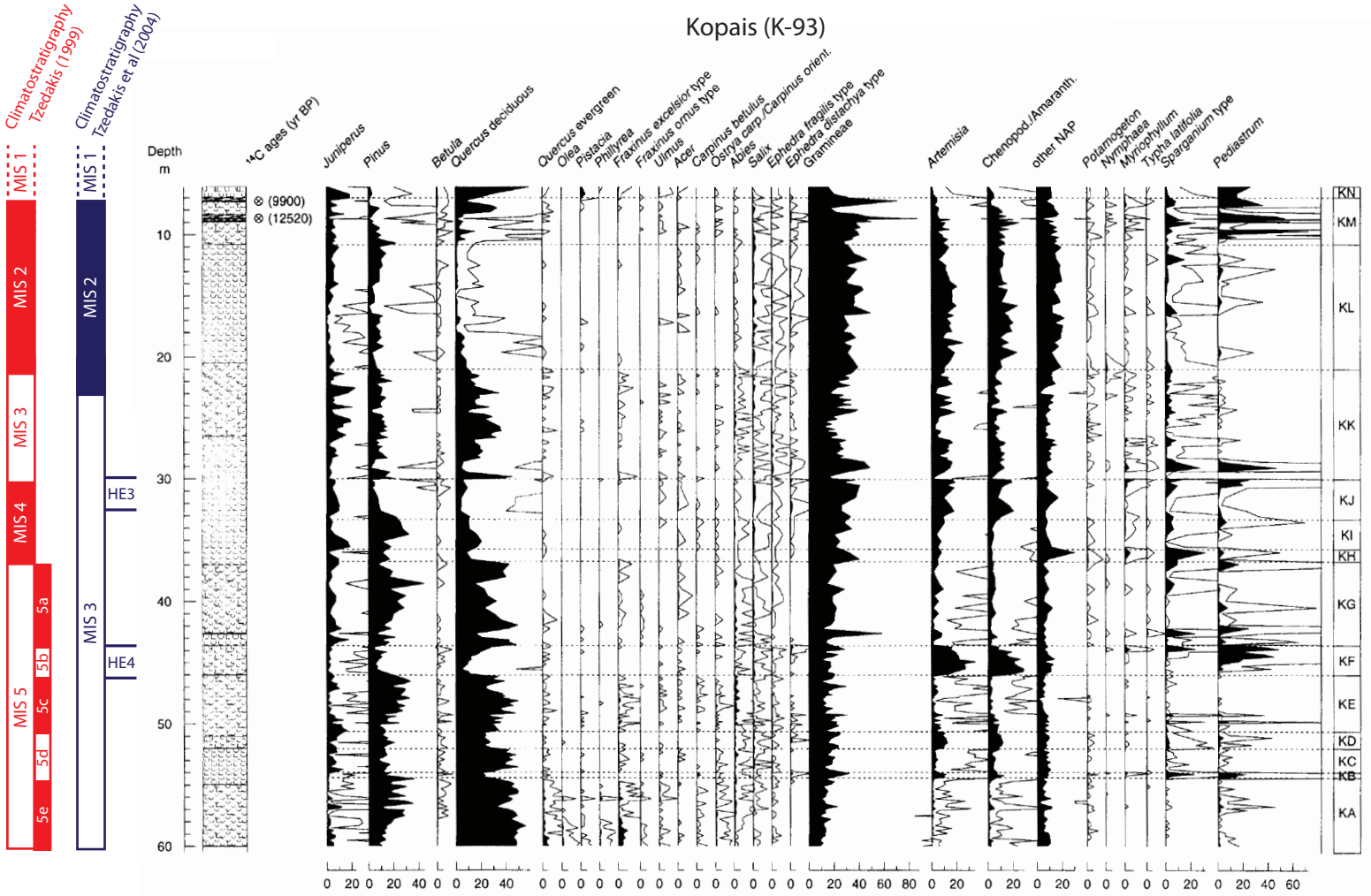

Figure 4.11 – Kopais (K-93) pollen stratigraphy from Tzedakis (1999). In addition the climatostratigraphic relationships proposed originally by Tzedakis (1999) and then by Tzedakis *et al.* (2002) of the Kopais pollen record to the MISs and also Heinrich events.

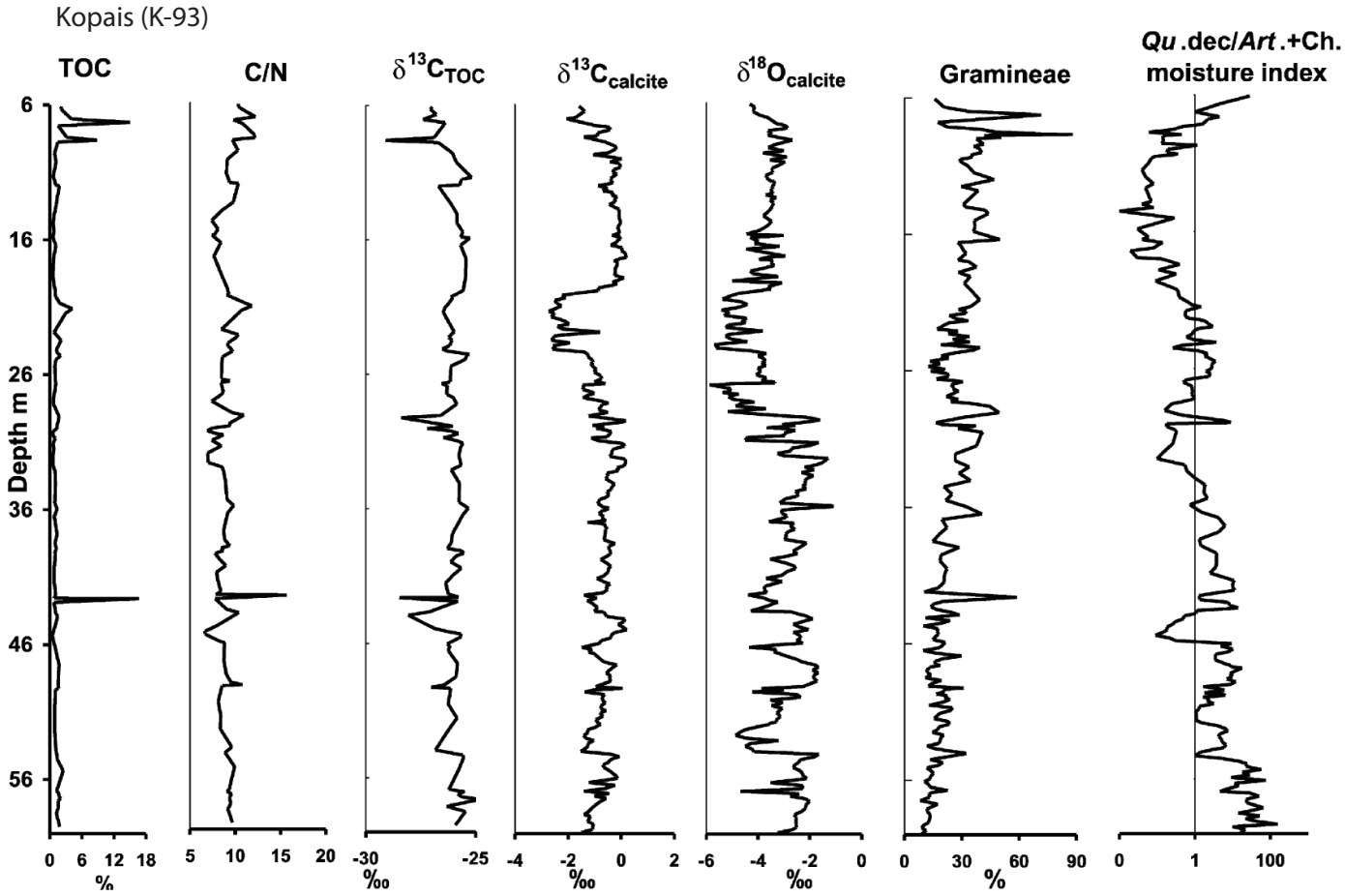

Figure 4.12 – Summary diagram of various palaeoenvironmental data for the Kopais (K-93) core including; C/N, Carbon isotopes on Total Organic Carbon (TOC) and calcite; Oxygen isotopes on calcite; Gramineae percentage and a moisture index curve based upon the pollen data of Tzedakis (1999). Diagram from Griffiths *et al.* (2002).

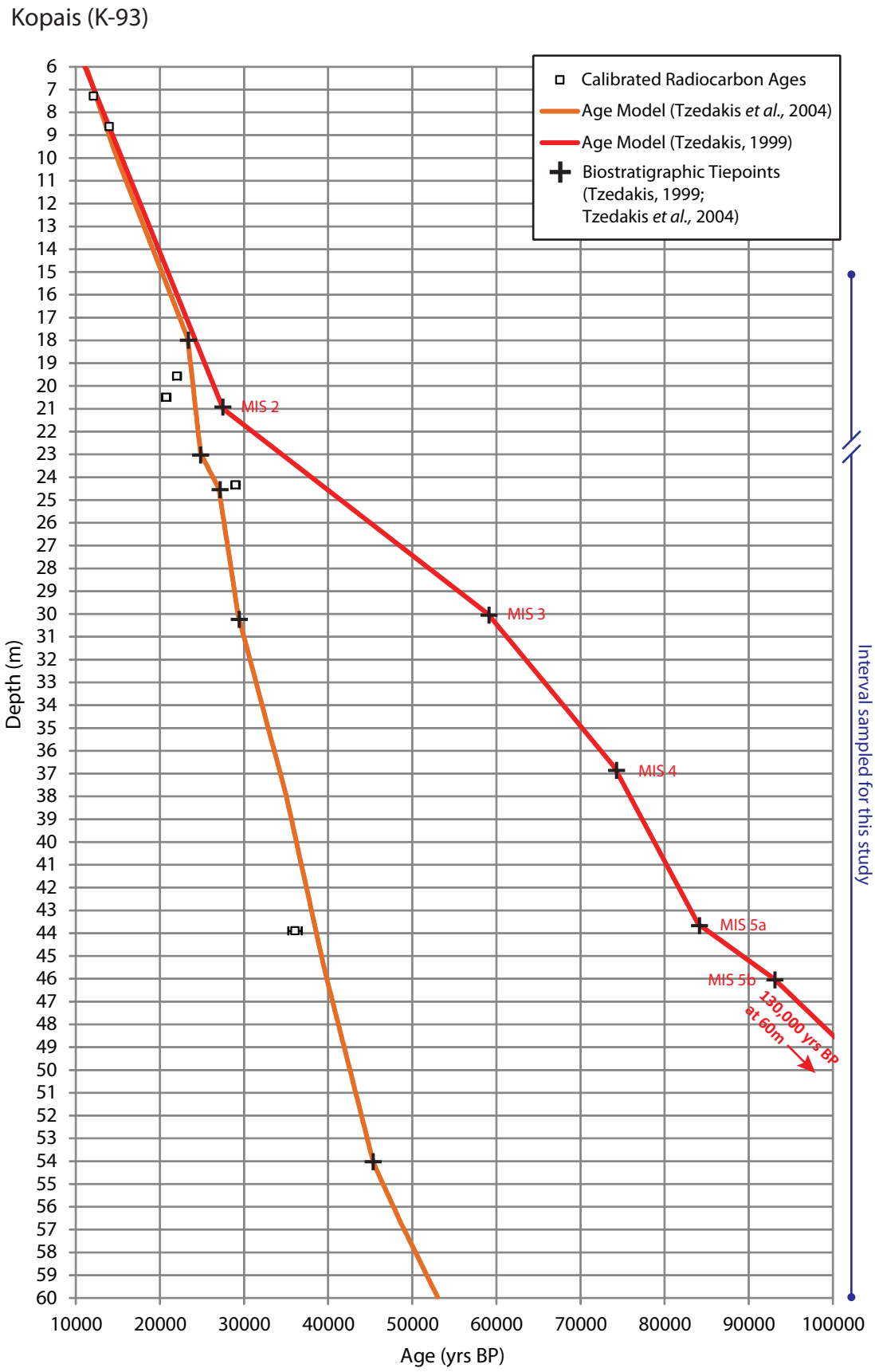

Figure 4.13 – Kopais (K-93) age determinations and the two suggested age models, the original model in red (Tzedakis, 1999) and the age-depth model suggested by Tzedakis *et al.* (2004) in orange. Both models are based upon using radiocarbon age as range finders and alignment to biostratigraphic tie points (see Fig. 4.7). The interval sampled for this study is highlighted.

dried out for an undetermined length of time. Tzedakis (1999) compared the Kopais pollen record to other long records from sites in southern Europe, and concluded an age of ~126 ka BP for the base of the sequence (see Fig. 4.11). Griffiths (2001) and Griffiths *et al.* (2002) concurred with this age model on the basis of their stable isotope stratigraphy, despite obtaining some new contradictory radiocarbon dates (AA35125; AA39647; AA35126).

Tzedakis *et al.* (2004) obtained additional radiocarbon dates, in particular one from 43.90m depth (see Table 4.5), which resulted in a markedly different age model for the site being proposed, which suggests that the whole sequence extends back to ~51 ka BP only. This new age model was based upon alignment of the Kopais pollen stratigraphy with the Ioannina (I-284) pollen stratigraphy and age-depth model. The I-284 age model is based upon a combination of radiocarbon dates and orbital tuning of pollen data for the last 21 ^{14}C ka years, and beyond that age is solely based on orbital tuning. The basis for each of the proposed chronologies for the Kopais sequence is summarised in Table 4.6.

Palaeoenvironmental significance for the LLG

The Kopais core K-93 provides a detailed near-continuous record of environmental and climatic shifts during the Last Glacial period in central Greece. These environmental shifts are particularly apparent in a detailed pollen stratigraphy generated by Tzedakis (1999; see Fig. 4.11) and also from a parallel oxygen isotope record based on the same core sequence (Griffiths *et al*., 2002; see Fig. 4.12). In this sequence there is clear evidence of forest expansions and collapses. Tzedakis *et al.* (2004) have related two of these collapses at 33.30 and 46m to Heinrich Events 3 and 4. Between 10-21m (c.16-24 ka BP) tree populations remain very subdued. See Figure 4.11 for all the climato-stratigraphic correlations that have been made for the K-93 sequence.

Previous tephra investigations of K-93

Tzedakis *et al.* (1999) reported that core sequence K-93 was examined in detail by B. Narcisi using magnetic susceptibility measures to detect the presence of volcanic tephra in an attempt to improve the chronology of the sequence, but no ash was detected. Following this, during the course of her PhD studies, Griffiths (2001) created 'smear' slides in an attempt to locate the tephra of the Campanian Ignimbrite eruption,

focusing on the depths which according to the Tzedakis (1999) age-model should contain shards of the CI (c.40 ka BP), but no tephra shards were found.

Table 4.5 – Accelerator Mass Spectrometer (AMS) radiocarbon dates obtained from Kopais (K-93).

Depth (m)	**Material**	**Radiocarbon Code**	**^{14}C age (BP)**	**Calibrated age range (IntCal09)**	**Comments**
7.29*	Charcoal	—	10310±70	12410-11825	
8.63*	Charcoal	—	12150±50	14163-13832	
19.57†	Microscopic charred grass fragments	AA35125	18580±160	22489-21558	
20.49-20.51†	Microscopic charred grass fragments	AA39647	17360±160	21257-20249	Sample picked in two batches, greater risk of contamination? (Griffiths, 2001)
24.34†	Microscopic charred grass fragments	AA35126	24200±220	29485-28488	
43.90*	Charcoal	—	31780±310	36855-35265	

Note: †-Values from Arizona lab (Griffiths *et al*., 2002) *- Results from Beta Analytic (Tzedakis *et al*., 2004)

Table 4.6 –The two different proposed age models for the Kopais (K-93) sequence

	Kopais (K-93)	
	Age Model 1	**Age Model 2**
References:	Tzedakis (1999); Griffiths (2001) Griffiths *et al.* (2002)	Tzedakis *et al*. (2004) C. Tzedakis, *pers. comm*. (2009)
Age of Base:	~130 Ka	~51 Ka
Basis:	1) Warm climate proxies recorded towards bottom of sequence.	1) Independent radiocarbon AMS dates firmly imply much faster depositional model. 2) Climatic and ecological shifts, assigned to the Last Glacial period, were more fully understood than was the case from other records.
Problems:	1) The radiocarbon evidence directly contradicts this age model. 2) No independent dates are available to support this age model. 3) No direct dates are available for the base (~18m) of the sequence	1) The ^{14}C dates are potentially too young due to contamination. 2) The age model has been fined-tuned using orbital tuning. 3) No direct dates available for the base (~18m) of the sequence

Tephra sampling

The Kopais cores were transported to the RHUL labs for cryptotephra sub-sampling in 2009. A total of 45 metres were sampled contiguously for cryptotephra analysis covering the interval of 15-60m, sampling to the base of the K-93 sequence. There is a small gap in sampling, from 22.4 to 23m, as the cores for these depths could not be located. Overall the cores, were found to be acceptable for sampling (although severely

dried out). The sediments are primarily composed of endogenic calcites with rare occasional organic horizons (Griffiths *et al*., 2002), while charcoal fragments were sometimes visible during sampling. The sampled sediment column covers the time interval 20-53 ka BP, according to the most recent age model proposed by Tzedakis *et al.* (2004), or 20-130 ka BP according to the original model based on biostratigraphic correlation (Tzedakis *et al*., 1999; Griffiths *et al*., 2002; see Fig. 4.11, Fig. 4.13 and Table 4.6 for details).

Site-specific aims

The key aim is to search for cryptotephra layers and, if found, to test the validity of the two age models outlined above (Fig. 4.13 and Table 4.6) as well as the radiocarbon dates on which these are partially based. A further aim is to refine the Kopais K-93 chronology by independently testing the robustness of the biostratigraphic correlation of pollen zone KF to Heinrich Event 4, as inferred by Tzedakis *et al.* (2004), using the widespread Campanian Ignimbrite tephra if discovered by the application of improved cryptotephra extraction techniques compared with those applied by Griffiths (2001) and B. Narcisi (Tzedakis *et al.,* 1999; see section 3.3.1).

4.2.5 Tenaghi Philippon, Anatoliki Makedonia, Greece

Site history

Tenaghi Philippon (alternatively known as the Philippi basin) is situated in the Drama basin of NE Greece. The basin formed during the Neogene as a result of tectonic processes (Christanis, 1983). The extensive peat deposit that now fills the basin has an aerial extent of 55 km^2. To the north of the Drama basin are the Pangaion Mountains, to the S-SW are the Lekanis Mountains and to the NE lies Falakron Mountain (Tzedakis *et al*., 2006). The area is separated from the Aegean Sea to the south by the Pangaion Range.

Tenaghi Philippon has a long history of Quaternary research tracing back to long core sequences recovered during the late 1960's which allowed a continuous vegetation reconstruction extending back to around 1 Ma BP. The TF2 sequence (280m deep) was analysed in three depth intervals over a 20 year period by Wijmstra (1969), 0-30m; Wijmstra & Smit (1976), 30-78m; and van der Wiel & Wijmstra, (1987), 78-120m. These vegetation reconstructions, although performed at low stratigraphic resolution,

nevertheless were thought to show climatostratigraphic similarities with the early deep-sea records and subsequently good correspondence with the SPECMAP curve published later (Imbrie *et al.,* 1984). Tzedakis *et al.* (2006) has re-evaluated the age of this sequence and has suggested the base of the pollen record to be older than first thought, dating to 1.35 Ma BP. The sequence has remained highly important to Quaternary research, with a number of reinvestigations undertaken (e.g. Tzedakis *et al*., 2003; 2004; Martrat *et al*., 2004; 2007). The Philippi basin has also been examined for its tephrostratigraphic potential with at least three visible tephra horizons recognised and assigned provisional ages by St Seymour *et al.* (2004). The tephrostratigraphic results from this work are discussed in more detail later in this section.

In 2005, partially in recognition of the importance of the Tenaghi Philippon site a new 60m long core (TP-2005) was drilled using a non-rotating probe powered by a DÜSTERLOH pneumatic hammer system resulting in an excellent recovery rate of 97.8% (see Pross *et al*., 2007 and Table 4.7 for details). A very high-resolution pollen record for the site was produced by Müller *et al.* (2011) and a chronology based on 20 radiocarbon determinations and two correlated visible tephra horizons (see Figs. 4.14 and 4.15). Unlike the TF2 pollen record aforementioned, the pollen sampling was undertaken at a much higher resolution (an average sampling resolution of 3.3 cm; Müller *et al*., 2011).

Table 4.7 – Summary of Tenaghi Philippon (TP 2005) setting and available data

Site Name:	Tenaghi Philippon
Country:	Greece
Grid Ref.	40°58’40”N, 24°13’42”E
Elevation:	40m
Modern Setting:	Drained peat bog
Core Code:	TP 2005
Sedimentology:	Peats, muds and lake marls with discrete visible tephra.
Proxy data available:	Pollen, Mag Sus, Radiocarbon dates.

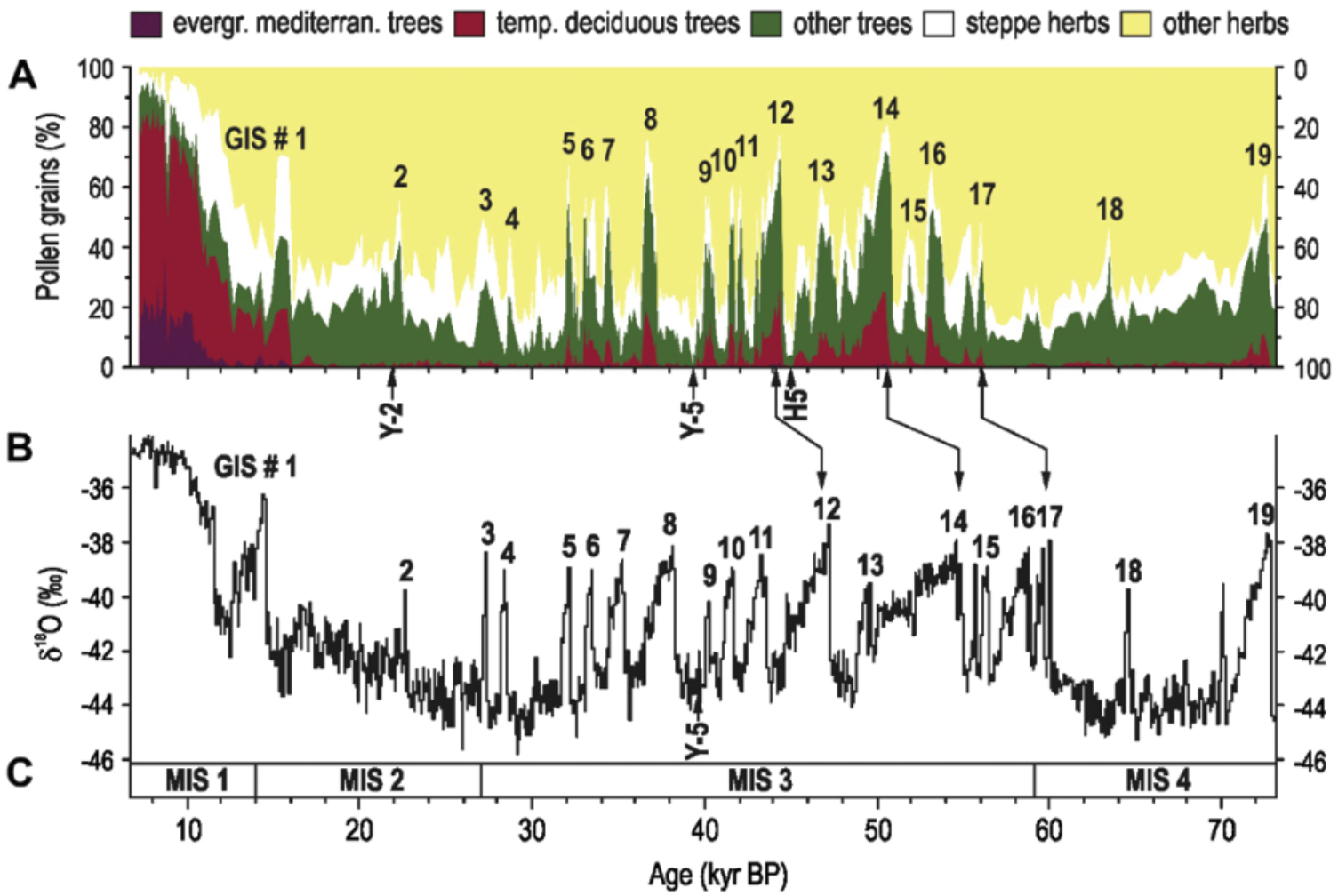

Figure 4.14 – The Tenaghi Philippon 2005 pollen record compared against NGRIP. Taken from Muller *et al.* (2011).

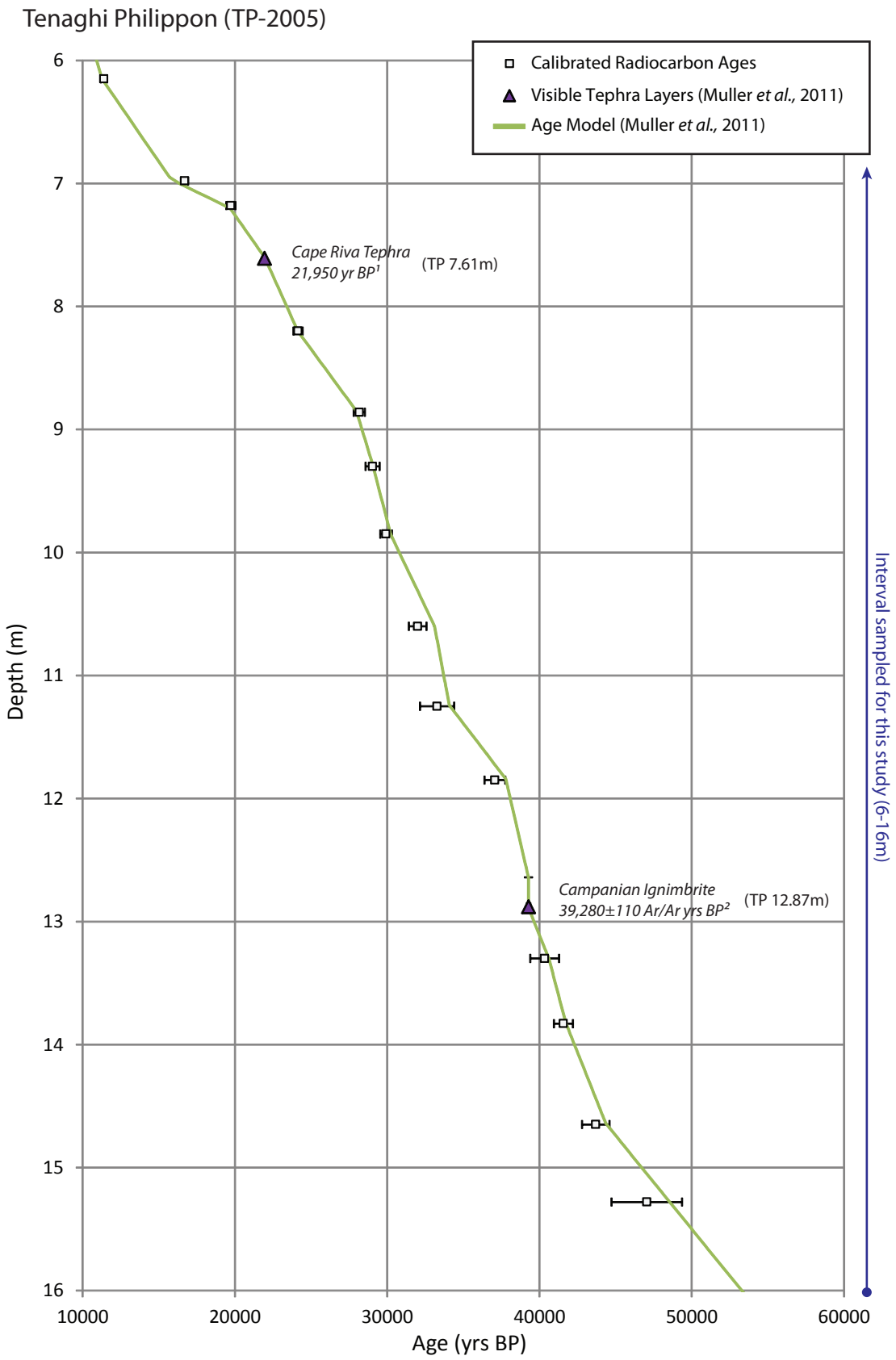

Figure 4.15 – Age-depth model for Tenaghi Philippon proposed by Muller *et al.* (2011) in green, is based upon 20 radiocarbon ages (also shown with 2 sigma error ranges) with the addition of two visible tephra layers (correlations and any imported ages are in italics, site tephra code shown alongside), beyond the radiocarbon dates the chronology is based upon tuning to the SPECMAP curve and NGRIP. The interval sampled for this study is highlighted. Note difference in the linear age model based on the calibrated radiocarbon ages and the Muller *et al.* (2011) age model is probably due to use of differing calibration curves (see text for details).

[1]Cape Riva age from Wulf *et al.* (2002) [2]Campanian Ignimbrite Ar/Ar age from De Vivo *et al.* (2001)

Palaeoenvironmental significance for the LLG

The new 2005 Tenaghi Philippon sequence represents one of the highest resolution pollen stratigraphies currently available of the LLG in the Eastern Mediterranean region. Compared to the older Tenaghi Philippon TF2 sequence (Wijmstra & Smit, 1976; Tzedakis *et al*., 2004) which, based on the evidence of c.30 counted pollen spectra, showed very subdued tree populations (<25 % arboreal pollen) throughout the LLG, the new sequence based upon around 270 pollen levels over the same interval shows much higher variability, with arboreal pollen reaching c.50% of total pollen at certain points. This variability between rapid increases in tree taxa that are punctuated regularly by often equally rapid increases in *Artemisia* and Chenopodiaceae and a sharp reduction in tree species, has been interpreted by Müller *et al.* (2011) to represent stadial and interstadial events during the LLG. Indeed, there is a marked visual similarity between the pollen fluctuations in the TP 2005 record and the NGRIP isotope record (see Fig. 4.14). It is likely that precipitation was the driving factor in Greece rather than temperature, with increases in rainfall allowing expansion of tree populations before they collapsed when rainfall decreased during stadial like events.

Current chronology for the LLG

The current chronology for the Tenaghi Philippon TP 2005 sequence is based upon 15 radiocarbon dates, two imported tephra ages and a biostratigraphic tie point based upon the pollen signal for the MIS 4/5 boundary (Müller *et al*., 2011). The detailed independent chronostratigraphic data available for Tenaghi Philippon TP 2005 means the sequence represents one of the most robust non-varved age models available for this period in this region (Figure 4.15).

The difference in the linear age model based on the calibrated radiocarbon ages shown in Figure 4.8 and the Müller *et al.* (2011) age model in part may reflect the different calibration curves utilised, with Müller *et al.* (2011) using the calibration curve proposed by Weninger & Jöris (2008), while the radiocarbon ages were re-calibrated for this PhD research project using IntCal09 (Reimer *et al*., 2009).

Tephrochronological significance for the LLG

The Philippi basin was first studied for volcanic ash horizons by St Seymour *et al.* (2004) who examined three short cores across the basin and described three visible

tephra layers from the site. In stratigraphical order from the top, these were named the PhT1, PhT2 and the PhT3 tephra layers. St Seymour *et al.* (2004) gained major element composition using EDS for all their layers and trace elemental data by 'bulk' ICP-MS for layers PhT1 and PhT2.

The PhT2 and PhT3 tephra layers were found to be present in all three cores with PhT3 being a particularly thick tuff deposit (>25 cm) and PhT2 much thinner (on average around 4 cm). PhT1 was present in two of the cores and also had an average thickness of around 4 cm. St Seymour *et al.* (2004) also supported the tephrostratigraphic data with radiocarbon dates obtained from peat directly below the tephra horizons (see Table 4.8). From these data, they concluded that PhT1 and PhT2 were geochemically very similar and probably originated from Santorini, correlating them to an as yet unknown Santorini eruption dated to around c. 13 ka BP (PhT1) and the Cape Riva (Y-2) eruption at c.22 ka BP (PhT2) respectively. St Seymour *et al.* (2004) concluded from the geochemical and chronological information that the likely correlative for the PhT3 was the Campanian Ignimbrite of the Campi Flegrei.

In the new long core TP-2005, Müller *et al.* (2011) detected only two visible tephra layers within the upper part of the sequence, TP 7.61, and TP 12.87m, from which they obtained major element analyses using EMPA-WDS. These data combined with the new chronology (see Fig. 4.15) indicate these tephra layers correlate with the Cape Riva and Campanian Ignimbrite eruptions respectively (see Table 4.8).

Table 4.8 – Currently available tephrostratigraphy and tephrochronology of Philippi peat basin, probable correlations and available ages shown both as uncalibrated (normal font) and calibrated (Italics).

St Seymour *et al.* (2004)			**Müller *et al.* (2011)**	
Ph-1	**Ph-2**	**Ph-3**	**TP-2005**	**Correlative event**
	PhT1 10,152±57[1] *(11410-12060)*	PhT1	?	Unknown Santorini event
PhT2 17,347±234[1] *(20130-21370)*	PhT2 18,527±145[1] *(21570-22430)*	PhT2 18,244±143[1] *(21420-22240)*	TP 7.61m (*21300-21890*[2]*)*	Cape Riva

PhT3	PhT3 31,577±570[1] *(34890-37410)*	PhT3	TP 12.87m *(38500-40240[2])*	Campanian Ignimbrite

[1]Ages based on radiocarbon date taken directly below the ash horizons.

[2]TP-2005 calibrated ages based upon linear interpolation between nearest radiocarbon ages.

Tephra sampling

The Tenaghi Philippon (TP 2005) sequence was sampled in June 2010 in Frankfurt, Germany. The depth interval sampled from 6-16m composed almost entirely of decomposed fen peats and peat muds with one section of lake marl (12.55-12.64m; Müller *et al*., 2011 supplementary information). The Tenaghi Philippon age model (see Fig. 4.15) suggests the interval sampled to roughly equate to c.10-50 ka BP.

Site-specific aims

An immediate aim was to confirm the correlation of TP 7.61 and TP 12.87 to the Cape Riva and Campanian Ignimbrite eruptions using single shard LA-ICP-MS trace element analysis. A second was to attempt to detect the PhT1 tephra of St. Seymour *et al.* (2004) and, if discovered, to 1) refine its geochemical signature via single shard LA-ICP-MS, 2) refine its age estimate, and 3) determine its palaeoenvironmental setting within the TP-2005 pollen stratigraphy. A third aim was to test and refine both the age model proposed by Müller *et al.* (2011) and the validity of the radiocarbon dates through tephrochronology.

4.2.6 Lesvos Island, Greece

Site History

Lesvos Island is located in the northeast of the Aegean Sea, near Greece. Margari (2004) carried out a geophysical survey and took four cores from the south-eastern part of the island within the Megali Limni basin finding a maximum sediment thickness of 40.2 m. This basin covers an area of around 1.48 km^2 at 323 m a.s.l. and is surrounded by four hills (max altitude at 507 m a.s.l.), the local bedrock being dominated by peridotites. Margari (2004) concluded that the basin originally initiated as a river valley which at some point became blocked by a landslide. In 1925 the lake was drained to allow the basin to be used for agriculture.

Of the four cores that were obtained from the Megali Limni basin, two cores have been studied in detail, one long core ML-01 from the deepest part of the basin (c.40.2m deep) and a shorter core ML-00 (c.8m). Margari *et al.* (2007) described 6 visible tephra layers (see below for more details) and presented the initial pollen record from this sedimentary sequence. Margari *et al.* (2009) then generated a more detailed pollen record by splicing the two pollen records from ML-00 and ML-01 together, to create a detailed pollen record thought to span the last 62 ka BP (see Fig. 4.16 and Table 4.9).

Table 4.9 – Summary of Lesvos (ML-00 and ML-01) setting and available data

Site Name:	Lesvos
Country:	Greece
Grid Ref.	39°06'08.9"N, 26°19'51.1"E
Elevation:	323m
Modern Setting:	Drained basin.
Core Code:	ML-00 and ML-01
Sedimentology:	Peats with discrete visible tephra.
Proxy data available:	Pollen, Magnetic susceptibility, Sedimentology, Radiocarbon dates.

Palaeoenvironmental significance for the LLG

The Lesvos sequence, which forms a unique palaeo-record from a Mediterranean island setting (Fletcher *et al.,* 2010), is also one of the very few high-resolution continuous records available for the Eastern Mediterranean. Margari *et al.* (2007; 2009) describe a number of distinct pollen fluctuations interpreted as reflecting shifts between steppe, forest-steppe and forest biomes. The most prominent of the tree expansions are interpreted as reflecting those Greenland interstadials which had the longest durations (e.g. GI-8, GI-12 and GI-14; see Fig. 4.17). Margari *et al.* (2009) inferred an increasing aridity during these interstadial events, with an increasing percentage of *Pinus* over other temperate taxa and in particular Mediterranean taxa in GI-14 (at 23.75m). This observation is important as it has hitherto not been described elsewhere within the Mediterranean region. Margari *et al.* (2007; 2009) proposed correlations to GI-2, GI-12, GI-13, GI-14 and GI-16 of which GI-12, GI-14 and GI-16 were used as chronological tie-points (see below). Fletcher *et al.* (2010) more recently proposed more correlations to Greenland interstadials (GIs 3, 4, 5, 6, 7, 8, 9, 10 and 11;

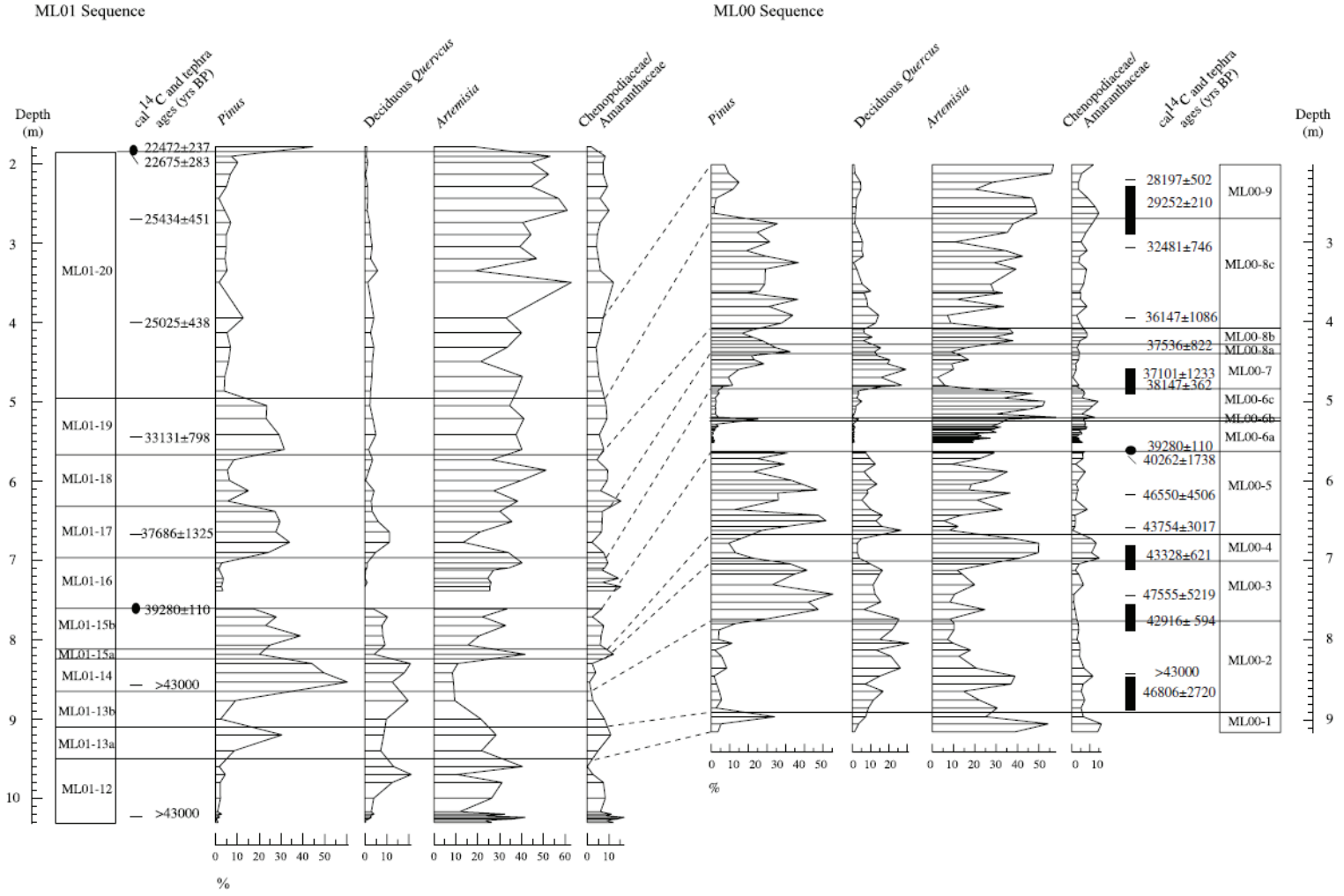

Figure 4.16 – The upper pollen record from ML-01 and the ML-00 pollen profile with the biostratigraphic correlations between them. Taken from Margari *et al.* (2009).

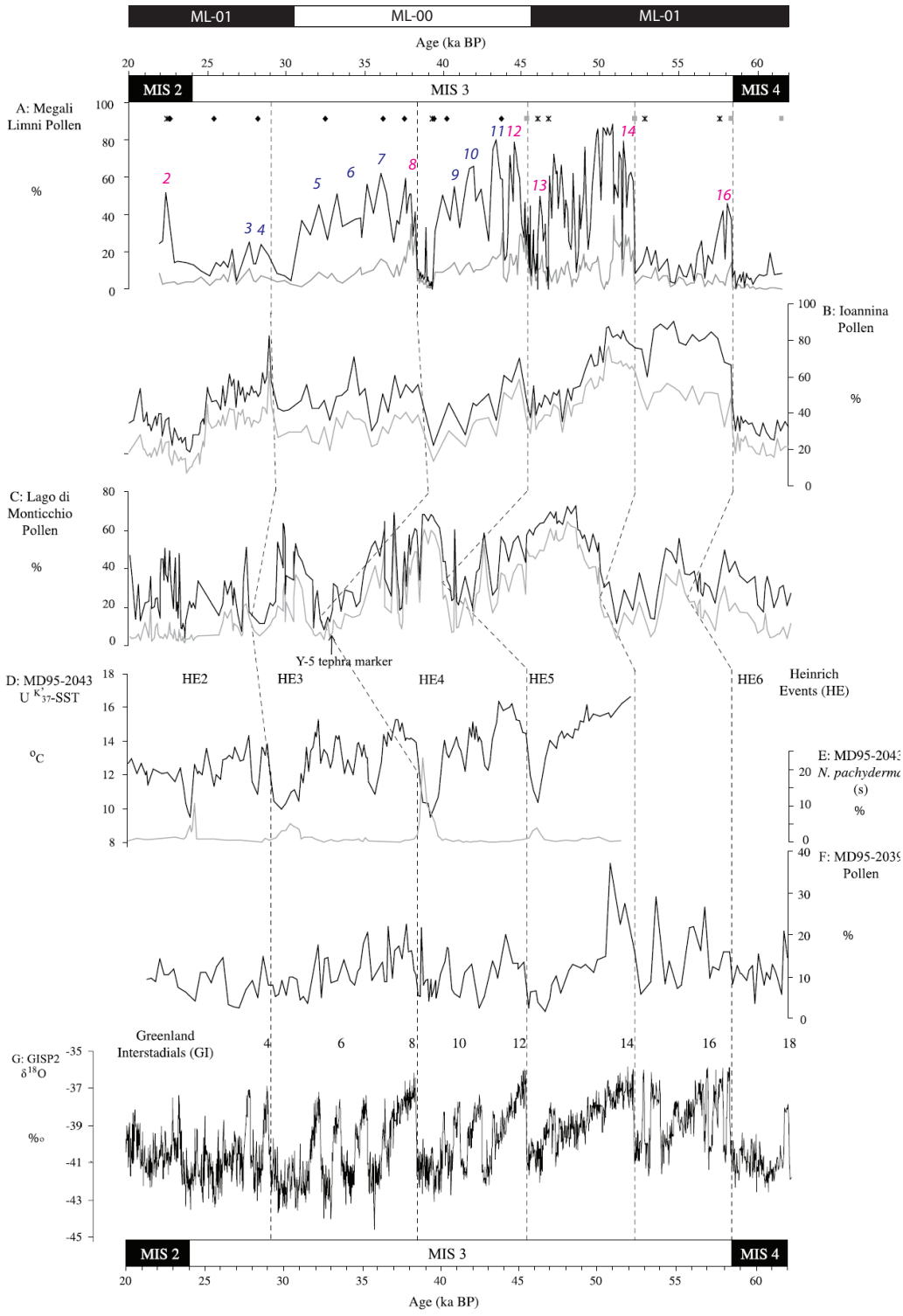

Figure 4.17 – Comparison of the combined Lesvos sequence against other palaeo-records including GISP2 (adapted from Margari *et al.*, 2009). Above the Lesvos record the chronological tie points are shown; Black diamonds represent calibrated radiocarbon dates (Fairbanks *et al.*, 2005) and tephra ages, grey squares alignment points and asterisks the position of the tephra layers ML-1 to ML-6. Correlations to Greenland Interstadials proposed by Margari *et al.* (2007; 2009; in magenta) and Fletcher *et al.* (2010; in blue) are also shown.

see Figs. 1.4 and 4.17) for the Lesvos pollen stratigraphy based upon the Margari *et al.* (2009) chronology and deciduous *Quercus* pollen fluctuations.

Current chronology for the LLG

The Lesvos chronology for sequence ML-00 and ML-01 is shown in Figs. 4.18 and 4.19. The age model is based upon 21 radiocarbon determinations (AMS and bulk taken on peat; Margari *et al.,* 2007; 2009) and upon an imported $^{40}Ar/^{39}Ar$ age for a tephra assigned to the Campanian Ignimbrite (see below). The independent age model extends to 9 m for ML-00 and to the CI (c. 40 ka BP) for the ML-01 sequence. Beyond 40 ka BP the age model is based primarily upon three biostratigraphic tie-points to Greenland interstadials 12, 14 and 16 (imported ages based upon the GISP2 chronology; Stuiver & Grootes, 2000) and tie point to the Ioannina pollen record at 36m (Tzedakis *et al.,* 2002, 2004), which suggests that the base of the sequence may date to around 71 ka BP though this is tentative since the base of the sequence is devoid of pollen grains (Margari *et al*., 2009).

Margari *et al.* (2004; 2009) also correlate Lesvos tephra ML-5 to the Pantelleria Green Tuff/ Y-6 which has $^{40}K/^{39}Ar$ ages available (41-54 ka BP; Civetta *et al.,* 1988; Madhood & Hildreth, 1986). These ages are plotted in the age-depth model that Margari *et al.* (2009) present, and was used to guide the alignment of the biostratigraphic tie-point to GI-14 at 23.75m but existing age estimates for the Green Tuff were not directly imported into the age model (see Fig. 4.19).

Margari *et al.* (2007; 2009) used the Fairbanks *et al.* (2005) calibration curve (Margari *et al*., 2009 used the updated 0108 version) to derive their age model. Here the radiocarbon dates presented in Figs. 4.18 and 4.19 have been re-calibrated using IntCal09 (Reimer *et al*., 2009). Significantly, recalibrating the ages with IntCal09 turns the lowermost radiocarbon date in sequence ML-01 at depth 11.625-11.63m from an age range of 41,815-50,071 (Fairbanks05) to 41,814-infinite (IntCal09).

Tephrochronological significance for the LLG

The Margari *et al.* (2007) paper sought to 'revisit' the Mediterranean tephra stratigraphy using six visible tephra layers which were uncovered in the Lesvos cores. The aims of this paper were:

1) To correlate the tephra layers using major, minor and trace elements.
2) To place the tephra layers found within a palaeo-environmental context.

3) To provide new ages for these tephra layers based upon the Lesvos age-model (see Figs. 4.18 and 4.19 and above for details).

Margari *et al.* (2007) determined major element geochemical compositions via Electron Microprobe Analysis (EPMA) for all the tephra layers and trace elements via 'bulk' ICP-MS for tephra layers ML-2, ML-3 and ML-4. On the basis of these data and the age model produced primarily via the pollen stratigraphy below c.8m in ML-01, Margari *et al.* (2007) assigned ML-1 to the Cape Riva eruption of Santorini and ML-2 to the Campanian Ignimbrite eruption from the Phlegrean fields.

ML-3 and ML-4 are very closely spaced stratigraphically within the ML-01 core (39 cm) and geochemically indistinguishable which led Margari *et al.* (2007) to question whether they were correlated to the Nisyros upper and lower eruptions and ML-5 to the Green Tuff (Y-6) of Pantelleria. The ML-6 tephra could not be correlated to any known eruptions although Margari *et al*. (2007) suggested an Aegean Volcanic Arc source. The core depths, thicknesses, correlations and ages based upon the ML core chronology and interpreted palaeoenvironmental contexts of each Lesvos tephra layer are outlined in Table 4.10. No cryptotephra analyses were carried out upon the Lesvos cores.

Table 4.10 – Ages of ML tephra and correlations to GI events from Margari *et al.* (2009).

Lesvos Tephra	**Depth (m)** (ML-00) *(ML-01)*	**Thickness (cm)**	**Correlation**	**Modelled age according to Margari *et al.* (2007)**	**Correlation to Greenland events Margari *et al.* (2007; 2009)**
ML-1	*1.80-1.82*	*2*	Cape Riva	22,647±374[1]	After GI-2
ML-2	7.44-7.60 *5.50-5.63*	16 *13*	Campanian Ignimbrite	40,361±1753[1]	End of GI 9 just before HE-4
ML-3	*10.33-10.50*	*17*	Nisyros Upper	46,000 ± 5690[2]	GI-13
ML-4	*11.89-12.00*	*11*	Nisyros Lower	46,800 ± 5690[2]	GI-13
ML-5	*24.21-24.25*	*4*	Green Tuff (Y-6)	53,600 ± 5690[2]	Slightly before GI-14 (GS-14?)
ML-6	*28.41-28.42*	*1*	unknown	58,000 ± 5690[1]	End of GI-16

[1]Calibrated AMS dates taken from below the tephra layers, calibrated using Fairbanks *et al*. (2005).
[2]Age errors is derived from the "calendrical age model of the ML sequence calculated as the quadrature of the age uncertainty of the GISP2 age scale and the resolution of the ML record"

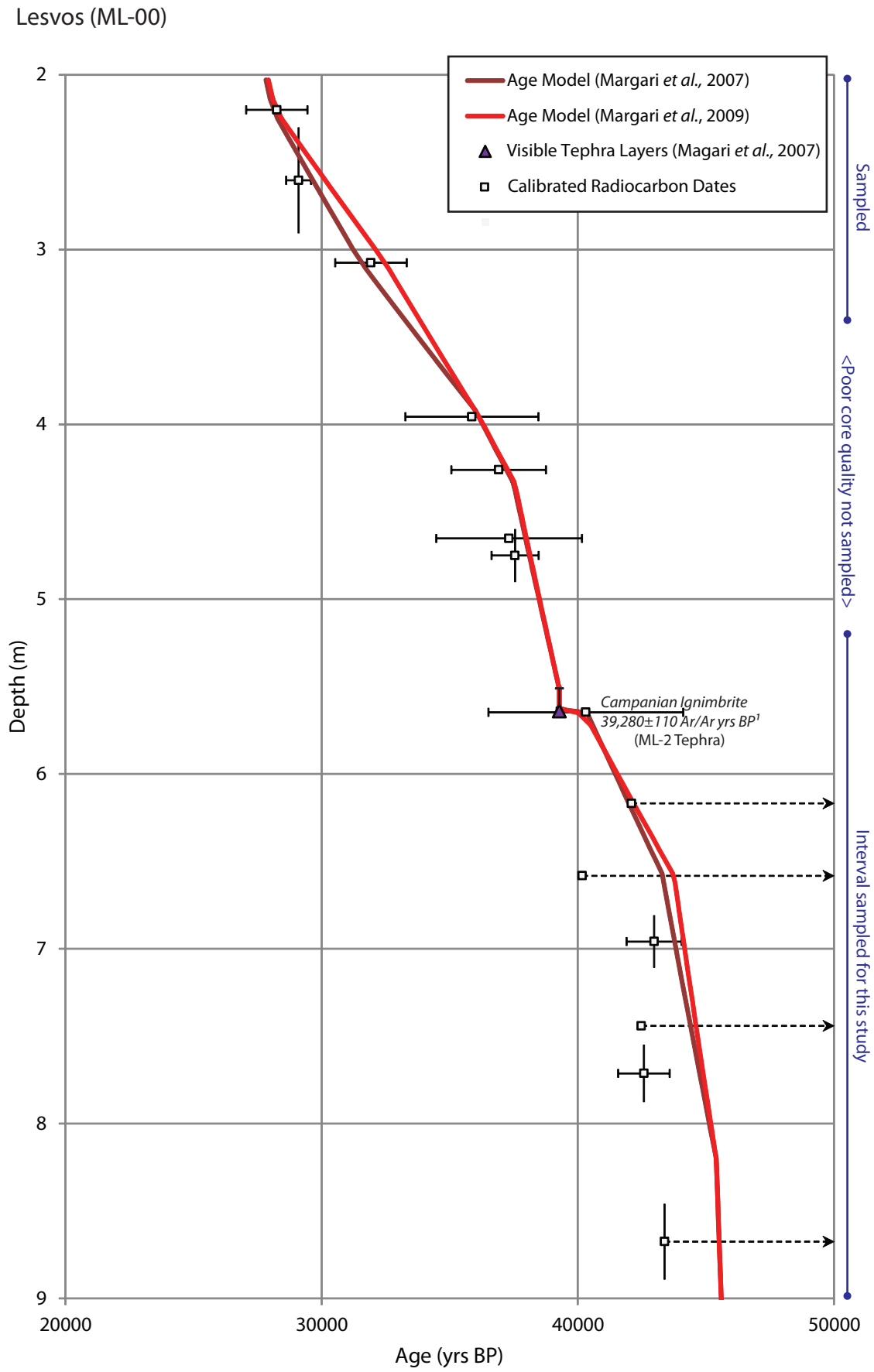

Figure 4.18 – Age-depth models for Lesvos short core ML-00 (Margari *et al.*, 2007; 2009). Arrows pointing to right indicate radiocarbon determinations with infinite maximum ages (these can however be used as minimum ages), 2 standard deviations are shown on the calibrated radiocarbon ages. The interval sampled for this study is highlighted.

[1]Campanian Ignimbrite Ar/Ar age from De Vivo *et al.* (2001)

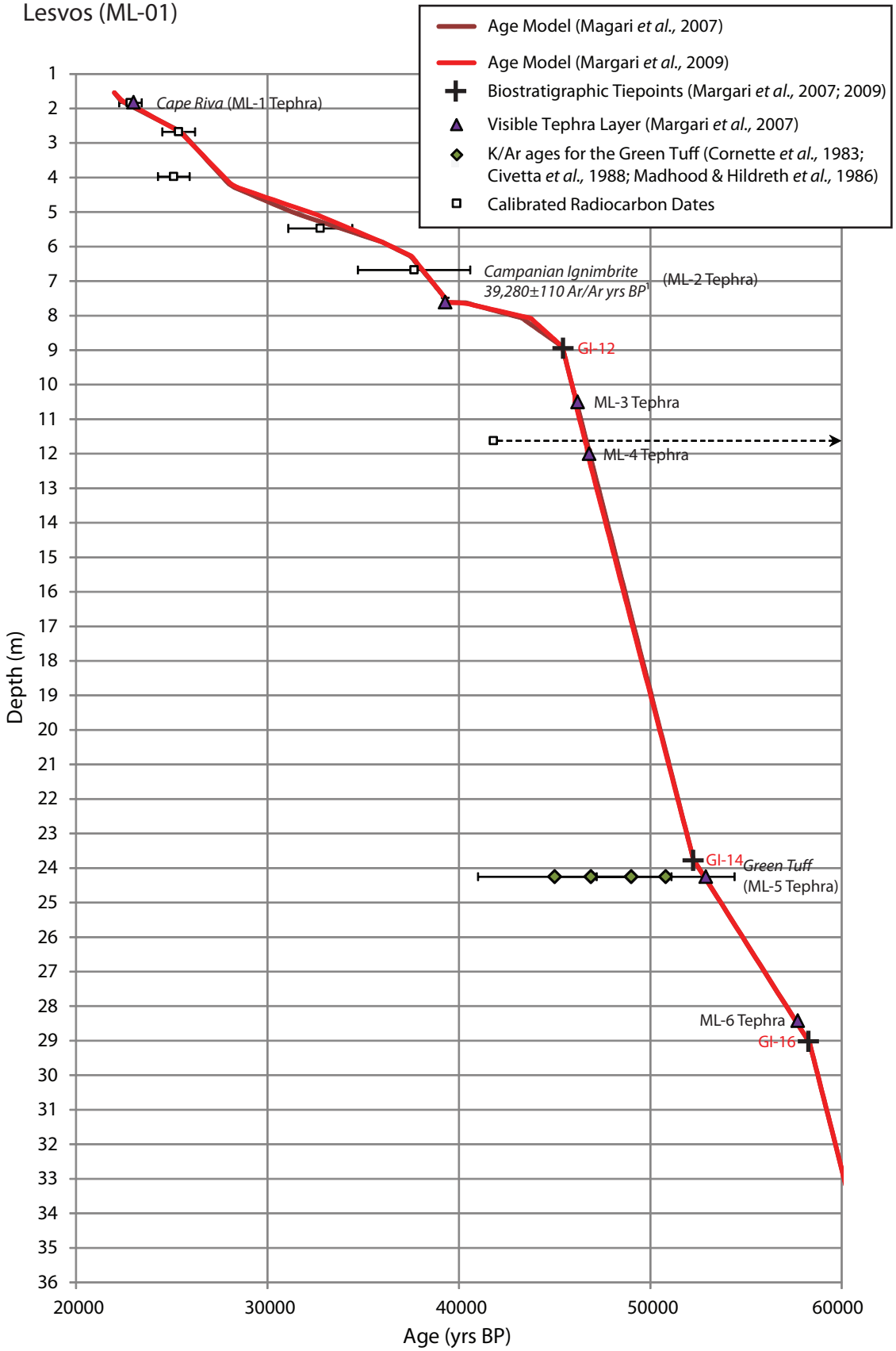

Figure 4.19 – Age-depth model for Lesvos long core ML-01. Visible tephras identified by Margari *et al.* (2007) are shown; tephrocorrelations and any imported tephra ages are in italics, site tephra code shown alongside. K/Ar ages of the Green Tuff shown by Margari *et al.* (2009) are also displayed. Arrows pointing to right of radiocarbon ages indicate a calibration with an infinite maximum age. Visible tephra layers ML-3 to ML-5 were sampled for this study.

[1]Campanian Ignimbrite Ar/Ar age from De Vivo *et al.* (2001)

Since the publication of Margari *et al.* (2007) there have been various reinterpretations of the data presented therein. Firstly Bichler *et al.* (2009) wrote a direct reply to the Margari *et al.* paper pointing out various data presentation oversights and also potential analytical issues with the methods used with respect to the ICP-MS analysis. In particular they questioned the effectiveness of the preparation technique used by Margari *et al*. to 'purify' the glass from the mineral fraction present in the visible tephra layers, and suggested that high Cr, Fe and Co values were probably due to detrital contamination of minerals. Also they point out that reference material from Nisyros analysed by Margari *et al.* has very high amounts of Zr which may relate to incomplete digestion of zircon crystals. This may suggest the ICP-MS data presented by Margari *et al.* (2007) should perhaps be treated with caution, the data perhaps being more in keeping (and comparable) with 'bulk' tephra measurements rather than 'pure' glass as assumed in the Margari *et al.* (2007) paper.

Alongside these criticisms Bichler *et al.* also questioned the robustness of the correlation of ML-3 and ML-4 to the Nisyros Upper and Lower eruptions, as outlined in Margari *et al.* (2007) suggesting firstly that the authors should have used a Eu/Ta versus Th/Hf plot to distinguish between the Nisyros Upper and Lower eruptions as suggested by Sterba *et al.* (2006). In fact Bichler *et al*. suggest the correlation can be discarded because of an Eu anomaly, and suggest a correlation instead to the Yali D eruption (*sensu* Bond, 1986). In the reply to this comment Pyle & Margari (2009) reject the claim that their trace element data cannot be used for comparison due to their preparation method and also reassert (using newly available data from Aksu *et al.,* (2008)) that the ML-3 and ML-4 tephra layers best correlate to the Nisyros Upper and Lower pumices even when using the suggested Eu/Ta–Th/Hf plot.

More recently more geochemical and tephrostratigraphical data have become available for Pantelleria, particularly from long lake records taken from Lake Ohrid which is situated on the Albanian–Macedonia border, from which a rich array of tephra information is now available (e.g. Wagner *et al*., 2008; Caron *et al*., 2010; Vogel *et al*., 2010; Sulpizio *et al*., 2010). In particular, in the longer cores studied by Vogel *et al.* (2010) and Sulpizio *et al.* (2010), both the Green Tuff (Y-6) and older P-11 (~131 ka BP) were interpreted as co-occuring within the same Ohrid core sequence (Ohrid tephra's OT0702-7 and OT0702-10 respectively). Both are sourced from Pantelleria but have very disparate age ranges at 41-54 ka (Civetta *et al*., 1988; Madhood & Hildreth, 1986) and ~131 ka BP (Paterne *et al*., 2008). Importantly, Vogel *et al.* (2010)

reinterpret the ML-5 tephra of Margari *et al.* (2007) as instead representing a distal occurrence of the P-11 tephra, via demonstrating it has a closer geochemical affinity.

Although Vogel *et al.* (2010) do not delve into the potential implications of reinterpreting ML-5 as a correlative to the P-11 tephra layer instead of the Green Tuff (Y-6), if correct, this clearly has profound implications for:

1. The Lesvos tephrostratigraphy.
2. The validity of the Lesvos chronological model and thus the suggested ML tephra ages (see Table 4.10).
3. Palaeoenvironmental implications based on the Lesvos record.

Tephra sampling

The Lesvos cores were transported to the RHUL labs for cryptotephra sub-sampling in 2011. Around 5 metres of core material was sampled for cryptotephra analysis covering the majority of the short core ML-00 (2-9m; see Fig. 4.18).

This core was chosen for study as the sequence is deemed to be more complete and has a higher percentage recovery due to the use of a Livingstone corer. The longer ML-01 sequence was extracted using a mechanical corer and thus small gaps between extracted segments become unavoidable (V. Margari, *pers. comm.*) also ML-00 was selected as a much higher frequency of radiocarbon dates are available (14 ^{14}C determinations) compared to the ML-01 sequence (5 ^{14}C determinations) for the LLG. Overall, most of the ML-00 cores were acceptable for sampling except for one core segment where the core had perished beyond the point where further sub-sampling was possible. Almost all the cores were heavily dried out and had high levels of shrinkage, despite this the previous sub-sampling points (for pollen and radiocarbon) were used to place new sub-samples onto the original depth scheme. Importantly Margari *et al.* (2007) noted two 'reworked' tephra layers at 5.4-5.5 m and 8.96-9.24 m in the ML-00 sequence.

Although no cryptotephra analysis was carried out on the longer core (ML-01) due partially to time constraints, the visible tephra layers ML-1 to ML-5 were sampled for further geochemical analysis.

Site specific aims

The specific aims for Lesvos are (a) to confirm the correlation of ML-1 and ML-2 to the Cape Riva and Campanian Ignimbrite via single shard LA-ICP-MS trace element analysis; (b) to test the correlation of ML-5 to the Pantelleria Green Tuff in light of new evidence from Lake Ohrid with hitherto unavailable trace element geochemistry; (c) to confirm the correlation of ML-3 and ML-4 to the Nisyros Upper and Lower eruptions via single shard LA-ICP-MS trace element analysis and comparison to recently acquired proximal RESET data; and (d) to carry out the first cryptotephra study on the Lesvos sediment sequence.

4.2.7 Summary of selected research sites

The sites described above represent a geographically and ecologically diverse range of sites (from southern Spain to eastern Greece; see Table 4.11) forming a W–E transect, and the potential to extend the European tephrostratigraphic framework. The sites also represent a diverse range of depositional environments with which the sampled sections have accumulated, from the peats of Padul, Tenaghi Philippon and Lesvos, to the primarily lacustrine sediments of Fimon (gyttja, clays, silts with peat horizons) and Kopais (calcareous lake silts). Villarquemado has the most complex LLG sedimentation history of all the sites with various phases of lacustrine deposits interrupted by alluvial units with potential fluvial influences as well (Moreno *et al*., 2012). Despite these differences cryptotephra has been proven to be preserved in a very large range of sedimentary environments (Lowe, 2011) so could theoretically be preserved in all these sites, except perhaps where coarse sand layers or high energy deposits are present.

All the sites have existing independent chronological data available (e.g. OSL and/or radiocarbon) and many contain chronological data based upon pollen-stratigraphic tie-points (e.g. Fimon, Kopais, Lesvos, Tenaghi Philippon). It is however not always clear how these differing chronological strands have been applied in terms of primacy (i.e. order of importance). For example, the pollen-stratigraphic tiepoints for Kopais were radically changed after new radiocarbon ages were obtained, changing the chronology by ~60 ka BP, suggesting the independent ages were viewed as more important than the ages based upon biostratigraphic alignment. In the case of Fimon the opposite appears to be true and the radiocarbon ages have been essentially *overruled* in favour of a biostratigraphically–based chronological scheme. In Lesvos it is not clear for instance if the correlation of ML-5 to the Green Tuff (Y-6) tephra was

Table 4.11 – Overview of study sites covering modern climate characteristics and chronological information, including how the current accepted age model was developed.

	Modern climate / geography						Chronological information					
Site (core code)	**Elevat-ion**	**Mean Annual Temp (°C)**	**Mean Annual Rainfall (mm) / *Length of dry season (months)***	**Biome**	**Core depths (m)**	**Sample interval for this study (m)**	**AMS**	**^{14}C**	**OSL**	**U/Th**	**Visible tephra layers**	**Age model (see figures and text for more details)**
Padul	714.2 m	*T*Jan 2.7 *T*Jul 31.2	453 *5-7*	Mediterranean	0-100	6.45-15.20	—	9	—	4	—	Based upon ^{14}C and U/Th ages, no detailed age-depth model proposed
Villarquemado	987m	*T*Jan 3 *T*Jul 20	484 *1-3*	Mediterranean	0-75	4-23	—	18	6	—	—	Based upon ^{14}C and U/Th ages, no detailed age-depth model proposed.
Fimon (PD core)	23m	*T*annual 12.8 *T*Jul 30.2	1038 *0-1*	Temperate (Broadleaf and mixed forests)	10-40	19-25	—	14	12	—	—	Based upon radiocarbon until 19.9m then solely upon biostratigraphic tie points.
Kopais (K-93)	92.4m	*T*Jan 9 *T*Jul 27	470 *>7*	Mediterranean	6-60	20-60	4	2	—	—	—	Most recent chronology (Tzedakis *et al*., 2004) based upon of 6 radiocarbon dates intertwined with biostratigraphic tuning.
Tenaghi Philippon (TP 2005)	40m	*T*Jan 3.4 *T*Jul 23.9	600 *1-4*	Mediterranean	0-60	4-19	—	20	—	—	2	Based upon 20 radiocarbon dates, 2 imported tephra ages intertwined with some biostratigraphic tuning to NGRIP which continues pre-50 ka BP.
Lesvos (ML-00 and *ML-01*)	323m	*T*win 10.4 *T*sum 26.1	725 *>7*	Mediterranean	1.8-9 *1-40*	1.8-9 *Selected visible Tephra's only*	— —	15 *9*	— —	— —	2 *5*	Based upon 15 radiocarbon dates and two tephra ages coupled with biostratigraphic tuning points. *Based upon 9 radiocarbon ages and three tephra ages coupled with biostratigraphic tie points.*

the guide to which the pollen-stratigraphic tie-points were based or *vice versa* while the Y-6 correlation was based upon the age derived from the pollen-stratigraphic tie-points. The order or superiority in which age information is evaluated is not a moot point as it has a large influence on how age-models develop and on the nature, perhaps validity, of the logic used to construct them.

Almost all of the sites described here have existing age–depth models (with the exception of Villarquemado) that allow ages to be determined for undated depths (see section 1.3.4). Most are based upon simple linear line plots through preferred mean ages (Kopais, Tenaghi Philippon and Lesvos) or through 2 sigma error ranges (Fimon). An exception is Padul which is based upon a polynomial regression curve. The current environmental and climatic contexts and age-model information for all the sites described here are summarised in Table 4.11.

Finally all sites have pollen stratigraphies available and throughout this study these have been primary compared and described via total tree pollen percentages. In the Mediterranean tree populations are thought to respond primarily to changes in precipitation, but can also by effected by changes in temperature (minimum winter temperatures are particularly important) and also to atmospheric CO_2 concentrations (Tzedakis *et al.,* 2004). Site specific factors are also important, such as altitude, topography, soils and microclimatic effects, such as sites sheltered from harsh winds (Fletcher *et al.,* 2010).

5.0 RESULTS

5.1 Spain

5.1.1 Padul borehole

Depths 15-6m were analysed for cryptotephra content (see section 3.3 for details) unfortunately no tephra shards were identified. No deposition of volcanic glass shards appears to have occurred between ~80-20 ka BP in Padul. It is however possible that glass shards may have been deposited and not preserved due to chemical or physical degradation which can be particularly prevalent in acidic environments that undergo desiccation phases (Matthews, 2009), though it seems unlikely that no evidence of tephra would be preserved.

5.1.2 Villarquemado

Depths 23-4m were sampled for cryptotephra analysis and although a few tephra shards (<5) were detected (at depths 5.90-6.00 and 12.30-12.50m) however these could not be replicated at higher 1 cm resolution and thus could not be confirmed nor allow geochemical data to be sought to validate the material as volcanic glass.

5.2 Italy

5.2.1 Fimon (PD core)

In the interval between 25-19m, first analysed by 10 cm scan samples, only very minimal trace amounts of tephra shards could be detected (1-3 total shards, 0.20-1.03 shards/per gram). Scans at higher resolution (1 cm) could only replicate more shards between 20.40-20.50 and 22.00-22.10m (shown and labelled in Figure 5.1; see also Table 5.1), these will now be discussed in more detail.

FIM-2042 has a total of 2 tephra shards between 20.41-20.43m. The shards found were small (<40μm) and platy. Unfortunately, attempts to gain geochemical data were unsuccessful. In the Pini *et al.* (2010) pollen stratigraphy this tephra occurs within a

Table 5.1 – Summary of Fimon PD tephra layers.

Tephra layer code	Full depth interval (m)	Distribution / skew	Peak shards/g dry wt.	Geochemical sampling depths (m)	Total WDS-EMPA analyses	Total LA-ICPMS analyses	Total SIMS analyses	Classification		
								Alkali status	Composition	K division
FIM-2042	20.41-20.43	*'Stump'*	0.76	—	—	—	—	—	—	—
FIM-2205	22.01-22.06	*Slightly negative*	5.37	*22.04-22.05* *22.00-22.10*	5 2	— —	— —	Alkaline	Tr/P	Shoshonite

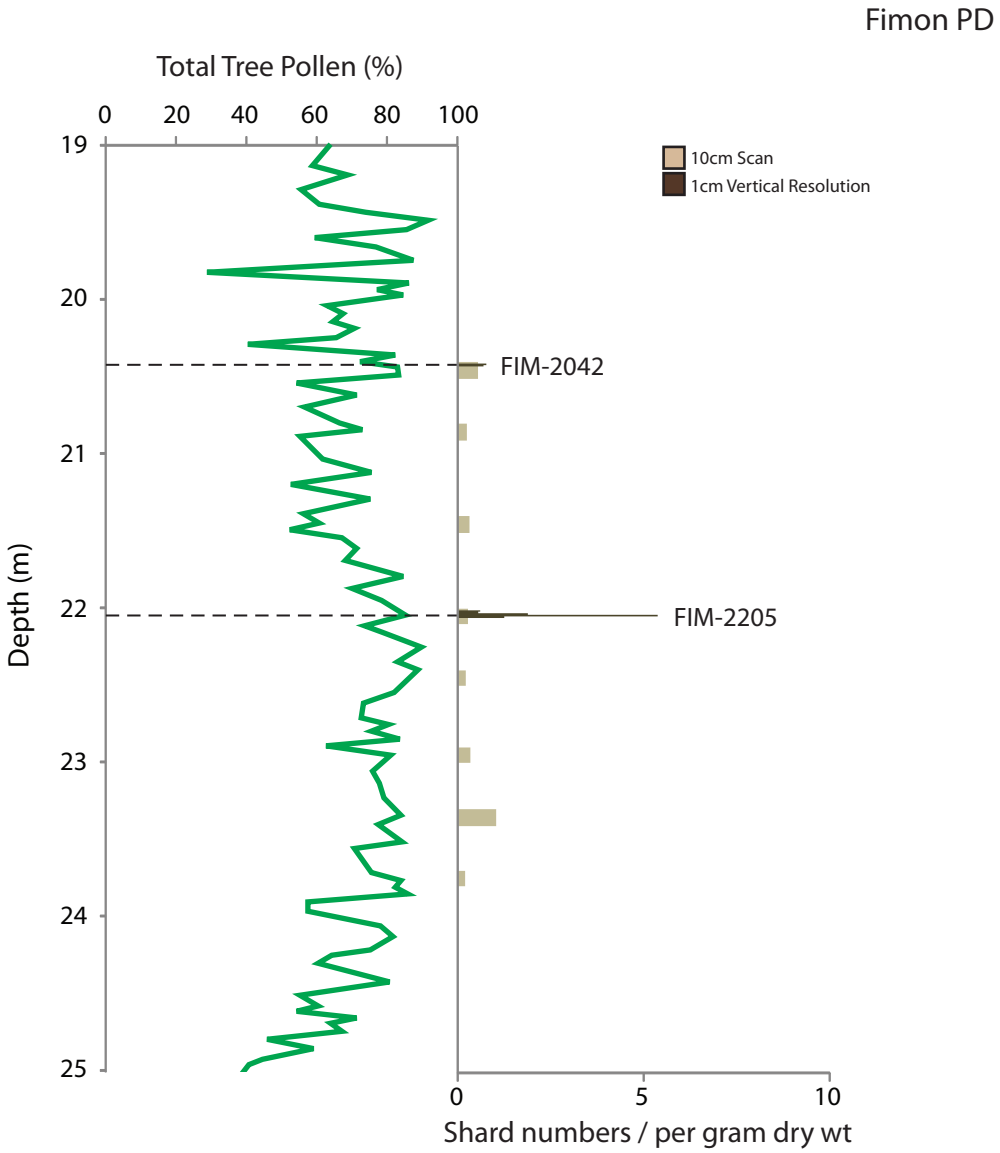

Figure 5.1 – Fimon PD shard counts and total tree pollen abundance (Pini *et al.,* 2010) against depth.

period of high *Pinus sylv/mugo* and much suppressed mixed-oak woody plants, *Tilia* becoming absent.

FIM-2205 represents the largest quantity of tephra shards found in Fimon PD in the sampled interval; the layer has a slightly negative skewed distribution and a very constrained layer (22.01-22.06m) with 5.37 shards/per gram at the peak. The dominant shard morphology is very fluted. Shards from this layer were successfully extracted and prepared in two batches for WDS-EMPA analyses where, overall, 7 assays were successfully acquired. The geochemical signature is trachyte/phonolite with geochemical ranges of 60.04–62.39 wt% SiO_2, 18.51–19.26 wt% Al_2O_3, 0.33–0.47 wt% TiO_2, 2.75–3.45 wt% FeO, 0.29–0.75 wt% MgO, 1.44–2.66 wt% CaO with a K_2O/Na_2O ratio of 1.50–2.02 (see Figure 5.2). In the pollen stratigraphy this tephra occurs after an increase in *Pinus sylv/mugo* and a decrease in mixed-oak woody plants.

5.3 Greece

5.3.1 Kopais (K-93)

The interval of 15-60m was sampled as part of this study (45 metres overall). Initial scan samples were completed at 10 or 20 cm resolution, where very low amounts of tephra shards were discovered, the highest being 31.51 per g dry wt. Despite this, many separate cryptotephra layers were apparent. Higher resolution scans carried out on these at 2 cm resolution only sometimes recovered tephra. Thirteen cryptotephra layers have been identified from the Kopais core on the basis of where layers had higher than 1 shard per g dry wt (see Fig. 5.3 and Table 5.2). Although this is clearly very low in shard numbers, several distinct layers are apparent, with varying distributions (e.g. normal or positively skewed), shard morphologies (Fig. 5.4) and geochemical signatures (see Figs 5.5, 5.6 and 5.7), will now be described in stratigraphic order.

KOP-1652, KOP-1759 are two discrete tephra layers present at the top of the sampled core interval (16.50-16.60, 17.50-17.58m). Both layers have a normal vertical distribution in shard abundance but contain very low shard numbers (<5 shards per/g dry wt). The shards have a primarily platy morphology. Only 2 geochemical assays (WDS-EMPA) were achieved for KOP-1652 determining a calc-alkaline rhyolitic composition (Fig. 5.5) with narrow geochemical ranges of 70.73–71.01 wt% SiO_2,

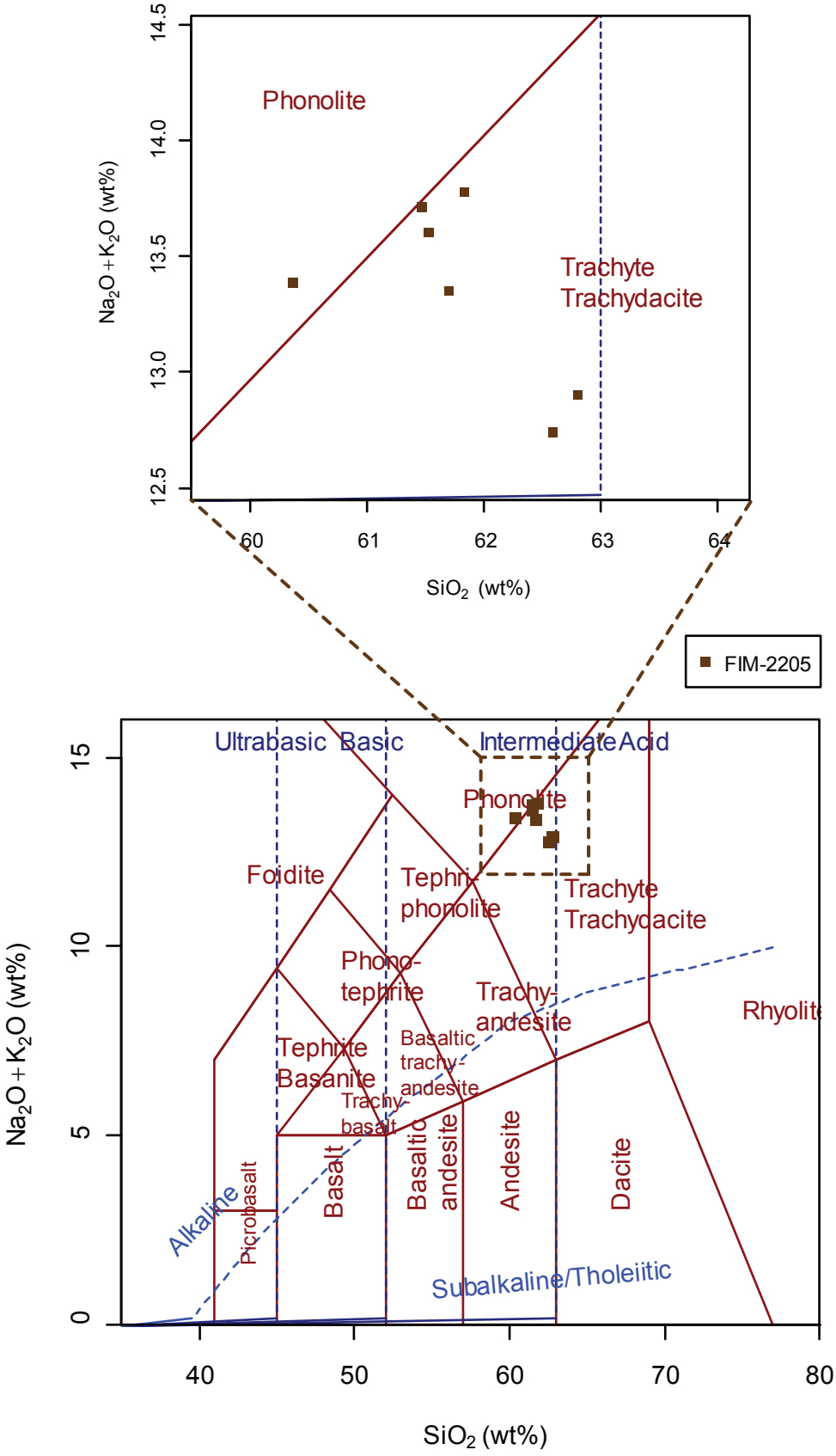

Figure 5.2 – Total alkali vs. silica plot (Le Bas *et al.,* 1986) for Fimon PD tephra layer FIM-2205.

Table 5.2 – Summary of Kopais (K-93) tephra layers.

Tephra layer code	Full depth interval (m)	Distribution / skew	Peak shards/g dry wt.	Geochemical sampling depths (m)	Total WDS-EMPA analyses	Total LA-ICPMS analyses	Total SIMS analyses	Classification		
								Alkali status	Composition	K division
KOP-1652	16.50-16.60	*Normal*	5	*16.50-16.60*	2			Sub-alkaline	Rhyolite	Calc-alkaline
KOP-1759	17.50-17.58	*Normal*	1	—	—	—	—	—	—	—
KOP-2317	23.10-23.35	*Normal*	25.33	*23.14-23.20*	7	—	—	Alkaline	Tr/P	Shoshonite
KOP-2637	26.30-26.61	*Normal*	31.51	*26.36-26.38*	20	—	—	Alkaline	Tr/P	Shoshonite
KOP-2698	26.88-26.99	*Negative*	13.99	*26.96-26.98*	4	—	—	Alkaline	Trachyte	Shoshonite
KOP-2763	27.62-27.73	*Positive*	4.84	*27.62-27.64*	2	—	—	Alkaline	Tr/P	Shoshonite
KOP-2910	29.00-29.20	—	1.29	—	—	—	—	—	—	—
KOP-3119	30.00-31.19	*Diffuse*	5.92	*30.54-30.56*	20	5	—	Alkaline	Tr/P	Shoshonite
KOP-3347	33.28-33.73	*Normal*	12.76	*33.44-33.50* *33.46-33.48*	2 14	— —	— —	Alkaline	P/Tr	Shoshonite
KOP-3900	39.00-39.40	*Positive*	2.34	—	—	—	—	—	—	—
KOP-4059	40.50-40.59	—	1.81	—	—	—	—	—	—	—
KOP-4815	47.90-49.09	*Diffuse with peak*	2.74	*48.10-48.20*	2	—	—	Sub-alkaline	Dacite-Trachyte	Medium to High-K
KOP-5678	56.78-56.79	*Diffuse*	0.53	*56.78-57.00*	23	—	—	Sub-alkaline	Rhyolite	High-K

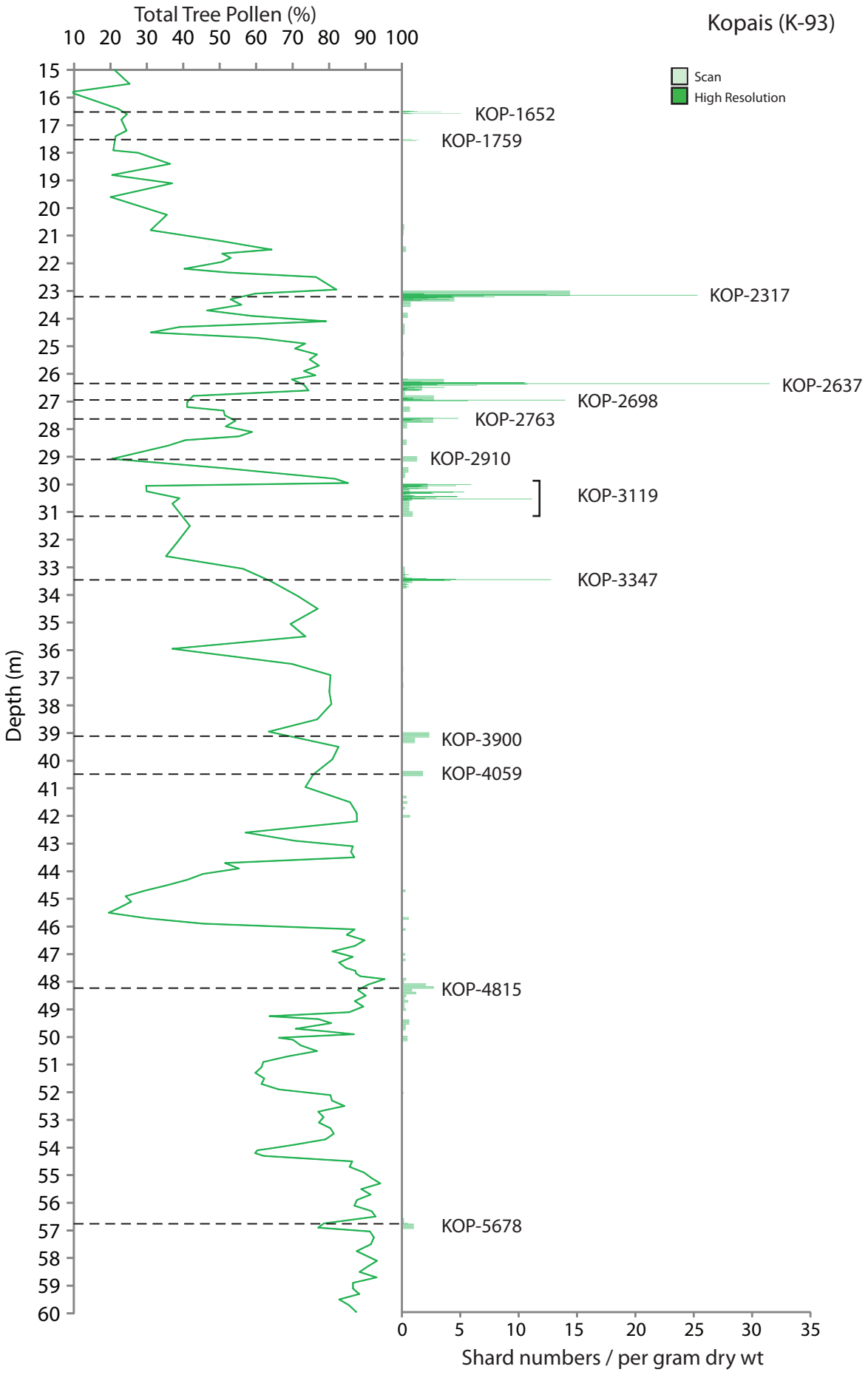

Figure 5.3 – Kopais (K-93) shard counts and total tree pollen abundance (Tzedakis, 1999) against depth.

14.44–14.48 wt% Al_2O_3, 5.37–5.46 wt% Na_2O and 2.90–2.94 wt% K_2O. No geochemical data could be attained for KOP-1759.

In terms of the pollen stratigraphy (Tzedakis *et al.*, 1999), both tephra layers sit within subdued (22-24%) total tree pollen periods.

KOP-2317 is the second largest tephra horizon sampled from the Kopais sequence with a peak of 25.33 per g dry wt. The peak forms a normal distribution between 23.10-23.35m. 7 elemental geochemical assays were attained from KOP-2317 demonstrating an alkaline trachytic-phonolitic composition, with geochemical ranges of 60.69–61.62 wt% SiO_2, 18.49–19.01 wt% Al_2O_3, 0.38–0.45 wt% TiO_2, 2.70–3.21 wt% FeO, 0.29–0.77 wt% MgO, 1.74–2.59 wt% CaO with a K_2O/Na_2O ratio of 1.11–1.73.

This tephra falls within a period of reduced total tree pollen percentages (c.38%) just before a sharp increase in tree pollen populations.

KOP-2637 – KOP-2763 these three cryptotephra; KOP-2637, KOP-2698 and KOP-2763 occur over a 2m segment of the Kopais cores and could represent a single event which is not fully seen due to very low shard counts, each layer appears to be dispersed over c.10-30 cm with various distributions (see Table 5.2) covering periods of both higher total tree pollen percentages (KOP-2637) and lower (KOP-2698). These layers have both trachyte/phonolite (KOP-2637 and KOP-2763) and trachyte (KOP-2698) geochemical compositions, as follows:

KOP-2637: 20 EMPA-WDS geochemical assays were attained for KOP-2637 demonstrating an alkaline trachytic-phonolitic composition with geochemical ranges of 60.69–61.97 wt% SiO_2, 18.12–18.67 wt% Al_2O_3, 0.34–0.45 wt% TiO_2, 2.73–4.56 wt% FeO, 0.28–0.71 wt% MgO, 1.67–2.69 wt% CaO with a K_2O/Na_2O ratio of 1.03–2.90.

KOP-2698: 4 EMPA-WDS geochemical assays were attained for KOP-2698 demonstrating an alkaline trachytic composition with geochemical ranges of 60.59–61.79 wt% SiO_2, 18.40–19.13 wt% Al_2O_3, 0.40–0.45 wt% TiO_2, 2.95–3.01 wt% FeO, 0.24–0.71 wt% MgO, 1.59–2.62 wt% CaO with a K_2O/Na_2O ratio of 1.14–3.15.

KOP-2763: 2 EMPA-WDS geochemical assays were attained for KOP-2763 demonstrating an alkaline trachytic-phonolitic composition with geochemical ranges of 60.78–62.25 wt% SiO_2, 18.69–18.87 wt% Al_2O_3, 0.34–0.40 wt% TiO_2, 2.81–2.88

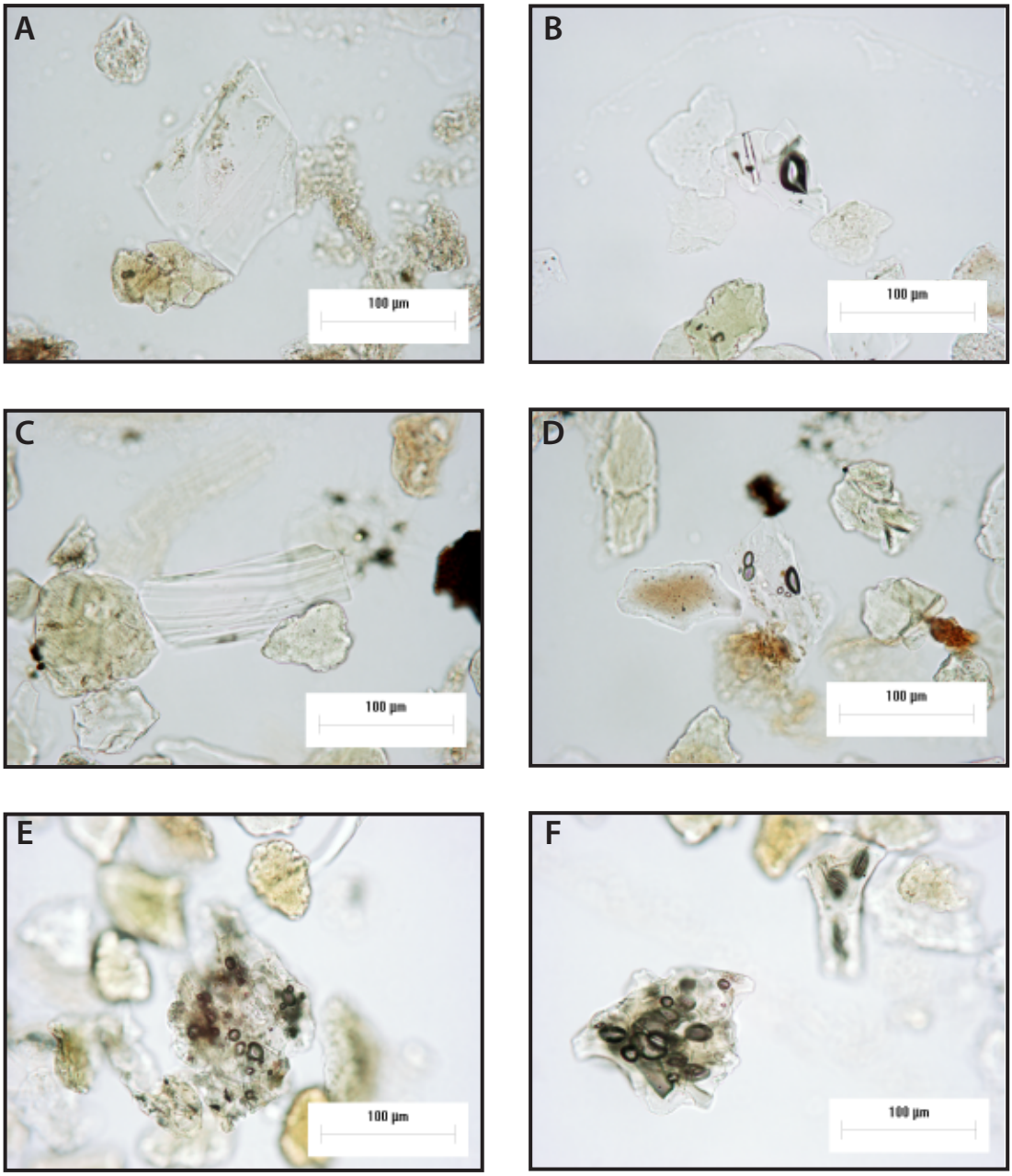

Figure 5.4 – Microphotographs showing the shard morphologies and characteristics of the Kopais (K-93) tephra layers. All were taken under transmitted light. (**A.**) A large platy shard from cryptotephra layer KOP-2637. (**B.**) A blocky vesicular shard with an microlite inclusion from KOP-2763. (**C.**) A large fluted shard from KOP-3347. (**D.**) A vesicular shard from KOP-3347. (**E**, **F.**) Two blocky, highly vesicular and microlite rich shards from tephra layer KOP-3900.

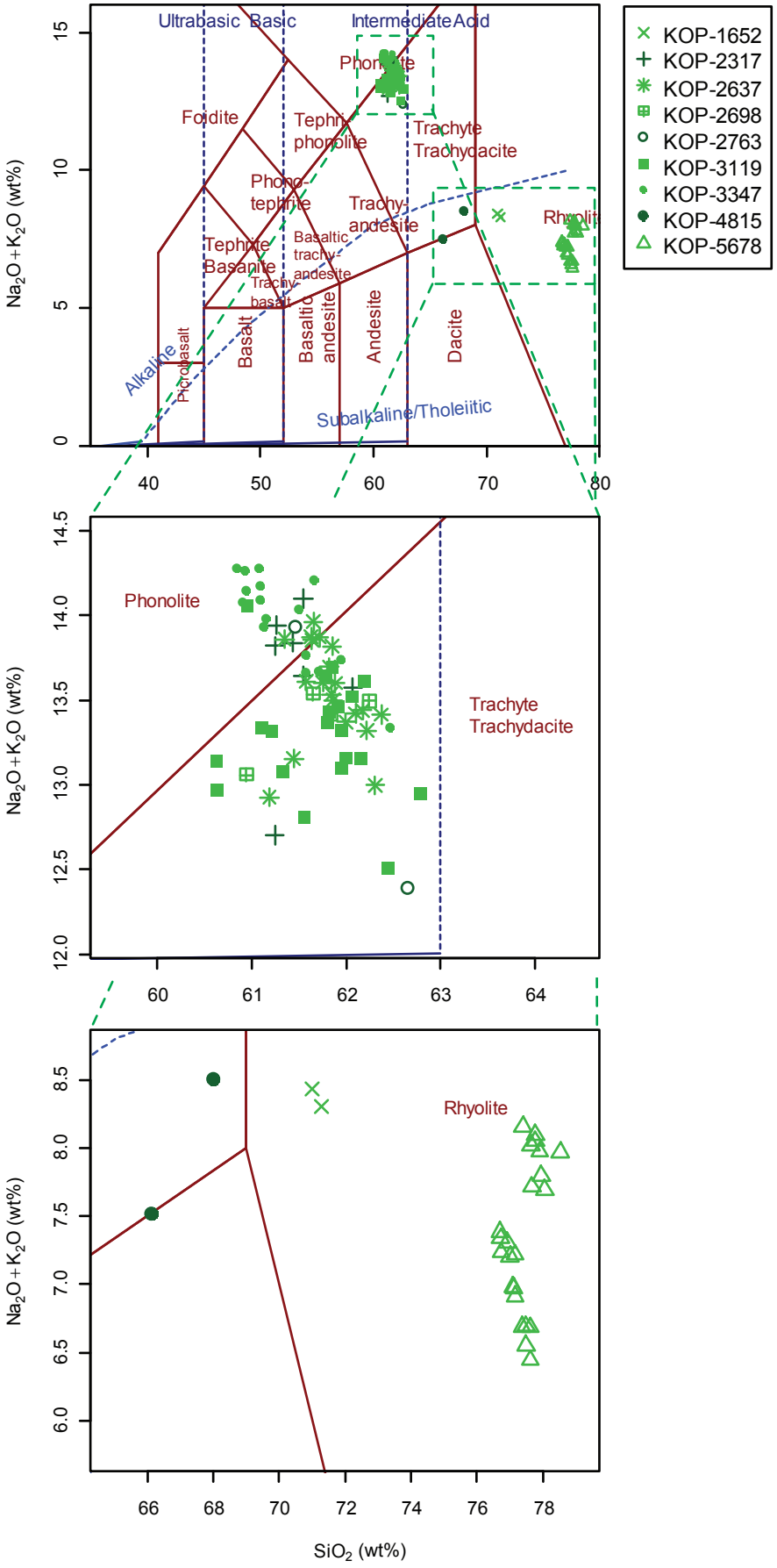

Figure 5.5 – Total alkali vs. silica plot (Le Bas *et al.,* 1986) for Kopais (K-93) tephra layers.

wt% FeO, 0.30–0.43 wt% MgO, 1.73–2.25 wt% CaO with a K_2O/Na_2O ratio of 1.11–2.19.

KOP-2910 is a tephra layer detedted in 10 cm scans but which could not be reproduced at higher resolution. It lies within a period a low total tree pollen percentages. No geochemical data could be achieved.

KOP-3119 is a tephra layer with a highest peak of 5.92 per g dry wt and with a very diffuse vertical distribution, with multi-modal distributions present. Compared to other surrounding layers the shard sizes are relatively larger with a-axis reaching >125µm. The morphology of the shards is mostly platy with some fluted. Due to the favourable shard sizes 5 trace element analyses could be achieved. 20 EMPA-WDS and 5 LA-ICP-MS geochemical assays were attained showing an alkaline trachytic-phonolitic composition. Geochemical ranges of 60.32–62.39 wt% SiO_2, 18.36–19.16 wt% Al_2O_3, 0.28–0.46 wt% TiO_2, 2.66–3.66 wt% FeO, 0.22–0.82 wt% MgO, 1.59–2.66 wt% CaO with a K_2O/Na_2O of 1.05–3.73. Trace element concentrations show a trimodal composition with full ranges of: 165–648 ppm Zr, 272–446 ppm Rb, 78.7–241 ppm Ce, 42–125 ppm La, 10.8–726 ppm Ba, 12.1–587 ppm Sr, 27.5–114 ppm Nb, 52.8–52.8 ppm Y, 12.2–49.3 ppm Th. TP 12.87 shows wide range of evolution from low to high (Zr/Sr = 0.2–33.3).

This tephra sits within total tree pollen percentages subdued to around c.40%.

KOP-3347 is a tephra layer with a normal discrete distribution with a shard peak of 12.76 shards per g dry wt. Overall 16 WDS-EMPA assays were secured showing a phonolitic-trachytic composition which are distinguishable on major elements (see Fig. 5.6) from the geochemistry of tephra layers KOP-2317–KOP-3119, which have identical overlapping geochemical envelopes. The shard morphology was primarily fluted. This layer lies within a period where total tree pollen populations are decreasing from a high point (c.60 %). KOP-3347 has geochemical ranges of 60.29–61.86 wt% SiO_2, 17.96–19.17 wt% Al_2O_3, 0.37–0.49 wt% TiO_2, 2.76–3.23 wt% FeO, 0.23–0.37 wt% MgO, 1.57–1.85 wt% CaO with a K_2O/Na_2O of 0.97–1.18.

KOP-3900 is a tephra detected by scan analysis but which could not be rediscovered at higher resolution. It appears to represent a positive distribution. Despite several attempts, no geochemical data could be attained, the tephra shards from this layer, although very distinctive, were mostly small (<80µm) with a high vesicularity

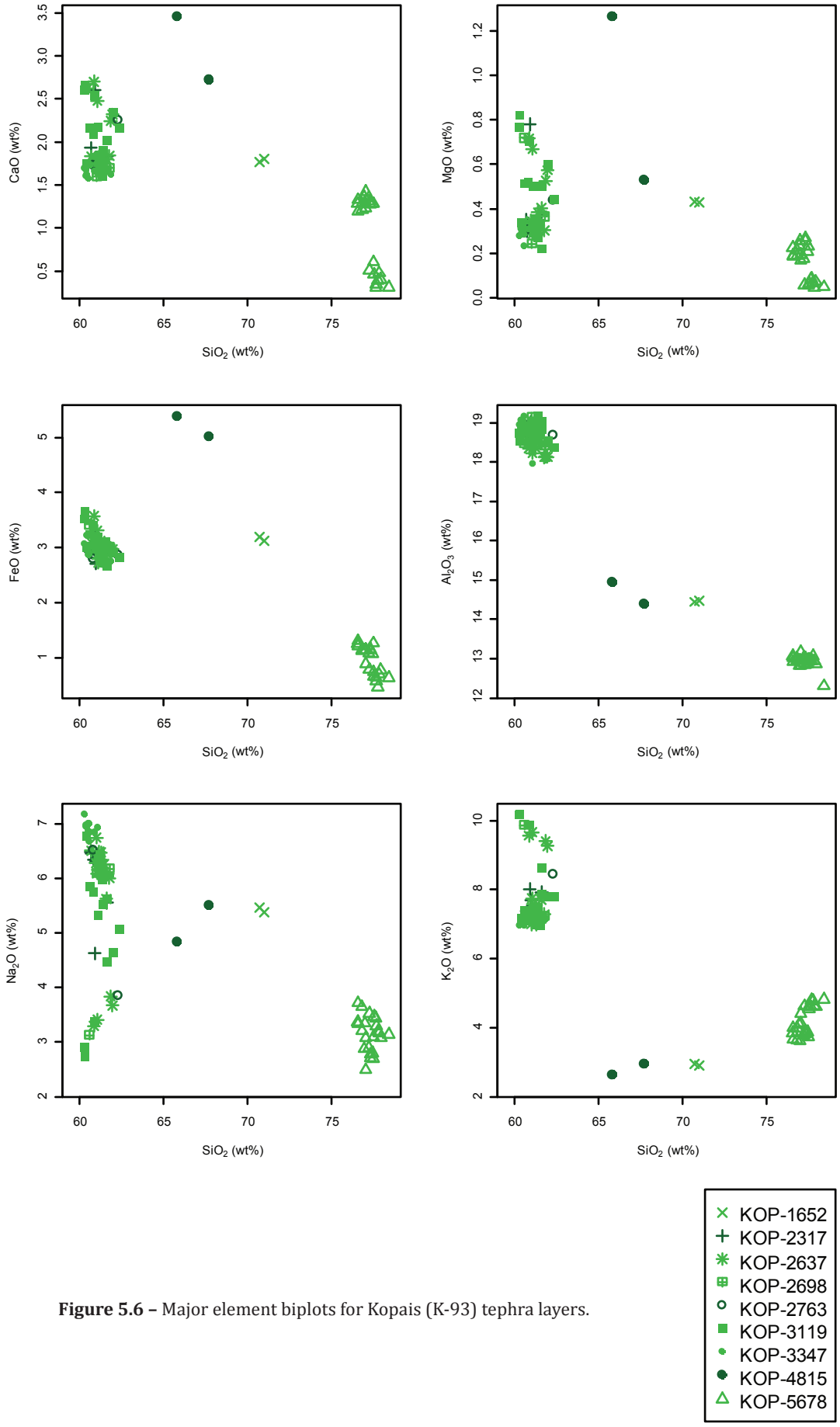

Figure 5.6 – Major element biplots for Kopais (K-93) tephra layers.

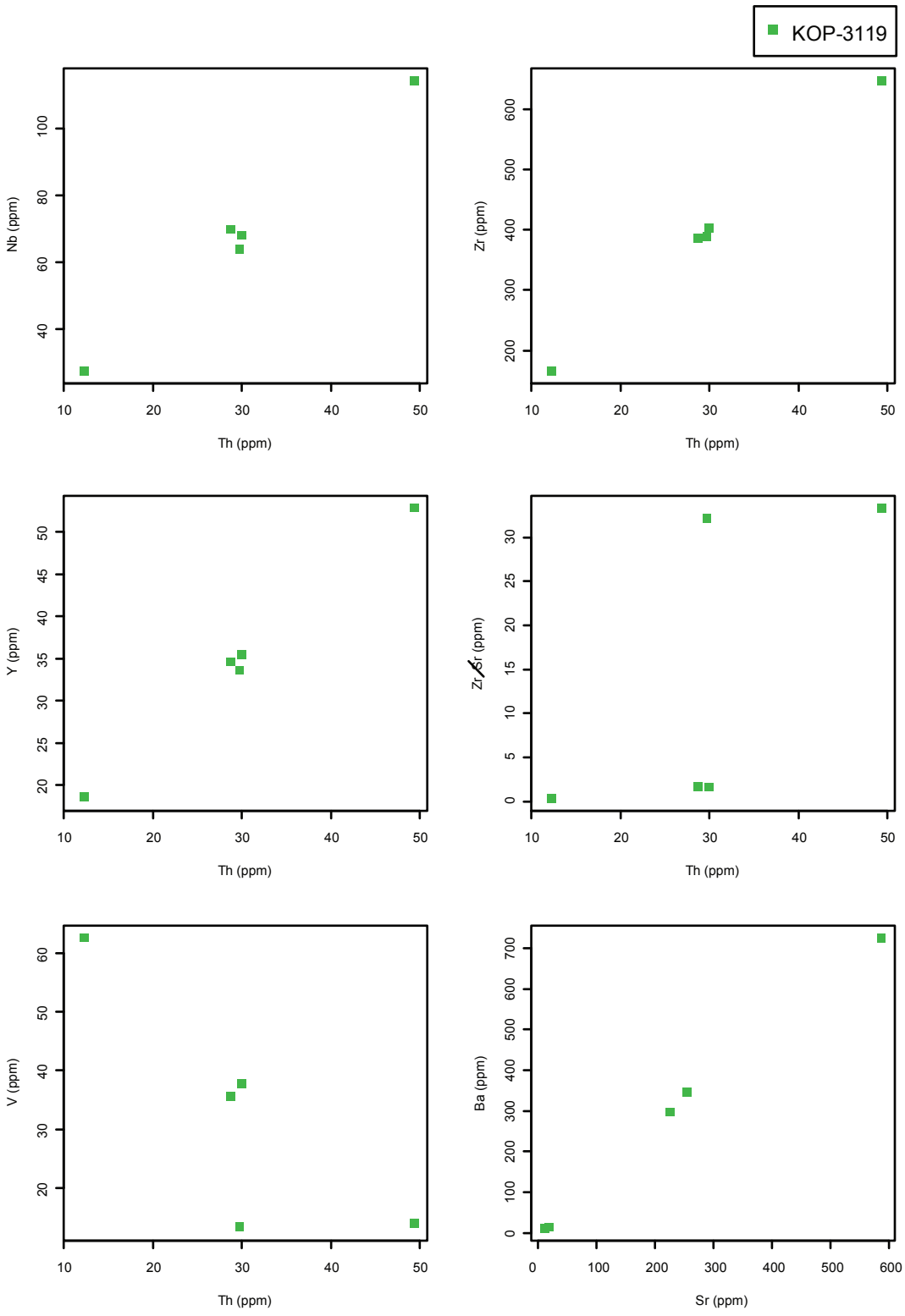

Figure 5.7 – Trace element biplots for Kopais (K-93) tephra layers.

containing high concentrations of mineral inclusions. The layer occurs during a decrease within relatively high total tree pollen percentages (c.70%).

KOP-4059 is a tephra where potentially significant numbers of shards were counted in the scan sample, but where no further tephra shards could be uncovered at 2 cm resolution. No geochemical data was attained and in comparison to the overlying KOP-3900, the shards were more platy, and without vesicles or mineral inclusions.

KOP-4815 is a tephra with a peak of 2.78 per g dry wt and despite no tephra shards being recovered at higher resolution, shards were recovered from the scan slide and two WDS-EMPA assays were attained showing a sub-alkaline medium to high-K dacite-trachyte composition. KOP-4815 has a wide geochemical range with ranges of 65.79–67.70 wt% SiO_2, 14.4–14.95 wt% Al_2O_3, 4.84–5.50 wt% Na_2O and 2.63–2.96 wt% K_2O. The layer appears to have a diffuse positive distribution which sits within a period of very high total tree pollen (c.88%).

KOP-5678 is the lowest stratigraphic tephra uncovered in the Kopais sequence with a peak in the higher resolution samples of 0.53 shards per g dry wt. The shards were large with some additional specimens also found within the retained fraction above >125µm. This allowed 23 WDS-EMPA assays to be gained for this tephra layer, showing two sub-alkaline rhyolitic compositions with a geochemical range of 76.56–78.4 wt% SiO_2, 12.31–13.18 wt% Al_2O_3, 2.49–3.71 wt% Na_2O and 3.61–4.81 wt% K_2O. The analytical totals were very low for this tephra, c.92% on average, which is suggestive of high glass water content. Environmentally this tephra sits within a short lived drop in total tree pollen (78%).

In Summary

Of the 13 cryptotephra layers identified in the K-93 core, 9 were successfully geochemically analysed via WDS-EMPA, at either high (e.g. 1 to 2 cm) or lower (10 cm or >10 cm) resolution (see Table 5.3 for details). These analysed tephra layers are classified using the TAS scheme put forward by Le Bas *et al.* (1986; Fig. 5.5). Trace elemental analysis was only successful on one layer, KOP-3119 (Fig. 5.7).

On the basis of the descriptions presented above and of the biplots presented in Figs. 5.5 and 5.6, KOP-1652, KOP-4815 and KOP-5678 are very distinct sub-alkaline geochemical populations. KOP-2317, KOP-2637, KOP-2698, KOP-2763, KOP-3119 are far more homogeneous, being indistinguishable on alkaline compositions on the basis

of Harker plots (Fig. 5.6). KOP-3347 is slightly different from KOP-2317 to KOP-3119 as it has a smaller geochemical range.

5.3.2 Tenaghi Philippon (TP-2005)

The Tenaghi Philippon sequence (TP-2005) was sampled for cryptotephra content between 16-6m with many layers discovered. The core was first processed using 10 cm contiguous scan samples. Where tephra shards were detected, the relevant intervals were resampled at 1 cm vertical resolution. In Figures 5.8 and 5.9 only the 1 cm-resolved counts and visible tephra layers are shown. Overall 17 tephra layers have been identified (see Figs. 5.8 and 5.9 and Table 5.3 for a summary) and overall 286 WDS-EMPA, 67 LA-ICP-MS and 46 SIMS geochemical assays were gained from Tenaghi Philippon tephra sampled material. Tephra layer stratigraphic position, shard morphology (Fig. 5.10) and geochemistry (see Figs 5.11, 5.12 and 5.13 for an overview) will now be described in stratigraphic order.

TP-707 is a cryptotephra with a peak of >10,000 shards per g dry wt which has a slightly negative distribution. The layer has a vertical spread of 11 cm and is thus quite stratigraphically defined. Both platy and fluted shards were present, mostly larger than 100µm with some rare microlites present. Larger shards were present in the >125µm size fraction, characteristically containing both enclosed and broken vesicles. 21 EMPA-WDS, 3 LA-ICP-MS and 3 SIMS assays were acquired demonstrating a calc-alkaline rhyolite composition (see Fig. 5.11) with narrow geochemical ranges of 70.79–71.67 wt% SiO_2, 14.17–14.76 wt% Al_2O_3, 5.05–5.68 wt% Na_2O and 2.75–3.08 wt% K_2O. This narrow homogenous geochemical envelope is also apparent within the trace element concentrations of Zr (302–376 ppm), Rb (79–109 ppm), Sr (66–80 ppm) and Th (15.3–17.1 ppm). TP-707 shows intermediate levels of evolution (Zr/Sr = 3.90–5.16).

Within the pollen stratigraphy (Müller *et al.*, 2011) this tephra sits in a period of lower tree pollen percentages (~25%).

TP-726 is a cryptotephra that sits 8 cm below TP-707 but forms another peak in shards (a distinct normal distribution) with a tephra peak of >10,000 shards per g dry wt. Both platy and fluted shards were present, mostly larger than 110µm. Enclosed vesicles were only present within the larger shards. 20 EMPA-WDS and 16 LA-ICP-MS

Table 5.3 – Summary of Tenaghi Philippon (TP-2005) tephra layers.

Tephra layer code	Full depth interval (m)	Distribution / skew	Peak shards/g dry wt.	Geochemical sampling depths (m)	Total WDS-EMPA analyses	Total LA-ICPMS analyses	Total SIMS analyses	Classification		
								Alkali status	Composition	K division
TP-707	7.03-7.14	*Slightly positive*	>10,000	*7.08-7.09*	21	3	3	Sub-alkaline	Rhyolite	Calc-alkaline
TP-726	7.22-7.33	*Normal*	>10,000	*7.24-7.28*	20	16	—	Sub-alkaline	Rhyolite	Calc-alkaline
TP 7.61[1]	7.43-7.61	*Negative*	Visible	*7.59-7.61*	46	11	—	Sub-alkaline	Rhyolite	Calc-alkaline
TP-890	8.88-8.92	*Positive*	275.22	—	—	—	—	—	—	—
TP-896	8.95-9.00	*Positive*	65.47	—	—	—	—	—	—	—
TP-923	9.20-9.26	*Negative*	56.21	*9.22-9.25*	17	—	8	Alkaline	Trachyte	Shoshonite
TP-938	9.34-9.43	*Slightly positive*	1257.75	*9.37-9.40*	7	—	7	Alkaline	Trachyte	Shoshonite
TP-951	9.44-9.56	*Negative*	1028.38	*9.48-9.51*	12	—	5	MIXED (9) Alkaline (1) Sub-alkaline	MIXED Trachyte Rhyolite	MIXED Shoshonite Calc-alkaline
TP-970	9.68-~9.76	*Highly Positive*	2059.84	*9.69-9.72*	15	9	—	MIXED (10) Alkaline (5) Sub-alkaline	MIXED Trachyte Rhyolite	MIXED Shoshonite Calc-alkaline
TP-978	~9.76-9.80	*Slightly negative*	952.38	*9.77-9.78*	3	4	—	Sub-alkaline	Rhyolite	Calc-alkaline
TP 12.87[1]	12.50-12.87	*Highly negative*	Visible	*12.77-12.87*	53	24	—	Alkaline	Tr/P	Shoshonite
TP-1325	13.24-13.27	*Positive*	1311.38	*13.24-13.26*	3	—	—	Alkaline	Tr/P	Shoshonite
TP-1328	13.27-13.30	*Positive*	1190.99	*13.29-13.30*	20	—	—	Alkaline	Tr/P	Shoshonite
TP-1334	13.31-13.35	*Negative*	3091.75	*13.33-13.34*	14	—	5	Alkaline	P/Tr	Shoshonite
TP-1354	13.50-13.55	*Negative*	1581.92	*13.52-13.55*	26	—	10	Alkaline	Tr/P	Shoshonite
TP-1392	13.90-13.93	*Normal*	2038.46	*13.90-13.93*	13	—	—	Alkaline	Tr/P	Shoshonite
TP-1450	14.46-14.54	*Diffuse*	39.77	*14.46-14.54*	16	—	8	Alkaline	P/Tr	Shoshonite

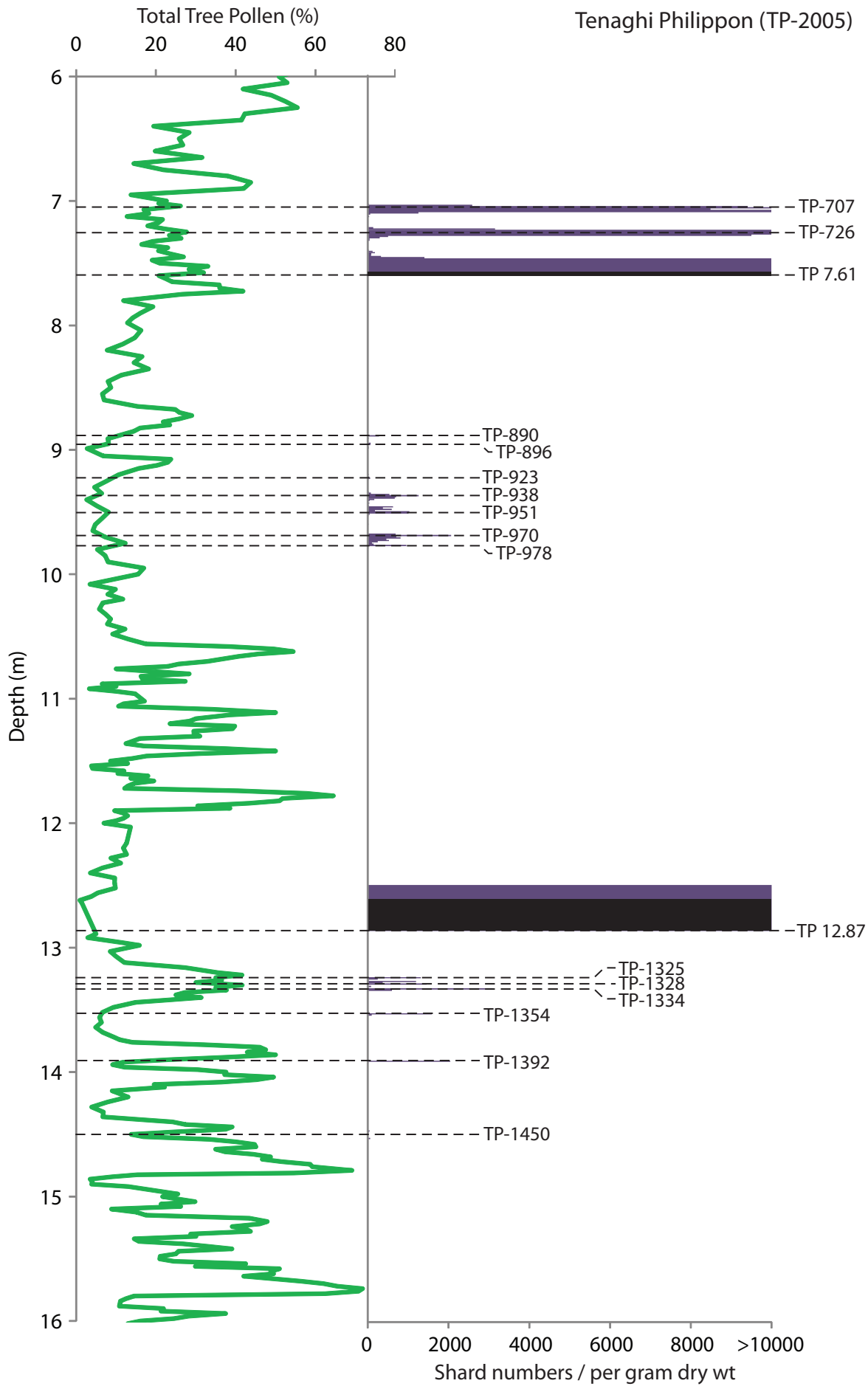

Figure 5.8 – Tenaghi Philippon (TP-2005) shard counts and total tree pollen percentages (Muller *et al.,* 2011) against depth. Black coloured shard numbers indicates visible tephra occurrence.

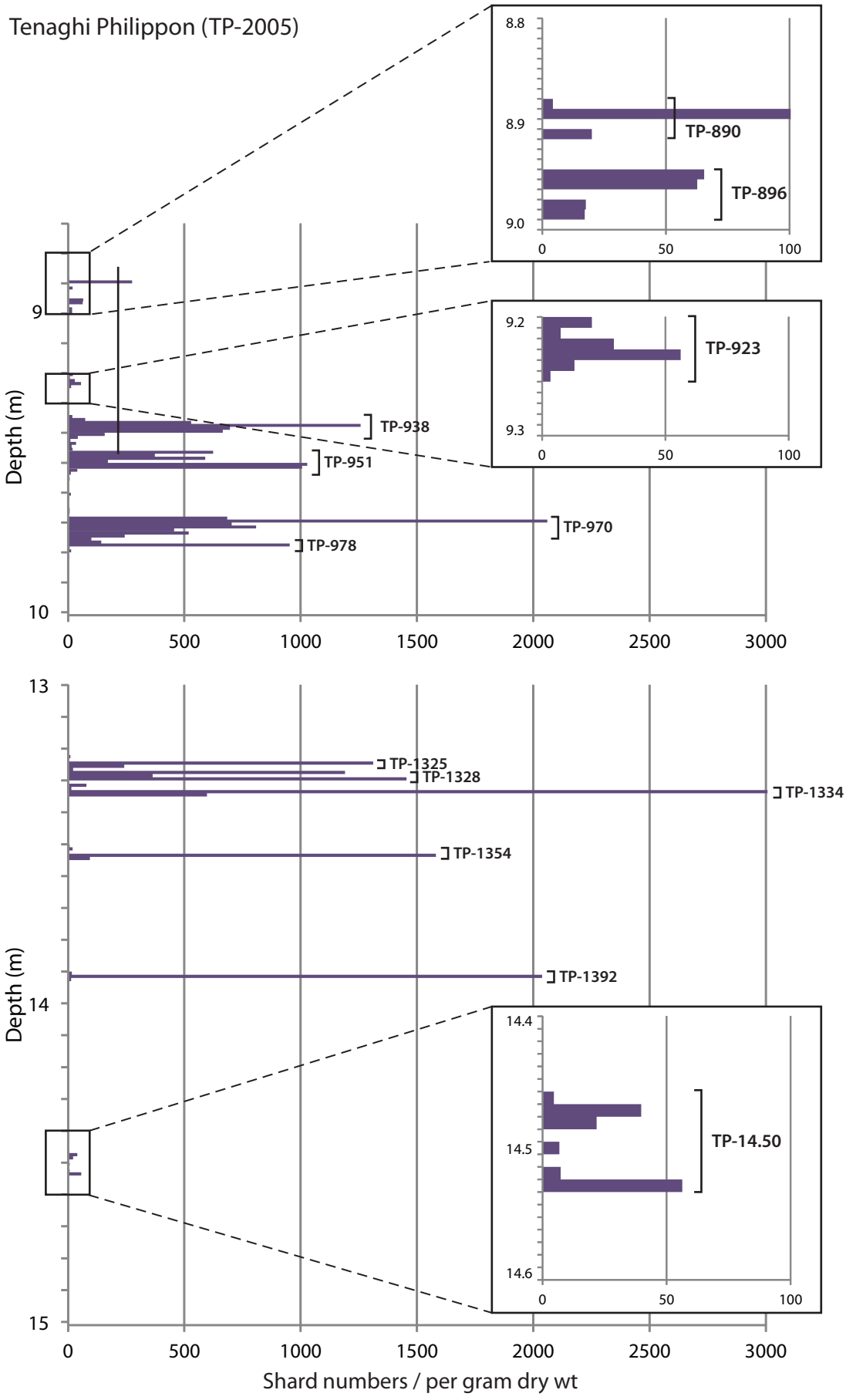

Figure 5.9 – Tenaghi Philippon (TP-2005) shard counts from selected depths.

geochemical assays showing a homogenous calc-alkaline rhyolitic composition (see Fig. 5.11). with narrow geochemical ranges of 70.56–71.39 wt% SiO_2, 14.27–14.68 wt% Al_2O_3, 5.12–5.69 wt% Na_2O and 2.81–2.96 wt% K_2O. This narrow envelope is mirrored within the trace element concentrations of Zr (281–337 ppm), Rb (104–111 ppm), Sr (68–85 ppm) and Th (12.86–17.63 ppm). TP-707 shows intermediate levels of evolution (Zr/Sr = 3.92–4.29).

This layer has a vertical spread of 10 cm and sits within a period of lower tree pollen totals (~27%).

TP 7.61 one of two visible tephra layers present in the Tenaghi Philippon core, sits between 7.59-7.61m although there is also a cryoptephra component which extends above the visible layer for a further 16 cm. Thus this tephra layer has a negative distribution. Both platy and fluted shards were present, mostly larger than 110µm (up to 500µm) with very rare occurrence of microlite inclusions. A very large component of the shards measured >125µm, within these larger shards commonly possessing enclosed vesicles (see Fig. 5.10B). 46 EMPA-WDS and 11 LA-ICP-MS geochemical assays were gained demonstrating a homogenous calc-alkaline rhyolitic composition (see Fig. 5.11), this geochemical envelope has an identical affinity to those of both TP-707 and TP-726. with narrow geochemical ranges of 70.90–71.98 wt% SiO_2, 14.65–14.65 wt% Al_2O_3, 4.80–5.55 wt% Na_2O and 2.75–3.11 wt% K_2O. This narrow envelope is also apparent within the trace element concentrations of Zr (289–322 ppm), Rb (104–109 ppm), Sr (72–80 ppm) and Th (14.47–16.69 ppm). TP-707 shows intermediate levels of evolution (Zr/Sr = 3.87–4.27).

TP 7.61 sits just after a sharp increase and contraction in total tree pollen percentages (c. 20%).

TP-890, TP-896 both represent the next evidence of cryptotephra in the Tenaghi Philippon sequence (see Figs. 5.6 and 5.7) but with relatively low tephra concentrations (<100 shards per g dry wt) showing multimodal shard abundance distributions. The shard morphology for both layers was mostly fluted, elongate shards measuring around 90µm average along the a-axis with some occasional enclosed vesicles present. Unfortunately geochemical data could not be attained due to time constraints. Both tephra layers sit within a period of very subdued but increasing total tree pollen percentages (2.7-8.1%).

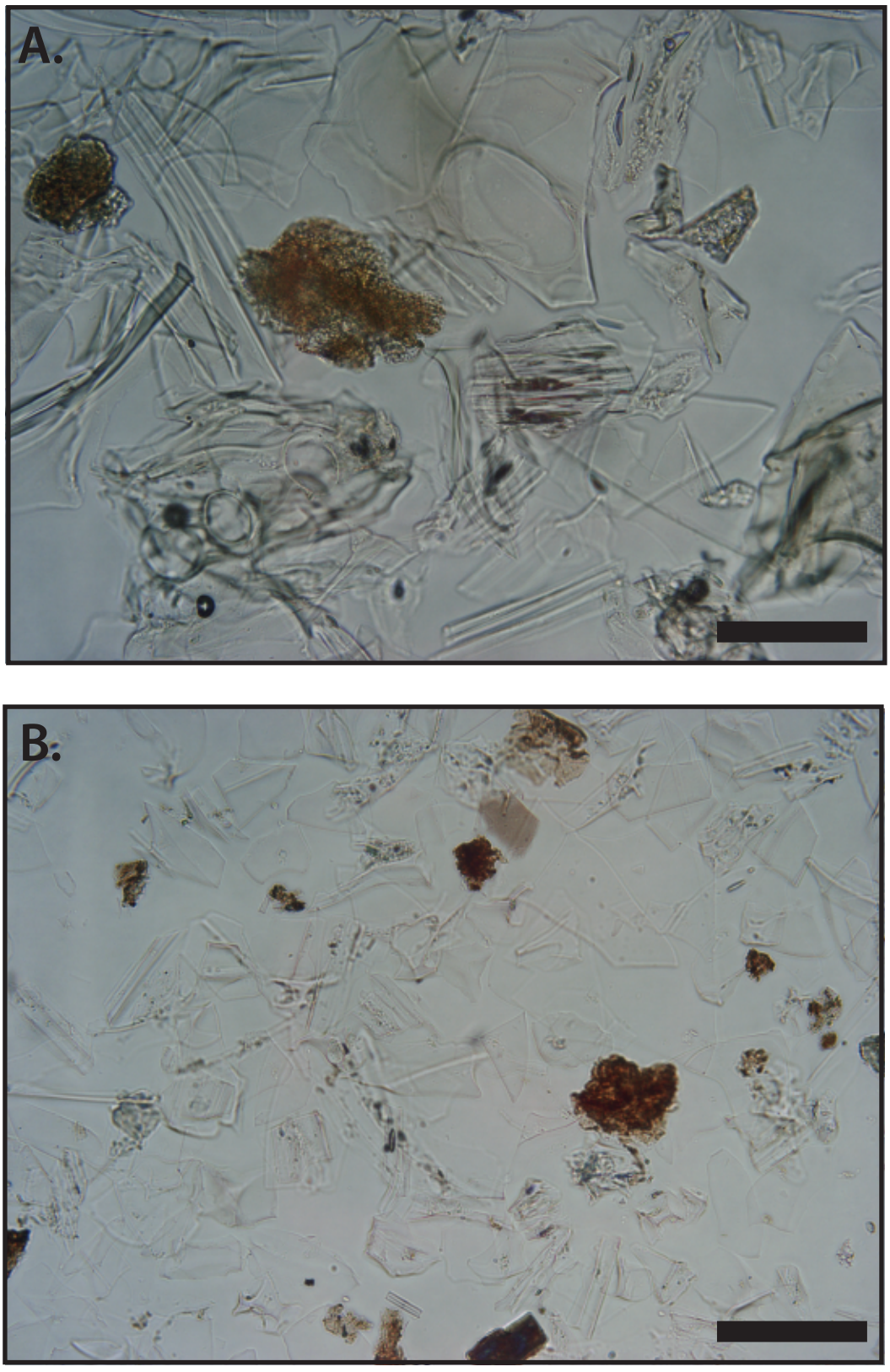

Figure 5.10 – Microphotographs showing the shard morphologies of visible tephra layers from the Tenaghi Philippon (TP-2005) sequence. Both were taken under transmitted light. (**A.**) Note large fluted shards, platy cuspate shards and highly vesicular shards all present within tephra layer TP 12.87. (**B.**) Clear and brownish coloured large platy shards from TP 7.61.

TP-923 is a cryptotephra with a peak of 56.21 shards per g dry wt that has a negative distribution over 6 cm. The observed shards from this layer were mostly small (<80μm) and platy. 17 EMPA-WDS and 8 SIMS geochemical assays were gained demonstrating a homogenous trachytic composition. Geochemical ranges of 60.09–62.79 wt% SiO_2, 18.01–18.71 wt% Al_2O_3, 0.31–0.44 wt% TiO_2, 2.64–3.81 wt% FeO, 0.06–0.18 wt% MgO, 2.04–2.76 wt% CaO with a K_2O/Na_2O of 1.80–3.73. Trace element concentrations also show a less homogenous composition with ranges of: 168–290 ppm Zr, 216–285 ppm Rb, 77.7–98.4 ppm Ce, 40.9–51.5 ppm La, 42–1290 ppm Ba, 164–685 ppm Sr, 21.8–37.6 ppm Nb, 17.5–24.8 ppm Y, 12.1–25.1 ppm Th. TP-923 shows low levels of evolution (Zr/Sr = 0.28–1.77).

The tephra sits within a period of increasing but relatively subdued total tree pollen percentages (c.5%).

TP-938, TP-951 represent two cryptotephra layers which sit alongside each other with and distributions that overlap slightly. TP-938 has a slightly normal distribution with a peak of 1257.75 shards per g dry wt and a vertical spread of 9 cm. The shard morphology is mostly fluted shards with some enclosed vesicles on average around 100μm a-axis size. TP-951, in contrast, has a negative distribution with a peak of 1028.38 shards per g dry wt and a vertical spread of 12 cm. The shard morphology for TP-951 is mostly thick platy shards with rare vesicles on average around 100μm a-axis size. WDS-EMPA and SIMS geochemical assays were attained for both tephra layers both showing the same trachytic geochemical composition and a single rhyolite composition point in TP-951.

TP-938 has a geochemical ranges of 60.57–63.127 wt% SiO_2, 18.15–18.50 wt% Al_2O_3, 0.33–0.43 wt% TiO_2, 2.72–3.55 wt% FeO, 0.35–0.82 wt% MgO, 2.01–2.73 wt% CaO with a K_2O/Na_2O of 1.65–3.16. Trace element concentrations also show a less homogenous composition with ranges of: 178–420 ppm Zr, 245–334 ppm Rb, 78.1–142 ppm Ce, 37.5–63.4 ppm La, 14.1–1221 ppm Ba, 99–674 ppm Sr, 28.9–56.8 ppm Nb, 19.4–28.8 ppm Y, 12.5–34.3 ppm Th. TP-923 shows low to intermediate levels of evolution (Zr/Sr = 0.3–4.2).

TP-951 trachytic component has a geochemical ranges of 60.81–63.06 wt% SiO_2, 18.04–18.51 wt% Al_2O_3, 0.32–0.42 wt% TiO_2, 2.78–3.70 wt% FeO, 0.35–0.87 wt% MgO, 2.10–2.88 wt% CaO with a K_2O/Na_2O of 1.84–2.86. Trace element concentrations also show a less homogenous composition with ranges of: 189–339 ppm Zr, 217–268

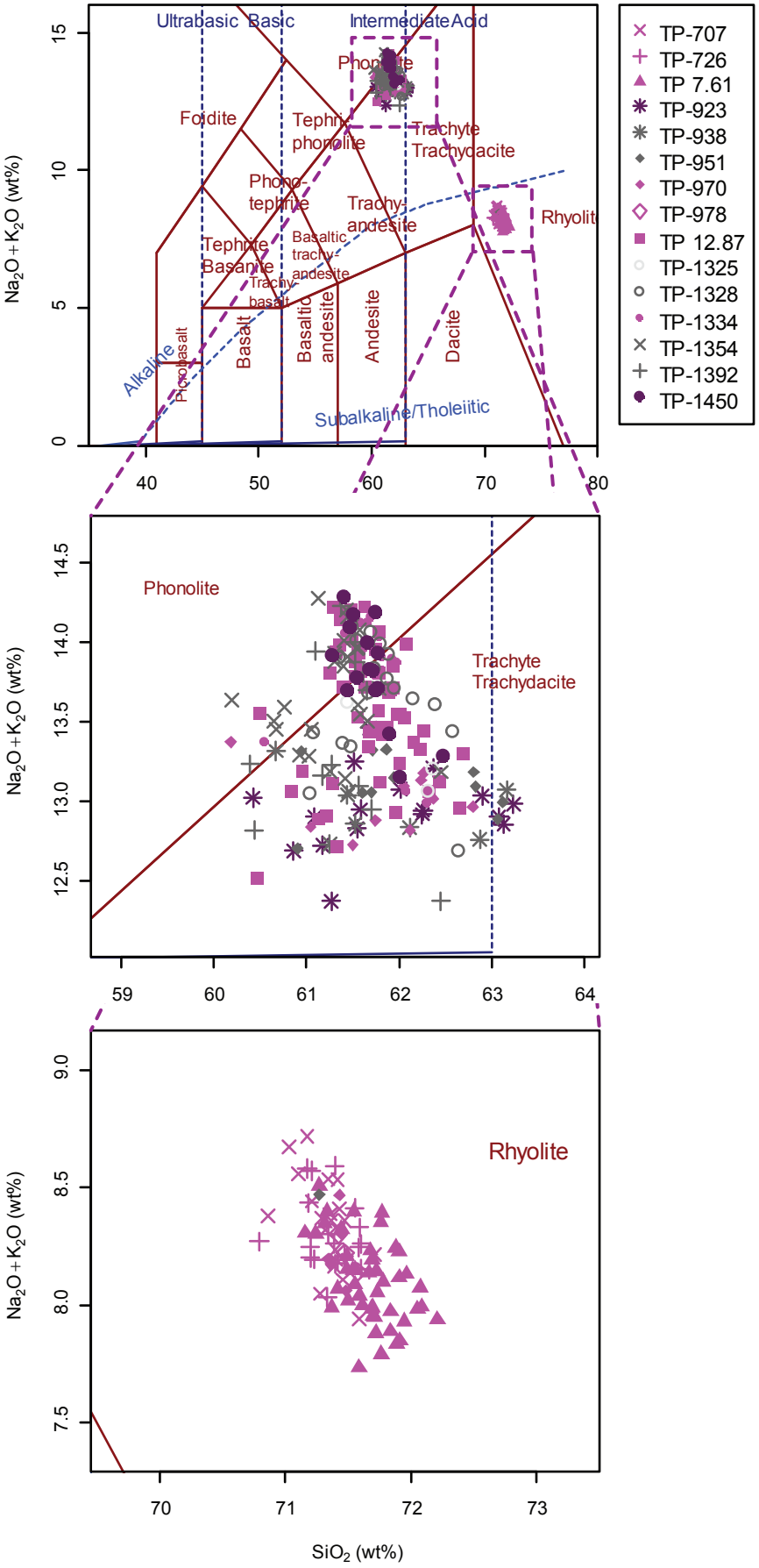

Figure 5.11 – Total alkali vs. silica plot (Le Bas *et al.,* 1986) for Tenaghi Philippon (TP-2005) tephra layers.

ppm Rb, 74.7–125 ppm Ce, 41.4–57.5 ppm La, 99–1625 ppm Ba, 246–782 ppm Sr, 29–48 ppm Nb, 20.4–26.5 ppm Y, 14.2–31.9 ppm Th. TP-923 shows low levels of evolution (Zr/Sr = 0.24–1.38).

Both these cryptotephra sit within the same environmental context with low total tree pollen percentages of ~7%.

TP-970, TP-978 represent two cryptotephra distributions merged into one another, firstly the much more stratigraphically spread and tephra rich TP-970 has a highly positive distribution with a peak of 2059.84 shards per g dry wt and has a vertical stratigraphic spread of 8 cm. Fluted and platy shards (with some broken vesicles) dominate layer TP-970 where shards were also found to be present in the >125µm fraction.

15 WDS-EMPA and 9 LA-ICP-MS geochemical assays were attained for TP-978 demonstrating a bi-modal mixed geochemical population of both alkaline trachyte and sub-alkaline rhyolite at a 2:1 ratio respectively. TP-970 trachytic component has geochemical ranges of 60.09–62.73 wt% SiO_2, 18.12–18.71 wt% Al_2O_3, 0.27–0.42 wt% TiO_2, 2.77–3.81 wt% FeO, 0.47–0.80 wt% MgO, 2.24–2.80 wt% CaO with a K_2O/Na_2O of 2.09–2.83. Trace element concentrations also show a less homogenous composition with ranges of: 211–307 ppm Zr, 300–347 ppm Rb, 92–115 ppm Ce, 49–63.4 ppm La, 145–1601 ppm Ba, 314–845 ppm Sr, 32.7–47.9 ppm Nb, 22.2–27.8 ppm Y, 17–25.6 ppm Th. TP-970 shows low levels of evolution (Zr/Sr = 0.25–0.94). The rhyolitic component of TP-970 is very homogenous geochemical ranges 71.28–71.45 wt% SiO_2, 14.41–14.57 wt% Al_2O_3, 5.09–5.48 wt% Na_2O and 2.89–2.97 wt% K_2O. This narrow homogenous geochemical envelope is also apparent within the trace element concentrations of Zr (309–335 ppm), Rb (106–112 ppm), Sr (76.1–82.1 ppm) and Th (14.69–14.95 ppm). TP-707 shows intermediate levels of evolution (Zr/Sr = 3.82–4.26).

TP-978 in comparison is a very tightly constrained (~4 cm) slightly negative distribution directly underlying TP-970 (see Fig. 5.9) with a peak of 952.38 shards per g dry wt. The shard morphology was predominantly highly fluted elongate shards which are comparatively larger on average than TP-970. 3 WDS-EMPA and 4 LA-ICP-MS geochemical assays were attained for TP-978 showing a sub-alkaline homogenous rhyolitic composition with ranges of: 71.28–71.45 wt% SiO_2, 14.41–14.57 wt% Al_2O_3, 5.09–5.48 wt% Na_2O and 2.89–2.97 wt% K_2O. This narrow envelope is mirrored

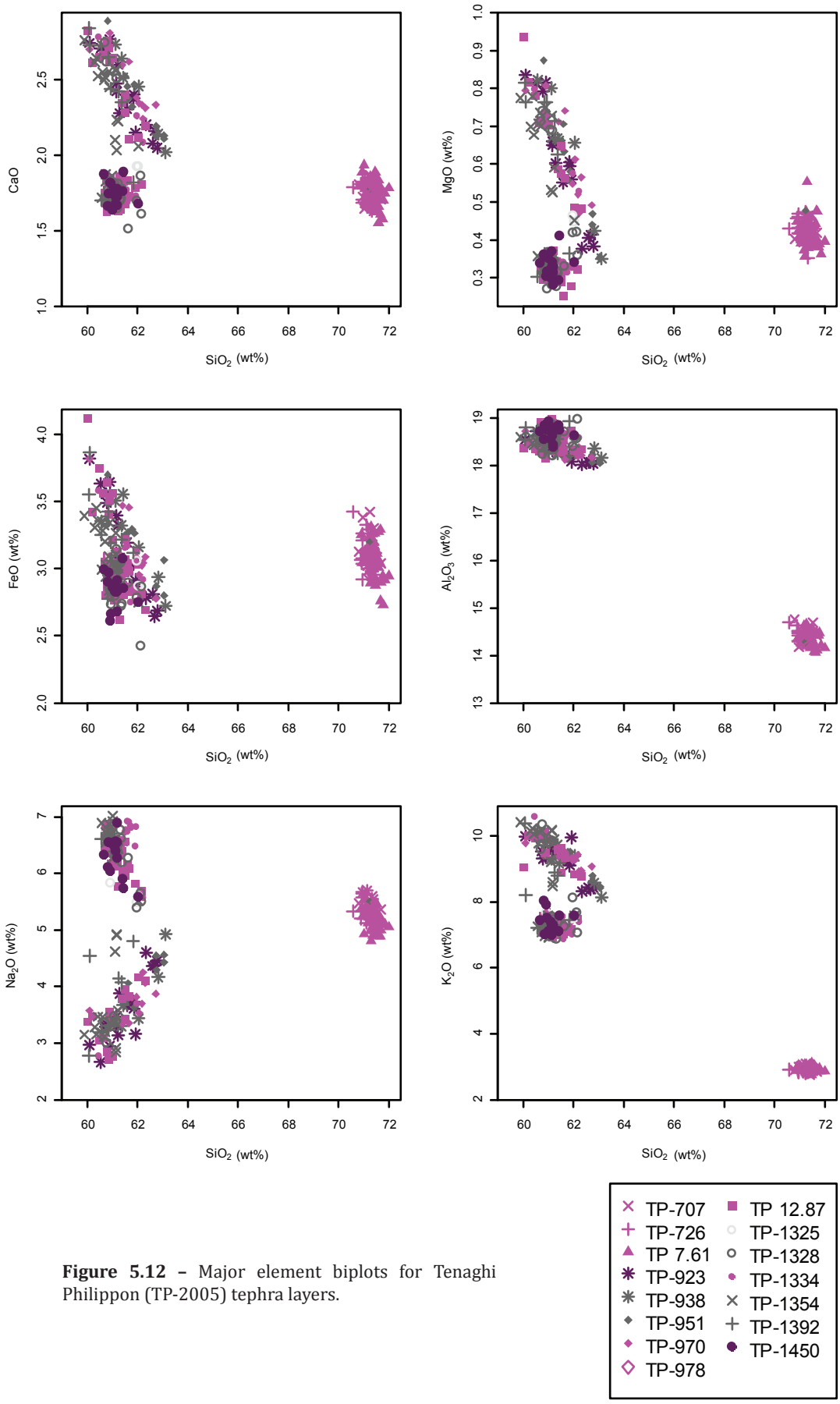

Figure 5.12 – Major element biplots for Tenaghi Philippon (TP-2005) tephra layers.

within the trace element concentrations of Zr (322–340 ppm), Rb (109–112 ppm), Sr (74.8–81.5 ppm) and Th (14.8–16.8 ppm). TP-707 shows intermediate levels of evolution (Zr/Sr = 4.172–4.312).

Both these cryptotephra sit within the same environmental context with low total tree pollen percentages of ~8%.

TP 12.87 is a visible tephra (the lowermost visible tephra layer in the Tenaghi Philippon core) and the visible component lies between 12.64-12.87m, there is also a cryptotephra component which lies up until 20 cm above, thus the tephra layer has a negative distribution. A wide array of shard morphology and very large range of shard sizes are present (including a very large fraction above 25-500μm). Morphology present in TP 12.87 include: featureless platy cuspate shards, highly fluted and highly vesicular shards as well as very 'blocky' shards with both planar and curviplanar intersecting surfaces. Well and poorly developed spherical and ovoid vesicles, both enclosed and broken, are present (see Fig. 5.10A). Mineral inclusions (feldspar) were rare. SEM imaging of unprocessed TP 12.87 (see Fig. 3.2) revealed very small shard and lithic fragments (1-3μm) fillings within larger shards.

53 EMPA-WDS and 24 LA-ICP-MS geochemical assays were attained demonstrating an alkaline trachytic-phonolitic composition. Geochemical ranges of 60.03–62.31 wt% SiO_2, 18.13–18.88 wt% Al_2O_3, 0.33–0.51 wt% TiO_2, 2.69–4.11 wt% FeO, 0.25–0.93 wt% MgO, 1.63–2.82 wt% CaO with a K_2O/Na_2O of 1.08–3.74. Trace element concentrations show a bimodal composition with ranges of: 176–678 ppm Zr, 276–477 ppm Rb, 83.9–251 ppm Ce, 44.1–133 ppm La, 13.1–662 ppm Ba, 18.3–563 ppm Sr, 28.4–126 ppm Nb, 19.2–55.5 ppm Y, 13.5–54.6 ppm Th. TP 12.87 shows a wide range of evolution from low to high (Zr/Sr = 0.3–35.6).

Just below the visible tephra the total tree pollen percentages are at 5% and above it, 1.4%, the lowest values recorded in the TP pollen stratigraphy.

TP-1325–TP-1334 represent three cryptotephra, TP-1325, TP-1328 and TP-1334 which form a tightly clustered three peaks between 13.24-13.34m, covering a 11 cm interval overall. TP-1325 is a very constrained layer (3 cm) with a peak of 1311.38 shards per g dry wt, only 3 EMPA-WDS geochemical assays could be attained demonstrating an alkaline trachytic-phonolitic composition. TP-1328 is another well

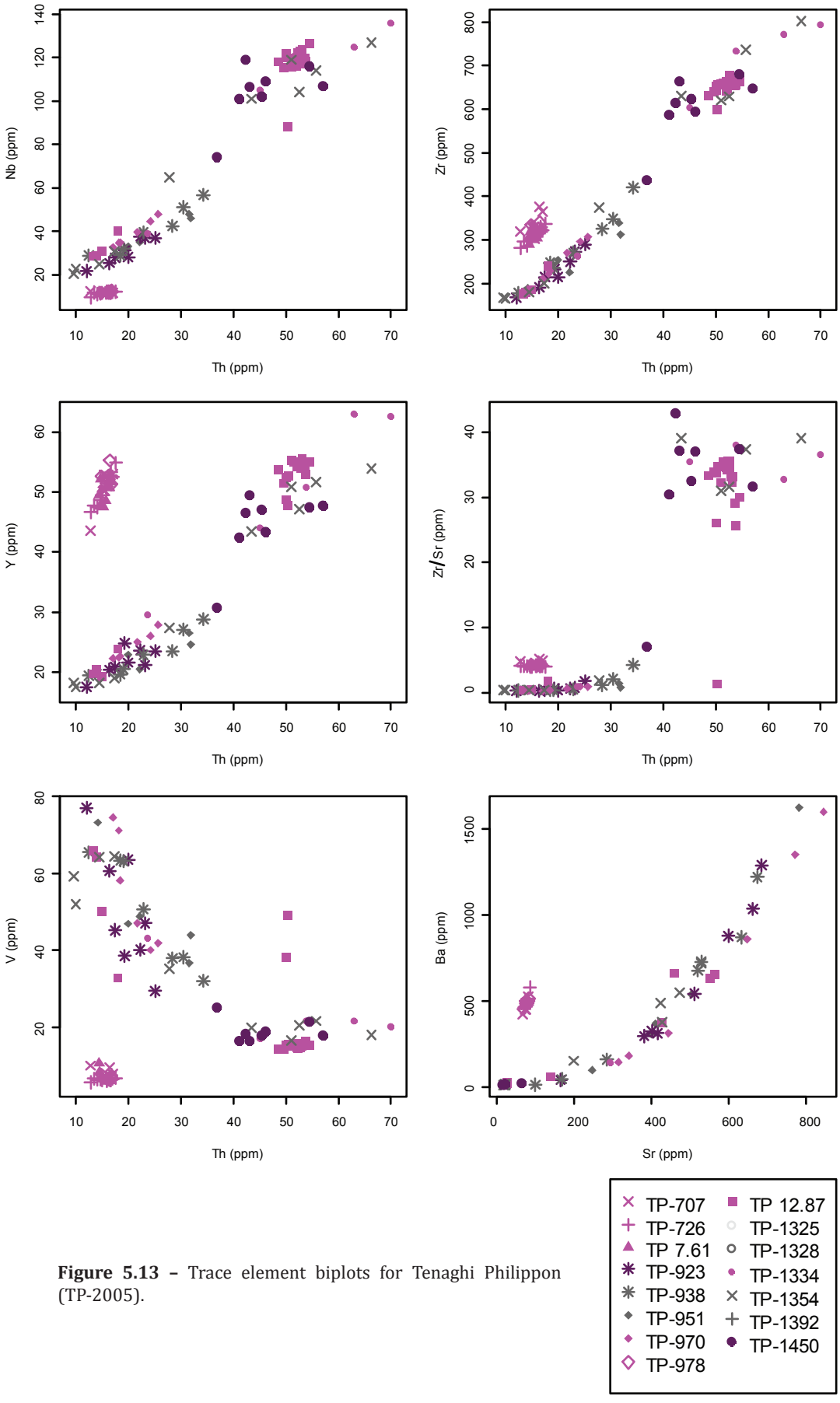

Figure 5.13 – Trace element biplots for Tenaghi Philippon (TP-2005).

constrained cryptotephra covering an interval of 3 cm from 13.27-13.30m with a peak of 1190.99 shards per g dry wt, 20 WDS-EMPA geochemical assays were attained demonstrating an alkaline trachytic-phonolitic composition identical to that of TP-1325. TP-1334 is the largest cryptotephra peak below the visible tephra at 12.87m at 3091.75 shards per g dry wt. The shard stratigraphic distribution skew is negative with a defined 1 cm peak.

3 EMPA-WDS geochemical assays were attained demonstrating an alkaline trachytic-phonolitic composition for TP-1325. TP-1325 has geochemical ranges of 60.91–62.01 wt% SiO_2, 18.51–18.87 wt% Al_2O_3, 0.37–0.41 wt% TiO_2, 2.87–3.09 wt% FeO, 0.32–0.46 wt% MgO, 1.76–1.92 wt% CaO with a K_2O/Na_2O of 1.31–1.36. 20 EMPA-WDS geochemical assays were attained showing also an alkaline trachytic-phonolitic composition for TP-1328 and has geochemical ranges of 60.69–62.15 wt% SiO_2, 18.20–18.97 wt% Al_2O_3, 0.32–0.46 wt% TiO_2, 2.42–3.36 wt% FeO, 0.27–0.74 wt% MgO, 1.51–2.74 wt% CaO with a K_2O/Na_2O of 1.01–3.43.

14 WDS-EMPA and 5 SIMS geochemical assays were attained for TP-1334 demonstrating an alkaline phonolitic- trachytic composition distinct from that of TP-1325 and TP-1328 with geochemical ranges of 60.43–62.22 wt% SiO_2, 18.31–18.80 wt% Al_2O_3, 0.32–0.46 wt% TiO_2, 2.75–3.58 wt% FeO, 0.31–0.79 wt% MgO, 1.68–2.78 wt% CaO with a K_2O/Na_2O of 0.99–3.81. Trace element concentrations also show a less homogenous composition with ranges of: 263–793 ppm Zr, 305–431 ppm Rb, 116–275 ppm Ce, 64.9–160 ppm La, 42–136 ppm Ba, 17–292 ppm Sr, 39–136 ppm Nb, 29.6–63 ppm Y, 23.6–70 ppm Th. TP-1334 shows low to high levels of evolution (Zr/Sr = 0.9–38).

TP-1325, TP-1328 and TP-1334 all sit within a period of elevated total tree pollen percentages (c. 30-40%).

TP-1354 is a cryptotephra which forms a constrained horizon with a negative distribution 5 cm in thickness, with a peak of 1581.92 shards per g dry wt. The tephra sits within a period with subdued total tree percentages (~6%)

TP-1354 has geochemical ranges of 59.89–62.04 wt% SiO_2, 18.34–18.74 wt% Al_2O_3, 0.27–0.47 wt% TiO_2, 2.74–3.45 wt% FeO, 0.30–0.77 wt% MgO, 1.67–2.75 wt% CaO with a K_2O/Na_2O of 0.99–3.57. Trace element concentrations also show a less homogenous composition with ranges of: 166–802 ppm Zr, 219–427 ppm Rb, 70.7–

269 ppm Ce, 39.8–128 ppm La, 12–721 ppm Ba, 16.1–528 ppm Sr, 20.6–127 ppm Nb, 17.5–53.9 ppm Y, 9.6–66.3 ppm Th. TP-1354 shows low to intermediate levels of evolution (Zr/Sr = 0.3–39.1).

TP-1392 is a tightly constrained cryptotephra with a peak of 2038.46 shards per g dry wt.

TP-1392 has geochemical ranges of 60.07–61.83 wt% SiO_2, 18.28–18.92 wt% Al_2O_3, 0.34–0.46 wt% TiO_2, 2.77–3.86 wt% FeO, 0.30–0.81 wt% MgO, 1.67–2.83 wt% CaO with a K_2O/Na_2O of 1.05–3.73. This cryptotephra sits within a period of rising total tree pollen percentages 1.4-7.9%.

TP-1450 is a relatively small cryptotephra horizon with a diffuse shard stratigraphic distribution (from 14.46-14.54 cm), the highest shard peak is 39.77 shards per g dry wt. In terms of environmental context the layer lies just after a period of high total tree percentages has subdued (3-6% total tree pollen).

TP-1450 has geochemical ranges of 60.67–62.01 wt% SiO_2, 18.39–18.92 wt% Al_2O_3, 0.37–0.47 wt% TiO_2, 2.61–3.07 wt% FeO, 0.28–0.41 wt% MgO, 1.63–1.89 wt% CaO with a K_2O/Na_2O of 1.04–1.35. Trace element concentrations also show a less homogenous composition with ranges of: 437–681 ppm Zr, 375–416 ppm Rb, 148–224 ppm Ce, 72.7–115 ppm La, 12.4–24 ppm Ba, 14.3–62.3 ppm Sr, 74.1–119 ppm Nb, 30.8–49.5 ppm Y, 36.8–57.1 ppm Th. TP-1450 shows intermediate to high levels of evolution (Zr/Sr = 7-43).

In Summary:

Of the 2 visible tephra layers first described by Müller *et al.* (2011), both were reanalysed here using both EPMA-WDS and LA-ICP-MS methods. When the EPMA data of this study are compared to the averaged EPMA presented in Müller *et al.* (2011) a good match is observed for most elements except for Na_2O which was higher by around 0.3 wt%.

Within the TP 2005 core 15 cryptotephra layers were identified and except for two layers (TP-890 and TP-896) all were successfully geochemically analysed via WDS-EMPA at mostly high (e.g. 1 cm) resolution (see Table 5.3 for details). These analysed tephra layers have been described here and classified based upon the TAS scheme put forward by Le Bas *et al.* (1986; see Fig. 5.11 and Table 5.3). Trace elemental analysis

were successful on both the visible horizons (TP 7.61 and TP 12.87) and on eleven of the cryptotephra horizons (see Fig. 5.13).

In summary on the basis of the descriptions provided above and the biplots presented in Figs. 5.11 to 5.13, the TP tephra layers can be geochemically grouped as follows: TP-923, TP-938, TP-951 and TP-970 form an indistinguishable trachytic range, while in contrast TP 12.87, TP-1325, TP-1328, TP-1354 and TP-1392 also fall into the trachyte range but also have an phonolitic component. TP-1334 and TP-1450 are similar to the aforementioned ranges but form a distinct smaller geochemical envelope. TP-707, TP-726, TP 7.61, TP-978 and smaller components of TP-951 and TP-970 all have identical alkaline composition, indistinguishable on major or trace elements.

5.3.3 Lesvos (ML-00 and ML-01)

Most of the Lesvos short core ML-00 was sub-sampled for cryptotephra and multiple tephra horizons were uncovered, the scan and high resolution results being presented here (see Figs. 5.14, 5.15 and Table 5.4 for a summary). Selected shard morphologies and characteristics for Lesvos ML-00 and Ml-01 tephra layers are presented and described in Figure 5.16. Due to time constraints cryptotephra layers ML00-785 to ML00-880 could not be resolved at higher stratigraphic resolution, though some geochemical data were obtained (see Figs 5.17, 5.18 and 5.19 for overview) and are described here for each tephra layer. The labelling follows that of Margari *et al*. (2007; 2009) for the previously–discovered visible tephra layers (ML-1 to ML-5), but new cryptotephra have been coded following the suggestions of Lowe (2011) using core code and depth information.

ML-00 Sequence

ML00-207 is the upper most cryptotephra layer and forms a discrete slightly positive distribution with a peak of 71.93 shards per g dry wt. The morphology was primarily platy with some fluted shards. 16 WDS-EMPA and 12 LA-ICP-MS analyses were obtained from this layer determining a tightly clustered subalkaline rhyolitic geochemical envelope with a geochemical ranges of: 70.89–71.69 wt% SiO_2, 14.18–14.81 wt% Al_2O_3, 4.98–5.56 wt% Na_2O and 2.78–3.08 wt% K_2O. This narrow homogenous geochemical envelope is also apparent within the trace element concentrations of Zr (288–326 ppm), Rb (102–111 ppm), Sr (72.0–80.9 ppm) and Th

Table 5.4 – Summary of Lesvos (ML00 & ML01) tephra layers

Tephra layer code	Full depth interval (m)	Distribution / skew	Peak shards/g dry wt.	Geochemical sampling depths (m)	Total WDS-EMPA analyses	Total LA-ICPMS analyses	Total SIMS analyses	Classification		
								Alkali status	Composition	K division
ML-00 Sequence										
ML00-207	2.02-2.18	*Positive*	71.93	*2.05-2.10*	16	12	—	Subalkaline	Rhyolite	Calc-alkaline
ML-2[2]	5.50-5.63	—	Visible	*5.50-5.63*	23	4	—	Alkaline	Tr/P	Shoshonite
ML00-583	5.80-5.87	*Normal*	77.01	*5.82-5.86*	14	—	—	MIXED (8) Subalkaline (4) Alkaline	MIXED Rhyolite Trachyte	MIXED High-K Shoshonite
ML00-716	7.04-7.16	*Negative*	2314.51	*7.16-7.17*	25	16	—	Subalkaline	Rhyolite	Calc-alkaline
ML00-785	7.73-8.01	—	12.16	*7.73-8.03*	8	—	—	Subalkaline	Rhyolite	High-K
ML00-815	8.11-8.19	—	27.76	*8.15-8.20*	6	—	—	Subalkaline	Rhyolite	High-K
ML00-845	8.27-8.64	—	40.65	*8.35-8.55*	23	6	—	Subalkaline	Rhyolite	High-K
ML00-880	8.70-8.85	—	19.11	*8.75-8.85*	22	5	—	MIXED (16) Subalkaline (5) Alkaline	MIXED Rhyolite P/Tr	MIXED High-K Shoshonite
ML-01 Sequence										
ML-1[2]	1.80-1.82	—	Visible	*1.80-1.82*	30	18	—	Subalkaline	Rhyolite	Calc-alkaline
ML-3[2]	10.33-10.50	—	Visible	*10.33-10.50*	28	19	—	Subalkaline	Rhyolite	High-K
ML-4[2]	11.89-12.00	—	Visible	*11.89-12.00*	30	16	—	Subalkaline	Rhyolite	High-K
ML-5[2]	24.21-24.25	—	Visible	*24.21-24.25*	24	8	—	MIXED (21) Alkaline (3) Subalkaline	MIXED Rhyolite Trachyte	MIXED Shoshonite High-K

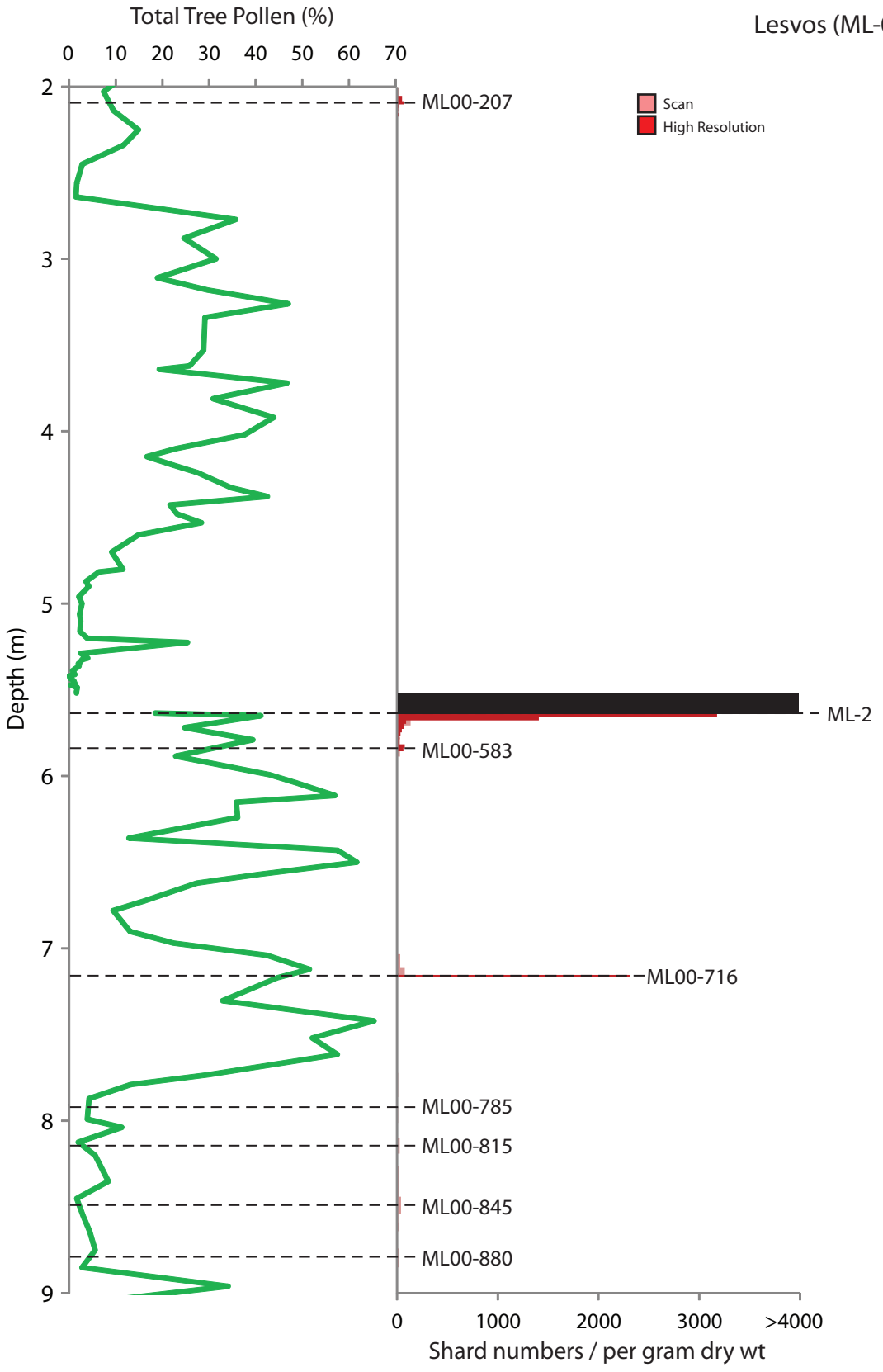

Figure 5.14 – Lesvos (ML-00) shard counts and total tree pollen percentages (Margari *et al.,* 2007; 2009) against depth.

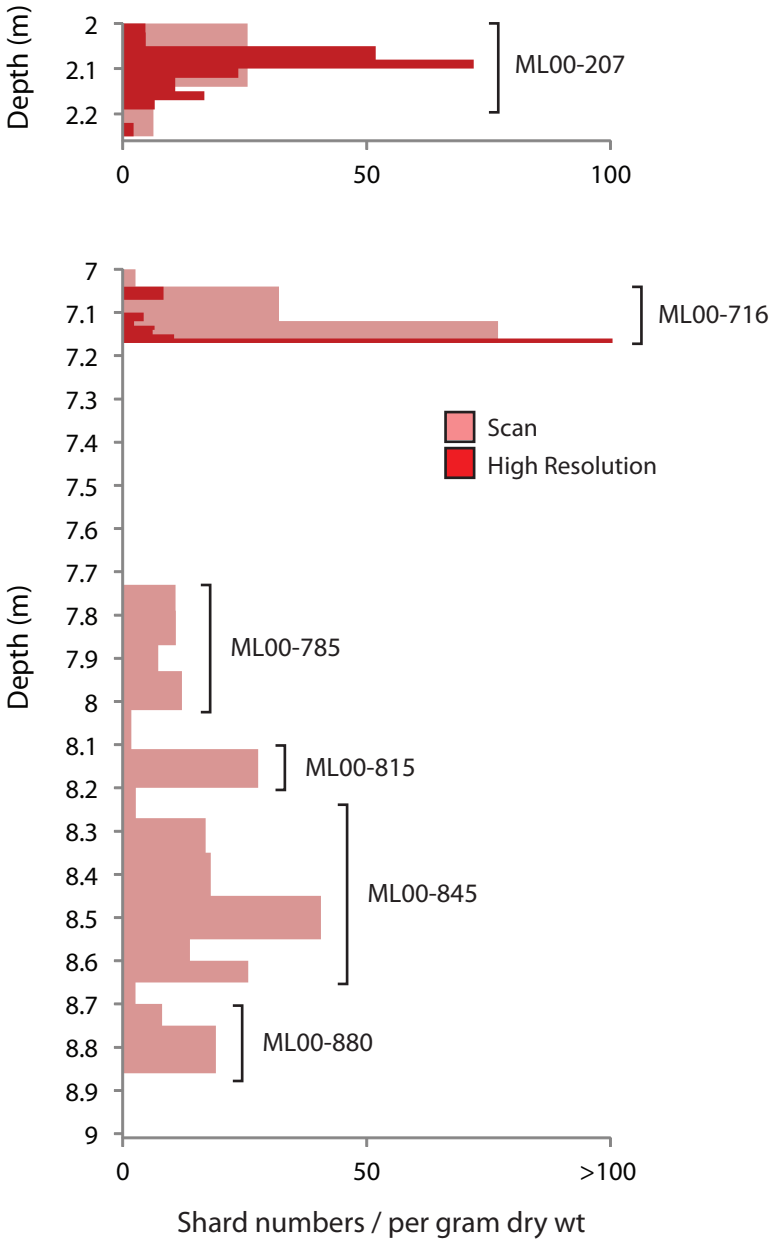

Figure 5.15 – Lesvos (ML-00) shard counts from selected depths.

(12.9–17.0 ppm). ML00-207 shows intermediate levels of evolution (Zr/Sr = 3.91–4.40).

This cryptotephra lies within a period of relatively low total tree percentages (c.10%).

ML-2 is a visible tephra horizon and lies at the depth interval 5.50-5.63 and was re-analysed (both 25->125µm size fractions) 22 WDS-EMPA and 4 LA-ICP-MS assays were achieved. ML-2 has a trachytic-phonolitic composition matching the data within Margari *et al.* (2007) with geochemical ranges of 60.91–62.42 wt% SiO_2, 18.11–18.79 wt% Al_2O_3, 0.33–0.51 wt% TiO_2, 2.66–3.19 wt% FeO, 0.26–0.51 wt% MgO, 1.67–2.17wt% CaO with a K_2O/Na_2O of 1.07–1.94. Trace element concentrations show a single compositional envelope with ranges of: 595–639 ppm Zr, 402–436 ppm Rb, 216–234 ppm Ce, 112–123 ppm La, 13.1–15.1 ppm Ba, 17.5–20.3 ppm Sr, 105–119 ppm Nb, 48.8–52.1 ppm Y, 46.2–49.7 ppm Th. TP 12.87 shows high levels of evolution (Zr/Sr = 31.5–35.5).

The shard morphology present in ML-2 tephra layer include: featureless platy cuspate shards, highly fluted and highly vesicular shards as well as very 'blocky' shards. This tephra layer lies within a period where tree percentages drop from 18 to 3%.

ML00-583 is a cryptotephra that underlies ML-2 and forms a normal distribution with a peak in 77 shards per g dry wt. The shards were both platy and fluted with some mineral inclusions apparent. 14 WDS-EMPA assays were achieved showing 2 distinct geochemical populations of sub-alkaline (76.69–77.73 wt% SiO_2, 12.44–13.17 wt% Al_2O_3, 3.37–3.60 wt% Na_2O and 3.96–4.71 wt% K_2O) and trachytic (61.17–62.04 wt% SiO_2, 18.60–19.24 wt% Al_2O_3, 0.34–0.47 wt% TiO_2, 2.80–2.85 wt% FeO, 0.35–0.47 wt% MgO, 1.63–1.95 wt% CaO with a K_2O/Na_2O of 1.14–1.74) compositions. This tephra lies within a period of semi-raised (c.30%) total tree percentages.

ML00-716 is the largest cryptotephra found in the ML-00 sequence forming a highly negatively distribution with a peak of 2314.51 shards per g dry wt. The layer contained very large shards (including shards in the retained >125µm fraction) which were primarily large thick fluted and platy shards with large vesicles apparent. This allowed 25 WDS-EMPA and 16 LA-ICP-MS analyses to be gained showing a tightly clustered subalkaline rhyolitic geochemical composition with geochemical ranges of 70.59-71.32 wt% SiO_2, 14.42-14.90 wt% Al_2O_3, 4.87–5.47 wt% Na_2O and 2.75–3.11 wt% K_2O. This narrow homogenous geochemical envelope is also apparent within the

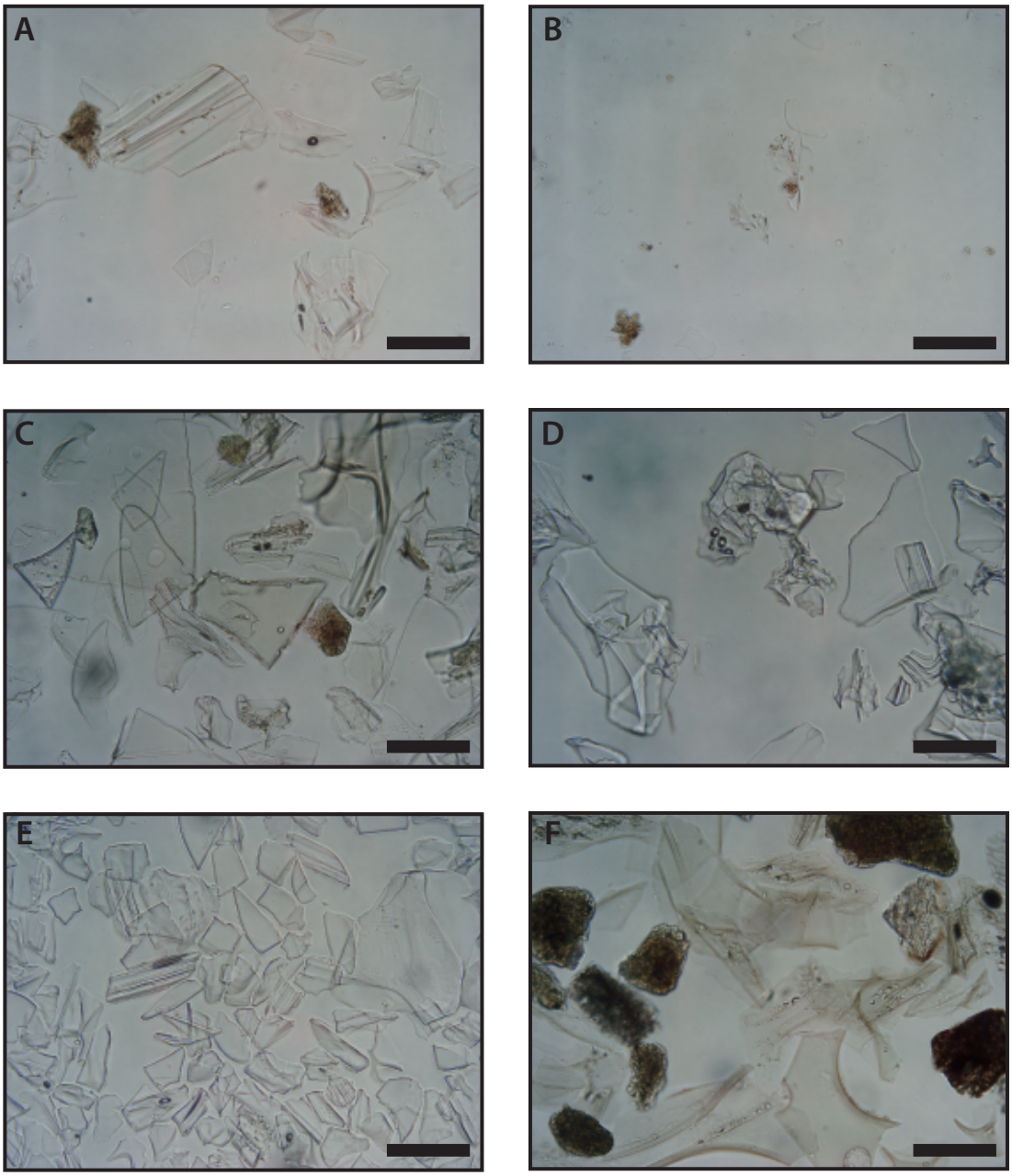

Figure 5.16 – Microphotographs showing the shard morphologies of Lesvos (ML-01, ML-00) tephra layers. All microphotographs were taken under transmitted light. (**A.**) Large fluted and platy shards from ML-1. (**B.**) Comparatively very small platy shards from cryptotephra ML00-207. (**C.**) Large platy and vesicular shards from ML-2. Note also some post depositional alteration features. (**D.**)Blocky and featureless platy shards from ML-3. (**E.**) Platy shards with rare vesicle occurrence from ML-4. (**F.**) Large greenish coloured shards showing both curviplanar and cuspate features from ML-5.

trace element concentrations of Zr (306–340 ppm), Rb (102–112 ppm), Sr (71.5–80.3 ppm) and Th (15.36–17.39 ppm). ML00-716 shows intermediate levels of evolution (Zr/Sr = 3.95-4.44).

This tephra layer lies within a period of higher tree pollen percentages (50%).

ML00-785–ML00-880 from 7.7-8.9m cryptotephra was apparent from around 10-40 shards per g dry wt (see Fig. 5.15) roughly four layers: ML00-785, ML00-815, ML00-845 and ML00-880 were identified from the scan samples (time constraints did not allow further high resolution sampling). All of these cryptotephra layers lie within a period of subdued total tree pollen percentages (1-10%) and all were sampled for geochemistry (see Table 5.4 for further details).

8 and 6 EMPA-WDS assays were gained from layers ML00-785 (74.45–76.97 wt% SiO_2, 12.53–14.34 wt% Al_2O_3, 3.46–4.35 wt% Na_2O and 3.95–4.33 wt% K_2O.) and ML00-815 (76.71–76.96 wt% SiO_2, 12.44–12.71 wt% Al_2O_3, 3.51–3.81 wt% Na_2O and 4.10–4.37 wt% K_2O.) respectively both showing near identical rhyolite compositions.

For the lower two layers ML00-845 and ML00-880 23, 21 EMPA-WDS and 6, 5 LA-ICP-MS assays were gained respectively. ML00-845 has a rhyolitic composition similar to that of the upper two layers with however an outlier population on certain biplots (see Fig. 5.18). The geochemical range for ML00-845 is 76.44–77.18 wt% SiO_2, 12.35–12.82 wt% Al_2O_3, 3.23–3.86 wt% Na_2O and 3.97–4.86 wt% K_2O with trace element concentrations of Zr (129–155 ppm), Rb (138–150 ppm), Sr (84.8–97.5 ppm) and Th (12.52–17.46 ppm). ML00-845 shows low levels of evolution (Zr/Sr = 1.42–1.61).

The lowermost cryptotephra (ML00-880) has a mixed geochemical population of predominantly rhyolitic and a smaller trachytic-phonolitic composition (see Table 5.4). The sub-alkaline geochemical population has ranges of 76.48–77.09 wt% SiO_2, 12.45–12.66 wt% Al_2O_3, 3.34–3.83 wt% Na_2O and 4.02–4.31 wt% K_2O. A narrow homogenous geochemical envelope is also apparent within the trace element concentrations of Zr (75.7–159 ppm), Rb (106–146 ppm), Sr (48.7–97.3 ppm) and Th (7.85–16.6 ppm). ML00-845 shows low levels of evolution (Zr/Sr = 1.55–1.65).

The alkaline component of ML00-880 has geochemical ranges of 60.40–61.68 wt% SiO_2, 18.68–19.14 wt% Al_2O_3, 0.41–0.50 wt% TiO_2, 2.72–3.08 wt% FeO, 0.31–0.43 wt% MgO, 1.56–1.93 wt% CaO with a K_2O/Na_2O of 1.05-1.97.

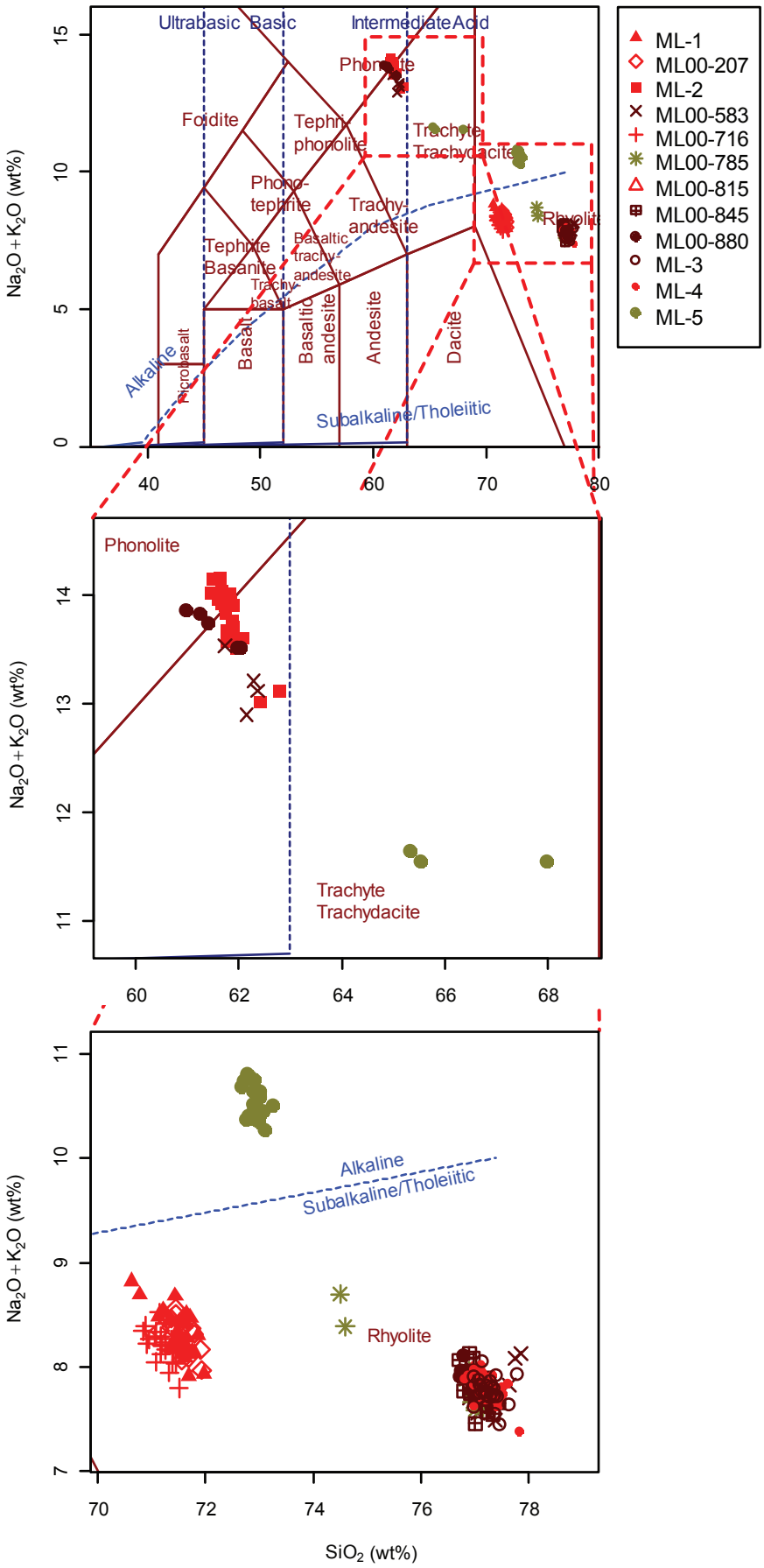

Figure 5.17 – Total alkali vs. silica plot (Le Bas *et al.,* 1986) for Lesvos (ML-00 & ML-01) tephra layers.

ML-01 Sequence

Four visible tephra layers were also analysed for WDS-EMPA and LA-ICP-MS assays, the coding is the same as that stated in Margari *et al.* (2007; 2009).

ML-1 lies at a depth of 1.80-1.82m in the ML-01 sequence and was sub-sampled (both the 25-125 and >125μm size fractions). 30 WDS-EMPA and 18 LA-ICP-MS assays were achieved. ML-1 has a calc-alkaline rhyolitic composition (Fig. 5.17) with narrow geochemical ranges of 70.37–71.71 wt% SiO_2, 14.06–14.55 wt% Al_2O_3, 5.06–5.74 wt% Na_2O and 2.71–3.15 wt% K_2O. This narrow homogenous geochemical envelope is also apparent within the trace element concentrations of Zr (224–331 ppm), Rb (100–107 ppm), Sr (58.5–80 ppm) and Th (10.8–17 ppm). ML-1 shows intermediate levels of evolution (Zr/Sr = 3.83–4.37). Within the pollen stratigraphy ML-1 lies between a period of low tree pollen percentages, c.20 %, before a sharp increase to 40%.

ML-3 lies at depths between 10.33-10.50m in the ML-01 sequence and was sub-sampled for geochemical analyse where 25 WDS-EMPA and 19 LA-ICP-MS assays were achieved. ML-3 has a high-K rhyolitic composition (Fig. 5.17) with narrow geochemical ranges of 75.53–77.55 wt% SiO_2, 12.03–12.95 wt% Al_2O_3, 3.34–4.13 wt% Na_2O and 4.01–4.41 wt% K_2O. This narrow homogenous geochemical envelope is also apparent within the trace element concentrations of Zr (169–139 ppm), Rb (140–147 ppm), Sr (84.1–100 ppm) and Th (13.6–17.9 ppm). TP-707 shows low levels of evolution (Zr/Sr = 1.54–1.69). Before the deposition of ML-3 total tree populations are falling and directly after the deposition of ML-3 total tree pollen percentages are very subdued (<5%).

ML-4 lies at depths between 11.89-12.00m in the ML-01 sequence was sub-sampled for geochemical analyse where 30 WDS-EMPA and 16 LA-ICP-MS assays were achieved. ML-4 (identical to ML-3; Fig. 5.17) has a high-K rhyolitic composition with narrow geochemical ranges between 76.59–77.60 wt% SiO_2, 12.07–12.48 wt% Al_2O_3, 3.13–3.77 wt% Na_2O and 4.12–4.43 wt% K_2O. This narrow homogenous geochemical envelope is also apparent within the trace element concentrations of Zr (147–164 ppm), Rb (144–152 ppm), Sr (91.2–110 ppm) and Th (15.5–17.8 ppm). TP-707 shows low levels of evolution (Zr/Sr = 1.38–1.75). Before the deposition of ML-4 total tree populations are falling and directly after the deposition of the tephra layer total tree pollen percentages are very subdued (<5%).

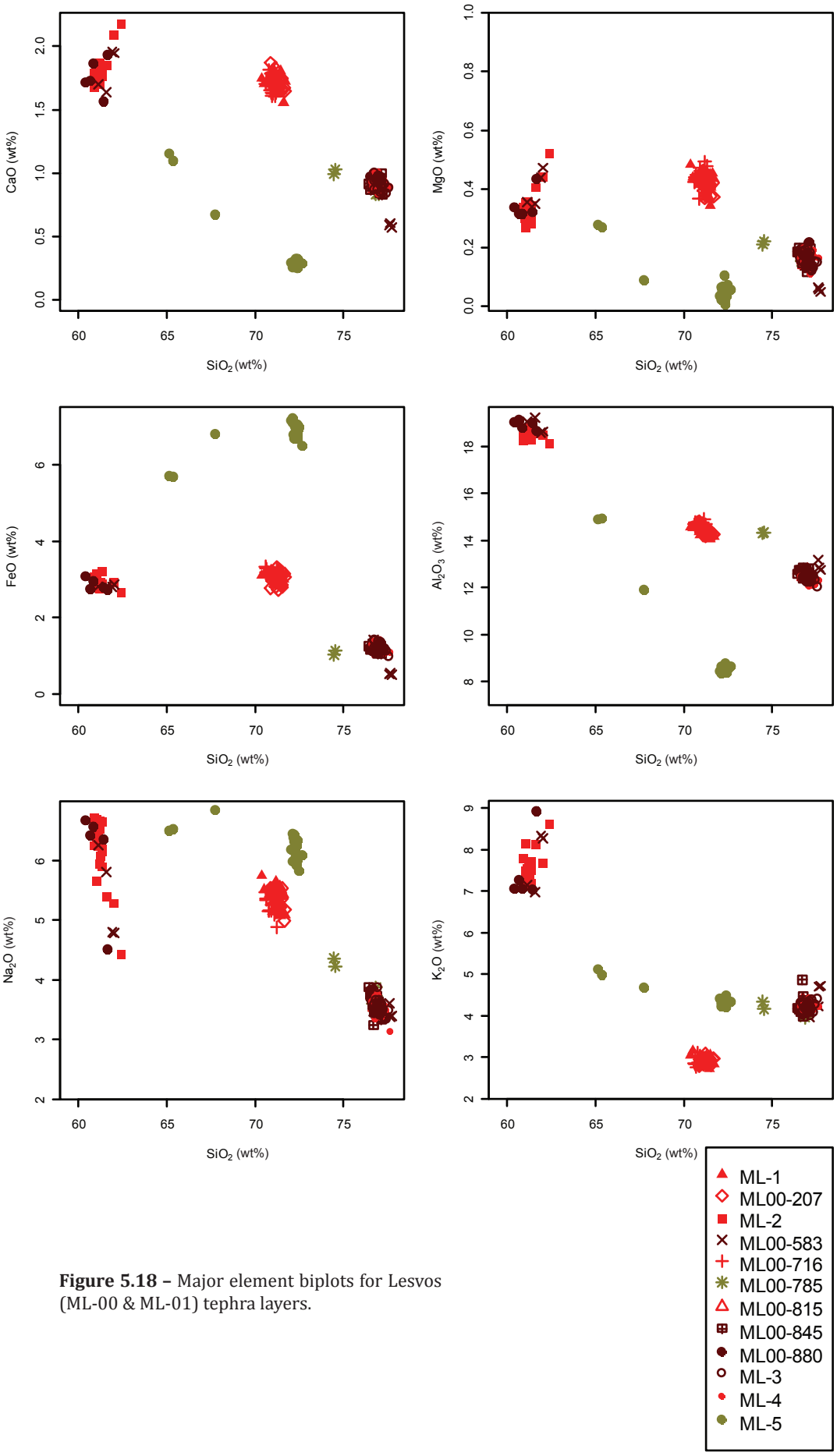

Figure 5.18 – Major element biplots for Lesvos (ML-00 & ML-01) tephra layers.

ML-5 lies at depths 24.21-24.25m in the ML-01 sequence and was sub-sampled for geochemical analysis (both 25-125 and >125μm size fractions) and 28 EMPA-WDS and 8 LA-ICP-MS assays were achieved showing an alkaline trachytic-rhyolitic composition. This bimodal geochemical population consisting of a far more populous rhyolitic component and a rarer trachytic component. ML-5 sits within a period of very subdued total tree pollen percentages both below and above the tephra.

By far the most common population is alkaline High-K rhyolitic composition (Fig. 5.17) with a very narrow geochemical range of 72.01–72.63 wt% SiO_2, 8.33–8.78 wt% Al_2O_3, 5.81–6.44 wt% Na_2O and 4.19–4.49 wt% K_2O. The rhyolitic population has trace element concentrations of: Zr (2267–2284 ppm), Rb (212–232 ppm), Sr (3.7–4.2 ppm) and Th (37.5–42.3 ppm). TP-707 shows very high levels of evolution (Zr/Sr = 532–593).

The trachytic component was only captured in 3 EMPA assays and is far less constrained with geochemical ranges of 65.15–67.73 wt% SiO_2, 11.90–14.92 wt% Al_2O_3, 0.57–0.67 wt% TiO_2, 5.68–6.81 wt% FeO, 0.08–0.27 wt% MgO, 0.67–1.15 wt% CaO with a K_2O/Na_2O ratio of 0.68–0.78 wt%. As with the WDS-EMPA data presented in Margari *et al.* (2007) the analytical totals were consistently low (~94%) for the EPMA data attained for ML-5.

In Summary:

Of the 5 visible tephra layers first described by Margari *et al.* (2007) all were reanalysed here using both EPMA-WDS and LA-ICP-MS methods. When the EPMA data of this study are compared to that of Margari *et al.* (2007) there are perplexing significant offsets (see Fig. 5.20), particularly between ML-2 and ML-5 which show little if any overlap on most biplots. For example on the TAS plot and the Si2O vs Na2O plots showing much lower Alkali and SiO_2 values. ML-2, ML-3 and ML-4 show stronger compositional matches to the Margari *et al.* (2007) dataset although there are subtle differences, ML-3 and ML-4 being indistinguishable from the data produced within this study than that of Margari *et al.* (2007).

Within the ML-00 core, 7 cryptotephra layers were identified and all were successfully geochemically analysed via WDS-EMPA at either high (e.g. 1 cm) or lower (10 cm or >10 cm) resolution (see Table 5.4 for details). These analysed tephra layers have been described here and classified based upon the TAS scheme of Le Bas *et al.* (1986; see

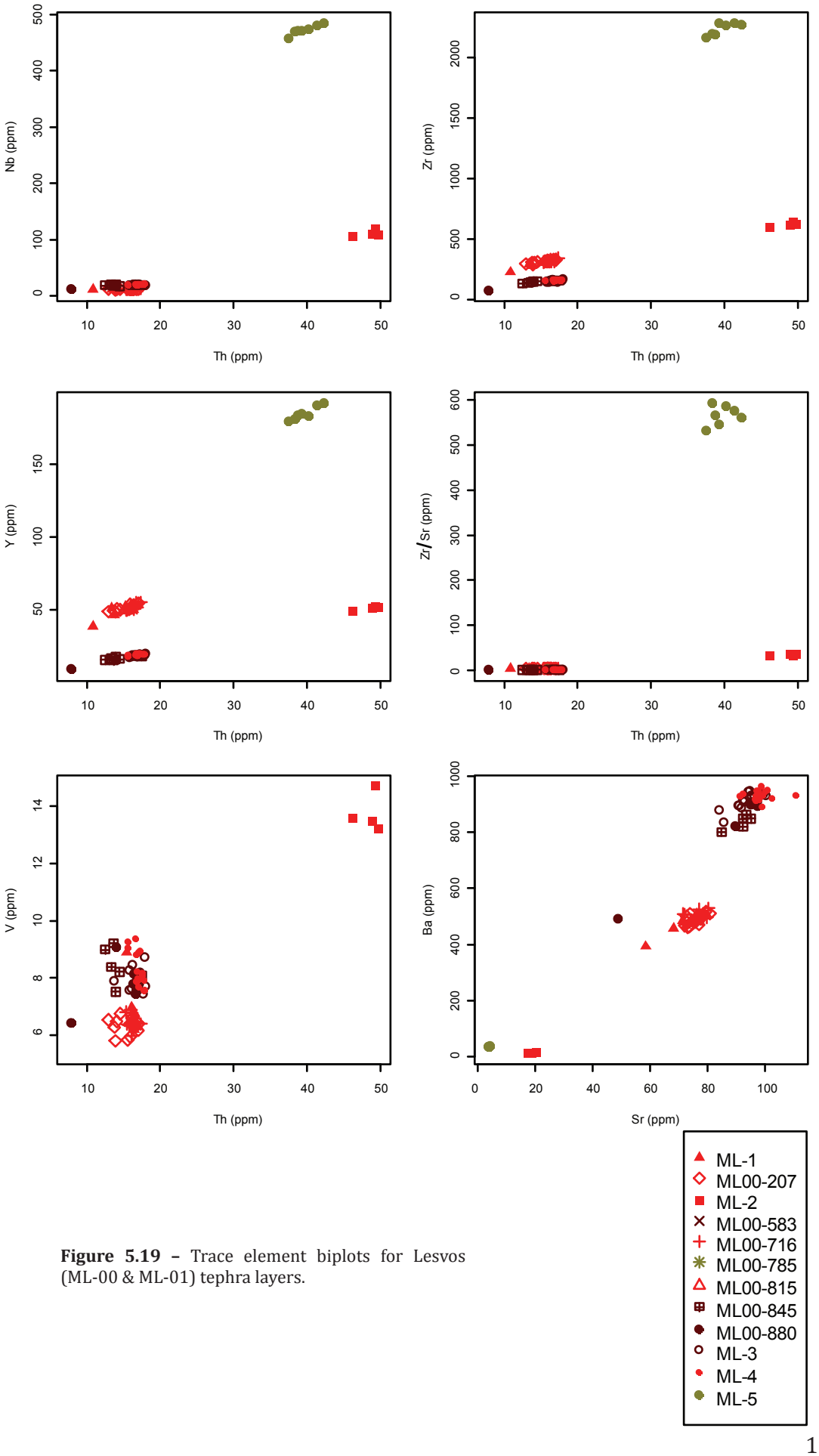

Figure 5.19 – Trace element biplots for Lesvos (ML-00 & ML-01) tephra layers.

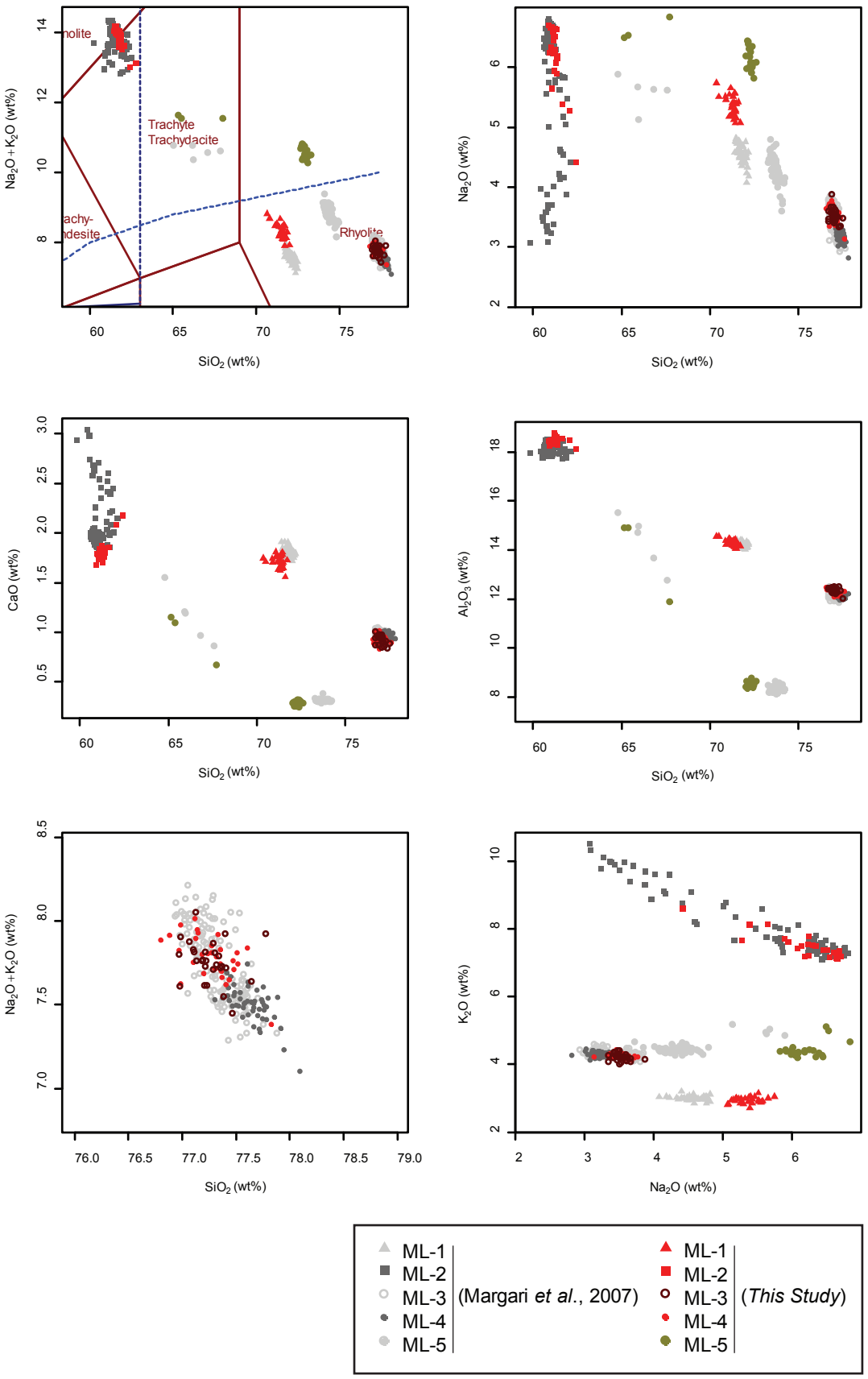

Figure 5.20 – Comparison between new data and Margari *et al.* (2007) geochemical data.

Fig. 5.17 and Table 5.4). Trace elemental analysis were only successful on four of the cryptotephra layers, ML00-207, ML00-583, ML00-845 and ML00-880 (Fig. 5.19).

On the basis of the descriptions provided above and the biplots presented in Figs. 5.17 to 5.19, the Lesvos tephra can be geochemically grouped as follows: ML-2 and ML00-583 form similar alkaline compositions with ML00-880 sitting within this composition but exhibiting a smaller geochemical range. ML-1, ML00-207 and ML00-716 have identical alkaline composition indistinguishable on major or trace elements. ML-5 has a very unique alkaline bimodal geochemical range. All the other tephra layers described from Lesvos within this study (ML-3, ML-4, ML00-785, ML00-815, ML00-845 and ML00-880) have a very similar sub-alkaline high-K geochemistry.

5.3.4 Geochemical grouping of all tephra layers

Figures 5.21, 5.22 and 5.23 combine all the geochemical data outlined above. When compared both between and within individual sites 8 geochemical groups can be recognised and are defined here on the basis of multiple biplots of both major and trace elements (where available). These groupings, outlined and described in Table 5.5, will help form the basis of the tephrocorrelation interpretations attempted within the next chapter.

In Figure 5.21 major element data are plotted against SiO_2 for all the alkaline geochemical tephra analysed within this study. Three different geochemical populations can be distinguished on CaO, MgO, Na_2O and K_2O against SiO_2 biplots. When compared to the other alkaline groups, group 1 has a higher percentage of CaO, MgO and K_2O and a SiO_2 range which extends to higher percentages. In contrast group 3 has a smaller geochemical range and lower CaO, MgO and K_2O and slightly elevated Na_2O percentages. Group 2 covers almost the entire geochemical range of groups 1 and 3.

In Figure 5.22 major element data are plotted against SiO_2 for all the sub-alkaline assays attained in this study which form mostly discrete geochemical clusters. When compared to the other groups, group 4 has very distinct FeO, Al_2O_3, Na_2O values and a wide SiO_2 range. Group 5 has a very distinct, if wide, geochemical range with comparatively lower SiO_2 values and high CaO and MgO values. Group 6 forms a very narrow geochemical envelope with FeO and MgO percentages which distinguish it

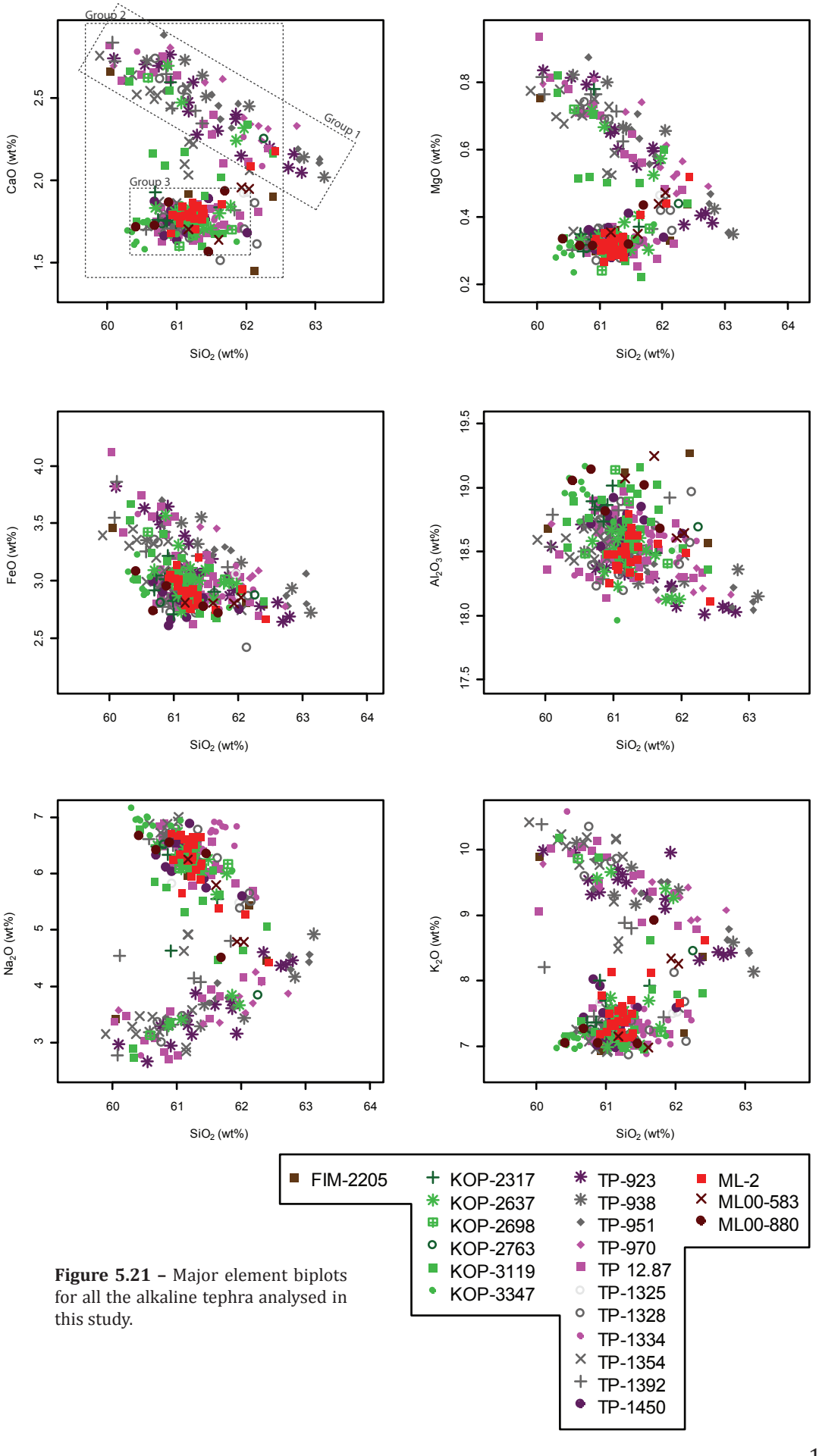

Figure 5.21 – Major element biplots for all the alkaline tephra analysed in this study.

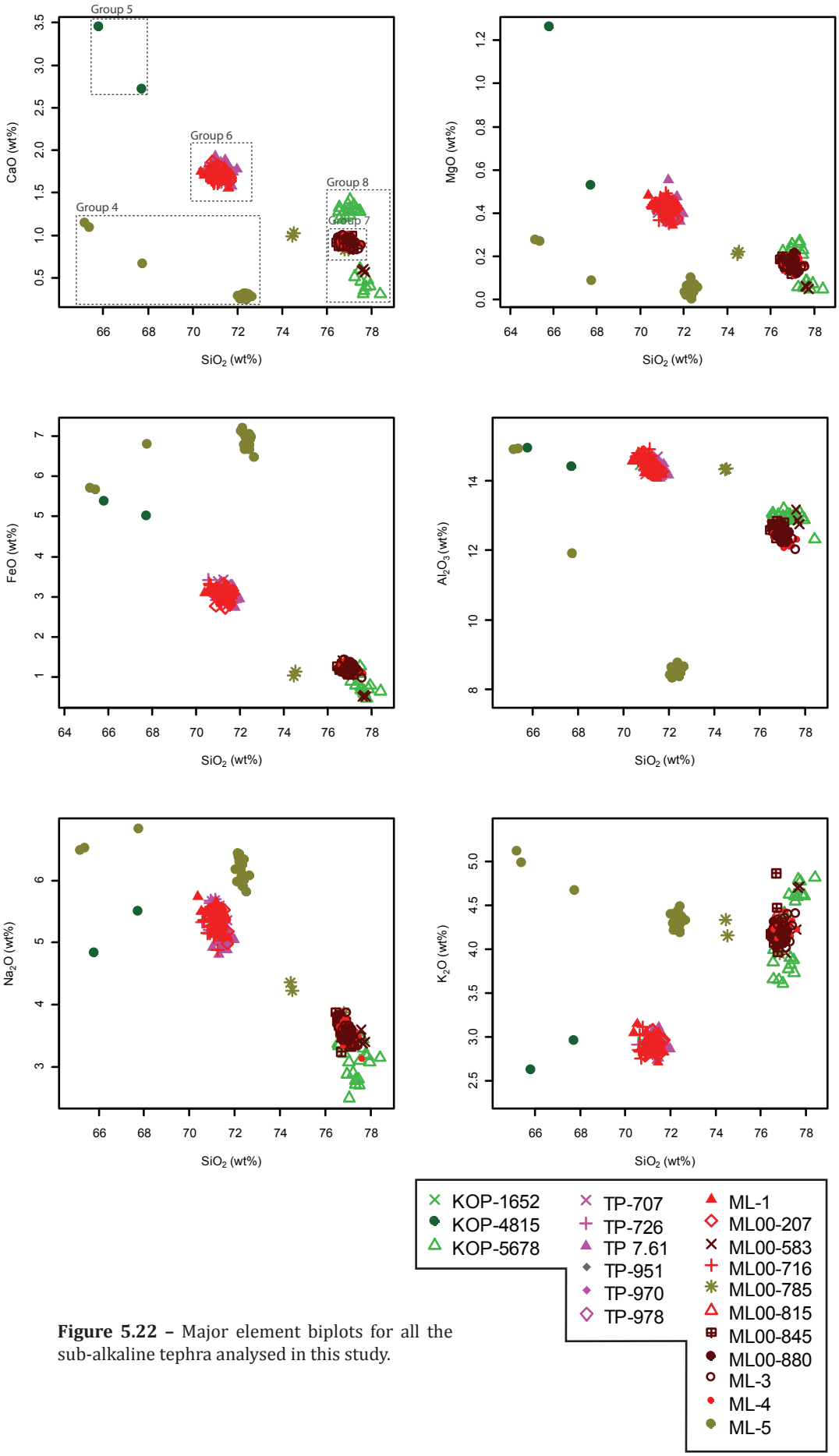

Figure 5.22 – Major element biplots for all the sub-alkaline tephra analysed in this study.

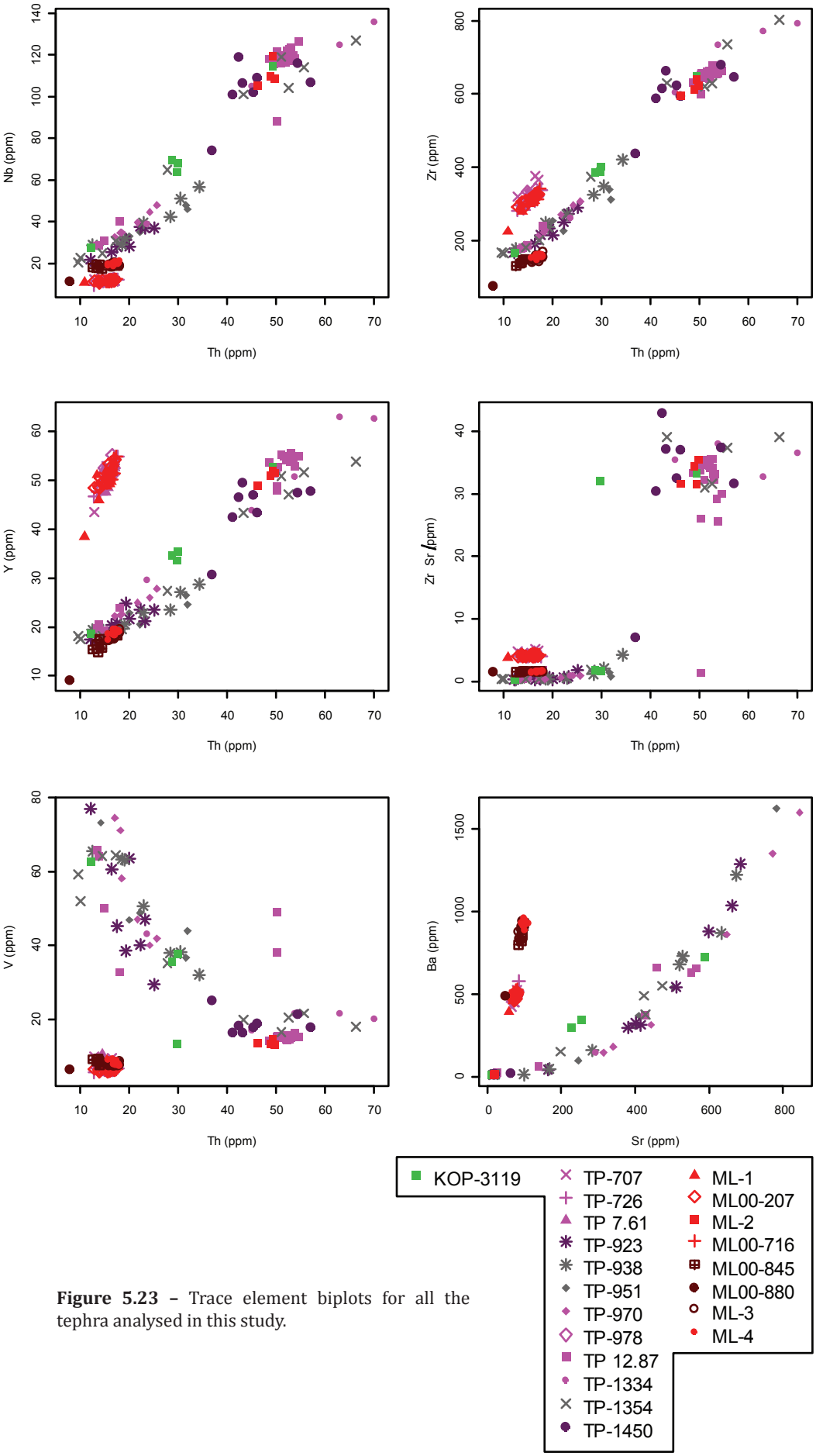

Figure 5.23 – Trace element biplots for all the tephra analysed in this study.

clearly from the other sub-alkaline groups. Group 7 has higher SiO_2 percentages (>76%) and a distinctive CaO range. There are two outlier geochemical assay points in Group 7 belonging to ML00-785, these do not fit into any of the groups although the majority of geochemical data from ML00-785 does fit into group 7. Finally Group 8, although similar to group 7, has lower Na_2O values and distinctive K_2O and CaO values which have a bi-modal distribution.

Table 5.5 – Geochemical grouping of all tephra layers (note tephra in italics are bimodal and thus may sit in more than one grouping).

Geochemical Grouping	Alkali status	Composition	K division	Tephra layer code/s
Group 1	Alkaline	Trachyte	Shoshonite	TP-923, TP-938, *TP-951, TP-970*
Group 2	Alkaline	Tr/P	Shoshonite	FIM-2205 KOP-2317, KOP-2637, KOP-2698, KOP-2763, KOP-3119 TP 12.87, TP-1325, TP-1328, TP-1354, TP-1392 ML-2, *ML00-583*
Group 3	Alkaline	P/Tr	Shoshonite	KOP-3347 TP-1334, TP-1450 *ML00-880*
Group 4	Alkaline	Tr/Rhy	High-K/Shos	ML-5
Group 5	Sub-alkaline	Dacite-Trachyte	Medium to High-K	KOP-4815
Group 6	Sub-alkaline	Rhyolite	Calc-alkaline	KOP-1652 TP-707, TP-726, TP 7.61, *TP-951, TP-970*, TP-978 ML-1, ML00-207, ML00-716
Group 7	Sub-alkaline	Rhyolite	High-K	ML-3, ML-4, *ML00-583*, ML00-785, ML00-815, ML00-845, *ML00-880*
Group 8	Sub-alkaline	Rhyolite	High-K	KOP-5678, *ML00-583*

6.0 CORRELATION OF TEPHRA LAYERS

6.1 Geochemical source regions and reference datasets

6.1.1 Defining source regions

Before specific tephrocorrelations can be applied (section 6.2) each geochemical group, defined at the end of Chapter 5, was compared to the RESET database (a database of both published data and data currently being produced within the RESET consortium) and defined by source regions (the Azores, Iceland, Massif Central, Eifel District, Hellenic Arc, Anatolian regions and various Italian tephra layers) in order to distinguish potential volcanic sources (see Fig. 6.1). The following distinctive groups are recognised, and this scheme forms the basis for classifying individual tephra layers detected in this study.

Group 1

Group 1 overlies Campi Flegrei, Somma-Vesuvius and Ischia compositions on majors and trace elements.

Group 2

Group 2 overlies Campi Flegrei, Somma-Vesuvius and Ischia compositions on majors but clearly matches Campi Flegrei alone on trace elements.

Group 3

Group 3 overlies Campi Flegrei, Somma-Vesuvius and Ischia compositions on majors but clearly matches the Campi Flegrei alone on the Th vs Zr plots.

Group 4

Group 4 is very distinctive on both trace and major element plots and correlates only to Pantelleria–sourced tephra, displaying very elevated Zr concentrations and very low Al_2O_3 percentages.

Group 5

Group 5 primarily overlies Hellenic, Icelandic and Pantelleria compositions. Unfortunately only major elements are available for group 5.

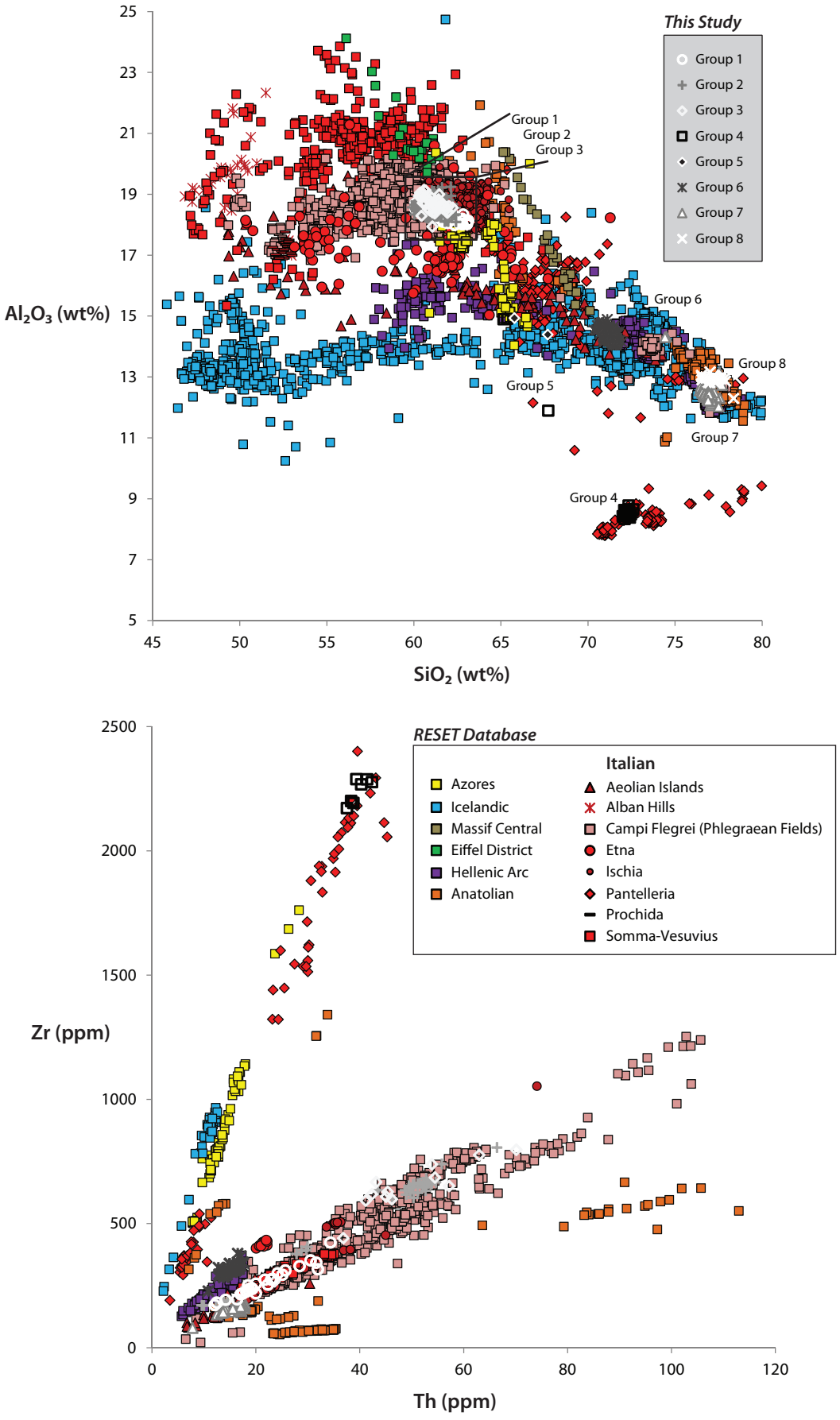

Figure 6.1 – Major and Trace element biplots of the geochemical groupings defined in this study compared against the RESET database defined by volcanic region (accessed 30/05/12).

Group 6

Group 6 primarily overlies Hellenic compositions but also some Icelandic and Aeolian data points on most major element plots. On trace elements, however, the group is clearly distinct from Icelandic and Aeolian composition, sitting solely on the Hellenic range.

Group 7

Group 7 overlies Icelandic, Hellenic and Anatolian compositions on major elements but can be separated from Icelandic evolution trends by trace element ratios which overlie Hellenic and Anatolian compositions.

Group 8

Only major elements are available for Group 8 which suggests Icelandic, Hellenic and Anatolian sources are all possible.

6.1.2 Reference Geochemical Databases

A wealth of tephra geochemical information exists for the Mediterranean region (see Chapter 2) with which to compare the data produced within this study and which will now be described before detailed comparisons are made on a site–by–site basis and an overall synthesis is provided at the end of the chapter.

RESET proximal geochemical dataset

Within RESET the same strategies have been used for distal and proximal volcanic samples including using the same EPMA-WDS and LA-ICP-MS operating protocols and analytical kit (see sections 3.4.7 and 3.4.8). Also the same secondary standards were run; this allows a robust comparison of geochemical data.

Within this chapter, proximal datasets primarily for the Campi Flegrei (CF; See Tomlinson *et al.,* 2012a), Santorini, Pantelleria and Anatolian proximal deposits are utilised (see Table. 6.1 for overview).

Having access to comparable proximal geochemical data is of great use as often these are the deposits where direct $^{40}Ar/^{39}Ar$ and $^{40}K/^{39}Ar$ dating can be achieved on associated minerals (see Table 6.1). However often proximal volcanic stratigraphy can

be complex and may not record all the eruptive products due to, for example, latter eruptions destroying earlier deposits or smaller eruptions leaving very small units. As an example of this 5-8 volcanic units are recognised by Pappalardo *et al.* (1999) proximally between the Neapolitan Yellow Tuff and CI units in the CF region whereas in Lago Grande di Monticchio 26 tephra layers are apparent between the Neapolitan Yellow Tuff and CI tephra layers (Wulf *et al.,* 2004; 2006; 2008).

Table 6.1 – Volcanic layers from proximal deposits used for geochemical comparison purposes within this study. All Radiocarbon dates presented are calibrated.

Tephra	***Source***	***Ages on Proximal Deposits***	***Reference***
Neapolitan Yellow Tuff	Campi Flegrei	14,900 ± 400 (Ar/Ar)[1]	Tomlinson *et al.* (2012a)
TLo	Campi Flegrei	—	Tomlinson *et al.* (2012a)
PRa	Campi Flegrei	16,100 ± 200 (Ar/Ar)[2]	Tomlinson *et al.* (2012a)
VRa	Campi Flegrei	30,300 ± 200(Ar/Ar)[2]	Tomlinson *et al.* (2012a)
VRb	Campi Flegrei		Tomlinson *et al.* (2012a)
Campanian Ignimbrite – Upper Flow	Campi Flegrei	39,280 ± 110 (Ar/Ar)[3]	Tomlinson *et al.* (2012a)
Campanian Ignimbrite – Lower and Intermediate Flow	Campi Flegrei	39,280 ± 110 (Ar/Ar)[3]	Tomlinson *et al.* (2012a)
Campanian Ignimbrite - Fall	Campi Flegrei	39,280 ± 110 (Ar/Ar)[3]	Tomlinson *et al.* (2012a)
TLf	Campi Flegrei	—	Tomlinson *et al.* (2012a)
TLc	Campi Flegrei	—	Tomlinson *et al.* (2012a)
TLa	Campi Flegrei	58,000 ± 3000 (Ar/Ar)[2]	Tomlinson *et al.* (2012a)
Cape Riva	Santorini	20540-22340 (^{14}C)[4] 21250-22270 (^{14}C)[5] 22025-23365 (^{14}C)[4]	(RESET database, Tomlinson *et al., in prep.*)
Upper Scoria 2	Santorini	38462-46197 (^{14}C)[6] 40575-49053 (^{14}C)[6] 54,000 ± 3000 (Ar/Ar)[7] 79,000 ± 8000 (K/Ar)[7]	(RESET database, Tomlinson *et al., in prep.*)
Upper Scoria 1	Santorini	—	(RESET database, Tomlinson *et al., in prep.*)
Vourvolous	Santorini	—	(RESET database, Tomlinson *et al., in prep.*)
Upper Nisyros	Nisyros	>47,450 (^{14}C)[13] 110,000 ± 40,000 (Fission Track)[14]	Tomlinson *et al.* (2012b)
Lower Nisyros	Nisyros	28,300-29,600 (^{14}C)[15]	Tomlinson *et al.* (2012b)
Green Tuff	Pantelleria	45,000 ± 4000 (K/Ar)[8] 46,900 ± 2000 (K/Ar)[9] 47,000 ± 3200 (K/Ar)[10] 49,900 ± 2100 (K/Ar)[9] 50,000 ± 4000 (K/Ar)[8] 50,800 ± 2200 (K/Ar)[9] 50,800 ± 3600 (K/Ar)[10] 59,000 ± 2000 (K/Ar)[10]	(RESET database, Tomlinson *et al., in prep.*)

Guneydag	Central Anatolia	23,800 ± 800 (U/Th)[11]	(RESET database, Tomlinson *et al., in prep.*)
Korudag	Central Anatolia	16,000 ± 3000 (fission track dating)[12] 24,900 ± 900 (U/Th)[11]	(RESET database, Tomlinson *et al., in prep.*)
Gölcük cycle III	Western Anatolia	Multiple eruptions between 72,700 ± 4700 and 24,000 ± 2000 (Ar/Ar)[12]	(RESET database, Tomlinson *et al., in prep.*)

[1]Deino *et al.* (2004) [2] Pappalardo *et al.* (1999) [3]De Vivo *et al.* (2001) [4] Pichler & Freidrich (1976) [5] Eriksen *et al.* (1990) [6] Mellors & Sparks (1991) [7] Druitt *et al*. (1999)[8] Madhood & Hildreth (1986) [9] Civetta *et al.* (1988) [10] Cornette *et al*. (1983) [11] Schmitt *et al.* (2011) [12] Bigazzi *et al.* 1993) [12] Platevoet *et al.* (2008) [13] Limburg & Varekamp (1991) [14] Barberi *et al.* (1988) [15] Keller *et al.* (1989).

Lago Grande di Monticchio

Lago Grande di Monticchio (LGdM) is largely recognised as one of the most comprehensive records of tephra layers in the Mediterranean region (Bourne *et al.,* 2010) and has a varve chronology available (Brauer *et al.,* 2000). The sequence covers the last 133,000 yrs and 349 discrete ash layers have been recognised, many of which have been geochemically analysed (Wulf *et al.,* 2004; 2006; 2008). Over this time frame the LGdM sequence registers tephra layers that have been correlated to the Alban Hills, Ischia, Somma-Vesuvius, Procida, Campi Flegrei, Etna, Stromboli and Pantelleria (Wulf *et al.,* 2004). Tephra layers from LGdM are labelled TM (Tephra Monticchio) and numbered on the basis of stratigraphy (e.g. TM-18 underlies TM-8). For the purposes of this investigation a broad range was taken from TM-8 to TM-22 covering a time range of 90 to 14 ka BP based on the varve chronology. LGdM tephra layers used for graphical comparison are listed in Table 6.2. Shard specfic LGdM EPMA-WDS data was made available by S. Wulf (*pers. comm.*) for use in this study, alongside this new LA-ICP-MS data are also available for some of the TM layers between TM-22 to TM-8 (Tomlinson *et al.,* 2012a). During the course of the comparisons a particular focus was placed on pre TM-18 Campi Flegrei tephra layers which were analysed for EPMA-WDS and LA-ICP-MS as part of this study by this author (TM-18-1d, TM-18-4, TM-18-9e) in order to aid this.

Table 6.2 – Tephra layers from LGdM used for correlative purposes within this study.

Tephra	***Varve Age***	***Source***	***Correlation***	***Reference***
TM-8	14,120 ± 710	CF	NYT	Wulf *et al.* (2004, 2008)

TM-9	14,560 ± 730	CF	Tufi Biancastri (GM1)	Wulf *et al.* (2004, 2008)
TM-10a	15,030 ± 750	CF	Lagno Amendolare (LA)	Wulf *et al.* (2004, 2008)
TM-10b	15,220 ± 760	CF	Lagno Amendolare (LA)	Wulf *et al.* (2004, 2008)
TM-10c	15,300 ± 770	CF	Lagno Amendolare (LA)	Wulf *et al.* (2004, 2008)
TM-10d	15,550 ± 780	CF	Lagno Amendolare (LA)	Wulf *et al.* (2004, 2008)
TM-10-1	15,820 ± 790	IS	St. Angelo Tuff	Wulf *et al.* (2006, 2008)
TM-11	16,440 ± 820	ET	Biancavilla	Wulf *et al.* (2004, 2008)
TM-12	17,560 ± 880	SV	Verdoline	Wulf *et al.* (2004, 2008)
TM-12-1	17,980 ± 900	ET	Ante-Biancavilla ?	Wulf *et al.* (2008)
TM-12-2a	18,500 ± 920	CF	Tufi Biancastri ?	Wulf *et al.* (2008)
TM-12-2b	18,540 ± 930	CF	Tufi Biancastri ?	Wulf *et al.* (2008)
TM-13	19,280 ± 960	SV	Pomici di Base	Wulf *et al.* (2004, 2008)
TM-14a	21,070 ± 1050	PR	Solchiaro CD1-b	Wulf *et al.* (2004, 2006)
TM-14b	21,260 ± 1060	PR	Solchiaro, white facies	Wulf *et al.* (2004, 2006, *in review*)
TM-14-1	21,350 ± 1070	IS	Faro di Punta Imperatore?	Wulf (*pers. comm.*)
TM-14-2	22,250 ± 1110	AB?	—	Wulf (*pers. comm.*)
TM-15	27,260 ± 1360	CF	Y-3	Wulf *et al*. (2004, 2006, *in review*)
TM-17a	29,920 ± 1500	CF	-	Wulf *et al*. (2004) Wulf (*pers. comm.*)
TM-17b	30,000 ± 1500	CF	-	Wulf *et al*. (2004) Wulf (*pers. comm.*)
TM-16a	30,240 ± 1510	SV	Coldola Top	Wulf *et al*. (2006)
TM-16b	31,120 ± 1560	SV	Codola Base	Wulf *et al*. (2006, in review)
TM-17bc	31,830 ± 1590	AB	Albano Unit 7	Wulf *et al*. (2004, in review)
TM-17c	33,770 ± 1690	CF	Taurano Pumice	Wulf *et al*. (2004) Wulf (*pers. comm.*)
TM-17d	33,920 ± 1700	CFPR	Taurano Pumice	Wulf *et al*. (2004) Wulf (*pers. comm.*)
TM-17e	33,360 ± 1700	CF	Taurano Pumice	Wulf *et al*. (2004) Wulf (*pers. comm.*)
TM-17-2	35,530 ± 1780	SV	Schiava, C-9	Wulf *et al*. (2006) Wutke (*submitted*)
TM-18	36,770 ± 1840	CF	Campanian Ignimbrite	Wulf *et al*. (2004, 2006, *in review*)
TM-18-1d*	37,360 ± 1870	CF	SMP1-a	Wulf *et al*. (2006) Wutke (*submitted*)
TM-18-4*	38,600 ± 1930	CF	—	Wulf (*pers. comm.*)
TM-18-7	40,170 ± 2010	PR ?	—	Wulf (*pers. comm.*)
TM-18-9e	41,690 ± 2090	IS	Citara	Wulf *et al.* (2006)
TM-18-12b	49,410 ± 2470	CF	Santa Lucia, C-15	Wulf *et al*. (2006)
TM-19	60,060 ± 3000	IS	Tufo Verde Epomeo	Wulf *et al*. (2004, 2006)
TM-20	61,370 ± 3070	IS	UMSA, Y-7	Wulf *et al*. (2004*, in review*)
TM-20-1a	64,050 ± 3200	IS	—	Wulf (*pers. comm.*)
TM-20-1b	64,140 ± 3200	IS	—	Wulf (*pers. comm.*)
TM-20-1c	64,470 ± 3220	IS	—	Wulf (*pers. comm.*)
TM-20-2a	68,620 ± 3430	CF	C-18	Wulf *et al*. (2006)
TM-20-5	72,940 ± 3650	IS	Pignatiello	Wulf *et al.* (2006)
TM-21	78,340 ± 3920	ST	Petrazza Tuffs, Y-9	Wulf *et al*. (2004, 2006, *in review*)
TM-21-1a	79,410 ± 3970	CF	C-20	Wulf *et al.* (2006)
TM-22	89,130 ± 4460	PA	Ante Green Ignimbrite, P-10	Wulf *et al*. (2004, 2006, *in review*)

AB: Alban Hills, CF: Ischia, ET: Etna, CF: Campi Flegrei, SV: Somma-Vesuvius, ST: Stromboli, PR: Procida, PA: Pantelleria.
*Major and trace elements gathered in this study.

Sicily Channel ODP Leg 160 Site 963A marine core

Geochemical group 4 (defined above) displays a unique Pantelleria geochemical signature. LGdM only has one tephra from this volcanic source currently described (TM-22; Wulf *et al.,* 2004), which could be due to Pantelleria eruptions not following an airfall distribution which covers LGdM due to its more southerly position. A more complete record of Pantelleria eruptive history is available from Sicily Channel ODP Leg 160 Site 963A (ODP963A; Tamburrino *et al.,* 2012), a marine core that lies 100 km to the east of Pantelleria. Six visible tephra horizons have been identified, labelled ODP1 to ODP6, all analysed with comparable EMPA-WDS and LA-ICP-MS techniques. Tamburrino *et al.* (2012) made correlations to the Pantelleria proximal volcanic stratigraphy (Mahood & Hildreth, 1986). A chronology for the core was attained via alignment of the isotope stratigraphy to SPECMAP (Imbrie *et al.,* 1984; Martinson *et al.,* 1987) suggesting the tephra layers cover a timeframe between c.200 – 40 ka BP. All the tephra layers are listed in Table 6.3.

Table 6.3 – Tephra layers from NGRIP and North Atlantic marine core MD04 used for geochemical comparison purposes within this study.

Tephra	*Age (ka)*	*Source*	*Correlations*	*Reference*
ODP1	42.5*	PA	Y-6, Green Tuff	Tamburrino *et al.* (2012)
ODP2	127.5*	PA	—	Tamburrino *et al.* (2012)
ODP3	128.1*	PA	P-11, Unit P	Tamburrino *et al.* (2012)
ODP4	129.1*	PA	—	Tamburrino *et al.* (2012)
ODP5	188.7*	PA	P-13, Unit I	Tamburrino *et al.* (2012)
ODP6	197.7*	PA	P-15, Unit I	Tamburrino *et al.* (2012)

PA: Pantelleria *Ages based on oxygen-isotope stratigraphy and eco-biostratigraphy (Tamburrino *et al.,* 2012).

Aegean marine tephra record

Several of the geochemical groupings display a potential Hellenic Arc signature. Within this region no single key tephrostratigraphic site exists or has been proposed, although over the last 30 years a large number of marine records in the region have been studied for visible tephra layer content, some correlated to proximal deposits and others not. These tephra layers have been summarised in Table 6.4 and follow the correlations proposed by Aksu *et al*. (2008). The geochemical data for these tephra come from a number of literature sources.

Table 6.4 – Tephra layers from the Aegean marine tephra record and references for the geochemical sources.

Tephra	***Age (ka)***	***Source***	***Proximal Correlation***	***References for geochemical data***
Y–2	18-21 ka BP	SA	Cape Riva	Keller *et al.* (1978); Vinci, (1985); Schwarz (2000); Wulf *et al* (2002); Aksu *et al.* (2008)
Santorini(?)	20–30 ka BP	SA	—	Vinci (1985)
Y–4	c. 30 ka BP	SA	—	Vinci (1985); Aksu *et al.* (2008)
Yali (Yali-C)	c.30 ka BP	YA	Yali 2	Federman & Carey (1980); Keller (1980); Vinci (1985); Aksu *et al.* (2008)
X–1	c.70 ka BP	AE	—	Keller *et al.* (1978); Vinci (1985); Aksu *et al.* (2008)
W–2	c.150 ka BP	SA	—	Vinci (1985)
W–3	c.161 ka BP	KO	Kos Plateau Tuff	Vinci (1985); C. Satow (*pers. comm*.)

SA: Santorini, YA: Yali, KO: Kos, AE: Aeolian Islands. Ages taken from Aksu *et al.* (2008).

Major elemental data (via EPMA) only is available for these layers and usually only mean values are given (Keller *et al.,* 1978; Keller, 1980; Federman & Carey, 1980; Vinci, 1985). Geochemical data were obtained by Aksu *et al.* (2008) using EPMA-WDS for major and minor elements and LAM-ICP-MS techniques for trace elements (trace element data are only available for Y–2 and Yali tephra layers) and are presented as mean values with standard deviations. Because of these constraints, comparison between the chemical dataset produced within this study and the Aegean marine tephra record outlined above should be viewed with caution.

For the W–3 tephra a full dataset of single–shard–specific values was made available by C. Satow (RESET database, Satow *et al., in prep.*) analysed following RESET protocols on the Jeol JXA8600 wavelength-dispersive electron microprobe at the Research Laboratory for Archaeology and the History of Art, University of Oxford. The same secondary standards were run as those employed within this study (see section 3.4.7).

NGRIP and MD04-2822

Geochemical groups 5 and 8 have elemental compositions which could indicate an Icelandic volcanic source. Despite the geographical distance between the palaeo-records studied within this study and Iceland (between 2,800 and 3,900 km) this possibility was not ruled out as recent tephrostratigraphic studies have detected

Icelandic ash in sites as far south as Slovenia, around 2,900 km from source (Lane *et al.,* 2011).

One of the most detailed tephrostratigraphic records currently available for Icelandic tephra during the LLG is the NGRIP record, which also has the advantage of providing confident age estimates for individual tephra layers via the GICC05 chronology (Andersen *et al.,* 2006; Svensson *et al.,* 2008). Tephrostratigraphic studies of the NGRIP record have focused on the intervals 26–31, 37–42 and 60–95 ka BP (Davies *et al.,* 2008; Davies *et al.,* 2010b and Abbott *et al.,* 2012; see Table 6.5). Shard specific major (and some trace) element data are available via EPMA-WDS and LA-ICP-MS techniques. Abbott *et al.* (2011) also presented LLG Icelandic tephrostratigraphic data from North Atlantic core MD04-2822 identifying two tephra layers dating to c. 70 ka BP. EPMA-WDS and LA-ICP-MS data for these are also available and included here for comparison.

Table 6.5 – Tephra layers from NGRIP and North Atlantic marine core MD04 used for geochemical comparison purposes within this study.

Tephra	***Age (1950 BP)***	***Source***	***Correlation***	***Reference***
NGRIP 1848.0–05 m	26,690 ± 390	H-V	FMAZ II	Davies *et al.* (2010b)
NGRIP 1855.7–8 m	27,150 ± 402	EVZ	—	Davies *et al.* (2010b)
NGRIP 1861.45–55 m	27,477 ± 410	Katla	—	Davies *et al.* (2010b)
NGRIP 1895.23–24 m	29,080 ± 456	Katla	—	Davies *et al.* (2010b)
NGRIP 1915.1–5 m	30,520 ± 504	EVZ	—	Davies *et al.* (2010b)
NGRIP 1915.5–63 m	30,520 ± 504	EVZ	—	Davies *et al.* (2010b)
NGRIP 2066.93–95 m	38,072 ± 723	GRI	FMAZ III	Davies *et al.* (2010b)
NGRIP 2441.14 m	61360 ± 1336	IRZ	—	Abbott *et al.* (2012)
NGRIP 2441.28 m	—	—	—	Abbott *et al.* (2012)
NGRIP 2454.9 m	63040 ± 1377	JM	—	Abbott *et al.* (2012)
NGRIP 2500.9 m	68,850 ± 1521	SFZ or EFZ	—	Abbott *et al.* (2012)
NGRIP 2548.35 m	74150 ± 1652	RE or V-B	—	Abbott *et al.* (2012)
NGRIP 2574.55 m	76110 ± 1701	Katla	—	Abbott *et al.* (2012)
NGRIP 2620.05 m	80100 ± 1800	GRI	—	Abbott *et al.* (2012)
NGRIP 2631.84 m	80980 ± 1822	Katla	—	Abbott *et al.* (2012)
NGRIP 2768.45 m	92310 ± 2102	SFZ or EFZ	—	Abbott *et al.* (2012)
MD04-2822 2327-2328 cm	c.70 ka BP*	—	—	Abbot *et al.* (2011)
MD04-2822 2359-2366 cm	c.74-76 ka BP*	—	—	Abbot *et al.* (2011)

H-V: Hekla-Vatnafjöll, EVZ: Eastern Volcanic Zone, SFZ: Southern Flank Zone, JM: Jan Mayen, GRI: Grímsvötn, RE: Reykjanes, V-B: Veidivötn-Bárdarbunga, IRZ: Icelandic Rift Zone. *Age based upon tuning.

Other geochemical data beside those outlined above have also been used for graphical comparison where required and this is highlighted within the text where relevant.

However, the majority of the data comparisons are with respect to the key data–sets outlined above.

6.1.3 Useful Geochemical discriminators

During this chapter various volcanic sources are compared to unknown data–sets, achieved via exploration of the data within GCDKit 3.0 Beta (Janoušek *et al.,* 2006). All data were explored using Harker variation diagrams and TAS plots (Le Bas *et al.,* 1986) and also via the use of other element biplots observed to be useful discriminators. For example for tephra layers of Italian origin Paterne *et al.* (1988), Wulf *et al.* (2004) and Bourne *et al.* (2010) all use an alkali ratio diagram (Na_2O+K_2O vs. $K2O/Na_2O$) to match tephra layers to source volcanoes in the Mediterranean region. Other major element biplots found to be useful for this volcanic region include CaO vs. MgO/TiO_2 (Calanchi and Dinelli, 2008) and FeO vs. CaO (Smith *et al.,* 2011). For the Hellenic Arc region K_2O vs. TiO_2 and SiO_2 vs. Al_2O plots have been found to allow discrimination (Wulf *et al.,* 2002).

When utilising trace elements the comparison of High Field Strength Elements (HFSEs; e.g. Zr, Nb, Th and U) should form compositional trends that remain uniform for the magma chamber whereas comparison of Light Rare Earth Elements (e.g. La, Sm) or Heavy Rare Earth Elements (HREEs; e.g. Eu, Y) to HFSEs may reflect more specific magmatic processes (Pearce & Peate, 1995). This is reflected in the common use of Th vs. Zr, Th vs. Nb and Th vs. Y, Th vs. La biplots (Smith *et al.,* 2011; Tamburrino *et al.,* 2012; Tomlinson *et al.,* 2012a,b).

6.2 Geochemical correlations

6.2.1 '*Orders*' of tephrocorrelations

The tephrostratigraphic framework is not fixed in time; indeed it is in a continual state of flux and re-evaluation. Existing tephra layers are being more robustly characterised or even reinterpreted and new tephra layers are being continually discovered. Indeed, as larger geographical regions are studied for cryptotephra, the number of tephra layers will only increase as in all probability will the overall complexity of the framework, at both local and regional geographical scales. The tephrocorrelations

made within this chapter should therefore be considered as reflecting the current best hypothesis that may require re-examination as new data becomes available. Because of this, the interpretations put forward here are presented in an order and manner that allow future researchers to easily disentangle sometimes complex correlation arguments and to consider alternative interpretations. This is not a trivial problem as very few volcanic eruptions have a truly unique geochemical signature, with the same volcanic centres often producing a similar geochemical product over different temporal scales. Therefore other factors such as stratigraphic or chronological information are often used to allow a tephrocorrelation to be achieved. As a key goal of this study is to test existing age-depth models using independent tephra age information, it is crucial to minimise the potential for circular argument and that associated caveats are made clear.

To help disentangle how interpretations are made in this investigation, three '*Orders*' of correlation have been defined for this thesis (see Fig. 6.2A) which will now be described in detail. Every correlation went through each step in succession and tephra layers from a site was interpreted in *Order* groups, for example all *First Order* tephrocorrelations were made first before continuing to *Second Order* ones and so on. This is to help ensure that as independent a tephrostratigraphy (and thus eventual tephrochronology) as possible is formed before other chronological information is used to allow a tephrocorrelations to be made.

Orders:

1. Tephrochronology rests on the correlation of tephra layers by demonstrating geochemical affinity between them, though other physical characteristics may also be used to help confirm correlation. Where a unique geochemical match is possible between two units a first order for a correlation is possible.
2. Some tephrocorrelations may require tephrostratigraphic or other types of stratigraphic information (e.g. simple principles of superposition *not* chronological information). Previously assigned *First Order* tephrocorrelations form the basis of the tephrostratigraphic framework.
3. Where multiple tephra layers exist with identical geochemical compositions chronological information may be required to allow a correlation. Where this is required two age-depth models should always be considered (see Fig. 6.2B) first the pre-existing age-depth model/s described in chapter 4 for each site

and also a *P_Sequence* age-depth model produced solely upon independent age information (e.g. radiocarbon ages) with the extraction of any previously imported tephra ages. It is important for this second *P_Sequence* model to be produced as it dates each tephra independently of former biostratigraphic tie-points and imported tephra ages (important in the case of Tenaghi Philippon and Lesvos) which would otherwise cause confirmation bias. Using just the original or the new *P_Sequence* model would be a biased test against either possibility. The ages for all the tephra layers described in chapter 5 are presented in Table 6.6 with both age estimates defined. OxCal model parameters for each site are presented in Appendix III. This should also be useful to future researchers for revaluation of the tephrocorrelations presented here. The final age-depth model for each site will be produced in Chapter 7; this is the step where tephrochronological information is incorporated into age-depth models. Although these orders could be deemed too simplistic they ensure a consistent, systemic approach and should help avoid potential confusion.

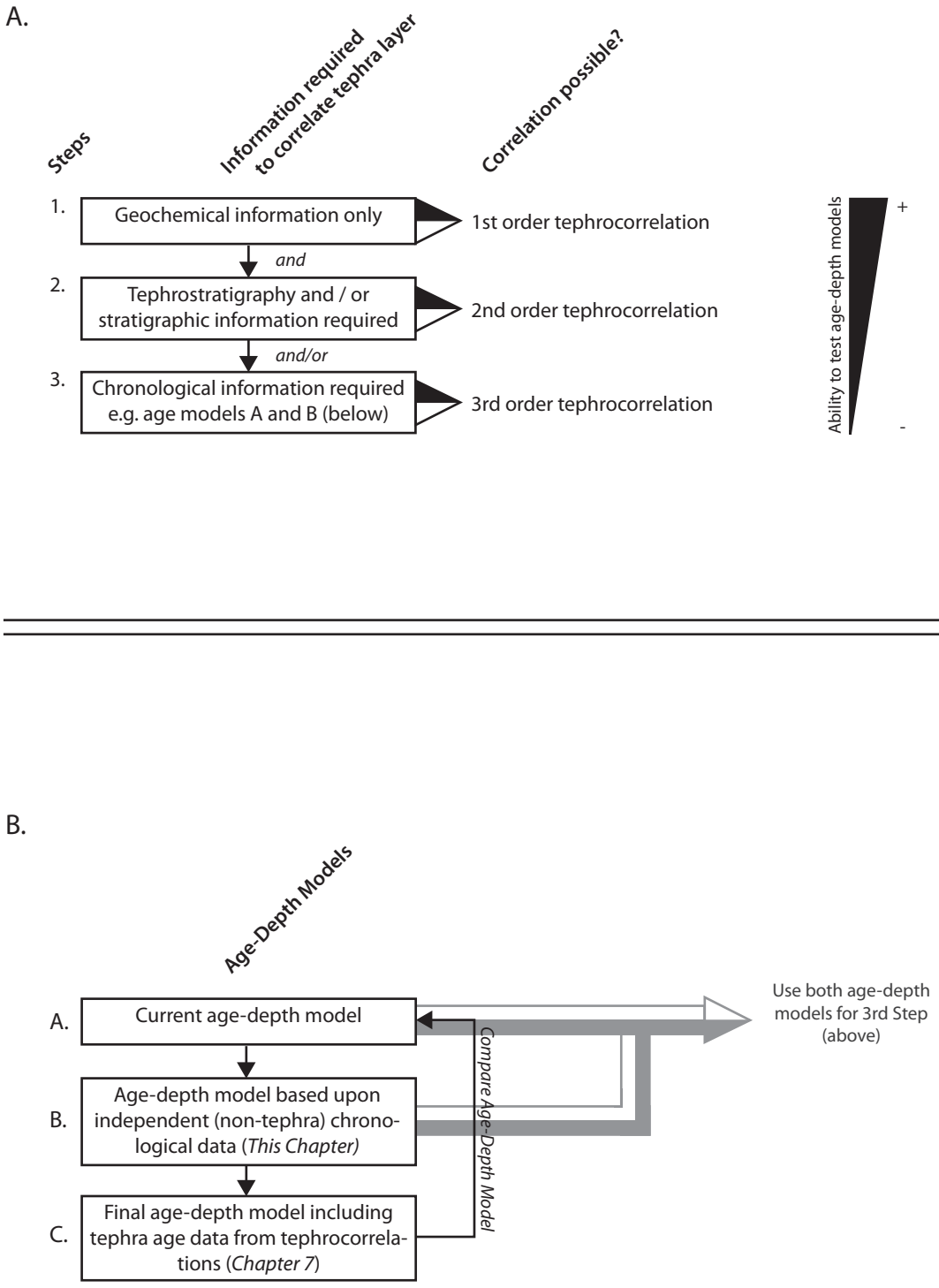

Figure 6.2 – (**A.**) Decision flowchart outlining type of correlation. (**B.**) Schematic of age model types used in this study.

Table 6.6 – Ages for each tephra layer identified within this study. Model B ages were determined using the OxCal *Date* function whereas original age models are based upon interpolation. Ages in Italics indicate ages where tephra ages have been imported.

Tephra layer code	Full depth interval (m)	Modelled Age (*Original Study/s*) **A**	Modelled Age with current independent Age Information **B**
FIM-2042	20.41-20.43	38450-38730	30730-33110
FIM-2205	22.01-22.06	65580-68130	36610-40730
KOP-1652	16.50-16.60	21830 (22600)	18580-21200
KOP-1759	17.50-17.58	22960 (23770)	19530-21830
KOP-2317	23.10-23.35	25140 (35095)	25570-28400
KOP-2637	26.30-26.61	27770 (46290)	28700-30270
KOP-2698	26.88-26.99	28020 (48430)	28880-30560
KOP-2763	27.62-27.73	28300 (50710)	29110-30880
KOP-2910	29.00-29.20	28900 (55850)	29600-31600
KOP-3119	30.00-31.19	29400 (61660)	30380-32530
KOP-3347	33.28-33.73	31770 (66770)	31210-33520
KOP-3900	39.00-39.40	35630 (77330)	33480-35780
KOP-4059	40.50-40.59	36570 (79640)	34170-36450
KOP-4815	47.90-49.09	41320 (99080)	*N/A*
KOP-5678	56.78-56.79	48740 (122100)	*N/A*
TP-707	7.03-7.14	17520	16980-19150
TP-726	7.22-7.33	20010	19520-20500
TP 7.61[1]	7.43-7.61	*21980*	20510-22470
TP-890	8.88-8.92	28100	27120-28480
TP-896	8.95-9.00	28250	27370-28670
TP-923	9.20-9.26	28910	28370-29230
TP-938	9.34-9.43	29250	28710-29530
TP-951	9.44-9.56	29520	28960-29800
TP-970	9.68-~9.76	29910	29370-30150
TP-978	~9.76-9.80	30070	29550-30270
TP 12.87[1]	12.50-12.87	*39280*	38360-40510
TP-1325	13.24-13.27	40450	39570-41090
TP-1328	13.27-13.30	40550	39670-41140
TP-1334	13.31-13.35	40700	39830-41250
TP-1354	13.50-13.55	41120	40390-41650
TP-1392	13.90-13.93	42040	41380-42480

TP-1450	14.46-14.54	43900	42720-44110

ML00

ML00-207	2.02-2.18	27990	N/A
ML-2[2]	5.50-5.63	*38600-42110*	40870-43370
ML00-583	5.80-5.87	40910	41070-43370
ML00-716	7.04-7.16	44330	42180-43660
ML00-785	7.73-8.01	45030	42380-44130
ML00-815	8.11-8.19	45350	42410-44470
ML00-845	8.27-8.64	45460	42420-44860
ML00-880	8.70-8.85	45550	N/A

ML01

ML-1[2]	1.80-1.82	22270-23020	21760-23530
ML-2	7.44-7.60	–	35670-41450
ML-3[2]	10.33-10.50	46000 ± 5690	>41601
ML-4[2]	11.89-12.00	46800 ± 5690	N/A
ML-5[2]	24.21-24.25	53600 ± 5690	N/A
ML-6[2]	28.41-28.42	–	N/A

6.2.2 *First Order* tephrocorrelations

Group 4

ML-5 is the only tephra assigned to Group 4 and has a very distinct Pantelleria geochemistry. ML-5 has previously been correlated to the Green Tuff (Y-6) by Margari *et al.* (2007) but was reinterpreted by Vogel *et al.* (2010) to correlate to the P-11 tephra. Here the new major, minor and trace elements from ML-5 (by-passing the critiques made of the Margari *et al.,* 2007 analytical approach; see section 4.2.6) have been compared to:

1. The two Lake Ohrid tephra layers with Pantelleria affinities, OT0702-7 and OT0702-10, correlated to the Green Tuff and P-11 respectively (Vogel *et al.,* 2010).
2. The recently available Sicily Channel ODP Leg 160 Site 963A which contains a detailed medial-distal Pantelleria tephrostratigraphic record from c.40-200 ka BP (ODP1-ODP6; Tamburrino *et al.,* 2012). From this record Tamburrino *et al.* (2012) correlated ODP1 to the Green Tuff (Y-6) and ODP3 to the P-11.
3. The only Pantelleria tephra found in LGdM (TM-22).
4. Geochemical data from the Green Tuff proximal deposit (RESET database, Tomlinson *et al., in prep.*).

Figures 6.3 and 6.4 show major element and trace elements plots of the data above. Trace element biplots follow those utilised by Tamburrino *et al.* (2012). It is clear that ML-5 can be clearly separated from the Green Tuff (and distal Green Tuff correlatives) on FeO and Ba values and shows close geochemical affinity to OT0702-10 and ODP3 (see Zr/Ba, FeO/Al_2O_3 and SiO_2/Al_2O_3 plots).

On this basis ML-5 most likely correlates to ODP3 and OT0702-10, both of which have been correlated to the P-11 marine layer via EDS data from Paterne *et al.* (2008; also shown in Fig. 6.3). The Unit P proximal deposit has been dated directly via $^{40}Ar/^{39}Ar$ to around c.133 ka BP (Mahood & Hildreth, 1986; see Table 6.7).

Table 6.7 – Direct ages defined for the P-11 deposit.

Deposit	***Dating Type***	***Age***	***Reference***
P-11	K/Ar	133,000 ± 5000	Mahood & Hildreth (1986)
P-11	K/Ar	134,000 ± 6000	Mahood & Hildreth (1986)
P-11	K/Ar	132,000 ± 6000	Mahood & Hildreth (1986)
P-11	K/Ar	133,100 ± 1500	Mahood & Hildreth (1986)
		133,080 ± 2720	*Oxcal Age Combine*

Underlying ML-5 in the ML-01 tephrostratigraphy is ML-6 which was interpreted as an unknown tephra from the Hellenic Arc by Margari *et al.* (2007). Margari *et al.* (2007) did consider a correlation between ML-6 and the Kos Plateau Tuff (KPT) but ruled this out on the basis that ML-6 was too young for the c.160 ka BP (Smith *et al.,* 1996) eruption. The new correlation of ML-5 to a much older eruption however suggests ML-6 should be reconsidered and also comparisons can be made on newly available datasets. Figure 6.5 shows several biplots which best separates similar Icelandic, Hellenic and Anatolian compositions. On the basis of these, ML-6 can be separated from known Anatolian compositions on FeO/CaO plots and best correlates to the W3 marine tephra which has been correlated to the KPT eruption (Vinci, 1985, C. Satow, *pers. comm.*). An average geochemical composition for the KPT proximal deposit is available (Federman & Carey, 1980) and shows some compositional overlap but the averaged nature of these data means it should be treated with some caution. The KPT was probably the largest eruption during the Quaternary in the Eastern Mediterranean region (Allen, 2001; Pe-Piper *et al.,* 2005).

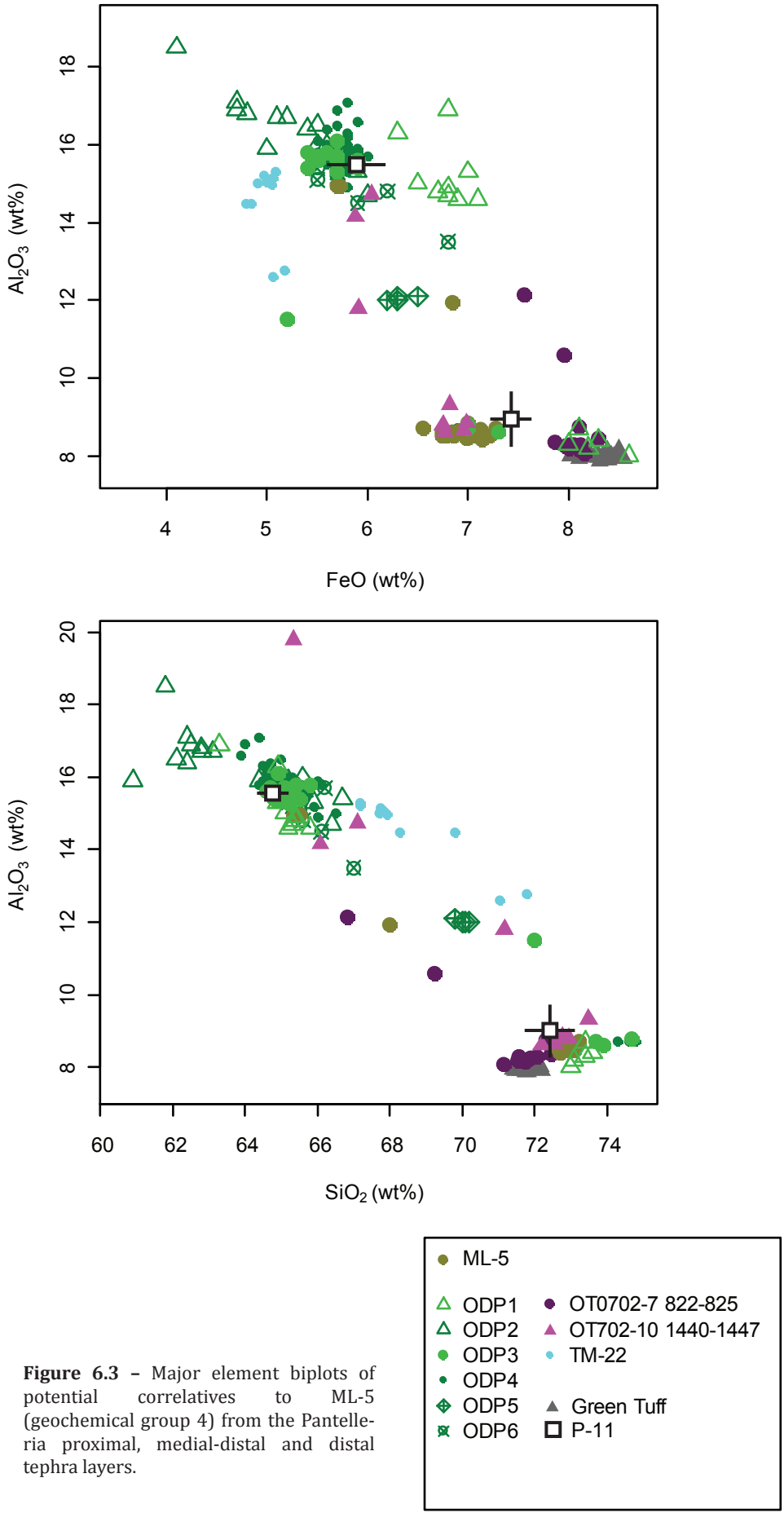

Figure 6.3 – Major element biplots of potential correlatives to ML-5 (geochemical group 4) from the Pantelleria proximal, medial-distal and distal tephra layers.

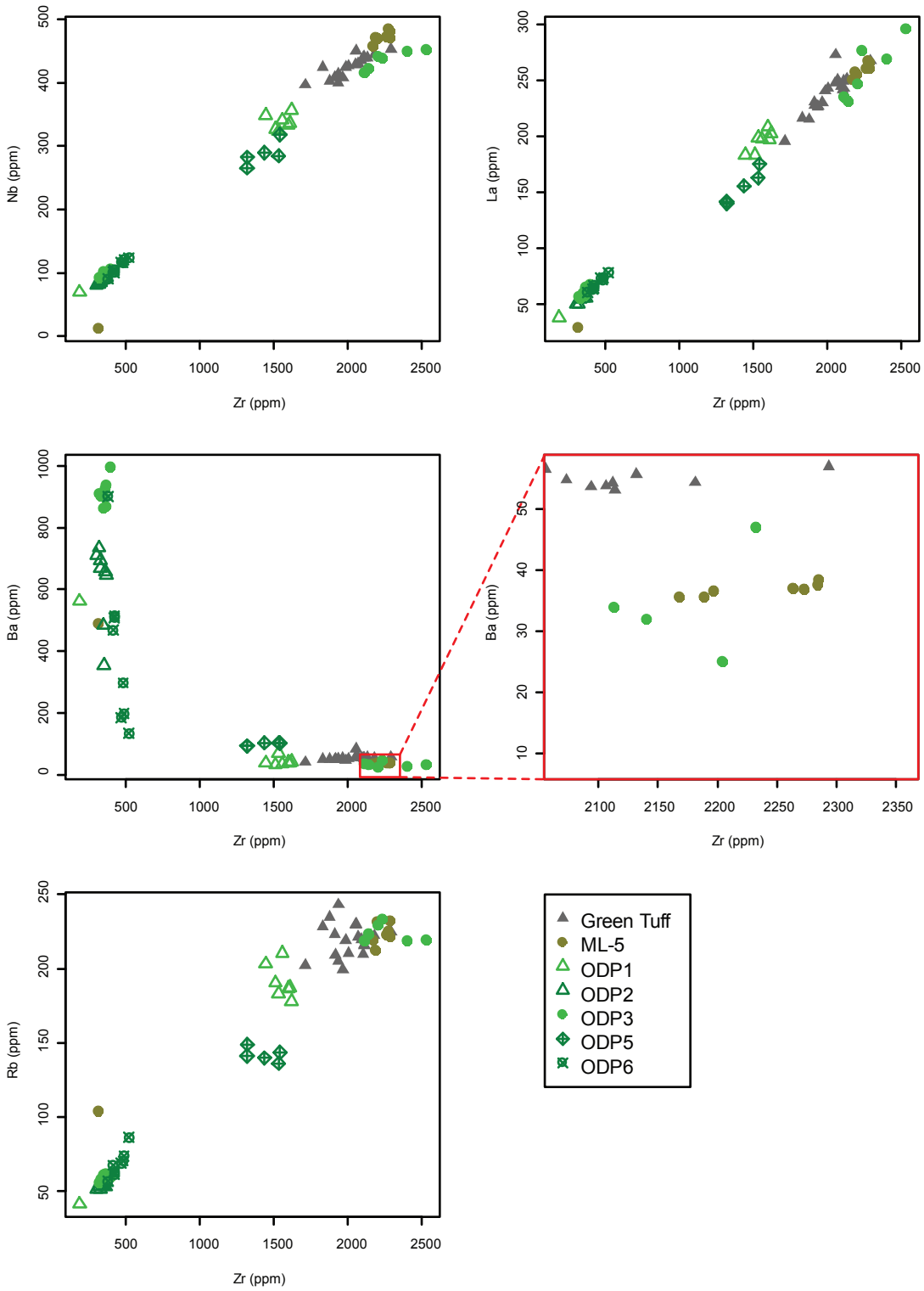

Figure 6.4 – Trace element biplots of potential correlatives to ML-5 (geochemical group 4) from the Pantelleria proximal, medial-distal and distal tephra layers.

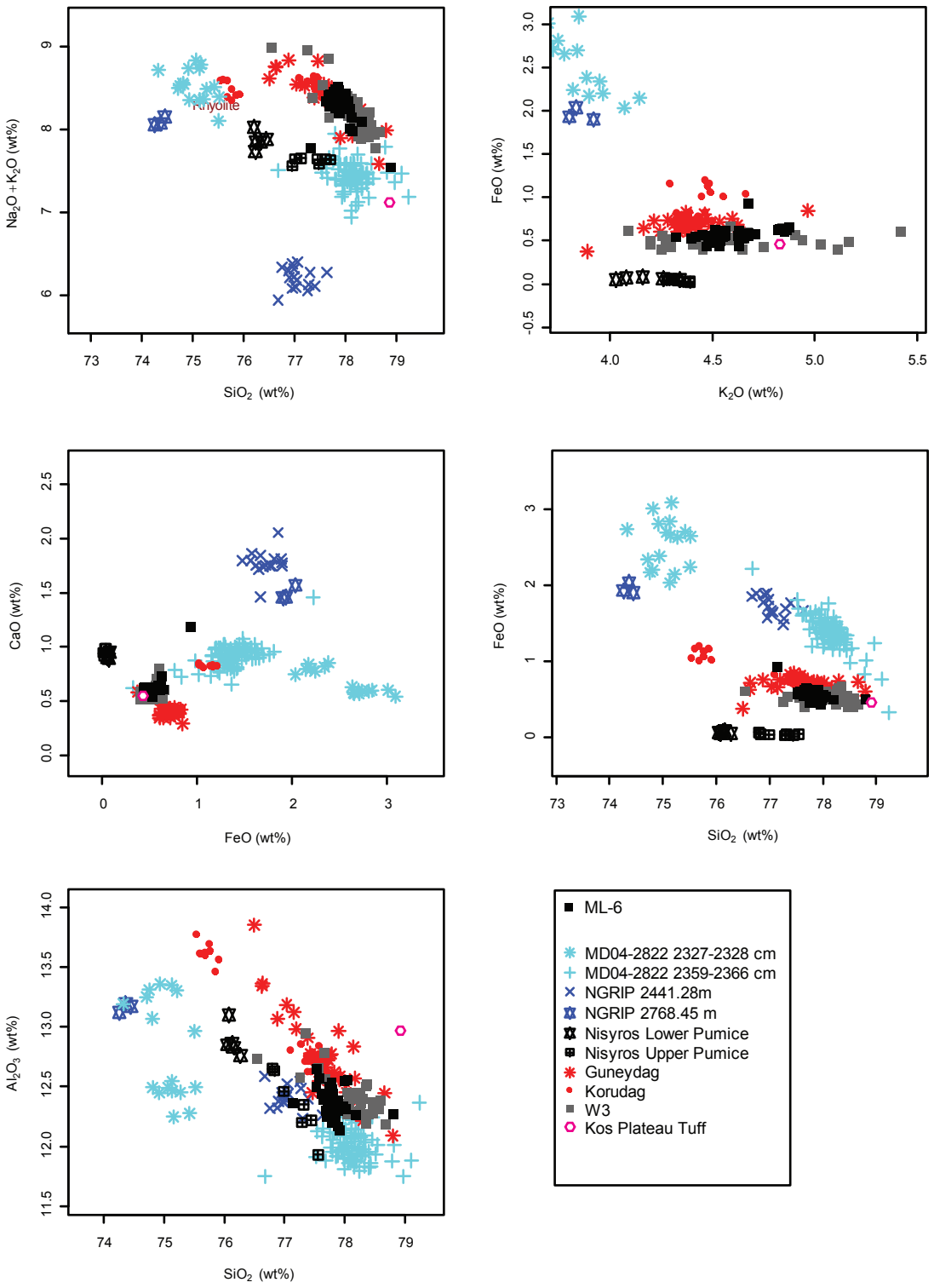

Figure 6.5 – Major element biplots of potential correlatives to ML-6 (Margari *et al.,* 2007).

The alkaline tephra (Groups 1, 3 and 2) are summarised here together and against the proximal and LGdM datasets in Figures 6.6, 6.7, 6.8, 6.9, 6.10 and 6.11.

Group 1

TP-923, TP-938, TP-951 and TP-970 were assigned to Group 1 and represent four cryptotephra peaks identified over a 60 cm vertical interval within the Tenaghi Philippon sequence. Group 1 could source from Campi Flegrei, Somma-Vesuvius or Ischia and extensive graphical comparisons were made to eruptions from these volcanic sources. On the basis of various major and trace element biplots (see Fig. 6.6 to 6.13) the TP-923 — TP-970 geochemical range overlies that of TM-15 on all plots. The Neapolitan Yellow Tuff, VRb, TM-8 and TM-9 can all be discarded on the basis of different MgO and TiO_2 values. TP-923 — TP-970 also overlies the rarer Upper Flow component of the CI, although the lack of the other CI components and distinctive Th vs Ba and Th vs Nb trends rule out the CI eruption as a potential correlative.

TP-923, TP-938, TP-951 and TP-970 all represent distinct cryptotephra peaks (see Fig. 5.9) suggesting that distinct but closely–spaced eruption events may be recorded in the Tenaghi Philippon sequence. The only geochemical match for these tephra layers is TM-15 within LGdM. This may indicate reworking of shards of this tephra into either younger or older sediments in the Tenaghi Philippon sequence. The largest cryptotephra peak between TP-923 — TP-970 is the lowest lying TP-970 (2059 shards per dry gram). A rhyolitic cryptotephra directly underlies TP-970, and this rhyolitic chemistry is also detected in TP-951 (see Table 5.3), suggesting upward reworking into younger sediment to be the most likely explanation.

On this basis TP-923, TP-938, TP-951 and TP-970 are correlated to TM-15 (see Figs. 5.12 and 5.13). This tephra has an LGdM varve age of 27,260 ± 1360 which is comparable to the 28-30 ka BP time frame suggested by both the Müller *et al.* (2011) age model and the independent non-tephra age model carried out within this study (see Table 6.6). TM-15 has been correlated to the Y-3 eruption of Keller *et al.* (1978) thought to originate from the CF region. Zanchetta *et al.* (2008) have suggested the Y-3 is best represented proximally by the SMP1-e and VRa deposits, the latter having a $^{40}Ar/^{39}Ar$ age determination of 30,100-30,500 ka BP. Geochemical data has recently become available for the VRa deposit (Tomlinson *et al.,* 2012a) which casts doubt on the correlation between VRa and TM-15. This can be seen in Figs. 6.12 and 6.13 with the VRa displaying a bi-modal population which is not a precise match for the TM-15

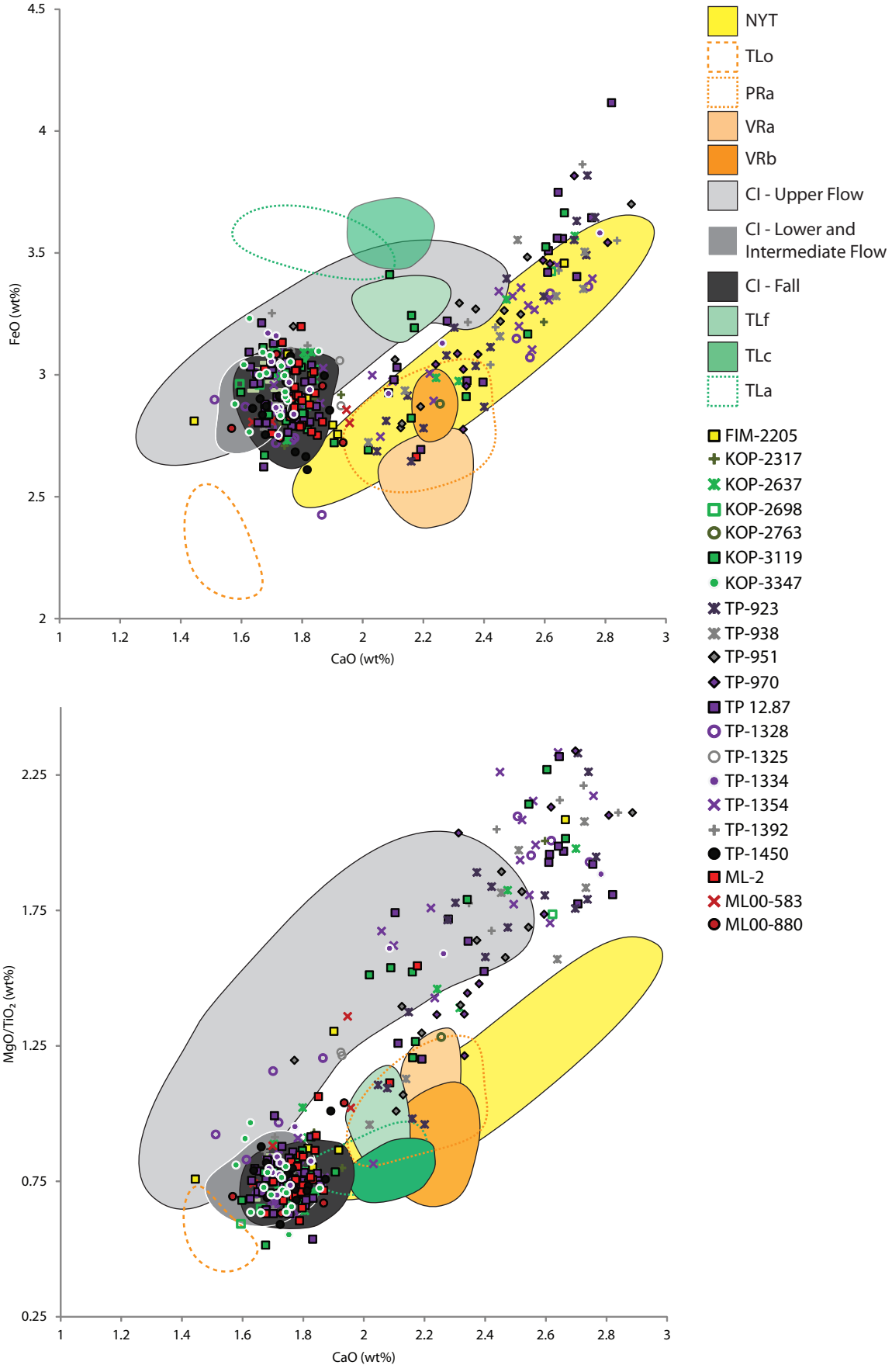

Figure 6.6 – Major element biplots of the alkaline tephra found in this study compared against the Campi Flegrei proximal tephrostratigraphic record.

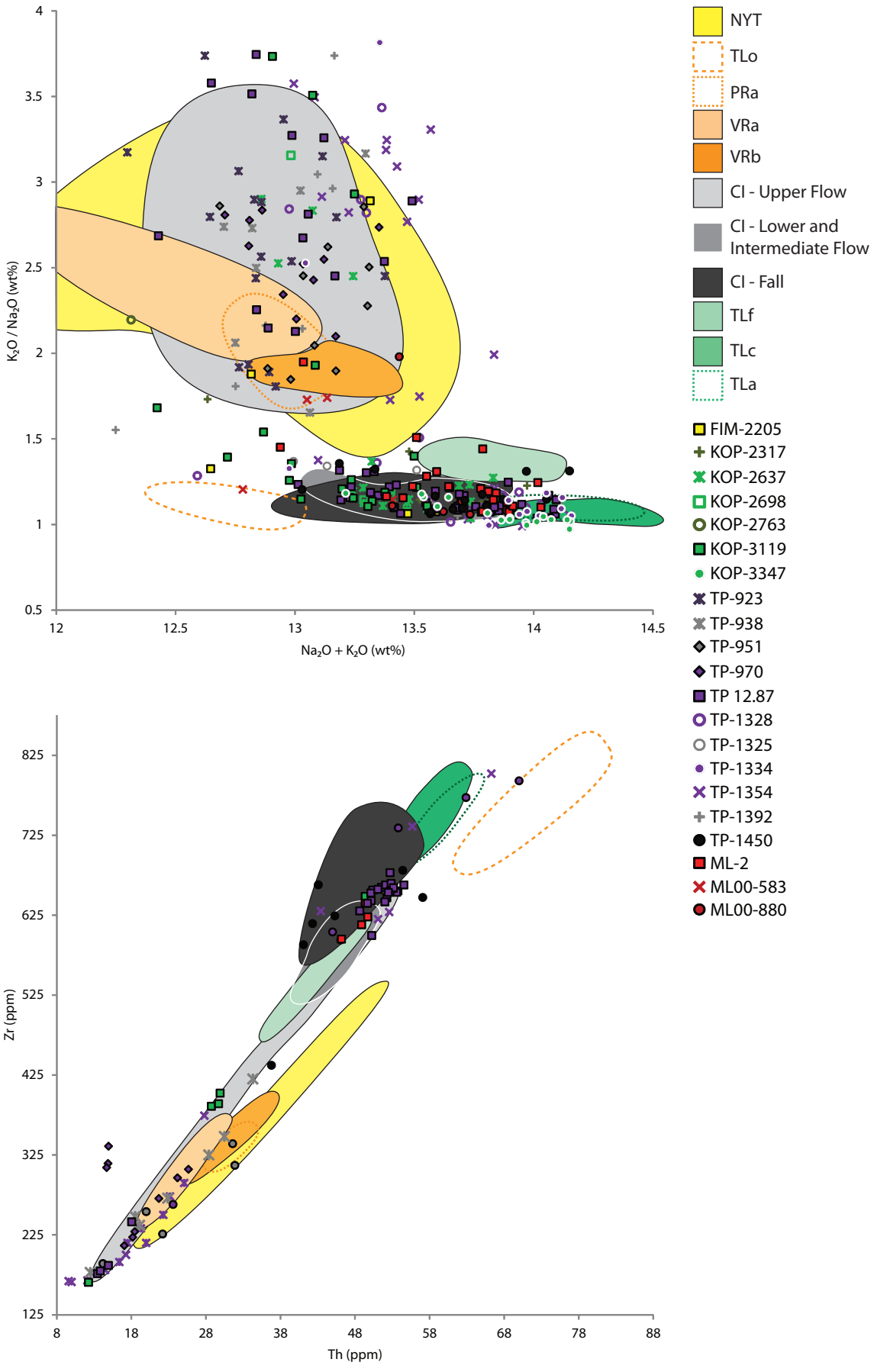

Figure 6.7 – Major and trace element biplots of the alkaline tephra found in this study compared against the Campi Flegrei proximal tephrostratigraphic record.

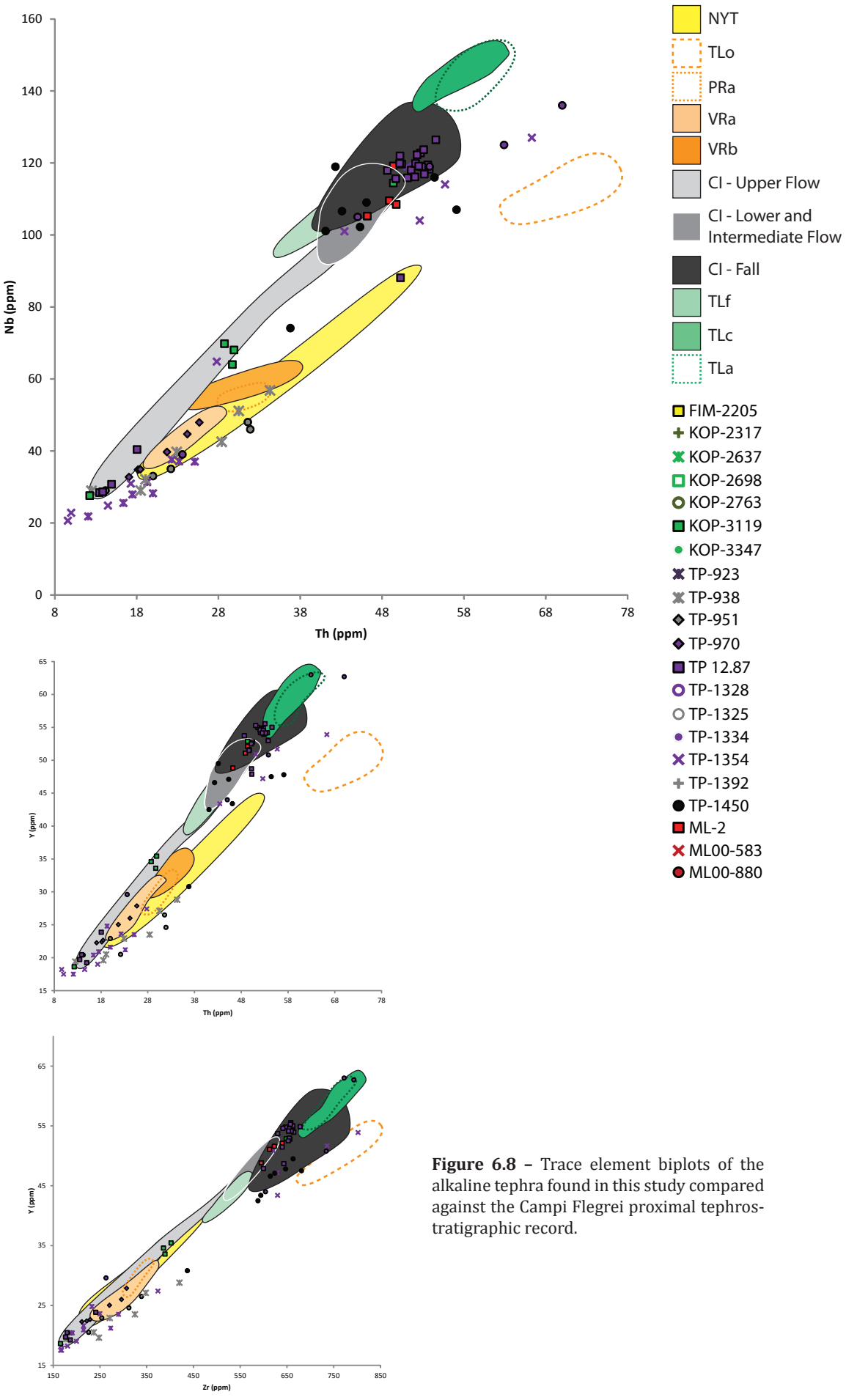

Figure 6.8 – Trace element biplots of the alkaline tephra found in this study compared against the Campi Flegrei proximal tephrostratigraphic record.

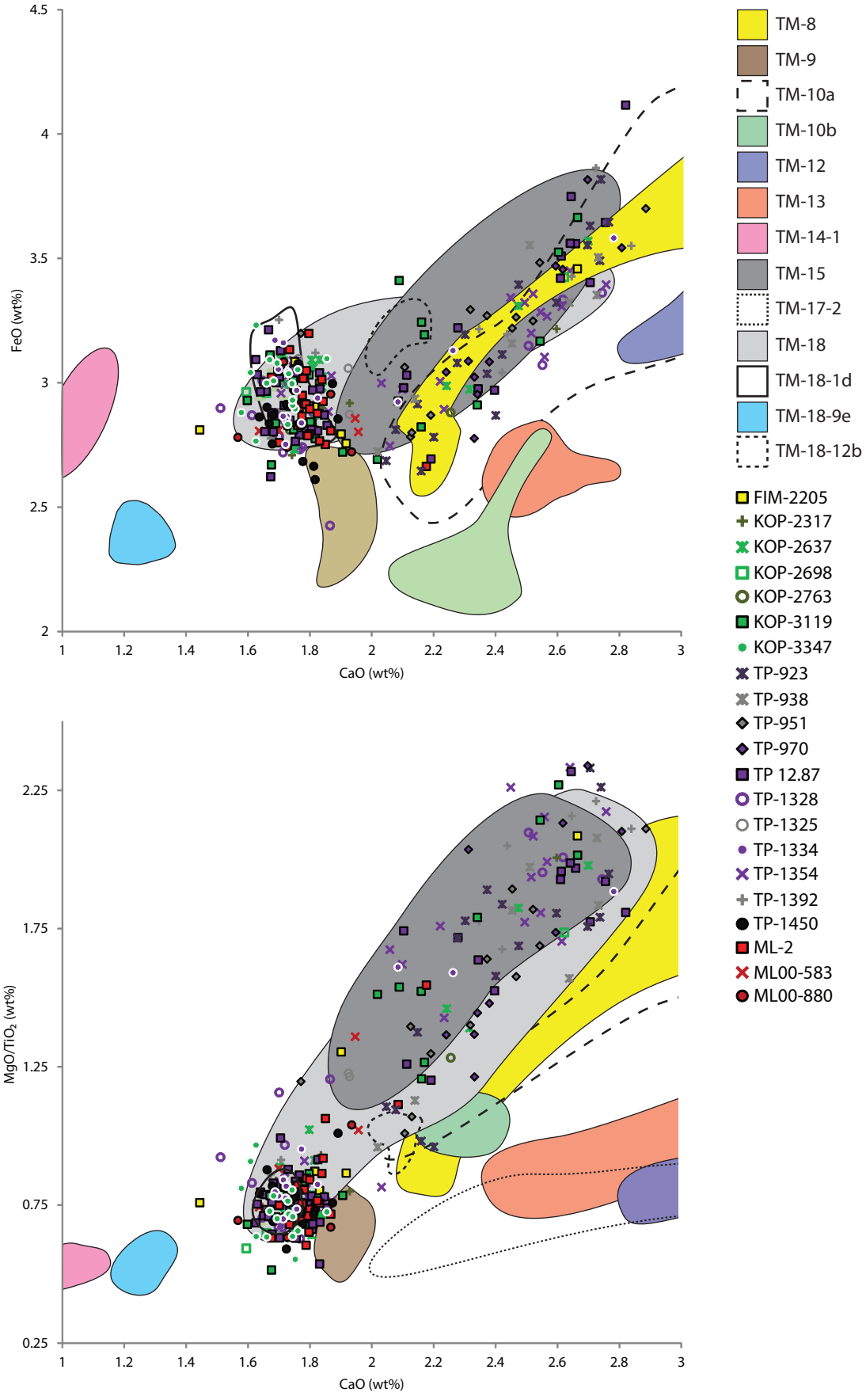

Figure 6.9 – Major element biplots of the alkaline tephra found in this study compared against LGdM tephra layers.

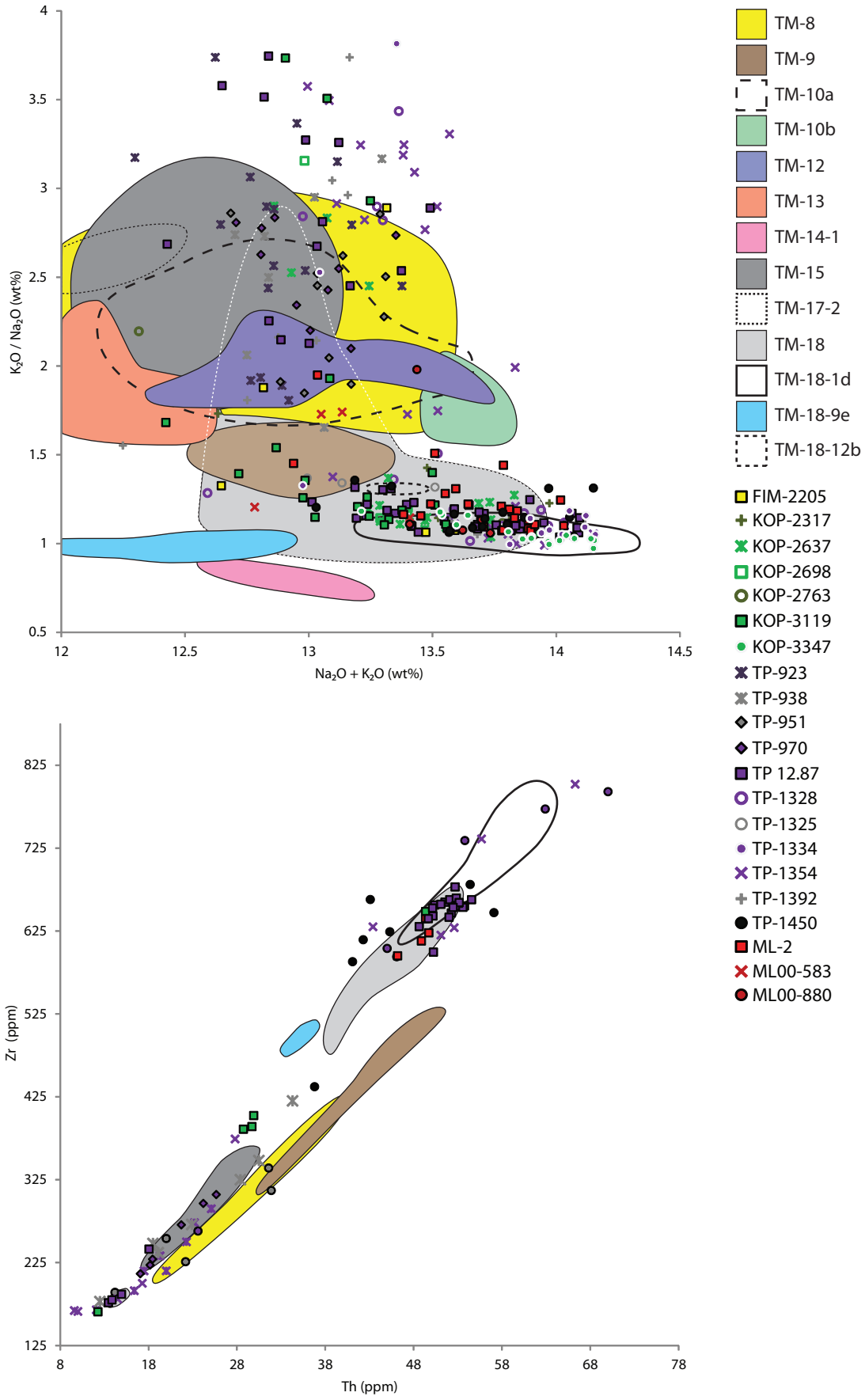

Figure 6.10 – Major and trace element biplots of the alkaline tephra found in this study compared against LGdM tephra layers.

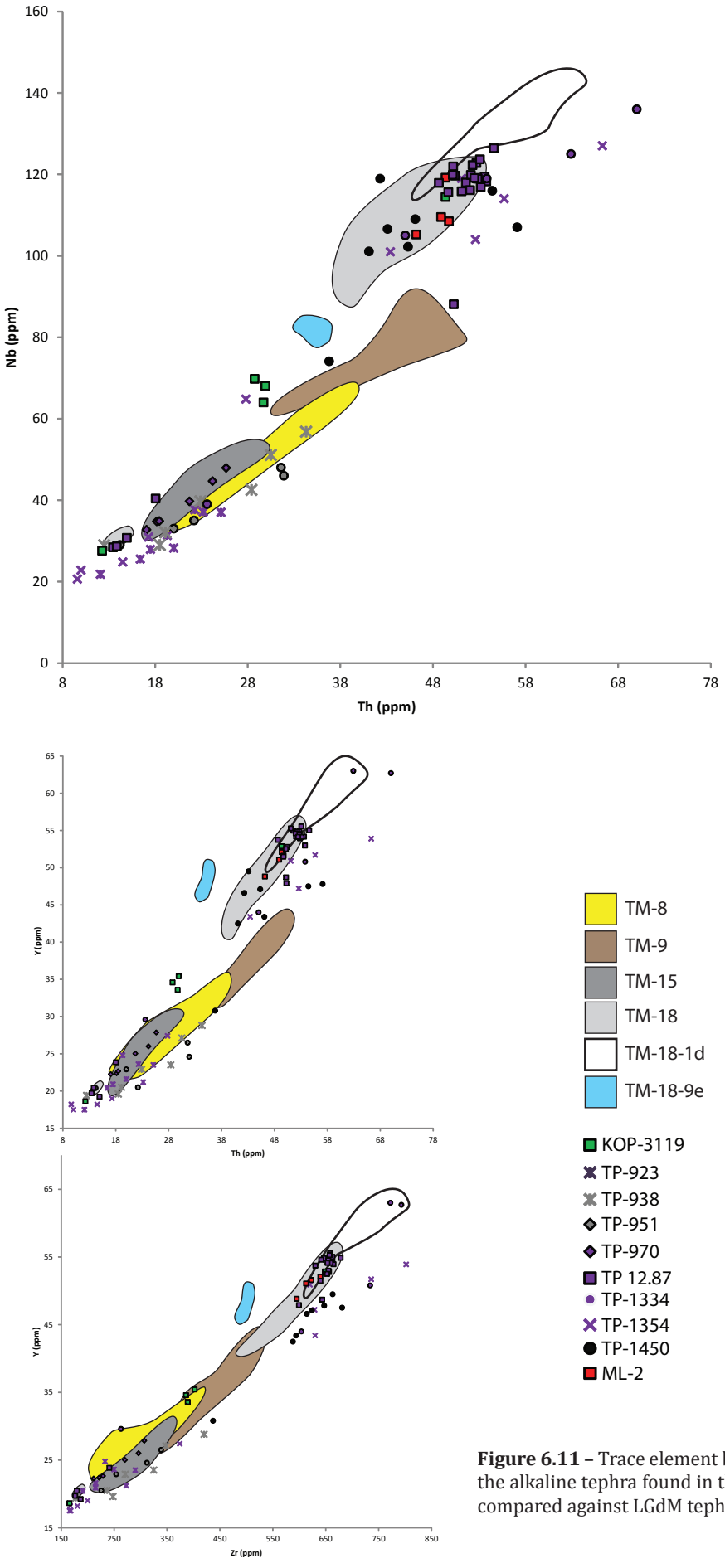

Figure 6.11 – Trace element biplots of the alkaline tephra found in this study compared against LGdM tephra layers.

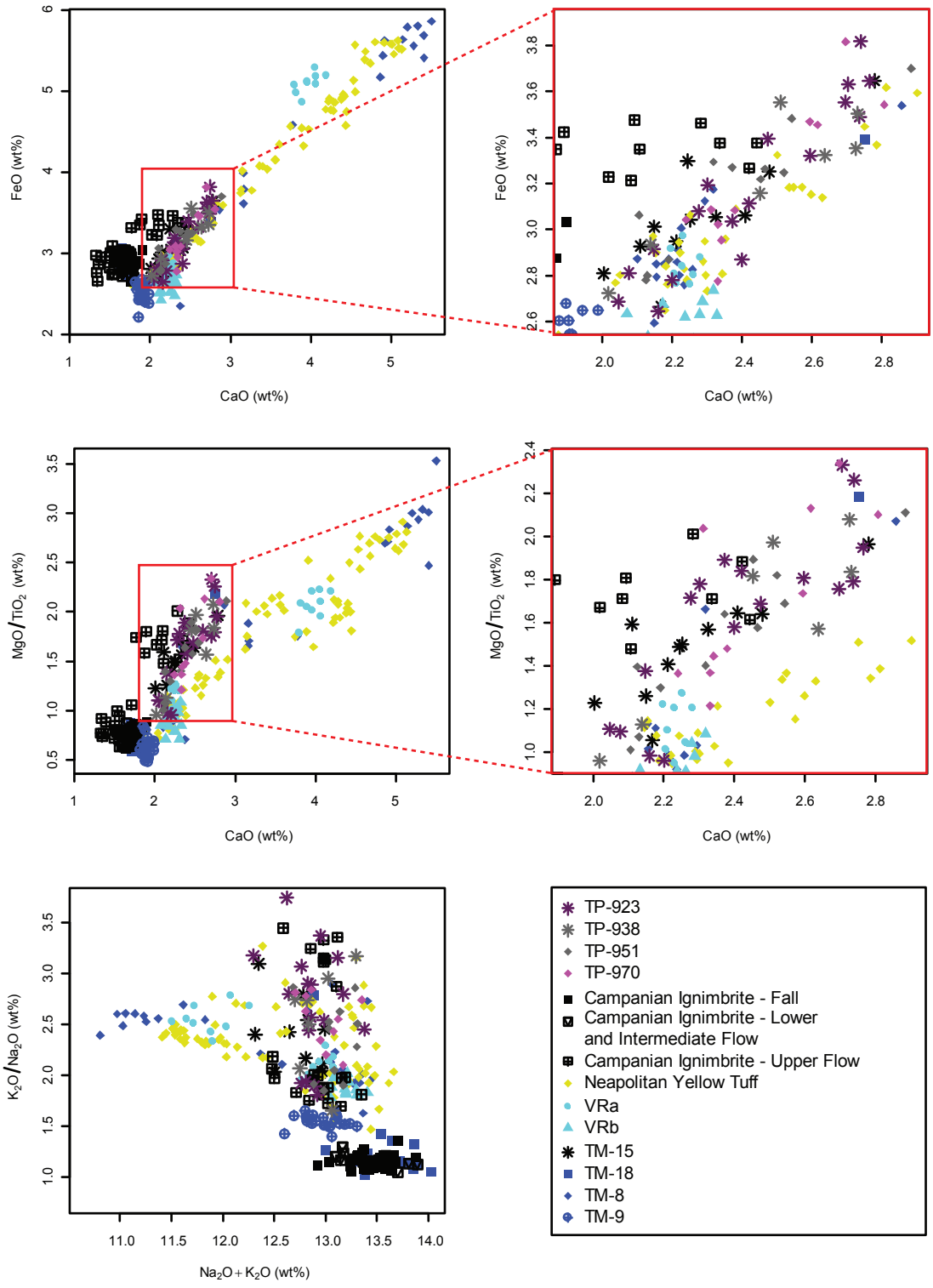

Figure 6.12 – Major element biplots of potential correlatives to geochemical group 1 tephra from the CF proximal and medial-distal LGdM record.

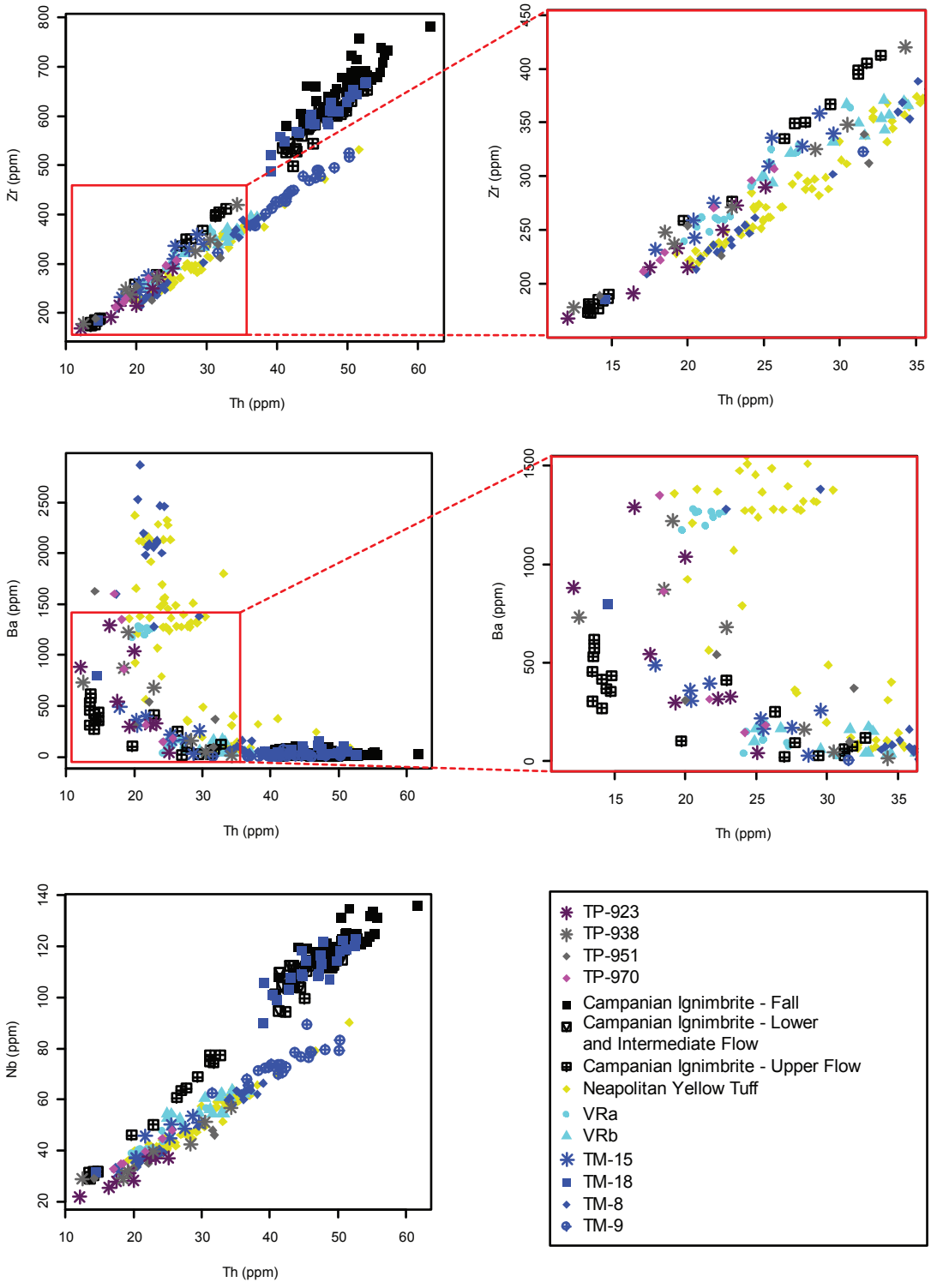

Figure 6.13 – Trace element biplots of potential correlatives to geochemical group 1 tephra from the CF proximal and medial-distal LGdM record.

compositional range, and hence this direct age cannot be confidently imported for TP-923 — TP-970. The identification of TM-15 within Tenaghi Philippon is the furthest easterly discovery of this tephra layer.

6.2.3 *Second Order* tephrocorrelations

Group 3

TP-1334, TP-1450, KOP-3347 and ML00-880 were all assigned to group 3 and are indistinguishable on major element biplots (see Fig. 6.14). These four tephra layers display phonolitic-trachytic compositions that suggest a CF source (see Figs. 6.6 to 6.8). Comparisons to the CF proximal (Tomlinson *et al.,* 2012a) and LGdM record show on major elements that all four tephra layers match the data for TM-18-1d and the CI Flow, but not the other CI components, ruling this out as a potential correlative (see Fig. 6.14).

TP-1334 and TP-1450 have trace elements available and can be differentiated from each other (e.g. Zr vs U/Th) and from the CI Flow component (e.g. Zr vs Y; Th vs U; Fig. 6.14). Using trace elements, TP-1334 clearly shows consistency with TM-18-1d whereas TP-1450 can be ruled out as a potential correlative to this tephra with no candidate from the reference dataset being apparent. Thus TP-1334 is likely to correlate to TM-18-1d on this basis.

TM-18-1d directly underlies TM-18 (correlated to the CI) in the LGdM record, being c.590 varve yrs older (Wulf *et al.,* 2006). The Tenaghi Philippon tephrostratigraphy shows that there is a very similar tephra to TM-18-1d (TP-1450), which underlies it, is indistinguishable on major element composition, but is separable on certain trace elements. As KOP-3347 and ML00-880 only have major elemental data available it is not possible without other stratigraphical information to correlate these tephra to either TM-18-1d or TP-1450. However these tephra must lie below the CI, based upon the tephrostratigraphic relationships outlined above.

Group 2

Group 2 contains tephra from all four sites which contain tephra content (Fimon, Kopais, Tenaghi Philippon and Lesvos) and has a composition which is highly suggestive of a CF source (see Figs 6.6 to 6.8). Based upon extensive graphical

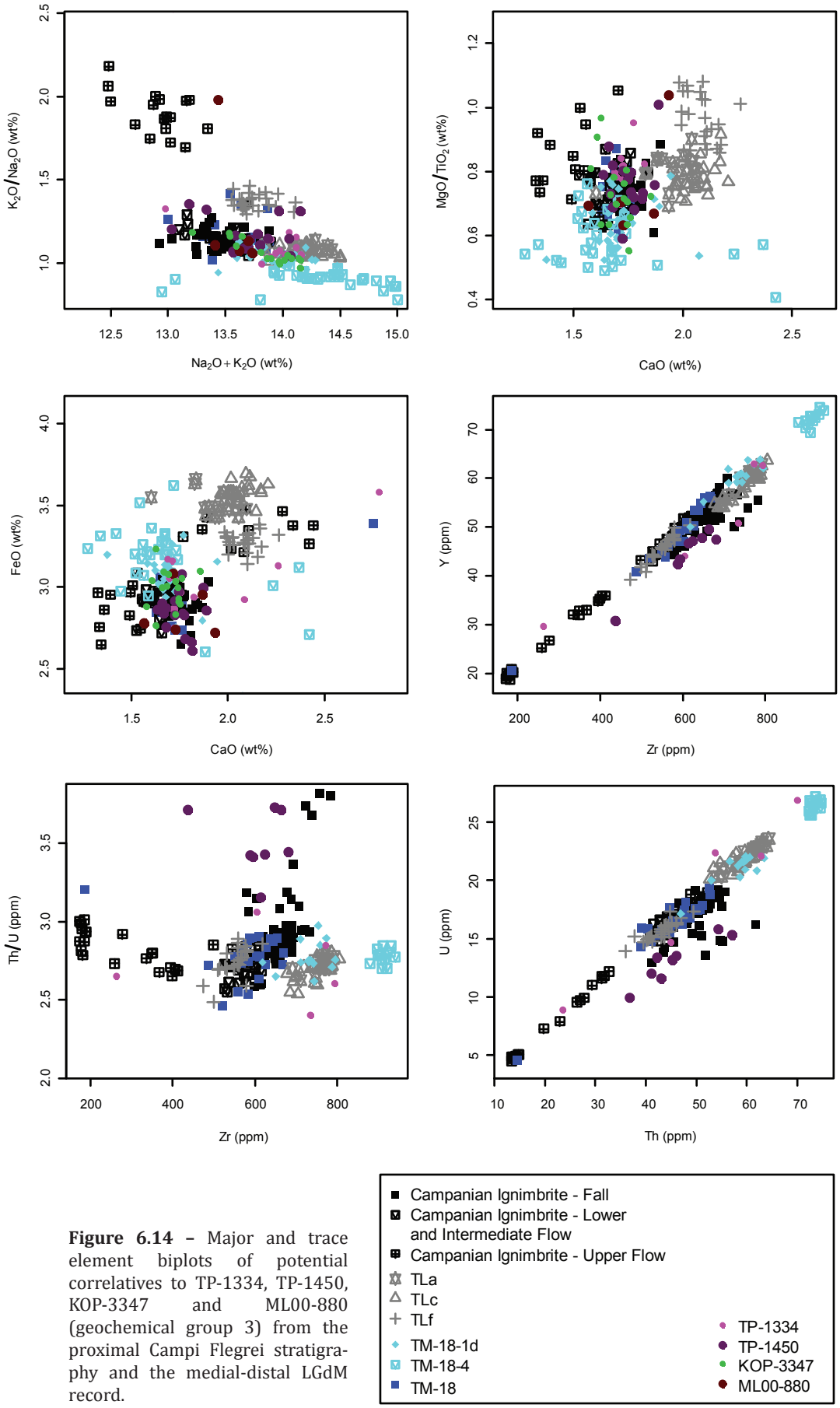

Figure 6.14 – Major and trace element biplots of potential correlatives to TP-1334, TP-1450, KOP-3347 and ML00-880 (geochemical group 3) from the proximal Campi Flegrei stratigraphy and the medial-distal LGdM record.

comparisons to both CF proximal deposits and the medial-distal LGdM tephra layers show that TM-18 and the CI form the most robust geochemical match for these tephra. The K_2O/Na_2O and MgO/TiO_2 ratios demonstrate that Group 2 tephra layers span the full geochemical range of TM-18 and also the CI correlating to its three main eruption phases: the fall, lower and intermediate and the upper flow (Tomlinson *et al.,* 2012a). The distinct bimodal geochemical signature for the CI is very distinctive and no other tephra in the LGdM sequence between TM-8 and TM-22 share it (Figs. 6.9 to 6.11) although they may cover smaller component parts of it on major elements (e.g. TM-18-1d and TM-15). Group 2 layers will now be discussed on a site by site basis. TM-18 has been correlated with the CI (Wulf *et al.,* 2004) an eruption from the Campi Flegrei dated by $^{40}Ar/^{39}Ar$ dating to 39,280 ± 110 BP (De Vivo *et al.,* 2001).

Fimon

Only one tephra in Fimon has geochemical data available, FIM-2205, which fits into group 2 and is thus correlated to TM-18 and the CI. The Pini *et al.* (2010) Fimon PD age model places FIM-2205 between 65-68 ka BP (see Table 6.6) however no tephra layer recorded within the LGdM record during this timeframe provide a more robust geochemical fit than the CI (see Fig. 6.15). Alternatively the Fimon age-depth model based upon independent age information alone (radiocarbon and OSL) suggest an age range of 36610-40730 BP which would be consistent with the $^{40}Ar/^{39}Ar$ age of the CI (De Vivo *et al.* 2001).

Lesvos

Within Lesvos the 13 cm thick visible layer, ML-2, fits the TM-18 and the CI on both major and trace element compositions (see Fig. 6.16). This confirms the correlation of ML-2 to the CI made by Margari *et al.* (2007) but increases its robustness via the application of trace elements and comparison to the recently available proximal CI dataset (Tomlinson *et al.,* 2012a). The Lesvos age-depth model based upon independent age information alone (radiocarbon) suggest an age range of 40865-43372 (ML-00) and 39065-39505 (ML-01) for ML-2 which is consistent with the $^{40}Ar/^{39}Ar$ age of the CI (De Vivo *et al.,* 2001). This correlation is also consistent with the correlation of the underlying ML00-880 tephra layer with TM-18-1d or TP-1450, both of which must underlie the CI. The position of ML00-880 3.17m below the ML-2 in the Lesvos sequence suggests a correlation to TP-1450 is more likely than one to TM-18-1d which is only 590 LGdM varve yrs older than the CI.

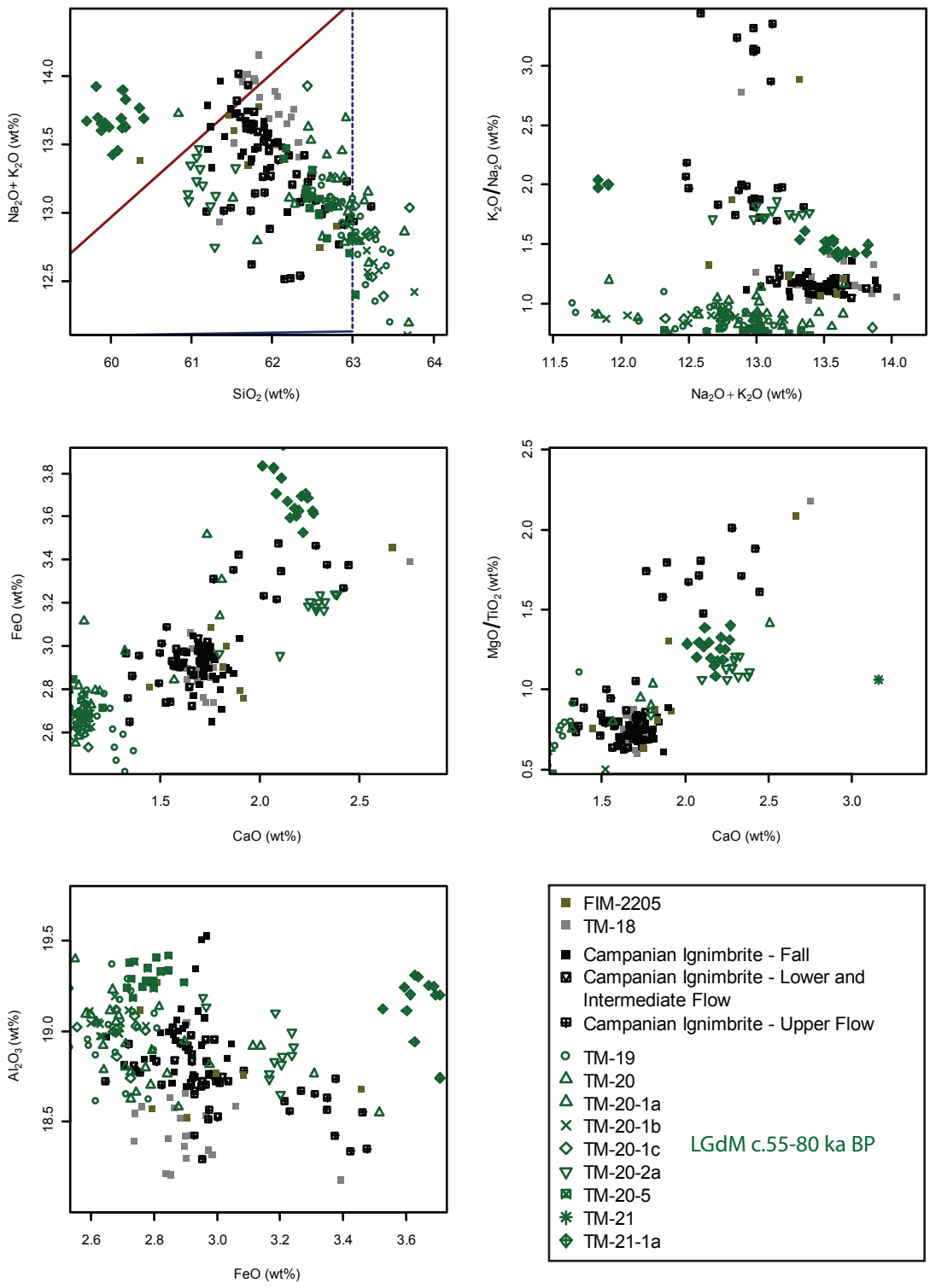

Figure 6.15 – Major element biplots of FIM-2205 compared against the CI proximal deposit, TM-18 and other LGdM tephra layers between 55 to 80 varve yrs BP.

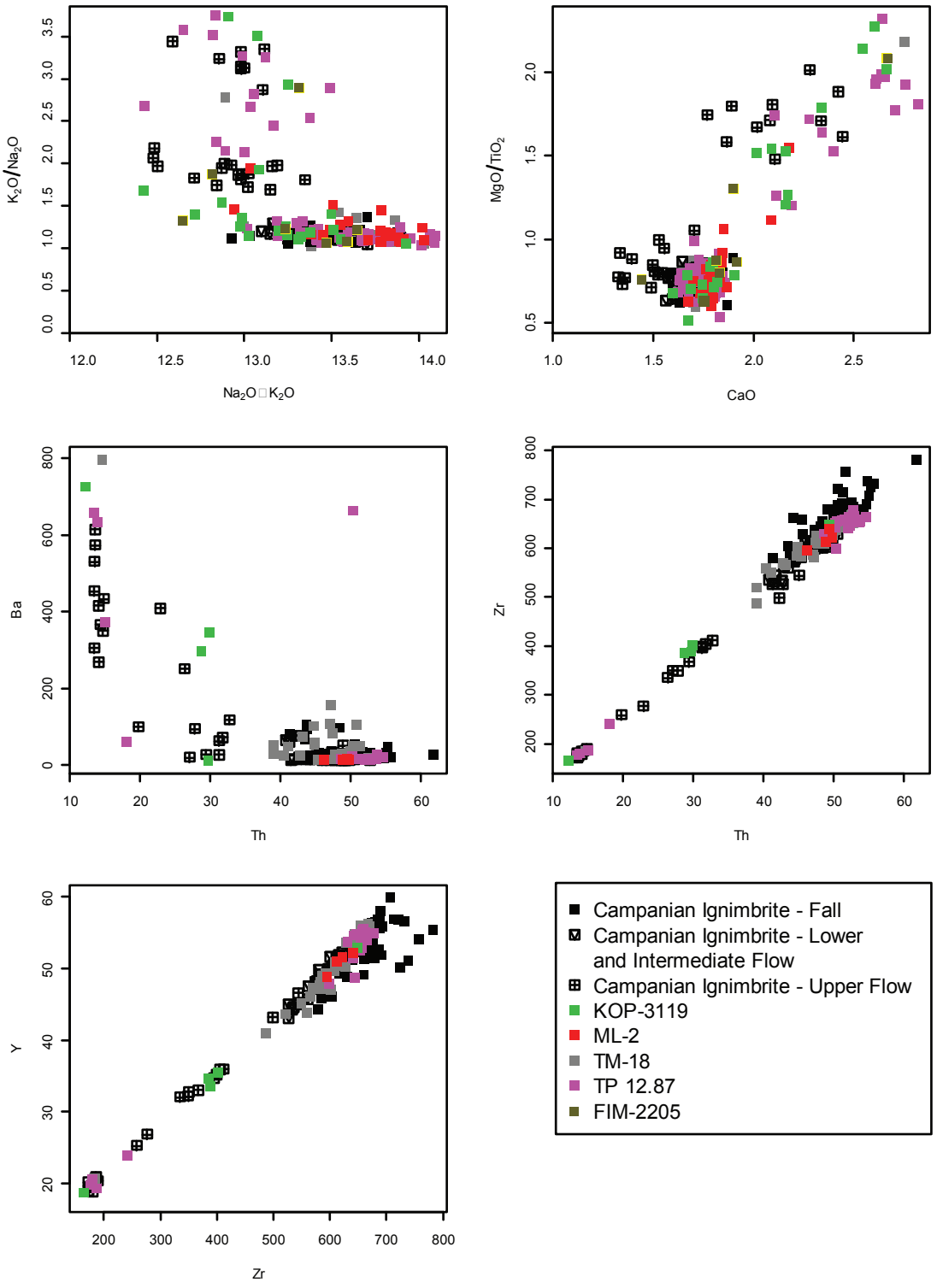

Figure 6.16 – Major and trace element biplots of all tephra layer correlated to the CI: KOP-3119, ML-2, TP 12.87 and FIM-2205 compared against the CI proximal deposit and TM-18.

Tenaghi Philippon

Within Tenaghi Philippon 5 tephra layers fit within group 2, one visible layer 37 cm thick: TP 12.87, and four cryptotephra layers which are dispersed over a 70 cm vertical interval: TP-1325, TP-1328, TP-1354 and TP-1392.

The correlation of TP-1334 to TM-18-1d rule out any tephra below this horizon (e.g. TP-1354 and TP-1392) due the stratigraphic relationship between TM-18-1d and the CI correlative TM-18 in the LGdM tephrostratigraphic record (see above). Considering that the CI was probably the largest eruption in the Mediterranean region during the last 200 ka BP (Barberi *et al.,* 1978) and is represented by visible tephra horizons as far east as Russia (Hoffecker *et al.,* 2008) the visible tephra TP 12.87 is the most likely correlative in the Tenaghi Philippon record. This confirms the correlation of TP 12.87 to the CI made by Müller *et al.* (2011) but increases its robustness via the application of trace elements and comparison to the recently available proximal CI dataset. The independent age determination (Model B) for TP 12.87 38363-40510 is consistent with the $^{40}Ar/^{39}Ar$ age of the CI (De Vivo *et al.,* 2001).

It is unclear if the CI like cryptotephra lying up to 1m (c. 2,000 yrs; see Table 6.6) below TP 12.87m represents previously unrecognised CF eruptions or reworking of the visible TP 12.87m downwards through the Tenaghi Philippon sequence.

Kopais

Six Kopais cryptotephra layers are in group 2: KOP-2317, KOP-2637, KOP-2698, KOP-2763, KOP-2910 and KOP-3119, all of which display indistinguishable geochemical envelopes. These tephra cover an 8 metre vertical interval in the sequence and either 4,000 or 26,000 yrs in time depending upon which age model is used (see Table 6.6). Extensive graphical comparisons to both the CF proximal record and the LGdM dataset show that TM-18 and the CI form the most robust geochemical match for tephra layers KOP-2317 to KOP-3119 (see Fig. 6.17).

It is apparent that more than one of these Kopais cryptotephra layers cannot be correlated to the CI and TM-18 unless they do not truly represent separate eruptions and instead are tephra shards from the same eruption reworked throughout the sequence. If the former is true the Kopais tephrostratigraphy records several previously unrecognised tephra layers which have an identical geochemical envelope to the CI tephra, this would have significant implications for the Mediterranean

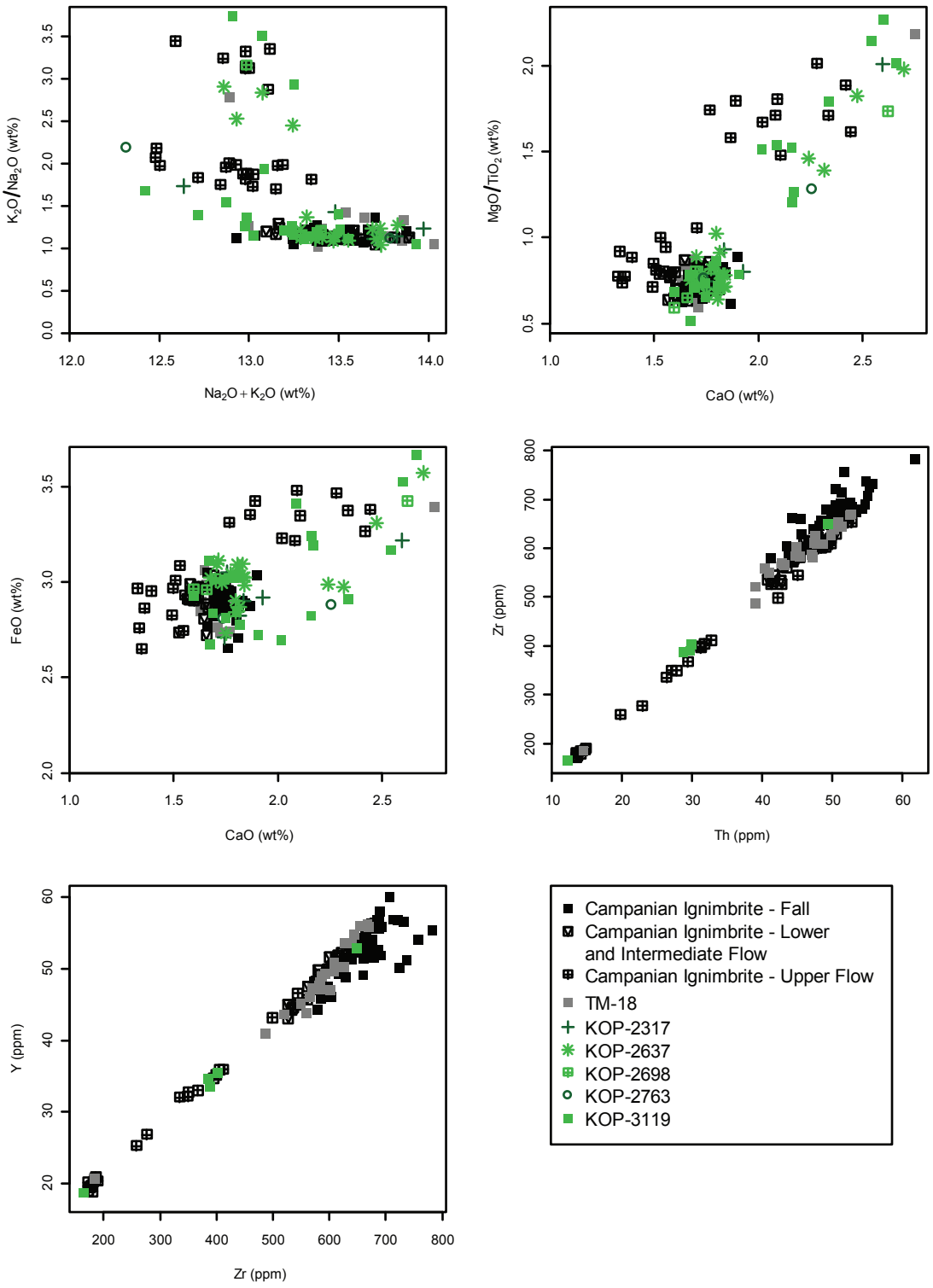

Figure 6.17 – Major and trace element biplots of KOP-2317, KOP-2637, KOP-2698, KOP-2763 and KOP-3119 compared against the CI proximal deposit and TM-18.

tephrostratigraphic lattice (including the correlations to the CI made above) and thus this possibility requires detailed consideration. KOP-2317 to KOP-3119 are tephra layers which are represented by very low shard numbers (1-30 shards per/g dry wt) and most of these layers represent distributions which would normally indicate a single depositional input events (i.e. have normal distributions) and are deposited during periods of both high and low tree pollen percentage's (see Fig. 5.3). This is perhaps odd as just 120 km to the south the CI tephra is represented as a visible tephra in a cave site (Lowe *et al.,* 2012) although it is possible other parts of the Kopais basin do record visible tephra (e.g. Pyne-O'Donnell, 2011).

The correlation of KOP-3347 to TM-18-1d or TP-1450 would suggest that KOP-3119 (the first input of compositionally matching CI tephra) is the most likely to represent the CI in Kopais as within LGdM TM-18 (correlated to the CI) directly overlies TM-18-1d. KOP-3119 was the only Kopais tephra layer where trace elements could be gained via LA-ICP-MS and clearly display the CI evolution trend.

It is unclear whether the tephra layers KOP-2317 to KOP-2910 represent some sort of reworking of KOP-3119 or are unique previously unrecognised tephra horizons, but the lack of any evidence from other tephrostratigraphic records east of the Campi Flegrei (e.g. LGdM, Ohrid) of multiple CI-like tephra would probably suggest the former.

If other evidence were to come to light the Kopais tephrostratigraphic record may require re-evaluation as it is replicated in another tephrostratigraphic record. It would, however be rash to attempt to change the current tephrostratigraphic framework here in light of the currently unclear evidence from Kopais.

The next four groupings interpreted (5, 7, 8 and 6) are sub-alkaline tephra and are summarised together and against relevant proximal and distal tephra datasets in Figures 6.18, 6.19 and 6.20 which are referenced within the following text.

Group 5

Only two EPMA-WDS geochemical assays are available for KOP-4815 but they form a distinctive geochemical range (Group 5), comparisons to Hellenic, Icelandic and Pantelleria tephra layers suggest that a Hellenic source is most likely, specifically Santorini (see Figs. 6.18, 6.21). KOP-4815 displays geochemical compositions which could correlate to the proximal Santorini deposits Upper Scoria 2, Vourvolous, or to

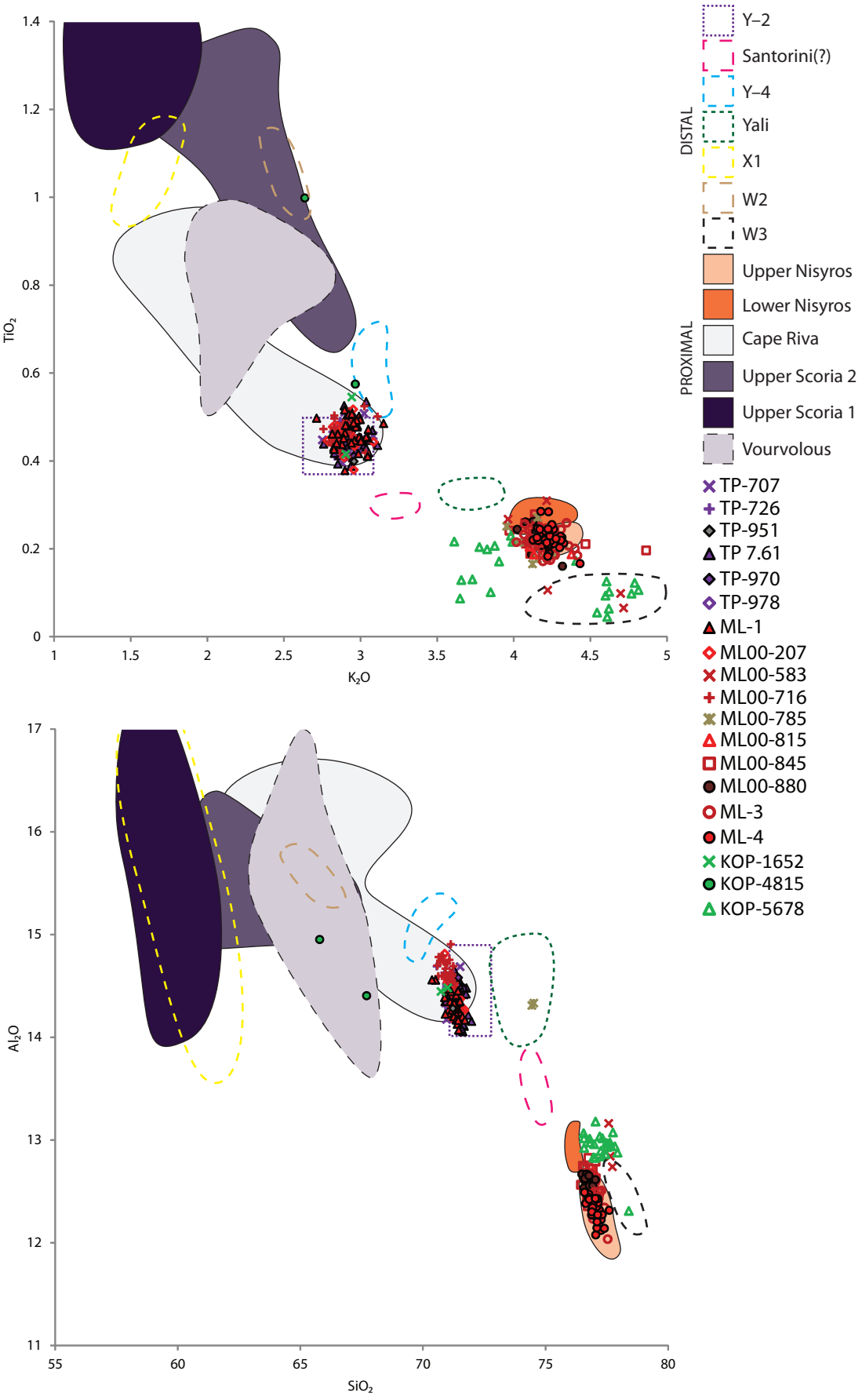

Figure 6.18 – Major element biplots of the sub-alkaline tephra found in this study compared against proximal and distal tephra datasets.

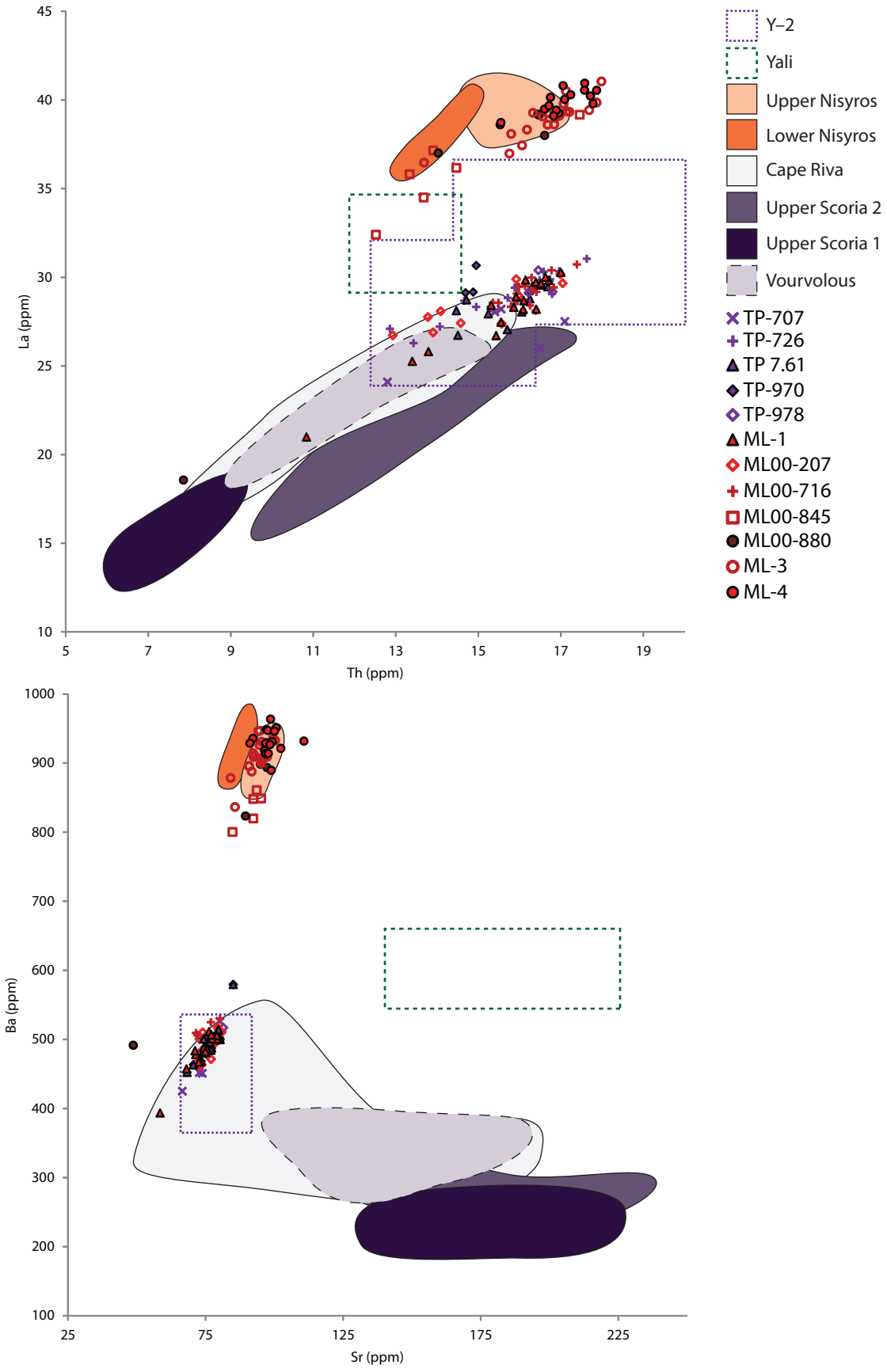

Figure 6.19 – Trace element biplots of the sub-alkaline tephra found in this study compared against proximal and distal tephra datasets.

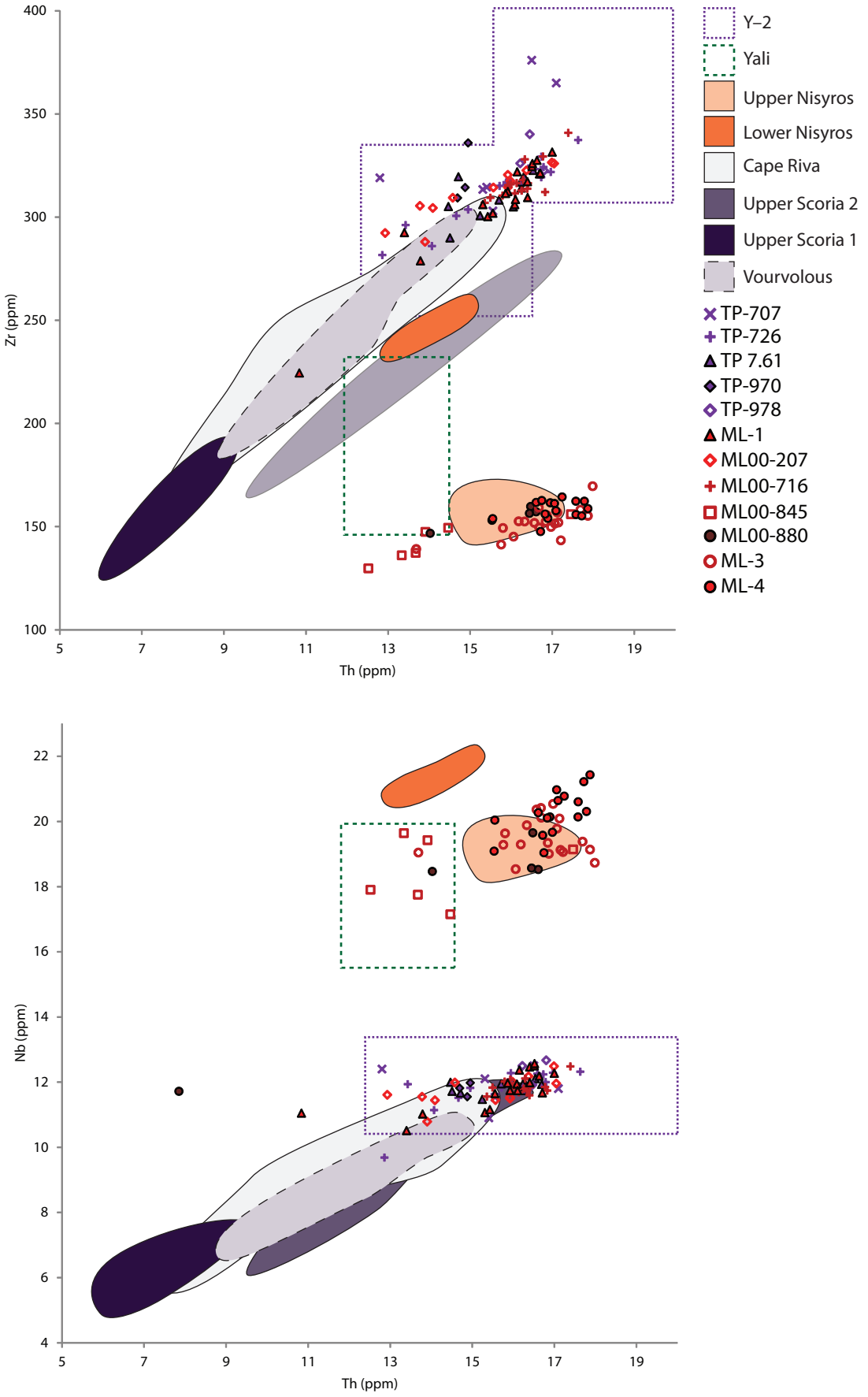

Figure 6.20 – Trace element biplots of the sub-alkaline tephra found in this study compared against proximal and distal tephra datasets.

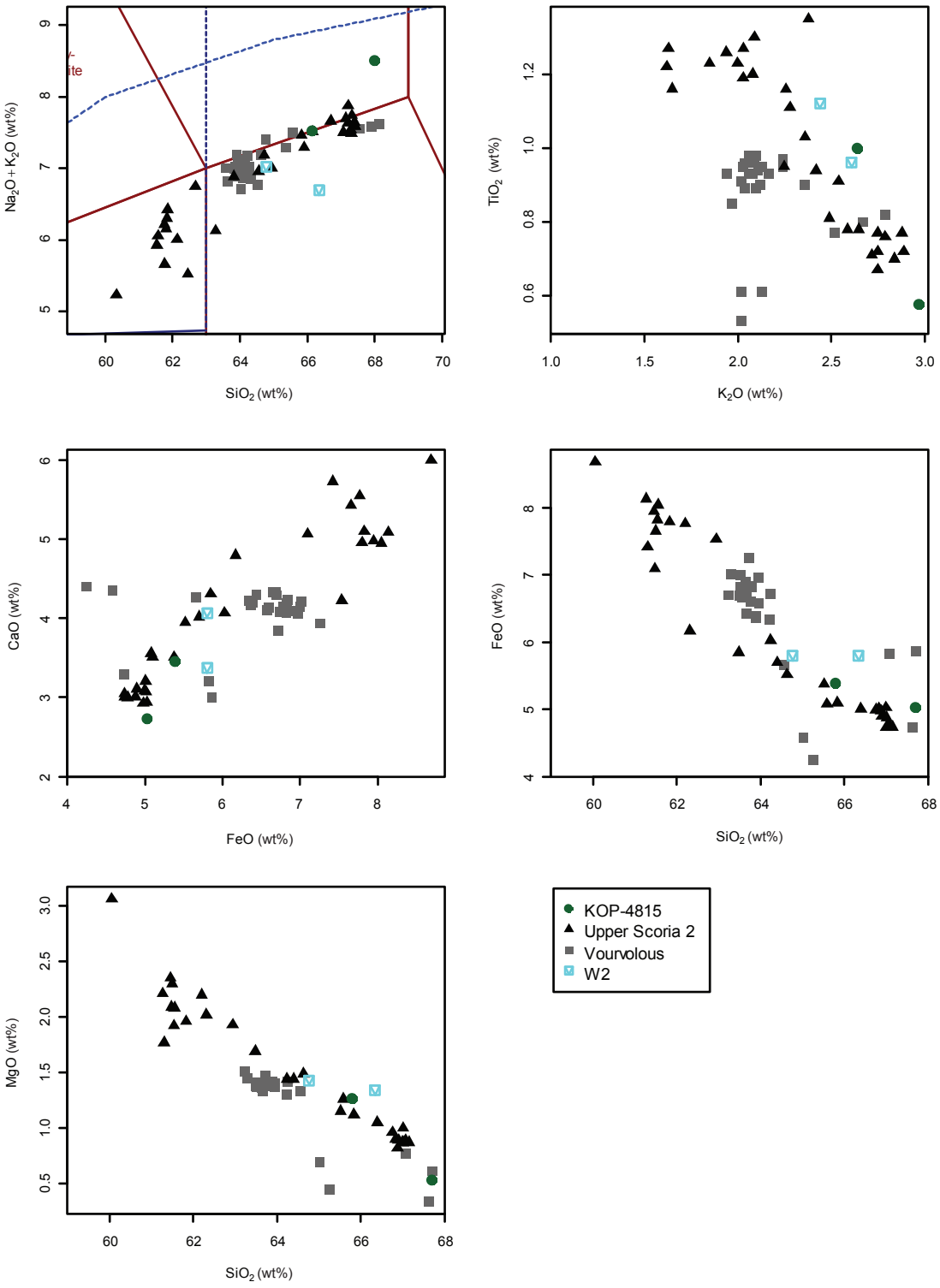

Figure 6.21 – Major and trace element biplots of potential correlatives to KOP-4815 (geochemical group 5) from the Santorini proximal and Aegean marine tephra layers.

the marine W–2 tephra. Without more geochemical data for KOP-4815 (in particular trace elements) it is difficult to correlate with confidence to a single one of these possible correlatives.

Upper Scoria 2 has several age determinations available including two radiocarbon ages taken from below the deposit on Santorini suggesting an age of 38400-49000 (Mellors & Sparks, 1991) and $^{40}Ar/^{39}Ar$ and $^{40}K/^{39}Ar$ determinations suggesting older ages of 54,000 ± 3000 and 79,000 ± 8000 respectively (Druitt *et al.,* 1999). The Vourvolous unit underlies Upper Scoria 2 in the Santorini stratigraphy and has not been dated. The W–2 marine tephra layer is thought to have an age older than 125 ka BP based upon its stratigraphic position underlying sapropel S5 (Vinci, 1985). KOP-4815 is dated in the Kopais age depth models to 99080 (Tzedakis, 1999) or 41320 yrs BP (Tzedakis *et al.,* 2004).

Group 7

Group 7 tephra consists of 6 tephra layers, 2 visible ML-3 and ML-4 and 4 cryptotephra ML00-785, ML00-815, ML00-845 and ML00-880 all from the Lesvos ML-00 and ML-01 sequences. This group could originate from either the Hellenic or Anatolian volcanic regions and extensive graphical comparisons were made to eruptions from these volcanic sources. On the basis of various major and trace element biplots (see Figs. 6.18 to 6.20) a Nisyros source was determined to be the closest compositional match for the tephra layers within Group 7.

Two large eruptions are known from the Nisyros region during the Last Glacial: the Upper Nisyros and the Lower Nisyros, which can be clearly distinguished on the basis of differing SiO_2, Al_2O_3, Zr, Ba and Nb values ((Tomlinson *et al.,* 2012b); see Fig. 6.22). On this basis all the group 7 tephra correlate to the Upper Nisyros and this can be seen clearly in SiO_2 vs Al_2O_3 and Sr vs Ba biplots (Figs. 6.18 and 6.19). This finding is in disagreement with both the correlations of Margari *et al.* (2007) who correlated ML-4 to the Lower Nisyros and ML-3 to the Upper Nisyros and Bichler *et al.* (2009) who subsequently suggested a correlation of ML-3 and ML-4 to the Yali-D eruption of Bond (1986). The correlation of both ML-3 and ML-4 to the Nisyros Upper was also recently proposed by Tomlinson *et al.* (2012b) based upon a reinterpretation of the Margari *et al.* (2007) dataset.

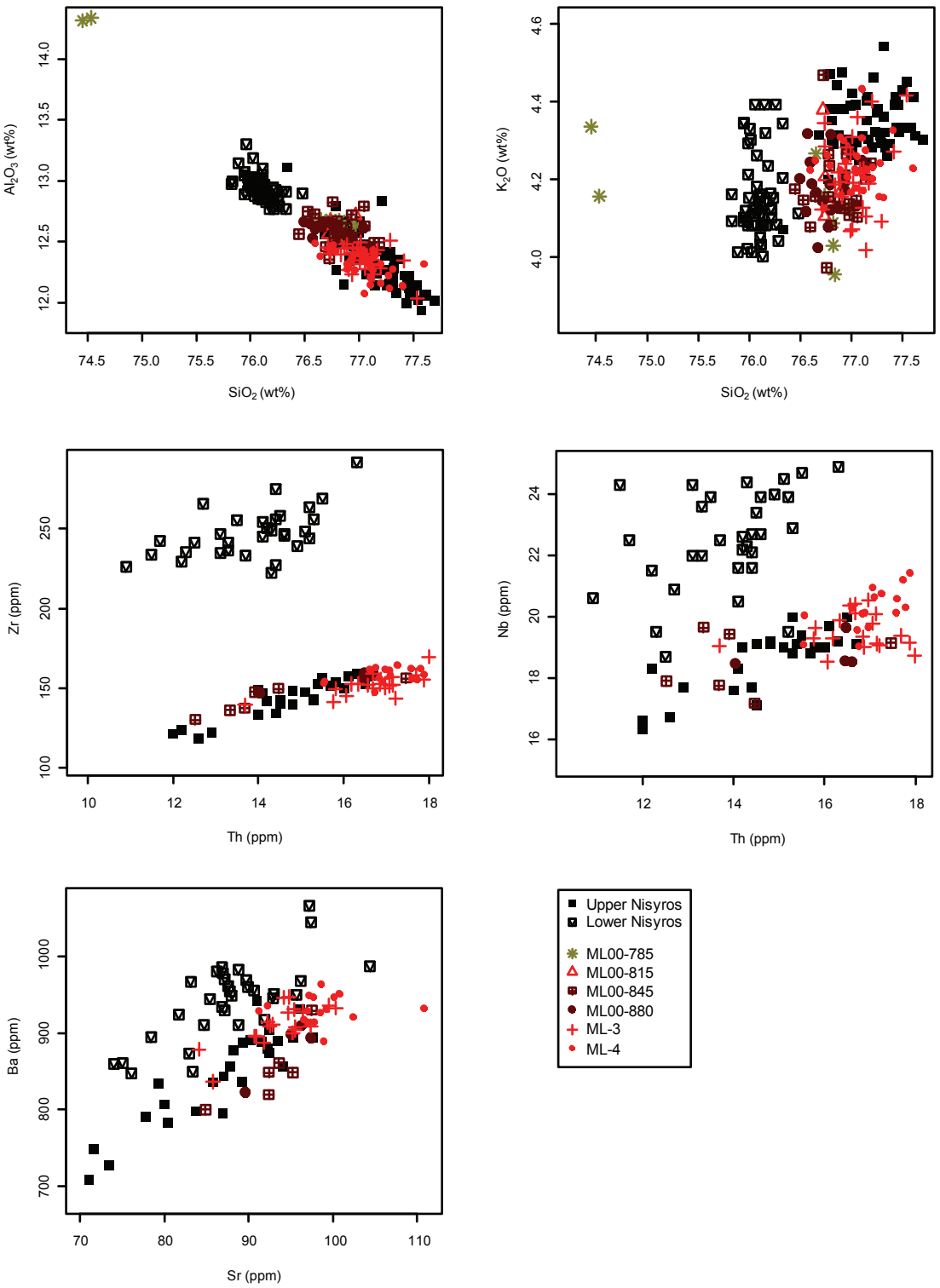

Figure 6.22 – Major and trace element biplots of potential correlatives to ML-3, ML-4, ML00-785, ML00-815, ML00-845, ML00-880 (geochemical group 7) with the Upper and Lower Nisyros.

Margari *et al.* (2007) did note reworking of tephra layers within the ML-00 sequence between 8.96-9.24m and it is a possibility that the cryptotephra layers at ML00-785, ML00-815, ML00-845 and ML00-880 represent reworking of the underlying ML-3 layer within ML-00 upwards through the sequence. Due to time constraints these cryptotephra were only defined to c.10 cm stratigraphic resolution and until a more detailed tephrostratigraphy is available for this part of the core it is difficult to assess the possibility that these layer may indeed be reworking from tephra layer ML-3 which underlie them (Margari *et al.* 2007).

Evidence against this possibility is that unique geochemical signatures are represented, for example ML00-880 contains a trachytic-phonolitic composition (Group 3). Also, where trace elements are available for ML00-845 and ML00-880 a slightly less evolved (e.g. on Ba and Th; see Fig. 6.22) composition is apparent from the chemical data from that of ML-3, this is more subtle but may also be seen from major element plots (e.g. SiO_2; Fig. 6.22) with all the group 8 cryptotephra (ML00-785 to ML00-880). Despite these slight differences all Group 8 tephra still best fit the Upper Nisyros tephra.

Group 8

KOP-5678 is the only tephra assigned to group 8 and this layer forms a unique geochemical envelope which on many biplots displays a bimodal compositional (e.g. K_2O/TiO_2, see Fig. 6.18). Comparisons to the RESET database suggest that Icelandic, Hellenic and Anatolian sources are all possible. Detailed graphical comparisons (see Fig. 6.23) suggest that there is no clear match for KOP-5678 with any specific layer from the reference database. However the data for KOP-5678 might suggest a central Anatolian origin, showing some geochemical affinity to the Guneydag proximal deposit (dated to c. 23 ka BP). Unfortunately little tephrostratigraphic and geochemical data currently exists for this volcanic region during the LLG.

6.2.4 *Third Order* tephrocorrelations

Group 6

Group 6 contains several tephra layers from three sites (Kopais, Tenaghi Philippon and Lesvos) and composition is highly suggestive of a Santorini source (see Figs. 6.18 and 6.19). Based upon extensive graphical comparisons to both Santorini proximal

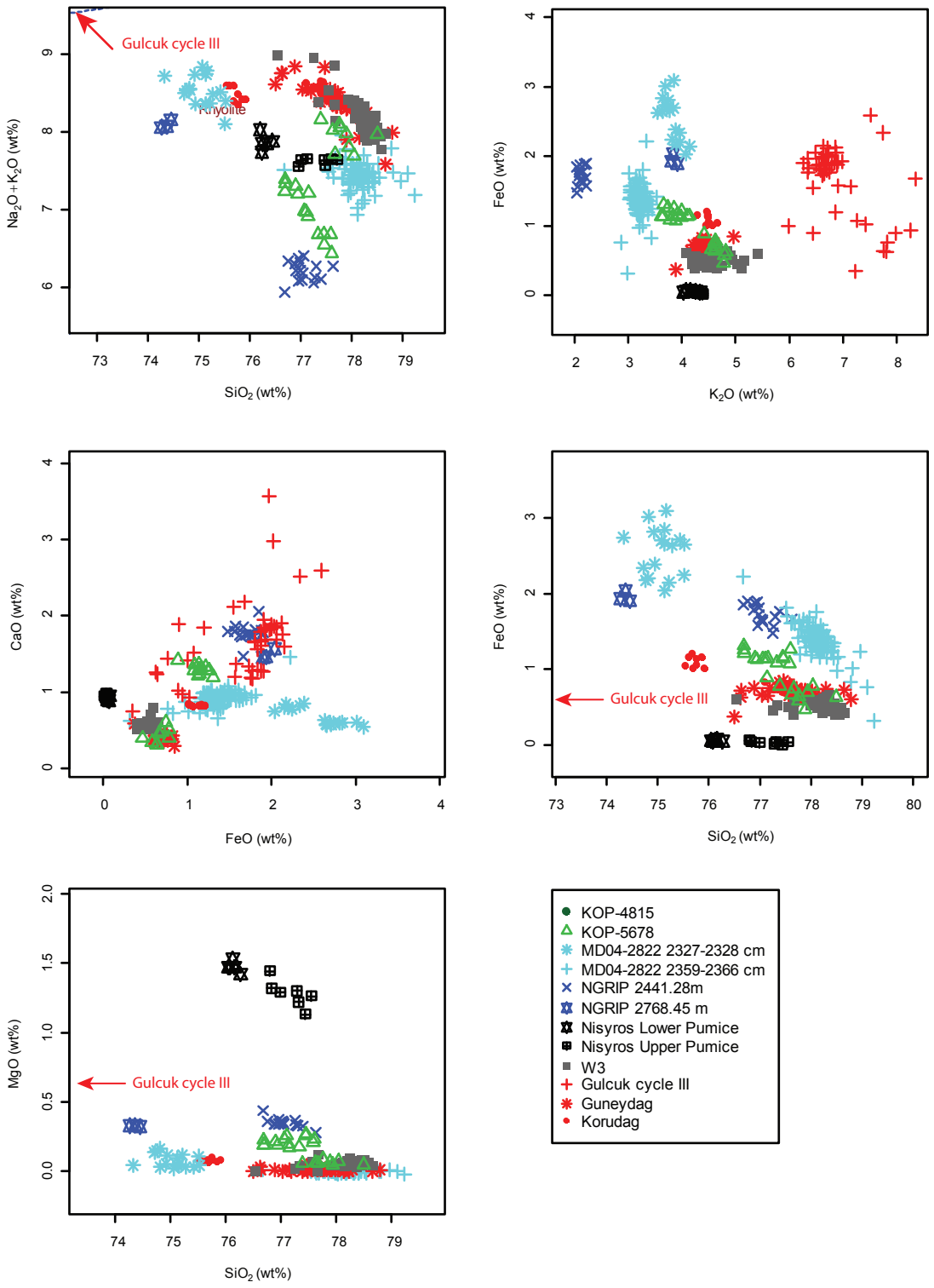

Figure 6.23 – Major element biplots of potential correlatives to KOP-5678 (geochemical group 8) from Icelandic, Hellenic and Anatolian sources.

deposits and the medial-distal Aegean marine tephra record show that the Cape Riva (and its correlated marine equivalent the Y–2 tephra) forms the most robust geochemical match for these tephra. All the group 6 tephra fit the most evolved end member of the Cape Riva geochemical range (see Fig. 6.24A) as does the Y–2 tephra. Detailed geochemical comparison of all the tephra layers within group 6 show that they are indistinguishable on both major and trace elements and suggest that several, previously unrecognised, Santorini layers with identical geochemical signatures to the Cape Riva tephra have been detected within this study in more than one site. This finding is not without precedence; with for example St Seymour *et al.* (2004) also finding multiple tephra layers with a Santorini Cape Riva signature. These several tephra layers will now be discussed.

In order to find out which layers within Group 6 may represent the Cape Riva tephra age information was required and was compared from both age-depth models A and B for each of the three sites (see Fig. 6.2 and Table 6.6) which are shown plotted against available proximal age information for the Cape Riva eruption of Santorini in Figure 6.24B. From this it can be seen that tephra layers TP-978 and ML00-207 from Tenaghi Philippon and Lesvos respectively, are considerably older in age than the Cape Riva tephra and, in contrast, TP-707 and TP-726 are too young on the basis of their age estimates. The only temporal matches for the Cape Riva in Tenaghi Philippon and Lesvos are tephra layers TP 7.61 and ML-1 which both sit within the age range of the Cape Riva, on this basis these tephra are correlated to the Cape Riva Eruption, this finding is in agreement with that of both Margari *et al.* (2007) and Müller *et al.* (2011). It is also worth noting that these tephra are the only visible layers present within Group 6 tentatively suggesting they represent larger magnitude eruptive events.

Two cryptotephra layers lie above TP 7.61 in the Tenaghi Philippon sequence, TP-726 and TP-707 and represent distinct tephra peaks with normal and slightly positive distributions respectively (see Fig. 5.8) suggesting they are not a result of reworking of the underlying visible tephra layer but represented distinct separate eruptions. This part replicates the results of St Seymour *et al.* (2004) who analysed visible tephra layers from three cores across the Tenaghi Philippon basin and found two visible tephra layers (their PhT1 and PhT2) within two of the cores which both had an identical geochemical signature to the Cape Riva eruption. On the basis of three radiocarbon dates they correlated PhT2 to the Cape Riva and PhT1 to a younger Santorini eruption. St Seymour *et al.* (2004) gained only one radiocarbon

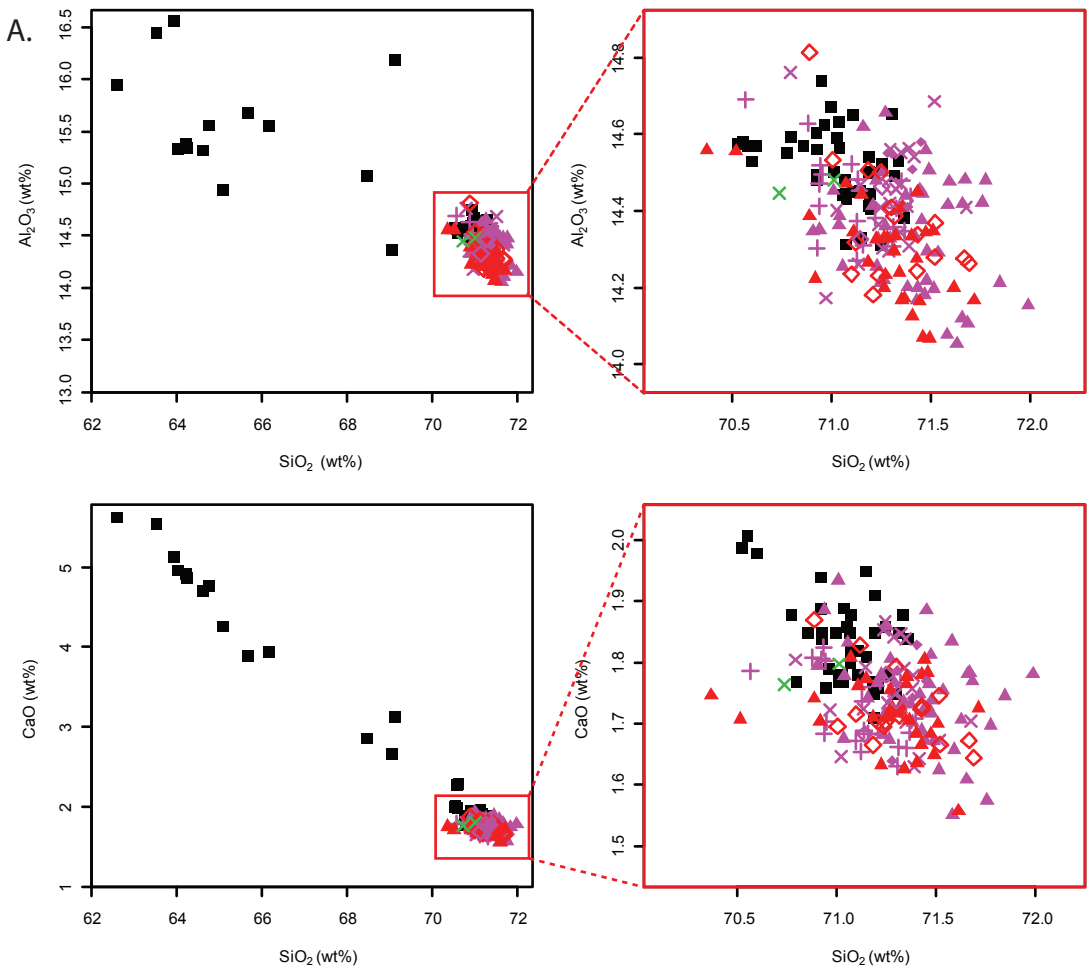

Figure 6.24 – (**A.**) Major element biplots of geochemical group 6 and the Cape Riva. (**B.**) Comparison of ages using age-depth models A (in grey) and B (in colour; see Fig. 6.2, Table 6.6 and text for details).

B.

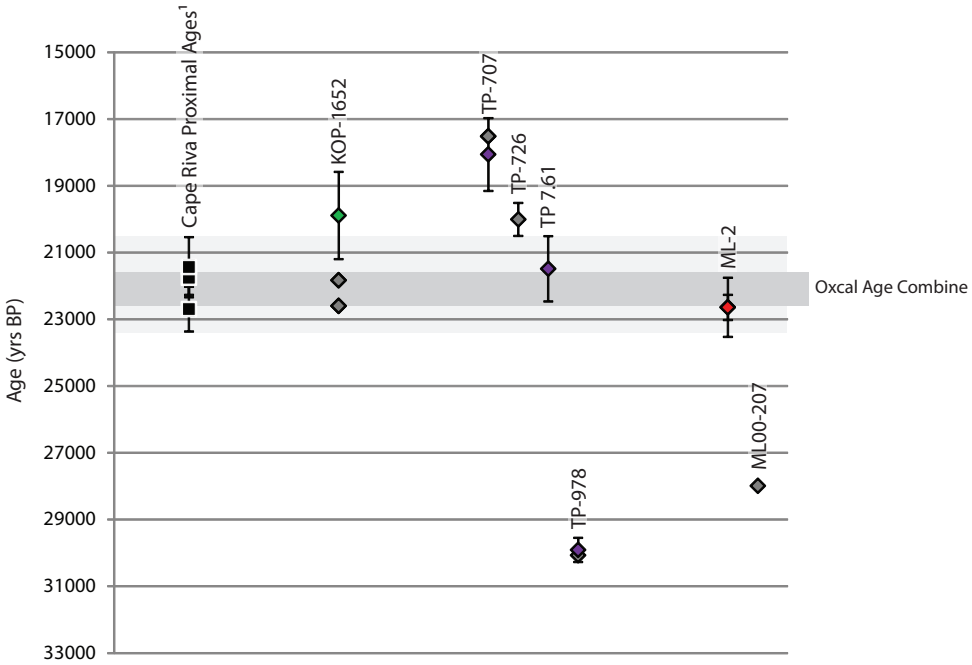

determination from below PhT1 suggesting an age of around 12 ka BP, however, rejected others radiocarbon dates from below PhT1 that gave erratic values on the basis of apparent contamination with older carbon. PhT1 lies around 30-100 cm above PhT2. On a stratigraphical basis a tentative correlation is made here between TP-707 and PhT1 as it sits a similar c.55 cm above TP 7.61 in the TP-2005 sequence. Despite the fact markedly older age ranges are apparent for TP-707 (Model A: 17520, Model B: 16980-19150 yrs BP) the lack of cryptotephra higher up in the TP-2005 sequence towards c.7 ka suggest this TP-707 probably represents St Seymour *et al.* (2004) PhT1 tephra layer. TP-726 is interpreted as representing a new previously undiscovered tephra layer.

The Group 6 layer from Kopais (KOP-1652) model A age estimates (interpolated from both the Tzedakis (1999) and Tzedakis *et al.* (2004) chronologies) suggest a good match with the Cape Riva eruption, however the model B age estimate (produced within this study) shows a younger age is possible, overlapping with both younger eruptive events present within the Tenaghi Philippon tephrostratigraphy (TP-707 and TP-726). It is thus not clear at this time which eruption KOP-1652 may represent, either the Cape Riva, TP-726 and TP-707 all possibilities, although it does represent the furthest east a tephra originating from Santorini has been discovered suggesting tephra from the Hellenic Arc can disperse far westwards not just to the N, E and S as observed by Hardiman (1999).

Based on the correlations made above, both TP-978 and ML00-207 underlie the Cape Riva tephra layer in Lesvos and Tenaghi Philippon (both by c.2m) and both lie above the CI tephra (by c.3m; see Fig. 6.25). They also display not dissimilar age estimates (c.28 to 30 ka BP; see Table 6.6). For these reasons these tephra layers are likely to represent distal occurrence of the same Santorini eruption, which is currently unrecognised in the proximal Santorini volcanostratigraphy. A Santorini eruption, the Y–4, is recognised in the Aegean marine tephrostratigraphic record by Vinci (1985) and has an estimate age of 30 ka BP (based upon stratigraphic position in relation to sapropel layers; Narcisi & Vezzoli, 1999) similar to the ages for TP-978 and ML00-207. The geochemical data for the Y–4 however (2 EPMA data-points from Vinci, 1985 and 1 from Keller *et al.,* 1978) although similar, does not match on Al_2O_3 or TiO_2 wt% (Fig. 6.18) thus a link cannot be made. However due to the paucity of the current geochemical dataset for the Y–4 tephra, re-evaluation may be required when and if more data become available.

ML00-716 is a cryptotephra which lies below the CI within the Lesvos ML-00 sequence (see Fig. 5.14) and has age estimates of 44330 (Model A; Margari *et al.,* 2007; 2009) and 42180-43660 (Model B; *this study*) and is the first occurrence of a tephra with a Cape Riva Santorini signature below the CI with no known correlations either in the proximal record or within the Aegean marine tephrostratigraphic record. This cryptotephra is situated at the very base of a core segment and could potentially represent contamination due to a coring artefact (V. Margari., *pers. comm.*). Because of this, the legitimacy of this layer should remain in doubt until it has been validated in another sequence.

6.2.5 Summary

Mostly *first* and *second order* tephrocorrelations were possible, however repeating geochemical signatures did complicate correlation and in the instance of the Cape Riva tephra chronological information was required to allow correlation. All the tephrocorrelations proposed above are listed in Table 6.8 alongside any previous correlations and shown in Fig. 6.25.

Many previously undetected tephra layers are described here (e.g. KOP-5678). The validity of these previously un-described tephra horizons is more robust where their presence has been confirmed in more than one record, for example, the c.30 ka Santorini eruption represented by both TP-978 and ML00-207 and the pre-CI CF eruption recorded distally by TP-1450 and ML00-880. Where multiple occurrences of the same tephra have been identified they have been named after the core where they were first discovered using the core code and depth of occurrence as recommended by Lowe (2011). Tephra layer ML00-583 was not grouped above but represents a tephra layer with at least three geochemical populations which might suggest that it may represent some form of core contamination or reworking. It is however difficult to prove conclusively core contamination where fine laminations or sediment layers are absent which can be particularly prevalent in peat records which is one of the reasons why tephra layers described in more than one sequence help confirmed their validity and help rule out contamination issues. Despite these problems it is unsurprising that new Hellenic tephra layers (without existing correlatives) have been uncovered within this study as it represents some of the first palaeo-records searched systematically for cryptotephra in the Eastern Mediterranean during the LLG timeframe. Other research

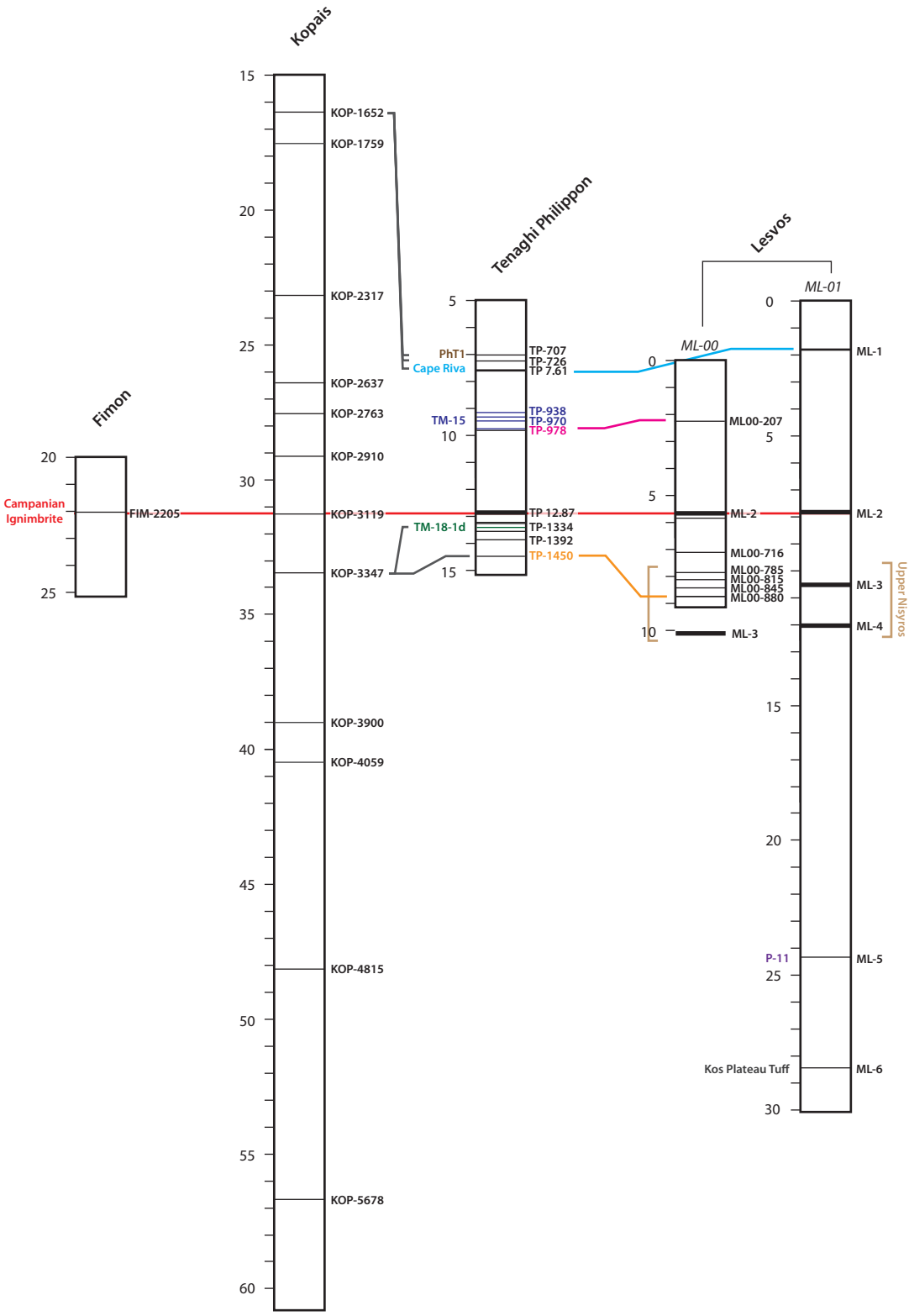

Figure 6.25 – Tephrocorrelations for and between records studied here plotted against depth. All records are aligned to the CI tephra.

in this vein is in progress as part of the RESET Project and new cryptotephra layers are also being uncovered in marine realm of this region (C. Satow, *pers. comm.*).

Often multiple layers were found to correlate to one proximal unit (interpreted to represent one eruptive event) this was the case with both the Cape Riva and Nisyros Upper suggesting either these distal tephra layers are not recognised proximally or that these proximal units may represent more than one eruption, these possibilities are further discussed and analysed within Chapter 8.

Where tephra layers could be linked to other existing deposits often their geographical range has been significantly improved, for example the CI (=FIM-2205) in Fimon represents the furthest NW occurrence of this tephra. TM-15 (=TP-978) in Tenaghi Philippon represents the furthest Eastern detection of this layer extending it distribution by up to c.300 km.

The implications of these correlations and identification of new tephra horizons to the wider Mediterranean tephrostratigraphy will be further discussed in Chapter 8.

Table 6.8 – Final tephrocorrelations made within this chapter alongside previous correlations, where available.

Tephra layer code	**Previous Correlations**	**Final Correlations (*This Study*)**
FIM-2042	—	—
FIM-2205	—	Campanian Ignimbrite
KOP-1652	—	PhT1 or TP-726 or Cape Riva
KOP-1759	—	—
KOP-2317	—	*Reworked CI?*
KOP-2637	—	*Reworked CI?*
KOP-2698	—	*Reworked CI?*
KOP-2763	—	*Reworked CI?*
KOP-2910	—	*Reworked CI?*
KOP-3119	—	Campanian Ignimbrite
KOP-3347	—	TM-18-1d or TP-1450

KOP-3900	—	—
KOP-4059	—	—
KOP-4815	—	Upper Scoria 2 or Vourvolous
KOP-5678	—	Unknown Anatolian Eruption?

TP-707	—	PhT1
TP-726	—	—
TP 7.61[1]	Cape Riva	Cape Riva
TP-890	—	—
TP-896	—	—
TP-923	—	Reworked TM-15
TP-938	—	Reworked TM-15
TP-951	—	Reworked TM-15
TP-970	—	TM-15
TP-978	—	—
TP 12.87[1]	Campanian Ignimbrite	Campanian Ignimbrite
TP-1325	—	—
TP-1328	—	—
TP-1334	—	TM-18-1d
TP-1354	—	—
TP-1392	—	—
TP-1450	—	—

ML00

ML00-207	—	TP-978
ML-2[2]	Campanian Ignimbrite	Campanian Ignimbrite
ML00-583	—	Reworking?
ML00-716	—	Reworking?
ML00-785	—	Upper Nisyros
ML00-815	—	Upper Nisyros
ML00-845	—	Upper Nisyros
ML00-880	—	Upper Nisyros and TP-1450

ML01

ML-1[2]	Cape Riva	Cape Riva
ML-2	Campanian Ignimbrite	Campanian Ignimbrite
ML-3[2]	Upper Nisyros	Upper Nisyros
ML-4[2]	Lower Nisyros	Upper Nisyros
ML-5[2]	Green Tuff	P-11
ML-6[2]	—	Kos Plateau Tuff

7.0 TESTING AND REFINING EXISTING AGE-DEPTH MODELS

This chapter aims to produce independent age models for each site where tephra horizons were discovered (i.e. the final age model C, see Fig. 6.2). The age model for each site will be based upon independent age information alone, free of biostratigraphic age correlation points used by other authors. Once completed the new age models (C) are compared and contrasted to the pre-existing age depth models described in Chapter 4. The palaeoenvironmental significance of any temporal differences will also be discussed. At the end of this chapter the sites will be compared against each other for LLG period via both the use of the independent chronologies developed within this chapter and tephrocorrelations between sites, before detailed comparison to other palaeoenvironmental data is undertaken within Chapter 8.

7.1 Imported Tephra ages

Several (often discordant) ages may exist for a volcanic eruption, it is thus necessary to ensure the most robust age estimates are imported into any age-model sequence. Ages determined from radiometric means were used here; not those acquired from alignment based chronologies. Where available $^{40}Ar/^{39}Ar$ and $^{40}K/^{39}Ar$ ages were preferentially used, due to these methods being free from radiocarbon calibration issues (see section 1.3.1) and thus providing a better independent cross test of radiocarbon based age models.

Many tephra ages are also available from the LGdM varve chronology (Table 6.2; Allen *et al.,* 1999; Wulf *et al.,* 2004; 2008; *in review*). However only around 10% of the total LGdM sediment sequence is varved with the intervening sections ages based upon estimated sedimentation rates, a 5% 'rough' error has been suggested for LGdM chronology (Wulf *et al.,* 2004). Brauer *et al.* (2000) have stated that the LGdM chronology is likely to underestimate the true age of events, and thus the LGdM chronology should be viewed as minimum age of events. Because of these caveats $^{40}Ar/^{39}Ar$ and $^{40}K/^{39}Ar$ ages were preferred over those from the LGdM chronology. The reference and final imported ages used within this study are shown in Table 7.1 and are discussed during the text but in summary were formed in these main ways:

Where overlapping age ranges exist for a tephra (e.g. the Cape Riva and P-11) the *Combine* function within OxCal was used to produce more precise ages at 95.4% confidence intervals (Bronk Ramsey, 1995). Where discordant age determinations were present, for example the Kos Plateau Tuff, an age range was assumed over where the bulk of the ages sit. For others the most precise age determination currently available was used (e.g. for the Campanian Ignimbrite). Imported tephra ages used within the age models below are outlined in Table 7.1.

Table 7.1 – Table listing all available age determinations with references and the final imported tephra age used within this study. All Radiocarbon dates presented are calibrated using IntCal09. See text for further details.

Tephra	Ages	References	Imported Age Range
Cape Riva	20540-22340 (^{14}C) 21250-22270 (^{14}C) 22025-23365 (^{14}C)	Pichler & Freidrich (1976) Eriksen *et al.* (1990)	21525 – 22340 *(R_Combine)*
TP-978	29550-30270 (^{14}C)	*This Study*	29550 – 30270
Campanian Ignimbrite	39,280 ± 110 (^{40}Ar/^{39}Ar)	De Vivo *et al.* (2001)	39170 – 39390
TM-18-1d	39,870 ± 170 (see text)	Wulf *et al*. (2006) Wutke (*submitted*) *This Study*	39700 – 40040
TP-1450	42720-44110 (^{14}C)	*This Study*	42720 – 44110
Upper Scoria 2	38462-46197 (^{14}C) 40575-49053 (^{14}C) 54,000 ± 3000 (^{40}Ar/^{39}Ar) 79,000 ± 8000 (^{40}K/^{39}Ar)	Mellors & Sparks (1991) Druitt *et al*. (1999)	>48000
P-11	132,000 ± 6000 (^{40}K/^{39}Ar) 133,100 ± 1500 (^{40}K/^{39}Ar) 132,000 ± 6000 (^{40}K/^{39}Ar) 133,000 ± 5000 (^{40}K/^{39}Ar) 134, 000 ± 6000 (^{40}K/^{39}Ar)	Mahood & Hildreth (1986)	131700 – 134400 *(C_Combine)*
KPT	161,000 ± 1000 (^{40}K/^{39}Ar) 165,000 ± 2000 (^{40}Ar/^{39}Ar) 166,100 ± 2000 (^{40}Ar/^{39}Ar) 177,600 ± 6600 (^{40}Ar/^{39}Ar)	Smith *et al*. (1996; 2000) Bachmann *et al*. (2010)	160000 – 168100

7.2 Fimon PD Core

7.2.1 New Age Model

The current Fimon PD age model (Pini *et al.,* 2010) is tied to radiocarbon dates until c.30 ka BP and then is based upon 10 pollen-stratigraphic alignment points back to c.50 ka BP (see Table 7.2). The biostratigraphic age information is discordant with the radiocarbon dates available for the lower part of the core, which Pini *et al.* (2010) rejected on the basis of the pollen-biostratigraphy and suggested some form of natural contamination effecting the radiocarbon ages (see section 4.2.3). The Pini *et al.* (2010)

Table 7.2 – *P_Sequence* model statistics for Fimon (PD) showing the K value used, age information and agreement indices.

FIMON PD CORE FINAL AGE MODEL (MODEL C)
K (7)

Amodel = 62.8
Aoverall = 62.8

OxCal Function	Name	Mean Depth	Unmodelled (BP)			Modelled (BP)				
			from	to	%	from	to	%	A	C
R_Date	UBA-7831	19.41	27743	26676	95	27805	26773	95	99	100
R_Date	UBA-7830	19.52	28491	27686	95	28455	27671	95	102	100
R_Date	UBA-7829	19.75	30151	29342	95	30145	29347	95	101	100
R_Date	UBA-7828	19.90	30675	29726	95	30610	29682	95	95	100
C_Date	OSL1	20.87	34088	22913	95	34683	31612	95	38	100
R_Combine	UBA-7827-1 and UBA-7827-2	21.58	36336	35094	95	36391	35178	95	100	100
C_Date	Campanian Ignimbrite	22.05	39500	39060	95	39494	39055	95	100	100
C_Date	OSL2	22.86	55280	38120	95	44927	41745	95	106	100
R_Date	UBA-7826	23.18	45461	44341	95	45490	44369	95	100	100
C_Date	OSL3	23.85	62077	42123	95	54030	45997	95	117	99
C_Date	OSL4	24.78	79570	53230	95	63178	49587	95	47	98

Dates Removed from Model

			Calibrated (BP) IntCal09	
Name	**^{14}C age**	**Depth (m)**	**from**	**to**
UBA-7825	49700 ± 520	23.45	…	48720
UBA-7824	47694 ± 491	24.35	48745	46765
UBA-7823	49922 ± 605	24.39	…	48792
UBA-7677	>64,200	27.00	…	…
UBA-7678	>58,352 ± 1108	27.21	…	…

model is also in disagreement with OSL ages which subsequently became available (S. Lowick, *pers. comm.*).

Within the Fimon PD sequence only one tephra layer, FIM-2205, was geochemically characterised and was correlated to the CI eruption of Campi Flegrei. The Pini *et al.* (2010) age–depth model (A) based upon biostratigraphic tie points at this depth suggests an age of 65,580-68,130 for FIM-2205 whereas the independent age model (B) suggests an age of 36,610-40,730 yrs BP which would be consistent with the $^{40}Ar/^{39}Ar$ age of the CI (De Vivo *et al.,* 2001). In fact age–depth models based on either OSL or radiocarbon information display age determinations consistent with the age of the CI. On this basis, and that there are no tephra horizons currently known in the 60-80 ka BP timeframe which display a geochemical signature similar to that of the CI (see Fig. 6.15), the biostratigraphic correlations made by Pini *et al.* (2010) appear to be incorrect and the age determinations of both the radiocarbon and OSL ages appear to be validated. The Fimon chronology is thus supported by three lines of independent evidence and final age model (C) for Fimon produced here reflects this. The Fimon age model was produced using the *P_Sequence* model function within OxCal ver 4.1 at 95.4% confidence limits (see section 3.6.1). Before the model was run four radiocarbon dates (UBA-7825, UBA-7823, UBA-7677 and UBA-7678) were excluded as these all produced infinite radiocarbon ages when calibrated (Table 7.2). A low K factor was first applied to the model to allow greater flexibility (i.e. rapidly varying depositional conditions) and one further date (UBA-7824) was removed at this stage as it produced a very low agreement indices. This dated interval at 24.35m returns an age very close to the limit of radiocarbon time (48.7 ka) and underlies the first radiocarbon date in the sequence that does return an infinite age (at 23.45m), considering the asymptotic radiocarbon effect (Higham, 2011), this is perhaps further reason to remove this date.

The K factor was then slowly increased and model re-run until the total model *Agreement Index* ($A_{overall}$ and A_{model}) remained no lower than 60% (Bronk Ramsey, 2008). The final model produced an $A_{overall}$ and A_{model} of 62.8% with most ages having agreement values above 95% (see Table 7.2). A graphical representation of this model is shown in Fig. 7.1 compared alongside Pini *et al.* (2010) age–depth model as described in chapter 4.

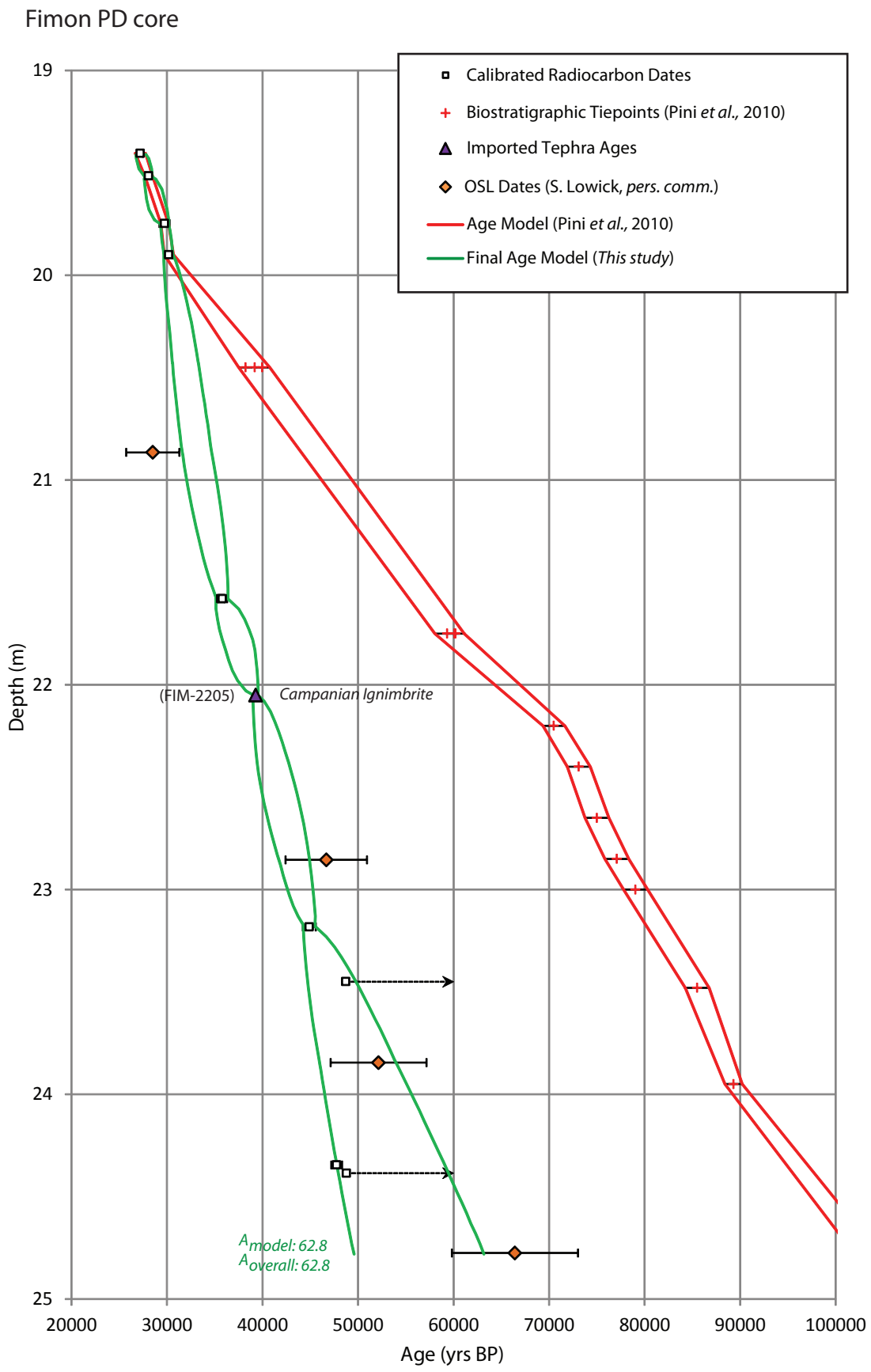

Figure 7.1 – Age–depth plot showing the chronological model developed within this study (at 95.4% confidence limits) compared against the age–depth model proposed by Pini *et al.* (2010) for Fimon PD. All radiocarbon and OSL ages (S. Lowick, *pers. comm.*) are shown alongside points where tephra ages have been imported (see table 7.1 for details). Error ranges are plotted at 2 standard deviations except for the OSL ages which are shown with 1 sigma errors.

From this comparison the following observations can be made: (a) the new model agrees with the Pini *et al.* (2010) model until around 20 m (b) the sedimentation rate of the new age–depth model appears to be more consistent with the sedimentation rate of the radiocarbon dates from 19-20m following the depositional gradient of these ages and (c) the new age–depth model produced here would suggest a much younger chronology for Fimon between 20–25 m by 10 increasing to a 30 thousand year offset.

7.2.2 Palaeoenvironmental Significance

Figure 7.2 shows the total tree pollen plotted against the Pini *et al.* (2010) age–depth model and the chronology produced here. It is apparent that the new chronology suggests a much younger sequence that sits within MIS 3 and potentially late MIS 4. This would suggest that increases in thermophilous taxa (*Quaercus, Ulmus* and *Tilia*) at 23.48m related to late MIS 5 events by Pini *et al.* (2010) actually occurred much later during MIS 3. Rises and falls in *Tilia* and *Picea* described by Pini *et al.* (2010) between 22.85 to 21.75m would relate to late to middle MIS 3 conditions (e.g. GI-7 to GI-12) with the new chronology rather than early MIS 4 as suggested by Pini *et al.* (2010).

In order to compare in detail the temporal offsets between the Pini *et al.* (2010) age–depth model and the chronological model produced here the biostratigraphic events identified in the Fimon pollen record by Pini *et al.* (2010) were dated upon the basis of the new age model, and were produced using the *Date* Function within OxCal ver 4.1. These are listed in Table 7.3 alongside the Pini *et al.* (2010) ages. These offsets will now be discussed in more detail.

Pini *et al.* (2010) correlate 20.45m to the onset of HE4 on the basis of a peak of xerophytes and the last occurrence of continuous *Tilia* presence within the pollen record. Interestingly on the basis of the new chronology proposed here 20.45m could correlate temporally to HE3 (see Fig. 7.3). This possibility is perhaps further strengthened by the position of the CI tephra which has been demonstrated in other investigations to sit just after the onset of HE4 (Rohling *et al.,* 2003; Lowe *et al.,* 2012). Within Fimon the CI (FIM-2205) lies below 20.45m within a period where mixed-oak woody plants have decreased in favour of *Pinus sylv/mugo* tree species which are

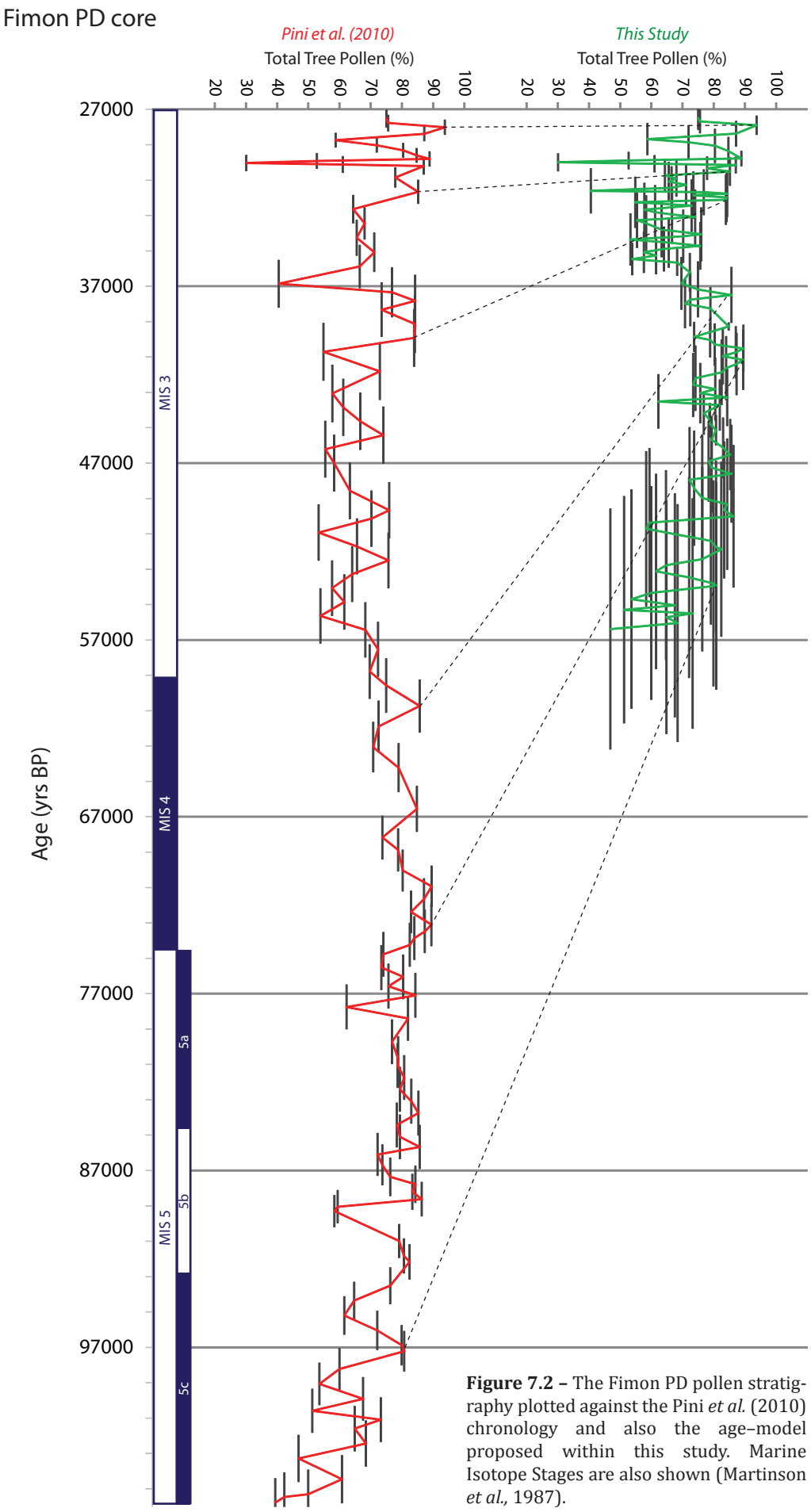

Figure 7.2 – The Fimon PD pollen stratigraphy plotted against the Pini *et al.* (2010) chronology and also the age–model proposed within this study. Marine Isotope Stages are also shown (Martinson *et al.,* 1987).

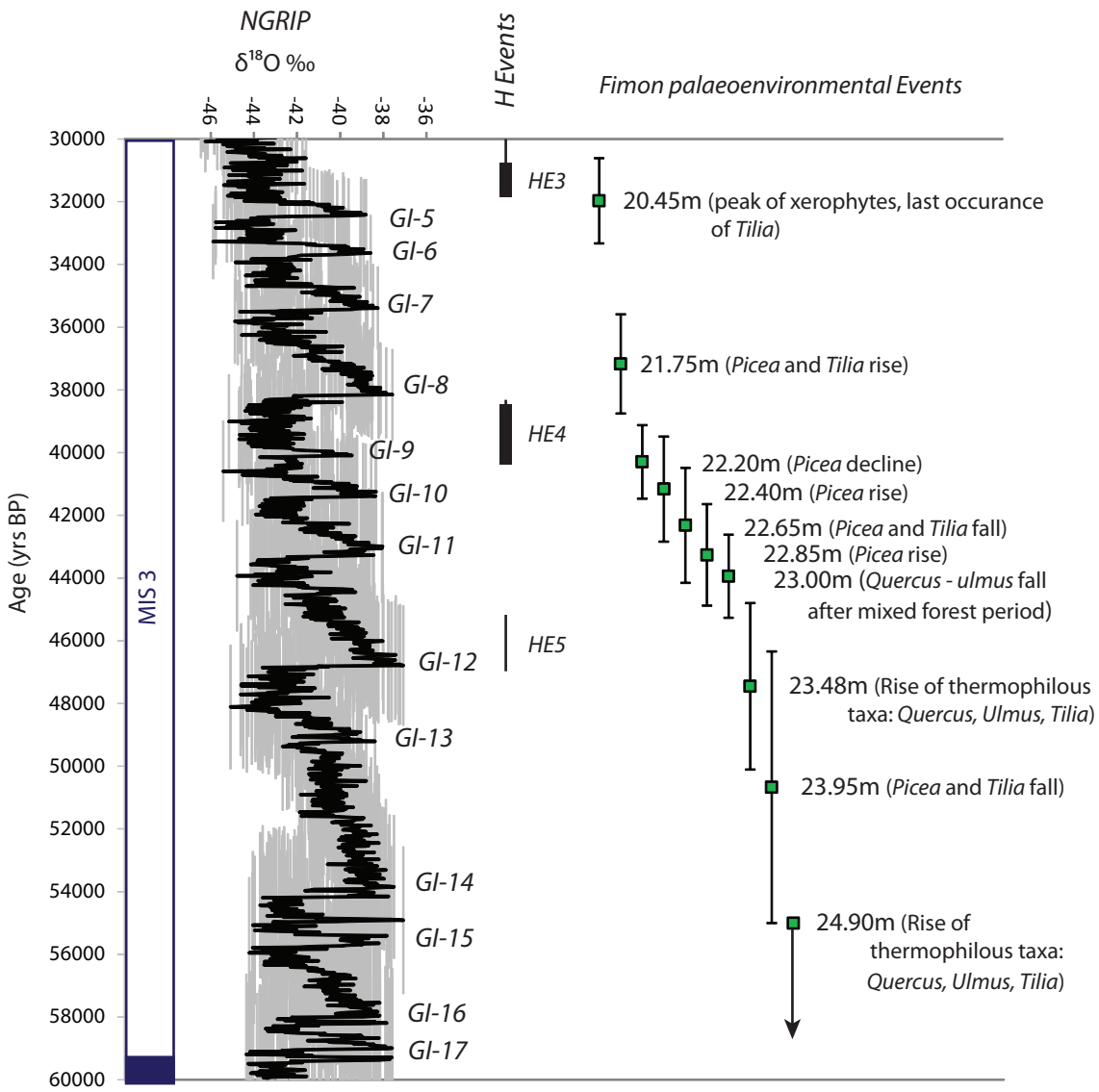

Figure 7.3 – Comparison between events in Fimon (PD) and the NGRIP oxygen isotope record based upon the GGIC05 timescale from Andersen *et al.* (2006) and Svensson *et al.* (2006). Calibrated age ranges for Heinrich (H) events 2, 3, 4 and 5 from western European records (Bard *et al.,* 2000; Sánchez Goñi *et al.*, 2002; de Abreu *et al.,* 2003) (thin lines) and calculated ages (Thouveny *et al.,* 2000) (black boxes). Marine Isotope Stages are also shown (Martinson *et al.,* 1987).

more adapted to dry conditions. Pini *et al.* (2010) very tentatively suggest graphically (see Fig. 4.9) this part of the Fimon pollen stratigraphy may represent the long

Table 7.3 – Correlations and imported ages for the Fimon PD sequence (from Pini *et al.,* 2010) alongside new age determinations produced within this study.

Pini *et al.* (2010)			***This study***
Pollen Stratigraphic event depth (m)	**Botanical or isotopic-correlated event**	**Imported Age/s**	**Modelled age (Model C)**
20.45	Onset of HE4	39200 ± 200[1] 39980 ± 1570[2] 38230 ± 1450	30610-33330
21.75	Base GI-17	60200 ± 400[3] 60100 ± 2000[1] 59330 ± 2570[2]	35590-38750
22.20	Top GI-19	70500 ± 2300[4]	39120-41470
22.40	Base GI-19	73100 ± 2400[4]	39490-42840
22.65	Top GI-20	75000 ± 2500[4]	40490-44150
22.85	Base GI-20	77100 ± 2500[4]	41640-44880
23.00	Top GI-21 End 2nd interstadial (St. Germain II)	79050 ± 2500[4]	42620-45270
23.48	Onset GI-21 Onset 2nd interstadial (St. Germain II)	85500 ± 2500[5]	44790-50110
23.95	End GI-22 End 1st interstadial (St. Germain 1)	89300 ± 1800[5]	46340-55000
24.90	Top GS-24 Top Montaigu event	105300 ± 2750[4]	>55000

[1]Sánchez Goñi *et al.* (2008); [2]Svensson *et al.* (2008); [3]Holzkämper *et al.* (2005); [4]NGRIP Members (2004); [5]Spötl and Mangini, (2006)

Greenland stadials of GS-18 or GS-19, the position of the CI would suggest instead this part of the core represents HE4. From Table 7.3 it can be seen that none of the new age determination agree (even within error) with the imported event ages used by Pini *et al.* (2010) to build their chronology (in particular Greenland events GI-17 to 22 or GS-24). When the Fimon pollen stratigraphic events, as dated within this study are compared against the NGRIP oxygen isotope record (on the GGIC05 timescale) a temporal relationship to a much younger range of GIs and GSs is instead potentially suggested (i.e. GI-7 to GI-14). Interesting periods where only *Picea* and *Tilia* vary

appear to relate temporally more to shorter duration GIs (e.g. GI-9 to GI-11) whereas Fimon palaeoenvironmental events where other more thermophiles species also respond (e.g. *Quercus* and *Ulmus*) appear to relate to longer duration GIs (e.g. GI-14 and GI-12).

Kaltenrieder *et al.* (2009) presented palaeoenvironmental data from a site situated in the nearby Euganean Hills region, only ~11km to the south east of the Fimon site. They presented both pollen and macrofossil evidence of thermophilous taxa (*Quercus, Ulmus* and *Tilia*) persisting during the Last Glacial Maximum (LGM) suggesting local hilly geography provided higher precipitation and could have sheltered warm loving tree species from cold winds. They suggest these small climatic pockets acted as refugia areas allowing the thermophilous taxa to survive during the LGM. It is then perhaps possible that Fimon (also situated within a hilly environment, the Berici Hills) might record higher than expected thermophilous taxa up until and during the LLG.

If the independent chronology proposed here is correct it would suggest that the biostratigraphic tie-point approach applied by Pini *et al.* (2009) between 20 to 25 m has led to an erroneous chronology, this could be due to localised environmental and climatic factors outlined briefly above which has skewed attempted cross correlations. Alternatively the three lines of independent chronological evidence, the radiocarbon, OSL and tephra (which cross validate between 21 to 23 m core depth) could be incorrect. This seems unlikely as it would imply three different chronological techniques are incorrectly offset by the same amount of time or a previously unrecognised CI like tephra exists. If coherent offsets may exist between different geochronological dating techinques it would have non-trivial implications for age modelling during the LLG.

7.3 Kopais (K-93)

7.3.1 New Age Model

Two age–depth models have been proposed for Kopais (K-93); one that proposes a chronology which would place the base of the Kopais sediment sequence at 130 ka BP (Tzedakis, 1999) and another, more recent, chronology that suggests a much younger sequence with the base dating to 52 ka BP (Tzedakis *et al.,* 2004). How both these models were formed is described in detail in section 4.2.4. Three new

tephrochronological tie points have been introduced here into the Kopais chronology which will now be described. Firstly the $^{40}Ar/^{39}Ar$ age of the CI (De Vivo *et al.* 2001) which was placed where the first input of the CI was detected in the sediment sequence (at 31.19 m) and secondly below this a tephra layer that could correlate to either TM-18-1d or TP-1450 is present at 33.47m (KOP-3347). The minimum and maximum ages for these tephra were imported into the sequence, thus allowing for both of these possibilities.

Over 15 m below KOP-3347 is the cryptotephra layer KOP-4815 which may correlate to three eruptions, the Upper Scoria 2, Vourvolous, or to the marine W–2 tephra. These tephra layers have various ages (see Tables 6.4 and 7.1). The youngest is the Upper Scoria 2 which has several age determinations including two radiocarbon ages taken from below the deposit on Santorini which date to 38460-49200 and 40570-49050 cal yrs BP (Mellors & Sparks, 1991) and $^{40}Ar/^{39}Ar$ and $^{40}K/^{39}Ar$ determinations suggesting older ages of 54,000 ±3000 and 79,000±8000 respectively (Druitt *et al.,* 1999). These radiocarbon dates have a large analytical radiocarbon error (c.2000 yrs) which is why the calibrated age ranges are so large. It seems unlikely that the younger age estimates (c.38-40 ka BP) are correct considering the CI and pre-CI tephra lie 15 m above KOP-4815 in the Kopais sequence and are of about this age (see Table 7.1). For these reason the younger $^{40}Ar/^{39}Ar$ age of the Upper Scoria 2 was imported in to the Kopais chronology. Due to the other two potential correlatives for KOP-4815 tephra (the Vourvolous tephra layer and the W–2 marine tephra layer) both of which are older than the Upper Scoria 2, the imported age estimate for KOP-4815 should be viewed as a youngest possible age estimate. Vourvolous underlies Upper Scoria 2 in the proximal Santorini stratigraphy, and no age estimates are available from this unit. The W-2 tephra is much older than the Upper Scoria 2 at c.150 ka BP, an age based upon marine oxygen isotope stratigraphy (Vinci, 1985). Although the age of the W-2 is significantly older than either age model currently suggested for Kopais, Tzedakis (1999) do describe a potential hiatus above KOP-4815 at 42.59-42.65m where an organic layer could be evidence that the lake completely dried out for an undetermined length of time, thus this possibility should not be ruled out.

The final Kopais age model was produced using the *P_Sequence* model function within OxCal ver 4.1 at 95.4% confidence limits (see section 3.6.1). *Boundary* functions were placed underneath dates where large (>5m) gaps were present between ages. Two radiocarbon dates had to be removed before the depositional model would run, both

dates (at 20.50 and 43.90m; listed in Table 7.4 and both shown in Fig. 7.4) caused age reversals. The age at 20.50m was slightly younger than the radiocarbon age directly above it (AA35125) and the radiocarbon age at 43.90m was significantly younger than the CI tephra and pre-CI tephra (either TM-18-1d or TP-1450) which lie ~10m above. Due to the paucity of ages in the Kopais sequence, large stratigraphic gaps between dated intervals and the potential uncertainty surrounding the CI correlation, the model was run with a K factor which kept the total model *Agreement Index* ($A_{overall}$ and A_{model}) very high to allow model prediction of rapidity varying deposition. The final model produced an $A_{overall}$ and A_{model} of 99.3 and 99.6 respectively with most ages having agreement values above 99% (see Table 7.4). A graphical representation of this model is shown in Fig. 7.4 compared alongside the two existing age–depth models for Kopais (K-93) as described in detail in chapter 4.

Comparison of the new chronological model proposed here for Kopais to those of Tzedakis (1999) and Tzedakis *et al.* (2004) (which are both represented as mean values) will now be described before the palaeoenvironmental significance is discussed in section 7.3.2.

Between depths 7 to 17m there is agreement between all the chronologies until 17 to 20m, where the new chronology becomes younger. Between 20 to 21m the large error ranges show potential agreement with both age models, between 21 to 24m the new age model agrees with the Tzedakis *et al.* (2004) age model. Below 24m up until 33.47m an age range younger than that of Tzedakis (1999) but older than the Tzedakis *et al.* (2004) age-depth model can be observed. Below 33.47m only a minimum age estimate is available although this does show ages which are older than that of the Tzedakis *et al.* (2004) curve but cannot be used to test the Tzedakis (1999) age-depth model in this part of the stratigraphy.

7.3.2 Palaeoenvironmental significance

Figure 7.5 shows the Kopais (K-93) total tree pollen plotted against the two former age–depth models and the chronology produced here. It can be seen that the new independent chronology is similar to the one produced by Tzedakis (1999) and Tzedakis *et al.* (2004) during MIS 2 (10 to 20 ka BP). During MIS 3 and before the original Tzedakis (1999) chronology increasingly disagrees with the age-depth model

Table 7.4 – *P_Sequence* model statistics for Kopais (K-93) showing the K value used, age information and agreement indices.

KOPAIS K-93 FINAL AGE MODEL (MODEL C)
K (0.5)

Amodel = 99.6
Aoverall = 99.3

OxCal Function	Name	Mean Depth	Unmodelled (BP)			Modelled (BP)				
			from	to	%	from	to	%	A	C
R_Date	uncoded1	8.63	12410	11825	95.4	12522	11836	95.4	97	100
R_Date	uncoded2	19.57	14163	13832	95.4	14143	13824	95.4	101	99
R_Date	AA35125	20.50	22489	21558	95.4	23212	21581	95.4	104	99
R_Date	AA35126	24.34	29485	28488	95.4	29115	28021	95.4	66	99
C_Date	Campanian Ignimbrite	31.19	39500	39060	95.4	39505	39065	95.4	100	99
C_Date	TM-18-1d *or* TP-1450	33.47	44498	39308	95.4	43328	39336	95.4	100	100
C_Date	Upper Scoria 2	48.15	59986	48015	95.4	59038	47395	95.4	99	98

Dates Removed from Model

			Calibrated (BP) IntCal09	
Name	**^{14}C age**	**Depth (m)**	**from**	**to**
AA39647	17360 ± 160	20.50	21257	20249
uncoded3	31780 ± 310	43.90	36855	35265

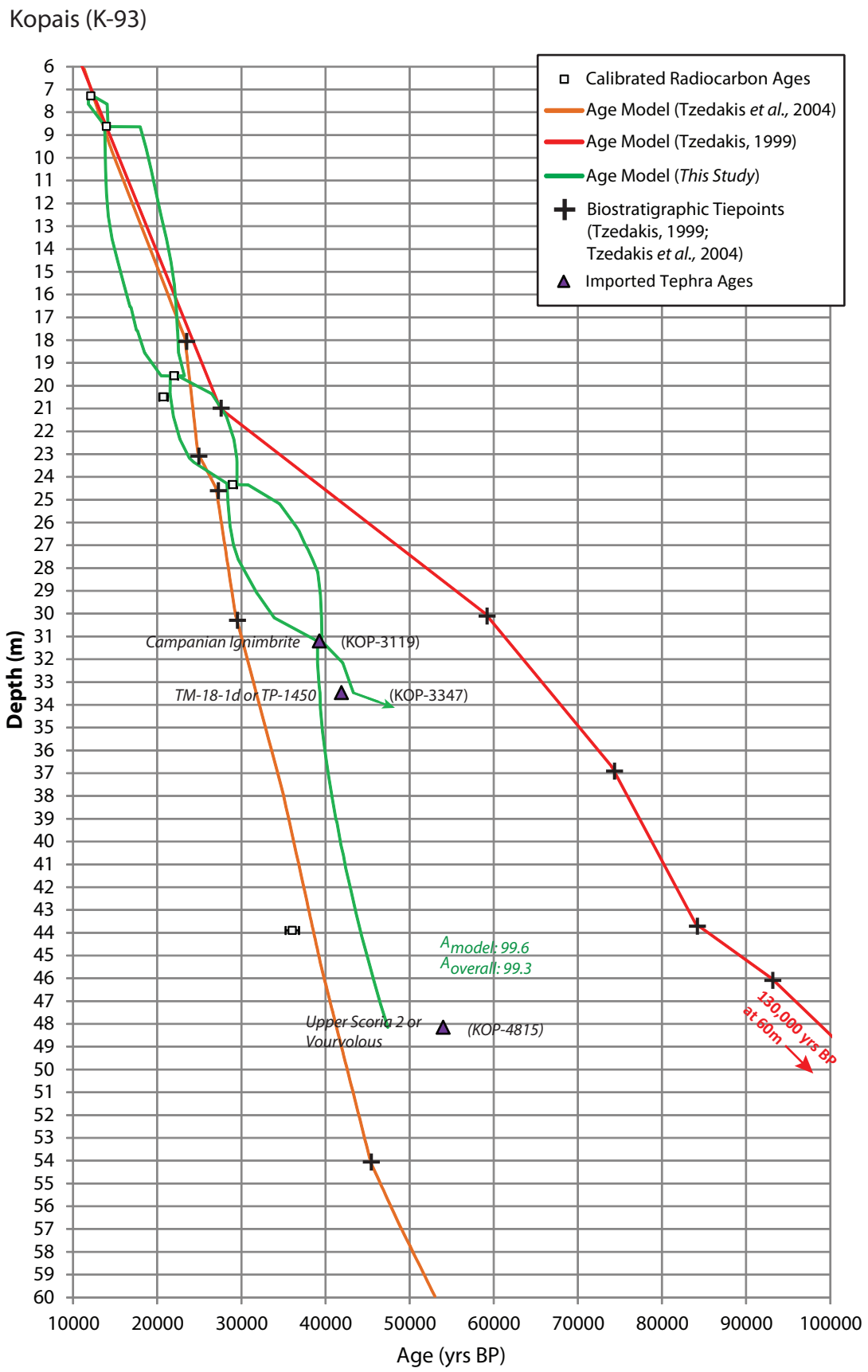

Figure 7.4 – Age–depth plot showing the chronological model developed within this study (at 95.4% confidence limits) compared against the models proposed by both Tzedakis (1999) and Tzedakis *et al.* (2004) shown in red and orange respectively for Kopais (K-93). All radiocarbon ages are shown alongside points where tephra ages have been imported (see table 7.1 for details).

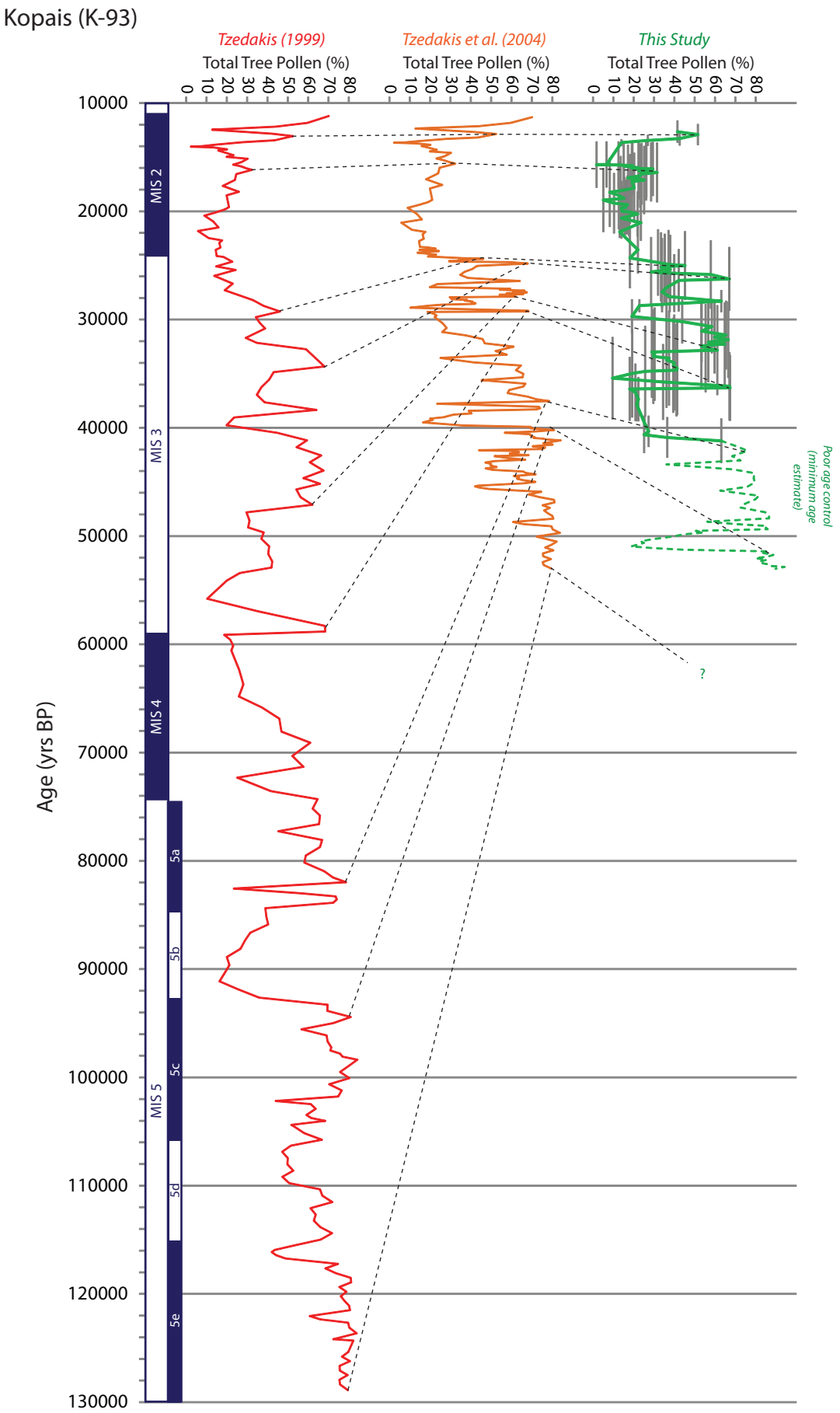

Figure 7.5 – The Kopais (K-93) pollen stratigraphy plotted against both Tzedakis (1999) and Tzedakis *et al.* (2004) timescales (shown in red and orange respectively) and the age–model proposed within this study. Marine Isotope Stages are also shown (Martinson *et al.,* 1987).

produced within this study, by up to 40 ka years. Below c.42 ka BP potential offsets are not possible to judge as only minimum age estimates are available for the new chronology although it is worth noting that this range does not rule out this lower part of the Tzedakis (1999) chronology.

During MIS 3 an increasing age offset becomes apparent between the Tzedakis *et al.* (2004) and new chronology, with the new chronology becoming older (within errors) suggesting the tree fluctuations represent an earlier period within MIS 3 than suggested by Tzedakis *et al.* (2004). Below c.42 ka BP the minimum age estimate suggests an older chronology is probable than that suggested by Tzedakis *et al.* (2004). The MIS 3 offsets are significant as Tzedakis *et al.* (2004) correlated tree pollen collapses at 33.30 and 46.00m to Heinrich Events 3 and 4. The new independent chronologies presented here would instead suggest age determinations for these depths which are inconsistent with these correlations and would instead suggest that the total tree pollen decline at 33.30 temporally relates to HE4 (c.39 ka BP; Thouveny *et al*. 2000) not HE3.

7.4 Tenaghi Philippon (TP-2005)

7.4.1 New Age Model

The existing age model for Tenaghi Philippon is based upon 15 radiocarbon dates, two imported tephra ages and one biostratigraphic tie point based upon the pollen signal for the MIS4/5 boundary (Müller *et al*., 2011). This age model is only represented by a mean value with no represented error ranges (see Fig. 4.15), also the radiocarbon ages were converted to calendar time using the Weninger & Jöris (2008) calibration curve.

Within Tenaghi Philippon several tephra layers (both visible and crypto) were identified, however relatively few ages have been imported into the Tenaghi Philippon age–depth model produced here from these, the reasons for this are discussed below.

TM-15 was identified within the Tenaghi Philippon sequence, this layer has been correlated to the Y-3 eruption of Keller *et al.* (1978). Zanchetta *et al*. (2008) and Di Vito *et al.* (2008) have suggested that the SMP1-e and VRa deposits represent proximal equivalents of the Y-3 eruption. The VRa deposit has a $^{40}Ar/^{39}Ar$ age of 30,300 ± 200 (Pappalardo *et al.,* 1999) however new geochemical data suggest that

TM-15 may not be the distal equivalent of VRa (Tomlinson *et al.* 2012a), this finding has been also observed within this study (Figs. 6.12 and 6.13) where the VRa displays a bi-modal population which is not a precise match for the TM-15 compositional range. A radiocarbon age range of 30,270 – 31,050 (cal yrs BP) exists for the SMP1-e, however a lack of detailed geochemical data from this layer preclude the import of this age into the Tenaghi Philippon chronology. The age of the TM-15 correlatives in Tenaghi Philippon, TP-970 is 29,350 – 30,150 on the basis of age model B and 29910 cal yrs BP according to the Müller *et al.* (2011) chronology. These ages are older than the LGdM varve age for TM-15 (25,900 – 28,620 yrs BP), attempts were made to import this age into the Tenaghi Philippon chronology, however very low agreement indices corrupted the model overall and meant this imported age had to be removed (see below). The LGdM age being too young is consistent with the observations of Wulf *et al.* (2004) and Brauer *et al.* (2000) who have stated that the LGdM chronology is likely to underestimate the true age of events. TM-15 then cannot at this time be used to increase the robustness of the Tenaghi Philippon chronology, although its use as an isochronous marker is still of value.

Despite the fact the LGdM varve chronology may have a consistent younger offset from real time in terms of absolute dates (which are likely to grow in the older parts of the record); the partial varved nature of the LGdM record does allow high precision differential dating. As an example of this TP-1334 was correlated to LGdM tephra layer TM-18-1d. TM-18-1d underlies the CI (=TM-18) in the LGdM record. TM-18 has a varve age of 34,930 – 38,610 yrs BP which is younger than the $^{40}Ar/^{39}Ar$ age of the CI (39,170 – 39,390 yrs BP; De Vivo *et al.* 2001) mirroring the younger age ranges of TM-15. TM-18-1d is only 590 varve years older than TM-18 (Wulf *et al.*, 2006) and a robust age was produced for this tephra within this study by adding 590 years onto the precise $^{40}Ar/^{39}Ar$ age of the CI (along with the 5% LGdM counting error; see Table 7.1). This age was then imported into the Tenaghi Philippon chronology along with the $^{40}Ar/^{39}Ar$ age of the CI for its correlative in Tenaghi Philippon (=TP 12.87m).

TP 7.61m was interpreted as correlating to the Cape Riva tephra and an age was imported into the age model. An age for the Cape Riva was gained via use of the OxCal ver 4.1 *R_Combine* function, which was used on the three radiocarbon ages available from charcoal fragments directly underlying the Cape Riva proximal deposit (see Table 7.1). This produces an age estimate of 21525 – 22340 cal yrs BP.

The final Tenaghi Philippon age model was produced using the *P_Sequence* model function within OxCal ver 4.1 at 95.4% confidence limits (see section 3.6.1). *Boundary* functions were placed where changes in lithostratigraphy were noted (Müller *et al*., 2011). No dates had to be removed, and the K factor was slowly increased and model re-run until the total model *Agreement Index* ($A_{overall}$ and A_{model}) remained no lower than 60% (as recommended by Bronk Ramsey, 2008). The final model produced an $A_{overall}$ and A_{model} of 60.1 and 60 respectively with most ages having agreement values above 60% (see Table 7.5). A graphical representation of this model is shown in Figure 7.6 compared alongside the Müller *et al.* (2010) age–depth model as described in chapter 4.

From 6 to 14.75m the new age model displays mostly agreement (within error) with the Müller *et al*. (2011) chronology with only minor offsets (e.g. 10.60 m and 11.85 m), because the original chronology does not have an error range it is difficult to estimate how significant these offsets are, they could also be due to the use by Müller *et al*. (2011) of a different calibration curve (Weninger & Jöris, 2008). To illustrate this the radiocarbon date at 10.60 m calibrates to 310 yrs older when the Weninger & Jöris (2008) calibration curve is used. It is unsurprising that the models are similar considering that they are based upon the similar data. What the new model does achieve is the quantification of a 2 sigma error range onto the Tenaghi Philippon LLG chronology and, in particular, constrains the chronology below the CI where the correlative to TM-18-1d essentially forces the chronology through a narrower time window. This has the effect of producing a comparatively slightly younger chronology for Tenaghi Philippon below 14.65m where the Müller *et al*. (2011) age model becomes older due the biostratigraphic tie point to the MIS 4/5 boundary at 19m (73 ka BP; Martinson *et al.,* 1987) this is discussed in more detail below.

7.4.2 Palaeoenvironmental significance

Figure 7.7 shows the Tenaghi Philippon total tree pollen plotted against the Müller *et al*. (2011) age–depth model and the chronology produced here. It is apparent that the new model closely follows that of the Müller *et al*. (2011) chronological scheme but as already mentioned from 43 ka BP and older, the new scheme suggests a younger age. Müller *et al*. (2011) suggest potential correlations between fluctuations within the Tenaghi Philippon pollen record and Greenland stadial and interstadial D–O events

Table 7.5 – *P_Sequence* model statistics for Tenaghi Philippon (TP-2005) showing the, K value used, age information and agreement indices.

TP FINAL AGE MODEL (MODEL C)
K (23)

Amodel =60
Aoverall = 60.1

OxCal Function	Name	Mean Depth	Unmodelled (BP)			Modelled (BP)				
			from	to	%	from	to	%	A	C
R_Date	Poz-15890	0.76	1986	1825	95.4	1988	1829	95.4	98.1	99.7
R_Date	Poz-15891	1.79	4848	4587	95.4	4838	4538	95.4	81.8	100
R_Date	Poz-15894	3.41	6715	6485	95.4	6671	6488	95.4	100.1	100
R_Date	Beta-244646	4.20	7417	7171	95.4	7424	7251	95.4	83.6	100
R_Date	Beta-244647	4.59	8537	8335	95.5	8473	8207	95.4	96.3	100
R_Date	Beta-244650	5.56	10156	9687	95.4	10159	9708	95.5	97.1	99.9
R_Date	Beta-244651	6.15	11602	11200	95.4	11694	11210	95.4	73.6	99.9
R_Date	Beta-244654	6.98	16933	16462	95.4	16948	16520	95.4	102.7	99.9
R_Date	Beta-244655	7.18	20034	19442	95.4	19878	19427	95.4	102	99.9
R_Combine	Cape Riva	7.61	22341	21526	95.4	22375	21589	95.4	102.6	99.4
R_Date	Beta-244637	8.20	24446	23846	95.4	24466	23898	95.4	99.6	99.9
R_Date	Poz-16295	8.86	28539	27809	95.4	28363	27054	95.4	76.6	99.8
R_Date	Beta-244638	9.30	29504	28582	95.4	29370	28575	95.4	95	99.9
R_Date	Beta-244639	9.85	30310	29545	95.4	30370	29693	95.4	103.2	99.9
R_Date	Beta-244640	10.60	32581	31419	95.4	32562	31504	95.4	96.5	99.9
R_Date	Beta-244641	11.25	34400	32162	95.4	34520	33210	95.4	36.5	99.8
R_Date	Beta-244642	11.85	37754	36387	95.4	37300	35722	95.4	108.9	99.8
C_Date	Campanian Ignimbrite	12.87	39500	39060	95.4	39456	39038	95.4	99.9	99.7
R_Date	Beta-244643	13.30	41286	39391	95.4	40292	39698	95.4	69.5	99.9
C_Date	TM-18-1d	13.32	40208	39533	95.4	40345	39775	95.4	73.8	99.9
R_Date	Beta-244644	13.83	42201	40952	95.4	41975	41035	95.4	110.1	99.9
R_Date	Beta-244645	14.65	44595	42801	95.4	44460	43054	95.4	110.5	99.7
R_Date	Beta-246628	15.28	49369	44735	95.4	46756	44487	95.4	105.6	97.2

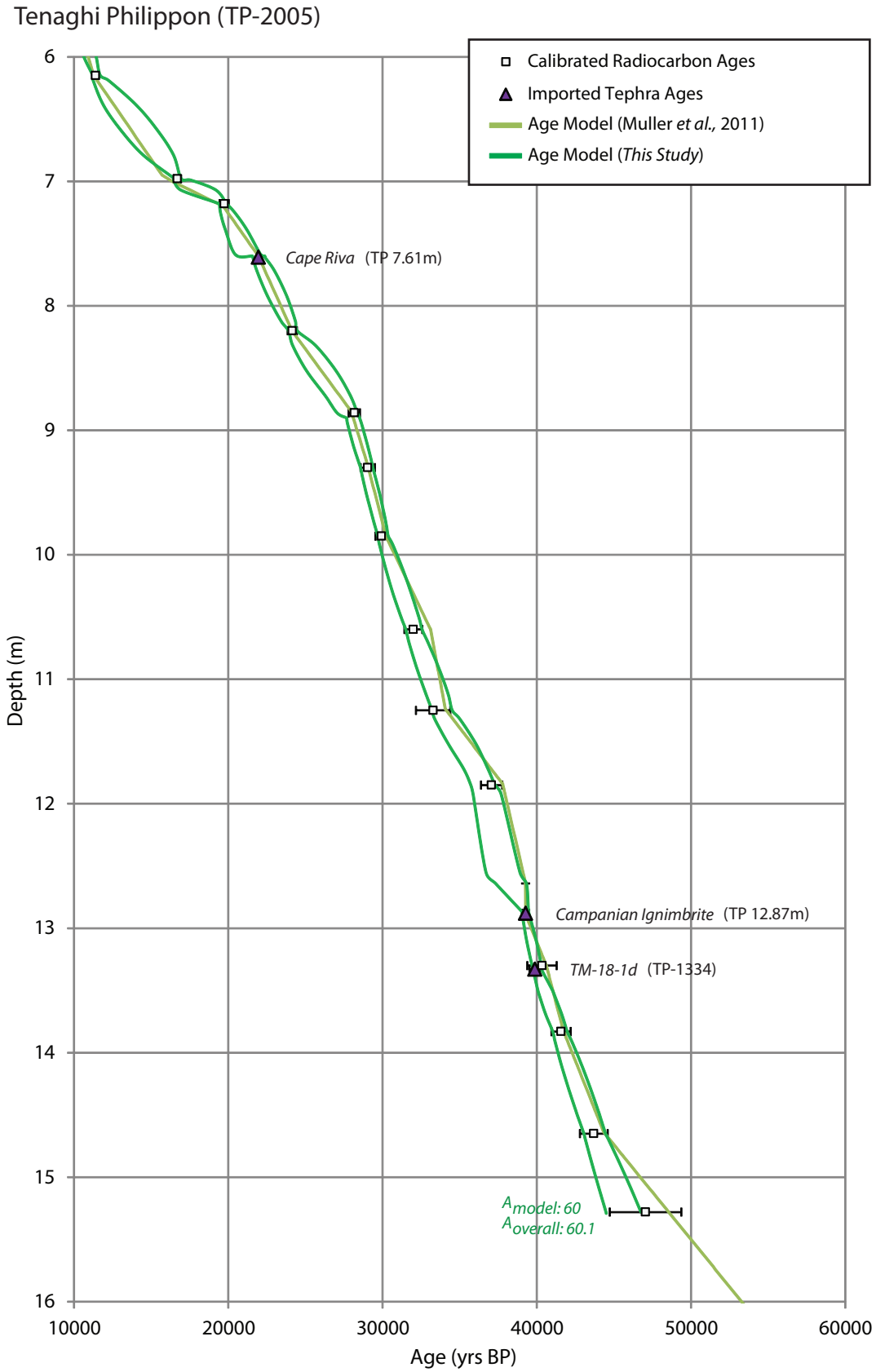

Figure 7.6 – Age–depth plot showing the chronological model developed within this study (at 95.4% confidence limits) compared against the model proposed by Muller *et al.* (2011) in green for Tenaghi Philippon (TP-2005). All radiocarbon ages are shown alongside points where tephra ages have been imported (see table 7.1 for details).

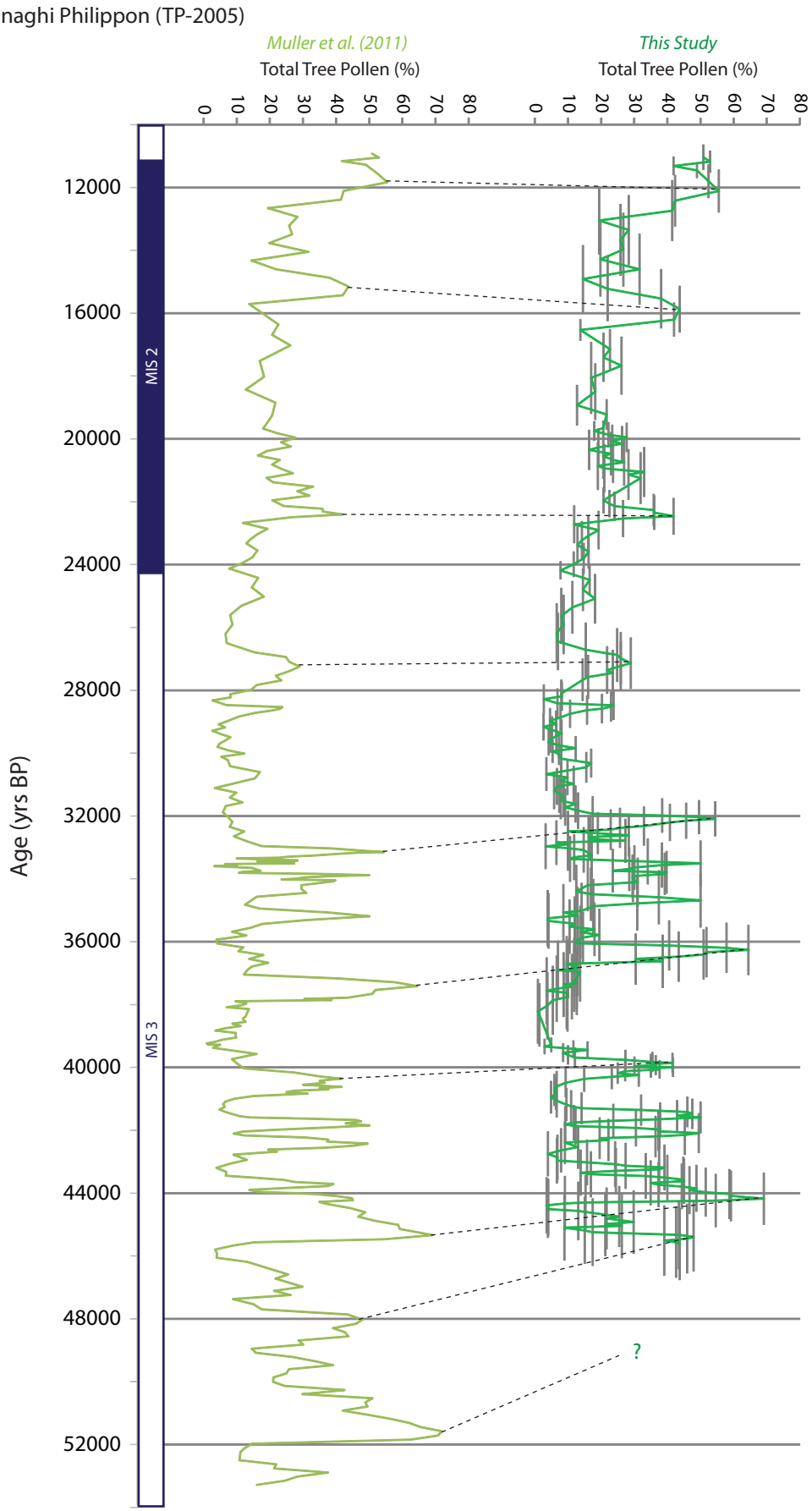

Figure 7.7 – The Tenaghi Philippon (TP-2005) pollen stratigraphy plotted against the Muller *et al.* (2011) chronology and also the age–model proposed within this study. Marine Isotope Stages are also shown (Martinson *et al.*, 1987).

(see Fig. 4.14). The new chronology produced here with 2 sigma error allows a detailed temporal comparison between these correlations, which are shown in Figure 7.8. Ages for the Tenaghi Philippon palaeoenvironmental events were calculated using the *Date* function within OxCal ver 4.1 (at 95.4% confidence limits) and are based upon the depth of the first peak in total tree pollen (as labelled in Fig. 4.14). From Fig. 7.8 it can be observed that most of the Tenaghi Philippon palaeoenvironmental events (TP GIs) lie within age error of their associated NGRIP interstadials (GI-2 to GI-12) when compared on their independent timescales, supporting the suggestion by Müller *et al*. (2011) that these events are associated by a shared climate mechanism. The Tenaghi Philippon palaeoenvironmental event correlated to GI-13 (TP GI-13) however does not temporally overlie this event in the Greenland stratigraphy. Although caution should be taken considering the radiocarbon dates within this part of the core are close to the limit of radiocarbon technique, the import of the ages of the CI and TM-18-1d (derived independently of radiocarbon via $^{40}Ar/^{39}Ar$ and via differential use of the LGdM varve chronology) however highly strengthen this new chronological model. These dates also lie within error of the radiocarbon chronology suggesting cross agreement between these differing chronological techniques. This might suggest that more events can be recognised from the Tenaghi Philippon sequence than within the Greenland event stratigraphy.

7.5 Lesvos (ML-00 and ML-01)

7.5.1 New Age Models

ML-00 Sequence

The shorter ML-00 sequence has two chronologies available from Margari *et al.* (2007) and Margari *et al.* (2009) which are very similar (see Fig. 4.18) and are based upon 14 radiocarbon dates (calibrated using the Fairbanks *et al.,* 2005 calibration curve) and the imported age of the CI tephra (De Vivo *et al.,* 2001). Both these age–depth models are represented as mean curve with no error ranges defined.

In the age model produced here two additional tephra ages have been imported into the sequence for tephra layers TP-978 (=ML00-207) and TP-1450 (=ML00-880). Both these tephra bracket the ML-00 sequence above and below the existing radiocarbon ages. Both these tephra were first defined in the Tenaghi Philippon sequence and

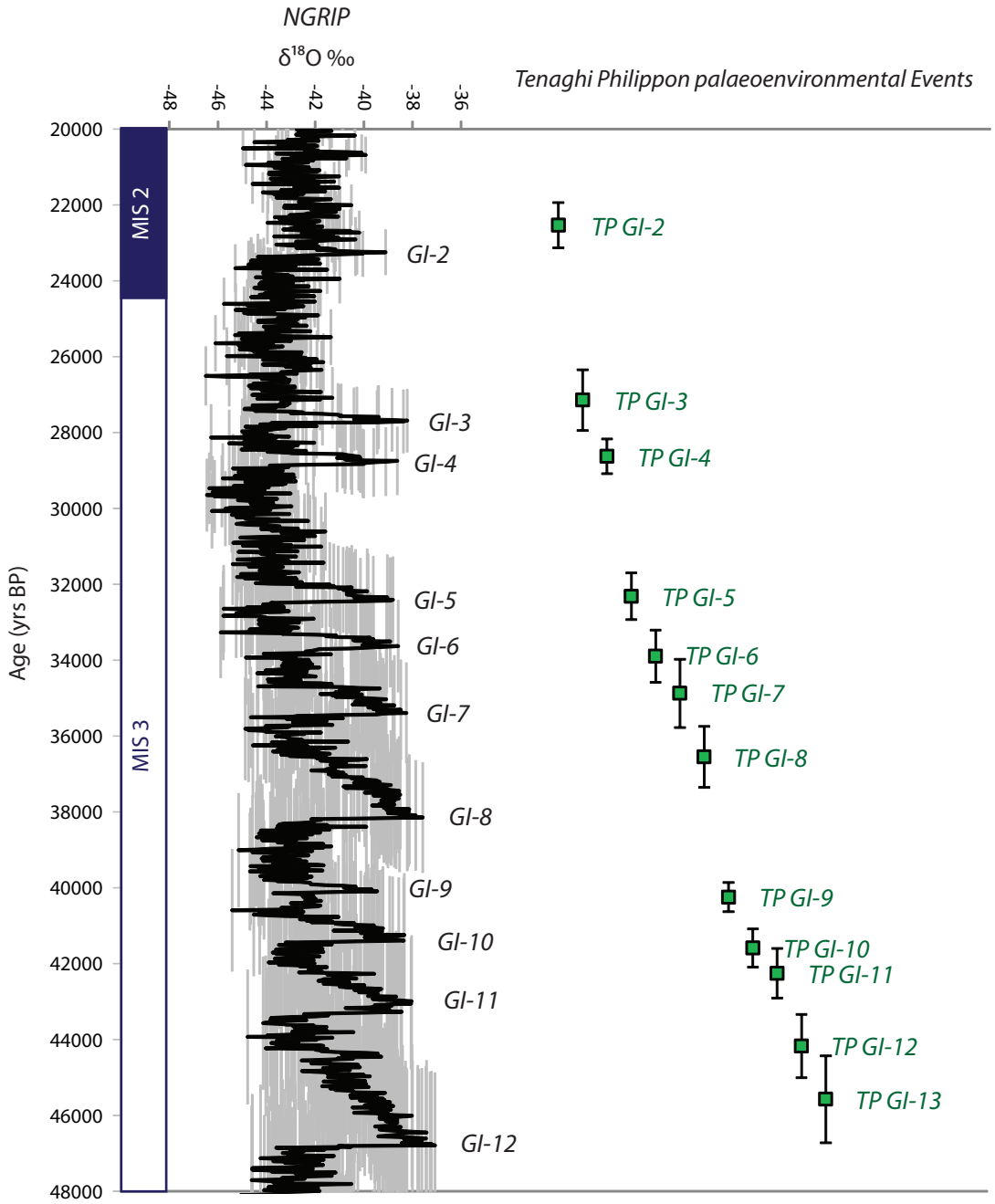

Figure 7.8 – Comparison between events in Tenaghi Philippon (TP-2005) and the NGRIP oxygen isotope record based upon the GGIC05 timescale from Andersen *et al.* (2006) and Svensson *et al.* (2006). Calibrated age ranges for Heinrich (H) events 2, 3, 4 and 5 from western European records (Bard *et al.,* 2000; Sánchez Goñi *et al.,* 2002; de Abreu *et al.,* 2003) (thin lines) and calculated ages (Thouveny *et al.,* 2000) (black boxes). Marine Isotope Stages are also shown (Martinson *et al.,* 1987).

modelled age estimates from this record have been imported (see Tables 6.6 and 7.1). The ML-00 age model proposed here was produced using the *P_Sequence* model function within OxCal ver 4.1 at 95.4% confidence limits (see section 3.6.1). *Boundary* functions were placed where changes in lithostratigraphy were noted (Margari *et al*., 2007). Two dates had to be removed before the model would run due to age reversals (Beta-147750 and SUERC-5862). After this the K factor was slowly increased and model re-run until the total model *Agreement Index* ($A_{overall}$ and A_{model}) remained no lower than 60% (as recommended by Bronk Ramsey, 2008). The final model produced an $A_{overall}$ and A_{model} of 64.6 and 62.5% respectively with most ages having agreement values above 60% (see Table 7.5). A graphical representation of this model is shown in Fig. 7.9 compared alongside the Margari *et al.* (2007; 2009) age–depth models as described in chapter 4.

Compared to the Margari *et al.* (2007; 2009) age models the new chronology proposed here shows that from 2 to 2.5 m a slightly older age range is suggested by the new chronology due to the imported TP-978 age. Although this new 95.4% error range still lies within the age error ranges of the two ML-00 radiocarbon ages between 2 and 3m despite their removal from the final model (see Table 7.6). Between 2.5 to 6.2m relatively good agreement can be observed, with only very slight offsets apparent (e.g. 4.5 to 5.5m). However below ~6.5m a younger age is suggested by the chronological model suggested here which is anchored by the imported age of TP-1450 at the base of the sequence. This would suggest that the infinite radiocarbon determinations above this are probably due to the large ^{14}C errors (c.2000-5000) whereas the two dates between the CI and TP-1450 which do not display infinite age ranges have much smaller ^{14}C errors (c.650). The import of the Tenaghi Philippon age for the TP-1450 essentially help cross-validate the Lesvos chronology.

ML-01 Sequence

The longer ML-01 sequence also has two chronologies available from Margari *et al.* (2007) and Margari *et al.* (2009) which are very similar (see Fig. 4.19) and are based upon 7 radiocarbon dates (calibrated using the Fairbanks *et al.,* 2005 calibration curve) and the imported age of the CI tephra (De Vivo *et al.,* 2001), below this the chronological framework is based upon the ages of GI-14 and 16 (ages from the GISP2 chronology; Stuiver and Grootes, 2000) correlated to palaeoenvironmental events at

Table 7.6 – *P_Sequence* model statistics for Lesvos (ML-00) showing the, K value used, age information and agreement indices.

LESVOS ML-00 FINAL AGE MODEL (MODEL C)
K (3)

Amodel = 62.5
Aoverall = 64.6

OxCal Function	Name	Mean Depth	Unmodelled (BP)			Modelled (BP)				
			from	to	%	from	to	%	A	C
C_Date	TP-978	2.07	30640	29167	95.4	30719	29232	95.4	98.4	99.4
R_Date	SUERC-5863	3.07	33325	30528	95.4	33435	30884	95.4	93.6	99.4
R_Date	SUERC-3019	3.96	38460	33268	95.4	36699	33919	95.4	123.8	99.2
R_Date	Beta-202262	4.26	38753	35069	95.4	37152	35132	95.4	111.1	99.7
R_Date	SUERC-5864	4.65	40162	34474	95.4	37837	35982	95.4	116.6	99.3
R_Date	Beta-147749	4.75	38469	36630	95.4	37838	36520	95.4	110.9	99.4
C_Date	Campanian Ignimbrite	5.63	39500	39060	95.4	39540	39095	95.4	96.9	99.1
R_Date	SUERC-3020	5.65	44111	36511	95.4	39913	38882	95.4	133.7	97.7
R_Date	SUERC-3022	6.17	...	42096	95.4	42560	39710	95.4	23.7	99.7
R_Date	SUERC-3023	6.58	...	40178	95.4	42975	40869	95.4	117.2	99.8
R_Date	Beta-145632	6.96	44054	41905	95.4	43137	41807	95.4	102.2	99.7
R_Date	SUERC-3026	7.44	...	42480	95.4	43514	42081	95.4	51.3	99.8
R_Date	Beta-145631	7.71	43587	41572	95.4	43688	42229	95.4	87.1	99.5
R_Date	Beta-145630	8.68	...	43385	95.4	44876	42872	95.4	68.2	98.8
C_Date	TP-1450	8.80	44796	42030	95.4	44992	42943	95.4	97.4	97

Dates Removed from Model

Name	^{14}C age	Depth (m)	Calibrated (BP) IntCal09 from	to
Beta-147750	24460 ± 150	2.60	29590	28618
SUERC-5862	27167 ± 686	2.20	33325	30528

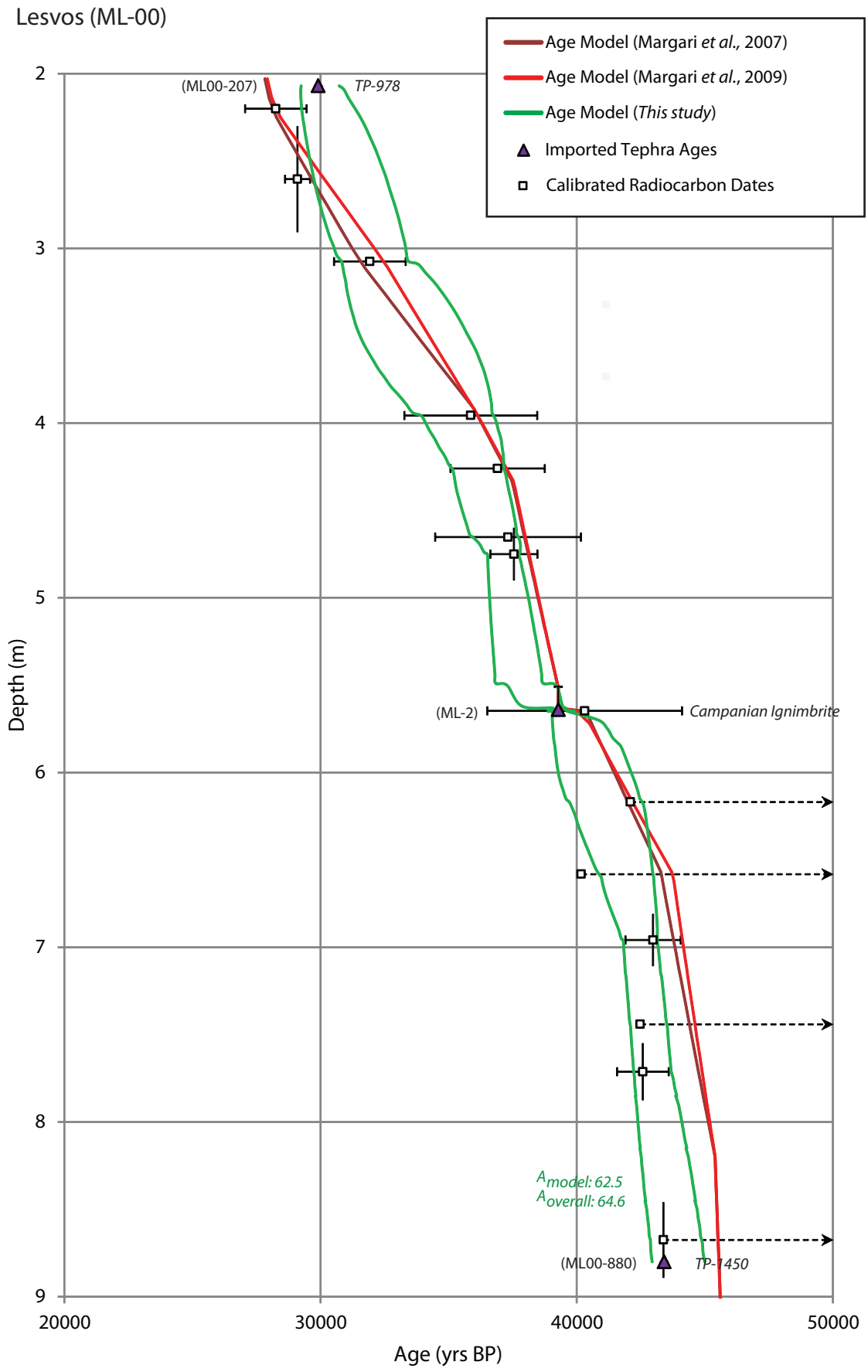

Figure 7.9 – Age–depth plot showing the chronological model developed within this study (at 95.4% confidence limits) alongside those proposed by Margari *et al.* (2007) and Margari *et al.* (2009) for the Lesvos short core sequence ML-00. Visible tephra layers identified by Margari *et al.* (2007) and cryptotephra layers described within this study are also shown (see table 7.1 for details on imported tephra ages).

23.75 and 29.06m respectively in the ML-01 sequence. Both these age–depth models are represented as a mean line with no error ranges defined.

In the age model produced here three additional tephra ages have been imported into the sequence for the Cape Riva (=ML-1), P-11 (=ML-5) and the Kos Plateau Tuff (=ML-6) eruptive events at 7.60, 24.25 and 28.42m respectively (see Table 7.1 for imported tephra age ranges). These provide new independent dates for the lower part of the ML-01 sequence.

The ML-01 age model proposed here was produced using the *P_Sequence* model function within OxCal ver 4.1 at 95.4% confidence limits. One radiocarbon date was removed before the model would run due to it returning an infinite age after calibration (SUERC-3032). The model was first run with a low K factor which was slowly increased and model re-run until the total model *Agreement Index* ($A_{overall}$ and A_{model}) remained no lower than 60% (as recommended by Bronk Ramsey, 2008). The final model produced an $A_{overall}$ and A_{model} of 68.2 and 63.7% respectively with all ages having agreement values above 60% (see Table 7.7). A graphical representation of this model is shown in Fig. 7.10 compared alongside the Margari *et al.* (2007; 2009) age–depth models as described in chapter 4. Compared to the Margari *et al.* (2007; 2009) age models the new chronology proposed here shows agreement between 1.5 to 11m (within errors), below this however a radically older chronology is suggested.

7.5.2 Palaeoenvironmental significance

ML-00 Sequence

Figure 7.11 shows the ML-00 total tree pollen plotted against the Margari *et al*. (2007; 2009) age–depth models and the chronology produced here. It is apparent that the new age–depth framework closely follows the Margari *et al*. (2007; 2009) chronological scheme. It can be observed that the upper and lower parts of the chronology have become slightly offset when compared to the Margari *et al*. (2007; 2009) chronological schemes (within 95.4% confidence intervals). One of the key biostratigraphic chronological tie-points used by Margari *et al.* (2007; 2009) in the construction of their chronology was that of GI-12 at 8.90m (which lies within the ML-00 sequence of the spliced record). Modelling of this depth using the new age model

Table 7.7 – *P_Sequence* model statistics for Lesvos (ML-01) showing the, K value used, age information and agreement indices.

LESVOS ML-01 FINAL AGE MODEL (MODEL C)
K (2) **Amodel = 63.7**
Aoverall = 68.2

OxCal Function	Name	Mean Depth	Unmodelled (BP)			Modelled (BP)				
			from	to	%	from	to	%	A	C
R_Date	SUERC-1287	0.65	1519	1360	95.4	1519	1361	95	100	100
R_Combine			22341	21526	95.4	22467	21650	95	85	99
R_Date	SUERC-5857	1.84	23428	22247	95.4	23249	22029	95	72	99
R_Date	SUERC-5858	2.68	26212	24501	95.4	25578	24315	95	75	100
R_Date	SUERC-5859	3.97	25928	24281	95.4	26287	24812	95	61	100
R_Date	SUERC-5860	5.47	34426	31091	95.4	33960	31060	95	104	100
R_Date	SUERC-3027	6.68	40595	34720	95.4	38238	34591	95	105	100
C_Date	Campanian Ignimbrite	7.60	39500	39060	95.4	39505	39063	95	100	100
C_Combine	P-11	24.25	134443	131723	95.4	134432	131737	95	99.8	96.4
C_Date	Kos Plateau Tuff	28.42	168271	160331	95.4	168284	160089	95	98.3	98

Dates Removed from Model

Name	^{14}C age	Depth (m)	Calibrated (BP) IntCal09 from	to
SUERC-3032	41384 ± 4128	11.63	...	41814

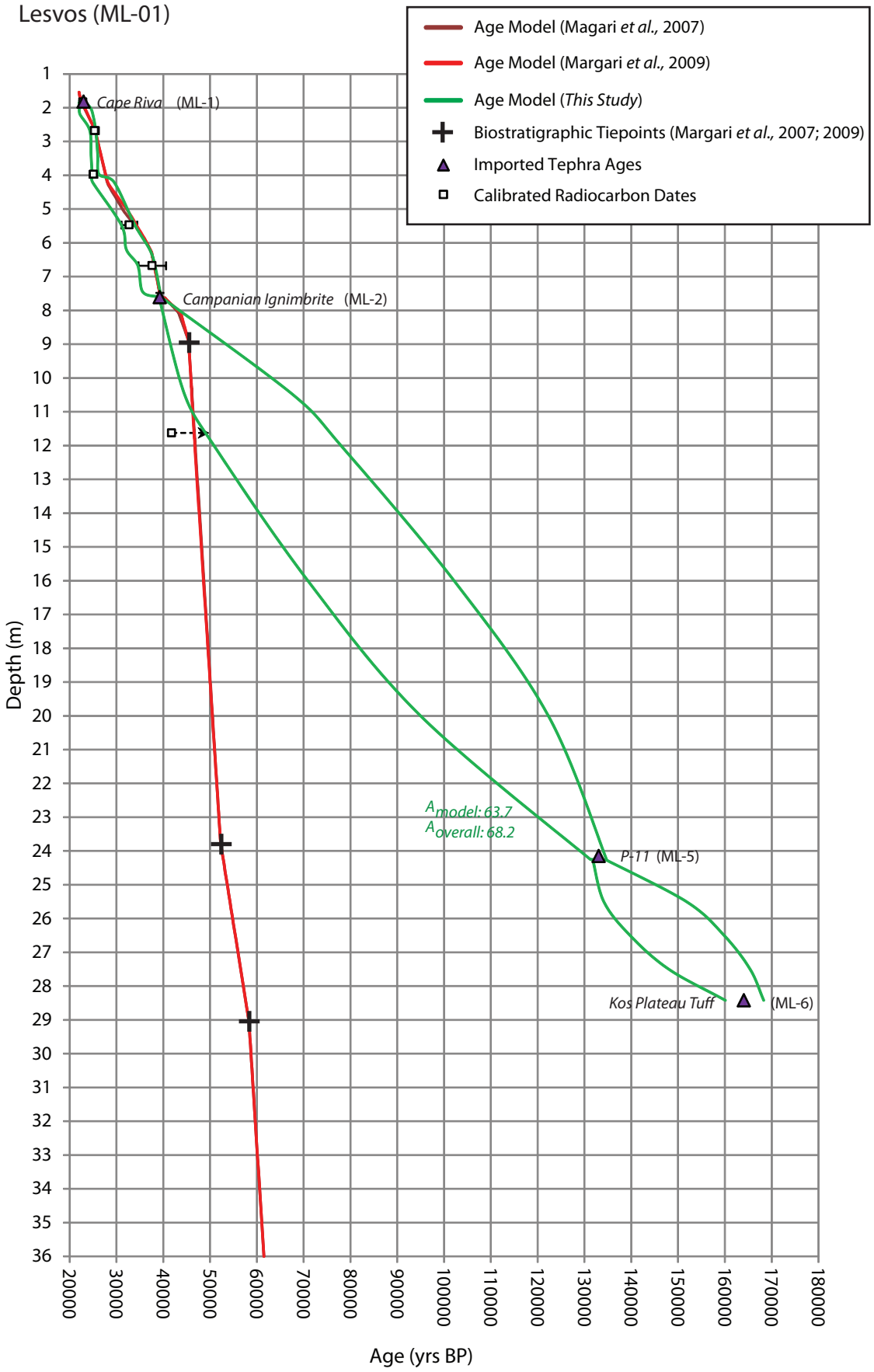

Figure 7.10 – Age–depth plot showing the chronological model developed within this study (at 95.4% confidence limits) alongside those proposed by Margari *et al.* (2007) and Margari *et al.* (2009) for the Lesvos long core sequence ML-01. Visible tephra layers identified by Margari *et al.* (2007) are shown alongside new correlations made within this study (see table 7.1 for details on imported tephra ages).

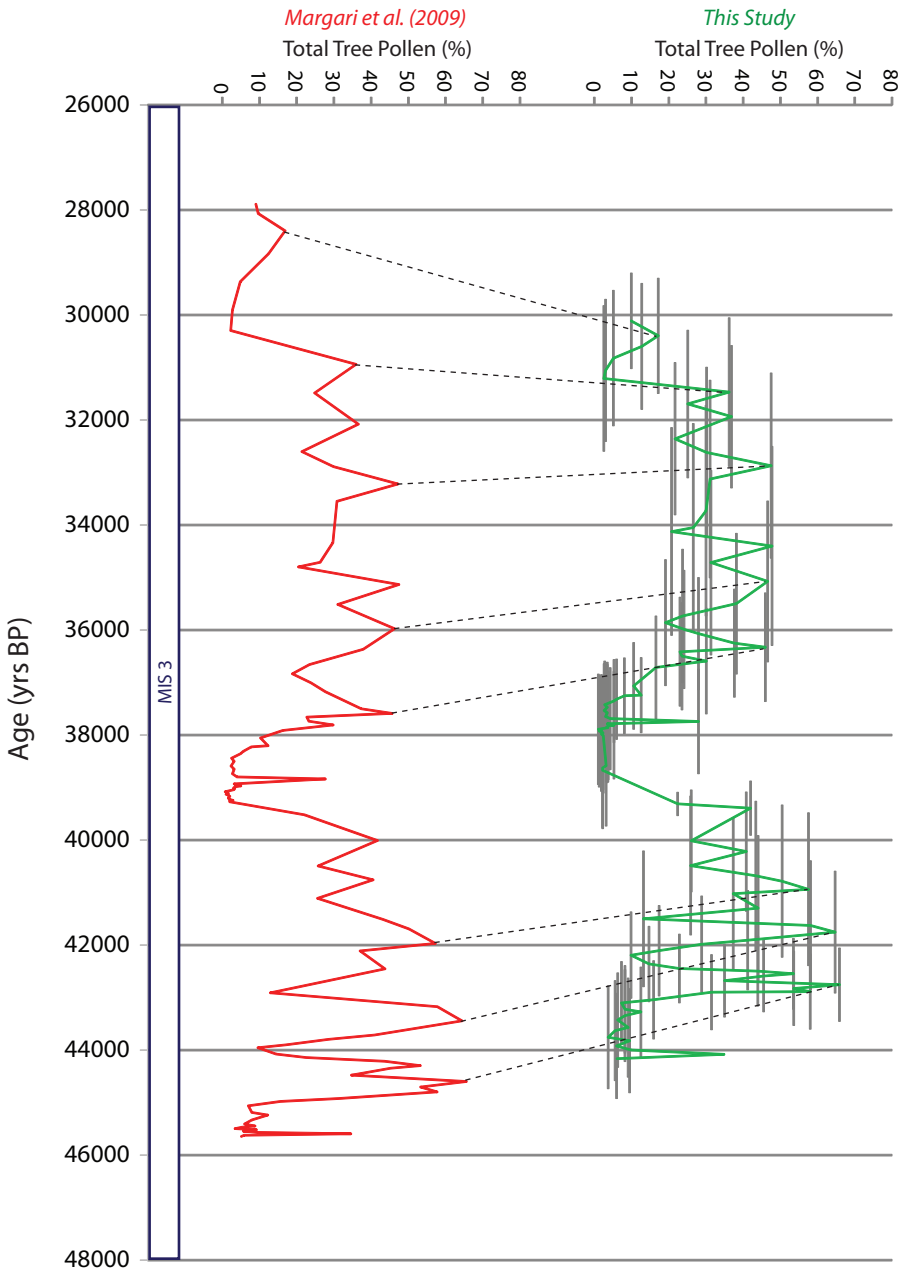

Figure 7.11 – The Lesvos ML-00 pollen stratigraphy plotted against the Margari *et al.* (2007) and Margari *et al.* (2009) chronologies and also the age–model proposed within this study. Marine Isotope Stages are also shown (Martinson *et al.,* 1987).

proposed here compared against the imported age of Margari *et al.* (2009) are shown in Table 7.8. This new age is slightly younger than the imported age of GI-12. Comparisons with the more recent GICC05 Greenland chronology places an age range of 44898-48722 yrs BP for GI-12 (Rasmussen *et al,.* 2008; Svensson *et al.*, 2008) thus the Margari *et al.* (2009) correlation of the pollen event at 8.90 with GI-12 appears to be incorrect on the basis of the new chronology.

Fletcher *et al.* (2010) went further than Margari *et al.* (2009) making further correlations to Greenland interstadials (GIs 3, 4, 5, 6, 7, 8, 9, 10 and 11) for the Lesvos pollen stratigraphy based upon the Margari *et al.* (2009) chronology, these correlations, along with the others made by Margari *et al.* (2007; 2009) will be discussed in more detail in section 7.6.

Table 7.8 – Correlations and imported ages for the ML-00 sequence (Margari *et al.,* 2007; 2009) alongside new age determinations produced within this study.

Margari *et al.* (2009)			***This study***
Pollen Stratigraphic event depth (m)	**Correlation to Greenland event**	**Imported Age**	**Modelled age**
7.80m	GI-12	45400[1]	42270–43820

[1]Ages from the GISP2 chronology (Stuiver and Grootes, 2000)

ML-01 Sequence

Figure 7.12 shows the ML-01 long sequence total tree pollen record plotted against the Margari *et al*. (2007; 2009) age–depth model and the new independent chronology produced here. As previously alluded to beneath 11m, a considerably older age range is suggested, if true this new chronology has non-trivial implications for the lower part of the Lesvos pollen record and the palaeoenvironmental interpretations and conclusions of Margari *et al.* (2009).

Three biostratigraphic tie points form the basis of the original chronology for Lesvos sequence ML-01 below 11m, two of which are based upon correlation of Greenland Interstadial events. The correlations are to the midpoints of the transitions from low tree pollen to high peaks in tree pollen at 23.75 and 29.06m correlated to GI-14 and GI-16 respectively. Table 7.9 shows the imported Greenland ages alongside age ranges

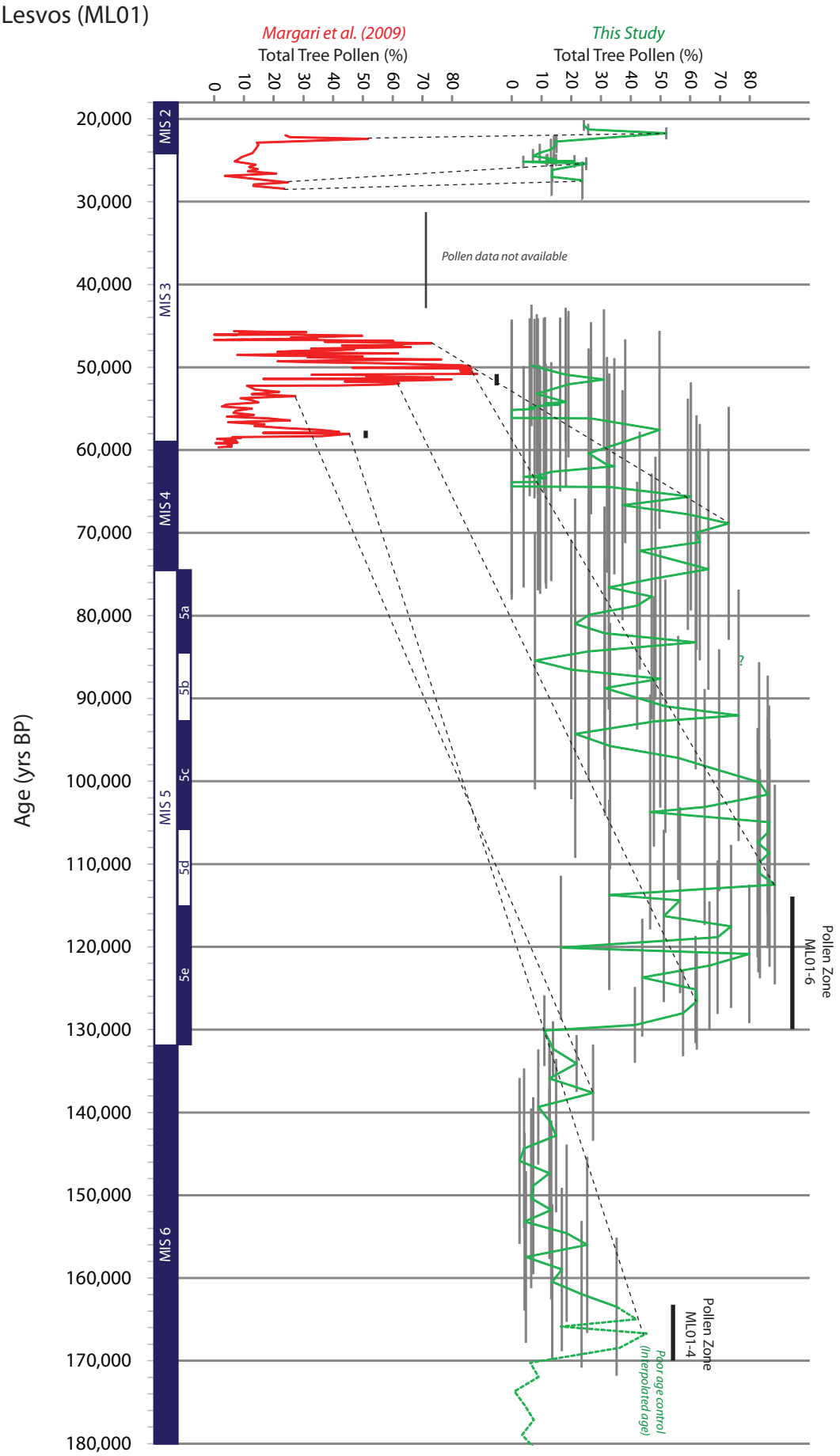

Figure 7.12 – The Lesvos ML-01 pollen stratigraphy plotted against the Margari *et al.* (2007) and Margari *et al.* (2009) chronologies and also the age–model proposed within this study. Marine Isotope Stages are also shown (Martinson *et al.,* 1987).

produced for these depths under the new age–model (at 95.4% confidence intervals). These new ages will now be discussed in terms of their palaeoenvironmental implications.

Table 7.9 – Correlations and imported ages for the ML-01 sequence (Margari *et al.,* 2007; 2009) alongside new independent age determinations produced within this study.

Margari *et al.* (2009)			***This study***
Pollen Stratigraphic event depth (m)	**Correlation to Greenland event**	**Imported Age**	**Modelled age**
8.90m	GI-12	45400	39850-55220
23.75m	GI-14	52250[1]	123870-134190
29.06m	GI-16	58320[1]	164490-173470*
36m	–	61500[2]	>170,000*

[1]Ages from the GISP2 chronology (Stuiver and Grootes, 2000)

[2]Age imported from Ioannina chronology (Tzedakis *et al.,* 2002, 2004)

*Extrapolated age range

Under the new chronostratigraphic scheme 23.75 dates to around 129 ± 5 ka BP, this would place it at the start of MIS 5 (Imbrie *et al.,* 1984). This range is also consistent with age determinations for the start of the Last Interglacial as dated via U-series in the southern European Antro del Corchia Italian Cave system (129 ± 1 ka BP; Drydale *et al.,* 2009). Clearly this age is significantly different to that of GI-14 suggested by Margari *et al.* (2009) which lies within MIS 3. Because of this large conflict it is worth assessing, in detail, if the ML-01 pollen stratigraphy in this part of the core could support an early MIS 5 age range.

Pollen zone ML01-6 is that correlated to GI-14 by Margari *et al.* (2009) and to around MIS 5e under the new chronology presented here and is highlighted in Fig. 7.12. In comparison to the younger pollen zones which are correlated to GI events (e.g. GI-8 and GI-12) ML01-6 has higher percentages of *Junipercus* and *Olea* and in general higher percentages of warm temperate forest species (Fletcher *et al.,* 2010; see Fig 1.4).

Recently Milner *et al.* (*in press*) have presented a new early MIS 5 pollen record from Tenaghi Philippon and describe the early part of the interglacial being dominated by sclerophyllous vegetation (species adapted to drier more seasonal precipitation

regimes) which relates to other evidence of highly evaporative summer conditions. This increase in sclerophyllous vegetation is also present within other southern Mediterranean records suggesting high summer aridity conditions was a southern European wide phenomenon (Milner *et al. in press*). Interestingly pollen zone ML01-6 contains the highest percentages of sclerophyllous pollen taxa (e.g. *Olea*) along with the most diverse range of woody taxa in the whole ML-01 sequence. As previously mentioned *Junipercus* also dominate this part of the pollen record, a taxa adapted to drier conditions. This period is also completely devoid of *Artemisia* probably indicating less cold conditions. After this pollen zone within Lesvos *Pinus* pollen percentages increase, this is in keeping with the early MIS 5 record of Tenaghi Philippon where the sclerophyllous Mediterranean vegetation is replaced by cool mixed forest taxa such as *Pinus* (Milner *et al. in press*).

Another chronological tie point Margari *et al.* (2009) used lower down in the ML-01 pollen stratigraphy is 29.06m (pollen zone ML01-4; see Fig 7.12) to GI-16. The age of this event under the new independent chronological scheme (see Table 7.9) would place it firmly within MIS 6. D–O like tree expansion events have been characterised from pollen records during MIS 6 (Margari *et al.,* 2010; Roucoux *et al.* 2011) and this will be discussed more in Chapter 8. Margari *et al*. (2009) do state that the GI-16 (=ML01-4) expansion, the ML-01 record is of a more subdued nature when compared to some other pollen records (e.g. Tzedakis *et al.,* 2002; 2004).

Finally Margari *et al.* (2009) state that the basal sediments of the ML-01 sequence appear to reflect a highly unstable environment with considerable erosion, which is likely to relate to a lack of vegetation in the surrounding basin. Margari *et al.* (2009) note this conflicts which the suggested MIS 4 age based on their age model, which would suggest widespread vegetation on the landscape; this apparent anomaly is perhaps rectified if these basal sediments instead represent the glacial conditions of MIS 6.

7.6 Significance for the LLG period; comparison between sites

Figures 7.13 and 7.14 highlight the differences between the palaeo-records for the LLG compared with the original and new chronological schemes, the latter proposed in the present study. Also listed are the correlations with GIs and HEs originally proposed for

each record by Tzedakis *et al.* (2004) for Kopais (see Fig. 4.11), Müller *et al.* (2011) for Tenaghi Philippon (see Fig. 4.14), Margari *et al.* (2009) and Fletcher *et al.* (2010) for the Lesvos sequences (see Fig. 4.17) and Pini *et al.* (2010) for Fimon (see Figs. 4.9 and 4.10).

Comparisons with the Greenland event stratigraphy using independent timescales as recommended by the INTIMATE Group (Lowe *et al.,* 2008; Blockley *et al.,* 2012) have already been presented in an earlier part of this chapter, where appropriate (e.g. Figs. 7.3 and 7.8), and are further discussed in section 8.4.5. This section will focus instead only on comparisons between the records under examination in this project. Special consideration is given to tephra layers present in more than one sequence that enable age estimates based on independent dating methods to be imported and that serve as isochronous marker horizons to test the robustness of correlations based on pollen-stratigraphic comparisons.

Only one tephra layer is common to all the records reviewed in this chapter: the Campanian Ignimbrite (CI). This tephra lies within intervals of relatively low total tree pollen in the Kopais, Tenaghi Philippon and Lesvos records, and in a period considered to reflect increased aridity in the Fimon record, indicated by lower percentages of *Picea* (Pini *et al.,* 2010). These events have previously been correlated with HE3 (Kopais), HE4 (for both Tenaghi Philippon and Lesvos) and tentatively to GS-18 or GI-19 for Fimon (but bracketed above and below by palynostratigraphic correlations made with more confidence to GI-19 and GI-17; see Table 7.3). The age of the CI eruption, dated by the $^{40}Ar/^{39}Ar$ method to 39,280 ± 110 yrs BP (De Vivo *et al.,* 2001), strongly supports a temporal relationship with HE4, dated to 39,380 ± 950 yr BP by Thouveny *et al.,* (2000), an association also proposed by others (e.g. Fedele *et al.,* 2008). The identification of the CI as cryptotephra layers in both the Kopais and Fimon palaeo-records demonstrates that there are wide discrepancies in alignment-based correlations; in the case of the Kopais record this is likely to have been caused by misalignment of an HE3-equivalent event with HE4 (see section 7.3.2).

By contrast some palynostratigraphic correlations are confirmed by the new tephra results or made more secure. For example, tephra layers TP-978 and the CI are both present in the Tenaghi Philippon and Lesvos (ML-00) sequences and bracket several palaeoenvironmental events. From this it can be observed that pollen signals related to GI-8, GI-7, GI-6 and GI-5 in both records show a consistency with the tephra layers

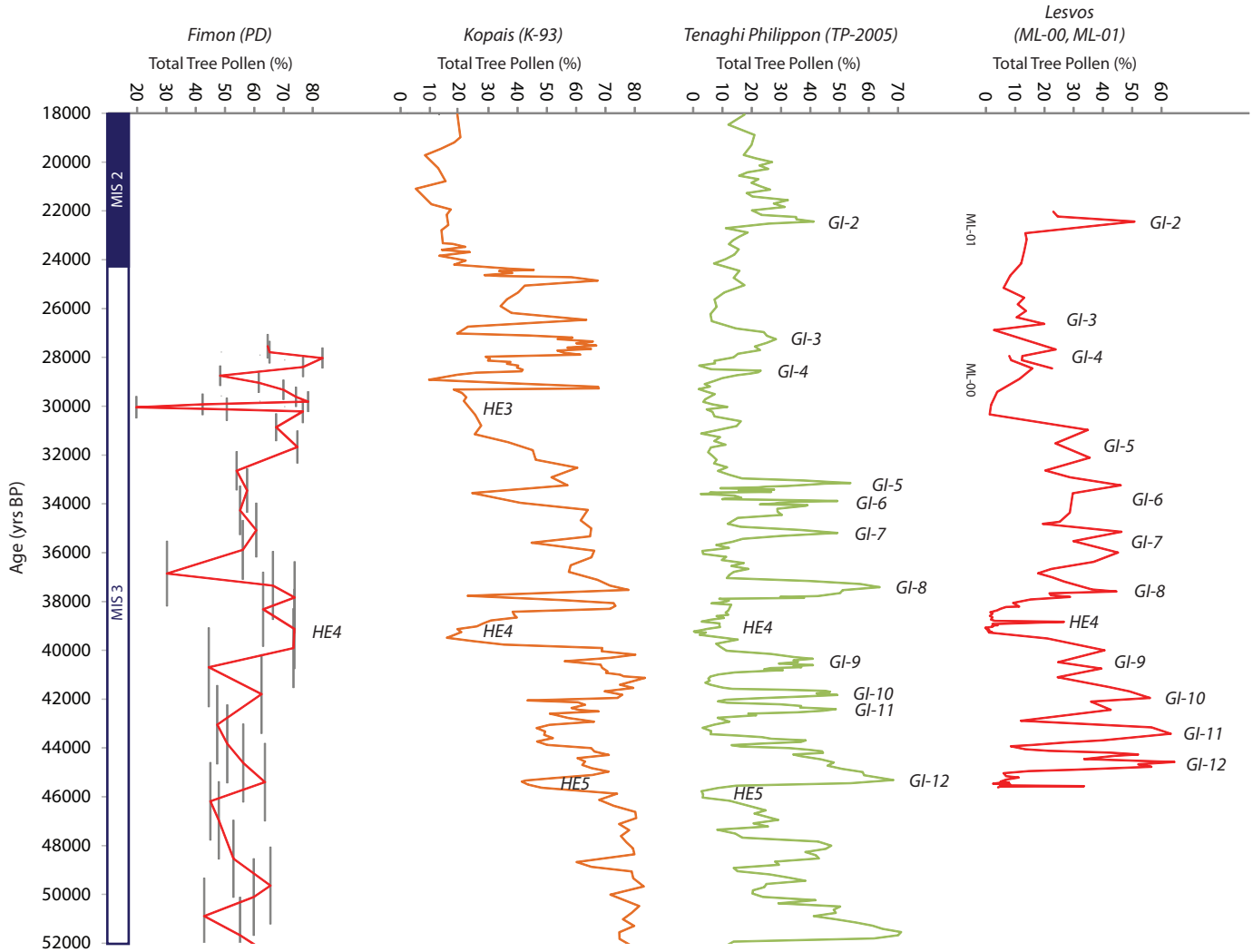

Figure 7.13 – LLG pollen records for Fimon (PD), Kopais (K-93), Tenaghi Philippon (TP-2005) and Lesvos (ML-00 and ML-01) plotted against their original age–depth models (Pini *et al.,* 2010; Tzedakis *et al.,* 2004; Margari *et al.,* 2009 respectively). The colour coding follows that of earlier diagrams. Also shown are correlated GIs and HEs from each record (Pini *et al.,* 2010; Tzedakis *et al.,* 2004; Margari *et al.,* 2009 and Fletcher *et al.,* 2010).

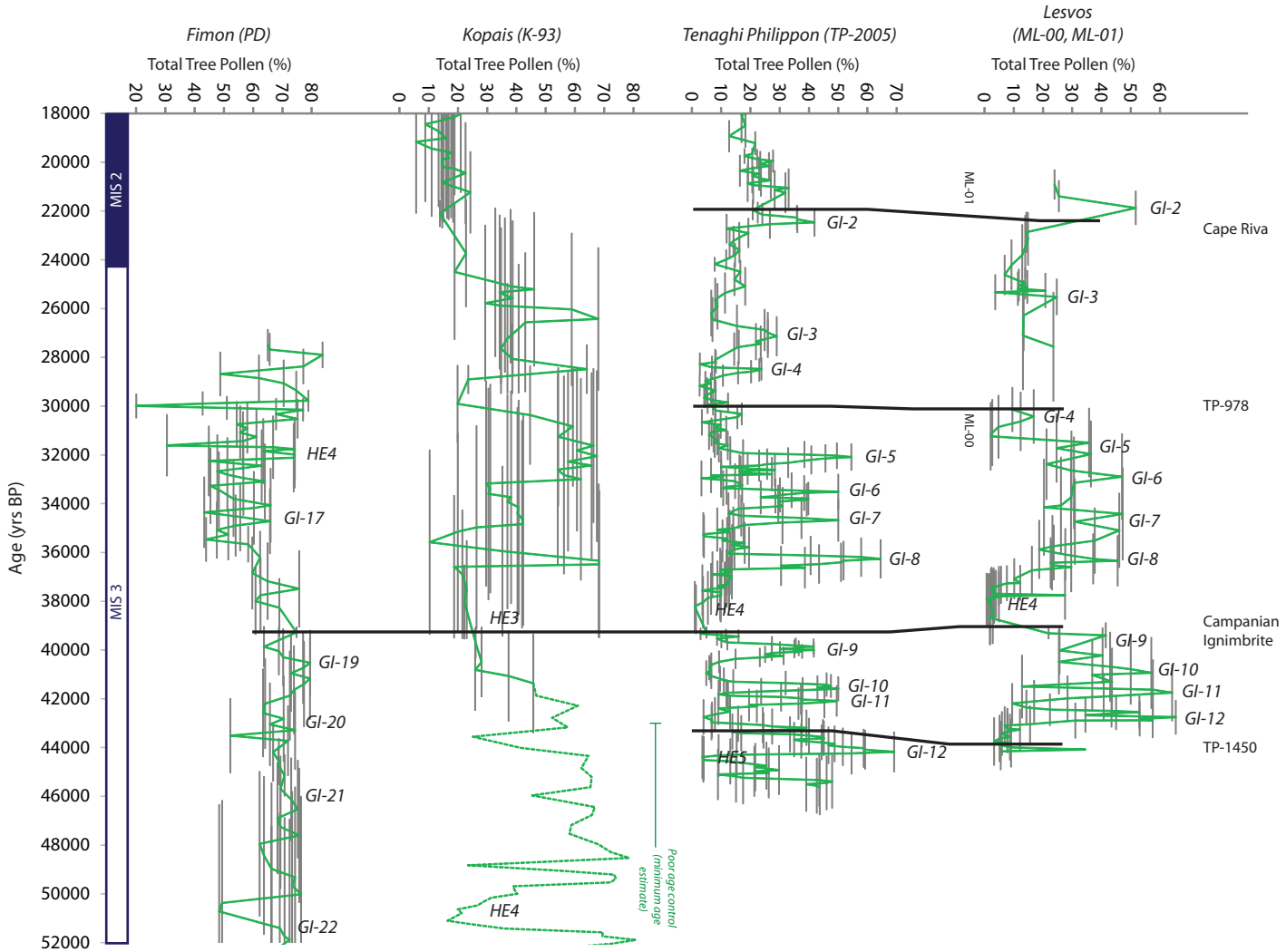

Figure 7.14 – LLG pollen records for Fimon (PD), Kopais (K-93), Tenaghi Philippon (TP-2005) and Lesvos (ML-00 and ML-01) plotted against the age–depth models proposed in this study shown alongside shared tephra layers. The colour coding follows that of earlier diagrams. Also shown are correlated GIs and HEs from each record as shown in Fig. 7.13 (taken from Pini *et al.,* 2010; Tzedakis *et al.,* 2004; Margari *et al.,* 2009 and Fletcher *et al.,* 2010).

and with the independent timescales (within dating uncertainties). Pollen events linked to GI-5 in particular are by far more closely constrained in the new age model (Fig. 7.14) by comparison with original models (Fig. 7.13).

It can also be concluded from the tephra results that GI-4 within the Lesvos (ML-00) pollen stratigraphy cannot equate with the GI-4 event recognised in the Tenaghi Philippon record, because the former underlies and the latter overlies the TP-978 tephra. One or both correlations must therefore be incorrect. Intriguingly, a small peak in total tree pollen percentages occurs beneath the TP-978 tephra layer in the Tenaghi Philippon record, which is not assigned to a GI event by Müller *et al.,* (2010), but which may equate with the pollen assemblage phase assigned to the GI-4 event in the Lesvos record.

Other pollen-stratigraphic features used for correlation occur between the CI and TP-1450 tephra layers. These include pollen-stratigraphic features in the Tenaghi Philippon and Lesvos (ML-00) sequences assigned to GI-9, GI-10 and GI-11 by Müller *et al.* (2011) and Margari *et al.* (2009). These are all temporally indistinguishable and therefore may reflect the same events. However, a pollen-stratigraphic feature assigned to GI-12 lies below the TP-1450 cryptotephra in the Tenaghi Philippon record but above it within the Lesvos record (ML-00 in Fletcher *et al.*,2010). These pollen signals cannot therefore reflect the same event, although both appear to sit in periods where tree pollen is declining into subdued total tree pollen percentages. Note, however, that that the cryptotephra layers in both sites are stratigraphically diffuse (Figs. 5.8, 5.9, 5.14 and 5.15). It is possible that the Lesvos record includes an 'extra' palaeoenvironmental event, or that GI-9, GI-10 and GI-11 are slightly misaligned. This perhaps highlights a point made by Ballie (1991) that there is always a risk of chronological uncertainties smearing relatively short lived events over longer timeframes, perhaps promoting miscorrelation.

The position of the Cape Riva tephra can also be used to constrain pollen events correlated to GI-2 in both the Tenaghi Philippon and Lesvos (ML-01) records by Fletcher *et al.* (2010) and Müller *et al.* (2011). Intriguingly, this tephra lies above the peak in total tree pollen percentages assigned to GI-2 in Tenaghi Philippon but below it within the Lesvos (ML-01) record, possibly suggesting a varying rate of environmental response between the two sites. Caution must be exercised here, however, as there are differences in sampling resolution between the two sites.

7.7 Summary

In summary the Cape Riva, TP-978, CI and TP-1450 tephra layers have allowed abrupt environmental transitions to be 'bracketed' between these isochrones, which has allowed a detailed comparison between, in this case, pollen signals and their suggested correlatives. The new tephra results have also generated new independent chronologies based upon imported radiocarbon determinations and OSL dates (where available) and Bayesian-based age models that are completely independent of biostratigraphic assumptions. All sites have had age–depth models defined using the same calibration curve (IntCal09) and tephra layer age determinations, and have been modelled using the same depositional *P_Sequence* function within OxCal 4.1 (Bronk Ramsey, 2008) (see section 3.6.1). This means that all records are on a common timescale with comparable quantified error ranges, following the recommendations of the INTIMATE Group (Lowe *et al.,* 2008; Blockley *et al.,* 2012).

Of the four pre-existing chronologies examined here, all were originally formed using linear interpolation between age points (both imported via alignment and from direct dating), but only in the case of the Fimon record was an attempt made to import published error ranges, although this was also done in a linear fashion (Pini *et al.,* 2010). It is likely this is due to error ranges being largely unavailable when the original chronologies were put together; NGRIP for example has only recently had age errors defined for GI and GS events within the LLG (Blockley *et al.,* 2012). It is however highly unlikely that accumulation rates do not change between the tie-points (Bennett, 1994) and the age models produced within this study reflect this. It is also apparent that some subtle temporal offsets observed may be artefacts of the use of different radiocarbon calibration curves in this study (e.g. Tenaghi Philippon). In three instances however (Fimon, Kopais and Lesvos (ML-01)) tephrochronological data have demonstrated considerable temporal offsets when compared against pre-existent age models. The potential significance of this is discussed further in section 8.3.1. Finally Tables 7.8, 7.9, 7.10 and 7.11 provide an overview of the pre-existing tephra layer correlations and age determinations (based upon age models A and B (see Fig. 6.2B)) arising from the new results reported in Chapters 6 and 7.

Table 7.8 – Original correlations and ages compared alongside the final correlations and ages of this investigation for Fimon (PD) tephra layers (see Fig. 6.2B for explanation of age models A, B and C). Note text in Italic signifies an imported tephra age; see Table 7.1 for details.

				This Study		
Tephra layer code	**Full depth interval (m)**	**Modelled Age (*Original Study/s*) A**	**Correlation (*Original Study*)**	**Modelled Age with current independent Age Information B**	**Final Modelled Age with imported Tephra Ages C**	**Correlation**
FIM-2042	20.41-20.43	38450-38730	—	30730-33110	30550-33250	—
FIM-2205	22.01-22.06	65580-68130	—	36610-40730	*39060-39490*	Campanian Ignimbrite

				This Study		
Tephra layer code	**Full depth interval (m)**	**Modelled Age (*Original Study/s*) A**	**Correlation (*Original Study*)**	**Modelled Age with current independent Age Information B**	**Final Modelled Age with imported Tephra Ages C**	**Correlation**
KOP-1652	16.50-16.60	21830 (22600)	—	18580-21200	16760-22250	PhT1 or TP726 or Cape Riva
KOP-1759	17.50-17.58	22960 (23770)	—	19530-21830	17670-22420	—
KOP-2317	23.10-23.35	25140 (35095)	—	25570-28400	23800-29440	*Reworked CI?*
KOP-2637	26.30-26.61	27770 (46290)	—	28700-30270	28750-36850	*Reworked CI?*
KOP-2698	26.88-26.99	28020 (48430)	—	28880-30560	29070-37600	*Reworked CI?*
KOP-2763	27.62-27.73	28300 (50710)	—	29110-30880	29650-38470	*Reworked CI?*
KOP-2910	29.00-29.20	28900 (55850)	—	29600-31600	31830-39370	*Reworked CI?*
KOP-3119	30.00-31.19	29400 (61660)	—	30380-32530	*39070-39510*	Campanian Ignimbrite
KOP-3347	33.28-33.73	31770 (66770)	—	31210-33520	*39340-43330*	TM-18-1d or TP-1450
KOP-3900	39.00-39.40	35630 (77330)	—	33480-35780	>41230	—
KOP-4059	40.50-40.59	36570 (79640)	—	34170-36450	>42120	—
KOP-4815	47.90-49.09	41320 (99080)	—		*>47400*	Upper Scoria 2 or Vourvolous
KOP-5678	56.78-56.79	48740 (122100)	—	*N/A*	*N/A*	Unknown Anatolian Eruption?

Table 7.9 – Original correlations and ages compared alongside the final correlations and ages of this investigation for Kopais (K-93) tephra layers (see Fig. 6.2B for explanation of age models A, B and C). Note text in Italic signifies an imported tephra age; see Table 7.1 for details.

Table 7.10 – Original correlations and ages compared alongside the final correlations and ages of this investigation for Tenaghi Philippon (TP-2005) tephra layers (see Fig. 6.2B for explanation of age models A, B and C). Note text in Italic signifies an imported tephra age; see Table 7.1 for details.

				This Study		
Tephra layer code	**Full depth interval (m)**	**Modelled Age (*Original Study/s*) A**	**Correlation (*Original Study*)**	**Modelled Age with current independent Age Information B**	**Final Modelled Age with imported Tephra Ages C**	**Correlation**
TP-707	7.03-7.14	17520	—	16980-19150	16930-19200	PhT1
TP-726	7.22-7.33	20010	—	19520-20500	19510-20480	**TP-726**
TP 7.61[1]	7.43-7.61	21980	Cape Riva	20510-22470	*21590-22380*	Cape Riva
TP-890	8.88-8.92	28100	—	27120-28480	27660-28510	—
TP-896	8.95-9.00	28250	—	27370-28670	27760-28670	—
TP-923	9.20-9.26	28910	—	28370-29230	28380-29250	TM-15
TP-938	9.34-9.43	29250	—	28710-29530	28710-29540	TM-15
TP-951	9.44-9.56	29520	—	28960-29800	28950-29820	TM-15
TP-970	9.68-~9.76	29910	—	29370-30150	29350-30150	TM-15
TP-978	~9.76-9.80	30070	—	29550-30270	29530-30270	**TP-978**
TP 12.87[1]	12.50-12.87	39280	Campanian Ignimbrite	38360-40510	*39040-39460*	Campanian Ignimbrite
TP-1325	13.24-13.27	40450	—	39570-41090	39600-40220	—
TP-1328	13.27-13.30	40550	—	39670-41140	39660-40260	—
TP-1334	13.31-13.35	40700	—	39830-41250	*39780-40350*	TM-18-1d
TP-1354	13.50-13.55	41120	—	40390-41650	40170-41150	—
TP-1392	13.90-13.93	42040	—	41380-42480	41210-42310	—
TP-1450	14.46-14.54	43900	—	42720-44110	42620-44070	**TP-1450**

Table 7.11 – Original correlations and ages compared alongside the final correlations and ages of this investigation for Lesvos (ML-00, ML-01) tephra layers (see Fig. 6.2B for explanation of age models A, B and C). Note text in Italic signifies an imported tephra age; see Table 7.1 for details.

				This Study		
Tephra layer code	**Full depth interval (m)**	**Modelled Age (*Original Study/s*) A**	**Correlation (*Original Study*)**	**Modelled Age with current independent Age Information B**	**Final Modelled Age with imported Tephra Ages C**	**Correlation**
ML-00						
ML00-207	2.02-2.18	27990	—	N/A	*29230-30730*	TP-978
ML-2[2]	5.50-5.63	38600-42110	Campanian Ignimbrite	40870-43370	*39090-39540*	Campanian Ignimbrite
ML00-583	5.80-5.87	40910	—	41070-43370	39120-41600	—
ML00-716	7.04-7.16	44328	—	42180-43660	41910-43300	—
ML00-785	7.73-8.01	45033	—	42380-44130	42300-43900	Upper Nisyros
ML00-815	8.11-8.19	45349	—	42410-44470	42470-44300	Upper Nisyros
ML00-845	8.27-8.64	45461	—	42420-44860	42680-44640	Upper Nisyros
ML00-880	8.70-8.85	45547	—	N/A	*42940-45000*	Upper Nisyros and TP-1450
ML-01						
ML-1[2]	1.80-1.82	22270-23020	Cape Riva	21760-23530	*21640-22470*	Cape Riva
ML-2	7.44-7.60	—	Campanian Ignimbrite	35670-41450	*39070-39510*	Campanian Ignimbrite
ML-3[2]	10.33-10.50	46000 ± 5690	Upper Nisyros	>41600	40380-47930	Upper Nisyros
ML-4[2]	11.89-12.00	46800 ± 5690	Lower Nisyros	N/A	41680-55810	Upper Nisyros
ML-5[2]	24.21-24.25	53600 ± 5690	Green Tuff	N/A	*130370-135780*	P-11
ML-6[2]	28.41-28.42	57580	—	N/A	*155040-171670*	Kos Plateau Tuff

8.0 DISCUSSION

8.1 Iberia as an ash-free zone?

One of the disappointing aspects of this research project was the lack of tephra evidence detected in palaeoenvironmental records sampled from the Iberian Peninsula (Padul and Villarquemado) and it is worth considering why volcanic eruptive products did not appear to have reached this western part of Europe during the LLG. One likely reason that ash from eastern volcanic sources such as the Massif Central and Italian volcanic systems did not reach Iberia is beacause the air circulation patterns were dominated by a strong northwestern component during the LLG (Moreno *et al.,* 2005), as they are today (Barry and Chorley, 1992). This essentially blocks atmospheric transport paths required for transport of ash from east to far west.

The Azores is a volcanic system which lies c.2000 km to the west of the two Iberian sites investigated within this study and that was highly active during the LLG producing multiple caldera-forming eruptions (Moore, 1990). It is unclear why tephra from those eruptions did not reach Iberia although it is possible that the distance is simply too great, although it is worth noting that cryptotephra from Icelandic eruptions has travelled up to 2800 km from source (Lane *et al.,* 2011). It is possible that the prevailing atmospheric circulation patterns in the North Atlantic during the LLG were simply not favourable for transport of ash from the Azores to Iberia. Another important consideration may be the high aridity that is thought to have existed for long intervals during the LLG in Iberia (Moreno *et al.,* 2010). Although still poorly understood it is thought that precipitation may be critical in promoting tephra deposition, as observed by Thorarinsson (1967) in the case of a modern Icelandic eruption. Thus very arid conditions in large parts of the Iberian peninsula during the LLG may have significantly reduced the potential for tephra deposition. The two sites analysed within this study are located in very arid districts today (see Table 4.11). In future tephrochronological studies therefore, it may be more profitable to target regions which experience higher rainfall (e.g. NW and NE Iberia). Also, terrestrial sites probably offer the best chances of detecting cryptotephra fall in the Iberia region, rather than Iberian Margin marine records, where regular IRD deposition are likely to complicate the assessment of pure airfall as against ice-rafted tephra particles.

During the course of this study the Icelandic Eyjafallajökull volcano erupted for 39 days in 2010 with the two most eruptive phases being between the 14–18 April and the 5–6 May (Stevenson *et al.,* 2012). This relatively small (if prolonged) eruption caused havoc to aviation activity and was observed and studied in great detail around Europe. In particular the atmospheric distribution of volcanic ash was modelled throughout the eruption allowing a valuable insight into how ash dispersal may shift with changing eruptive and atmospheric conditions. These findings have implications for the potential of tephra reaching and being deposited in Iberia.

Figure 8.1 shows the predicted presence of the Eyjafallajökull ash cloud at different altitudes between the 14–21 April and the 7–10 of May. Most of the active eruptive period was characterised by low eruptive columns and the tropospheric dispersal of ash. Under these conditions, ash dispersal was multi-directional from Eastern Europe to Greenland and beyond, but did not encroach on to the Iberian peninsula during 14 to 21 of April (Fig. 8.1). However as the eruptive column became more elevated and entrained in the jet stream, the dispersal directions became more uni-directional and passed over the Iberian peninsula between 7 and 10 of May. This modelled ash cloud distribution was confirmed on the ground in Spain by Revuelta *et al.* (2012) who reported large elevations in sulphur dioxide and sulphate between the 6 and 15 of May, that were three times higher than the average level for 2010 above Madrid.

On the 7th and 8th of May, as the main low level ash cloud passed over Spain (see Fig. 8.1) volcanogenic particles were confirmed at ground level in Madrid (Revuelta *et al.,* 2012) though these were very small in diameter (0.1 to 0.7μm), much smaller than the Eyjafallajökull tephra shards found in NW Europe which have reported modal grain sizes of ~25 μm (Stevenson *et al.,* 2012).

This is evidence that volcanic ash may be deposited in Iberia, but suggests it may only fall in very small quantities and size fractions. However, the 2010 Eyjafallajökull eruption was small compared with many late Quaternary eruptions (Davies *et al.,* 2010a) so transport of larger tephra grains sizes during older eruptions cannot be ruled out. In the PhD project 15μm was the smallest mesh size used, but if most tephra fall over Iberia falls within a much smaller particle size range sieves with smaller mesh diameters may need to be employed in future tephrostratigrapical investigations. This has non-trivial implications for both identifying tephra at these small sizes and acquiring geochemical data: as the smallest EPMA-WDS beam size currently available

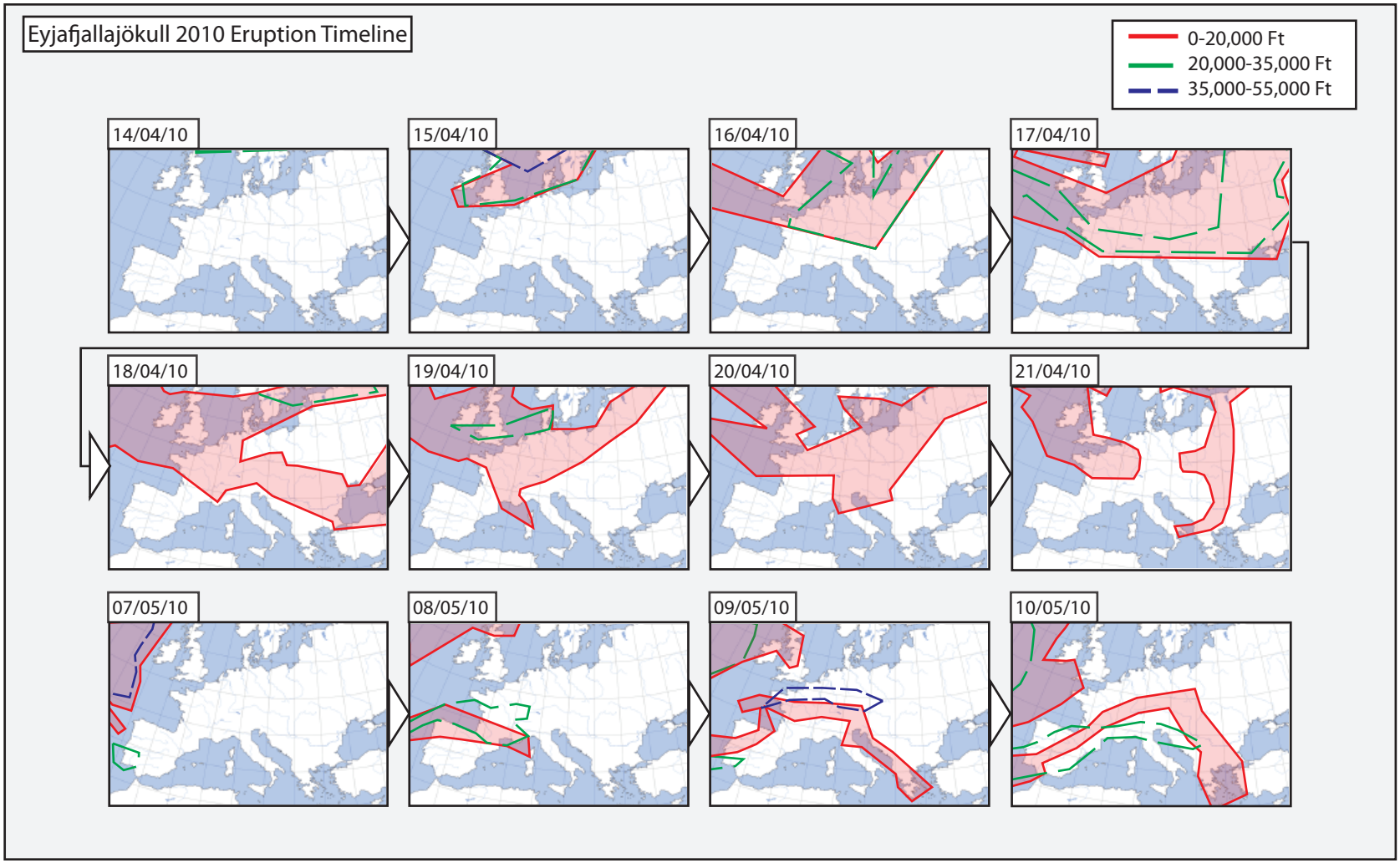

Figure 8.1 – Diagram showing the ash dispersal over Europe between the 14th to the 21st of April and the 7th to 10th of May 2010 based upon simulations by atmospheric dispersal models by the UK Met Office at 0-20, 20-35 and 35-55 thousand feet above ground level. Adapted from Crown copyright data supplied by the Met Office (UK).

is 3μm (Haywood, 2012). It is clear that a more comprehensive and robust assessment of late Quaternary sediment sequences in Iberia may be required to establish the absence or presence of non-visible ash layers more conclusively.

8.2 Significance of results to the tephra lattice

8.2.1 Augmenting the tephra framework of southern Europe

Figure 8.2 highlights how the sites investigated here contrast with those discussed in Chapter 2. From this it can be seen that a number of new tephra layers and terrestrial sequences have been added to the tephrostratigraphic framework which will now be discussed.

Figures 8.3A–C and 8.4 A–C show current reported occurrences of tephra layers taken from the RESET database and literature compared with the new findings of this investigation. The majority of distal occurrences described in this study are largely consistent with, though sometimes extending, the existing distributions. For example the eastward geographic of three Italian tephra layers, TM-15, TM-18-1d and the P-11, have had their eastward geographic range extended by their discovery in terrestrial palaeo-records from the N and NE of the Aegean, demonstrating the value of exploring sequences for cryptotephra content. There are however two notable exceptions, the CI in Fimon and the Kos Plateau Tuff (W–3) in Lesvos (ML-01), which will now be discussed.

The new correlation of the Kos Plateau Tuff (W–3) to tephra layer ML-6 in the ML-01 sequence is one of the first descriptions of this tephra travelling to the north of Kos (see Fig. 8.4C), with its distribution hitherto thought to be primarily to the SW and SE lying within marine sequences positioned to the southeast of Crete (Vinci, 1985) and in the Levantine Basin (Ducassou *et al.* 2007). The KPT (W–3) is present as a visible 1 cm thick layer in the ML-01 sequence and its apparent absence until now to the north of Kos might be an artefact caused by the rarity of records which extend into MIS 6 in this region (e.g. Aksu *et al.,* 2008). The KPT was probably one of the largest, if not the largest, eruptions in the Eastern Mediterranean region during the Quaternary (Allen, 2001; Pe-Piper *et al.,* 2005). There is a strong likelihood that this tephra has a vast geographical distribution, particularly as a cryptotephra layer.

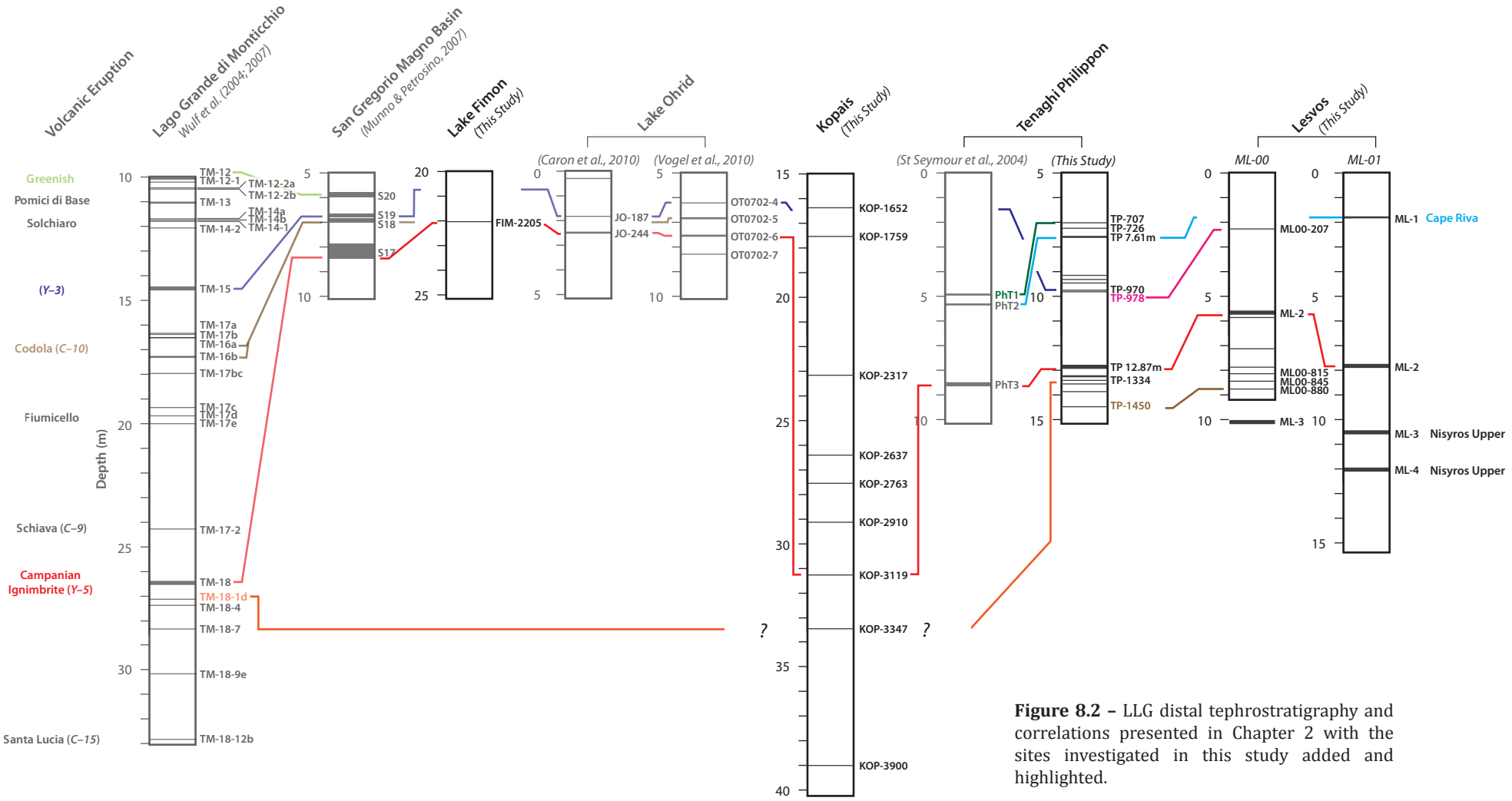

Figure 8.2 – LLG distal tephrostratigraphy and correlations presented in Chapter 2 with the sites investigated in this study added and highlighted.

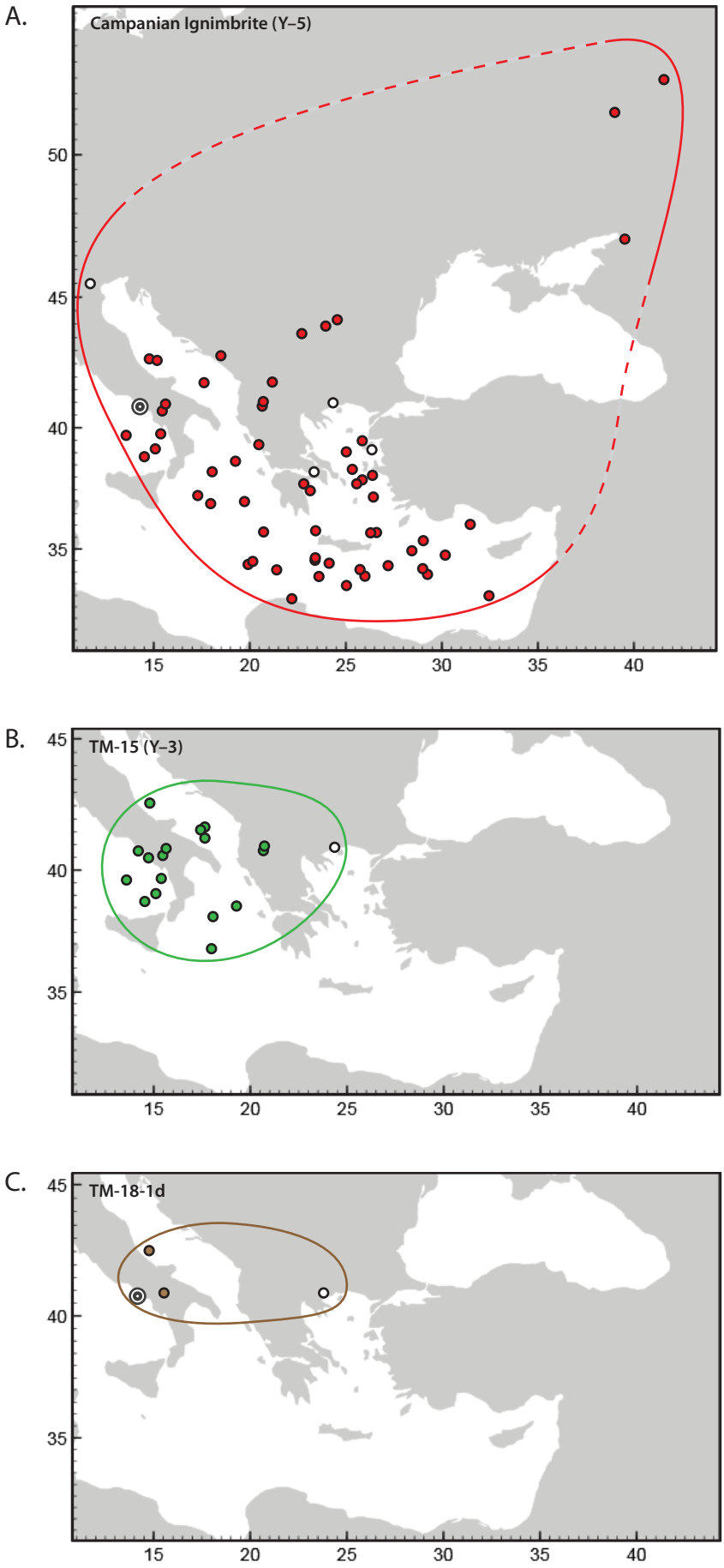

Figure 8.3 –Distal occurrences of selected eruptions based and suggested geographical distribution for (**A.**) the Campanian Ignimbrite (Y–5); (**B.**) TM-15 (Y–3); (**C.**) TM-18-1d. White circles indicate sites investigated within this study and coloured circles are occurrences taken from the RESET database (assessed 05/07/12) the eruption source is also indicated where available.

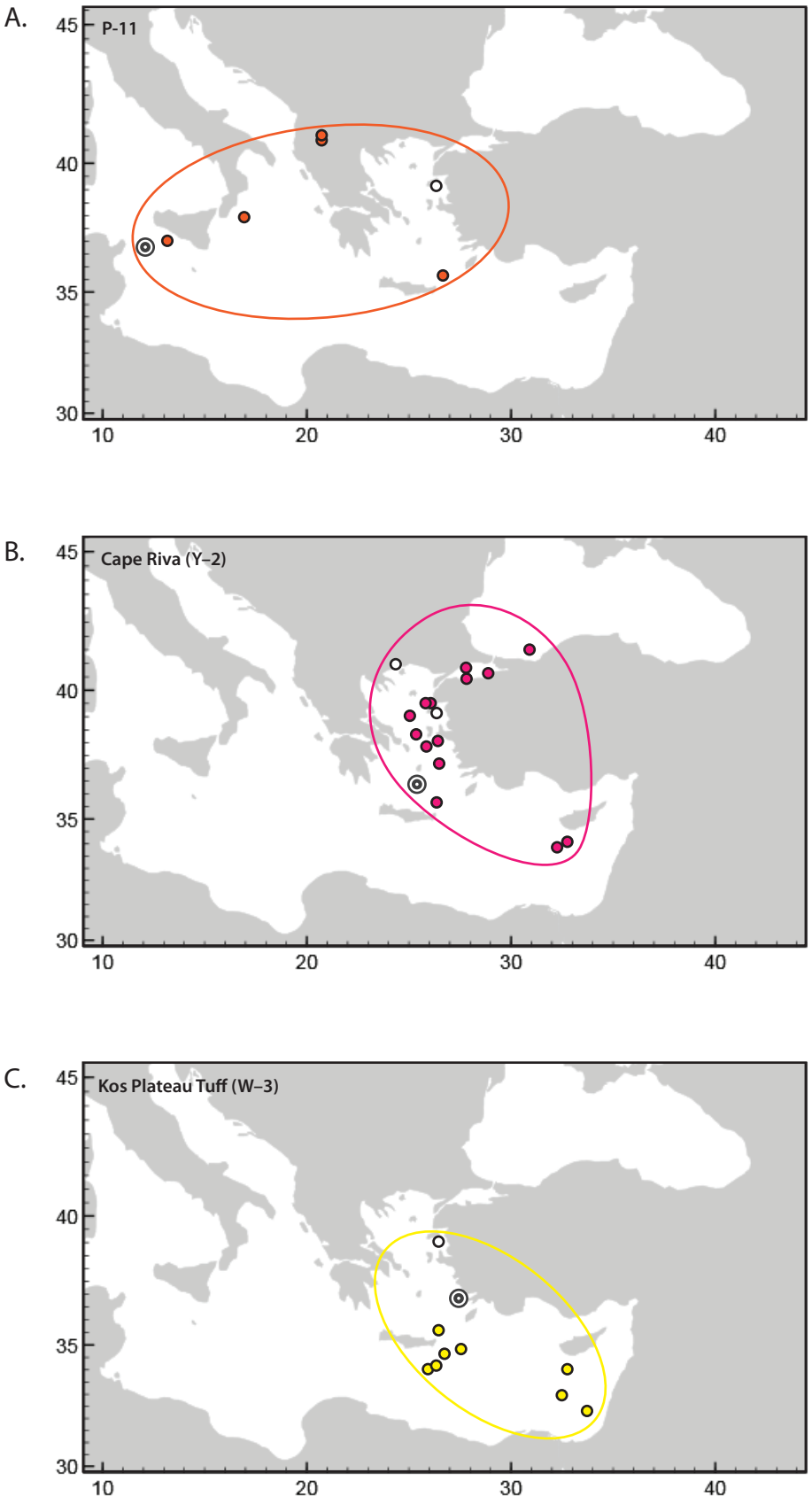

Figure 8.4 –Distal occurrences of selected eruptions based and suggested geographical distribution for (**A.**) P-11; (**B.**) Cape Riva (Y–2); (**C.**) Kos Plateau Tuff (W–2). White circles indicate sites investigated within this study and coloured circles are occurrences taken from the RESET database (assessed 05/07/12) the eruption source is also indicated where available.

The only tephra layer to have been found in all four of the tephra-bearing sequences investigated in this study is the CI, the presence of which was confirmed in both the Tenaghi Philippon (TP-2005) and Lesvos (ML-00 and ML-01) sequences and described for the first time from Kopais (K-93) and Fimon (PD). The presence of the CI in Fimon (NE Italy) is of particular significance as this is the furthest north this tephra has been hitherto discovered in Italy, extending the northward range of this important marker horizon (Fig. 8.3A). It should be noted that the cryptotephra shards corresponding to the CI in Fimon (FIM-2205) are in very low concentration, just 5.37 shards per/g dry wt, which could indicate that a low quantity of volcanic material travelled northwards in Italy to leave a feint imprint. Apart from the CI, only one other cryptotephra layer was identified in the Fimon sequence, FIM-2042, but this tephra remains unidentified due to unsuccessful attempts to obtain geochemical data. Fimon is one of the first sites in the north of Italy to be investigated for cryptotephra content during the LLG, and the results suggest that very few tephra layers were deposited in this region during this timeframe, probably because most Italian eruptions had a predominantly eastward dispersal (see Figs. 8.3A–C and 8.4A). The lack of tephra in Fimon from other volcanic sources lying to the west, such as the Massif Central might indicate either known eruptive events (see Fig. 2.3) were not explosive enough to reach northern Italy or prevailing atmospheric circulation patterns were simply not favourable with the Alps forming a geographical block. While Fimon provides a useful foundation, analysis of other north Italian palaeo-records spanning the LLG is required to further explore and understand the tephrostratigraphy of this region, although Fimon forms a useful foundation.

8.2.2 TM-15; its age relationship to the Y–3

TM-15 was identified in Tenaghi Philippon (TP-970), showing an excellent geochemical match on both major and trace elements (Wulf *et al.,* 2004; Tomlinson *et al.,* 2012a). TM-15 has been related to the Y–3 tephra (Wulf *et al.,* 2004) first described by Keller *et al.* (1978) which has a very wide distribution over the central Mediterranean region and is thought to have originated from Campi Flegrei (Zanchetta *et al.,* 2008). The geographical spread extends to the SW of central southern Italy where it has been found in the Tyrrhenian Sea (Paterne, 1985; Munno & Petrosino, 2004), to the NE in the Adriatic (Bourne *et al.,* 2010) and also to the East in several

palaeo-records taken from Lake Ohrid (Wagner *et al.,* 2008; Vogel *et al*., 2010; Caron *et al*., 2010), located between Albania and Macedonia (see Fig. 8.3B).

Di Vito *et al.* (2008) have suggested that the proximal deposits SMP1-e and VRa represent proximal equivalents of the Y–3 eruption with the VRa outcrop lying within the Campi Flegrei caldera itself and the SMP1-e unit lying further away, over 30 km to the SE. Both these deposits have age determinations with a radiocarbon age from charcoals underlying the SMP1-e deposit giving a calibrated age of 30210–31110 (Di Vito *et al.,* 2008) and direct $^{40}Ar/^{39}Ar$ dating on the VRa unit giving a similar age of 30300 ± 200 (Pappalardo *et al.,* 1999). Geochemical data recently available from the VRa unit (Tomlinson *et al.,* 2012a), has however, demonstrated that this unit is bimodal and does not show a definitive match to TM-15 with significantly different FeO, CaO and SiO_2 values and trace element ratios which do not cover the full geochemical span of TM-15 (see Figs. 6.12 and 6.13). In light of this evidence, which may suggest multiple eruptions in a short timespan, it is worth re-examining distal layers which have been previously correlated to the Y–3 tephra in order to 1) better determine the geochemical homogeneity of these layers and 2) evaluate available independent ages for these layers in the light of the new data produced in the present study. Figures 8.5 and 8.6 show all available geochemical data for layers correlated to the Y–3 and available ages which will now be discussed.

The original Y–3 deposit of Keller *et al.* (1978) shows some similarities with TM-15, but are hard to evaluate robustly as no standard deviation range is available; until this becomes available it is recommended that correlation is not made to this deposit but instead with others where larger datasets are available, such as the LGdM dataset of TM-15 and the VRa proximal deposit (Tomlinson *et al.,* 2012a).

The majority of the other marine deposits all demonstrate reasonable matches with TM-15, except perhaps KET8004 which has some overlap with one component of the VRa. The PRAD 1332 tephra layer from the Adriatic core PRAD 1–2 (Bourne *et al.,* 2010) is very different and has a distinct bimodal population which partly covers one end of the VRa and TM-15 geochemical range which may suggest that this tephra relates to the VRa eruption and not TM-15 as suggested by Bourne *et al.* (2010). Trace elements may be required to robustly correlate this layer. It can be observed that the Ohrid tephra layers correlated to the Y–3 (JO187, OT0702-4, 896-897 cm) also match TM-15 reasonably well on major elements covering the full range displayed by the TM-

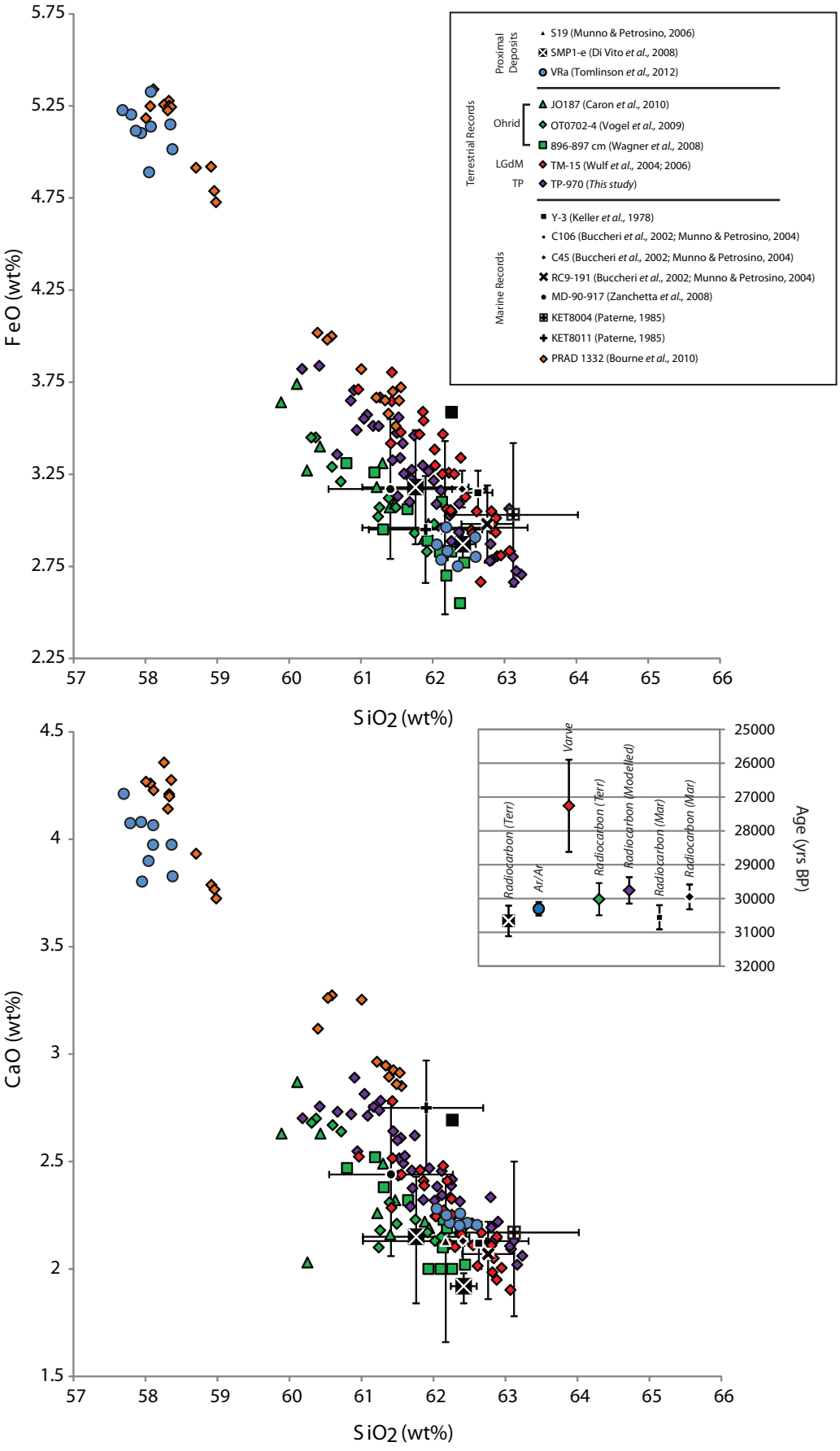

Figure 8.5 – Major element biplots of proximal and distal tephra layers correlated to the TM-15 / Y–3 (see key for references). Where available independent age determinations are also shown, see the main text for details.

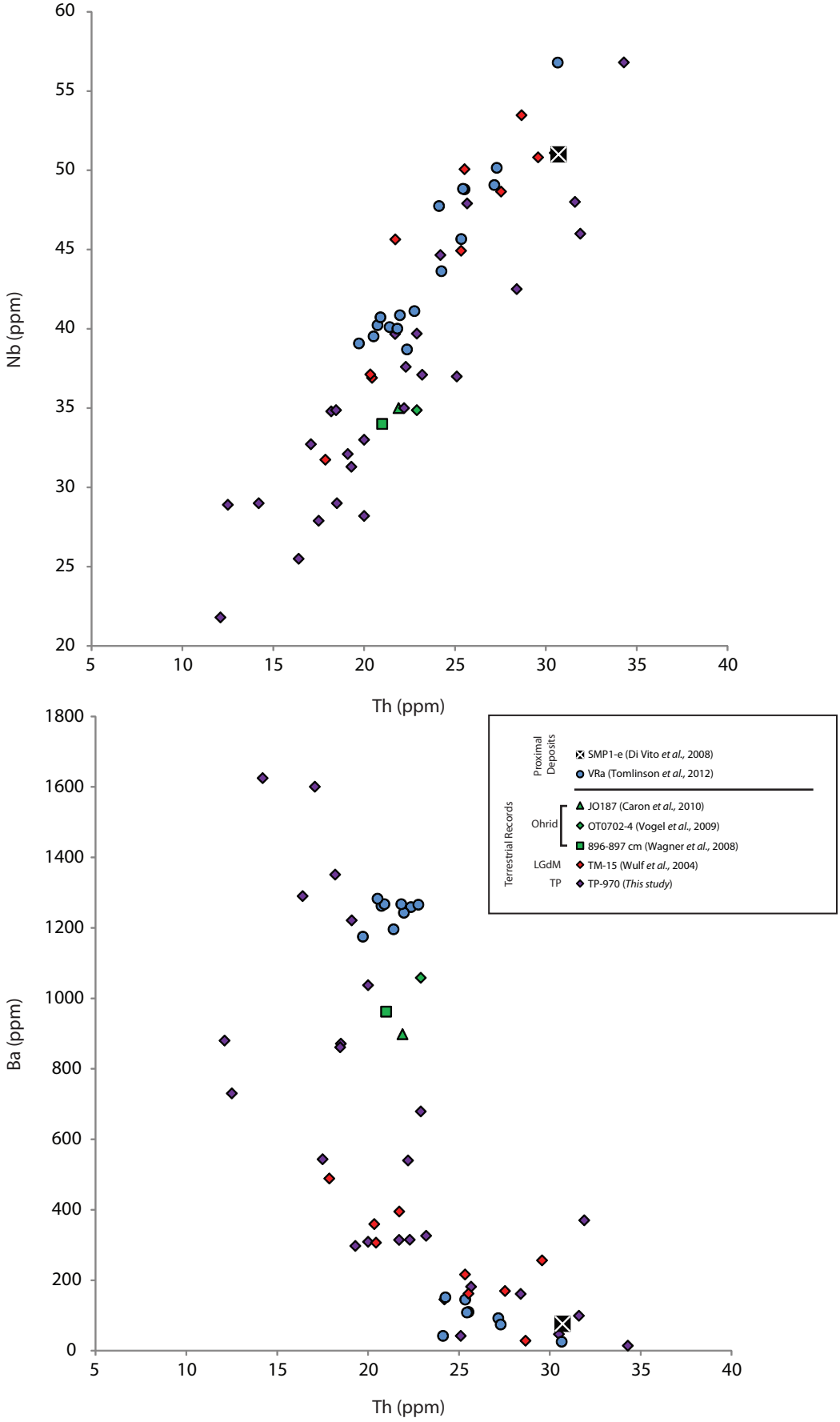

Figure 8.6 – Trace element biplots of proximal and distal tephra layers correlated to the TM-15 / Y–3 (see key for references). Symbols follow those of Fig. 8.5.

15 dataset. The trace elements also show a good match, even if this should be treated with more caution as only bulk glass ICP-MS data are available. Geochemical data for SMP1-e from Di Vito *et al.* (2008) also shows good agreement with the TM-15 data, although a single-grain dataset for this layer is required for a more robust correlation. The geochemical dataset produced within this study from Tenaghi Philippon layer TP-970 (and reworked layers above; see section 6.2.2) currently forms the largest dataset available for TM-15, particularly on trace element data where TP-970 covers the whole range of layers correlated to TM-15 (e.g. TM-15, SPMP-e and the Ohrid layers). One of the most useful trace element plots for distinguishing TM-15 from the VRa is Ba/Th where Ba values of between 200–1000 ppm and Th values of between 10–20ppm are diagnostic of TM-15. Considering the paucity of detailed geochemical data (especially trace elements) for SMP1-e and other tephras correlated with Y–3 that are based on selected individual tephra shards, it is recommended here that correlations are made to TM-15 datasets until better geochemical datasets become available.

There are several independent age determinations available from the distal deposits described above (which do show good matches to TM-15) which will now be briefly described. Two radiocarbon age determinations are available from marine sequences C106 and C45, both of which are located in the Salerno Gulf. Foraminifera underlying these tephra layers were used as the dating material (Buccheri *et al.,* 2002a; 2002b; Munno & Petrosino, 2004). Calibration with Marine09 (Reimer *et al.,* 2009) indicates age ranges of 30200–30910 for C106 and an indistinguishable age of 29580–30320 for C45, but these age estimates should be treated as oldest probable ages for the tephra layer which overlie the dated material, while uncertain marine reservoir offsets may complicate this view. The radiocarbon age for SMP1-e should also be considered a maximal age as the dated charcoals were taken from material underlying this deposit. In contrast, a radiocarbon date from directly above tephra layer OT0702-4 from Lake Ohrid core Co1202 (Vogel *et al.,* 2010) should be treated as a minimal potential age estimate, calibrated using IntCal09 it is 29550–30480 yrs BP. Taking these stratigraphic relationships into account, these age estimates are fairly consistent and are employed in Fig. 8.5. A significant offset is apparent, however, between these ages and the LGdM varve age for TM-15 which is significantly younger (27,260 ± 1360 yrs BP). This can be viewed as further evidence that the LGdM varve chronology is apparently 'missing' years, confirming the view of Brauer *et al.* (2000) that the LGdM chronology is likely to underestimate the true age of events.

A very robust modelled age of 29370-30150 yrs BP for TM-15 has been obtained in this study from the Tenaghi Philippon sequence (=TP-970); unlike the other age estimates outlined above, the TP-970 age is defined on the basis of radiocarbon ages obtained from both below and above the tephra. This probably represents the most robust age estimate currently available for TM-15 and corresponds well with other estimates, being either indistinguishable at 95.4% confidence limits, as with layers OT0702-4 and C45, or slightly younger when compared against oldest possible ages of SMP1-e and C106. All these ages can be visually compared in Fig. 8.5.

All the above age estimates of TM-15 are based upon radiocarbon dating, however, which has inherent uncertainties, particularly with respect to the reliability of the calibration for this timeframe (see section 1.3.1). It is worth noting, nevertheless, that the radiocarbon based age for the CI in Tenaghi Philippon (38360–40510) is in very good agreement with the $^{40}Ar/^{39}Ar$ age of the CI determined by De Vivo *et al.* (2001; 39,280 ± 110). It is however preferable that an age estimate that is independent of radiocarbon is also gained for the TM-15 layers, in order to test the age ranges outlined above. More complex Bayesian age modelling incorporating all or most of these age estimates should also be performed in future studies, when additional data become available, using the approach demonstrated for younger eruptions by Blockley *et al.* (2007b).

Finally the age of TM-15 is similar to independent age determinations of the HE3 (c.31; Thouveny *et al.,* 2000) and indeed Watts *et al.* (1996) concluded from their analysis of the LGdM sequence that tephra TM-15 (=L10 in Watts *et al.,* 1996) marked the beginning of an arid period which they equated with the onset of HE3. This relationship is discussed further in section 8.4.3.

8.2.3 Pre-CI Campi Flegrei tephra layers TM-18-1d and TP-1450

Campi Flegrei tephra layers predating the CI were discovered in three sequences, Kopais, Tenaghi Philippon and Lesvos (TP-1334, TP-1450, KOP-3347 and ML00-880). Other layers underlying the CI were also discovered in Tenaghi Philippon though these have chemical signatures indistingushable from the CI and probably represent downward reworking of the overlying visible CI tephra.

On the basis of their geochemical match, TP-1334 was correlated to the LGdM layer TP-18-1d. The older ML00-880 was correlated to TP-1450 on the basis of both geochemistry and stratigraphy, apparently this is the first discovery of this tephra (see section 6.2.3 and Fig. 6.25) with no apparent correlative from reference dataset used within Chapter 6 (see section 6.1.2). It remains unclear if KOP-3347 represents TP-18-1d or TP-1450, though this might be resolved by acquisition of trace element ratios for this layer. Both TM-18-1d and TP-1450 are indistinguishable on major elements but importantly may be distinguished from the overlying CI on the basis of both major and trace elements, with trace elements allowing unmistakable distinction.

Only in Tenaghi Philippon are both these tephra layers represented (sitting 1.16m apart) and trace elements obtained by SIMS analysis are available for both TP-1334 and TP-1450; the data suggest that these two layers may be separated on certain trace element biplots (e.g. Zr vs U/Th and Zr vs Y plots).

During the course of this study, as it became apparent that these pre-CI Campi Flegrei eruptions could be detected distally, samples were gathered from other sequences for trace elemental composition measurements (major elements were largely available) in an attempt to better correlate and geochemically define these layers. Figure 8.7 shows schematics of these sequences, their locations, tephrostratigraphic details and the layers analysed as part of this study (denoted with an asterisk), the key points being as follows.

Cryptotephra layers PRAD 1752 and SA03-03-427 from Adriatic marine sequences PRAD1-2 and SA03-03 have both been correlated to TM-18-1d by Bourne *et al.* (2010) and Bourne (2012) and trace elemental data was acquired in the present study. Major and trace elemental data were also obtained from LGdM layers TM-18-1d and TM-18-4, both interpreted to originate from CF (Wulf *et al.,* 2006; S. Wulf, *pers. comm.*) as part of this study (data presented in chapter 6). LGdM tephra layer TM-18-12b is also interpreted to originate from CF although no trace elements are currently available for this layer. The proximal Pre-CI volcanostratigraphy is perhaps best defined at the Trefola and SMP1 localities (Pappalardo *et al.,* 1999; Di Vito *et al.,* 2008) although geochemical data from the glass component is currently scarce with only the largest eruptive units having been analysed: TLf, TLc, TLa from Trefola (Tomlinson *et al.,* 2012a); and SMP1-a from SPM1 (Di Vito *et al.,* 2008). Figures 8.8 and 8.9 show geochemical biplots of all the tephra layers and units described above.

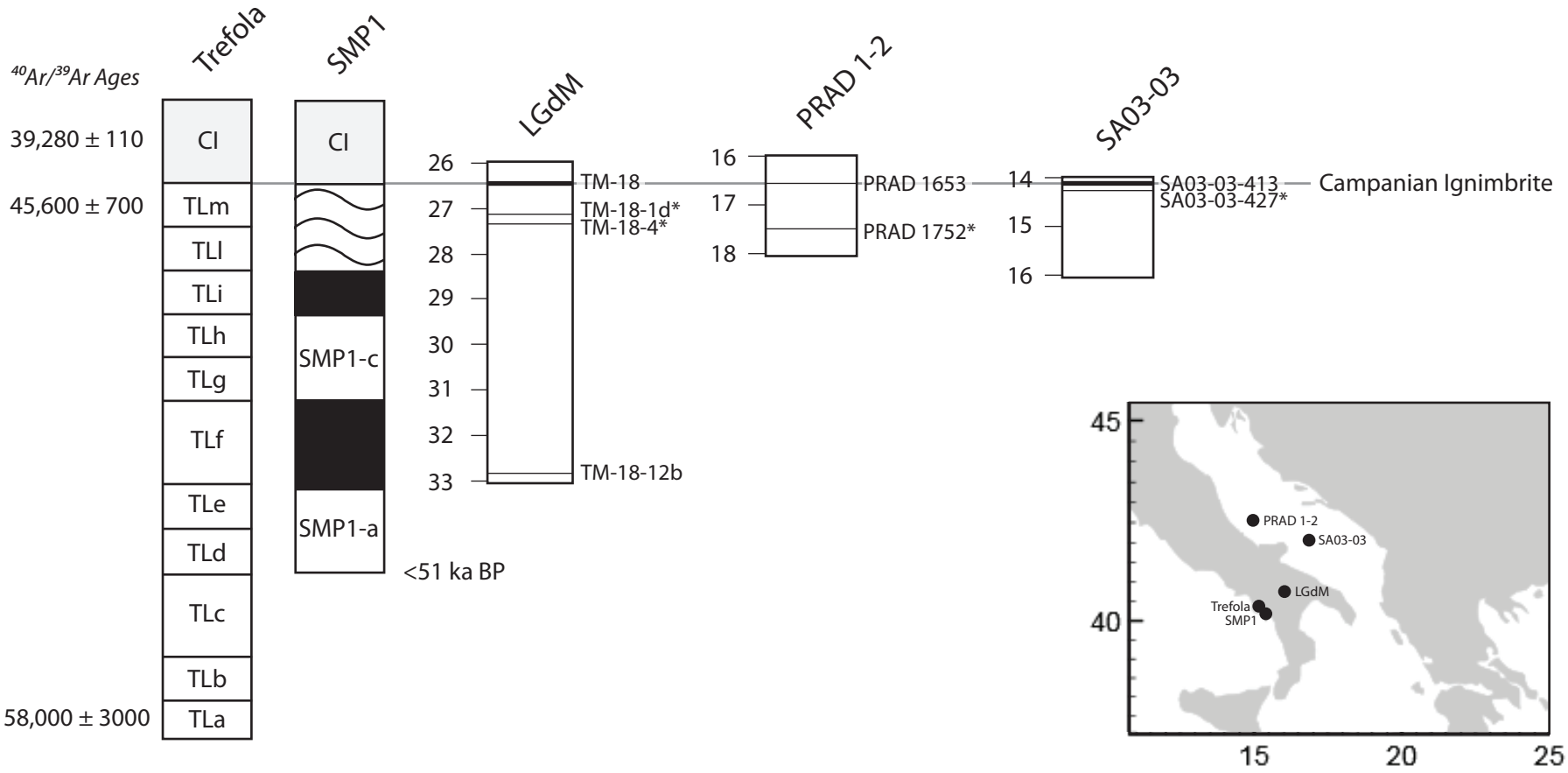

Figure 8.7 – Pre-CI tephrostratigraphy of proximal and distal records taken from Pappalardo *et al.* (1999); Di Vito *et al.* (2008); Bourne *et al.* (2010) and Bourne (2012).

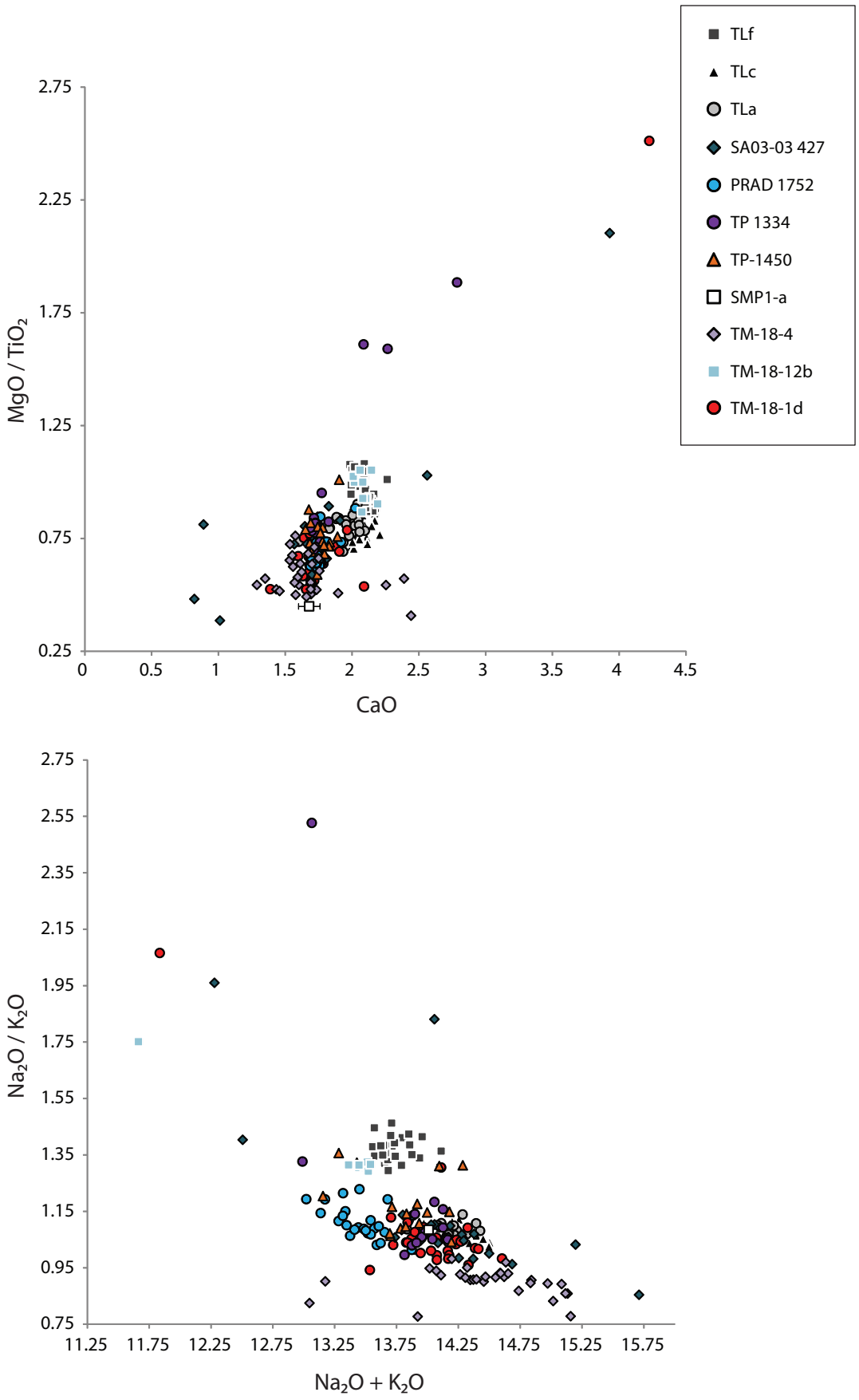

Figure 8.8 – Major element biplots of proximal and distal tephra layers /units which sit below the CI. Data from: Wulf *et al.* (2006); Bourne *et al.* (2010; Bourne (2012); Tomlinson *et al.* (2012a) and this study.

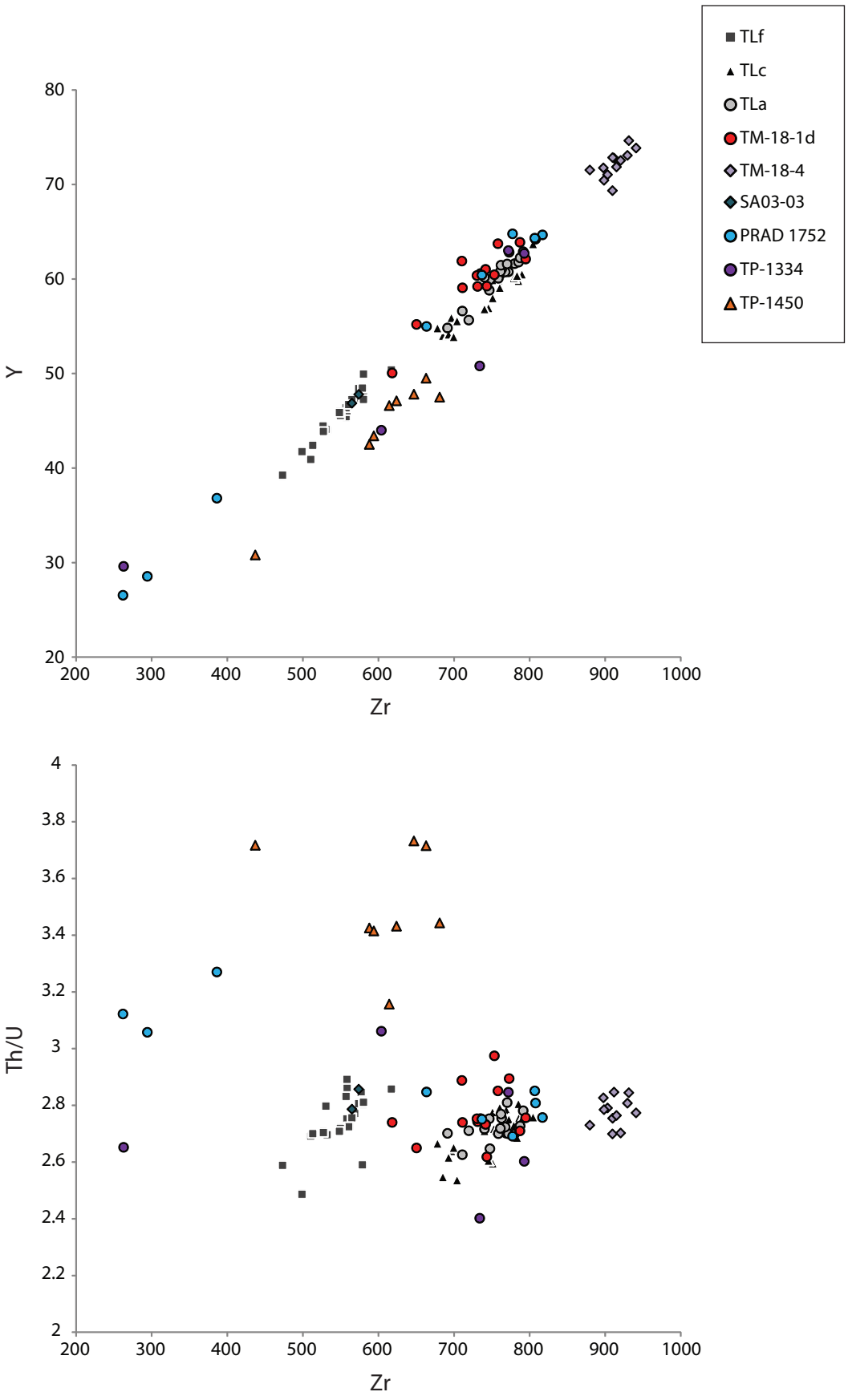

Figure 8.9 – Trace element biplots of proximal and distal tephra layers /units which sit below the CI. Symbols follow those of Fig. 8.8. Data from: Tomlinson *et al.* (2012a) and this study.

From these data it can be ascertained that the PRAD 1752 tephra layer of Bourne *et al.* (2010) demonstrates a good match to TM-18-1d and its correlative TP-1334 on both major and trace elements, confirming the interpretations of Bourne *et al.* (2010). SA03-03-427 by comparison, although overlying the geochemical range of TM-18-1d on major elements (despite a more scattered distribution), does not show affinity to the TM-18-1d geochemical range when trace elements are compared. The new trace elements from SA03-03-427 then cast doubt on the Bourne (2012) correlation of this layer to TM-18-1d.

TM-18-4 and TM-18-12b both underlie TM-18-1d and are separated in LGdM by 1240 and 12050 varve yrs respectively (see Table 6.2 for details). Both TM-18-4 and TM-18-12b have alkali ratio values which allow geochemical distinction from TM-18-1d on major elements. Further to this TM-18-4 has a very distinctive trace element composition (e.g. very high Zr and Y values). Interestingly, TM-18-12b shows an excellent match with the proximal Trefola unit TLf (Fig. 8.8).

Wulf *et al.* (2006) have suggested that TM-18-1d may relate to the proximal SMP1-a unit of Di Vito *et al.* (2008), for averaged glass major element data from this unit show good conformity with both TM-18-1d and TP-1450; hence this unit could potentially represent either of these distal tephra layers. These potential connections remain tentative, however, until single-grain major and trace geochemical data become available for SMP1-a. It is also worth noting that the SMP1-c unit (which overlies SMP1-a; see Fig. 8.7) glass fraction remains unanalysed.

Comparison of the Trefola units (TLf, TLc, TLa) to TM-18-1d and TP-1450 suggests that 1) none of these correlate to TP-1450 on the basis of trace element biplots and 2) both TLc and TLa demonstrate some geochemical similarity to TM-18-1d on trace elemental and alkali ratios (see Figs. 8.8 and 8.9) but differ significantly on SiO_2, Al_2O_3 and CaO values (see Fig. 6.14). An $^{40}Ar/^{39}Ar$ age of 58,000 ± 3000 yrs BP is available for the lowermost TLa unit, which would make it markedly older than independent ages obtained for TM-18-1d from distal sites (see below), particularly in the LGdM sequence where TM-18-1d is estimated to be only 590 varve years older than the CI. TLc overlies TLa but also would appear too old as it lies four units below a deposit $^{40}Ar/^{39}Ar$ dated to 45,600 ± 700 yrs BP (Pappalardo *et al.,* 1999). These units (TLc and TLa) can therefore be ruled out as proximal equivalents on both geochemical and chronological grounds, although the trace element similarities between these units

and TM-18-1d suggest they may have originated from the same pre-CI magma source (Tomlinson *et al.,* 2012a).

In summary distal layers TP-1334 and PRAD 1752 can be robustly correlated to TM-18-1d. The older TP-1450 tephra layer may be separated from this layer on the basis of trace element ratios only (see Fig. 8.9) and because of this it is presently unclear whether the proximal deposit SPM1-a relates to TM-18-1d or to TP-1450. Both these eruptions had very significant eastward dispersals, extending far into Greece as cryptotephra horizons.

The current best age estimate for the TM-18-1d tephra layer is derived from the LGdM varve chronology, as outlined in section 7.4.1. This involves adding the 590 varves years separating the CI (=TM-18) from TM-18-1d onto the precise $^{40}Ar/^{39}Ar$ age of the CI, taking into account the 5% LGdM varve counting error (see Table 7.1). This approach utilises the precise age control available from the LGdM chronology while by-passing the accumulative 'missing' years problem identified by Brauer *et al.* (2000) and noted within the present study. The resulting age estimate of 39,870 ± 169 yrs BP is within errors of the modelled age (39830-41250 yrs BP) for TM-18-1d from the Tenaghi Philippon radiocarbon chronology (Model B). The Tenaghi Philippon radiocarbon chronology (Model B) also provides a relatively precise age of 42720-44110 yrs BP for TP-1450.

These tephra layers should form key targets for future tephrostratigraphic investigations in the Mediterranean region as they both have reasonable age limits and secure tephrostratigraphic positions, directly below the widespread CI tephra, which means targeted sampling can be applied. Both also sit very close to evidence for rapid palaeoenvironmental change, discussed further in section 8.4.

8.2.4 Significance of previously unrecognised Santorini eruptions

There is tentative evidence of multiple Santorini eruptions which all share the Cape Riva (Y–2) geochemical characteristics. St Seymour *et al.* (2004) first described two visible tephra layers with a geochemical signature identical to that of the Cape Riva tephra from Tenaghi Philippon (PhT1 and PhT2; see section 4.2.5). Research undertaken within the present study conducted on a new core sequence also from the Tenaghi Philippon basin (TP-2005; Müller *et al.,* 2010) confirms these findings: tephra

layer TP 7.61 is equated with PhT2 and TP-707 with PhT1, and while two other, previously unrecognised, Santorini tephra layers which also have chemical signatures indistinguishable from the Cape Riva (TP-726 and TP-978; see section 6.2.4 for details). Based upon suggested correlations within the present research, two of these tephra horizons overlie the distal equivalent of the Cape Riva tephra at c.18 and 20 ka BP and one is older, dating to around 30 ka BP. This older Santorini tephra is also found in the Lesvos record (ML00-207). These tephrostratigraphic relationships are summarised in Table 8.1 alongside available age determinations.

Table 8.1 – Correlations between Santorini eruptions.

St Seymour *et al.* (2004)	**This Study**	**This Study**	
Tenaghi Philippon		*Lesvos*	Correlative(s)
Ph-1, Ph-2, Ph-3	*TP-2005*	*ML-00, ML-01*	
PhT1 *(11410-12060)*[1]	**TP-707** *(16980-19150)*[2]	—	?
—	**TP-726** *(19520-20500)*[2]	—	?
PhT2 *(20130-21370)*[1] *(21420-22240)*[1] *(21570-22430)*[1]	**TP 7.61** *(20510-22470)*[2]	**ML-1** *(21760-23530)*[2]	**Cape Riva (Y–2)** *(20540-22340)*[1] *(21250-22270)*[1] *(22025-23365)*[1]
—	**TP-978** *(29550-30270)*[2]	**ML00-207**	**?**

[1]Ages based on radiocarbon date taken directly below ash horizons (see Tables 4.8 and 7.1 for details).

[2]Modelled age ranges from this study based upon independent (non-tephra) chronological data (age model B; see Fig. 6.2B and Table 7.11).

The Cape Riva (Y–2) tephra has been identified primarily in marine records (Keller *et al.,* 1978; Vinci, 1985; Wulf *et al.,* 2002; Aksu *et al.,* 2008) but in very few terrestrial records prior to this study (e.g. Roeser *et al.* 2012). In all these existing examples only visible tephra layers were analysed, with no search for cryptotephra layers, which might explain why only one Cape Riva tephra has previously been observed. Another reason may be that the sediment accumulation rates of marine records are usually much lower than in terrestrial sequences which could merge together several tephra

layers deposited in a short time, while turbidites (some related to volcanic activity) may also mask or complicate the identification of closely-spaced eruption events. With these caveats in mind, there is tentative evidence of multiple Cape Riva tephra horizons from the work of Aksu *et al.* (2008) who analysed the visible tephra horizons identified in 13 marine core sequences from within the Aegean Sea. Evidence of multiple Cape Riva eruption events was found in at least three of these (MAR2-89, MAR2-113 and MAR3-3), which all lie to the N and NE of Santorini. One of these, MAR2-89, is shown in Fig. 8.10 alongside the Tenaghi Philippon tephrostratigraphy.

Presently there are no known proximal equivalents to these 'extra' Santorini eruptions, though original descriptions of the Cape Riva deposits on Santorini describe four separate eruptive units, which from the base comprise of the CR-A, CR-B, CR-C and CR-D eruptive units. Druitt (1985) interprets these to represent four phases of a single eruption on the basis that intervening soil layers are absent and that all four units are geochemically indistinct. Radiocarbon dates for the CR-B unit of the Cape Riva eruption suggest an age of c.22 ka BP (Pichler & Friedrich, 1976; see Table 7.1). There is one other radiocarbon age from the Cape Riva proximal stratigraphy reported by Eriksen *et al.* (1990), although it is unclear from which part of the Cape Riva proximal stratigraphy it was obtained.

If the Pichler & Friedrich (1976) radiocarbon dates relate specifically to eruptive unit CR-B, then one eruptive unit (CR-A) lies below and two (CR-C, CR-D) above, which would fit neatly with the distal tephrostratigraphic observations of the present study, suggesting four separate eruptions events rather than a single eruption. This question may be resolved by new dating evidence for the proximal Santorini stratigraphy or if hiatuses are discovered between these units. Alternatively Vespa *et al.* (2006) provide evidence for some volcanic activity between the Cape Riva eruption and the next large eruption, the Minoan, though this phase of activity is poorly studied in terms of its geochemistry and age.

The existence of 4 geochemically indistinct Santorini tephra layers described within this study raises the distinct possibility that current distal tephra correlations to a single Cape Riva event in the proximal stratigraphy (see Fig. 8.4B) could be incorrect. Although the Cape Riva eruption appears to be the largest eruption to the north of Santorini (see Fig. 8.10) this may not be true over broader geographical areas (e.g. in NW Turkey; Roeser *et al.* 2012). The use of the Cape Riva as an isochron is therefore

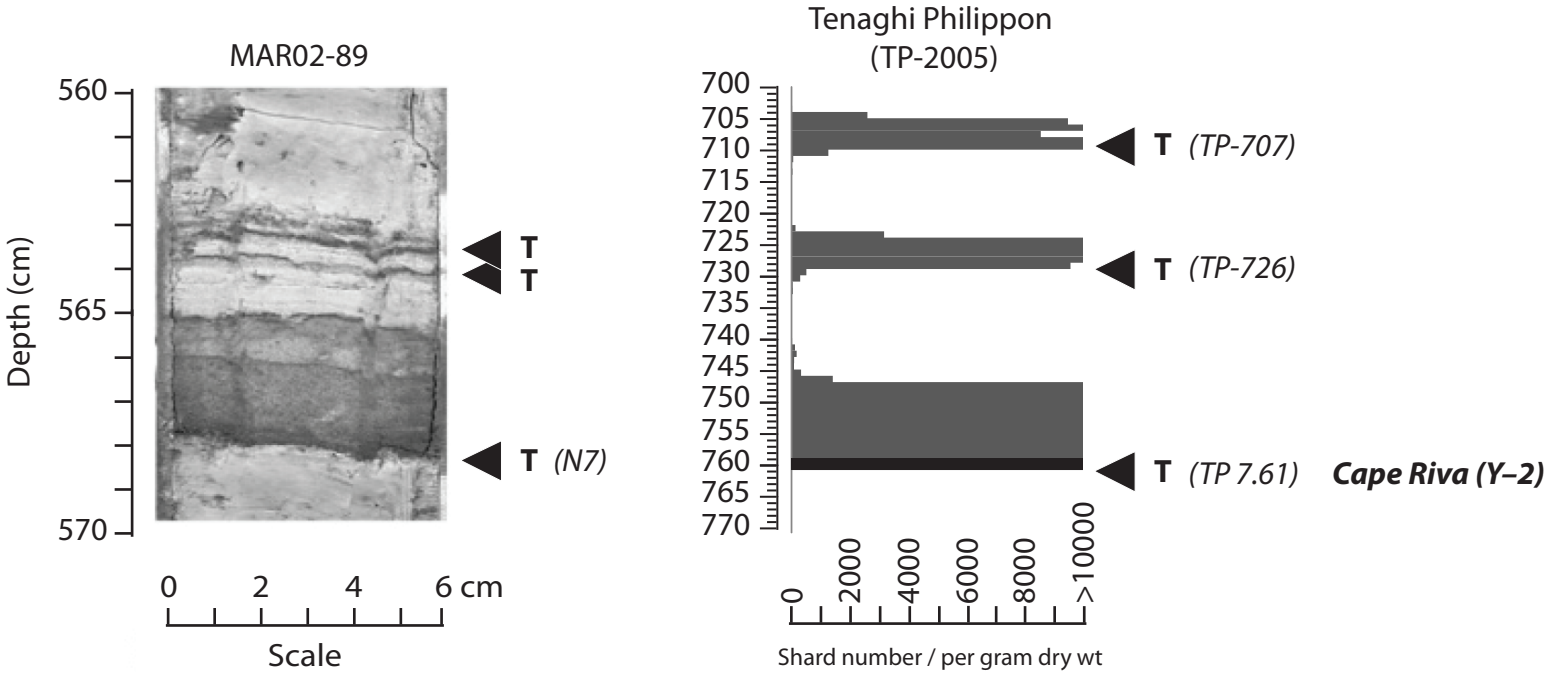

Figure 8.10 – Comparison of the MAR02-89 and Tenaghi Philippon tephrostratigraphic record. Black triangles indicate onset of tephra layer deposition. Note that the black line indicates visible tephra in the Tenaghi Philippon sequence and the grey cryptotephra. In both sequences the lowermost layer has been correlated to the Cape Riva (Y–2) tephra. The photograph of the MAR02-89 sequence has been adapted from Asku *et al.* (2008).

compromised where other geochronological or stratigraphical data are not available to allow distinction. This negates the use of these tephra layers as independent test of age–depth models, indeed the very similar ages of the Cape Riva, TP-726 and PhT1 (see Table 8.1), for example, may mean that a broader age range encompassing all of these upper units (e.g. 16980–22470) should be imported into age models where little geochronological information is available.

There is no current evidence for the older c.30 ka BP Santorini tephra identified within this investigation which is formally named TP-978 here, after its first place of identification (Lowe, 2011). Within both Tenaghi Philippon (TP-978) and Lesvos ML-00 (ML00-207) this layer is represented as relatively small cryptotephra horizons, 952 and 71.9 shards per g dry wt, in each respective sequence (see Figs. 5.8 and 5.14). This eruption then appears to have a smaller eruptive magnitude compared to the other Santorini layers which resemble the Cape Riva in terms of their geochemistry.

The best age estimate for this tephra layer is 29550-30270 yrs BP which has been attained from the Tenaghi Philippon chronology (see Table 8.1). Around this timeframe one tephra layer has been identified from the Aegean marine tephrostratigraphic record as originating from Santorini, the Y–4 (Keller *et al.,* 1978; Vinci, 1985). The Y–4 is thought to date to around c.30 ka BP based upon tuning based chronologies (Vinci, 1985). Unfortunately the geochemical range of the Y–4 does not show a satisfactory geochemical affinity to TP-978 to allow correlation at this time (see Fig. 6.18); although revaluation may be required when and if larger chemical datasets becomes available for the Y–4. Another line of evidence which might suggest these tephra layers do not represent the same eruption is the observed southward dispersal of the Y–4 which is discordant with the northwards dispersal of TP-978 (see Fig. 8.11).

Another Hellenic Arc tephra layer, the Yali-2 (= Yali-C; Keller *et al.,* 1978; Federman & Carey, 1980; Vinci, 1985) also occurs around this timeframe with ages of ~31 ka BP based upon oxygen isotope stratigraphy (Federman & Carey, 1980) and ~35 ka BP based on astronomically tuned ages of sapropels (Smith *et al.,* 1996). This timeframe would appear to be a very active period within the Hellenic Arc volcanic system. Currently the Y–4 and Yali-2 tephra have not been found in the same sequence making their precise stratigraphic relationship unclear (Narcisi & Vezzoli, 1999). Two further previously unrecognised tephra layers may have also been discovered by Aksu *et al.*

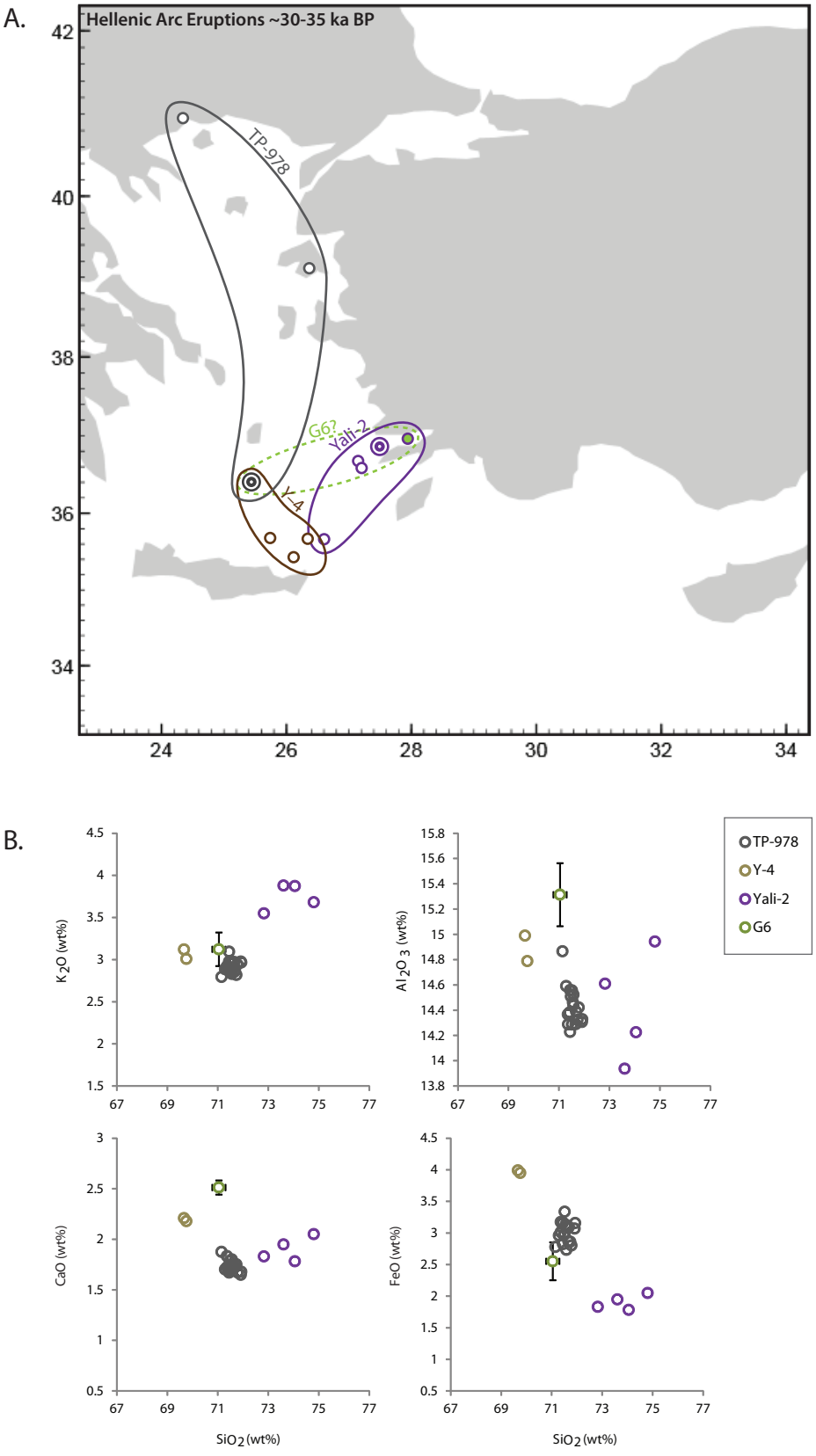

Figure 8.11 – Overview of Hellenic Arc eruptions ~30-35 ka BP. (**A.**) Map showing distributions of four eruptions, occurrences taken from the RESET database (assessed 05/07/12) and this study. The eruption sources are also indicated. (**B.**) Biplots Data from: Vinci (1985); Asku *et al.* (2008) and this study.

(2008) who find two visible tephra layers, G6 and U2, closely bracketing the Yali-2 in the Aegean Sea sequence MAR03-24. Unfortunately only G6 has geochemical data available and although it may correspond to the Y–4, geochemical differences cast some doubt on this (Aksu *et al.,* 2008; see Fig. 8.11) and although tentatively on some major elements bi-plots this tephra shows some affinity with TP-978, on trace elements it appears to be very distinct. Therefore this tephra probably represents another eruption, most likely originating from Santorini (Aksu *et al.,* 2008).

A key aim in future investigations in the Eastern Mediterranean region should aim to more fully understand the tephrostratigraphic relationships between these various deposits during this time, a period which closely corresponds to important climatic events such as HE 3 (Thouveny *et al.,* 2000). This could potentially be invaluable to the Mediterranean tephrostratigraphic lattice, particularly considering the stratigraphic relationship observed between TP-978 and the Italian TM-15 tephra in Tenaghi Philippon, which would suggest near coeval timings (~150 yrs) that the TP-978 can be effectively used as a surrogate for TM-15 significantly increasing the range at which this tephra can be used for synchronizing purposes.

8.2.5 The tephrostratigraphy and chronology of the 'Upper Nisyros'

Within the course of this investigation only one study site, Lesvos, was found to record tephra fall originating from the Hellenic Arc volcanic island of Nisyros. Two visible layers, the ML-3 and ML-4, were previously described and correlated by Margari *et al.* (2007) to the Lower and Upper Nisyros. New data acquired during this work (including LA-ICP-MS analyses) and comparison to newly available proximal datasets from the proximal Nisyros stratigraphy (Tomlinson *et al.,* 2012b) demonstrate robustly that both these layers geochemically correlate to the Upper Nisyros. This interpretation is in agreement with the wider work of Tomlinson *et al.* (2012b) who compared the proximal Nisyros dataset produced in their study to all published distal occurrences of the Upper and Lower Nisyros and interpreted them all to correspond to the Upper Nisyros and not the lower as suggested by some authors (e.g. Aksu *et al.,* 2008).

The two visible layers in Lesvos would suggest that the Upper Nisyros was formed of two eruptions spaced fairly close in time (they are separated by 1.5m in ML-01).

Margari *et al.* (2007) rule out the possibility of reworking of tephra layers ML-3 and ML-4 with high resolution grain-size and x-ray analysis. Cryptotephra lying above ML-3 in the shorter Lesvos core ML-00 also displayed an Upper Nisyros geochemical signature (ML00-785, ML00-815, ML00-845 and ML00-880; see Fig. 6.22); currently these layers have only been refined at low stratigraphic resolution (c.10 cm) and could represent basin reworking of the underlying visible ML-3 tephra layer (Margari *et al.,* 2007). Evidence against this possibility are subtle geochemical differences between the cryptotephra layers and the underlying visible ML-3 and ML-4 layers which display a more evolved geochemical range (see Fig. 6.22).

In terms of its tephrostratigraphy the Upper Nisyros tephra layers described here from Lesvos sequences ML-00 and ML-01 underlie the CI and sit stratigraphically above the P-11 tephra. Figures 8.12A and 8.12B show the proximal Nisyros volcanostratigraphy alongside the tephrostratigraphy of both Lesvos sequences. The Upper Nisyros proximal deposit has been dated both via radiocarbon and fission track dating which produced discordant ages of >47,700 yrs BP and 110,000 ± 40,000 yrs BP (Barberi *et al.,* 1988; Limberg & Varekamp, 1991). Confusingly ages below the Upper Nisyros are younger (see Fig. 8.12A) which suggests at least some (if not all) of these ages should be viewed with caution. Distally the delta tephra of Aksu *et al.* (2008) correlated to the Upper Nisyros by Tomlinson *et al.* (2012b) has an age determination of between 42.4 to 44.1 ka BP on the basis of linear extrapolation through the oxygen isotope stratigraphy in two marine cores. Both these authors cite the original ages proposed by Margari *et al.* (2007) for layers ML-3 and ML-4 to 46000 ± 5690 and 46800 ± 5690 yrs BP respectively, these ages are however based upon an age-model adjusted significantly in chapter 7 (see section 7.5). New age determinations for both ML-3, ML-4 and the other Upper Nisyros cryptotephra are shown in Fig. 8.12B. There are based on the new independent chronology produced for ML-00 and ML-01 in this study in which the lower part of the sequence is based primarily on the tephrocorrelations to the P-11 and KPT (see Fig. 7.10). The Upper Nisyros activity can be limited to a period between 42300 and 55810 yrs BP which is consistent with both the ages for the Upper Nisyros as determined by Aksu *et al.* (2008) and the radiocarbon date taken directly from the Upper Nisyros surge deposits by Limberg & Varekamp (1991).

In summary the Upper Nisyros eruption (or eruptions) remains somewhat enigmatic or in flux (Aksu *et al.,* 2008). The evidence from this study suggest it may well

A.

	Proximal volcano-stratigraphy	Age (yrs BP)	Method	Reference
	Yali-C Pumice	~31,000 / *~35,000*	Tuning	Federman & Carey (1980) / *Smith et al. (1996)*
Upper Nisyros	Surges & Flows (more dilute)	>47,700	^{14}C	Limberg & Varekamp (1991)
Upper Nisyros	Surges (pumiceous)	110,000 ± 40,000	Fission Track	Barberi *et al.* (1988)
Upper Nisyros	Fall (stratified)			
	Nikia Lavas			
Lower Nisyros	Flows			
Lower Nisyros	Lithic-rich Fall			
	Palaeosol	28,8000 ± 600	^{14}C	Rehren (1988)
	Undated Units			
	Panagia Kyra sequence	37,000 ± 24,000 39,000 ± 26,000	^{40}K/^{40}Ar ^{40}K/^{40}Ar	Rehren (1988) Rehren (1988)
	Dacite Lava	38,000 ± 2000	^{40}K/^{40}Ar	Keller *et al.* (1990)

B.

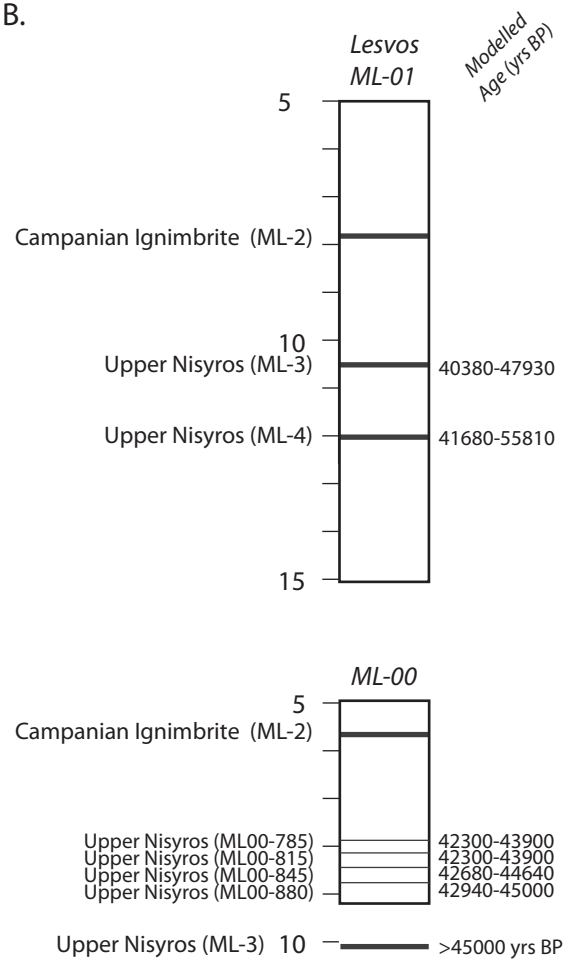

Figure 8.12 – (**A.**) Proximal volcanostratigraphy of Nisyros also showing units, available direct age determinations and references. (**B.**) Lesvos sequences ML-00 and ML-01 with tephra layers with Upper Nisyros geochemical signatures highlighted. Calculated age ranges are also shown (at 95.4% confidence intervals).

represent multiple phases of volcanic activity although currently this evidence comes from only one site (Lesvos) and confirmation is required before the exact nature of this eruption/s can be more fully understood.

On the basis of the evidence presented above for the Hellenic Arc region and the new independent modelled ages available from this study (see Table 7.11) an updated LLG tephrochronology and tephrostratigraphy is put forward in Fig. 8.13 and contrasted with the pre-existing tephrostratigraphy and tephrochronology described in chapter 2.

8.3 Importance of tephrochronology for testing and refining age models; advantages and limitations

8.3.1 Validating the tephrochronological approach

Two key aims of the study were to firstly test existing chronological schemes for the LLG timeframe using tephrochronology, and to secondly produce independent age–depth models free of the assumptions inherent in the curve alignment approach. These aims can now be evaluated and the wider implications considered for the four sites studied here in which a number of tephra layers were found.

In three instances the tephrochronological data demonstrate considerable temporal offsets when compared against pre-existing chronologies based primarily upon palynostratigraphically-based alignment. In the Lesvos (ML-01) sequence a considerably older age model was suggested towards the base of the sequence, in Fimon (PD) a younger chronology and for the Kopais (K-93) sequence the tephra-based age model is considerably younger than the intial chronology proposed by Tzedakis (1999) but older than a more recent model proposed by Tzedakis *et al.* (2004)

In the case of Fimon (PD) two divergent age models are apparent (see Fig. 4.10). The identification of just one cryptotephra layer (in this case correlated to the CI) provided strong evidence that the chronostratigraphy based upon both radiocarbon and OSL dates, which both separately predict an age range that agrees with the $^{40}Ar/^{39}Ar$ age of the CI (De Vivo *et al.,* 2001), are more reliable than the discordant alignment-based chronology (see Fig. 7.1). An offset of about 26 to 28 ka is apparent between the age of the CI tephra and the tuned chronology of Pini *et al.* (2010).

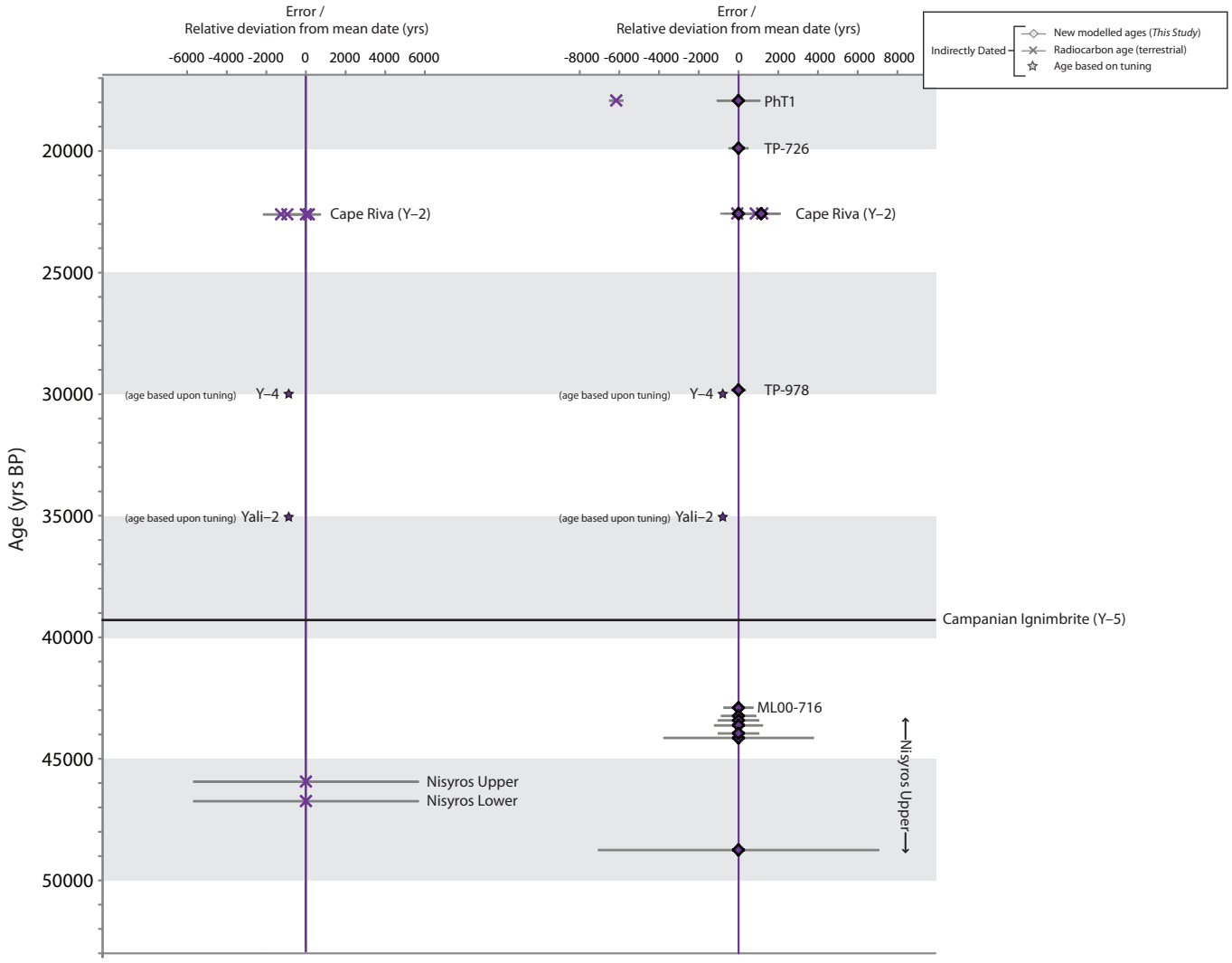

Figure 8.13 – Ages for Hellenic Arc eruptions as presented in Chapter 2 and updated on the basis of the results from this study including new previously undiscovered tephra layers. See text for details.

The Kopais (K-93) sequence also had two pre-existing chronological schemes, both based in part upon biostratigraphic alignment points (see Fig. 4.13). The identification of three dated cryptotephra horizons (see Fig. 7.1) between 31 to 47 m suggests an age model discordant with either that suggested by Tzedakis (1999) or Tzedakis *et al.* (2004) by between 10 to 20 thousand years. However apparently reworked tephra (see section 6.2.3) far up sequence suggest more needs to be understood about sediment catchment reworking particularly within very large carbonate catchments.

The tephrochronological data from the longer Lesvos sequence (ML-01) suggested that below the last radiocarbon date only one (the correlations of 8.90m to GI-12; Margari *et al.,* 2007; 2009; see Table 7.10) out of the four alignment tie points are in agreement with the independent chronology produced here. Whereas the bottom three alignment tie-points at 23.75, 29.06 and 36.00m are discordant with the independent chronology by ~77, ~110 and >108 thousand years respectively. The base of the Lesvos (ML-01) chronology was constrained by two tephra layers; the P-11 (=ML-5) and the Kos Plateau Tuff (=ML-6), both of which are robust chronostratigraphic markers as they are both geochemically distinct and both have direct proximal age determinations available (Mahood & Hildreth, 1986; Smith *et al.,* 1996; 2000; Bachmann *et al.,* 2010). Interestingly the final age model proposed here follows a more consistent sedimentation rate with the upper part of the ML-01 record between 1 to 8m where the chronological model proposed in this study is in agreement with the Margari *et al.* (2007; 2009) chronological scheme (see Fig. 7.10). For the upper part of the sequence between 1 to 8 m the sedimentation rate is ~0.3 mm / per year, which is consistent with 0.2 mm / per year for the lower part of the core (23 to 36m) calculated with the new chronology here. The Margari *et al.* (2007; 2009) age model, in contrast, produces a value four times higher between these lower depths at 1.3mm / per year. This significant change in sedimentation rate is directly related to the switch from the independent age model to the alignment based chronology at ~9m by Margari *et al.* (2007; 2009).

Undoubtedly the miscorrelation by Margari *et al.* (2007) of ML-5 to the much younger Green Tuff eruption (in part caused by a lack of geochemical data for the P-11 at the time of publication) complicated the lower chronology of Lesvos and may have helped misdirect Margari *et al.* (2007; 2009) into selecting erroneous palynostratigraphic alignment points. This clearly acts as a warning against treating tephrocorrelations with excessive deference and during the course of this study where significant

chronological offsets have been observed attempts have been made to discuss other lines of evidence, both dating and palaeoenvironmental information (see Chapter 7). Despite this the potential miscorrelation of the start of the Eemian (an interglacial) with GI 14 (an interstadial) perhaps highlights that pollen based alignment chronologies, where unavoidable, should always be treated with a certain amount of caution. The implications of these findings for using palynostratigraphic correlations to build chronological schemes are discussed further in section 8.4.1.

During the LLG period, in the sites analysed in this study, there were not enough widespread tephra layers or indeed associated ages to form independent chronologies with low sub-millennial error ranges from tephrochronology alone, and within this study the final age models produced here (i.e. the model C) tephrochronological data was coupled with other independent data which were combined via Bayesian statistical approaches. Of course often these data may disagree; this can be seen particularly in the case of Kopais (K-93) where a radiocarbon date at 43.9m (see Fig. 7.4) is much younger than the tephrochronological data would suggest. Where this was the case the tephrochronological data was given precedence during the Bayesian modelling date removal phase, where dates with low agreement index values are removed to allow the model to run and form acceptable satisfactory agreement indices (see section 3.6.1 for details of this process). Far more often however there was very good agreement with the tephra layer ages imported and the pre-existing independent age controls which often predicted the age of the tephra layers. This is demonstrated in Figure 8.14 using the CI tephra in the Fimon (PD), Tenaghi Philippon (TP-2005) and Lesvos (ML-00) records where both age models B (Bayesian Age-depth model based upon independent (non-tephra) chronological data) and C (final Bayesian age-depth model including imported tephra age and independent data; see Fig. 6.2B) are shown plotted together alongside individual age determination. From this it can be observed that the age of the CI is predicted well in both the Fimon (PD) and Tenaghi Philippon (TP-2005) chronostratigraphic schemes where no tephra age data has been imported. In comparison the Lesvos (ML-00) Bayesian model B predicts an age slightly too old although a radiocarbon date closely underlying the CI does cover the CI $^{40}Ar/^{39}Ar$ age (De Vivo *et al.,* 2001). This evidence indicates that the Lesvos radiocarbon based age model maybe less reliable; probably due to containing radiocarbon ages with larger laboratory error ranges (see Fig. 7.9 and appendix III for details). This evidence may also tentatively suggest that the consensus IntCal09 radiocarbon calibration curve

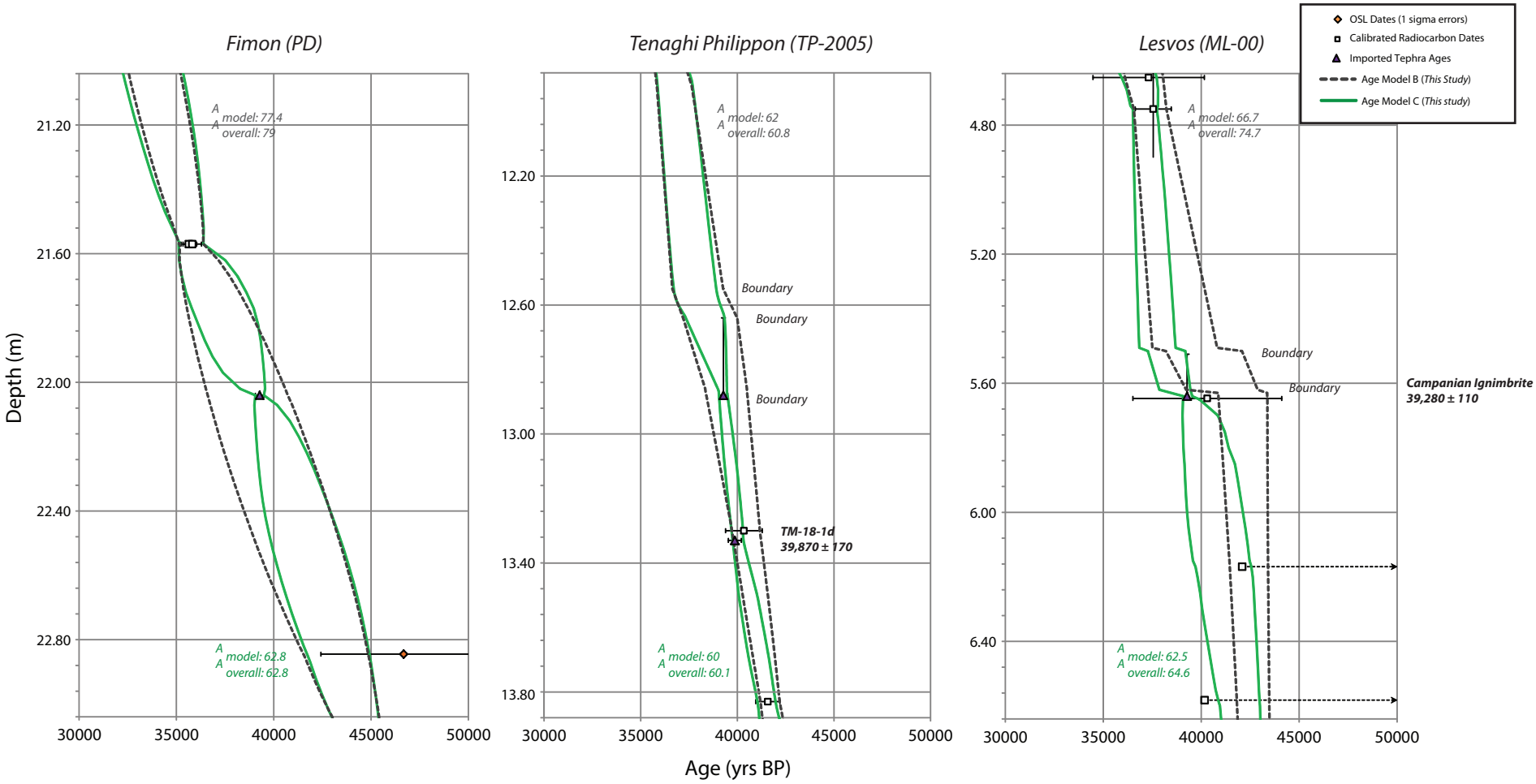

Figure 8.14 – Age–depth models B and C (see Fig. 6.2) for Fimon (PD), Tenaghi Philippon (TP-2005) and Lesvos (ML-00) around the CI tephra layer. Agreement indices and individual ages are also shown.

used within this study appears to be operating correctly during this period of the LLG (e.g. 35-45 ka BP) where the IntCal09 calibration curve is based primarily upon datasets from marine records from the Cariaco Basin (Hughen *et al.,* 2006) and Iberian Margin (Bard *et al.,* 2004) both of which are based upon alignment chronologies, and on an independently dated coral record from Barbados (Fairbanks *et al.,* 2005).

Tenaghi Philippon (TP-2005) has another imported tephra age for a cryptotephra underlying the CI, TM-18-1d (=TP-1334) which has been produced utilising the $^{40}Ar/^{39}Ar$ age of the CI (De Vito *et al.,* 2001) and the relationship of these tephra layers in the LGdM varve chronology (where they are separated by only 590 varve years; Wulf *et al.* 2006). The combination of both these tephra ages significantly increases the precision of the TP-2005 chronology between 12.80–13.50m (see Fig. 8.14) and also allows the Bayesian model to remain more constrained below the TM-18-1d layer. This example demonstrates that very constrained age control that can be achieved for non-varved records during parts of the LLG with the combined use of tephrochronology, Bayesian age modelling and differential dating techniques. Differential dating when combined with precise ages in particular (e.g. a varve or $^{40}Ar/^{39}Ar$ age) can allow comparable or even superior absolute age errors to be achieved than is currently possible in the Greenland ice-core records, where the error range is around 4% for this period compared to ~0.5% possible between the CI and TM-18-1d tephra layers, the ages of which also by-pass potential radiocarbon calibration complexities. This allows an increasingly robust independent comparison of relative timings of palaeoenvironmental events between distant palaeo-records and establishment of localised stratotypes in which to test regional questions (as recommended by the INTIMATE group; see section 8.4.5). One potential limitation of having very precise ages is it increases the need for accurate determination of the first 'input' event (see Fig. 3.5) if, for example, a tephra layer is very stratigraphically diffused (i.e. spread over many tens of cm's) or displays evidence of reworking it may be difficult to place with certainty the depth at which the precise age should be placed. This is less of an issue for tephra layers with larger age range errors (e.g. >1000 yrs error) which are more likely to mask any potential offset caused by stratigraphic misplacement (Matthews, 2009).

Age models based upon multiple lines of chronological evidence, like those described above, are more robust and can be treated with more confidence (Blockley *et al.,* 2012). However even in instances where very precise $^{40}Ar/^{39}Ar$ (or other) age

determinations are not available and the only ages available for tephra layers are those derived indirectly from radiocarbon age depth models are still important tools for cross-checking chronologies. For example ages determined for tephra layers TP-978 and TP-1450 from the Tenaghi Philippon (TP-2005) chronostratigraphy were imported into the Lesvos (ML-00) sequence where they bracketed the existing age information. The age for TP-1450 is firmly within radiocarbon time (42720 – 44110 yrs BP) and helped validate both the lower part of the ML-00 sequence where many existing radiocarbon ages taken from the sequence returned infinite ages after calibration (Margari *et al.,* 2009; see Fig. 7.9). After the age of tephra layer TP-978 was imported into the ML-00 sequence a slightly older modelled age became apparent (while still overlapping the 94.5% confidence limits of the radiocarbon dates available between 2 to 3m; see Fig. 7.9). A potential limitation of this approach is that it makes the assumption that the site which defined the indirect age (in this case the TP-2005 chronology) is more robust or reliable, as tephra ages were given precedence. Although the evidence discussed already for predicting the age of the CI may well suggest the Tenaghi Philippon (TP-2005) chronology produced within this study is more reliable this may not be the case for different parts of the LLG. Modelling techniques are becoming available within OxCal which allow multiple site *P_Sequences* to be run within the same overarching model, this allows the model to find the best intra-sequence age for shared tephra without direct age determinations (Bronk Ramsey, *pers. comm.*).

In this section examples from this study have been outlined which demonstrate the validity of tephrochronology as a chronological approach, including firstly its use as a tool to allow cross checks between differing chronological techniques (e.g. $^{40}Ar/^{39}Ar$ and radiocarbon or alignment ages) and secondly how tephrochronology may be used to produce precise chronologies on absolute temporal scales free of radiocarbon calibration issues which are superior to that of even the Greenland ice cores, although this is often limited to very small periods of time where tephra layers with precise ages are present (e.g. the CI and TM-18-1d). Also the age–depth models produced within this study and discussed here (and in Chapter 7) may be easily updated or re-modelled in the future where either improved dates for individual volcanic eruptions become available, as improved calibration curves are proposed and also as new modelling techniques become available.

Finally the use of tephra horizons as isochrones to allow intra-site comparisons of abrupt environmental transitions has not been discussed in detail here but is considered in more detail in sections 8.4.3 and 8.4.4.

8.3.2 Potential pitfalls of the tephrochronological approach; repeating geochemical signatures

This study has highlighted instances of several successive tephra layers with indistinguishable geochemical signatures, even where trace element data were available. Some of these have been interpreted as probable reworking (e.g. in the case of Kopais cryptotephra KOP-2910 to KOP-2317) and others as discrete separate eruptive events (e.g. Tenaghi Philippon layers TP-707, TP-726 and TP 7.61) particularly where they have been demonstrated in more than one locality (e.g. cryptotephra TP-978 and ML00-207 from Tenaghi Philippon and Lesvos respectively).

This problem has also been observed in Icelandic and New Zealand volcanic systems (Lowe, 2011). For example Matthews *et al.* (2011a) and Lane *et al.* (2012) between them describe at least six separate tephra layers which all originate from the Icelandic Katla volcano over a timeframe of around 15 to 8 ka BP and share an identical geochemical fingerprint. These include the Suðuroy Tephra, dated to ca. 8 ka BP, AF555 which occurs near the end of the Younger Dryas, two layers which sits within the Younger Dryas; the Vedde Ash and a tephra which predates it by 100 years in the NGRIP record (Mortensen *et al.,* 2005) the IA2 which is associated with GI-1 (Bond *et al.,* 2001) and finally the Dimna ash which pre-dates this (>15 ka BP; Koren *et al.,* 2008).

From this it is clear that volcanic systems, apparently particularly those which produce highly silicic eruptive products, tend to reach the same end products via either similar volcanological conditions or dynamics being required for an eruption to take place or alternatively via different pathways which converge to a similar eruptive product (equifinality). That these eruptions can take place over very short periods highlights a significant pitfall of tephrochronology, as this may lead to erroneous correlation of distal tephra layers representing multiple eruptions to the same event. This underlines the need to consider stratigraphic position (including the tephrostratigraphy) and other independent chronological controls when accessing

potential correlations (Davies *et al.*, 2012), care must also be taken however to avoid circular reasoning. The possibility of unknown tephra layers being present should always be considered particularly when assessing a record in a region where little or no cryptotephra work has been carried out, as, for example, the Eastern Mediterranean.

This reduces the capacity for using tephra layers to test age-models and also underlines the importance of separate age model construction, i.e. the site specific dating of each tephra layer discovered both before and after importation of available tephra ages (e.g. see Tables 7.8, 7.9, 7.10, 7.11). This allows future workers to easily reassess correlations in light of new data, it is also recommended that when the indirect ages for volcanic eruptions are taken from one sequence and imported into another, where possible the modelled age transferred is that which is independent of any imported tephra ages (e.g. the age model B of this study rather than the final model C). Although perhaps a minor point this helps keep separate tephrochronological based information (which may change) from the specific age of a tephra layer from a core (which is perhaps less likely to do so) it also makes comparison of independent ages between sequences simpler with less caveats. Of course for many tephra layers, particularly those older than the limit of radiocarbon, this is simply not possible and ages derived from relationships of under and overlying tephra layers are still of great value (e.g. Bourne, 2012).

The tephrostratigraphic framework is ever evolving as new data, such as new tephra layers, larger geochemical datasets and new age determinations become available. It is likely that this tephrostratigraphic lattice will only increase in its complexity with some layers being rendered of less or more use. For example in this study the P-11 tephra of Pantelleria was found to be a very useful marker as it is geochemically very distinct and is thus a very useful horizon with which to test pre-existing age models whereas other tephra layers require pre-existing age information in order to allow correlation (e.g. the Cape Riva) and are of less use in directly testing existing age models.

Despite this, just because a tephra horizon may lose its use as a direct site to site synchronizing tool due to many closely spaced similar eruptions, does not mean it is of no use as a geochronological tool. For example LGdM layers TM-17a and TM-17b (Wulf *et al.,* 2006) are both geochemically similar but separated by just ~80 varve yrs.

Even the complex Upper Nisyros where found distally, may still be of use as, for example, it must be older than the CI and its overall age range may still be imported (e.g. 42.3-55.8 ka BP) into sequences which offer age errors which still allow correlation to particular marine isotope stages, in this case to MIS 3. Careful evaluation is always required of what chronostratigraphic information may be ascertained or derived from different volcanic marker layers.

8.4 Palaeoenvironmental significance

8.4.1 Implications for building age models for the LLG using palynostratigraphic tuning

Often debates surrounding the rationale for tuning environmental records focus on the notion that this form of alignment precludes the ability to assess 'leads' and 'lags' between different palaeo-records (e.g. Tzedakis *et al.,* 2004). This matter is becoming more widely recognised, with Blaauw (2012) stating un-categorically that nothing can be implied about synchroneity with alignment-based chronologies. In line with these views, the present project has highlighted incidences of often significant temporal offsets exist between alignment-based and independently-dated chronological schemes that range on scales of 10s to 100s of thousand years. This suggests that unrelated climatic events may be being aligned in different palaeo records. Where such errors are evident, and it is only through establishing independent chronological control can this be determined, the ability to judge leads and lags is a moot point.

An example of this may be observed within the Kopais (K-93) record where the independent chronology suggests an event originally correlated to HE3 is more likely to correspond to HE4 (Fig. 7.14). While this example suggests offsets of c. 10 ka in an abrupt climatic event between aligned and independent chronologies a more problematic issue can be identified where pollen signals are correlated to palaeoenvironmental events of markedly different climatic context and timescale, for example in the Lesvos record where an event correlated to GI-14 (Margari *et al.,* 2009) may actually represent the onset of the interglacial conditions of MIS 5e (see Fig. 7.10). This finding illustrates a relevant point made by Wunch (2006), that a major limitation of alignment techniques are 'false-positives' or in other words where the visual similarity of two proxy records are in reality completely unrelated. In the case of correlation using pollen signals, 'false-positives' may be a symptom of contrasting

sensitivities between different proxy records, especially when the 'target' alignment records against which pollen-stratigraphic records are being compared to are oxygen isotopes stratigraphies (e.g. NGRIP). When comparisons are made between pollen records from the same region these are often used in 'bridging' manner as the comparison pollen records frequently lack independent chronologies and are themselves aligned to target palaeo-records. This 'double tuning' may lead to the formation of 'coherent myths' (*sensu* Oldfield, 2001) which can only be tested by the development of independent chronologies (Blaauw, 2012). Not all palynostratigraphic correlations made in order to allow chronologies to be built tested within this study were, however, in disagreement for example the correlation of GI-12 within Lesvos sequence ML-01 at c.9m (see Fig. 7.10) and also tie-points between 21 and 23m within Kopais (K-93; see Fig. 7.4) all were within error margin of the independent age models.

In two sites switches by the original authors between independent and alignment based chronological information resulted in marked changes in sediment accumulation rates, for example Lesvos (ML-01) at c.9m where the sediment accumulation rate increased dramatically (see Fig. 4.19) and Fimon (PD) at c.20m where sediments accumulation rate reduced (see Figs. 4.10). When the age-depth relationship of these sites are remodelled using the independent age models produced within this study it shows much more consistency over both of these sequences (see Figs. 7.1 and 7.10). While it is highly unlikely sedimentation rates remain constant over time in long sequences, caution should away be taken when large shifts occur when switching between different chronological information, particularly where no significant changes in lithology are observed.

When debating the application of tuning vs independent chronologies Skinner (2008) suggested that "stratigraphy may be risky, but 'chronological absolutism' is downright dangerous" (p.S450). This point, of course, might be valid and independent chronologies may be erroneous despite attempts to quantify reasonable uncertainty limits (Telford *et al.,* 2012). However, it is worth noting that a large array of differing independent chronological techniques does allow cross checking, even within the LLG (see section 8.3.1). I would suggest that stratigraphic or alignment 'absolutism' is equally dangerous, perhaps more so in the sense uncertainties cannot be easily (if at all) be assessed or calculated. An emerging practise within alignment-based chronology building is the importation of ages from target records, e.g. NGRIP, along

with associated errors (e.g. Pini *et al.,* 2010). Although the purpose of this approach is no doubt an attempt to robustly capture chronological uncertainties and is, to an extent, a logical extension of the alignment method, it may lead some to interpret 'real' absolute *in-sequence* errors.

Alignment based chronological schemes require testing which can only be achieved via formation of independent chronologies; this process may also operate in reverse (e.g. Skinner, 2008; Lowick *et al.,* 2010). Where temporal offsets are apparent these need to be explained or discussed and all conflicting data should always be published (e.g. Pini *et al.,* 2010), this should help prevent against the formation and persistence of 'coherent myths' and increase the understanding of the kind of chronological offsets feasible. Ideally all chronologies would be based upon several lines of dating evidence however in reality this is rarely possible, particularly as one travels further back in time. Alignment (or stratigraphy) will then still be required to ask valuable questions, although the uncertainties inherent should always be made clear (Blaauw, 2012).

8.4.2 Relating tephra layers to abrupt environmental transitions (AETs) during the LLG

Using tephra layers as isochronous marker horizons is perhaps one of the most useful applications of tephrochronology and one of the key aims of this study was to assess how well AETs may be chronologically constrained and correlated over wide geographical areas, which will now be discussed.

How useful tephra layers are as isochronous marker horizons is somewhat dependent upon how well a tephra layer may be defined stratigraphically (see section 3.3.5). This question can be broken into two parts when considering palaeoenvironmental questions: first, how well tephra horizons can be stratigraphically defined in relation to AETs, and second, how well the timing of volcanic eruptions coincide usefully with AETs that are of interest and allow phase relationships to be better understood (Tzedakis, 2009). These questions are evaluated below and within section 8.4.3.

On the first point, many tephra layers in this study form useful, well defined distributions that allowed detailed pinpointing within existing pollen stratigraphies, while in other cases this was much less precise. Where visible tephra layers are concerned (contained in both peat records, Tenaghi Philippon and Lesvos), these

tended to have very sharp, well-defined contacts with underling sediment. In these cases the pollen samples taken from directly underneath the tephra can be used to infer the palaeoenvironmental conditions that persisted immediately before the tephra was deposited (Newnham & Lowe, 1999). In the example of the CI, the pollen stratigraphy at Tenaghi Philippon and Lesvos show that treeless conditions were already in existence before the CI eruption occurred (Margari *et al.,* 2009; Müller *et al.,* 2011) suggesting arid conditions were already prevalent, this event coincided with the HE4 event (Lowe *et al.,* 2012). It has been shown that large deposition of ash across landscapes can affect the local ecology, usually on decadal to centennial scales (e.g. Giles *et al.,* 1999; Allen & Huntley, 2011), so care should be taken when considering palaeoenvironmental analyses taken from directly above large visible ash layers.

Perhaps paradoxically, it was found harder during this study to assign cryptotephra layers to particular abrupt environmental events. The main reason for this is that cryptotephra lack a defined discrete contact associated with visible tephra layers; even though a 'peak' in shard concentrations may be used for this purpose, this approach was often compromised by apparently reworked tephra often occurring above the first stratigraphic occurrence. This is particularly the case with the TM-15 tephra layer within the Tenaghi Philippon record (tephra TP-970) which had separate multiple peaks lying above it which probably relate to the same eruption/tephra (TP-951, TP-938, TP-923; see Fig. 5.9). This problem has also been highlighted by other authors (Davies *et al.,* 2007; Pyne-O'Donnell *et al.,* 2008) and highlights the importance of understanding post-depositional processes which may affect cryptotephra deposition (Davies *et al.,* 2012).

Fortunately, some cryptotephra layers could be clearly related to a particular AET, a good example being layer TP-978 in the Lesvos sequence (=ML00-207) which covers 16 cm vertically but with a very defined peak confined to c.3 cm (see Fig. 5.15) which allows sharp correspondence with the well resolved pollen stratigraphy of Margari *et al.* (2009). Within the Tenaghi Philippon sequence, cryptotephra layer TP-978 has a very constrained 1 cm peak (see Fig. 5.9) but potentially extends upwards in the sequence by possibly as much as 20 cm, probably due to upward reworking (see section 6.2.2 and above). Despite their upward 'spread', representing the potential stratigraphic error around each shard peak, both layers can be confidently assigned to AETs and both seem to cap minor increases in total tree pollen percentages (see Fig. 7.14).

Ash layers P-11 and KPT are examples of ash layers that can be used to clarify the expression and phasing of AETs. Both layers occur within the Lesvos (ML-01) sequence (tephra ML-5 and ML-6) and have direct ages available of around 131–134 and 160–168 ka BP respectively (Mahood & Hildreth., 1986; Smith *et al.,* 1996; 2000; Bachmann *et al.,* 2010). The P-11 is widely deposited across the central and Eastern Mediterranean (see Fig. 8.4A) whereas the KPT occurrences are currently more confined to the East (see Fig. 8.4C). Within Lesvos the P-11 tephra layer sits within a period of subdued total tree pollen percentages just before the onset of a marked increase in tree percentages. The P-11 has also been identified within Lake Ohrid (Lezine *et al.,* 2010) where it is located within a period where calcite content is increasing, which has been interpreted as reflecting the inception of the Last Interglacial (MIS 5). Compared visually in Figure 8.15, both records show that the P-11 was deposited just before an increase in total tree pollen percentages; from this evidence it would appear that both these records appear to reflect broadly the same phasing.

Within the Lesvos (ML-01) sequence the KPT lies within a period of increased total tree percentages originally interpreted by Margari *et al.* (2009) as reflecting an increase in precipitation which correlates with GI-16. The position of the KPT near the midpoint of this palaeoenvironmental event (and the P-11 tephra lying stratigraphically above) would instead suggest an age within MIS 6 (see Fig. 7.12). The KPT has also been identified within marine cores off the coast of Egypt in the Levantine Basin (Ducassou *et al.,* 2007) where it is positioned within an isotopic excursion which displays a similar character to the pollen signal in Lesvos (ML-01), and which also occurs after the deposition of Sapropel 6. Taken together, these strands of evidence seem to suggest that the KPT coincides with a short period of both enhanced precipitation and warmth in the Eastern Mediterranean region, which may represent the expression of a GI-like event within MIS 6. Intriguingly, recent work by Roucoux *et al.* (2011) from the Ioannina terrestrial sequence in NW Greece also identifies an expansion in total tree pollen which appears to have a similar timing to that observed in the Lesvos record. All of these records are compared on their respective timescales in Figure 8.16. The age of the KPT eruption is fortuitous, for it can be used to directly date this palaeoenvironmental event, albeit rather coarsely, and to link with other records in order to test its occurrence and expression within the Eastern Mediterranean region as a whole. Likewise the P-11 forms a very useful

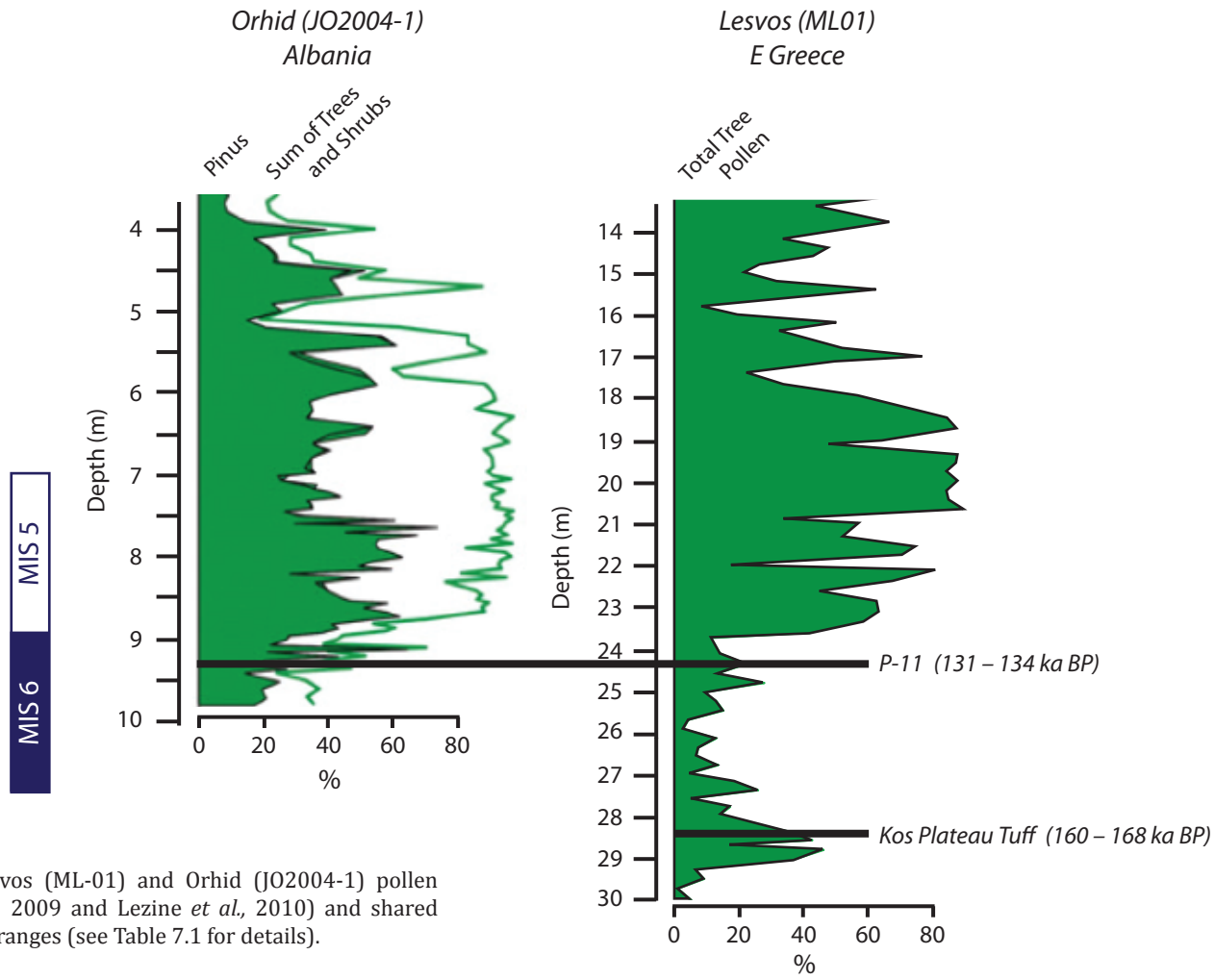

Figure 8.15 – Comparison of Lesvos (ML-01) and Orhid (JO2004-1) pollen records (taken from Margari *et al.,* 2009 and Lezine *et al.,* 2010) and shared tephra horizons and associated age ranges (see Table 7.1 for details).

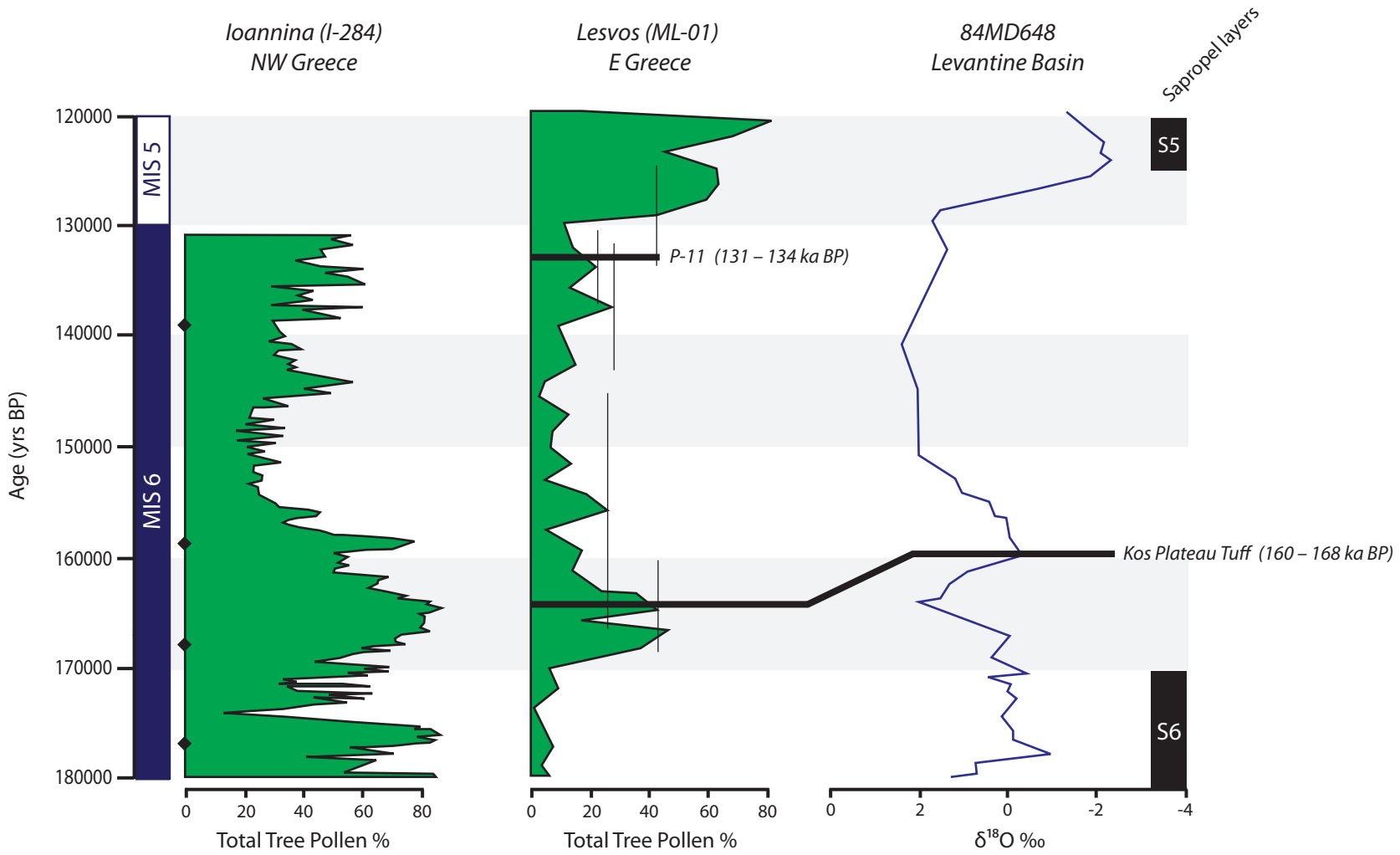

Figure 8.16 – Comparison of Lesvos (ML-01) sequence plotted on its independent timescale with the Ioannina (I-284) pollen record (Roucoux *et al.,* 2011) and the 84MD648 Levantine Basin marine oxygen isotope record with sapropel layers (from Ducassou *et al.,* 2007) also shown. Both sequences are plotted on their own timescales (black diamonds on the Ioannina record indicate alignment points used to construct the age model; see Roucoux *et al.,* 2011). Shared tephra horizons and associated age ranges are also shown (see Table 7.1 for details).

marker occurring just before or at the inception of the Last Interglacial. These two tephra layers can therefore be used effectively to stratigraphically 'bracket' the end of MIS 6.

8.4.3 Determining potential leads and lags in vegetation response

Tzedakis (2009) suggested that the proxy curve alignment approach precludes the ability to assess phase relationships (i.e. leads or lags) between AETs, as almost all independent dating techniques yield large error ranges for events dating to within the LLG, the error ranges often being greater than the duration of the AETs in question (Tzedakis *et al.,* 2004). Ballie (1991) also identified this problem suggesting that independent chronological uncertainties can sometimes 'smear' relatively short-lived events over longer intervals, perhaps promoting miscorrelation.

This section will assess whether potentially diachronous pollen signals may be detected and even possibly quantified using the tephrostratigraphic scheme and associated age models developed in this study. Due reference is also made to other relevant records, in particular the LGdM tephra archive for the LLG period. Rather than focus on different proxy responses, here consideration will focus on pollen signals alone, since these should be more directly comparable.

In order to address this question using tephra layers found in more than one sequence, the following data are provided in Tables 8.2 and 8.3: vertical sampling distance (in cm) of both the first pollen sample taken both above and below each tephra horizon and secondly an estimated time gap between these two horizons, calculated by interpolation of mean values obtained from the the final age model (C) outlined in Chapter 7. As most of the records being compared here are either non-varved or partially varved (e.g. LGdM) the time gap value should be seen as a coarse comparative guide rather than as a precise fixed value without uncertainties. All of the pollen records within this section are also shown in Figure 8.17 for visual comparison.

Table 8.2 – Vertical sampling distance and estimated time gap (calculated via interpolation of mean values for the final age model (C)) between tephra layers and the first underlying and overlying pollen analysis sample for sites investigated within this study. Note that for cryptotephra layers the peak tephra shards or mean value was used as the comparative depth value.

	Fimon (PD)					Kopais (K-93)					Tenaghi Philippon (TP-2005)					Lesvos (ML-00, *ML-01*)			
Tephra	Distance below Tephra (cm)	Time gap (yrs)	Distance above Tephra (cm)	Time gap (yrs)		Distance below Tephra (cm)	Time gap (yrs)	Distance above Tephra (cm)	Time gap (yrs)		Distance below Tephra (cm)	Time gap (yrs)	Distance above Tephra (cm)	Time gap (yrs)		Distance below Tephra (cm)	Time gap (yrs)	Distance above Tephra (cm)	Time gap (yrs)
Cape Riva											2	78	1	28		*8*	*816*	*4*	*181*
TM-15											<1	<3	5	94					
TP-978											2	40	3	53		7	162	4	185
Campanian Ignimbrite	<1	<1	10	1012		31	72	49	919		2	33	23	920		~5	638	11	580
TM-18-1d											<1	<5	2	37					
TP-1450											<1	<2.5	2	50		5	570	5	656

Table 8.3 – Vertical sampling distance and estimated time gap (calculated via the LGdM varve chronology; Allen *et al.,* 1999) between tephra layers and the first underlying and overlying pollen analysis sample for Lago Grande di Monticchio, Italy.

	LGdM			
Tephra	Distance below Tephra (cm)	Time gap (varve yrs)	Distance above Tephra (cm)	Time gap (varve yrs)
TM-15	N/A	112	N/A	1
Campanian Ignimbrite	N/A	70	N/A	1
TM-18-1d	N/A	230	N/A	3

The CI can be used to assess the relative timing of the drop in total tree pollen (probably relating to HE4) in the Kopais and Tenaghi Philippon records. The pollen sample below the tephra horizon (at ~72 and ~33 yrs respectively) shows that total tree pollen was already fully subdued in both records. This may also be seen in LGdM where a pollen spectra level is available at a similar temporal interval (~70 varve yrs) below the CI tephra which also shows this trend (see Fig. 8.18).

In Fimon a pollen sample available from directly below the CI cryptotephra layer (<1 cm) shows, in contrast, increases in total tree pollen. This increase is, however, reflective of taxa requiring higher precipitation levels (e.g. mixed-oak woody plants and *Tilia*) being replaced with those that are more adapted to arid conditions (e.g. *Pinus sylv/mugo*). Finally within Lesvos, the pollen sample beneath the CI shows decreasing total tree pollen percentages, although not the fully subdued percentages values observed after the deposition of the CI in this site. This difference may be due to the potential larger temporal gap between the tephra and the first underlying pollen sample (see Table 8.2).

Taken together then the records described above appear to show that the AET (related to an increase in arid conditions, probably relating to HE4) had a broadly synchronous timing within each palaeo-record, with its inception just before the deposition of the

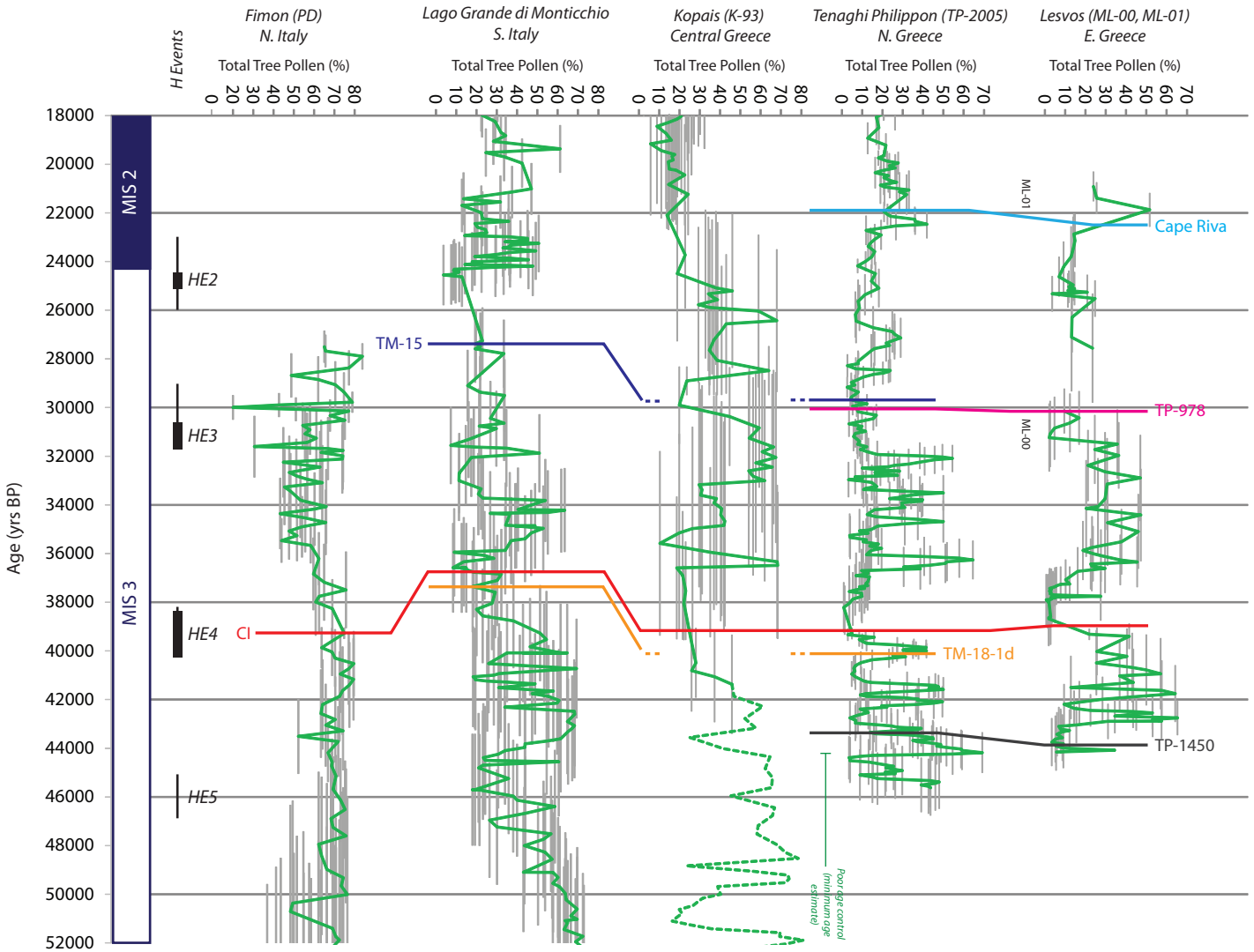

Figure 8.17 – The total tree pollen records of Fimon (PD), Kopais (K-93), Tenaghi Philippon (TP-2005) and Lesvos (ML-00 and ML-01) plotted on the final age models outlined in Chapter 7 compared against the Lago Grande di Monticchio (LGdM) pollen record for the 18–52 ka BP. The LGdM pollen record is taken from Allen *et al.* (1999) and the timescale and has been adjusted on the basis of the most recent tephra varve age information outlined in Wulf *et al.* (2004; 2006), a 5% counting error is assumed (Brauer *et al.,* 2000). Also shown are calibrated age ranges for Heinrich (H) events 2, 3, 4 and 5 from western European records (Bard *et al.,* 2000; Sánchez Goñi et al., 2002; de Abreu *et al.,* 2003) (thin lines) and calculated ages (Thouveny *et al.,* 2000) (black boxes) and Marine Isotope Stages (from Martinson *et al.,* 1987).

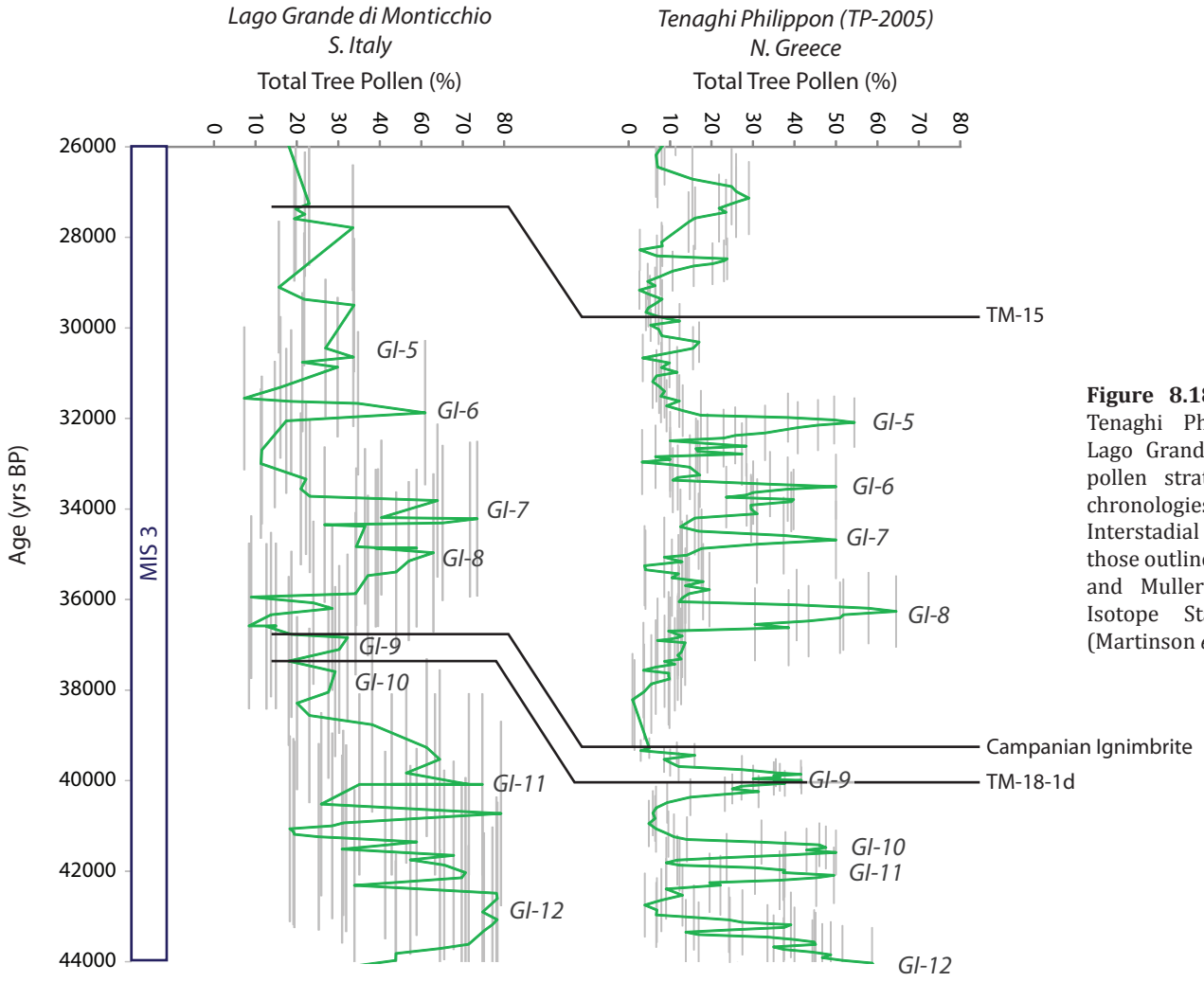

Figure 8.18 – Comparison of the Tenaghi Philippon (TP-2005) and Lago Grande di Monticchio (LGdM) pollen stratigraphies following the chronologies of Fig. 8.17. Greenland Interstadial number labelling follow those outlined in Fletcher *et al.* (2010) and Muller *et al.* (2011). Marine Isotope Stages are also shown (Martinson *et al.*, 1987).

CI. Also highlighted are different regional expressions to the same environmental event, as within Fimon there is a switch in percentages between differing tree species rather than a fall in total tree pollen percentages overall, as seen in the three other sites. This difference is probably due to different physiographic conditions where precipitation remained high enough in the Fimon area to maintain a tree presence. Indeed this may be seen from the modern climate characteristics where the Fimon region records significantly higher mean annual rainfall when compared to Kopais, Tenaghi Philippon and Lesvos (see Table 4.11).

Another tephra layer, TP-978, present in both Tenaghi Philippon and Lesvos can also be utilised to 'bracket' a decrease in total tree pollen (from a small peak observed in both records; see sections 7.6 and 8.4.5). The position of this cryptotephra also appears to demonstrate a broadly coeval pollen signal timing (see Fig. 8.17). The TM-15 tephra layer (which is almost coeval with the TP-978 tephra; see Fig. 8.17) may also be traced from Tenaghi Philippon into the LGdM sequence where a similar decrease in total tree pollen from a small peak may also be observed (see Fig. 8.18).

In contrast tephra layers TM-18-1d and the Cape Riva may be used to assess the phasing of where increases in total tree pollen percentages are occuring. The TM-18-1d tephra layer occurs within both Tenaghi Philippon and the LGdM sequences. Within Tenaghi Philippon the tephra layer sits within a period of increased tree pollen percentages whereas in LGdM a pollen sample from directly above the tephra layer indicates subdued total tree pollen values before a later increase post tephra deposition (see Fig. 8.18). This would suggest that Tenaghi Philippon is responding faster than LGdM if indeed both of these events are responses to the same forcing.

The Cape Riva tephra may also allow assessment, if at a coarser resolution, of a tree expansion event correlated to GI-2 in both Tenaghi Philippon and Lesvos (Fletcher *et al.,* 2010; Müller *et al.,* 2011). Based upon their original chronologies the AET occurs at the same time (see Fig. 7.13) and these palaeoenvironmental events cannot be distinguished temporally on absolute chronological error either (see Fig. 8.17). However the position of the Cape Riva in both cores may suggest an offset in peak total tree pollen response, with the Tenaghi Philippon sequence seemingly responding first before a decline in tree pollen percentages occurs, whereas the main significant oscillation within Lesvos (ML-01) occurs after the Cape Riva has been deposited. The lower pollen sampling resolution of the Lesvos sequence (see table 8.2) does make

detailed assessment of a potential lead and lag highly uncertain at this stage although efforts are underway to improve the Lesvos pollen spectra resolution to allow a more robust direct comparison (V. Margari, *pers. comm.*).

Within this section examples have been highlighted where fairly in phase or synchronous timings can be observed (e.g. the total tree pollen drop before the CI) and also where apparent asynchronous environmental responses are operating between sites (e.g. the total tree pollen increase associated with TM-18-1d). In all these cases asynchronous and synchronous AETs would remain invisible or 'hidden' without the utilisation of tephra layers as isochronous markers due to chronological uncertainties (see Fig. 8.17). Tenaghi Philippon appears to respond rapidly during tree expansion events in comparison to other records (e.g. LGdM and potentially Lesvos). This finding is in agreement with the suggestion by Müller *et al.* (2010) that the Tenaghi Philippon site is ideally suited to record abrupt climatic improvements without large lags due to its proximity to glacial tree refugia areas, which reduces migration lags.

Finally it is worth noting that here comparisons have largely only been made using total tree pollen percentages, although this does give a good indication of changing aridity and to lesser extent changing temperatures in the Mediterranean, much more detailed comparisons are required, using individual taxa. This would add much value when considering the questions outlined here and when making such inter-site comparisons.

8.4.4 Applying the INTIMATE approach

The final part of this chapter will very briefly consider the application of the Greenland ice–core record as a regional stratotype event stratigraphy for the Mediterranean region during the LLG. The INTIMATE Group has proposed the Greenland record as a stratotype for the North Atlantic area and suggests it may also be used over wider regions (Lowe *et al.,* 2008). Many authors have implied direct relationships between palaeoenvironmental events in the Mediterranean region and Greenland, indeed this is the most common way for alignment based chronologies to be constructed, as has been described in this study (e.g. Pini *et al.,* 2010; Margari *et al.,* 2007; 2009). Via the use of the independent chronologies (and errors) produced here we can assess these potential linkages, this will be done for the Tenaghi Philippon and Lesvos pollen

records as these have smaller age errors and strong stratigraphical linkages via shared common tephra horizons. Firstly although no direct stratigraphical correlations can be made between the Greenland and the Mediterranean pollen records under discussion here, a partial relationship may be determined via the position of the Laschamp geomagnetic excursion and the CI, which have both recently been observed within the same marine core sequence from the Black Sea (Nowaczyk *et al.,* 2012). This may be used to provide an ordering of events as the Laschamp event has been correlated to a ^{10}Be flux in the NGRIP record situated within GI-10 (41,200 ± 1628 yrs BP; shown in Fig. 8.19). Combined with this the Laschamp excursion has been directly dated to 40,700 ± 950 b2k by Singer *et al.* (2009; also shown). Comparison between the NGRIP event stratigraphy and the two pollen records suggests remarkable visual similarities, with Tenaghi Philippon in particular recording (within age error) very distinctive events which temporally may correlate with GI events (particularly GI-5 to 8; see Fig. 7.8) this is largely in agreement with the findings of Müller *et al.* (2011). It can be observed, however, that the pollen events within Tenaghi Philippon, unlike the GI events (see Fig. 1.2), display sharp increases and falls (rather than just sharp increases) which could be reflecting differing proxy thresholds.

Austin *et al.* (2012) found evidence for a warm interval within GS-3 from several North Atlantic marine sequences dated to c.25 ka BP, which is apparently absent from the Greenland ice–core record event stratigraphy, this event was named NEA-GS-3b (shown in Fig. 8.19). Intriguingly a small increase in tree pollen percentages may be observed from the Tenaghi Philippon and potentially Lesvos records during this timeframe. This would be in agreement with the findings of Tzedakis (2007) who also noted this apparent trend in the Mediterranean, which is suggestive of interstadial conditions persisting up until around 24 ka BP.

A similar, but older, palaeoenvironmental event may also be observed within both the Tenaghi Philippon and Lesvos sequences (both capped by the TP-978 cryptotephra). The age control available from the Tenaghi Philippon sequence allows this event to be temporally distinguished from either GI-4 or GI-5 and other pollen events within Tenaghi Philippon seem, instead, to coincide with these GI events (see Fig. 8.19). There is no labelled event within the current INTIMATE event stratigraphy and therefore this may represent a regional palaeoenvironmental event recorded in the Eastern Mediterranean record around 30.2 ka. Alternatively this event may be present within the Greenland record but as a mooted signal that has not been labelled. It occurs near

the onset of HE3 and appears to show a very brief climatic improvement that allowed a small tree expansion. Tentatively this event is labelled here EMR-GS-5b (EMR: Eastern Mediterranean Region). The position of the TM-15 tephra directly after this event within Tenaghi Philippon (EMR-GS-5a) allows this event to be tested for in other high resolution palaeo-records, particularly those which might record a more direct climate signal.

From this evidence it would appear that the Greenland record forms a useful comparison event stratigraphy for the Eastern Mediterranean although in the future direct independent comparisons to the more regional Soreq speleothem isotope record, which has a high precision U-Th chronology available, may also be desirable; particularly to see if the EMR event described here is present. Currently however this is somewhat hampered by low proxy resolution during parts of the LLG (Bar-Matthews *et al.,* 1999; 2003).

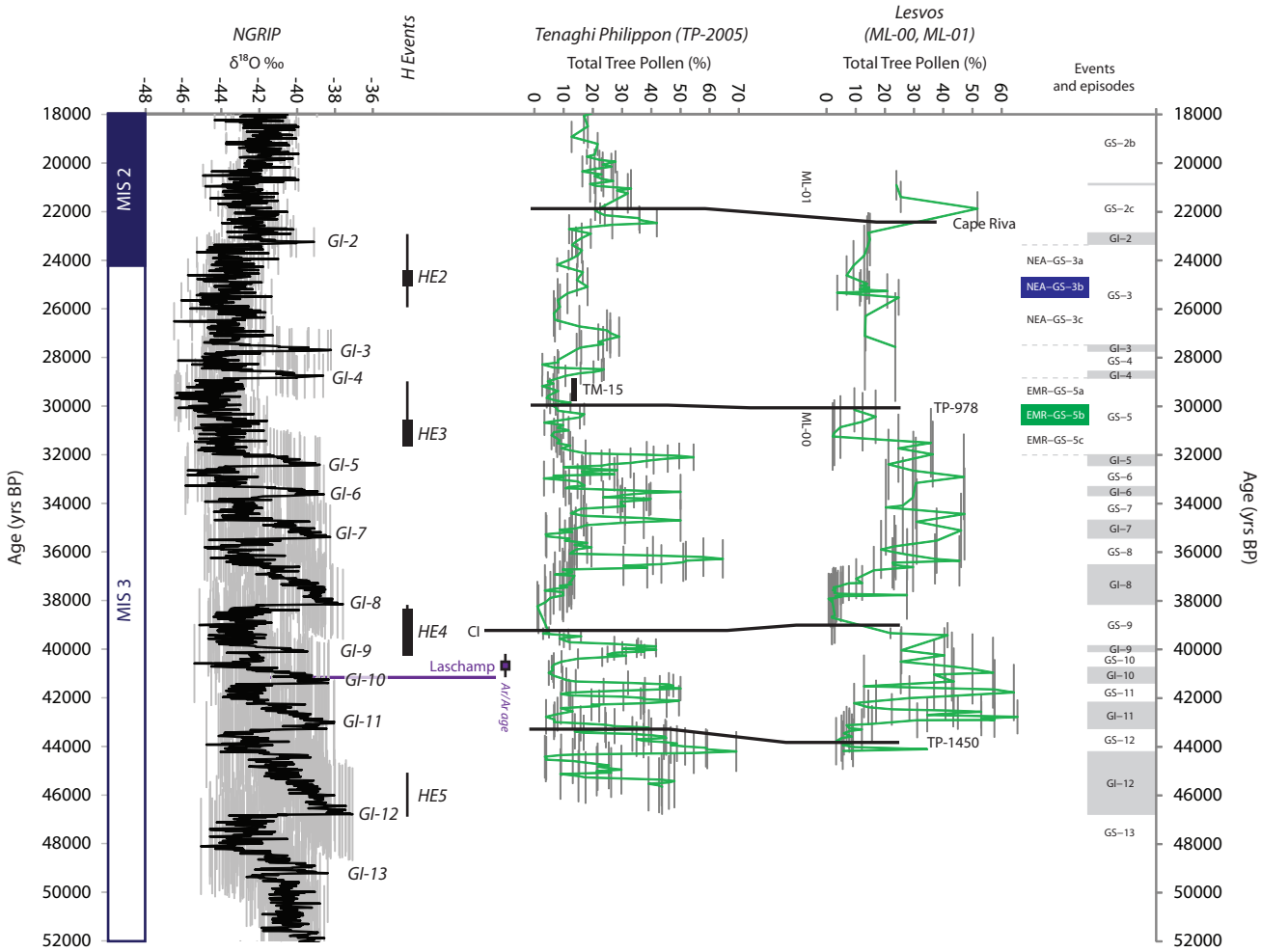

Figure 8.19 – Shown from left to right: The 18,000–52,000 yrs BP record of: Marine Isotope Stages (from Martinson *et al.,* 1987). The NGRIP oxygen isotope record (Rasmussen *et al.,* 2006; Svensson *et al.,* 2008). The interpreted position of the Laschamp geomagnetic excursion in NGRIP is also shown (Svensson *et al.,* 2008) along with a direct $^{40}Ar/^{39}Ar$ age for this event (Singer *et al.,* 2009). Also shown are calibrated age ranges for Heinrich (H) events 2, 3, 4 and 5 from western European records (Bard et al., 2000; Sánchez Goñi et al., 2002; de Abreu *et al.,* 2003) (thin lines) and calculated ages (Thouveny *et al.,* 2000) (black boxes). Tenaghi Philippon (TP-2005) and Lesvos (ML-00 and ML-01) plotted against the final age–depth models proposed within this study. The INTIMATE event stratigraphy is also shown (Lowe *et al.,* 2008; Blockley *et al.,* 2012) alongside regional events recognised by Austin *et al.* (2012; in blue) and in this study (in green). Note all data have been adjusted to a yrs BP (1950) timescale.

9.0 CONCLUSIONS

9.1 Key Findings

The findings of this research can be separated into three sections: firstly the tephrochronological findings, secondly the palaeoenvironmental, and finally the chronological implications for LLG terrestrial sequences:

Tephrochronological findings

- Several discrete tephra layers have been detected and characterised across four study sites, both extending the distribution of previously identified volcanic layers (e.g. TM-15) into the Eastern Mediterranean and also identifying widespread but previously unrecognised tephra layers (e.g. TP-1450).
- Previously unrecognised Santorini tephra layers have also been identified and dated at 29,910±360 (TP-978) and 20010±490 yrs BP (TP-726). A new age is suggested for the PhT1 tephra layer of St Seymour *et al.* (2004) to 18065±1085 yrs BP (=TP-707). All these tephra share an identical geochemistry to the Cape Riva tephra (c.22 ka BP) which has implications for the robust identification of this tephra in the Quaternary record and impinges upon its use as a chronostratigraphic marker.
- A more refined age for the TM-15 tephra has been derived from the Tenaghi Philippon chronostratigraphy at 29370-30150 yrs BP. TM-15 also shares an almost coeval timing with a newly identified Santorini eruption, the TP-977 tephra (named after its first observation in Tenaghi Philippon). This increases the geographical range at which this time-parallel marker may be utilised as TP-977 and can be effectively used as a surrogate for the TM-15 tephra. This represents an important addition to the tephrochronological framework of the Eastern Mediterranean region. These tephra layers also lie within a period of a marked reduction in total tree pollen percentages which temporally relates to a period just after the onset of HE3 and also marks the end of an Eastern Mediterranean region palaeoenvironmental event (EMR–GS–5b).

Palaeoenvironmental findings

- This research has highlighted evidence of both asynchronous and synchronous pollen signals during the LLG via the use of tephrostratigraphy. Using tephra layers in this way reveals potentially important palaeoenvironmental data currently 'hidden' or obscured via the use of alignment techniques. During the LLG testing the synchroneity of pollen responses requires the presence of coeval tephra horizons. This study has highlighted where these tephra layers exist and thus where future studies considering this question should focus.

Chronological Implications

- New tephrochronological results have both revealed and help confirm significant chronological off-sets between alignment based chronologies and those derived via independent chronological methods alone. These offsets are at resolutions of 10^3–10^4 years in scale and highlight the need to treat alignment based chronologies, specifically those based upon palynostratigraphic correlations, with some caution.
- This study has demonstrated that very precise age control can be achieved for non-varved records during parts of the LLG with the combined use of tephrochronology, Bayesian age–depth modelling and differential dating techniques. Differential dating when combined with precise $^{40}Ar/^{39}Ar$ ages in particular, allow comparable or even superior absolute age errors to be achieved than is currently possible in the GICC05 Greenland ice core chronology as well as by-passing radiocarbon calibration complexities. This allows robust independent comparison of relative timings of abrupt palaeoenvironmental events between distant palaeo-records.

9.2 Recommendations for further work

- During this study qualitative graphical means (i.e. bi-plots) were used to compare geochemical data and distinguish or correlate between tephra layers. This method, though thorough, is highly time consuming and as geochemical database sizes grow automated statistical measures will have to be applied in order to allow practical time efficient assessment of potential correlatives (which can then be assessed graphically). Efforts are underway to this end with, for example, tools being developed for the RESET database including the potential usage of multi-dimensional kernel density statistics (C. Bronk Ramsey, *pers. comm.*).
- Some results within this study require independent confirmation in other tephrostratigraphical records, particularly in the Eastern Mediterranean where very few cryptotephra records are currently available for comparison. Ideally records with differing sedimentary environments should be assessed (i.e. lacustrine alongside peat bogs) as different stores are less likely to be afflicted by the same re-working issues. This should also aid our understanding of tephra deposition as well as perhaps allowing different sedimentary environments to be correlated and contrasted.
- Within this study evidence has emerged of probable tephra reworking, which may relate to catchment reworking processes or through the vertical displacement of shards through sediment sequences. Understanding these processes, particularly for cryptotephra layers, and how to better differentiate between primary and secondary tephra deposition should be a key aim for tephrochronologists. Strategies to this end may involve thin section micromorphology (e.g. Matthews *et al.,* 2011b) or x-ray microtomography. Also horizontal cross core sampling for cryptotephra (compared to the more standard vertical sampling) may also allow cryptotephra distributions and potential reworking to be better understood (Pyne-O'Donnell, 2004). This may also help explain instances where, for example, tephra shards cannot be replicated during resampling due to patchy distributions.

10 REFERENCES

Abbott, P.M., (2005) Towards a tephrochronology for a southern Adriatic deep marine sequence. MSc Thesis, University of London, unpublished.

Abbott, P.M., Davies, S.M., Austin, W.E.N., Pearce, N.J.G., Hibbert, F.D. (2011) Identification of cryptotephra horizons in a North East Atlantic marine record spanning marine isotope stages 4 and 5a (~60,000–82,000 a b2k). Quaternary International 246, 177–189.

Abbott, P.M., Davies, S.M., Steffensen, J.P., Pearce, N.J., Bigler, M., Johnsen, S.J., Seierstad, I.K., Svensson, A., Wastegård, S. (2012) A Detailed Framework of Marine Isotope Stages 4 and 5 Volcanic Events recorded in two Greenland Ice-cores Quaternary Science Reviews 36, 59–77.

Aksu, A.E., Jenner, G., Hiscott, R.N., Isler, E.B. (2008) Occurrence, stratigraphy and geochemistry of Late Quaternary tephra layers in the Aegean Sea and the Marmara Sea. Marine Geology 252, 174–192.

Alessio, M., Bella, F., Improta, S., Belluomini, G., Calderoni, G., Cortesi, C., Turi, B. (1976) University of Rome carbon-14 dates XIV. Radiocarbon 18, 321–349.

Allen, H.D. (1986) Late Quaternary of the Kopais Basin, Greece: Sedimentary and Environmental History. Unpublished PhD Thesis, University of Cambridge.

Allen, H.D. (1990) A postglacial record from the Kopais Basin, Greece. In: Bottema, S., Entjes-Nieborg, Van Zeist, W. (eds) Man's Role in the Shaping of the Eastern Mediterranean. Balkema, Rotterdam, 173–182.

Allen, J. & Huntley, B. (2011) Effects of ash falls on vegetation – a palynological study. Poster Presentation at INQUA, Bern, Switzerland. (21–27th July).

Allen, J.R.M., Brand, U., Brauer, A., Hubbertens, H.W., Huntley, B., Keller, J., Kraml, M., Mackensen, A., Mingram, J., Negendank, J.F.W., Nowaczyk, N.R., Oberhansli, H., Watts, W.A., Wulf, S., Zolitschka, B. (1999) Rapid environmental changes in southern Europe during the last glacial period. Nature. 400, 740–743.

Allen, S.R. (2001) Reconstruction of a major caldera-forming eruption from pyroclastic deposit characteristics: Kos Plateau Tuff, eastern Aegean Sea. Journal of Volcanology and Geothermal Research 105, 141– 162.

Alley, R. B., Meese, D. A., Shuman, C. A., Gow, A. J., Taylor, K. C., Grootes, P. M., White, J. W. C., Ram, M., Waddinton, E. D., Mayewski, P. A., Zielinski, G. A. (1993) Abrupt increase in Greenland snow accumulation at the end of the Younger Dryas. Nature. 362, 527–529.

Alloway, B.V., Larsen, G., Lowe, D.J., Shane, P.A.R., Westgate, J.A. (2007) QUATERNARY STRATIGRAPHY: Tephrochronology. In: Encyclopedia of Quaternary Science. S. A. Elias. Oxford.

Anastasakis, G. & Pe-Piper, G. (2006) An 18 m thick volcaniclastic interval in Pantelleria Trough, Sicily Channel, deposited from a large gravitative flow during the Green Tuff eruption. Marine Geology 231, 201–219.

Andersen, K.K., Svensson, A., Rasmussen, S.O., Steffensen, J.P., Johnsen, S.J., Bigler, M., Röthlisberger, R., Ruth, U., Siggaard-Andersen, M.-L., Dahl-Jensen, D., Vinther, B.M., Clausen, H.B. (2006) The Greenland ice core chronology 2005, 15–42 ka. Part 1: constructing the time scale. Quaternary Science Reviews 25, 3246–3257.

Anderson, R.Y., Nuhfer, E.B., Dean, W.E. (1984) Sinking of volcanic ash in uncompacted sediment in Williams Lake, Washington. Science 225, 505–508.

Andrews, J.T., Erlenkeuser, H., Tedesco, K., Aksu, A.E., Jull, A.J.T. (1994) Late Quaternary (Stage 2 and 3) meltwater and Heinrich events, northwest Labrador Sea, Quaternary Research, 41, 26–34.

Andrews, J.T., Eberl D.D., Kristjansdóttir, G.B. (2006) An exploratory method to detect tephras from quantitative XRD scans: Examples from Iceland and east Greenland marine sediments. The Holocene 16, 1035–1042.

Andronico, D., Branca, S., Del Carlo, P. (2001) The 18.7 Ka phreatomagmatic flank eruption on Etna (Italy): relationship between eruption activity and sedimentary basement setting. Terra Nova 13, 235-240.

Andronico, D., Calderoni, G., Cioni, R., Sbrana, A., Sulpizio, R., Santacroce, R. (1995) Geological map of Somma-Vesuvius Volcano. Periodico di Mineralogia 64, 77–78.

Aruga, R. (2004) Multivariate classification of constrained data: problems and alternatives. Analytica Chimica Acta 527 (1), 45–51.

Austin, W.E.N., Hibbert, F.D., Rasmussean, S.O., Peters, C., Abbott, P.M., Bryant, C.L. (2012) The synchronization of palaeoclimatic events in the North Atlantic region during Greenland Stadial 3 (ca 27.5 to 23.3 kyr b2k). Quaternary Science Reviews 36, 154-163.

Austin, W.E.N., Wilson, L.J., Hunt, J.B. (2004) The age and chronostratigraphical significance of North Atlantic Ash Zone II. Journal of Quaternary Science 19, 137–146.

Bachmann, O., Schoene, B., Schnyder, C., Spikings, R. (2010) The $^{40}Ar/^{39}Ar$ and U/Pb dating of young rhyolites in the Kos-Nisyros volcanic complex, Eastern Aegean Arc, Greece: Age discordance due to excess ^{40}Ar in biotite. Geochemistry Geophysics Geosystems 11, 1–14.

Baillie, M.G.L. (1991) Suck-in and smear — two related chronological problems for the 90s. Journal of Theoretical Archaeology 2, 12–16.

Baines, P.G. & Sparks, R.S.J. (2005) Dynamics of giant volcanic ash clouds from supervolcanic eruptions. Geophysical Research Letters 32, L24808.

Balascio, N., Bradley, R.S., Francus, P. (2008) Improving methods for locating cryptotephra in minerogenic lacustrine sediment of the Canadian High Arctic. 38th International Arctic Workshop. University of Colorado at Boulder, Colorado, USA.

Balter, M. (2006) Mild climate, lack of moderns let last Neanderthals linger in Gibraltar, News of the week Science 313, 1557.

Barberi, F., Innocenti, F., Lirer, L., Munno, R., Pescatore, T., Santacroce, R. (1978) The Campanian ignimbrite: a major prehistoric eruption of the Neapolitan area (Italy). Bull. Volcanol. 41, 10–31.

Barberi, F., Navarro, J.M., Rosi, M., Santacroce, R., Sbrana, A. (1988) Explosive interaction of magma with ground water: insights from xenoliths and geothermal drillings. Rendiconti della Societa Italiana di Mineralogica e Petrologica 43, 901–926.

Bard E, Rostek F, Ménot-Combes G. (2004b) Radiocarbon calibration beyond 20,000 ^{14}C yr B.P. by means of planktonic foraminifera of the Iberian Margin. Quaternary Research 61(2), 204–214.

Bard, E., Rostek, F., Ménot-Combes, G. (2004a) A better radiocarbon clock. Science 303(5655), 178–179.

Bard, E., Rostek, F., Turon, J.-L., and Gendreau, S. (2000) Hydrological impact of Heinrich events in the Subtropical Northeast Atlantic. Science 289, 1321–1324.

Bar-Matthews, M., Ayalon, A., Kaufman, A., and Wasserburg, G. J. (1999) The eastern Mediterranean paleoclimate as a reflection of regional events: Soreq cave, Israel. Earth and Planetary Science Letters 166(1–2), 85–95.

Barry, R.G. & Chorley, R.J. (1992) Atmosphere, Weather and Climate. Routledge, London.

Bartov, Y., Goldstein, S.L., Stein, M., Enzel, Y. (2003) Catastrophic arid episodes in the Eastern Mediterranean linked with the North Atlantic Heinrich events. Bulletin of the Geological Society of America 31, 439–442.

Beaudouin, C., Suc, J–P, Escarguel, G., Arnaud, M., Charmasson, S. (2007) The significance of pollen signal in present-day marine terrigenous sediments: The example of the Gulf of Lions (western Mediterranean Sea). Geobios 40, 159–172.

Bennett, K.D. (1988) Holocene pollen stratigraphy of central East Anglia, England, and comparison of pollen zones across the British Isles. New Phytologist 109, 237–253.

Bennett, K.D. (1994) Confidence intervals for age estimates and deposition times in late-Quaternary sediment sequences. The Holocene 4, 337–348.

Bibus, E., Frechen, M., Kösel, M., Rähle, W. (2007) Das jungpleistozäne Lössprofil von Nussloch (SW-Wand) im Aufschluss der Heidelberger Zement AG. Eiszeitalter und Gegenwart, 56, 227–255.

Bichler, M., Pearce, N., Steinhauser, G., Sterba, J.H., 2009. More than just a convoluted table? A comment on Margari et al. (2007) Journal of Volcanology and Geothermal Research 181, 247–250.

Bigazzi, G., Yegingil, Z., Ercan, T., Oddone, M., Ozdogan, M. (1993) Fission track dating obsidians in central and northern Anatolia. Bulletin of Volcanology 55, 588-595.

Björck, S., Walker, M.J.C., Cwynar, L., Johnsen, S.J., Knudsen, K.-L., Lowe, J.J., Wohlfarth, B., INTIMATE Members. (1998) An event stratigraphy for the last termination in the North Atlantic region based on the Greenland Ice Core record: a proposal by the INTIMATE group. Journal of Quaternary Science 13, 283–292.

Blaauw, M. (2012) Out of tune: the dangers of aligning proxy archives. Quaternary Science Reviews 36, 38–49.

Blaauw, M., van Geel, B., Kristen, I., Plessen, B., Lyaruu, A., Engstrom, D.R., van der Plicht, J., Verschuren, D. (2011) High-resolution ^{14}C dating of a 25,000-year lake-sediment record from equatorial East Africa. Quaternary Science Reviews 30, 3043–3059.

Blaauw, M., van Geel, B., Mauquoy, D., van der Plicht, J. (2004) Radiocarbon wiggle-match dating of peat deposits: advantages and limitations. Journal of Quaternary Science 19, 177-181.

Blaauw, M., Wohlfarth, B., Christen, J.A., Ampel, L., Veres, D., Hughen, K.A., Preusser, F., Svensson, A. (2008) Were last glacial climate events simultaneous between Greenland and western Europe? Climate of the Past 4, 1203–1217.

Blockley, S., Lowe, J., Walker, M., Asioli, A., Trincardi, F., Coope, G., Pollard, A., Donahue, R. (2004) Bayesian analysis of radiocarbon chronologies: examples from the European Lateglacial. Journal of Quaternary Science 19, 159–175.

Blockley, S.P.E., Blaauw, M., Bronk Ramsey, C., van der Plicht, J. (2007a) Building and testing age models for radiocarbon dates in Lateglacial and Early Holocene sediments. Quaternary Science Reviews 26, 1915–1926.

Blockley, S.P.E., Bronk Ramsey, C., Pyle, D.M. (2007b) Improved age modelling and high-precision age estimates of late Quaternary tephras, for accurate palaeoclimate reconstruction. Journal of Volcanology and Geothermal Research 177, 251–262.

Blockley, S.P.E., Lane, C.S., Hardiman, M., Rasmussen, S., Seierstad, I., Turney, C.S., Bronk Ramsey, C. (2012) Synchronisation of palaeoenvironmental records over the last 60,000 years, an extended INTIMATE group protocol. Quaternary Science Reviews 36, 2–12.

Blockley, S.P.E., Pyne-O'Donnell, S.D.F., Lowe, J.J., Matthews, I.P., Stone, A., Pollard, A.M., Turney, C.S.M., Molyneux, E.G. (2005) A new and less destructive laboratory procedure for the physical separation of distal glass tephra shards from sediments. Quaternary Science Reviews 24, 1952–1960.

Blockley, S.P.E., Ramsey, C.B., Lane, C.S., Lotter, A.F. & Blockley, S. (2008) Improved age modeling approaches as exemplified by the revised chronology for the Central European varved lake Soppensee. Quaternary Science Reviews 27(1-2), 61–71.

Bond, A. (1976). Multiple sources of pumice in the Aegean. Nature 259, 194–195.

Bond, G. & Lotti, R. (1995) Iceberg discharges into the North Atlantic on millennial time scales during the last glaciation. Science 267, 1005–1010.

Bond, G., Broecker, W., Johnsen, S., McManus, J., Labeyrie, L., Jouzel, J., Bonani, G., (1993) Correlations between climate records from North Atlantic sediments and Greenland ice. Nature 365, 143–147.

Bond, G.C., Heinrich, H., Broecker, W., Labeyrie, L., McManus, J., Andrews, J., Huon, S., Jantschik, B., Clasen, S., Simet, C., Tedesco, K., Klas, M., Bonani, G., Ivy, S., (1992) Evidence for massive discharges of icebergs into the North Atlantic ocean during the last glacial period. Nature 360, 245–249.

Bond, G.C., Mandeville, C., Hoffmann, S. (2001) Were rhyolitic glasses in the Vedde Ash and in the North Atlantic's Ash Zone 1 produced by the same volcanic eruption? Quaternary Science Reviews 20, 1189–1199.

Bourne, A. (2012) The late Quaternary tephrochronology of the Adriatic region: implications for the synchronisation of marine records. unpublished PhD, Royal Holloway, University of London.

Bourne, A., Lowe, J.J., Trincardi, F., Asioli, A., Blockley, S.P.E., Wulf, S., Matthews, I.P., Piva, A., Vigliotti, L. (2010) Distal tephra record for the last ca 105,000 years from core PRAD 1-2 in the central Adriatic Sea: implications for marine tephrostratigraphy. Quaternary Science Reviews 29 (23–24), 3079–3094.

Boygle, J. (1999) Variability of tephra in lake and catchment sediments, Svínavatn, Iceland. Global and Planetary Change 21, 129–149

Brauer, A., Mingram, J., Frank, U., Günter, C., Schettler, G., Wulf, S., Zolitschka, B., Negendank, J.F.W. (2000) Abrupt environmental oscillations during the Early Weichselian recorded at Lago Grande di Monticchio, southern Italy. Quaternary International 73/74, 79-90.

Brendryen, J., Haflidason, H., Sejrup, H.P. (2010) Norwegian Sea tephrostratigraphy of marine isotope stages 4 and 5: Prospects and problems for tephrochronology in the North Atlantic region. Quaternary Science Reviews 29, 847–864.

Broecker, W.S. (1994) Massive iceberg discharges as triggers for global climate-change. Nature 372, 421–24.

Broecker, W.S., Bond, G.C., Klas, M., Clark, E., McManus, J.F. (1992), Origin of the northern Atlantic's Heinrich events. Climate Dynamics 6, 265–273.

Bronk Ramsey, C. (1995). Radiocarbon calibration and analysis of stratigraphy: The OxCal program. Radiocarbon 37(2), 425-430.

Bronk Ramsey, C. (1999) Oxcal. Radiocarbon calibration and stratigraphic analysis program, Research Laboratory for Archaeology. Oxford University, Oxford.

Bronk Ramsey, C. (2000) Comment on the use of Bayesian statistics for C-14 dates of chronologically ordered samples: a critical analysis. Radiocarbon 42, 199–202.

Bronk Ramsey, C. (2001) Development of the radiocarbon calibration program OxCal. Radiocarbon 43 (2), 355–363.

Bronk Ramsey, C. (2008) Deposition model for chronological records. Quaternary Science Reviews, 27 (1–2), 42–60.

Bronk Ramsey, C. (2009), Bayesian analysis of radiocarbon dates, Radiocarbon, 51 (1), 337–360.

Brook, E.J., Harder, S., Severinghaus, J., Steig, E.J., Sucher, C.M. (2000) On the origin and timing of rapid changes in atmospheric methane during the last glacial period. Global Biogeochemical Cycles 14 (2), 559–572.

Buccheri, G., Bertoldo, G., Coppa, M.G., Munno, R., Pennetta, M., Siani, G., Valente, A., Vecchione, C. (2002a) Studio multidisciplinare della succession sedimentaria tardo-quaternaria proveniente dalla scarpata continentale del Golfo di Policastro (Tirreno meridionale). Bollettino della Societa` Geologica Italiana 121, 187–210.

Buccheri, G., Capretto, G., Di Donato, V., Esposito, P., Ferruzza, G., Pescatore, T., Russo Ermolli, E., Senatore, M. R., Sprovieri, M., Bertoldo, M., Carella, D.,Madonna, G. (2002b) A high resolution record of the last deglaciation in the southern Tyrrhenian Sea: environmental and climatic evolution. Marine Geology 186, 447–470.

Butler, S. (1992) X-radiography of archaeological soil and sediment profiles. Journal of Archaeological Science 19, 151–61.

Cacho, I., Grimalt, J.O., Pelejero, C., Canals, M., Sierro, F.J., Flores, J.A., Shackleton, N. (1999) Dansgaard–Oeschger and Heinrich event imprints in Alboran Sea paleotemperatures. Paleoceanography 14 (6), 698–705.

Calanchi, N., Cattaneo, A., Dinelli, E., Gasparotto, G., Lucchini, F. (1998) Tephra layers in Late Quaternary sediments of the central Adriatic Sea. Marine Geology 149, 1–4.

Caron, B., Sulpizio, R., Zanchetta, G., Siani, G., and Santacroce, R. (2010) The Late Holocene to Pleistocene tephrostratigraphic record of Lake Ohrid (Albania). Comptes Rendus Geoscience 342, 453–466.

Caseldine, C., Baker, A., Barnes, W.L. (1999) A rapid, non-destructive scanning method for detecting distal tephra layers in peat. The Holocene 9 (5), 635–638.

Chambers, F.M., Daniell, J.R.G., Hunt, J.B., Molloy, K., O'Connell, M. (2004) Tephrostratigraphy of An Loch Mor, Inis Oirr, western Ireland: implications for Holocene tephrochronology in the northeastern Atlantic region. Holocene 14 (5), 703–720.

Chapman, M. R., and Shackleton, N. J. (1998) Millennial-scale fluctuations in North Atlantic heat flux during the last 150,000 years. Earth Planetary Science Letters 159, 57–70.

Chappell, J., Head, J., Magee, J. (1996) Beyond the radiocarbon limit in Australian archaeology and Quaternary research. Antiquity 70, 543–52.

Christanis, K. (1983) Genese und Fazies der Torflagerstätte von Philippi (Griechisch-Mazedonien) als Beispiel der Enstehung einer Braunkohlen-Lagerstätte vom stark telematischen Typ. PhD-thesis at the Naturwissenschaftliche Fakultät of the Technische Universität Braunschweig, 179 pp.

Civetta, L., Cornette, Y., Gillot, P.-Y., Orsi, G. (1988) The eruptive history of Pantelleria (Sicily Channel) in the last 50 ka. Bulletin of Volcanology 50, 47–57.

Combourieu Nebout, N., Peyron, O. & Dormoy, I. (2009) Rapid climatic variability in the west Mediterranean during the last 25 000 years from high resolution pollen data, Climate Past Discussion, 5, 671-707.

Conard, N.J. & Bolus, B. (2003) Radiocarbon dating the appearance of modern humans and timing of cultural innovations in Europe: new results and new challenges. Journal of Human Evolution 44, 331–371.

Condomines, M., Morand, P., Camus, G., Duthou, L. (1982) Chronological and geochemical study of lavas from the Chaîne des Puys, Massif Central, France: evidence for crustal contamination. Contributions to Mineralogy and Petrology 81, 296–303.

Cook, G.T., van der Plicht, J. (2007) RADIOCARBON DATING: Conventional Method. In: Elias (Ed) Encyclopaedia of Quaternary Science. Elsevier.

Coope, G. R., Lemdahl, G. (1995) Regional differences in the Lateglacial climate of northern Europe based on coleopteran analysis. Journal of Quaternary Science 10 (4) 391-395.

Coope, G. R., Lemdahl, G., Lowe, J. J. & Walkling, A. (1998) Temperature gradients in northern Europe during the last glacial-Holocene transition (14{9 ka BP) interpreted from coleoptern assemblages. Journal of Quaternary Science 13, 419-433.

Cornette, Y., Crisci, G.M., Gillot, P.Y., Orsi, G. (1983) Recent volcano history of Pantelleria: A new interpretation. Journal of Volcanology and Geothermal Research 17, 361–373.

Cortijo, E., Duplessy, J.-C., Labeyrie, L., Duprat, J., Paillard, D. (2005) Heinrich events: hydrological impact. Comptes Rendus Geoscience 337(10), 897-907.

Cortijo, E., Labeyrie, L., Vidal, L., Vautravers, M., Chapman, M., Duplessy, J.-C., Elliot, M., Arnold, M., Turon, J.-L., Auffret, G. (1997) Changes in sea surface hydrology associated with Heinrich event 4 in the North Atlantic Ocean between 40° and 60°N. Earth and Planetary Science Letters 146, 29–45.

Coulter, S.E., Pilcher, J.R., Hall, V.A., Davies, S.M. (2010) Testing the reliability of the JEOL FEGSEM 6500F electron microprobe for quantitative major element analysis of glass shards from rhyolitic tephra. Boreas 39, 163–169.

d'Errico, F., Sánchez Goñi, M.F. (2004) 'A Garden of Eden for the Gibraltar Neanderthals? A reply to Finlayson et al.' Quaternary Science Reviews 23, 1205-1216.

d'Errico, F., Zilhão, J., Julien, M., Baffier, D., & Pélegrin, J. (1998) Neanderthal acculturation in western Europe? A critical review of the evidence and its interpretation. Current Anthropology 39, 1–44.

Dansgaard, W., Johnsen, S .J., Clausen, H. B., Dahl-Jensen, D., Gundestrup, N. S., Hammer, C. U., Hvidberg, C. S., Steffensen, J. P., Sveinbjörnsdottir, A. E., Jouzel, J., Bond, G. (1993) Evidence for general instability of past climate from a 250-Kyr ice-core record. Nature 364, 14. 218-220.

Davies, S.M., Abbott, P.M., Pearce, N.J.G., Wastegård, S., Blockley, S. P. E. (2012) Integrating the INTIMATE records using tephrochronology: rising to the challenge. Quaternary Science Reviews 36, 11–27.

Davies, S.M., Elmquist, M., Bergman, J., Wohlfarth, B., Hammarlund, D. (2007) Cryptotephra sedimentation processes within two lacustrine sequences from west central Sweden. The Holocene 17, 319–330.

Davies, S.M., Hoek, W.Z., Bohncke, S.J.P., Lowe, J.J., Pyne O'Donnell, S., Turney, C.S.M. (2005) Detection of Lateglacial distal tephra layers in the Netherlands. Boreas 34, 123–135.

Davies, S.M., Branch, N.P., Lowe, J., Turney, C.S.M. (2002) Towards a European tephrochronological framework for Termination 1 and the Early Holocene. Philosophical Transactions of the Royal Society of London Series a-Mathematical Physical and Engineering Sciences. 360 (1793), 767-802.

Davies, S.M., Larsen, G., Wastegård, S., Turney, C.S.M., Hall, V.A., Coyle, L., Thordarson, T. (2010a) Widespread dispersal of Icelandic tephra: how does the Eyjafjöll eruption of 2010 compare to past Icelandic events? Journal of Quaternary Science 25(5), 605–611.

Davies, S.M., Turney, C.S.M., Lowe, J.J. (2001) Identification and significance of a visible, basalt-rich Vedde Ash layer in a Late-glacial sequence on the Isle of Skye, Inner Hebrides, Scotland. Journal of Quaternary Science 16, 99–104.

Davies, S.M., Wastegård, S., Abbott, P.M., Barbante, C., Bigler, M., Johnsen, S.J., Rasmussen, T.L., Steffensen, J.P., Svensson, A. (2010b) Tracing volcanic events in the NGRIP ice-core and synchronising North Atlantic marine records during the last glacial period. Earth and Planetary Science Letters 294, 69–79.

Davies, S.M., Wastegård, S., Rasmussen, T.L., Johnsen, S.J., Steffensen, J.P., Andersen, K.K., Svensson, A. (2008) Identification of the Fugloyarbanki tephra in the NGRIP ice-core: a key tie-point for marine and ice-core sequences during the last glacial period. Journal of Quaternary Science 23, 409–414.

Davies, W (2007) Neanderthal Demise. In: Elias (Ed) Encyclopaedia of Quaternary Science. Elsevier.

de Abreu, L., Shackleton, N.J., Schönfeld, J., Hall, M., and Chapman, M.R. (2003) Millennial scale oceanic climate variability off the Western Iberian margin during the last two glacial periods. Marine Geology 196, 1–20.

de Beaulieu, J–L., Tzedakis, P., Ponel, P., Frédéric, G. (2007) Southern Europe. In: Elias (Ed) Encyclopedia of Quaternary Science. Elsevier.

de Goër de Herve, A., Camus, G., Miallier, D., Sanzelle, S., Falguères, C., Fain, J., Montret, M., Pilleyre, T. (1993). Le puy de Gravenoire et ses coulées, dans l'agglomération de Clermont-Ferrand (Massif central français): un modèle inhabituel d'avalanche de débris, déclenchée par une e´ruption strombolienne en climat périglaciaire. Bulletin de la Société Géologique de France 164, 783–793.

De Vivo, B., Rolandi, G., Gans, P.B., Calvert, A., Bohrson,W.A., Spera, F.J., Belkin, H.E. (2001) New constraints on the pyroclastic eruptive history of the Campanian volcanic plain (Italy). Mineralogy and Petrology 73, 47–65.

Deino, A.L., Orsi, G., de Vita, S., Piochi, M. (2004) The age of the Neapolitan Yellow Tuff caldera-forming eruption (Campi Flegrei caldera — Italy) assed by $^{40}Ar/^{39}Ar$ dating method. Journal of Volcanology and Geothermal Research 133, 157 170.

Deino, A.L., Orsi, G., de Vita, S., Piochi, M. (2004) The age of the Neapolitan Yellow Tuff caldera-forming eruption (Campi Flegrei caldera — Italy) assed by 40Ar/39Ar dating method. Journal of Volcanology and Geothermal Research 133, 157–170.

Deino, A.L., Southon, J., Terrasi, F., Campajola, L., Orsi, G. (1994) ^{14}C and $^{40}Ar/^{39}Ar$ dating of the Campanian Ignimbrite, Phlegrean Fields, Italy. In: Abstracts, ICOG, Berkeley, CA.

Di Vito, M.A., Sulpizio, R., Zanchetta, G., D'Orazio, M. (2008) The late Pleistocene pyroclastic deposits of the Campanian Plain: new insights into the explosive activity of Neapolitan volcanoes. Journal of Volcanology and Geothermal Research 177, 19–48.

Druitt, T.H., Edwards, L., Mellors, R.M., Pyle, D.M., Sparkes, R.S.J., Lanphere, M., Davies, M., Barriero, B. (1999) Santorini. Volcanol. Geol. Soc. Spec. Publ., 19. Geological Society of London. 165 pp.

Drysdale, R.N., Hellstrom, J.C., Zanchetta, G., Fallick, A.E., Sánchez Goñi, M.F., Couchoud, I., McDonald, J., Maas, R., Lohmann, G., Isola, I. (2009) Evidence for obliquity forcing of glacial Termination II. Science 325, 1527–1531.

Ducassou, E., Capotondi, L., Murat, A., Bernasconi, S.M., Mulder, T., Gonthier, E., Migeon, S., Duprat, J., Giraudeau, J., Mascle, J. (2007) Multiproxy Late Quaternary stratigraphy of

the Nile deep-sea turbidite system — Towards a chronology of deep-sea terrigeneous systems. Sedimentary Geology 200, 1–13.

Dugmore, A.J., Larsen, G., Newton, A.J., Sugden, D.E.. (1992). Geochemical stability of fine-grained silicic Holocene tephra in Iceland and Scotland. Journal of Quaternary Science 7, 173–183.

Dugmore, A.J. (1989) Icelandic volcanic ash in Scotland. Scottish Scotland Geographical Magazine 105, 168–172.

Dugmore, A.J. and Newton, A.J. (1992) Thin tephra layers in peat revealed by X-radiography. Journal of Archaeological Science 19, 163– 70.

Dugmore, A.J., Larsen, G., Newton, A.J. (1995) Seven tephra isochrons in Scotland. The Holocene 5, 257–266.

Dunbar, N.W. & Kurbatov, A.V. (2011) Tephrochronology of the Siple Dome ice core, West Antarctica: correlations and sources. Quaternary Science Reviews 30, 1602–1614.

Edwards, K.J., Whittington, G., Tipping, R. (2000) The incidence of microscopic charcoal in late glacial deposits. Palaeogeography Palaeoclimatology Palaeoecology 164, 263–278.

Elliot, M., Labeyrie, L., Duplessy, J.-C. (2002) Changes in North Atlantic deep-water formation associated with the Dansgaard–Oeschger temperature oscillations (60–10 ka). Quaternary Science Reviews 21, 1153–1165.

Enache, M.D., Cumming, B.F. (2006) The morphological and optical properties of volcanic glass: A tool to assess density-induced vertical migration of tephra in sediment cores. Journal of Palaeolimnology 35 (3), 661–667.

EPICA community members (2006) One-to-one coupling of glacial climate variability in Greenland and Antarctica. Nature 444, 195–198.

Eriksen, U., Friedrich, W.L., Buchardt, B., Tauber, H., Thomson, M.S. (1990) The Stronghyle Caldera: geological, paleontological and stable isotope evidence from radiocarbondated stromatolites from Santorini. In: Hardy, D.A., Keller, J., Galanopoulos, V.P., Flemming, N.C., Druitt, T.H. (Eds.), Thera and the Aegean World III. Santorini, Greece, pp. 139–150.

Etlicher, B., Janssen, C.R., Juvigné, E., van Leeuwen, J. (1987) Le Haut Forez (Massif Central, France) après le pléniglaciaire würmien: environnement et téphra du volcan de la Nugère. Bulletin de l'Association française pour l'Etude du Quaternaire 1987, 229–239.

Fairbanks, R.G., Mortlock, R.A., Chiu, T.-C., Cao, L., Kaplan, A., Guilderson, T.P., Fairbanks, T.W., Bloom, A.L., Grootes, P.M., Nadeau, M.-J. (2005) Radiocarbon calibration curve spanning 0 to 50,000 years BP based on paired 230Th/234U/238U and 14C dates on pristine corals. Quaternary Science Reviews 24, 1781–1796.

Fedele, F.G., Giaccio, B., Hajdas, I. (2008) Timescales and cultural process at 40,000 BP in the light of the Campanian Ignimbrite eruption, Western Eurasia. Journal of Human Evolution 55, 834–857.

Federman, A.N., Carey, S.N. (1980) Electron microprobe correlation of tephra layers from eastern Mediterranean abyssal sediments and the island of Santorini. Quaternary Research 13, 160–171.

Finlayson, C., Fa, D., Finlayson, G., Giles-Pacheco, F., Rodríguez-Vidal, J.R. (2004) 'Did the moderns kill off the Neanderthals? A reply to d'Errico and Sánchez-Goñi'. Quaternary Science Reviews 23, 1205–1209.

Fletcher, W.J. & Sanchez Goñi, M.F. (2008) Orbital and sub-orbital scale climate impacts on the vegetation of the W. Mediterranean basin during the last 48 000 years. *Quaternary Research* 70, 451–464.

Fletcher, W.J., Goni, M.F.S., Allen, J.R.M., Cheddadi, R., Combourieu-Nebout, N., Huntley, B., Lawson, I., Londeix, L., Magri, D., Margari, V., Mueller, U.C., Naughton, F., Novenko, E., Roucoux, K., Tzedakis, P.C. (2010) Millennial-scale variability during the last glacial in vegetation records from Europe. Quaternary Science Reviews, 29, 2839-2864.

Florschütz, F., Menéndez Amor, J., Wijmstra, T.A. (1971) Palinology of a thick Quaternary succession in southern Spain. Palaeogeography, Palaeoclimatology, Palaeoecology 10, 233–264.

Flückiger, J., Blunier, T., Stauffer, B., Chappellaz, M., Spahni, R., Kawamura, K., Schwander, J., Stocker, T.F., Dahl-Jensen, D. (2004) N2O and CH4 variations during the last glacial epoch: insight into global processes. Global Biogeochemical Cycles 18 (1) GB1020.

Froggatt, P.C. & Gosson, G.J. (1982) Techniques for the preparation of tephra samples for mineral or chemical analysis and radiometric dating. Geology Department, Victoria University of Wellington Publication 23, 1–12.

Froggatt, P.C. (1992) Standardization of the chemical analysis of tephra deposits. Report of the ICCT Working Group. Quaternary International 13/14, 93–96.

Fuhrer, K., Wolff, E.W., Johnsen, S.J. (1999) Timescales for dust variability in the Greenland Ice Core Project (GRIP) ice core in the last 100,000 years. Journal of Geophysical Research 104 (D24), 31043–31052.

G. Guerin, P.-Y. Gillot, R. Brousse, Age subactuel des dernie`res manifestations eruptives du Mont-Dore et du Cezallier, C. R. (1981) Acad. Sci. Paris, Ser. II 262, 855–857.

Gibbard, P., Head, M.J., Walker, M.J.C. & The Sub-commission on Quaternary Stratigraphy (2010) Formal ratification of the Quaternary System/Period and the Pleistocene Series/Epoch with a base at 2.58 Ma. Journal of Quaternary Science 25, 96–102.

Giles, T.M., Newnham, R.M., Lowe, D.J., Munro, A.J., (1999) Impact of tephra fall and environmental change: a 1000 year record from Matakana Island, Bay of Plenty, North Island, New Zealand. In: Firth, C.R. _Ed.., Volcanoes in the Quaternary, Geological Society London. Special Publication.

Gillot, P-Y., Labeyrie, J., Laj, C., Valladas, G., Guérin, G., Poupeau, G., Delibrias, G. (1979) Age of the Laschamp paleomagnetic excursion revisited. Earth and Planetary Science Letters 42, 444–450.

Gögen, K., Wagner, G.A. (2000) Alpha-recoil track dating of Quaternary volcanic. Chemical Geology 166, 127-137.

Greig, J.R.A. & Turner, J. (1974) Some pollen diagrams from Greece and their archaeological significance. Journal of Archaeological Science 1, 177–194.

Griffiths, S.J. (2001) Late Quaternary palaeolimnology of Lake Kopais, Central Greece. Unpublished PhD Thesis, University of Wales Swansea.

Griffiths, S.J., Street-Perrott, F.A., Holmes, J.A., Leng, M.J., Tzedakis, C. (2002) Chemical and isotopic composition of modern water bodies in the Lake Kopais Basin, central Greece: analogues for the interpretation of the lacustrine sedimentary sequence. Sedimentary Geology 148, 79–103.

Grimm, E.C., Watts, W.A., Jacobson, G.L., Hansen, B.C.S., Almquist, H.R., Dieffenbacher-Krall, A.C. (2006) Evidence for warm wet Heinrich in Florida. Quaternary Science Reviews 25, 2197–2211.

Grousset, F.E., Cortijo, E., Huon, S., Hervé, L., Richter, T., Burdloff, D., Duprat, J., Weber, O. (2001), Zooming in on Heinrich layers. Paleoceanography 16(3), 240–259.

Grousset, F.E., Labeyrie, L. Sinko, J.A., Cremer, M., Bond, G., Duprat, J., Cortijo, E., Huon, S. (1993) Patterns of icerafted detritus in the glacial North Atlantic (40–55N). Paleoceanography 8(2), 175–192.

Grousset, F.E., Pujol, C., Labeyrie, L., Auffret, G., Boelaert, A. (2000), Were the North Atlantic Heinrich events triggered by the behaviour of the European ice sheets? Geology 28, 123–126.

Guérin G. (1983) La thermoluminescence des plagioclases, method de datation du volcanisme. Applications au domaine volcanique francais: Chaîne des Puys, Mont Dore et Cezallier, Bas Vivarais. These de Doctorat d'Etatès Sciences, Physique, Université Pierre et Marie Curie.

Guérin, G., Gillot, P-Y. (2007) Nouveaux elements de chronologie du volcanisme pléistocène du bas Vivarais (Ardeche, France) par thermoluminescence. C. R. Geoscience, 339, 40–49.

Guérin, G., Valladas, G. (1980) Thermoluminescence dating of volcanic plagioclases. Nature 286: 697–699.

Guest, J.E., Gaspar, J.L., Cole, P.D., Queiroz, G., Duncan, A.M., Wallenstein, N., Ferreria, T., Pacheco, J.-M. (1999) Volcanic geology of Furnas Volcano, São Miguel, Azores. Journal of Volcanology and Geothermal Research 92, 1–29.

Gutiérrez, M., Gutiérrez, F., Desir, G. (2006) Considerations on the chronological and causal relationships between talus flatirons and palaeoclimatic changes in central and northeastern Spain. Geomorphology 73, 50–63.

Gwiazda, R. H., Hemming, S.R., Broecker, W.S. (1996) Provenance of icebergs during Heinrich event 3 and the contrast to their sources during other Heinrich episodes, Paleoceanography 11(4), 371–378.

Haase-Schramm A., Goldstein S. L. and Stein M. (2004) U–Th dating of Lake Lisan (late Pleistocene Dead Sea) aragonite and implications for glacial East Mediterranean climate change. Geochimica et Cosmochimica acta 68, 985–1005.

Hagleberg, T.K., Bond, G., deMenocal, P. (1994) Milankovitch band forcing of sub-Milankovitch climate variability during the Pleistocene. Paleoceanography 9, 545–558.

Hardiman, J.C. (1999) Deep sea tephra from Misyron Island, eastern Aegean Sea, Greece. In: Firth, C.R., McGuire, W.J. (Eds.), Volcanoes in the Quaternary. Geological Society of London, Special Publication, 161.

Hays, J. D., Imbrie, J., and Shackleton, N. J. (1976). Variations in the Earth's Orbit: Pacemaker of the Ice Ages. Science 194, 1121–1132.

Haywood, C. (2012) High spatial resolution electron probe microanalysis of tephras and melt inclusions without beam-induced chemical modification. The Holocene 22 (1), 119–125.

Heinrich, H. (1988), Origin and consequences of cyclic ice rafting in the northeast Atlantic Ocean during the past 130,000 years, Quaternary Research 29, 142–152.

Hemming, S.R. (2004) Heinrich Events: Massive Late Pleistocene detritus layers of the North Atlantic and their global climate imprint. Review of Geophysics 42, RG1005.

Higham, T. (2011) European Middle and Upper Palaeolithic radiocarbon dates are often older than they look: problems with previous dates and some remedies. Antiquity 85, 235–249.

Hoffecker, J.F., Anikovich, M.V., Sinitsyn, A.A., Holliday, V.T., Levkovskaya, G.M., Pospelova, G.A., Forman, S.L., Giaccio, B. (2008) From the Bay of Naples to the River Don: The Campanian Ignimbrite eruption and the Middle-Upper Paleolithic transition in Eastern Europe. In: Adler, D.S., Joris, O. (Eds.), Setting the Record Straight: Toward a Systematic Chronological Understanding of the Middle to Upper Paleolithic Boundary in Eurasia. Journal of Human Evolution 55, 858–870.

Holzkämper, S., Spötl, C., Mangini, A. (2005) High-precision constrains on timing of Alpine warm periods during the middle to late Pleistocene using speleothem growth periods. Earth and Planetary Science Letters 236, 751–764.

Huber, C., Leuenberger, M., Spahni, R., Flückiger, J., Schwander, J., Stocker, T. F., Johnsen, S., Landais, A., Jouzel, J. (2006) Isotope calibrated Greenland temperature record over Marine Isotope Stage 3 and its relation to CH4. Earth and Planetary Science Letters 243, 504–519.

Hughen K, Southon J, Lehman S, Bertrand C, Turnbull J. (2006) Marine-derived C-14 calibration and activity record for the past 50,000 years updated from the Cariaco Basin. Quaternary Science Reviews 25 (23–24), 3216–3227.

Hulbe, C.L. (1997) An ice shelf mechanism for Heinrich layer production. Paleoceanography 12(5), 711–717.

Hunt, A.G. and Malin, P.E. (1998) Possible triggering of Heinrich events by ice load-induced earthquakes. Nature 393, 155–158.

Hunt, J.B., Hill, P.G. (1993) Tephra geochemistry: a discussion of some persistent analytical problems. The Holocene 3, 271–278.

Hunt, J.B., Hill, P.G. (2001) Tephrological implications of beam sizeesample-size effects in electron microprobe analysis of glass shards. Journal of Quaternary Science 16, 105–117.

Imbrie, J., Hays, J.D., Martinson, D.G., McIntyre, A., Mix, A.C., Morley, J.J., Paces, N.G., Prell, W.L., Shackleton, N.J. (1984) The orbital theory of Pleistocene climate: Support from a revised chronology of the marine d18O record, in Milankovitch and Climate, Part 1, edited by A. Berger et al., pp. 269-305, D. Reidel, Norwell, Mass.

Janoušek, V., Farrow, C. M. & Erban, V. (2006) Interpretation of whole-rock geochemical data in igneous geochemistry: introducing Geochemical Data Toolkit (GCDkit). Journal of Petrology 47(6), 1255–1259.

Jochum, K.P., Stoll, B., Herwig, K., Willbold, M., Hofmann, A.W., Amini, M., Aarburg, S., Abouchami, W., Hellebrand, E., Mocek, B., Raczek, I., Stracke, A., Alard, O., Bouman, C., Becker, S., Dücking, M., Brätz, H., Klemd, R., de Bruin, D., Canil, D., Cornell, D., de Hoog, C., Dalpé, C., Danyushevsky, L., Eisenhauer, A., Gao, Y., Snow, J.E., Groschopf, N., Günther, D., Latkoczy, C., Guillong, M., Hauri, E., Höfer, H.E., Lahaye, Y., Horz, K., Jacob, D.E., Kasemann, S.A., Kent, A.J.R., Ludwig, T., Zack, T., Mason, P.R.D., Meixner, A., Rosner, M., Misawa, K., Nash, B.P., Pfänder, J., Premo, W.R., Sun, W.D., Tiepolo, M., Vannucci, R., Vennemann, T., Wayne, D., Woodhead, J.D. (2006) MPI-DING reference glasses for in situ microanalysis: new reference values for element concentrations and isotope ratios. Geochemistry Geophysics Geosystems 7, Q02008.

Johnsen, S. J. & Vinter, B. M. (2007) ICE CORE METHODS: Greenland Stable Isotopes. In: Elias (Ed) Encyclopaedia of Quaternary Science. Elsevier.

Johnsen, S. J., Clausen, H. B., Dansgaard, W., Gundestrup, N.S., Hammer, C.U., Andersen, U., Andersen, K.K., Hvidberg, C.S., Dahl-Jensen, D., Steffensen, J.P., Shoji, H., Sveinbjörnsdóttir, Á.E., White, J., Jouzel, J., Fishe, D. (1997). The d18O record along the Greenland Ice Core Project deep ice core and the problem of possible Eemian climatic instability. Journal of Geophysical Research 102(C12), 26,397–26,410.

Johnson, R. G. and Lauritzen, S,-E. (1995), Hudson Bay-Hudson Strait jökulhlaups and Heinrich events: A hypothesis, Paleogeography Paleoclimatology Paleoecology 117, 123–137.

Juvigné, E., Bastin, B., Delibrias, G., Evin, J., Gewelt, M., Gilot, E., Streel, M. (1996) A comprehensive pollen- and tephra-based chronostratigraphic model for the late glacial and Holocene period in the French Massif Central. Quaternary International. 34–36, 113–120.

Juvigné, E.T., Porter, S.C. (1985) Mineralogical variations within two widespread Holocene tephra layers from Cascade Range volcanoes, U.S.A. Géographie Physique et Quaternaire 39, 7–12.

Kaltenrieder, P., Belia, C.A., Hofstetter, S., Ammann, B., Ravzzi, C., Tinner, W. (2009) Environmental and climatic conditions at a potential Glacial refugial site of tree species near the Southern Alpine glaciers. New insights from multiproxy sedimentary studies at Lago della Costa (Euganean Hills, Northeastern Italy). Quaternary Science Reviews 28, 2647–2662.

Kaufman A. (1993) An evaluation of several methods for determining ^{230}Th/U ages in impure carbonates. Geochimica et Cosmochimica acta 57, 2303–2317.

Keller, J. (1980) Prehistoric pumice tephra on Aegean islands. Thera Aegean World, II: 49–56.

Keller, J., Gillot, P.Y., Rehren, T., Stadkbauer, E. (1989) Chronostratigraphic data for the volcanism in the eastern Hellenic Arc: Nisyros and Kos. Terra Abstracts 1, 354.

Keller, J., Ryan, W.B.F., Ninkovich, D., Altherr, R. (1978) Explosive volcanic activity in the Mediterranean over the past 200,000 yr as recorded in deep-sea sediments. Geological Society of America Bulletin 89, 591–604.

Kenny, E.J.A. (1935) The ancient drainage of the Copais. In: Droop, J.P. (Ed.), Annals of Archaeology and Anthropology. Liverpool Univ. Press, Liverpool, pp. 189–206.

Knauss, J. (1984) Die Wasserbauten der Minyer in der Kopais – die alteste Flussregulierung Europas (Kopais 1), Wasserbau und Wasserwitschaft, No. 50, Technische Universität München.

Knauss, J. (1987) Die Melioration des Kopaisbeckens durch die Minyer im 2 Jt. V. Chr. Wasserbau und Siedlungsbedingungen im Altertum (Kopais 2) – Wasserbau und Wasserwirtschaft, No. 57, Technische Universität München.

Koren, J.H., Svendsen, J.I., Mangerud, J., Furnes, H. (2007) The Dimna Ash — a 12.8 ^{14}C Ka-old volcanic ash in Western Norway. Quaternary Science Reviews 27, 85–94.

Kuehn, S. C. and D. G. Froese (2010) Tephra from Ice-A Simple Method to Routinely Mount, Polish, and Quantitatively Analyze Sparse Fine Particles. Microscopy and Microanalysis 16 (2), 218–225.

Kuehn, S.C., Froese, D.G., Shane, P.A.R. (2011) INTAV Intercomparison Participants. Quaternary International 246 (1–2), 19–47.

Kylander, M.E, Wastegård, S, Lind-Mettävainio, E., Löwemark, L., Wohlfarth, B. (2010). The Itrax and organic rich sediments: Tephrochronology and humification. Itrax 2010 Meeting, Lipari, Italy.

Kylander, M.E., Lind, E.M., Wastegård, S., Löwemark, L. (2012) Recommendations for using XRF core scanning as a toll in tephrochronology. The Holocene 22, 1–5.

Labeyrie, L., Heclaire, H., Waelbroek, C., Cortijo, E., Duplessy, J.-C., Vidal, L., Elliot, M., Lecoat, B., Auffret, G. (1999) Insolation forcing and millennial scale variability of the north west Atlantic ocean: surface versus deep water changes. In: Clark, P.U., Webb, R., Keigwin, L. (Eds.), Chapman Conference on Millennial Scale Climate Variability, AGU Monographs. American Geophysical Union, Washington, DC, Snowbird, Utah, 77–98.

Landais, A., Caillon, N., Goujon, C., Grachev, A.M., Barnola, J.M., Chappellaz, J., Jouzel, J., Masson-Delmotte, V., Leuenberger, M. (2004) Quantification of rapid temperature change during DO event 12 and phasing with methane inferred from air isotopic measurements. Earth and Planetary Science Letters 225 (1–2), 221–232.

Lane, C.S. (2008) Exploring the variability of microtephra deposits: chemical characterisation and discrimination methods. Unpublished D.Phil Thesis. Research Laboratory for Archaeology and the History of Art, University of Oxford.

Lane, C.S., Andric, M., Cullen, V.L., Blockley, S.P.E. (2011) The occurance of distal Icelandic and Italian tephra in the Lateglacial of Lake Bled, Slovenia. Quaternary Science Reviews 30, 1023–1018.

Lane, C.S., Blockley, S., Smith, V.C., Mangerud, J, Matthews, I. & Lotter, A.F. (2012) Was the 12.1 ka Icelandic Vedde Ash one of a kind? Quaternary Science Reviews 33(6), 87–99.

Lanphere, M.A. (2003) Application of K-Ar dating to the chronology of young volcanic centers. Eos. Transactions of the American Geophysical Union 84(46), Fall Meeting Supplement, Abstracts.

Larsen, G., Dugmore, A., Newton, A. (1999) Geochemistry of historical-age silicic tephras in Iceland. Holocene 9(4), 463-471

Lauaterbach, S., Brauer, A., Andersen, N., Danielopol, D.L., Dulski, P., Hüls, M., Milecka, K., Namiotko, T., Obremska, M., Von Grafenstein, U. and Declakes Participants. (2011) Environmental responses to Lateglacial climatic fluctuations recorded in the sediments of pre-Alpine Lake Mondsee (northeastern Alps). 26(3), 253–267.

Lézine, A.-M., von Grafenstein, U., Anderson, N., Belmecheri, S., Bordon, A., Caron, B., Cazet, J.-P., Erlenkeuser, H., Fouache, E., Grenier, C., Huntsman-Mapila, P., Hureau-Mazaudier, D., Manelli, D., Mazaud, A., Robert, C., Sulpizio, R., Tiercelin, J.-J., Zanchetta, G., Zeqollari, Z. (2010) Lake Ohrid, Albania, provides an exceptional multi-proxy record of environmental changes during the last glacial–interglacial cycle. Palaeogeography, Palaeoclimatology, Palaeoecology 287, 116–127.

Lian, O.B. (2007) Optically-Stimulated Luminescene. In: Elias (Ed) Encyclopedia of Quaternary Science. Elsevier.

Limburg, E.M., Varekamp, J.C. (1991) Young pumice deposits on Nisyros, Greece. Bulletin of Volcanology 54 (1), 68–77.

Lirer, L., Rolandi, G., Rubin, M. (1991) 14C age of the ‘‘Museum Breccia’’ (Campi Flegrei) and its relevance for the origin of the Campanian Ignimbrite. Journal of Volcanology and Geothermal Research 48, 223–227.

Lowe, D.J. (2011) Tephrochronology and its application: A review. Quaternary Geochronology. 6, 107–153.

Lowe, J. J. (2001) Abrupt climatic changes in Europe during the last glacial–interglacial transition: the potential for testing hypotheses on the synchroneity of climatic events using tephrochronology. Global and Planetary Change 30, 73–84.

Lowe, J., Barton, N., Blockley, S., Ramsey, C.B., Cullen, V.L., Davies, S.W.G., Gamble, C., Grant, K., Hardiman, M., Housley, R., Lane, C.S., Lee, S., Lewis, M., MacLeod, A., Menzies, M., Muller, W., Pollard, M., Price, C., Roberts, A.P., Rohling, E.J., Satow, C., Smith, V.C., Stringer, C.B., Tomlinson, E., White, D., Albert, P., Arienzo, I., Barker, G., Carandente, A., Civetta, L., Farrand, W., Ferrier, C., Gaudelli, J-L., Karkanas, P., Koumouzelis, M., Muller, U.C., Orsi, G., Pross, J., Rosi, M., Shalamanov-Korobar, L., Sirakov, N., Tzedakis, P.C. & Boric, D. (2012) Volcanic ash layers illustrate the resilience of Neanderthals and early modern humans to natural hazards. Proceedings of the National Academy of Sciences of the United States of America 109 (34), 13532-13537.

Lowe, J.J., Blockley, S., Trincardi, F., Asioli, A., Cattaneo, A., Matthews, I.P., Pollard, M., Wulf, S. (2007) Age modelling of late Quaternary marine sequences in the Adriatic: towards improved precision and accuracy using volcanic event stratigraphy. Continental Shelf Research 27, 560–582.

Lowe, J.J., Hoek, W., INTIMATE Group. (2001) Inter-regional correlation of palaeoclimatic records for the Last Glacial-Interglacial Transition: a protocol for improved precision recommended by the INTIMATE project group. Quaternary Science Reviews 20, 1175–1187.

Lowe, J.J., Rasmussen, S.O., Bjorck, S., Hoek, W.Z., Steffensen, J.P., Walker, M.J.C., Yu, Z.C. (2008) Synchronisation of palaeoenvironmental events in the North Atlantic region during the Last Termination: a revised protocol recommended by the INTIMATE group. Quaternary Science Reviews 27, 6–17.

Lowe, J.J., Walker, M.J.C., Porter, S.C. (2007). Understanding Quaternary Climatic Change. In: Elias (Ed) Encyclopaedia of Quaternary Science. Elsevier.

Lowe, J.J., Walker, M.J.C., Scott, E.M., Harkness, D.D., Bryant, C.L., Davies, S.M. (2004) A coherent high-precision radiocarbon chronology for the Lateglacial sequence at Sluggan Bog, Co. Antrim, Northern Ireland. Journal of Quaternary Science 19, 147–158.

Lowick, S., Preusser, F., Pini, R., Ravazzi, C. (2010) Underestimation of fine grain quartz OSL dating towards the Eemian: Comparison with palynostratigraphy from Azzano Decimo, northeastern Italy. Quaternary Geochronology 5, 583-590.

MacAyeal, D. R. (1993) Binge/Purge oscillations of the Laurentide ice sheet as a cause of the north Atlantic's Heinrich Events. Paleoceanography. 8(6), 775–784.

Macera, P., Gasperini, D., Piromallo, C., Blichert-Toft, J., Bosch, D., Moro, D.A., Martin, S. (2003) Geodynamic implications of deep mantle upwelling in the source of Tertiary volcanics from the Veneto region (South-Eastern Alps). Journal of Geodynamics 36, 563–590.

Mackie, E., Davies, S. M., Turney, C. S. M., Dobbyn, K., Lowe, J. J. & Hill, P. (2002) The use of magnetic separation techniques to detect basaltic microtephra in last glacial–interglacial transition (LGIT: 15–10 ka cal. BP) sediment sequences in Scotland. Scottish Journal of Geology 38, 21–30.

Magri, D. & Parra, I. (2002) Late Quaternary Mediterranean pollen records and African winds. Earth and Planetary Science Letters. 3–4, 401–408.

Mahood, G.A. & Hildreth, W. (1986) Geology of the peralkaline volcano at Pantelleria, Strait of Sicily. Bulletin of Volcanology 48, 143–172.

Margari, V. (2004) Late Pleistocene vegetational and environmental changes on Lesvos Island, Greece, Ph.D. thesis, University of Cambridge.

Margari, V., Gibbard, P.L., Bryant, C.L., Tzedakis, P.C. (2009) Character of vegetational and environmental changes in southern Europe during the last glacial period; evidence from Lesvos Island, Greece. Quaternary Science Reviews 28 (13-14), 1317–1339.

Margari, V., Pyle, D.M., Bryant, C., Gibbard, P.L. (2007) Mediterranean tephra stratigraphy revisited: Results from a long terrestrial sequence on Lesvos Island, Greece. Journal of Volcanology and Geothermal Research 163, 34–54.

Martinson, D.G., Pisias, N.G., Hays, J.D., Imbrie, J., Moore, T.C., Shackleton, N. J. (1987) Age dating and the orbital theory of the Ice Ages: Development of a high-resolution 0–300,000 year chronostratigraphy. Quaternary Research 27, 1–29.

Martrat, B., Grimalt, J.O., Lopez-Martinez, C., Cacho, I., Sierro, F.J., Flores, J.A., Zahn, R., Canals, M., Curtis, J.H., Hodell, D.A. (2004) Abrupt temperature changes in the Western Mediterranean over the past 250 kyr. Science 306, 1762–1765.

Martrat, B., Grimalt, J.O., Shackleton, N.J., de Abreu, L., Hutterli, M.A., Stocker T.F. (2007) Four climate cycles of recurring deep and surface water destabilizations on the Iberian margin. Science 317, 502–507.

Maslin, M., Seidov, D., Lowe, J. (2001). Synthesis of the nature and causes of rapid climate transitions during the Quaternary. Geophysical monograph. Geophysical Monograph Series 126, 9 –52.

Matthews, I.P. (2003) Toward a Holocene tephrochronological framework for the southern central Andes: the applicability of tephrochronology to sites in the Machu Picchu and Cuzco regions, Peru. Unpublished M.Sc. Thesis, Royal Holloway, University of London.

Matthews, I.P. (2009) The potential of tephrostratigraphy in the investigation of wetland archaeological records. Unpublished PhD Thesis, Royal Holloway, University of London.

Matthews, I.P., Birks, H.H., Bourne, A.J., Brooks, S.J., Lowe, J.J., Macleod, A. & Pyne-O'Donnell, S.D.F. (2011a) New age estimates and climatostratigraphic correlations for the Borrobol and Penifiler Tephras: evidence from Abernethy Forest, Scotland. Journal of Quaternary Science 26(3), 247–252.

Matthews, I.P., Palmer, A.P., Folkes, H., Trincardi, F. (2011b) Understanding tephra layers in marine sediments, the potential of thin section micromorphology to investigate depositional and taphonomic processes. Oral Presentation at the Marine Tephrochronology Meeting, Geological Society of London. (26th October).

Mellors, R. A. and Sparks, R. S. J. (1991) Spatter-rich pyroclastic flow deposits on Santorini, Greece. Bulletin of Volcanology, 53, 327–42.

Mertes, H. (1983) Aufbau und Genese des Westeifel Vulkanfelds. Bochumer Geologische und Geotechnische Arbeiten 9, 415.

Meyer, M.C., Spötl, C., Mangini, A. (2008) The demise of the Last Interglacial recorded in isotopically dated speleothems from the Alps. Quaternary Science Reviews 27, 476–496.

Milankovitch, M. (1941). Kanon der Erdbestrahlung und seine Anwendung auf das Eiszeitenproblem. Académie Royale Serbe Editions Speciales. Section des Sciences Mathématiques et Naturelles 133.

Milner, A.M., Collier, R.E.L., Roucoux, K.H., Müller, U.C., Pross, J., Kalaitzidis, S., Christanis, K., Tzedakis, P.C. (*in press*) Enhanced seasonality of precipitation in the Mediterranean during the early part of the Last Interglacial. Geology.

Mokgalaka, N. & Gardea-Torresdey, J. (2006) Laser Ablation Inductively Coupled Plasma Mass Spectrometry: Principles and Applications. Applied Spectroscopy Reviews 41 (2), 131–150.

Monegato, G., Pini, R., Ravazzi, C., Reimer, P.J., Wick, L. (2011) Correlating Alpine glaciation with Adriatic sea-level changes through lake and alluvial stratigraphy. Journal of Quaternary Science 26 (8) 791–804.

Moore, R.B. (1990) Volcanic geology and eruption frequency, São Miguel, Azores. Bulletin of Volcanology 52, 602–614.

Moreno, A., Cacho, I., Canals, M., Grimalt, J.O., Sanchez-Goni, F., Shackleton, N., Sierro, F.J. (2005) Links between marine and atmospheric processes oscillating on a millennial time-scale. A multi-proxy study of the last 50,000 yr from the Alboran Sea (Western Mediterranean Sea). Quaternary Science Reviews, 24, 1623-1636.

Moreno, A., G., González-Sampériz, P., Morellón, M., Valero-Garcés, B.L., Flectcher, W.J. (2012) Northern Iberian abrupt climate change dynamics during the last glacial cycle: A view from lacustrine sediments. Quaternary Science Reviews 36, 139–153.

Müller, U.C., Pross, J., Tzedakis, P.C., Gamble, C., Kotthoff, U., Schmiedl, G., Wulf, S., Christanis, K. (2011) The role of climate in the spread of modern humans into Europe. Quaternary Science Reviews 30, 273–279.

Müller, W., Shelley, M., Miller, P., Broude, S. (2009) Initial performance metrics of a new custom-designed ArF eximer LA-ICP-MS system coupled to a two-volume laser ablation cell. Journal of Analytical Atomic Spectrometry 24, 209–214.

Munno, R., Petrosino, P. (2004) New constraints on the occurrence of Y-3 Upper Pleistocene tephra marker layer in the Tyrrhenian sea. Il Quaternario, 17, 11–20.

Munno, R., Petrosino, P. (2007) The late Quaternary tephrostratigraphical record of the San Gregorio Magno basin (southern Italy). Journal of Quaternary Science, 22, 247-266.

Murray, A.S. and Olley, J.M. (2002) Precision and accuracy in the optically stimulated luminescence dating of sedimentary quartz: a status review. Geochronometria 21, 1-15.

Nakagawa, T., Gotanda, K., Haraguchi, T., Danhara, T., Yonenobu, H., Brauer, A., Yokoyama, Y., Tada, R., Takemura, K., Staff, R.A., Payne, R., Bronk Ramsey, C., Bryant, C., Brock, F., Schlolaut, G., Marshall, M., Tarasov, P., Lamb, H., Suigetsu 2006 Project Members. (2011). SG06, a fully continuous and varved sediment core from Lake Suigetsu, Japan: stratigraphy and potential for improving the radiocarbon calibration model and understanding of late Quaternary climate changes. Quaternary Science Reviews.

Narcisi, B., Vezzoli, L. (1999) Quaternary stratigraphy of distal tephra layers in the Mediterranean — an overview. Global and Planetary Change 21, 31–50.

Nesse, W. (2000) Introduction to Optical Mineralogy. Oxford University Press, New York, USA, 442 pp.

Nestares, T., Torres, T. (1998) Un nuevo sondeo de investigación paleoambiental del Pleistoceno y Holoceno en la turbera de Padul (Granada, Andalucía). Geogaceta 23, 99–102.

Newham, R.M. & Lowe, D.J. (1999) Testing the synchroneity of pollen signals using tephrostratigraphy. Global and Planetary Change 21, 113–128.

Newnham, R.M. & Lowe, D.J. (1999) Testing the synchroneity of pollen signals using tephrostratigraphy 21, 113–128.

North Greenland Ice Core Project Members (2004). High-resolution record of Northern Hemisphere climate extending into the last interglacial period. Nature 431, 147–151.

Nowell, D.A.G., Jones, M.C., Pyle, D.M. (2006) Episodic Quaternary volcanism in France and Germany. Journal of Quaternary Science 21(6), 645-675

Ojala, A.E.K., Francus, P., Zolitschka, B., Besonen, M., Lamoureux, S.F. (2012) Characteristics of sedimentary varve chronologies – A review. Quaternary Science Reviews 43, 45–60.

Okuda, M., Yasuda, Y., Setoguchi, T. (1999) Latest Pleistocene and Holocene pollen records from Lake Kopais, Southeast Greece. The Journal of the Geological Society of Japan 105, 450–455.

Okuda, M., Yasuda, Y., Setoguchi, T. (2008) Middle to Late Pleistocene vegetation history and climatic changes at Lake Kopais, southeast Greece. Boreas 1, 73–82.

Oldfield, F. (2001) A question of timing: a comment on Hong, Jiang, Lui, Zhou, Beer, Li, Leng, Hong and Qin. The Holocene 11, 123–124.

Orsi, G., De Vita, S., Di Vito, M. (1996) The restless, resurgent Campi Flegrei nested caldera (Italy): constraints on its evolution and configuration. Journal of Volcanology and Geothermal Research 74, 179–214.

Ortiz, J.E., Torres, T., Delgado, A., Julià, R., Lucini, M., Llamas, F.J., Reyes, E., Soler, V., Valle, M. (2004) The palaeoenvironmental and palaeohydrological evolution of Padul Peat Bog (Granada, Spain) over one million years, from elemental, isotopic, and molecular organic geochemical proxies. Organic Geochemistry. 35 (11–12), 1243–1260.

Ortiz, J.E., Torres, T., Delgado, A., Llamas, J.F., Soler, V., Valle, M., Julià, R., Moreno, L., Díaz-Bautista, A. (2010) Palaeoenvironmental changes in the Padul Basin (Granada, Spain) over the last 1 Ma based on the biomarker content. Palaeogeography, Palaeoclimatology, Palaeoecology 298, 286–299.

Papadopoulou-Vrynioti, K.A. (1990) Geomorphological study of the Kopais area Boeotia (in Greek). PhD Thesis, University of Athens, Athens.

Pappalardo, L., Civetta, L., D' Antonio, M., Deino, A., Di Vito, M., Orsi, G., Carandente, A., de Vita, S., Isaia, R., Piochi, M. (1999) Chemical and Sr-isotopical evolution of the Phlegrean magmatic system before the Campanian Ignimbrite and the Neapolitan Yellow Tuff eruptions. Journal of Volcanology and Geothermal Research 91, 141–166.

Pastre, J-F., Debard, E., Chennaoui, K. (1994) Un tephra-repère du volcanisme phréatomagmatique du Vivarais dans la séquence Pléistocène supérieur de l'abri Moula (Soyons, Ardèche, France). Comptes rendus l'Académie des Sciences, Paris, série II 319, 937–943.

Paterne, M. (1985) Reconstruction de l'activitè explosive des volcans de l'Italie du Sudpar tèphrochronologie marine. PhD. Thesis University of Paris Sud, Paris, 144 pp.

Paterne, M., Guichard, F., Duplessy, J.C., Siani, G., Sulpizio, R., Labeyrie, J. (2008) A 90,000–200,000 yrs marine tephra record of Italian volcanic activity in the Central Mediterranean Sea. Journal of Volcanology and Geothermal Research 177, 187–196.

Pearce N.J.G., Perkins W.T. Westgate J.A. and Wade S.C. (2011a) Trace element microanalysis by laser ablation ICP-MS: the quest for comprehensive chemical characterisation of single sub-10um volcanic glass shards**.** Quaternary International 246, 57–81.

Pearce, N., Perkins, B., Westgate, J. (2011b) Laser ablation ICP-MS analysis of individual glass shards from tephra deposits – recent developments in trace element micro-analysis and Pb isotope determination. Conference presentation, INQUA 2011, Bern.

Pearce, N.J.G., Bendall, C.A., Westgate, J.A. (2008) Comment on "Some numerical considerations in the geochemical analysis of distal microtephra" by A.M. Pollard, S.P.E. Blockley and C.S. Lane. Applied Geochemistry 23 (5), 1353–1364.

Pearce, N.J.G., Denton, J.S., Perkins, W.T., Westgate, J.A., Alloway, B.V. (2007) Correlation and characterisation of individual glass shards from tephra deposits using trace element laser ablation ICP-MS analyses: current status and future potential. Journal of Quaternary Science 22, 721–736.

Pe-Piper, G., Piper, D.J.W., Perissoratis, C. (2005) Neotectonics and the Kos Plateau Tuff eruption of 161 ka, south Aegean arc. Journal of Volcanology and Geothermal Research 139, 315–338.

Pichler, H., Friederich, W. (1976). Radiocarbon dates of the Santorini volcanics. Nature 262, 373–374.

Pilcher, J.R., Hall, V.A. (1992). Towards a tephrochronology for the Holocene of the north of Ireland. Holocene 2 (3), 255–259.

Pini, R., Ravazzi, C., Reimer, P.J. (2010) The vegetation and climate history of the last glacial cycle in a new pollen record from Lake Fimon (southern Alpine foreland, N-Italy). Quaternary Science Reviews 29, 3115–3137.

Platevoet, B., Scaillet, S., Guillou, H., Blamart, D., Nomade, S., Massault, M., Poisson, A., Eltok, O, Özgür, N., Yagmurlu, F., Yilmaz, K. (2008) Pleistocene eruptive chronology of the Gölcük volcano, Isparta angle, Turkey. Quaternaire 19 (2), 147–156

Plewinski, B. and Kamp. P. (1984) Sodium metatungstate, a new medium for binary and ternary density gradient centrifugation. Mak-romolekulare Chemie 185, 1429–1439.

Polacci, M., Pioli, L., Rosi, M. 2003. The Plinian phase of the Campanian Ignimbrite eruption (phlegrean fields, Italy): Evidence from density measurements and textural characterization of pumice. Bulletin of Volcanology 65(6), 418-432

Poli, S., Chiesa, S., Gillot, P.-Y., Gregnanin, A., Guichard, F. (1987) Chemistry versus time in the volcanic complex of Ischia (Gulf of Naples, Italy): evidence of successive magmatic cycles. Contributions to Mineralogy and Petrology 95, 322–335.

Pollard, A. M., Blockley, S.P.E. & Lane, C.S. (2006) Some Numerical Considerations in the Geochemical Analysis of Distal Microtephra, Applied Geochemistry 21, 1692–1714.

Pons, A., Reille, M. (1988) The Holocene and upper Pleistocene pollen record from Padul (Granada, Spain): a new study. Palaeogeography, Palaeoclimatology, Palaeoecology 66, 243–263.

Prentice, I.C. (1985) Pollen representation, source area, and basin size: toward a unified theory of pollen analysis. Quaternary Research 23, 76–86.

Pross, J., Tzedakis, C., Schmiedl, G., Christanis, K., Hooghiemstra, H., Müller, U.C., Kotthoff, U., Kalaitzidis, S., Milner A. (2007) Tenaghi Philippon Re-Visited: Drilling a Continuous Lower-Latitude Terrestrial Climate Archive of the Last 250,000 Years. Scientific Drilling 5, 30–32.

Pyle, D.M. & Margari, V. (2009) Reply: Correlation of a widespread Pleistocene tephra marker from the Nisyros–Yali volcanic complex, Greece. Journal of Volcanology and Geothermal Research 181, 251–254.

Pyle, D.M. (1989) The thickness, volume and grainsize of tephra fall deposits, Bulletin of Volcanology, 51, 1-15.

Pyle, D.M., Ricketts, G.D., Margari, V., van Andel, T.H., Sinitsyn, A.A., Praslov, N.D., Lisitsyn, S. (2006) Wide dispersal and deposition of distal tephra during the Pleistocene 'Campanian Ignimbrite/Y5' eruption, Italy. Quaternary Science Reviews 25, 2713–2728.

Pyne-O'Donnell S.D.F. (2011) The taphonomy of Last Glacial–Interglacial Transition (LGIT) distal volcanic ash in small Scottish lakes. Boreas 1, 131–145.

Pyne-O'Donnell, S.D.F. (2007) Three new distal tephras in sediments spanning the Last Glacial-Interglacial Transition in Scotland. Journal of Quaternary Science 22, 559–570.

Pyne-O'Donnell, S.D.F., Blockley SPE, Turney CSM, Lowe JJ. (2008) Distal volcanic ash layers in the Lateglacial Interstadial (GI-1): problems of stratigraphic discrimination. Quaternary Science Reviews 27, 72–84.

Pyne-O'Donnell, S.D.F. (2005) The factors affecting the distribution and preservation of microtephra particles in lateglacial and early Holocene lake sediments., Unpublished PhD thesis, University of London.

Rashid, H., Hesse, R., Piper, D. J. W. (2002) Distribution, thickness and origin of Heinrich layer 3 in the Labrador Sea. Earth and Planetary Science Letter 205, 281–293.

Rasmussen, S.O., Andersen, K.K., Svensson, A.M., Steffensen, J.P., Vinther, B.M., Clausen, H.B., Siggaard-Andersen, M.L., Johnsen, S.J., Larsen, L.B., Dahl-Jensen, D., Bigler, M., Röthlisberger, R., Fischer, H., Goto-Azuma, K., Hansson, M.E. & Ruth, U. (2006) A new Greenland ice core chronology for the last glacial termination. Journal of Geophysical Results 111 (D6), D061202.

Rasmussen, S.O., Seierstad, I.K., Andersen, K.K., Bigler, M., Dahl-Jensen, D., Johnsen, S.J. (2008) Synchronization of the NGRIP, GRIP, and GISP2 ice cores across MIS 2 and palaeoclimatic implications. Quaternary Science Reviews 27, 18–28.

Rasmussen, T.L., Thomsen, E. (2004) The role of the North Atlantic Drift in the millennial timescale glacial climate fluctuations. Palaeogeography, Palaeoclimatology., Palaeoecology 210, 101–116.

Rasmussen, T.L., Thomsen, E., van Weering, T.C.E. (1998) Cyclic sedimentation on the Faeroe Drift 53–10 ka BP related to climatic variations. Geological Society Special Publications 129, 255–267.

Rasmussen, T.L., Thomsen, E., van Weering, T.C.E., Labeyrie, L. (1996) Rapid changes in surface and deep water conditions at the Faeroe Margin during the last 58,000 years. Palaeoceanography 11, 757–771.

Raynal, J-P., Paquereau, M., Daugas, J-P., Miallier, D., Fain, J., Sanzelle, S. (1985) Contributions à la datation du volcanisme quaternaire du Massif central franc¸ais par thermoluminescence des inclusions de quartz et comparaison avec d'autres approches: implications chronostratigraphiques et paléoenvironnementales. Bulletin de l'Association française pour l'étude du Quaternaire 1985, 183–207.

Reed, S.J.B. (2005) Electron Microprobe Analysis and Scanning Electron Microscopy in Geology, second ed. Cambridge University Press, Cambridge, UK, pp. 1–206.

Reimer, P.J., Baillie, M., Bard, E., Bayliss, A., Beck, J.W., Blackwell, P.G., Bronk, Ramsey, C., Buck, C.E., Burr, C.E., Edwards, R.L., Friedrich, M., Grootes, P.M., Guilderson, T.P., Hajdas, I., Heaton, T.J., Hogg, A.G., Hughen, K.A., Kaiser, K.F., Kromer, B., McCormac, F.G., Manning, S.W., Reimer, R.W., Richards, D.A., Southon, J.R., Talamo, S., Turney, C.S.M., van der Plicht, J., Weyhenmeyer, C.E. (2009) INTCAL09 and MARINE09 radiocarbon age calibration curves, 0–50,000 years cal BP. Radiocarbon 51, 1111–1150.

Reimer, P.J., Baillie, M., Bard, E., Bayliss, A., Beck, J.W., Blackwell, P.G., Bronk,Ramsey, C., Buck, C.E., Burr, C.E., Edwards, R.L., Friedrich, M., Grootes, P.M., Guilderson, T.P., Hajdas, I., Heaton, T.J., Hogg, A.G., Hughen, K.A., Kaiser, K.F., Kromer, B., McCormac, F.G., Manning, S.W., Reimer, R.W., Richards, D.A., Southon, J.R., Talamo, S., Turney, C.S.M., van der Plicht, J., Weyhenmeyer, C.E. (2009) INTCAL09 and MARINE09 radiocarbon age calibration curves, 0–50,000 years cal BP. Radiocarbon 51, 1111–1150.

Reimer, P.J., Reimer, R.W. (2007) RADIOCARBON DATING: Calibration. In: Elias (Ed) Encyclopaedia of Quaternary Science. Elsevier.

Revuelta, M.A., Sastre, M., Fernández, A.J., Martin, L., Gómez-Moreno, F.J., Artinano, B., Pujadas, M., Molero, F. (2012) Characterization of the Eyjafjallajökull volcanic plume over the Iberian Peninsula by lidar remote sensing and ground-level data collection. Atmospheric Environment 48, 46–55.

Roberts, N., Moreno, A., Valero-Garcés, B., Corella, J.P., Jones, M., Allcock, S., Woodbridge, J., Morellón, M., Luterbacher, J., Xoplaki, E. (2012) Palaeolimnological evidence for an east-west climate see-saw in the Mediterrean since AD 900. Global and Planetary Change 84–85, 23–34.

Roeser, P.A., Franz, S.O., Litt, T., Ülgen, U.B., Hilgers, A., Wulf, S., Wennrich, V., Ön, S.A., Viehberg, F.A., Çağatay, M.N. (2012) Lithostratigraphic and geochronological framework for the palaeoenvironmental reconstruction of the last ~36 ka cal BP from a sediment record from Lake Iznik (NW Turkey). Quaternary International 1–13.

Rohling, E.L., Mayewski, P.A., Challenor, P. (2003) On the timing and mechanism of millennial-scale climate variability during the last glacial cycle. Climate Dynamics 20, 257–267.

Rolandi, G., Bellucci, F., Heizler, M.T., Belkin, H.E., De Vivo, B. (2003) Tectonic controls on the genesis of ignimbrites from the Campanian Volcanic Zone, southern Italy. Mineral. Petrol. 79, 3–31.

Rose, N.L., Golding, P.N.E., Battarbee, R.W. (1996) Selective concentration and enumeration of tephra shards from lake sediment cores. The Holocene 6, 243–246.

Roucoux, K. H., de Abreu, L., Shackleton, N. J., and Tzedakis, P. C. (2005) The response of NW Iberian vegetation to North Atlantic climate oscillations during the last 65 kyr. Quaternary Science Reviews 24, 1637–1653

Roucoux, K.H., Tzedakis, P.C., Lawson, I.T., Margari, V. (2011) Vegetation history of the penultimate glacial period (Marine Isotope Stage 6) at Ioannina, north-west Greece. Journal of Quaternary Science 26(6), 616–626.

Ruth, U., Bigler, M., Rothlisberger, R., Siggaard-Andersen, M.L., Kipfstuhl, S., Goto-Azuma, K., Hansson, M.E., Johnsen, S.J., Lu, H.Y., Steffensen, J.P. (2007) Ice coreevidence for a

very tight link between North Atlantic and east Asian glacialclimate. Geophysical Research Letters 34 (3), L03706.

Sanchez Goni, M.F. & Harrison, S.P. (2010) Millennial-scale climate variability and vegetation changes during the Last Glacial: Concepts and terminology. Quaternary Science Reviews 29, 2823–2827.

Sánchez Goñi, M.F., Cacho, I., Turon, J.-L., Guiot, J., Sierro, F.J., Peypouquet, J.-P., Grimalt, J.O., Shackleton, N.J. (2002) Synchroneity between marine and terrestrial responses to millennial scale climatic variability during the last glacial period in the Mediterranean region. Climate Dynamics 19, 95–105.

Sanchez Goñi, M.F., Landais, A., Fletcher, W.J., Naughton, F., Desprat, S., Duprat, J. (2008) Contrasting impacts of Dansgaard–Oeschger events over a western European latitudinal transect modulated by orbital parameters. Quaternary Science Reviews 27, 1136–1151.

Sanchez Goñi, M.F., Turon, J.L., Eynaud, F., Gendreau, S. (2000) European climatic response to millenial-scale changes in the atmosphere-ocean system during the Last Glacial period. Quaternary Research 54, 394–403.

Sanchez-Goni, M.F., Landais, A., Fletcher, W.J., Naughton, F., Desprat, S., Duprat, J. (2008) Contrasting impacts of Dansgaard-Oeschger events over a western European latitudinal transect modulated by orbital parameters. Quaternary Science Reviews 27 (11–12), 1136–1151.

Sanzelle, S., Pilleyre, T., Montret, M., Fain, J, Miallier, D., Camus, G., de Goër de Hervé, A., Defleur, A. (2000) Datation par thermoluminescence: étude d'une corrélation chronologique possible entre le maar de La Vestide-du-Pal et un niveau de téphra de La Baume-Moula-Guercy (Arde`che, France). Comptes rendus l'Académie des Sciences, Paris, série II 321, 541–546.

Schmitt, A.K., Danisik, M., Evans, N.J., Siebel, W., Kiemele, E., Aydin, F., Harvey, J.C. (2011) Acigöl rhyolite field, Central Anatolia (part 1): high resolution dating of eruption episodes and zircon growth rates 162, 1215–1231.

Schrag, D.P. and R.B. Alley. Ancient lessons for our future climate. (2004) Science, 306, 821-822.

Schwander, J., Sowers, T., Barnola, J.-M., Blunier, T., Malaizé, B., Fuchs, T. (1997) Age scale of the air in the summit ice: implication for glacial–interglacial temperature change. Journal of Geophysical Research 102, (D16) 19483–19494.

Schwarz, M. (2000). Tephrakorrelation im östlichen Mittelmeer (Meteor M40/4 Kerne). Diploma Thesis, Universität Freiburg, Germany.

Scott, E.M. (2007) RADIOCARBON DATING: Sources of Error. In: Elias (Ed) Encyclopaedia of Quaternary Science. Elsevier.

Scourse, J.D., Hall, I.R., McCave, I.N., Young, J.R., Sugdon, C. (2000), The origin of Heinrich layers: Evidence from H2 for European precursor events. Earth Planetary Science Letters 182, 187–195.

Sedov, S., Solleiro-Rebolledo, E., Morales-Puente, P., Arias-Herreia, A., Vallejo-Gòmez, E., Jasso-Castañeda, C. (2003) Mineral and organic components of the buried paleosols of

the Nevado de Toluca, Central Mexico as indicators of paleoenvironments and soil evolution. Quaternary International 106-107, 169–184.

Shackleton, N. J., Chapman, M., Sanchez-Goni, M. F., Pailler, D., Lancelot, Y. (2002). The classic marine isotope substage 5e. Quaternary Research 58, 14–16.

Shackleton, N.J., Fairbanks, R.G., Chiu, T-C., Parrenin, F. (2004) Absolute calibration of the Greenland time scale: implications for Antarctic time scales and for $\Delta^{14}C$. Quaternary Science Reviews 23(14–15), 1513–22.

Siani, G., Paterne, M.,Michel, E., Sulpizio, R., Sbrana, A., Arnold, M., Haddad, G. (2001) Mediterranean sea-surface radiocarbon reservoir age changes since the last glacial maximum. Science 294, 1917–1920.

Siani, G., Sulpizio, R., Paterne, M., Sbrana, A., 2004. Tephrostratigraphy study for the last 18,000 ^{14}C years in a deep-sea sediment sequence for the South Adriatic. Quaternary Science Reviews 23, 2485–2500.

Siddall, M., Rohling, E.J., Blunier, T., Spahni, R. (2010) Patterns of millennial variability over the last 500 ka. Climate of the Past 6, 19–13.

Skinner, L.C. (2008) Revisiting the absolute calibration of the Greenland ice-core age-scales. Climate of the Past 4, 295–302.

Smith, P. E., N. M. Evensen, and D. York (2000) Under the volcano: A new dimension in Ar–Ar dating of volcanic ash, Geophysical Research Letters 27, 585–588.

Smith, P.E., York, D., Chen, Y., Evensen, N.M. (1996) Single crystal ^{40}Ar–^{39}Ar dating of a late Quaternary paroxysm on Kos, Greece: concordance of terrestrial and marine ages. Geophysical Research Letters 23 (21), 3047–3050.

Smith, V.C., Isaia, R., Pearce, N.J.C. (2011) Tephrostratigraphy and glass compositions of post-15 kyr Campi Flegrei eruptions: implications for eruption history and chronostratigraphic markers. Quaternary Science Reviews 30 (25–26), 3638–3660.

Snoeckx, H., F. Grousset, M. Revel, and A. Boelaert (1999) European contribution of ice-rafted sand to Heinrich layers H3 and H4. Marine Geology, 158, 197–208.

Snyder, C.W. (2010) The value of paleoclimate research in our changing climate. Climatic Change, 100, 407–418.

Sparks, R.S.J., Bursik, M.I., Carey, S.N., Gilbert, J.S., Glaze, L.S., Sigurdsson, H., Woods, A.W. (1997) Volcanic Plumes. Wiley, Chichester, 1–590.

Spötl, C., Mangini, A. (2006) U/Th age constraints on the absence of ice in the central Inn Valley (eastern Alps, Austria) during Marine Isotope Stages 5c to 5a. Quaternary Research 66, 167–175.

Spray, J.G. and Rae, D.A. (1995) Quantitative electron-microprobe analysis of alkali silicate glasses: a review and user guide. Canadian Mineralogist, 33(2), pp. 323–332.

St. Seymour, K., Christanis, K., Bouzinos, A., Papazisimou, S., Papetheodorou, G., Moran, E., Dénès, G. (2004) Tephrostratigraphy and tephrochronology in the Philippi peat basin, Macedonia, Northern Hellas (Greece). Quaternary International 121, 53–65.

Standford, J.D., Rohling, E.J., Bacon, S., Roberts, A.P., Grousset, F.E., Bolshaw, M. (2011) A new concept for the paleoceangraphic evolution of Heinrich event 1 in the North Atlantic. 30, 1047–1066.

Sterba, J.H., Steinhauser, G., Bichler, M. (2006) Application of NAA to develop a chemostratigraphy of volcanic deposits on Nisyros and Telos, Greece. Czech J. Phys. 56, D283–D289.

Stevenson, J.A., Loughlin, S., Rae, C., Thordarson, T., Milodowski, A.E., Gilbert, J.S., Harangi, S., Lukács, R., Højgaard, B., Árting, U., Pyne-O'Donnell, S., MacLeod, A., Whitney, B., Cassidy, M. (2012) Distal deposition of tephra from the Eyjafjallajökull 2010 summit eruption Journal of Geophysical Research 117, B00C10.

Stokes, S., Lowe, D.J. (1988) Discriminant function analysis of late Quaternary tephras from five volcanoes in New Zealand using glass shard major element chemistry. Quaternary Research 30, 270–283.

Stuiver, M., Grootes, P.M. (2000). GISP2 oxygen isotope ratios. Quaternary Research 53, 277–284.

Sulpizio, R., Zanchetta, G., D'Orazio, M., Vogel, H., Wagner, B. (2010) Tephrostratigraphy and tephrochronology of lakes Ohrid and Prespa, Balkans. Biogeosciences Discussions 7, 3931–3967.

Sulpizio, R., Zanchetta, G., Paterne, M., Siani, G. (2003) A review of tephrostratigraphy in central and southern Italy during the last 65 ka. Il Quaternario 16, 91–108.

Svensson, A., Andersen, K. K., Bigler, M., Clausen, H. B., Dahl-Jensen, D., Davies, S. M., Johnsen, S. J., Muscheler, R., Rasmussen, S. O., Röthlisberger, R., Steffensen, J. P. and Vinther, B. M. (2006) The Greenland Ice Core Chronology 2005, 15-42 ka. Part 2: Comparison to other records. Quaternary Science Reviews 25, Shackleton special issue 24.

Svensson, A., Andersen, K.K., Bigler, M., Clausen, H.B., Dahl-Jensen, D., Davies, S.M., Johnsen, S.J., Muscheler, R., Parrenin, F., Rasmussen, S.O., Röthlisberger, R., Seierstad, I.K., Steffensen, J.P., Vinther, B.M., (2008) A 60 000 year Greenland stratigraphic ice core chronology. Climate of the Past 4, 47-57.

Tamburrino, S., Insinga, D.D., Sprovieri, M., Petrosino, P & Tiepolo, M. (2012) Major and trace element characterization of tephra layers offshore Pantelleria Island: insights into the last 200 ka of volcanic activity and contribution to the Mediterranean tephrochronology. Journal of Quaternary Science 27(2), 129–140.

Telford, R.J., Heegaard, E., Birks, H.J.B. (2012) All age–depth models are wrong: but how badly? Quaternary Science Reviews 23, 1–5.

Thorarinsson, S. (1944) Tefrokronologiska studier pa Island; Thjorsardalur och dess foeoedelse; Tephrochronological studies in Iceland. Geografiska Annaler 31, 1–217.

Thorarinsson, S. (1967) The eruptions of Hekla in historical times. A tephrochronological study. The eruption of Hekla 1947-48. 1, 1-170.

Thordarson, T., Larsen, G. (2007) Volcanism in Iceland in historical time: Volcano types, eruption styles and eruptive history. Journal of Geodynamics 43(1), 118-152

Thornalley, D.J.R., McCave, I.N., Elderfield, H. (2011) Tephra in deglacial ocean sediments south of Iceland: Stratigraphy, geochemistry and oceanic reservoir ages. Journal of Quaternary Science 26(2), 190–198.

Thouveny, N., Moreno, E., Delanghe, D., Candon, L., Lancelot, Y., Shackleton, N.J. (2000) Rock magnetic detection of distal ice-rafted debries: clue for the identification of Heinrich layers on the Portuguese margin. Earth and Planetary Science Letters 180, 61–75.

Tomlinson, E.L., Arienzo, I., Civetta, L., Wulf, S., Smith, V.C., Hardiman, M., Lane, C.S., Carandente, A., Giovanni, O., Rosi, M., Muller, W., Thirlwall, M., Menzies, M.A. (2012a) Geochemistry of the Phlegraean Fields (Italy) proximal sources for major Mediterranean tephras: Implications for the dispersal of Plinian & co-ignimbritic components of explosive eruptions. Geochimica et Cosmochimica acta 93, 102–128.

Tomlinson, E.L., Kinvig, H.S., Smith, V.C., Blundy, J.D., Gottsmann, J., Müller, W., Menzie, M.A. (2012b) The Upper and Lower Nisyros Pumices: Revisions to the Mediterranean tephrostratigraphic record based on micron-beam glass geochemistry. Journal of Volcanology and Geothermal Research 243–244, 69–80.

Tomlinson, E.L., Thordarson, T., Muller, W., Thirlwall, M. & Menzies, M.A. (2010) Microanalysis of tephra by LA-ICP-MS - Strategies, advantages and limitations assessed using the Thorsmork ignimbrite (Southern Iceland). Chemical Geology 279 (3–4), 73–89.

Ton-That, T., Singer, B., Paterne, M. (2001) $^{40}Ar/^{39}Ar$ dating of latest Pleistocene (41 ka) marine tephra in the Mediterranean Sea: implications for global climate records. Earth and Planetary Science Letters 184, 645–658.

Turner, J. & Greig, R.A. (1975) Some Holocene pollen diagrams from Greece. Review of Palaeobotany and Palynology 20, 171–204.

Turney, C.S.M. (1998) Extraction of rhyolitic component of Vedde microtephra from minerogenic lake sediments. Journal of Paleolimnology 19 (2), 199–206.

Turney, C.S.M., Fifield, L. K., Hogg, A.G., Palmer, J.G., Hughen, K., Baille, M.G.L., Galbraith, R., Ogden, D., Lorrey, A., Tims, S.G., Jones, R.T. (2010) The potential of New Zealand kauri (Agathis australis) for testing the synchronicity of abrupt climate change during the Last Glacial Interval (60,000–11,700 years ago) Quaternary Science Reviews 29, 3677–3682.

Turney, C.S.M., Harkness, D.D., Lowe, J.J. (1997) The use of microtephra horizons to correlate Late-glacial lake sediment successions in Scotland. Journal of Quaternary Science 12 (6), 525–531.

Turney, C.S.M., Lowe, J.J., Davies, S.M., Hall, V.A., Lowe, D.J., Wastegård, S., Hoek, W.Z., Alloway, B.V. (2004) Tephrochronology of Last Termination sequences in Europe: a protocol for improved analytical precision and robust correlation procedures (a joint SCOTAV–INTIMATE proposal). Journal of Quaternary Science 19, 111–120.

Turney, C.S.M., van den Burg, K., Wastegard, S., Davies, S.M., Whitehouse, N.J., Pilcher, J.R., Callaghan, C. (2006) North European last glacial-interglacial transition (LGIT; 15-9 ka) tephrochronology: Extended limits and new events. Journal of Quaternary Science 21(4), 335-345

Twyman, R.M. (2007) K/Ar AND Ar/Ar DATING. In: Elias (Ed) Encyclopedia of Quaternary Science. Elsevier.

Tzedakis, P.C. (1999) The last climatic cycle at Kopais, Central Greece. Journal of the Geological Society, London 156, 425–434.

Tzedakis, P.C. (2009) Cenozoic climate and vegetation change, in J.C. Woodward (ed.), The Physical Geography of the Mediterranean. Oxford University Press, Oxford, 89–137.

Tzedakis, P.C., Andrieu, V., Birks, H.J.B., de Beaulieu, J.-L., Crowhurst, S., Follieri, M., Hooghiemstra, H., Magri, D., Reille, M., Sadori, L., Shackleton, N.J., Wijmstra, T.A. (2001) Establishing a terrestrial chronological framework as a basis for biostratigraphical comparisons. Quaternary Science Reviews 20, 1583–1592.

Tzedakis, P.C., Frogley, M.R., Lawson, I.T., Preece, R.C., Cacho, I., de Abreu, L. (2004) Ecological thresholds and patterns of millennial-scale climate variability: the response of vegetation in Greece during the last glacial period. Geology 32, 109–112.

Tzedakis, P.C., Hooghiemstra, H., Pälike, H. (2006) The last 1.35 million years at Tenaghi Philippon: revised chronostratigraphy and long-term vegetation trends. Quaternary Science Reviews 25, 3416–3430.

Tzedakis, P.C., Lawson, I.T., Frogley, M.R., Hewitt, G.M., Preece, R.C. (2002) Buffered Tree Population Changes in a Quaternary Refugium: Evolutionary Implications. Science 297, 2044–2047.

Tzedakis, P.C., McManus, P.C., Hooghiemstra, H., Oppo, D.W., Wijmstra, T.A. (2003) Comparison of changes in vegetation in northeast Greece with records of climate variability on orbital and suborbital frequencies over the last 450,000 years. Earth and Planetary Science Letters 212, 197–212.

Valero-Garcés, B., González-Sampériz, P., Morellón, M., Rico, M., Moreno, A., Navas, A., Machín, J., Mata, M.P., Rubio, J.C. (2007) Climate and Tectonics for the last 100 kyrs in the Iberian Range (NE Spain) based on the Villarquemado Lacustrine Record. Fourth International Limnogeology Congress, Barcelona, Spain.

Valle, M., Rivas, M.R., Lucini, M., Ortiz, J.E., Torres, T. (2003) Interpretación paleoecológica y paleoclimática del tramo superior de la turbera de Padul (Granada, España) a partir de datos palinológicos. Polen 13, 85–95.

van den Bogaard, C., Dörfler, W., Glos, R., Nadeau, M.-J., Grootes, P.M.,Erlenkeuser, H. (2002) Two tephra layers bracketing late Holocene paleoecological changes in northern Germany. Quaternary Research 57, 314–324.

van den Bogaard, P., Schmincke, H.U. (1985) Laacher See Tephra; a widespread isochronous late Quaternary tephra layer in Central and Northern Europe. Bulletin of the Geological Society of America 96(12), 1554-1571.

van der Wiel, A.M., Wijmstra, T.A. (1987) Palynology of the lower part (78-120 m) of the core Tenaghi Philippon II, middle Pleistocene of Macedonia, Greece. Review of Palaeobotany and Palynology 52, 73–88.

Van Kreveld, S. A., Knappertsbusch, M., Ottens, J., Ganssen, G. M., Hinte, J. (1996) Biogenic carbonate and ice-rafted debris (Heinrich layer) accumulation in deep-sea sediments from a Northeast Atlantic piston core. Marine Geology 131, 21–46.

van Kreveld, S. M., Sarnthein, H., Erlenkeuser, P., Grootes, S., Jung, M. J., Nadeau, A., Pflaumann, U. and Voelker, A. (2000), Potential links between surging ice sheets, circulation changes, and the Dansgaard-Oeschger cycles in the Irminger Sea, 60–18 kyr, Paleoceanography, 15(4), 425–442.

Vandergoes M.J., Newnham R.M., Preusser F., Hendy C.H., Lowell T.V., Fitzsimons S.J., Hogg A.G., Kasper H.U., Schluchter C. (2005) Regional insolation forcing of late Quaternary climate change in the Southern Hemisphere. Nature, 436, 242–245.

Veres. D., Davies, S.M., Wohlfarth, B., Preusser, F., Wastegård, S., Ampel, L., Hormes, A., Possnert, G., Raynal, J., Vernet, G. (2008) Age, origin and significance of a new middle MIS 3 tephra horizon identified within a long-core sequence from Les Echets, France. Boreas 37, 434-443.

Vidal, L., Labeyrie, L., Cortijo, E., Arnold, M., Duplessy, J.C., Michel, E., Becque, S., van Weering, T.C.E. (1997) Evidence for changes in the North Atlantic deep water linked to meltwater surges during the Heinrich events. Earth and Planetary Science Letters 146, 13–27.

Vinci, A. (1985) Distribution and chemical composition of tephra layers from Eastern Mediterranean abyssal sediments. Marine Geology 64, 143–155.

Vinci, A. (1987) The 'Cape Riva tephra layer' Y-2 (Santorini volcano) in deep-sea sediments from Eastern Mediterranean Sea. Bolletino di Oceanologia teorica ed applicata 5, 117–123.

Voelker, A. H. L. (2002) Global distribution of centennial-scale records for marine isotope stage (MIS) 3: A database, Quaternary Science Reviews 21(10), 1185–1212.

Vogel H, Zanchetta G, Sulpizio R, Wagner B, Nowaczyk N (2010) A tephrostratigraphic record for the last glacial–interglacial cycle from Lake Ohrid, Albania and Macedonia. Journal of Quaternary Science 25(3), 320–338.

Von Grafenstein, U., Erlenkeuser, H., Müller, J., Jouzel, J., Jognsen, S. (1998) The cold event 8200 years ago documented in oxygen isotope records of precipitation in Europe and Greenland. Climate Dynamics 14, 73–81.

von Post, L. (1916) Om skogsträdspollen i sydsvenska torfmosse-lagerföljder (föredragsreferat). Geologiska Föreningens i Stockholm Förhandlingar 38, 384–394.

von Post, L. (1918) Skogsträdpollen i sydsvenska torvmosselagerföljder. Det 16 bog deposits, translation by Davis M.B. & Fægri, K. (1967) Pollen et spores 9, 375-401.

Wagner, B., Sulpizio, R., Zanchetta, G., Wulf, S., Wessels, M., and Daut, G. (2008) The last 40 ky tephrostratigraphic record of Lake Ohrid, Albania and Macedonia: a very distal archive for ash dispersal from Italian volcanoes. Journal of Volcanology and Geothermal Research 177, 71–80.

Walker, M.J.C., Björck, S., Lowe, J.J., Cwynar, L., Johnsen, S., Knudsen, K.-L., Wohlfarth, B., INTIMATE group (1999) Isotopic 'events' in the GRIP ice core: a stratotype for the Late Pleistocene. Quaternary Science Reviews 18, 1143–1150.

Wastegård, S., Rasmussen, T.L., Kuijpers, A., Nielsen, T., van Weering, T.C.E. (2006) Composition and origin of ash zones from Marine Isotope Stages 3 and 2 in the North Atlantic. Quaternary Science Reviews 25, 2409–2419.

Watts, W.A., Allen, J.R.M., Huntley, B. (1996) Vegetation history and palaeoclimate of the last glacial period at Lago Grande di Monticchio, southern Italy. Quaternary Science Reviews 15, 133–153.

Weninger, B., Jöris, O. (2008) A ^{14}C age calibration curve for the last 60 ka: the Greenland-Hulu U/Th timescale and its impact on understanding the Middle to Upper Paleolithic transition in Western Eurasia. Journal of Human Evolution 55, 772–781.

Wijmstra, T.A. (1969) Palynology of the first 30m of a 120m deep section in northern Greece. Acta Botanica Neerlandica 18, 511–527.

Wijmstra, T.A., Smit, A. (1976) Palynology of the middle part (30–78 m) of the 120m deep section in northern Greece (Macedonia). Acta Botanica Neerlandica 25, 297–312.

Woda, C., Mangini, A., Wagner, G.A. (2001) ESR dating of xenolithic quartz in volcanic rocks. Quaternary Science Reviews 20, 993–998.

Wohlfarth, B., Veres, D., Ampel, L., Lacourse, T., Blaauw, M., Preusser, F., Andrieu- Ponel, V., Kéravis, D., Lallier-Vergés, E., Björck, S., Davies, S., de Beaulieu, J.-L., Risberg, J., Hormes, A., Kasper, H.U., Possnert, G., Reille, M., Thouveny, N., Zander, A. (2008) Rapid ecosystem response to abrupt climate changes during the last glacial period in western Europe 40–16 ka. Geology 36, 407–410.

WoldeGabriel, G., Hart, W.K., Katoh, S., Beyene, Y., Suwa, G. (2005) Correlation of Plio-Pleistocene tephra in Ethiopian and Kenyan rift basins: temporal calibration of geological features and hominid fossil records. Journal of Volcanology and Geothermal Research 147, 81–108.

Wolff, E.W., Chappellaz, J., Blunier, T., Rasmussen, S.O., Svensson, A. (2010) Millenial-scale variability during the last glacial: the ice core record. Quaternary Science Reviews 29, 21–22, 2828–2838.

Wulf, S., Brauer, A., Mingram, J., Zolitschka, B., Negendank, J.F.W. (2007) Distal tephras in the sediments of Monticchio maar lakes. In: Principe, C. (Ed.), Geologia del Monte Vulture. Bollettino della Società Geologica Italiana, 105–122.

Wulf, S., Kraml, M., Brauer, A., Keller, J., Negendank, J.F.W. (2004) Tephrochronology of the 100 ka lacustrine sediment record of Lago Grande di Monticchio (southern Italy). Quaternary International 122, 7–30.

Wulf, S., Kraml, M., Keller, J. (2008) Towards a detailed distal tephrostratigraphy in the Central Mediterranean: The Last 20,000 yrs record of Lago Grande di Monticchio. Journal of Volcanology and Geothermal Research 177, 118–132.

Wulf, S., Kraml, M., Kuhn, T., Schwarz, M., Inthorn, M., Keller, J., Kuşçu, I., Halbach, P. (2002) Marine tephra from the Cape Riva eruption (22 ka) of Santorini in the Sea of Marmara. Marine Geology 183, 131–141.

Wunsch, C. (2006) Abrupt climate change: an alternative view. Quaternary Research 65, 191–203.

Yeloff, D., Bennett, K. D., Blaauw, M., Mauquoy, D., Sillasoo, Ü., van der Plicht, J., van Geel, B. (2006) High precision ^{14}C dating of Holocene peat deposits: A comparison of Bayesian calibration and wiggle-matching approaches. Quaternary Geochronology 1, 222-235.

Zanchetta, G., Sulpizio, R., Giaccio, R., Siani, G., Paterne, M., Wulf, S., D'Orazio, M. (2008) The Y-3 tephra: a stratigraphic marker for the Last Glacial successions of the Central Mediterranean Basin. Journal of Volcanology and Geothermal Research 177, 145–154.

Zielinski, G.A., Mayewski, P.A., Meeker, L.D., Whitlow, S.I. & Twickler, M.S. (1996) A 110 000 year record of explosive volcanism from the GISP2 (Greenland) ice core. Quaternary Research 45, 109–118.

Zöller, L., Streme, H.E., Wagner, G.A. (1988) Löss-Paläoboden-Sequenzen von Nieder-, Mittel- und Oberrhein. Chemical Geology, 73, 39–62.